Design and Manufacture of Molded Micro Products Using Concurrent Engineering

Marhöfer, David Maximilian

Publication date:
2016

Document Version
Publisher's PDF, also known as Version of record

Ph.D. Thesis

Design and Manufacture of Molded Micro Products Using Concurrent Engineering

Maximilian Marhöfer

2016

Technical University of Denmark

"*Wissenschaft wird von Menschen gemacht.*"

—Werner Karl Heisenberg,
German physicist and Nobel laureate

Preface

The present thesis was composed as one of the requirements of the Ph.D. degree at the Technical University of Denmark, Kongens Lyngby, Denmark. The related work has been carried out from February 2013 to January 2016 at the Technical University of Denmark (DTU), Kongens Lyngby, Denmark, at the Department of Mechanical Engineering (MEK) under the supervision of Assoc. Prof. Guido Tosello, senior researcher Aminul Islam, and Prof. Hans Nørgaard Hansen.

From October to December 2014, three months were spent at the Karlsruhe Institute of Technology (KIT), Eggenstein-Leopoldshafen, Germany, at the Institute for Applied Materials (IAM) under the supervision of Volker Piotter, Klaus Plewa, and Prof. Thomas Hanemann.

I would like to express my gratitude to all my supervisors for their inspiration and contribution to my work. Particularly, I would like to very much appreciate my main supervisor Guido Tosello for his inspiring consultations, fabulous collaboration, and highly valuable contribution to my work. Furthermore, I would like to thank Guido Tosello and Prof. Hans Nørgaard Hansen for providing me the possibility to accomplish my Ph.D. project at the Technical University of Denmark.

The team of the Karlsruhe Institute of Technology is thanked for the opportunity of the research stay, for the excellent hospitality, and the considerable contribution to my work regarding the material characterization and powder injection molding experiments.

This work was funded by the Technical University of Denmark which is greatly acknowledged. Financial aid by the project "Hi-MICRO" (High Precision Micro Production Technologies) supported by the European Commission in the 7th Framework Programme (Grant agreement no: 314055) for my Ph.D. project in general and by the KNMF (Karlsruhe Nano Micro Facility) for my external research stay in Karlsruhe is also gratefully acknowledged.

Kongens Lyngby
January 2016

Maximilian Marhöfer

Abstract (English)

The matter of this thesis is the design and manufacture of micro parts made by micro and powder injection molding. Multiple aspects of the design process towards the final micro component were investigated with the aim of establishing the optimal micro part and mold design in a holistic design approach. The focus was on simulation-aided design for manufacture and assembly.

First, the state-of-the-art of injection molding technology and of process simulations in the area of micro injection molding is presented in the theoretical part of this thesis as foundation for the following issues. Furthermore, the mathematical background of injection molding simulations is outlined.

In correspondence to the holistic design procedure, the experimental part of the thesis commences with the discussion of the conducted comprehensive material characterization of several feedstocks. The characterization contained mainly the thermal and rheological material properties and led to a material model enabling process simulations of powder injection molding.

Subsequently, the process simulations of polymer micro injection molding were evaluated regarding the comprehensiveness of the model and the experimental validation. The simulation-assisted approach was applied in the design for manufacture and assembly of a microfluidic plastic part and its feed system in the early product development phase and in absence of the mold. In two design iterations based on the design of experiment approach, the most suitable material and gate concept were selected, and the part quality was successfully optimized, so that the part complied with the requirement of a maximum flatness of 10 µm by implementing a 900 µm wide pin gate.

Process simulations were also utilized for the design optimization of the actual component and the mold of a second microfluidic device. The concurrent investigations covered the whole development from the first concept to the manufactured mold. Hence, the material selection and testing, the iterative simulation-aided optimization of the gating conception, and the implementation of the mold are presented. The examination on the gate design resulted in the realization of a film gate with 560 µm thickness minimizing the risk of degradation due to excessive shear and the best packing performance. The molded parts of the two aforementioned micro components were moreover employed in additional simulation validations.

Similar to the polymer injection molding, the powder injection molding in this thesis starts with the simulation validation. The established material models of the characterized feedstocks were used for a comparison between simulations and experiments to assess the applicability of simulations in powder molding. In an additional short shot study, the impact of the melt cushion on the flow length and injection pressure could be revealed.

Afterwards, the focus was on the design optimization of the mold and cooling of a ceramic micro-mechanical component. The comprehensive analysis elaborated on different facets of the simulation model and their influence on the simulation outcome regarding part quality. The process simulations were proven as valuable tool for the part, mold, and cooling optimization.

Keywords: design for manufacture and assembly, micro injection molding, powder injection molding, process simulation.

Resumé (Danish)

Dette Ph.D. projekt behandler designet og fremstillingen af mikrodele produceret ved hjælp af mikro- og pulversprøjtestøbning. Flere aspekter af designprocessen mod den endelige mikrokomponent blev undersøgt med formålet at etablere den optimal design i en holistisk tilgang. Der var fokus på design understøttet af simuleringer i udsigten til fremstilling og montage.

Den nyeste udvikling af sprøjtestøbeteknologi og processimuleringerne inden for mikrosprøjtestøbning er først præsenteret i den teoretiske del af denne afhandling som fundament for nedenstående problemer. Ydermere er den matematiske baggrund af simulationerne af sprøjtestøbning skitseret.

I overensstemmelse med den holistisk designprocedure begynder den eksperimentelle del af afhandlingen med diskussionen af den gennemførte omfattende karakterisering af flere pulverfeedstocks. Karakteriseringen indeholder primært de termisk og reologisk materialeegenskaber og førte til en materiale model som muliggjorde processimuleringer af pulversprøjtestøbning.

Efterfølgende blev processimulationerne af polymer mikrosprøjtestøbning evalueret med hensyn til omfanget af modellering og til eksperimentel validering. Fremgangsmåden med assistancen gennem processimulationer blev anvendt i fremstillings- og samlingsorienteret design af en mikrofluidisk plastdel i den tidlige produktudviklingsfase og fravær af støbeformen. I to design iterationer som var baseret på design af eksperimenter tilgang blev det mest egnede materiale og indløbkoncept valgt og den del kvalitet blev optimeret. Delen overholdt kravet om en maksimal fladhed på 10 µm ved at gennemføre en 900 µm stor stift indløb.

Processimuleringerne blev også anvendt til designoptimeringen af komponenten og formen af en anden microfluidisk enhed. De samtidige undersøgelser dækkede hele udviklingen fra den første designidé til den fremstillede form. Det forbundene materialevalg og afprøvning, den iterative designoptimering af indløbkonceptet gennem simuleringer, og realiseringen af støbeformen er præsenteret. Undersøgelsen af indløbdesignet resulterede i realiseringen af en filmindløb med 560 µm tykkelse hvilket minimerede risikoen for nedbrydning på grund af høj forskydning og viste den bedste eftertrykopførsel. Den støbte dele af de to ovennævnte komponenter var benyttet i yderligere valideringer af mikrosprøjtestøbnings simuleringen.

I lighed med polymersprøjtestøbning begynder pulversprøjtestøbning i denne afhandling med validering af simuleringen. Den etablerede materialemodeller af den karakteriserede feedstocks blev anvendt til en sammenligning mellem simuleringer og eksperimenter for at vurdere anvendeligheden af simulationer inden for pulverstøbningen. I en yderligere undersøgelse om indsprøjtning kunne virkningen af puden på flydelænge og indsprøjtningstryk blive afsløret.

Bagefter var fokus på designoptimeringen af støbeformen og af kølingen af et keramisk mikromekanisk element. Den omfattende analyse uddyber forskellige facetter af simulationsmodellen og deres indflydelsen på simulerings resultater angående kvalitet af plastdelen. Processimuleringer kunne bevises som et værdifuldt værktøj for optimeringen af delen, formen, og af kølingen.

Nøgleordene: fremstilling- og montageorienteret design, mikrosprøjtestøbning, pulversprøjtestøbning, processimuleringer.

Zusammenfassung (German)

Die vorliegende Arbeit behandelt den Entwurf und die Herstellung von Mikrokunststoffkomponenten, die mit Hilfe von Mikro- und Pulverspritzguss gefertigt werden. Verschiedene Aspekte des Entwicklungsprozesses hin zum fertigen Produkt wurden mit dem Ziel eines optimierten Designs von Bauteil und Werkzeug als Ergebnis eines gesamtheitlichen Ansatzes untersucht. Der Schwerpunkt lag beim simulationsgestützen fertigungs- und montageorientierten Produktentwurf.

Zunächst werden die Grundlagen für die vorliegende Arbeit gelegt, indem eine Einführung in die Spritzgusstechnologie und eine Diskussion zum Entwicklungsstand der Prozesssimulationen im Bereich Mikrospritzguss erfolgt. Des Weiteren wird der mathematische Hintergrund der Simulationen angeschnitten.

Auf Grund des gesamtheitlichen Ansatzes wird der experimentelle Teil der Arbeit mit der durchgeführten, umfassenden Werkstoffcharakterisierung mehrerer Pulverfeedstocks eingeleitet. Die Charakterisierung beinhaltete unter anderem die Bestimmung der thermischen und rheologischen Materialeigenschaften und führte zu einem Materialmodell für die Prozesssimulation des Pulverspritzgusses.

Danach erfolgte die Untersuchung der Leistungsfähigkeit und Validierung der Mikrospritzgusssimulationen von Kunststoffen. Anschließend wurde der Simulationsansatz im Rahmen des Entwurf eines Mikrobauteils in der frühen Phase der Produktentwicklung zur Optimierung des Bauteils und Angusssystems eingesetzt. In zwei Iterationen auf Basis statistischer Versuchsplanung konnte sowohl ein geeigneter Werkstoff und Anschnittkonzept ausgewählt wie auch die Bauteilqualität erfolgreich optimiert werden. Der geforderte Maximalwert der Ebenheit von 10 µm wurde durch die Realisierung eines 900 µm großen Punktangusses erreicht.

Die Prozesssimulationen fanden ebenfalls Anwendung beim Entwurf des eigentlichen Bauteils und des Werkzeugs eines mikrofluidischen Chips. Die Betrachung umfasste die komplette Entwicklung vom ersten Entwurf bis zum fertigen Werkzeug. Die damit einhergehenden Werkstoffauswahl und Materialtests, die iterative Optimierung des Angusssytems und die Ausarbeitung des Werkzeugs werden vorgestellt. Die Untersuchungen bezüglich des Angusses resultierten in der Umsetzung eines Filmanschnitts mit 560 µm Dicke, welcher die Gefahr von Degradation durch exzessive Scherraten minimierte und das beste Nachdruckverhalten zeigte. Der Spritzguss der beiden genannten Komponenten ermöglichte eine weitere Validierung der durchgeführen Simulationen.

Wie auch der Kunststoffspritzguss beginnt der Abschnitt zum Pulverspritzguss mit der Validierung. Die auf Basis der Werkstoffcharakterisierung erstellten Modelle werden beim Vergleich zwischen Simulation und Experiment eingesetzt, um die Anwendbarkeit von Prozesssimulationen beim Pulverspritzguss abzuschätzen. In einer zusätzlichen Füllstudie konnte die Auswirkung des Materialkissens auf die Fließlänge und den Einspritzdruck aufgezeigt werden.

Darauffolgend steht das Design eines keramischen mikromechanischen Bauteils im Vordergrund. Die breit angelegte Analyse behandelte diverse Gesichtspunkte des Simulationsmodells und deren Einfluss auf die vorhergesagte Ergebnisse bezüglich der Bauteilqualität. Die Eignung von Prozesssimulationen als wertvolles Hilfsmittel bei der Optimierung und Auslegung von Mikrobauteil, Werkzeug und Kühlung konnte nachgewiesen werden.

Stichwörter: Fertigungs- und montageorientiertes Design, Mikrospritzguss, Pulverspritzguss, Prozesssimulation.

Contents

Preface v

Abstract (English) vii

Resumé (Danish) ix

Zusammenfassung (German) xi

List of Figures xix

List of Tables xxix

List of Mathematical Symbols xxxiii

List of Acronyms xxxvii

1 Introduction and objective 1
- 1.1 Introduction . . . 1
- 1.2 Project definition and objectives . . . 3
- 1.3 Motivation and research questions . . . 4
- 1.4 Hi-MICRO project . . . 5
- 1.5 Structure of the thesis . . . 7

2 State-of-the-art of injection molding technology 9
- 2.1 Conventional injection molding . . . 9
- 2.2 Micro injection molding . . . 10
- 2.3 Powder injection molding . . . 13
- 2.4 Summary and conclusion . . . 16

3 Process simulations of injection and micro injection molding 17
- 3.1 Why simulate the injection molding process? . . . 17
- 3.2 Mathematical modeling background . . . 19
  - 3.2.1 Viscosity of plastics . . . 19
  - 3.2.2 Viscosity of powder feedstocks . . . 21
  - 3.2.3 Flow of plastics . . . 23
  - 3.2.4 Thermodynamics . . . 24

3.3 Simulation software . . . 25
3.3.1 Commercially available software packages . . . 25
3.3.2 Meshing strategies . . . 26
3.3.3 Mold and cooling analysis . . . 27
3.4 State-of-the-art of micro injection molding process simulations . . . 28
3.4.1 Issues of micro injection molding simulations . . . 28
3.4.2 Simulation and validation of polymer micro injection molding 29
3.4.3 Simulation and validation of micro powder injection molding . 31
3.4.4 Recommendations for micro injection molding process simulations 32
3.4.5 Systematic concept and methodology for the concurrent development of molded micro parts . . . 33
3.4.6 Software and standard settings for this work . . . 36
3.5 Summary and conclusion . . . 38

4 Materials and material characterization 41
4.1 State-of-the-art . . . 41
4.2 Necessary material properties for simulations . . . 43
4.3 Powder feedstocks used and characterized in this work . . . 44
4.4 Molding of disc samples for measurements of density and thermal properties . . . 46
4.5 Powder content determination . . . 46
4.5.1 Measurement methods . . . 46
4.5.2 Results and discussion . . . 47
4.6 Density measurements . . . 48
4.7 Measurements of the specific heat capacity . . . 49
4.8 Measurements of the thermal conductivity . . . 50
4.8.1 Measurement method . . . 50
4.8.2 Theoretical determination . . . 53
4.8.3 Results and discussion . . . 53
4.9 Theoretical background of rheological and thermodynamic measurements 57
4.9.1 Rheometers . . . 57
4.9.2 Fitting method . . . 58
4.9.3 Mathematical corrections . . . 59
4.10 Viscosity measurements . . . 60
4.10.1 Measurement method . . . 60
4.10.2 Results and discussion . . . 61
4.11 Measurements of pvT data . . . 62
4.11.1 Measurement method . . . 62
4.11.2 Results and discussion . . . 65
4.11.3 Material compressibility . . . 71
4.12 Summary and conclusion . . . 72

5 Validation of polymer micro injection molding simulations 75
5.1 Study case . . . 75

5.2 Molding . . . 76
5.3 Simulation . . . 78
5.3.1 Models . . . 78
5.3.2 Venting . . . 79
5.3.3 Meshing . . . 80
5.3.4 Simulation settings . . . 83
5.4 Results and discussion . . . 84
5.5 Summary and conclusion . . . 86

6 Simulation-aided part design 89
6.1 Study case . . . 89
6.1.1 Component . . . 89
6.1.2 Material selection . . . 90
6.1.3 Initial gate designs . . . 91
6.2 First design iteration . . . 94
6.2.1 Introduction . . . 94
6.2.2 Design of experiments . . . 94
6.2.3 Simulation set up . . . 96
6.2.4 Flow front comparison . . . 99
6.2.5 Filling analysis . . . 103
6.2.6 Warpage analysis . . . 106
6.3 Second design iteration . . . 110
6.3.1 General simulation set up . . . 110
6.3.2 Design of experiments for filling and packing analysis . . . 112
6.3.3 Filling and packing analysis . . . 113
6.3.4 Design of experiments for warpage analysis . . . 117
6.3.5 Warpage analysis . . . 119
6.3.6 Mold . . . 123
6.4 Simulation validation . . . 124
6.4.1 Molding and sample preparation . . . 124
6.4.2 Simulation set up . . . 124
6.4.3 Results and discussion . . . 125
6.5 Summary and conclusion . . . 128

7 Complete part and mold design and manufacture 131
7.1 Study case . . . 131
7.2 Material selection . . . 133
7.3 Material testing . . . 135
7.3.1 Purpose . . . 135
7.3.2 Sample preparation . . . 135
7.3.3 Tensile testing . . . 137
7.3.4 Data processing . . . 137
7.3.5 Results and discussion . . . 140
7.4 Design of press-fit connections . . . 141

7.5 Mold design and gate optimization—pin gates . . . 144
7.5.1 Gate properties . . . 144
7.5.2 Simulation set up . . . 144
7.5.3 Settings for gating location analysis . . . 145
7.5.4 Results and discussion of gating location analysis . . . 146
7.5.5 Settings for pin gate analysis . . . 147
7.5.6 Results and discussion of pin gate analysis . . . 148
7.6 Mold design and gate optimization—film gates . . . 153
7.6.1 Gate design considerations . . . 153
7.6.2 Feed system design . . . 154
7.6.3 Simulation set up . . . 155
7.6.4 Results and discussion . . . 157
7.7 Mold design and manufacture . . . 162
7.7.1 Mold block . . . 162
7.7.2 Inserts . . . 162
7.8 Validation of simulations . . . 166
7.8.1 Molding and sample preparation . . . 166
7.8.2 Simulation set up . . . 167
7.8.3 Results and discussion . . . 167
7.9 Summary and conclusion . . . 171

8 Validation of powder injection molding simulations 173
8.1 Study case . . . 173
8.1.1 Part . . . 173
8.1.2 Mold . . . 174
8.2 Experiments . . . 176
8.2.1 Full shot study . . . 176
8.2.2 Short shot study with design of experiments . . . 177
8.3 Simulation set up . . . 178
8.4 Results and discussion . . . 181
8.4.1 Experimental results of full shot study . . . 181
8.4.2 Comparison of full shot study and simulations . . . 182
8.4.3 Short shot study . . . 186
8.5 Summary and conclusion . . . 191

9 Ceramic micro component design and manufacture 193
9.1 Study case . . . 193
9.1.1 Actual component . . . 193
9.1.2 Mold conception of early design stage . . . 195
9.1.3 Mold conception of late design stage . . . 195
9.2 Comparison of homogeneous and multi-scale mesh . . . 197
9.2.1 Simulation set up . . . 197
9.2.2 Results and discussion . . . 201

9.3 Influence of mold and cooling implementation . . . 204
9.3.1 Investigated simulation models . . . 204
9.3.2 Meshing . . . 205
9.3.3 Simulation settings . . . 207
9.3.4 Results and discussion . . . 209
9.4 Simulation validation of powder injection molding . . . 211
9.4.1 Molding . . . 211
9.4.2 Simulation models and meshing . . . 212
9.4.3 Simulation settings . . . 214
9.4.4 Results and discussion . . . 214
9.5 Summary and conclusion . . . 216

10 Executive summary **219**
10.1 Improved simulation strategy – entities to model . . . 219
10.2 Improved simulation strategy – implementation procedure . . . 221

11 Conclusion and outlook **229**
11.1 Conclusion . . . 229
11.2 Outlook . . . 232

Bibliography **235**

List of Publications **249**

A Supplementary information to chapter 4 **253**
A.1 Processing data of the disc samples . . . 253
A.2 DSC curves for powder content determination of feedstocks . . . 258
A.3 Viscosity and pvT fitting for Catamold® TZP-A . . . 261
A.4 Viscosity and pvT fitting for Catamold® 17-4PHA . . . 265
A.5 Viscosity and pvT fitting for GoMikro ZrO_2 . . . 270
A.6 Viscosity and pvT fitting for GoMikro 17-4PH . . . 274

B Supplementary information to chapter 5 **279**
B.1 Technical drawing of the micro channel test structure . . . 279
B.2 Averaging of speed profile of injection molding machine . . . 281
B.3 Machine geometry . . . 289

C Supplementary information to chapter 6 **291**
C.1 Main effect and interaction plots of first design iteration . . . 291
C.2 Main effect and interaction plots of second design iteration . . . 304
C.3 Pictures of instruments of the simulation validation . . . 313

D Supplementary information to chapter 7 **315**
D.1 Supplementary data to the tensile tests . . . 315
D.2 Supplementary calculations to the dimensioning of the press-fits . . . 318

D.3 Technical drawings of mold and mold components 323
D.4 Part list of the mold block 331

E Supplementary information to chapter 8 **333**
E.1 Experimental molding of KIT double spiral 333
E.2 Simulations of KIT double spiral 337

F Supplementary information to chapter 9 **341**
F.1 Molding settings of molding machine for ceramic lever 341

Acknowledgments **345**

List of Figures

1.1 Examples of micro plastic products made by micro injection molding [7]. 2
1.2 Polymer micro injection molding market share by application in 2013 [8]. 2

2.1 The different phases of the process cycle of injection molding with a conventional machine [15]. 11
2.2 Schematic of the machine concept of the micro injection molding machines "MicroPower" of Wittmann-Battenfeld with small screw for plastication and plunger for injection and the "formicaPlast®" of Klöckner DESMA Schuhmaschinen with plungers for plastication and injection. 13
2.3 Schematic of the typical process chain of powder injection molding. Optional finishing processes like polishing, plating, or grinding after sintering are not shown. The blue part (left) is usually covered by the material supplier, the pink part (right) is covered by the component manufacturer. [22] 14

3.1 Terms of the Cross viscosity model with comparison to Newtonian and power-law fluid. 20
3.2 Comparison of shear rate profile, velocity profile, and viscosity of the simple Cross-WLF viscosity model (used for plastics) and the Cross-WLF viscosity model with Herschel-Bulkley extension (used for powder feedstocks to fit the viscosity increase at low shear rates) [45]. 22
3.3 Proposed compilation for the systematic concept and its aspects for the concurrent development of molded micro parts. 34
3.4 Proposed flow diagram for the systematic methodology for the concurrent development of molded micro parts. 35

4.1 Measured values for the specific heat capacity of the investigated feedstocks and typical values for POM from BASF (from ASMI data base [100]). The measurement was directly done by a DSC analysis. The values are the average of three heating and cooling cycles at a rate of 10 °C min^{-1}, the error bars represent the standard measurement uncertainty, confidence level: 95 %. 52

4.2 Measured values for the thermal conductivity of the investigated feedstocks and typical values of pure POM from BASF (from ASMI data base [100]). The measurement was indirectly done by measuring the thermal diffusivity with a laser flash analysis. The values are the average of five measurements. The error bars represent the standard measurement uncertainty, confidence level: 95 %. 56
4.3 Schematic (left) and real device (right) of the high pressure capillary rheometer used for the material characterization of the powder feedstocks. The piston compresses the heated plastic material which flows through the orifice while the resulting pressure drop is monitored. . . 58
4.4 Example of measured raw viscosity data of the investigated feedstocks at their typical processing temperature and for a capillary ratio of $L/D = 10$. 63
4.5 Fitted viscosity curves of the investigated feedstocks at their typical processing temperature and reference curves of POM according to the Cross-WLF model and the parameters from Table 4.10. 64
4.6 Measured pvT data and fitting curves for BASF Catamold® TZP-A. . 66
4.7 Measured pvT data and fitting curves for BASF Catamold® 17-4PHA. 67
4.8 Measured pvT data and fitting curves for GoMikro ZrO_2. 68
4.9 Measured pvT data and fitting curves for GoMikro 17-4PH. 69
4.10 Normalized specific volume of the Catamold® feedstocks and the pure POM binder to illustrate the pressure dependency of the specific volume and compressibility of the materials. 71

5.1 Model and dimensions of the micro channel test structure [119]. . . . 76
5.2 Monitored speed profile versus time of the used injection molding machine for the molding of the micro channel test structure. The error bars denote the standard deviation of the data points with a maximum value of about $\pm 1.8\,\mathrm{mm\,s^{-1}}$. 77
5.3 Schematic (not true to scale) of the implementation of the venting structure for the venting analysis in ASMI. The grey areas illustrate the implemented venting channels. Their dimensions were given by the part position and the mold size. The dimensions of the venting channels are listed in Table 5.3. 80
5.4 Meshed model of the micro channel test structure. The part and gate were meshed with smaller, individual specific element edge lengths. . 82
5.5 Meshed model of the part with feed system, additional machine geometry modeled as hot runner, and pointers indicating the venting channels. The geometry resembles the actual nozzle and barrel of the machine. 83
5.6 Injection time, injection pressure, and part weight of the experiments and different simulation models of the micro channel test structure. The studies A, B, C, D, E refer to the models described in subsection 5.3.1. 84

5.7 Injection pressure versus time for experiments and the simulated models of the micro channel test structure. The error bars indicate the standard deviation of the experimentally recorded pressure with a maximum value of about ±3 MPa. 85
5.8 Comparison of the flow fronts of the different simulation models of the micro channel test structure at two positions. The shape of the flow front did not differ significantly between the studies. Color scale: fill time from 0.15 s to 0.25 s (blue to red). 87

6.1 CAD model of the microfluidic dispenser which was used as study case for the simulation-assisted part design, captured in SolidWorks®. Shown is the front part, the back looked exactly the same because of the part symmetry. 90
6.2 CAD models of the different gate configurations with the part for the microfluidic dispenser, captured in SolidWorks®. 92
6.3 Drawings of the different gate designs for the microfluidic dispenser, made in SolidWorks®. All dimensions in mm. 93
6.4 Meshed models of the proposed gate designs of the microfluidic dispenser in ASMI. 98
6.5 Meshed model of the actual part of the microfludic mixer with detailed view on some of the micro features and highlighted assigned specific element edge length. 99
6.6 Visualization of predicted flow front in the part cavity of the different gate designs of the microfluidic mixer. Color scale from red to blue: normalized filling time from 0 to 1. 100
6.7 Visualization of predicted flow front in the part cavity of the different gate designs of the microfluidic mixer. Color scale from red to blue: normalized filling time from 0 to 1. 101
6.8 Influence of the ribbing and coring out of the microfluidic dispenser on the plastic flow. The ribs act as flow restrictor, because they are thinner than the bulk part which exhibited a large thickness variation. The color index represents the fill time. 102
6.9 Design optimization at the microfluidic dispenser. It was equipped with one more rib for more uniform flow on both sides. 103
6.10 Main effect plots of the responses of the DOE investigating the influence of the gate type and position as well as the material on the process and part quality of the microfluidic dispenser. 105
6.11 Main effect and interaction plots for the examination of the influence of the gate type and position as well as the material on the warpage of the microfluidic dispenser. 107

6.12 Exemplary visualization of the z-component (along the shortest side of the part) of the warpage of the microfluidic dispenser with different gate design. Please note the different deflection range for design A. Because of the inclusion of the sprue, the color scales were adjusted to match the deflection of the part only. 108
6.13 Meshed microfluidic dispenser with feed system and indicated mesh densities in ASMI. 111
6.14 Main effect plots of the DOE analyzing the effect of the input factors "gate thickness" and "ASMI version" on the simulated process outcome of the microfluidic dispenser with pin gate. 116
6.15 Maximum shear rate during filling at the investigated pin gates of different size in ASMI 2014. The presented results are also representative for ASMI 2015, since the shear rate results of both software releases were very close. Color scales from blue to red: shear rate from $0\,s^{-1}$ to $250\,000\,s^{-1}$. 117
6.16 Definition of flatness according to ISO 1101 and as applied for the flatness measurements in the second design iteration of the microfluidic mixer [127]: the flatness of a surface is the distance between the two planes enclosing this surface. 118
6.17 Exemplary surface selection and flatness evaluation of warped microfluidic dispenser in the deployed evaluation software. The flatness was in both cases evaluated according to GD&T, ISO 1101, and ISO 12781 as the distance between the two parallel planes enclosing the investigated surface. Displayed values in mm. 119
6.18 Main effect and interaction plots of the DOE analyzing the effect of the input factors "gate size", "ASMI configuration", and "evaluation software" on the simulated flatness of the microfluidic dispenser with pin gate. 121
6.19 Comparison of z-component (along the shortest dimension of the part) of the part warpage of the microfluidic dispenser for different gate thicknesses. The view is in the direction of the gate on the face with the fluidic inlet, the gate is indicated on the left. Color scale: deflection from $-5\,\mu m$ to $5\,\mu m$. 122
6.20 Finalized mold with the machined cavity of the microfluidic dispenser with 0.90 mm large semi-circular pin gate. The design was based on the knowledge gained in the simulation-aided optimization. 123
6.21 Comparison of molded short shots and the simulated flow front pattern on global part level of the microfluidic dispenser. 126
6.22 Comparison of molded short shots and the simulated flow front pattern on local feature level of the microfluidic dispenser. 127

7.1 Schematic CAD models of the initial design of the microfluidic mixer with two chambers. The BOT was relevant for this investigation. The blue structure is the TPE used for sealing, the brownish part is the thermoplastic base. 132
7.2 2k injection molding of material samples for bonding strength tests in relation to the material selection of the microfluidic mixer. The used mold is multi-purpose, so that other cavities are integrated, but not active. 136
7.3 PP specimens being clamped in the tensile testing machine and showing necking during test and comparison between the initial and stretched PP sample. Break could not be reached, because the material elongation exceeded the machine working distance. 138
7.4 Exemplary originally monitored and filtered data of the 2k tensile test. The highlighted difference after sample break was considered for calculating the tensile strength. 139
7.5 Exemplary frequency spectrum of the FFT analysis of the measured tensile test data for a 2k specimen. 139
7.6 Results of the tensile tests of the 1k and 2k specimens. The shown values are the average of five measurements. The error bars mark the standard measurement uncertainty, confidence level: 95 %. 140
7.7 Schematic of the shaft and hub of a press-fit with the major dimensions and the resulting stresses in the material and pressure between the shaft and the hub [133]. 141
7.8 Mechanical FEM simulation of the von-Mises stress distribution in BOT for PS. The stress distribution for COC matched PS, the numerical values varied. The simulation showed that the von-Mises stresses for both materials were clearly below the yield strengths. 143
7.9 Overview and details of the meshed microfluidic mixer. The global edge length was 0.6 mm. The mesh refinement at the gate and micro features is due to the use of the chord height control. 145
7.10 Results of the gating suitability analysis. Color scale from “best” to “worst”. 147
7.11 Filling analysis of two pin e microfluidic mixer with indicated possible air entrapment because of the rib acting as flow restrictor. Color scale: fill time from 0 s to 0.11 s. 149
7.12 Weld line analysis in ASMI for the investigated pin gate configurations. The lines show the formation of weld lines where flow fronts meet at an angle of up to 135° (the default value of ASMI). Larger values were assumed to not cause any mechanically weak spots or surface notches. Critical weld lines are particularly highlighted. Color scales: weld line angle from 0° to 135°. 150

7.13 Analysis of volumetric shrinkage in ASMI for the investigated pin gate configurations. The configuration with three gates at the front was preferred, as it gave the lowest shrinkage. Color scale: average volumetric shrinkage from 0 % to 5 %. 152
7.14 Bottom part (BOT) of the microfluidic mixer with the proposed film gate, runner, and sprue. The gate thickness was varied, the feed system showed an ejection spot and a sprue puller. 153
7.15 Overview and closeup of the meshed microfluidic mixer, captured in ASMI 2015. The global edge length was 0.8 mm. The mesh refinement at the gate and micro features is due to the assignment of the highlighted local mesh densities. 156
7.16 Flow front visualization of the microfluidic mixer with film gate in ASMI 2015. Color scale from blue to red: filling time from 0 s to 0.46 s. 158
7.17 Cross-sectional view of the flow inside the cavity of the microfluidic mixer with distinct hesitation effect at the micro pillars: the filling in bulk direction is faster than in the direction of the micro pillars, i.e. the flow length a in bulk direction is larger than the flow length b in direction of the micro pillars. Color scale from blue to red: filling time from 0 s to 0.46 s. 159
7.18 Predicted shear rate at the film gates of different thickness. Only the largest gate showed acceptable shear rates. Color scales from blue to red: shear rate from 0 s^{-1} to 40 000 s^{-1} (allowed limit for COC). . . . 161
7.19 Predicted average volumetric shrinkage of BOT for different film gate thicknesses. The packing performance increases with thickness. Color scales from blue to red: shrinkage from 0 % to 4.5 %. 161
7.20 Cross-sectional view of the created prototype mold for the BOT of the microfluidic mixer. The two-plate mold consisted of Hasco standard parts and featured four interchangeable inserts for flexibility of the molded plastic parts enabling the 2k production of the BOT and TOP as well as other parts in the future. 163
7.21 CAD models of the initial mold concept with plugged insert (highlighted in yellow) clamped from the back by the back-up plate. The heating was supposed to be fully electrical. The film gate is not shown at the insert. 164
7.22 CAD models of the final, realized mold concept with inserts fixed by four screw joints and liquid heating of the cavity plates and electrical heating of the inserts. 165
7.23 EDM electrode in copper for fabricating the holes of the micro pillars and finished mold insert of the microfluidic mixer. The cavity design was machined by milling and EDM accordingly to the finalized design based on the findings in the simulations. The insert was provided with an additional venting channel. Scale in mm. 166

7.24 Comparison of molded short shots and the simulated flow front pattern on global part level of the microfluidic mixer. [a] Filling time in simulation of the best fit to the actual short shot. 169
7.25 Comparison of molded short shots and the simulated flow front pattern on local feature level of the microfluidic dispenser. [a] Filling time in simulation of the best fit to the actual short shot. 170

8.1 CAD model and real part of the test spiral being used for the powder injection molding simulations and experiments. 174
8.2 Drawing of the cavity layout of the double spiral. The mold enables to investigate the pressure and temperature evolution in the cavity with three integrated pressure sensors (pressure signals denoted as p1, p2, and p3) in one spiral and three integrated temperature sensors (not used) in the other spiral. All values in mm. 175
8.3 Stationary half of the double spiral test mold with pressure and temperature sensors (not visible) and their connections (cables on the right) used for the powder injection molding experiments. 175
8.4 Meshed double spiral with sprue and defined injection location, captured in ASMI. 178
8.5 Comparison of the true and constant speed profile used for the simulation of the double spiral in ASMI. The curves are exemplary shown for Catamold® TZP-A. 180
8.6 Comparison of the molded spirals for all four used feedstocks. Shown scale in cm. 182
8.7 Comparison of the predicted injection pressure over time for the two implemented simulation with the implemented constant and true speed and the experimental results for Catamold® 17-4PHA. 183
8.8 Injection pressure over time of the experiments and simulations with three different feedstocks. The plot contains the pressure signals from the pressure sensors (p1, p2, p3) and the machine (pM). 185
8.9 Graphs of the results of the short shot DOE with GoMikro ZrO_2. . . 187
8.10 Overview of the different short shot studies with varying stroke length at an injection speed of $v = 30\,\mathrm{mm\,s^{-1}}$. Scale in cm. 189
8.11 Overview of the different short shot studies with varying stroke length at an injection speed of $v = 40\,\mathrm{mm\,s^{-1}}$. Scale in cm. 190
8.12 Normalized specific volume versus pressure of the Catamold® feedstocks and the pure POM binder to illustrate the pressure dependency of the specific volume and the compressibility of the materials. 191

9.1 Drawing and CAD model of the ceramic lever for a micro-mechanical system [141]. All dimensions in mm. 194
9.2 Mold conception for the ceramic lever with two inserts, integrated cooling channels, and actual part in the early design stage. 196

9.3 Mold conception for the ceramic lever in the later design stage. The gating of the part was changed, and the part cavity was incorporated in a single insert in the movable half of the mold. 198
9.4 Realized mold (movable half) with mounted insert made by SLS. . . . 199
9.5 Comparison between homogeneous and multi-scale mesh applied to the micro-mechanical lever. The homogeneous mesh was created with 500 µm mesh size, the multi-scale mesh comprised mesh sizes in the range from 40 µm to 500 µm. The part (magenta), one of the cooling channels (yellow or beige), and partially the insert (blue) are shown. . 200
9.6 Comparison between the coolant flow and velocity inside the cooling channels of the planned insert for the homogeneous and multi-scale mesh of the ceramic lever. Color scale from blue to red: velocity from $0\,\mathrm{m\,s^{-1}}$ to $1.3\,\mathrm{m\,s^{-1}}$. 203
9.7 Comparison between the total warpage (sum of x, y, and z-component of deflection) of the ceramic lever for the homogeneous and multi-scale mesh. The original shape of the part is indicated and the deflection is scaled by a factor ten. Color scale from blue to red: deflection from 14 µm to 121 µm. 203
9.8 Meshed micro-mechanical ceramic lever with feed system (sprue is not shown completely), detailed views on micro features, and indicated mesh densities in ASMI. 206
9.9 Meshed mold block with insert, part, and cooling channels of the SC model of the ceramic lever. The mold plate of the stationary half is not shown, the cooling inlet and outlet are indicated. 206
9.10 Meshed cooling channels and part and indicated insert of the CC model of the ceramic lever. The mold plates are not shown. 207
9.11 Comparison of filling of the cavity for the three different simulation models of the ceramic lever. Color scale from blue to red: filling time from 0 s to 0.3 s. 210
9.12 Comparison of the total deflection (sum of x, y, and z-component) for the three different simulation models of the ceramic lever. Color scale from blue to red: deflection from 0 mm to 0.1054 mm 211
9.13 Meshed part and mold assembly with indicated machine geometry modeled as hot runner beam elements. The mesh is based on a simplified version of the mold block. 214
9.14 Comparison of the experiments and the two investigated models of the simulations of the lever made of ceramic feedstock. 215

10.1 Recommended aspects to consider for a comprehensive simulation model of micro plastic parts. 220
10.2 Simplification of the full CAD model of a mold including all components such as screws and bolts (top) to a reduced version suitable for process simulations in ASMI (bottom), captured in SolidWorks®. . . . 222

10.3 Implementation procedure for process simulations of micro plastic parts with ASMI. 223
10.4 Imported assembly for the simulation including the mold platens, the insert, the cooling channels, and the actual part, captured in ASMI 2015. 226
10.5 Meshed insert of stationary half (blue) and meshed cooling channel (greyish) with cooling inlet and outlet and overlay of original CAD model (green), captured in ASMI 2015. 227

A.2 Coefficients of the ASMI data fit for the viscosity of Catamold® TZP-A. 261
A.4 Coefficients of the ASMI data fit for the *pvT* data of Catamold® TZP-A. 261
A.1 ASMI data fit for the viscosity of Catamold® TZP-A. 262
A.3 ASMI data fit for the *pvT* data of Catamold® TZP-A. 263
A.5 SigmaSoft®data fit for the *pvT* data of Catamold® TZP-A. 264
A.6 Coefficients of the SigmaSoft®data fit for the *pvT* data of Catamold® TZP-A. 265
A.8 Coefficients of the ASMI data fit for the viscosity of Catamold® 17-4PHA. 265
A.7 ASMI data fit for the viscosity of Catamold® 17-4PHA. 266
A.9 ASMI data fit for the *pvT* data of Catamold® 17-4PHA. 267
A.10 Coefficients of the ASMI data fit for the *pvT* data of Catamold® 17-4PHA. 268
A.12 Coefficients of the SigmaSoft®data fit for the *pvT* data of Catamold® 17-4PHA. 268
A.11 SigmaSoft®data fit for the *pvT* data of Catamold® 17-4PHA. 269
A.14 Coefficients of the ASMI data fit for the viscosity of GoMikro ZrO_2. . 270
A.16 Coefficients of the ASMI data fit for the *pvT* data of GoMikro ZrO_2. 270
A.13 ASMI data fit for the viscosity of GoMikro ZrO_2. 271
A.15 ASMI data fit for the *pvT* data of GoMikro ZrO_2. 272
A.17 SigmaSoft®data fit for the *pvT* data of GoMikro ZrO_2. 273
A.18 Coefficients of the SigmaSoft®data fit for the *pvT* data of GoMikro ZrO_2. 274
A.20 Coefficients of the ASMI data fit for the viscosity of GoMikro 17-4PH. 274
A.19 ASMI data fit for the viscosity of GoMikro 17-4PH. 275
A.21 ASMI data fit for the *pvT* data of GoMikro 17-4PH. 276
A.22 Coefficients of the ASMI data fit for the *pvT* data of GoMikro 17-4PH. 277
A.24 Coefficients of the SigmaSoft®data fit for the *pvT* data of GoMikro 17-4PH. 277
A.23 SigmaSoft®data fit for the *pvT* data of GoMikro 17-4PH. 278

C.1 Polaron Thermo VG Scientific SC7620 sputter coater. 313
C.2 JEOL JSM-5900 scanning electron microscope. 314

E.1 Arburg Allrounder 420 C 600-100 injection molding machine. 333
E.2 Mold installed on the injection molding machine. 334

E.3 Stationary half of the double test spiral geometry with sprue and pressure sensors. 335
E.4 Movable half of the double test spiral geometry with cavity. 336
E.5 Positions of the pressure measurements on the spiral with pressure curves for Catamold® 17-4PHA. 337
E.6 Positions of the pressure measurements on the spiral with pressure curves for Catamold® TZP-A. 338
E.7 Positions of the pressure measurements on the spiral with pressure curves for GoMikro 17-4PH. 339

List of Tables

1.1 Hi-MICRO project partners and their role in the project: academic partner (AP), technology provider (TP), or end user (EU). 5

2.1 Capabilities of the summarized micro molding processes applied to micro components. The statements are typical values, actual values depend on the machined material, the process conditions, and on the exact process variant. 16

4.1 Key specifications of the characterized commercial powder feedstocks from BASF. 45
4.2 Key specifications of the characterized non-commercial powder feedstocks from KIT. 45
4.3 Processing conditions of the circular disc specimen for the material characterization of the feedstocks. 46
4.4 Determined powder content of the commercial powder feedstocks. . . 48
4.5 Determined densities of the used powder feedstocks. 49
4.6 Measured values for the specific heat capacity of the investigated feedstocks. The measurement was directly done by a DSC analysis. The values are the average of three heating and cooling cycles at a rate of 10 °C min^{-1}, confidence level: 95 %. 51
4.7 Measured values for the thermal conductivity of the investigated feedstocks. The measurement was indirectly done by measuring the thermal diffusivity with a laser flash analysis. The values are the average of five measurements, confidence level: 95 %. 55
4.8 Measured and theoretical thermal conductivities of the powder feedstocks as well as of the pure powders and binders. Approximated and averaged values for temperatures of about 25 °C to 200 °C. 57
4.9 Chosen temperature levels for the viscosity measurements and recommended processing window of the investigated feedstocks for reference. 61
4.10 Data-fitted parameters for the Cross-WLF model describing the viscosity of the feedstocks and reference values of a pure POM from BASF (from ASMI data base [100]). The values given are partially rounded for easier perception. 62

4.11 Data-fitted parameters for the modified 2-domain Tait model describing the pvT data of the investigated feedstocks, determined with ASMI and SigmaSoft®, and reference values of a pure POM from BASF (from ASMI data base [100]). The values are shown as generated by the fitting software. 70

5.1 Process settings for the molding and simulation of the micro channel test structure. 77
5.2 Incorporated entities of the different simulation models of the micro channel test structure to assess the influence of the machine geometry and venting analysis on the predicted process outcome. 79
5.3 Dimensions of the implemented venting channels of the models C, D, E of the micro channel test structure. The numbering of the venting channels corresponds to Figure 5.3. All dimensions in mm, corresponding to length × width × thickness. 81
5.4 Meshing settings of the micro channel test structure. Unspecified settings were kept at the default values. 81
5.5 Additional simulation settings of the micro channel test structure. Unspecified settings were kept at the default values. 84

6.1 Factors and the chosen factor levels of the DOE for the first design iteration of the microfluidic dispenser. 96
6.2 Meshing settings of the microfluidic dispenser with pin gate for the simulation validation. Unspecified settings were kept at the default values. 97
6.3 Machine and process settings of the microfluidic dispenser with film gate. Unspecified settings were kept at the default values. 97
6.4 Results of the simulation DOE for the analysis of the influence of the gate type and position and the material on the process and part quality of the microfluidic dispenser. 104
6.5 Meshing settings of the microfluidic dispenser with pin gate for the simulation validation. Unspecified settings were kept at the default values. 111
6.6 Machine and process settings of the microfluidic dispenser with film gate. Unspecified settings were kept at the default values. 112
6.7 Factors and the chosen factor levels of the DOE analyzing the filling and packing of the microfluidic dispenser. 113
6.8 General simulation results for the second design iteration of the microfluidic dispenser with different gate size in ASMI. 115
6.9 Factors and the chosen factor levels of the DOE analyzing the flatness of the microfluidic dispenser. 119
6.10 Simulation results of the DOE for analyzing the flatness of the microfluidic dispenser with different gate sizes. 120

6.11 Simulation process settings of the microfluidic dispenser for the simulation validation. Unspecified settings were kept at the default values. 125

7.1 Meshing settings of the microfluidic mixer with film gate. Unspecified settings were kept at the default values. The total number of elements varies slightly due to the different thickness of the investigated film gates. . . . 145
7.2 Machine and process settings for the simulations of the microfluidic mixer with pin gate. Unspecified settings were kept at the default values. . . . 146
7.3 Machine and process settings for the simulations of the microfluidic mixer with pin gate. Unspecified settings were kept at the default values. . . . 148
7.4 Simulation results for the predicted values of the injection time and pressure and the shear rate of the pin gate analysis. . . . 149
7.5 Meshing settings of the microfluidic mixer with film gate. Unspecified settings were kept at the default values. The total number of elements varied slightly due to the different thickness of the investigated film gates. . . . 157
7.6 Machine and process settings for the simulations of the microfluidic mixer with film gate. Unspecified settings were kept at the default values. . . . 159
7.7 General simulation results for the second design iteration of the microfluidic dispenser in ASMI 2015. . . . 160
7.8 Process settings for the molding of the short shots of the microfluidic mixer in PP. . . . 167
7.9 Machine and process settings of the simulations of the microfluidic mixer with film gate. Unspecified settings were kept at the default values. . . . 168

8.1 Process settings for the molding of the full shots of the double spiral geometry with all four characterized feedstocks. . . . 176
8.2 Input factors and their factor levels for the DOE with the GoMikro ZrO_2 feedstock. . . . 177
8.3 Meshing settings of the double spiral together with the feed system. Unspecified settings were kept at the default values. . . . 179
8.4 Additional simulation settings of the simulations of the test spiral. The process settings were in accordance to the experiments (see Table 8.1). Unspecified settings were kept at the default values. . . . 180
8.5 Experimental results for the full shots of the molded test spirals. . . . 181
8.6 Predicted process results of the simulations with constant and true speed profile of the test spirals and experimental results from above for comparison (given in the row denoted by “experiment”). . . . 183

9.1 Meshing settings of the homogeneous mesh (HM) and multi-scale mesh (MM) of the micro-mechanical lever with insert and cooling. Unspecified settings were kept at the default values. The numbers of elements are rounded. 199
9.2 Machine and process settings of the simulations for the comparison of the homogeneous and multi-scale mesh of the ceramic lever. Unspecified settings were kept at the default values. 201
9.3 Major simulation results of the homogeneous and multi-scale mesh of the ceramic lever. 202
9.4 Incorporated entities of the different simulation models of the ceramic lever to assess the influence of mold and cooling circuit on the simulation outcome. 204
9.5 Meshing settings of the microfluidic dispenser with pin gate for the simulation validation. Unspecified settings were kept at the default values. The numbers of elements are rounded. 205
9.6 Machine and process settings of the simulations models of the ceramic lever. Unspecified settings were kept at the default values. 208
9.7 Major simulation results of the three different models of the ceramic lever. 209
9.8 Machine and process settings of the powder injection molding experiments of the ceramic lever. 212
9.9 Meshing settings of the micro-mechanical lever. Unspecified settings were kept at the default values. The numbers of elements are rounded. 213
9.10 Machine and process settings of the powder injection molding simulation of the ceramic lever. Unspecified settings were kept at the default values. 215

List of Mathematical Symbols

Symbol	meaning	SI unit
Latin		
a	thermal diffusivity	$\mathrm{m^2\,s^{-1}}$
A	data-fitted constant	s^n
	geometrical factor	1
A_1	data-fitted constant	1
A_2	data-fitted constant	K
$b_{1\mathrm{m}}$	data-fitted constant	$\mathrm{m^3\,kg^{-1}}$
$b_{2\mathrm{m}}$	data-fitted constant	$\mathrm{m^3\,kg^{-1}\,K^{-1}}$
$b_{3\mathrm{m}}$	data-fitted constant	Pa
$b_{4\mathrm{m}}$	data-fitted constant	$\mathrm{K^{-1}}$
$b_{1\mathrm{s}}$	data-fitted constant	$\mathrm{m^3\,kg^{-1}}$
$b_{2\mathrm{s}}$	data-fitted constant	$\mathrm{m^3\,kg^{-1}\,K^{-1}}$
$b_{3\mathrm{s}}$	data-fitted constant	Pa
$b_{4\mathrm{s}}$	data-fitted constant	$\mathrm{K^{-1}}$
b_5	data-fitted constant	K
b_6	data-fitted constant	$\mathrm{K\,Pa^{-1}}$
b_7	data-fitted constant	$\mathrm{m^3\,kg^{-1}}$
b_8	data-fitted constant	$\mathrm{K^{-1}}$
b_9	data-fitted constant	$\mathrm{Pa^{-1}}$
B	pressure sensitivity (data-fitted constant)	K
	geometrical factor	1
Bi	Biot number	1
c_p	specific heat capacity (at constant pressure)	$\mathrm{J\,kg^{-1}\,K^{-1}}$
d_{10}	particle diameter of 10 %	m
d_{50}	particle diameter of 50 %	m
d_{90}	particle diameter of 90 %	m
d_i	inner shaft diameter	m
d_o	outer shaft diameter	m
D_1	data-fitted constant	Pa s
D_2	reference temperature (data-fitted constant)	K
D_3	data-fitted constant	$\mathrm{K\,Pa^{-1}}$
D_i	inner hub diameter	m
D_o	outer hub diameter	m

Symbol	**meaning**	**SI unit**
E	elastic modulus	Pa
f	flatness	m
f_f	flatness of front	m
f_b	flatness of back	m
F	axial bearing capacity	N
$\boldsymbol{g}$	gravitational acceleration (vector)	$\mathrm{m\,s^{-2}}$
h	heat transfer coefficient	$\mathrm{W\,m^{-2}\,K^{-1}}$
L	length of hub and shaft interference	m
m	consistency index (data-fitted constant)	$\mathrm{Pa\,s}^n$
	mass	kg
m_f	total mass after fill	kg
m_p	total mass after pack	kg
m_pp	part mass after pack	kg
n	power-law or flow index (data-fitted constant)	1
p	pressure	Pa
	fill/injection pressure	Pa
s	volumetric shrinkage	1
s_max	maximum volumetric shrinkage	1
s_min	minimum volumetric shrinkage	1
s_avg	average volumetric shrinkage	1
t	time	s
	fill/injection time	s
T	absolute temperature	K
T_0	reference temperature (data-fitted constant)	K
T_t	transition temperature	K
$\boldsymbol{u}$	velocity (vector)	$\mathrm{m\,s^{-1}}$
V_p	powder volume	$\mathrm{m^3}$
V_tot	total volume	$\mathrm{m^3}$
W	geometrical factor	1

Symbol	meaning	SI unit
Greek		
β	coefficient of volumetric thermal expansion	K^{-1}
$\dot{\gamma}$	shear rate	s^{-1}
$\dot{\boldsymbol{\gamma}}$	shear rate (tensor)	s^{-1}
$\dot{\gamma}_{\mathrm{max}}$	maximum shear rate	s^{-1}
Δ	difference	1
η	viscosity	$\mathrm{Pa\,s}$
η_0	zero shear rate viscosity	$\mathrm{Pa\,s}$
η_{app}	apparent viscosity	$\mathrm{Pa\,s}$
η_{b}	viscosity of the binder	$\mathrm{Pa\,s}$
κ	thermal conductivity	$\mathrm{W\,m^{-1}\,K^{-1}}$
λ	thermal conductivity	$\mathrm{W\,m^{-1}\,K^{-1}}$
μ	coefficient of friction	1
ρ	density	$\mathrm{kg\,m^{-3}}$
$\rho_{25\,^\circ\mathrm{C}}$	density at 25 °C and atmospheric pressure	$\mathrm{kg\,m^{-3}}$
$\boldsymbol{\sigma}$	stress (tensor)	Pa
τ	shear stress	Pa
$\boldsymbol{\tau}$	shear stress (tensor)	Pa
τ^*	critical shear stress	Pa
τ_0	yield stress	Pa
σ_{y}	yield strength	Pa
ϕ	powder volume fraction	1
ϕ_{max}	maximum powder volume fraction	1
ϕ_{vol}	powder volume fraction	1
ϕ_{wt}	powder weight fraction	1

List of Acronyms

Abbreviation	meaning
2k	two-component
ABS	acrylonitrile butadiene styrene
AP	academic partner
app	apparent
ASMI	Autodesk Simulation Moldflow Insight®, molding simulation software made by Autodesk, San Rafael, CA, USA
a.u.	arbitrary unit
avg	average
BOT	bottom part of microfluidic mixer
CAD	computer-aided design
CC	conformal cooling
CIM	ceramic injection molding
COC	cyclic olefin copolymer
CT	computer tomography
DEV	complete device of microfluidic mixer
DOE	design of experiments
DTU	Technical University of Denmark
e.g.	for example (from Latin: exempli gratia)
et al.	and others (from Latin: et alii)
etc.	and so on (from Latin: et cetera)
EU	end user
FDM	finite difference method
FEA	finite element analysis
FEM	finite element method
GD&T	geometric dimensioning and tolerancing
GOM	GOM Inspect V8 Hotfix 10, metrology software made by GOM Gesellschaft für optische Messtechnik, Braunschweig, Germany
HM	homogeneous mesh
HTC	heat transfer coefficient
i.e.	that is (from Latin: id est)
IAM	Institute of Applied Materials, KIT

Abbreviation	**meaning**
IM	injection molding
KIT	Karlsruhe Institute of Technology
LCP	liquid crystal polymer
max	maximum
MEK	Department of Mechanical Engineering, DTU
MIM	metal injection molding
min	minimum
MM	multi-scale mesh
n.a.	not available
PE	polyethylene
PEEK	polyether ether ketone
PEI	polyetherimide
Ph.D.	Doctorate of Philosophy (from Latin: doctor philosophiae)
PIM	powder injection molding
PMMA	polymethyl methacrylate
PO	part only
POM	polyoxymethylene
PP	polypropylene
PS	polystyrene
SC	simple cooling
SEM	scanning electron microscope
SLS	selective laser sintering
STL	stereolithography CAD file
SUB	middle segment of microfluidic mixer
TOP	top part of microfluidic mixer
TP	technology provider
TPE	thermoplastic elastomer
TPE-S	styrene thermoplastic elastomer
TPS	styrene thermoplastic elastomer
vs	versus
WLF	Williams-Landel-Ferry

1 Introduction and objective

1.1 Introduction

Micro systems are among the essential drivers of the technological evolution and among the key technologies in the information age. Micro systems engineering and micro technology as the engineering discipline and the manufacturing technology behind enable to combine product miniaturization and functionality in complex high-performance multi-material micro products. Consequently, these products have a tremendous impact on process chains and the manufacturing industry in general. However, the production of such components also comes along with an increasing demand on the applied design and manufacturing tools.

The key for the success of micro systems is their reliable, cost-effective, and high-volume production. As a result of the increasing demand, the well established large-scale production technology of injection molding was developed further in the recent decades, finally leading to micro injection molding (µIM). Micro injection molding is adapted to and nowadays widely applied for the production of precise three-dimensional micro plastic parts. It appears as one of the most suitable processes for the successful replication of micro structures at large scale, full automation, excellent dimensional control, and low unit costs. [1–4]

Micro products became a part of our daily life. The number of applications of micro systems is constantly growing, and they are spreading into new application areas. Established applications cover a broad and diverse spectrum of industrial fields such as life sciences, medical and healthcare, sensors, consumables, automation, and telecommunications. Typical examples in these fields are microfluidic devices for diagnostics (shown in Figure 1.1a), minimally invasive surgery tools (shown in Figure 1.1b), airbag or pressure sensors in the automotive industry, gyroscopes and acceleration sensors in smart phones, displays in consumer electronics, nozzles of ink jet printers, micro mechanical parts in hearing aids and watches, or optical wave guides, switches, and connectors in digital data transmission. [2, 3, 5, 6]

The global market just for polymer components made by micro injection molding is expected to reach about $ 900 million in 2020 compared to $ 350 million in 2013. This is equal to a growth of about 14.4 % p.a. in average. The main shares and drivers are the medical and healthcare industry, the automotive sector, telecommunications, and micro drive systems as illustrated in Figure 1.2. [8]

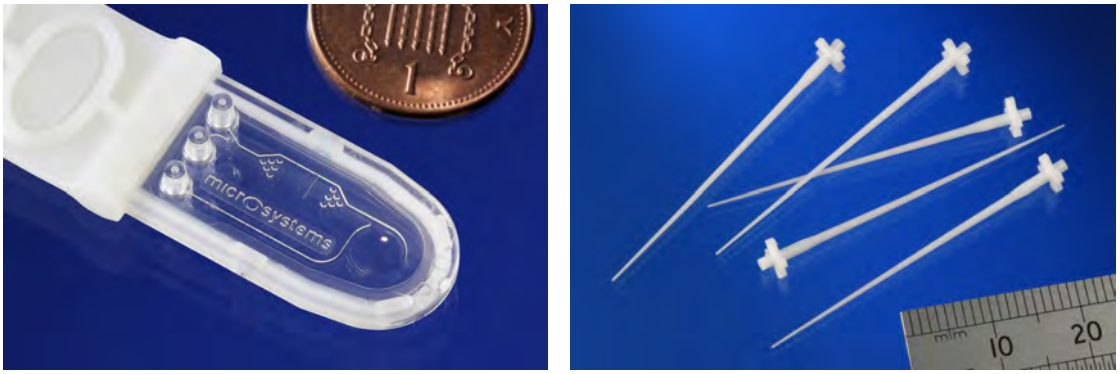

(a) Microfluidic chip.

(b) Micro dental surgery tool for root canal treatment and tip diameter of 180 µm.

Figure 1.1: Examples of micro plastic products made by micro injection molding [7].

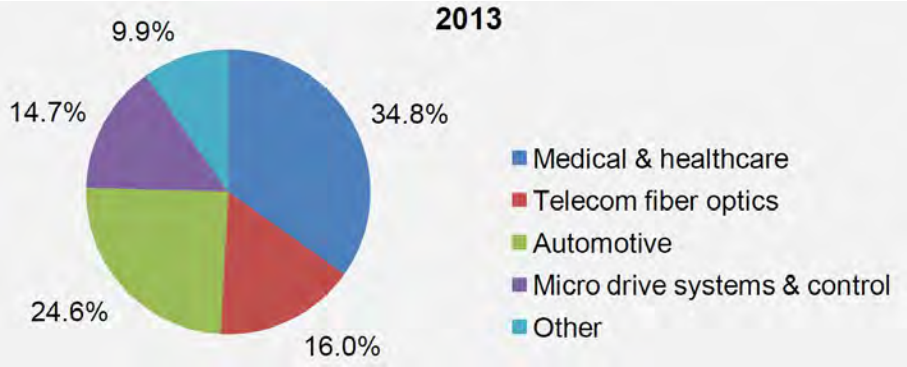

Figure 1.2: Polymer micro injection molding market share by application in 2013 [8].

Similar to conventional injection molding, related process variants of micro injection molding exist such as multi-component micro injection molding, micro powder injection molding (µPIM), or in-mold labeling. Micro powder injection molding enables the cost efficient medium to large-scale production of geometrically complex and net-shaped micro components in metals and ceramics. [1]

However, micro injection molding of plastics, metals, and ceramics is not just a scaling down of the well known conventional injection molding process. Instead, a rethinking of basically the whole process chain is necessary. Different aspects such as design guides, tolerance rules, simulation tools, the manufacturing process, and the deployed machinery must be addressed to fully develop the potential of micro injection molding. [2, 5]

1.2 Project definition and objectives

It was the ambition of the present Ph.D. project to pick up the aforementioned aspects and implement a novel holistic approach for the development and manufacture of complex three-dimensional micro parts made by micro injection molding. The over-all objective of the project was to develop, validate, and define a methodology for manufacturing-oriented micro product design. This was done by applying a systematic approach based on process simulation, concurrent engineering, design for manufacture, dimensional and geometrical tolerancing and metrology, as well as analysis and experimental characterization of the micro injection molding process.

The objective of the project could be divided into the following sub-tasks:

- development of a systematic methodology to establish the performance and applicability of process simulation software in micro injection molding applications,
- optimization of micro component and product design based on the concurrent micro engineering approach, i.e. including validated micro injection molding process simulations,
- characterization of the micro injection molding process of polymers, metals, and ceramics by means of experimental and simulation studies,
- investigations on the applicability of process simulations for micro product development within the process chain of micro powder injection molding,
- material research on the applied materials to enable concurrent simulation-aided design methods in the area of powder injection molding.

1.3 Motivation and research questions

The design and manufacture of micro products require a full understanding of miniaturization laws and their implementation on engineering materials as well as on entire manufacturing process chains employed to shape these materials at the micro scale. In particular, micro injection molding is established as one major player for the efficient replication of micro plastic parts, but miniaturization rules and design tools for micro parts and micro molds are still pending.

A powerful and promising tool to predict material behavior and processing is reported by multi-scale integrated modeling. This modeling approach in injection molding combines the fundamental analysis of the process and material with the established methods of computer-aided and simulation-supported design. The holistic characterization of the process, the materials, the part, and the design and simulation tools is essential.

Any simulation is nonetheless subject to limitations. One limitation is the finite amount of available resources, e.g. time and computation power. For that reason, simulations must also be economical. To make them the most economical, the simulation models should be as simple as possible. However, this simplification of the real world naturally impairs the accuracy and validity of the generated simulation results. In the context of micro injection molding, it is thus necessary to find out how extensive the simulation model shall be to remain economical, but still yield satisfying results.

Another limitation results from the fact that any simulation model is only valid in a certain context—so are hence the simulation results. Applying the simulations to a different set of parameters and conditions can lead to false results. Consequently, the validation of simulation models in any application case is essential.

Further limitations can be for instance the inaccuracy of input data or insufficient knowledge about the real phenomena that are simulated. Here, the quality of the used material data comes into play in injection molding simulations. Parts of this work were motivated by the urge to collect reliable material data for a solid foundation of the material models which are applied in the process simulations.

When looking into literature and industry, the simulation of the injection molding process is common practice—on the macro level. However, simulations are a new and barely applied tool in the area of micro injection molding. This work intends to prove simulations as valuable and effective tool for micro molded parts, too.

Further motivation for driving the simulations forward in micro injection molding was the fact that it is actually not possible to easily and effectively rework or modify fragile micro-structured molding tools. Computer simulations of each step in the process chain—and therefore also for the molding—would be remarkably beneficial to prevent from serious and costly mistakes. [9, 10]

1.4 Hi-MICRO project

This Ph.D. thesis reports work undertaken in connection to the project "Hi-MICRO" (High Precision Micro Production Technologies, http://www.hi-micro.eu/), mostly Task 1.2: Micro Injection-Moulding Oriented Product Design. Hi-MICRO was a collaborative project supported by the European Commission in the 7th Framework Programme (Grant agreement no: 314055). The project duration was from October 2012 until September 2015.

The project partners were from different countries in central Europe and are listed in Table 1.1. In detail, there were four academic partners (AP) which supported the research and development activities with their expertise. Moreover, there were seven industrial partners of which four were the so-called end users (EU), because they aimed to fabricate a demonstrator device. Besides, there were three technology providers (TP) which contributed by providing machinery which was supposed to be improved by the project activities.

Table 1.1: Hi-MICRO project partners and their role in the project: academic partner (AP), technology provider (TP), or end user (EU).

Name	origin		role
University of Bremen	Bremen	GER	AP
Technical University of Chemnitz	Chemnitz	GER	AP
Technical University of Denmark	Kongens Lyngby	DK	AP
Katholieke Universiteit Leuven	Leuven	BE	AP
Klöckner DESMA Schuhmaschinen	Achim	GER	TP
LayerWise	Leuven	BE	TP
X-Tek Systems	Tring	UK	TP
Formatec Technical Ceramics	Goirle	NED	EU
Polyoptics	Kleve	GER	EU
Sophion Bioscience	Ballerup	DK	EU
XAAR Technology	Cambridge	UK	EU

The detailed goals of the project and the consortium were as follows [11, 12]:

- using additive manufacturing (AM) to produce monolithic tool inserts with integrated complex internal channels for efficient thermal management and process control,
- developing and enabling precision manufacturing technologies to post-process the tool insert features,
- applying special metrology techniques based on computer-tomography (CT) to control the quality of the integrated complex internal channels,

- developing the handling system and high-speed in-line quality control system for non-statistic quality control and integrating it into an industrial production platform.

In summary, the different project partners of course wanted to benefit from the project and strengthen their position in their market or research area. The academic partners aimed at deepening their expertise and fostering international collaboration. The technology providers sought to improve their products in order to gain a better position in the European and international market. The end users strove for the successful fabrication of their prototype as great part of the development of novel and improved products.

Currently, the process chain for complex micro injection molded micro parts is usually characterized by segmentation into specialized steps, often even further limited by available manufacturing processes at shop floor level. The Hi-MICRO project proposed therefore an innovative process chain for precision micro injection molding (µIM) and micro powder injection molding (µPIM). It realized an innovative approach for the design, manufacturing, and quality control of tool inserts to achieve a significant breakthrough in mass production of precision 3D micro parts.

The project partners thus improved the performance of industrial equipment for mass production of precision 3D micro parts through modular design of monolithic tool inserts with improved thermal management capability, development of an on-machine handling system and an in-line quality control system. The project activities covered the entire value chain of mass production of precision 3D micro parts from product and tool insert design, manufacturing of tool inserts, micro injection molding processes to the production equipment and quality control.

Contribution from the Hi-MICRO consortium to the present Ph.D. thesis is greatly acknowledged. Some project partners provided their prototype from the project as study cases for the application of the simulations. They were hence entirely or partially subject of the investigations, design, and manufacture presented in this work. Also, the financial support to the present Ph.D. project coming from the Hi-MICRO project is thankfully acknowledged.

If not otherwise specified, explicit prototype functionality or decisive dimensions and tolerances could not be disclosed in this Ph.D. because of considerateness towards the enterprise know-how of and confidentiality arrangements with the industrial partners.

1.5 Structure of the thesis

The structure of this Ph.D. thesis follows the elaborated objectives and related tasks from section 1.2. The different chapters treat roughly one of the identified sub-objectives.

The thesis starts over with a state-of-the-art overview on different molding technologies in chapter 2. The investigation examines conventional injection molding, micro injection molding, and powder injection molding and finishes up with an overview on their key specifications.

In chapter 3, the thesis elaborates on the concept of computer simulations and their application in the area of injection molding. The mathematical background of the modeling, available simulations tools, and their limitations regarding micro molding are presented. The chapter ends with the presentation of the state-of-the-art related to simulations in micro molding.

Afterwards, chapter 4 treats the material characterization of the powder feedstocks used for the experiments and simulations of powder injection molding. After the discussion of the state-of-the-art, the actual material characterization comprises the measurements of essential material properties, mainly thermal and rheological data which are necessary to enable the simulation of the powder injection molding process.

The subsequent chapter 5 deals with the simulation validation of the micro injection molding process of a micro channel test structure. The experimental molding of the part is described. Furthermore, the simulation set up and the implementation of differently complex simulation models are outlined. In the end, the experimental molding and the predicted simulation results are compared and the influence of the model comprehensiveness is investigated.

In chapter 6, the simulation-aided part design is carried out for one industrial study case, a microfluidic dispenser. Several design iterations are described leading to an optimized part and gate design of the investigated micro plastic part. The chapter is rounded up with a simulation validation by comparing the actually molded part with the outcome of according simulations.

Chapter 7 deals with the concurrent part and mold design of a microfluidic mixer, the second industrial study case made from plastics. By means of simulations, the part design is optimized, a possible gate design is is systematically established, and the mold is built up. The manufactured mold and the molded parts are introduced, demonstrating the application of the previously gained insight from the simulations to industrial manufacture. The chapter finishes with the simulation validation by comparing molded part to simulation results.

The carried out powder injection molding experiments and simulation validations are the topic of chapter 8. First, the deployed geometry and machinery as well

as the conducted experimental investigations are outlined. Afterwards, the related simulations and models for the investigation about the applicability of process simulations on the powder injection molding process are presented. The chapter closes with the discussion of the experimental and simulation results and their comparison for the validation of the simulation performance.

Chapter 9 continues with the powder injection molding topic and applies the manufacture-oriented design to another industrial study case, a micro mechanical part made from ceramics. The practical applicability of the concurrent engineering supported by simulations is analyzed. Novel aspects such as the mold design optimization with regard to integrated conformal cooling channels are examined and discussed.

Ultimately, the carried out work and findings are compiled and summarized in chapter 10. The chapter comprises an improved simulation strategy for micro plastic parts made by micro injection molding which is concluded from the work of this Ph.D. project.

The summary is followed by a conclusion on the major outcome and achievements of this project in chapter 11. Additionally, possible future work related to this project and ideas how to enhance the done work are outlined.

2 State-of-the-art of injection molding technology

Abstract An overview of existing manufacturing processes in the area of injection molding technology is given. The most important and for this work relevant process variations are introduced: conventional, micro, and powder injection molding. The processes and their properties are briefly described. In the end, a summary of the process capabilities can be found.

It is not intended to discuss all details, further details regarding injection molding can be found in the corresponding literature, further details about the technologies employed during the project, such as simulations and material characterization, can be found in the respective chapters.

2.1 Conventional injection molding

Conventional injection molding is the most common technology for the production of parts made from thermoplastics, elastomers, and thermosets. It enables the economic large-scale production of complex and net-shaped plastic parts with tight tolerances. Post-processing like finishing is usually not necessary. The production can often be fully automated. In general, pure or filled plastics are used in plastics injection molding. [13–15]

The process of plastics injection molding is discontinuous, but cyclic. The sequence of the different phases of the cycle on an injection molding machine is shown in Figure 2.1. The cycle can be divided into the following process phases [4, 13–15]:

- Filling (injection)
  In the injection phase, the molten plastic material is pushed into the mold under high pressure to fill the cavity. The screw moves forward and a pre-defined amount of material is injected into the mold.
- Packing
  After the filling is completed, the packing commences. During the packing stage, more material is pushed into the cavity to compensate for the shrinkage of the plastic which starts to cool down and contract.

- Plastication and metering
  After the filling and packing are completely finished, the machine starts the metering and plastication for the shot of the subsequent cycle. The screw rotates and moves back to dose the material. The plastic is molten by external electrical and internal frictional heating.
- Cooling and solidification
  After the packing and parallel to the plastication and metering, the cooling phase happens in which the plastic inside the cavity continues to cool down and shrink. Sometimes, the injection unit is contracted from the mold to prevent from further heat transfer to the mold.
- Mold opening
  When the plastic part has reached the ejection temperature and gained sufficient dimensional stability, the mold opens.
- Ejection
  As soon as the mold is open, the plastic part is automatically ejected by the ejector system mechanically or pneumatically, for delicate parts sometimes assisted by a handling system like a robot arm.

Typical cycle times for thermoplastic materials are in the order of 1 s with the produced parts having typical wall thicknesses of few millimeters. Typical injection pressures are in the order of 1000 bar. [13, 15]

2.2 Micro injection molding

When dealing with micro injection molding, the question arises about what exactly is the definition of "micro" or how small the parts are supposed to be considered in the micro injection molding domain. After some proposals and revisions, three common definitions of different types of micro-molded plastic products nowadays exist [1–3, 5, 16, 17]:

1. Micro-patterned parts
   Micro-featured parts with outer dimension in the millimeter range or larger, but locally featuring structures in the micrometer range, typically less than 100 µm down to sub-micrometer range.
2. Single micro parts
   Micro parts with very small outer dimensions, typically 1 mm to 2 mm or even entirely in the micrometer range, and shot weights in the order of milligrams.
3. Micro precision parts
   Parts with larger dimensions, but dimensional tolerances in the micrometer range.

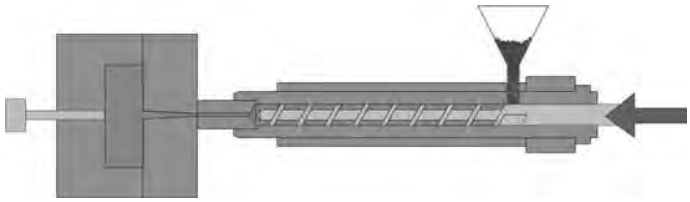

(a) Filling and packing.

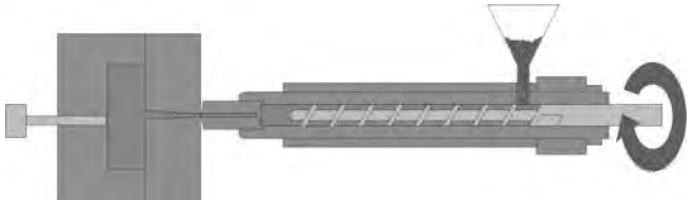

(b) Plastication and metering.

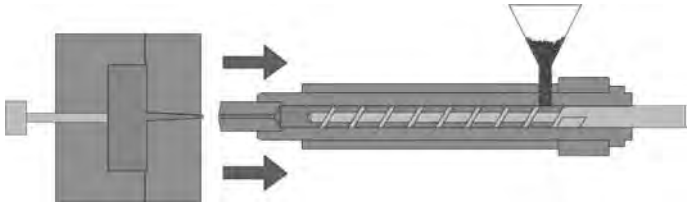

(c) Cooling and solidification.

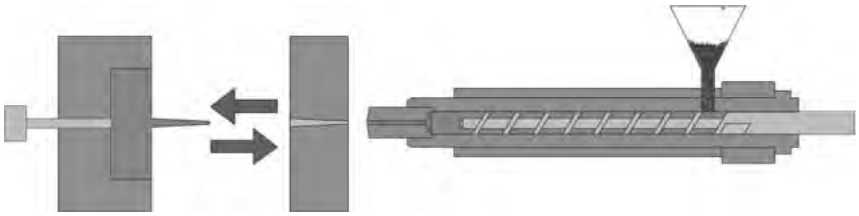

(d) Mold opening.

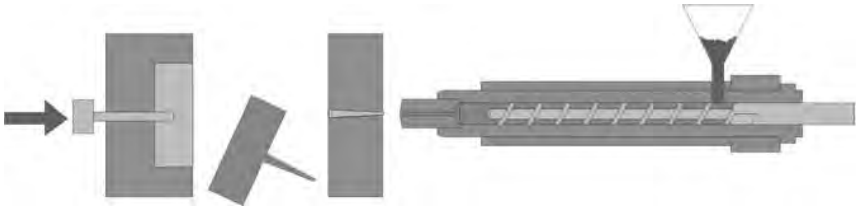

(e) Ejection.

Figure 2.1: The different phases of the process cycle of injection molding with a conventional machine [15].

Micro injection molding is based on the conventional injection molding process and equipment. The processing of the material follows the same cycle as described in the previous section. Nonetheless, it can be derived from the aforementioned definitions that the application of conventional injection molding machines to micro plastic parts is possible, but challenging and comes with some disadvantages. Hence, modifications of process and equipment are necessary. [1]

Regarding the plastic part, the resulting sprue accounts for a large part of the total volume and is often even larger than the actual part. This leads first of all to a great waste of material. In addition, the large sprue dominates the cooling and thus the cycle time. Because of the generally very small shot size, the plastic material can experience long residence times inside the heated barrel which causes the risk of material degradation. [18, 19]

Moreover, it becomes more difficult to dose the right amount of material and control the filling process. The response time, reproducibility of the injection speed, and positioning accuracy of the screw of a conventional machine might not be sufficient for meeting tight tolerances in production of micro plastic parts. The large melt cushion and possible deviations caused by the shut-off ring at the screw makes the control of the plastic flow and the packing more difficult. [4, 15, 20]

Furthermore, more precise positioning and control of the mold motion and ejector system are necessary in order to prevent from deformation during mold opening and ejection. The ejection with simple ejector pins might not be applicable to single micro parts simply because of their size in the same order as the ejector pins. New handling and demolding concepts are necessary. [4]

In order to overcome these drawbacks of conventional machines, some machine manufacturer developed dedicated micro injection molding units and machines. These machines differ from the conventional machines in a way that they provide fully electric and consequently more precise drives. For better metering and injection precision, they are moreover equipped with plunger or mixed plunger-screw systems instead of a single reciprocating screw like shown in Figure 2.2.

Furthermore, the metering and dosing of the plastic is often spatially separated into two segments in the machine. Both structural changes lead to better dosing and smaller residence time in the machine. The smaller and lighter machine parts improves the response time, acceleration, and positioning accuracy. Some examples for micro injection molding machines are

- the “MicroPower” (predecessor: “MicroSystem”) developed by Wittmann-Battenfeld, Kottingbrunn, Austria,
- the “formicaPlast®” made by KLÖCKNER DESMA Schuhmaschinen, Achim, Germany,
- and the nameless micro-injection module made by Arburg, Lossburg, Germany.

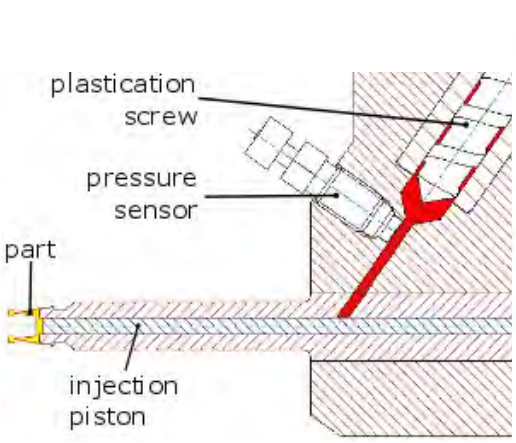

(a) "MicroPower" [20].

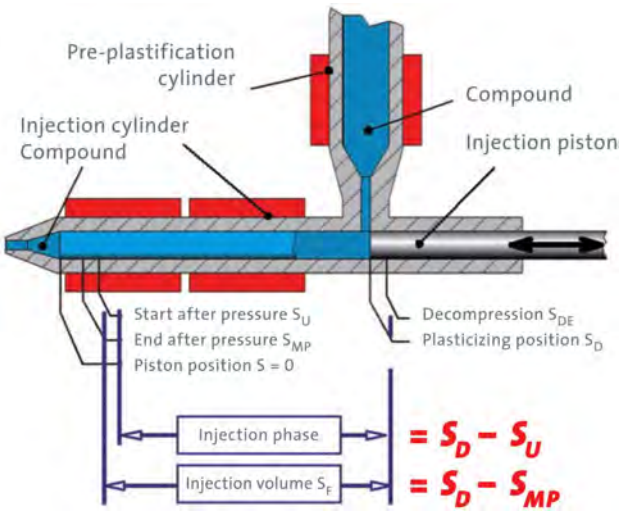

(b) "formicaPlast®" [21].

Figure 2.2: Schematic of the machine concept of the micro injection molding machines "MicroPower" of Wittmann-Battenfeld with small screw for plastication and plunger for injection and the "formicaPlast®" of Klöckner DESMA Schuhmaschinen with plungers for plastication and injection.

Insufficient venting and premature solidification because of the large surface-to-volume ratio are issues for micro parts, too. Therefore, classical venting concepts are sometimes not applicable anymore and elevated mold temperatures, sometimes above the no-flow temperature of the used material, must be used. In order to overcome the first problem, the evacuation of the mold is sometimes applied. The second problem and the connected increase in cycle time can be counteracted by the so-called variotherm process. In this process, the mold is actively heated up for injection and cooled down for ejection. [1]

2.3 Powder injection molding

Powder injection molding is very similar to the conventional injection molding process of plastics. However, the processed raw materials, the so-called feedstocks, consist of a polymer binder, usually thermoplastics or wax, and a large fraction of fine metal or ceramic powder. Therefore, the particular processes are usually referred to as metal injection molding (MIM) or ceramic injection molding (CIM). The binder enables the actual injection molding and provides the viscous properties. Furthermore, it provides also the structural stability of the molded parts. The powder filling can reach up to about 70 % by volume (>90 % by weight) [22]. Usually, the feedstocks also contain little amounts of additives for better flowability, lubrication, demolding,

anti-foaming, wetting of the powder, etc. The feedstocks are mixed prior to the actual injection molding process at the compounding. [1, 9, 23, 24]

The complete process chain of powder injection molding in brief is introduced in Figure 2.3. The shaping happens in the same cyclic way as in conventional injection molding. The feedstock is

1. melted by electrical and frictional heating,
2. injected under high pressure into the mold until the cavity is full,
3. packed to compensate for the material contraction when cooling,
4. cooled down to stable shape,
5. and finally ejected from the mold.

Figure 2.3: Schematic of the typical process chain of powder injection molding. Optional finishing processes like polishing, plating, or grinding after sintering are not shown. The blue part (left) is usually covered by the material supplier, the pink part (right) is covered by the component manufacturer. [22]

The part resulting from the injection molding is referred to as green part. The binder has only temporary function, so that subsequently the green part is debound thermally, catalytically or by a solvent. The resulting brown part still has a porous structure. The following sintering of the brown part happens at high temperatures in a special sintering furnace. After sintering, the final part reaches almost the full bulk density of the used metal or ceramic. Post-processing like densification (pressing), annealing (heating), hardening, machining, or plating can follow. [1, 22, 25]

The major differences of powder injection molding in comparison to plastic injection molding arise from the usage of the feedstocks. The extensive powder content and the heavy powder weight compared to the lightweight polymer binder leads to a serious increase in inertia of the material flow. As a result, the powder feedstocks tend to show jetting and wall-slip. Moreover, powder-binder separation due to high shear rates can be sometimes observed leading to local differences in viscosity, powder content and hence shrinkage behavior while sintering. [9, 16, 26, 27]

In addition, feedstocks exhibit significantly increased heat conductivity due to the metal and ceramic filler, but at the same time generally lower heat capacity than plastics. The different thermal properties lead to an increase of the heat loss and more rapid solidification of the melt which negatively influences filling and replication performance. Besides, the feedstocks have lower compressibility and lower temperature-dependent change in density. [28]

The quality of the fabricated product is very sensitive to the process settings, because powder injection molding has a narrow process window compared to plastics injection molding. The sintering of the part leads to tremendous shrinkage which must be already considered in the tool design phase to reach the required dimensions of the final product. The powder particles will sinter together, but they will not completely melt. The fusion of the material is achieved by diffusion processes within and between the material grains. The micro structure can thus still be recognized in the sintered product. Hence, the particle size of the chosen powder affects the part properties and process performance, e.g. smallest feature sizes, surface roughness, material strength. [16, 23, 27]

As a rule of thumb, the particle size should be smaller than one tenth of the smallest part feature. The typical average particle size d_{50} for steels is about 1 µm to 10 µm. For metal injection molding, mainly stainless steel of the grades AISI 17-4PH (typically 1.4542, X5CrNiCuNb16-4) and AISI 316L (typically 1.4404, X2CrNiMo17-12-2) are used. The typical average particle size d_{50} for ceramic powders is about 0.1 µm to 1.0 µm. In case of ceramic injection molding, zirconium dioxide (ZrO_2) and aluminum oxide (Al_2O_3) are the predominant materials. [9, 16, 29]

Due to the smaller particle size, ceramic injection molding enables to reproduce finer structural details. However, the powder particle size is still much larger compared to the polymer chains. Consequently, powder injection molding shows in general worse performance regarding reproduction accuracy, aspect ratio, and surface roughness (see also in the next section in section 2.4). The ceramic and metal particles in the feedstocks have an abrasive effect on the machine parts, so that specially hardened steel is usually deployed for all machine parts in contact with the feedstock such as the barrel, screw, and nozzle. [28]

An advantage of powder injection molding over subtractive processes like turning and milling is the much lower waste production. The parts are produced close to net shape, finishing steps are hardly necessary. Typical products made by powder injection

molding come from the areas of the automotive industry, household appliances, electronics, and the medical industry. [1]

2.4 Summary and conclusion

Table 2.1 gives an overview of the presented micro molding technologies. Typical numbers for the achievable accuracy, features, and roughness of the processes are listed. Additionally, the main impacts on the tolerances and precision of every technology are briefly summarized in the table. The values in the table prove that it is important to distinguish between materials when dealing with micro injection molding, as the process capabilities and the major influences vary.

Table 2.1: Capabilities of the summarized micro molding processes applied to micro components. The statements are typical values, actual values depend on the machined material, the process conditions, and on the exact process variant.

Molding process	plastics (µIM)	metals (µMIM)	ceramics (µCIM)
feature size	$> 10\,\mu m$	$> 50\,\mu m$	$< 10\,\mu m$
aspect ratio	> 20	> 10	< 15
precision	$> 1\,\mu m$[b] $> 0.1\,\mu m$[c]	$< 10\,\mu m$	$< 3\,\mu m$
roughness (R_a)	$< 0.01\,\mu m$	$< 1\,\mu m$	$< 0.2\,\mu m$
major impacts on tolerance and precision	shrinkage melt viscosity packing	sintering particle size feedstock viscosity powder load	sintering particle size feedstock viscosity powder load
references	[2, 5, 30–32]	[9, 16, 27, 31, 33]	[9, 16, 27, 31, 33]

[b] with conventional injection molding machines
[c] with dedicated micro injection molding machines

3 Process simulations of injection and micro injection molding

Abstract This chapter first deals with the questions what are simulations used for in general and why the injection molding process is simulated. Afterwards, the underlying mathematical models which are applied in the numerical simulations of injection molding are presented. Besides, available software tools, their functions, and their drawbacks are introduced; followed by a greater discussion of the state-of-the-art regarding micro injection molding simulations. Ultimately, the simulation software and supplementary information used in this work are briefly introduced.

3.1 Why simulate the injection molding process?

> "A computer simulation is any computer-implemented method for exploring the properties of mathematical models where analytic methods are unavailable." [34]

In other words, computer simulations can be described in general as the numerical computation of the solution of equations and their related boundary conditions which govern a mathematical model. They are applied to these mathematical models, if an analytic solution is not available or too complex. As physical and mathematical models are available for many issues in engineering and technology, simulations are consequently widely applied in any field of engineering. Simulations cover areas like structural analyses, meteorology process simulations, fluid dynamics, logistics, or electric and electronic circuits to name a few.

Computer simulations are applied because of the following motives which are relevant for this work [35]:

- Simulations enable to investigate systems in detail. In reality, it might not be possible to observe the system for pragmatic reasons, e.g. because the system works too fast or very slow or parts are inaccessible for some reason. Examples are the climate development, chemical reactions, heat transfer, plastic flow, etc.

- Simulations enable to quickly and easily manipulate the investigated system. In reality, these changes are often too costly, too laborious, or simply impossible, e.g. changes of the design of a product, changes in process conditions of a chemical reactor, or the used materials in any construction, etc.
- Simulations enable to investigate systems which do not exist yet and assist the preselection, e.g. different layouts for a building, different configurations of a cooling or electrical circuit, etc.
- Simulations enable to visualize and improve the understanding of the underlying system. In reality, the visualization or implementation of the system might be too costly or too dangerous, e.g. the inside of a combustion engine, training flights, the motion of a mechanical system without building a prototype, the deformation of an object under load, etc.

These reasons can also be applied and transferred to the area of injection molding. In particular, the following goals can thus be derived for simulations of the injection molding process [10, 36–43]:

- shorten the development time and the time-to-market for a new product,
- assist the part design at an early stage in the design process when the molds or tools do not exist yet,
- avoid design errors at the costly mold and subsequently necessary re-engineering actions,
- assist the material selection,
- eliminate the need or reduce the amount of physical prototyping and experiments,
- optimize the part and mold design as well as the parameter settings of the manufacturing process,
- predict and improve the part quality e.g. morphology and properties,
- gain a better understanding of the process characteristics,
- visualize the process and the final product, e.g. possible air entrapment, warpage and shrinkage, weld lines, etc.

In conclusion, simulations are widely applied and accepted as helpful and efficient tool. Due to the complexity of the injection molding cycle, the equipment, and the used materials as well as the increasing requirements on the part quality, process simulations of injection molding are indeed very attractive and relevant and still gain more attention. Process simulations in the plastic injection molding area have been in fact established for decades now and are common practice in the plastic industry, whereas they are still on the rise in the powder injection molding area. Because of

the rising number of applications of micro injection molded components, the interest and demand of simulations in this area increases rapidly, too. [44, 45]

However, carrying out simulations also comes with some drawbacks. It must not be forgotten that the underlying models incorporate usually idealizations, approximations, and assumptions—no matter how realistic or accurate the results might appear. In addition, the underlying model must be understood and there must be evidence to believe in the applicability and validity of the model independently from how good the real data is reproduced. [35]

3.2 Mathematical modeling background

3.2.1 Viscosity of plastics

The micro injection molding process consists of the filling, the packing, and the cooling phase. During the filling phase, the plastic flows into the cavity driven by the applied pressure of the injection molding machine. Hence, the plastic's viscosity is of major importance during the filling. In 1687, Isaac Newton called the viscosity "the lack of slipperiness" of a fluid [42], i.e. the viscosity is the resistance of the fluid to deformation.

Mathematically, the viscosity links the applied shear rate to the shear stress that the fluid experiences. For complex flows, this relationship is given in tensor notation as

$$\boldsymbol{\tau} = \eta \, \dot{\boldsymbol{\gamma}} \tag{3.1}$$

where $\boldsymbol{\tau}$ denotes the shear stress, η the viscosity, and $\dot{\boldsymbol{\gamma}}$ the shear rate.

Newtonian fluids show a strictly linear behavior, i.e. the viscosity is independent of the shear rate. In contrast, polymers are non-Newtonian fluids and therefore, the viscosity is a function of the applied shear rate. When polymers experience shear, two effects come into play leading to a decrease in viscosity, the so-called shear thinning effect: the heat dissipation and the alignment of the polymer chains [46].

In order to mathematically describe the viscosity, the power-law model was introduced in the 1920s [42]. It is one of the simplest and most common models for non-Newtonian fluids. According to the power-law model, the viscosity of a plastic melt depends exponentially on the shear stress and is given as [47]

$$\eta(\dot{\gamma}) = m \cdot \dot{\gamma}^{n-1} \tag{3.2}$$

where m is the viscosity at a shear rate of one reciprocal second and n is the power-law index which are both data-fitted constants. Generally, $n \leq 1$ for plastic melts which reflects the shear thinning effect, $n = 1$ for purely Newtonian fluids, and $n \geq 1$ for shear thickening. This model describes the viscosity of plastics well at high shear

rates. Nonetheless, injection molding is not only a high shear rate process. The shear rate is highest at the wall of the mold and decreases towards the center of the fountain flow where the shear actually vanishes completely and the polymer melt exhibits the so-called zero shear rate viscosity.

Consequently, the power law model is insufficient. Instead, the Cross model is widely applied [37]. This model describes the shear rate dependency of the viscosity over a wide range of shear rates very well, because it combines a Newtonian region at low shear rates with a power-law shear thinning region at higher shear rates [42]. The viscosity is mathematically given by the Cross model as [46, 48]

rates with a power law shear thinning region at higher shear rates [17]. The viscosity is mathematically given by the Cross model as [18, 28]

$$\eta(\dot{\gamma}) = \frac{\eta_0}{1 + \left(\frac{\eta_0 \dot{\gamma}}{\tau^*}\right)^{1-n}} \tag{3.3}$$

$$\eta(\dot{\gamma}) = \frac{\eta_0}{1 + \left(\frac{\eta_0 \dot{\gamma}}{\tau^*}\right)^{1-n}}, \tag{4.3}$$

where η_0 denotes the zero shear rate viscosity and τ^* is the critical stress level at the transition between the Newtonian plateau and the power-law region which is determined by curve fitting. The term $1-n$ describes the slope of the viscosity curve in the power law region when logarithmically plotted versus the shear rate with n being equal to the power law index. The terms of the Cross model and the comparison to the power law model can be found in Figure 4.1.

where η_0 denotes the zero shear rate viscosity and τ^* is the critical stress level at the transition between the Newtonian plateau and the power law region which is determined by curve fitting. The terms $1-n$ describes the slope of the viscosity curve in the power law region when logarithmically plotted versus the shear rate with n being equal to the power law index. The terms of the Cross model and the comparison to the power law model can be found in Figure 4.1.

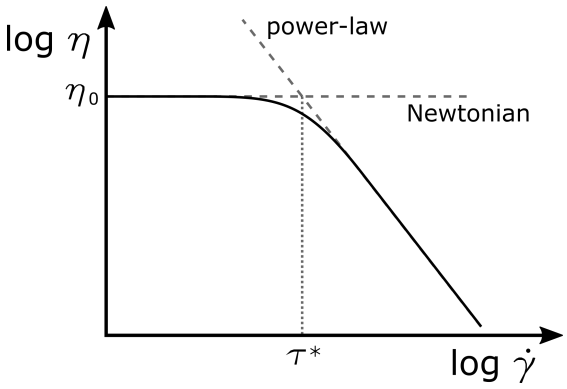

Figure 4.1: Terms of the Cross viscosity model with comparison to Newtonian and power-law fluid.

Figure 3.1: Terms of the Cross viscosity model with comparison to Newtonian and power-law fluid.

In order to understand and simulate the flow of the polymer during the filling phase, it is however not enough to look only at the viscosity. The applied viscosity model must also account for the temperature changes happening during the entire injection molding cycle. The concept of time-temperature superposition can also be applied to the viscosity. The core of the concept is to shift the known viscosity curve at a reference temperature along the time axis in order to gain the viscosity curve at any temperature different from the reference temperature. The shift factor is given by the Williams-Landel-Ferry (WLF) equation which can be also applied to the zero shear rate viscosity to introduce the temperature dependency. This step yields the Cross-WLF model with the zero shear rate viscosity given as [18]

In order to understand and simulate the flow of the polymer during the filling phase, it is however not enough to look only at the viscosity. The applied viscosity model must also account for the temperature changes happening during the entire injection molding cycle. The concept of time-temperature superposition can also be applied to the viscosity.
The concept of time-temperature superposition can also be applied to the viscosity. The core of the concept is to shift the known viscosity curve at a reference temperature along the time axis in order to gain the viscosity curve at any temperature different

$$\eta_0(T) = D_1 \exp\left[-\frac{A_1 (T - T_0)}{A_2 + T - T_0}\right], \tag{4.4}$$

where D_1, A_1, and A_2 are constants, T is the temperature, and T_0 is the reference temperature (which is often chosen as the glass transition temperature of the polymer).

from the reference temperature. The shift factor is given by the Williams-Landel-Ferry (WLF) equation which can be also applied to the zero shear rate viscosity of the Cross model to introduce the temperature. This step yields the Cross-WLF model with its zero shear rate viscosity given as [37, 48]

$$\eta_0(T,p) = D_1 \exp\left[-\frac{A_1\,(T - D_2 - D_3\,p)}{A_2 + T - D_2}\right] \tag{3.4}$$

where A_1, A_2, D_1, and D_3 are constants, T is the temperature, and $D_2 = T_0$ is the reference temperature[1]. The viscosity is also dependent on the pressure as given in Equation 3.4. In most simulations or material models, this pressure dependency is commonly neglected by assuming $D_3 = 0$. The pressure dependency is nevertheless quite relevant, because the injection molding process exhibits often high injection pressures. [37]

Besides the aforementioned, more models exist to describe the viscosity of plastics. Common examples which will not be discussed in more detail in this work are the Carreau or the Carreau-Yasuda model which are described for instance in [47] or the second-order model used by Autodesk and described in [49].

3.2.2 Viscosity of powder feedstocks

Powder feedstocks can be understood as extremely filled plastics. In fact, the binder provides the viscous properties and acts as carrier for the rigid powder particles. The powder particles contribute though to a large extend of the volume of the feedstock. The feedstocks therefore show noticeably different flow properties compared to pure plastics. The powder particles influence the flow and viscosity because of the complex interaction between the binder and the particles. In contrast to the binder, they can be assumed as being incompressible and carry much more momentum owing to their weight. Furthermore, their size and shape affect the viscosity.

As a consequence of these differences, the aforementioned models for the viscosity are insufficient to describe the viscous nature of feedstocks properly. In literature, different or modified viscosity models are proposed. The important Cross-WLF model with Herschel-Bulkley extension is based on the Cross-WLF model shown in Equation 3.4. The difference is depicted in Figure 3.2. The Herschel-Bulkley extension accounts for the increase in viscosity and a Bingham-like behavior of the feedstocks at low shear rates. In fact, the velocity profile of feedstocks, the so-called plug flow, looks more like an oblate parabola. This is due to the increase in viscosity in the center of the shear-governed fountain flow in injection molding.

[1] This reference temperature can be any temperature, but it is often chosen as the glass transition temperature of the polymer.

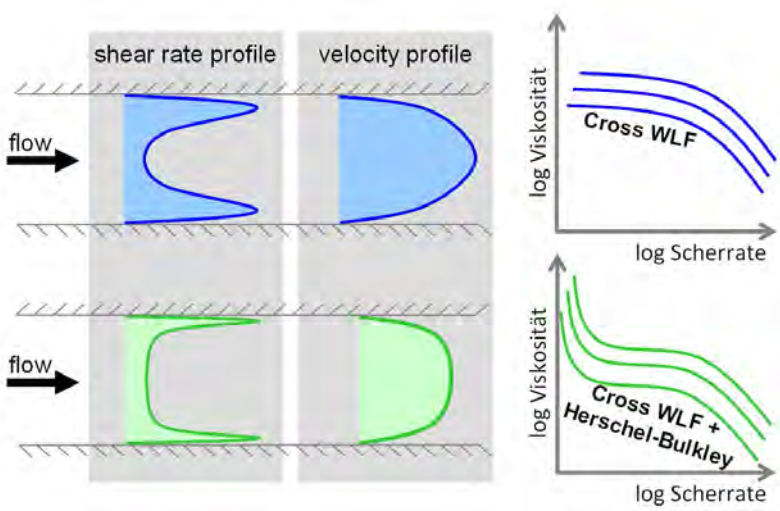

Figure 3.2: Comparison of shear rate profile, velocity profile, and viscosity of the simple Cross-WLF viscosity model (used for plastics) and the Cross-WLF viscosity model with Herschel-Bulkley extension (used for powder feedstocks to fit the viscosity increase at low shear rates) [45].

Mathematically, the shear stress τ differs in the Herschel-Bulkley model from Equation 3.1 by the addition of the yield stress τ_0 below which there is no flow. It is thus described as [48, 50]

$$\tau = \tau_0 + m\,\dot{\gamma}^n \tag{3.5}$$

where m is the consistency index (corresponds to the viscosity in Equation 3.1), $\dot{\gamma}$ the shear rate, and n the flow index. The viscosity of the Herschel-Bulkley model is likewise given as an extension of Equation 3.2 as

$$\eta(\dot{\gamma}) = \frac{\tau_0}{\dot{\gamma}} + m\,\dot{\gamma}^{n-1}. \tag{3.6}$$

Another proposed model is the so-called equivalent-viscosity model which takes the actual particle size and size distribution of the powder into account. The viscosity is given as [51]

$$\eta(\dot{\gamma}) = \frac{A\,\eta_{\text{app}}}{\dot{\gamma}^n}\frac{d_{90}}{d_{10}\,d_{50}}\,\exp\left(\frac{B}{T}\right)\left[\frac{1-\phi}{\left(1-\frac{\phi}{\phi_{\max}}\right)^2}\right] \tag{3.7}$$

where A and B are data-fitted parameters, η_{app} is the apparent viscosity, d_{10}, d_{50}, and d_{90} are the particle diameter of 10 %, 50 %, and respectively 90 % of the particles, ϕ is the powder volume fraction, and $\phi_{\max}$ is the maximum powder volume fraction.

The simplified Krieger-Dougherty viscosity model has fewer parameters. This model is suitable for the prediction of the viscosity of feedstocks with high powder load.

The viscosity of the feedstock η is given by the viscosity of the binder η_b according to [52, 53]

$$\eta(\dot{\gamma}) = \frac{\eta_\mathrm{b}(\dot{\gamma})}{\left(1 - \frac{\phi}{\phi_\mathrm{max}}\right)^2}. \tag{3.8}$$

It must be mentioned that the effect of powder-binder segregation is not accounted for by any of the presented models. For the identification of the powder-binder segregation, multi-phase material models would be necessary [9]. This effect can nonetheless locally influence the viscosity of the feedstock. The models do not either explicitly comprise any particle interaction which can in fact lead to shear thickening of the feedstock.

3.2.3 Flow of plastics

The flow of molten plastics is of anisothermal, compressible, and viscous nature and can consequently be described by the Navier-Stokes equations. The Navier-Stokes equations are a system of non-linear partial differential equations. They are the fundamental mathematical model in general fluid dynamics and consist of:

- the continuity equation which describes the conservation of mass,
- the momentum equation which describes the conservation of momentum,
- the energy equation which describes conservation of energy.

These equations govern also the simulation tools for injection molding. The continuity equation is commonly given by [54]

$$\frac{\partial \rho}{\partial t} + \boldsymbol{\nabla} \cdot (\rho \, \boldsymbol{u}) = 0 \tag{3.9}$$

with the density ρ, and the velocity $\boldsymbol{u}$ in vector notation. The momentum equation is ordinarily formulated as [42]

$$\rho \frac{\mathrm{D}\,\boldsymbol{u}}{\mathrm{D}t} = -\boldsymbol{\nabla}\, p + \boldsymbol{\nabla} \cdot \boldsymbol{\sigma} + \rho \, \boldsymbol{g} \tag{3.10}$$

with the pressure p, the stress $\boldsymbol{\sigma}$ in tensor notation, and the gravity $\boldsymbol{g}$ in vector notation. Finally, the energy equation, sometimes also referred to as heat-transfer equation, is commonly given as [42]

$$\rho \, c_\mathrm{p} \frac{\mathrm{D}\,T}{\mathrm{D}t} = \beta \, T \frac{\mathrm{D}\,p}{\mathrm{D}t} + p \, \boldsymbol{\nabla} \cdot \boldsymbol{u} + \boldsymbol{\nabla} \cdot (\kappa \, \boldsymbol{\nabla}\, T) + \boldsymbol{\sigma} : \boldsymbol{\nabla}\, \boldsymbol{u} \tag{3.11}$$

with the specific heat capacity c_p at constant pressure, the absolute temperature T, the coefficient of volume expansion β, and the thermal conductivity κ.

Semi-crystalline polymers show a sudden and significant increase in viscosity at their melting temperature due to the incipient formation of crystalline domains inside the material. The aforementioned models do not comprise this viscosity increase due to crystallization [42].

3.2.4 Thermodynamics

Besides the viscosity, information about the thermodynamic properties of materials is necessary for computer simulations of the injection molding process. These can be derived from the equation of state of the material which links the pressure, the specific volume (i.e. the inverse of the density), and the temperature. It is therefore also called pvT data. [42]

For plastics, this data is usually provided as pvT diagrams which show the specific volume v as a function of the pressure p and the absolute temperature T. The commonly used model for describing the curves of such a diagram is the 2-domain Tait model which is mathematically given as [1, 24]

$$v(p,T) = v_0(T) \cdot \left[1 - C \, \ln\left(1 + \frac{p}{B(T)}\right)\right] + v_\mathrm{t}(p,T) \tag{3.12}$$

where $C = 0.0894$ is a universal constant, and the function $B(T)$ denotes the pressure sensitivity of the material. The two domains are equal to the solid and molten phase of the plastic which are separated by the transition temperature T_t. The transition temperature is again given as

$$T_\mathrm{t} = b_5 + b_6 \, p. \tag{3.13}$$

In the lower temperature region, i.e. the solid phase with $T \leq T_\mathrm{t}$, the missing functions of Equation 3.12 are given as

$$\begin{aligned} v_0(T) &= b_{1\mathrm{s}} + b_{2\mathrm{s}} \, (T - b_5) \\ B(T) &= b_{3\mathrm{s}} \, \exp\left[-b_{4\mathrm{s}} \, (T - b_5)\right] \\ v_\mathrm{t}(p,T) &= \begin{cases} b_7 \, \exp\left[b_8 \, (T - b_5) - b_9 \, p\right] & \text{if semi-crystalline} \\ 0 & \text{if amorphous} \end{cases} \end{aligned} \tag{3.14}$$

and the upper temperature region, i.e. the molten phase with $T > T_\mathrm{t}$, is respectively described by

$$\begin{aligned} v_0(T) &= b_{1\mathrm{m}} + b_{2\mathrm{m}} \, (T - b_5) \\ B(T) &= b_{3\mathrm{m}} \, \exp\left[-b_{4\mathrm{m}} \, (T - b_5)\right] \\ v_\mathrm{t}(p,T) &= 0 \end{aligned} \tag{3.15}$$

where the unknowns $b_{1\mathrm{s}}$, $b_{2\mathrm{s}}$, $b_{3\mathrm{s}}$, $b_{4\mathrm{s}}$, $b_{1\mathrm{m}}$, $b_{2\mathrm{m}}$, $b_{3\mathrm{m}}$, $b_{4\mathrm{m}}$, b_5, b_6, b_7, b_8, and b_9 in Equation 3.14 and Equation 3.15 are all data-fitted coefficients. The data is usually collected from measurements with rheometers. Because of the ease of use and the ability to reproduce high shear rates, high-pressure capillary rheometers are often deployed.

3.3 Simulation software

3.3.1 Commercially available software packages

Process simulations in the plastic injection molding area have been established for decades, whereas they are still on the rise in the powder injection molding area [45]. Nowadays, different sophisticated software packages are commercially available on the market. They offer the possibility to simulate the conventional injection molding process, but also related processes like multi-component injection molding, rubber molding, gas-assisted molding, foam molding, etc. Some of the most common software packages today are:

- Autodesk Simulation Moldflow®, made by Autodesk, San Rafael, CA, USA,
- Moldex3D®, developed by CoreTech System, Chupei City, Taiwan,
- SigmaSoft®, developed by SIGMA Engineering, Aachen, Germany,
- Simpoe-Mold®, made by Dassault Systèmes, Vélizy-Villacoublay, France.

The equations and models presented in section 3.2 are the basis for the numerical simulation of the injection molding process. The listed software tools use the Navier-Stokes equations to describe the flow of the plastic during the injection molding process. The contributions of gravity and inertia in the flow are considered in simulation software packages, and options to switch the effects on or off are offered.

The pvT data is described by the 2-domain Tait model. For the viscosity, the Cross-WLF model is commonly applied, because it fits experimental data from material characterization the most accurate [48]. SigmaSoft® uses the Cross-WLF model with Herschel-Bulkley extension and provides therefore more accurate results for the simulation of the powder injection molding process according to the manufacturer [10, 45, 55, 56].

In the field of injection molding, process simulations are based on the method of finite element analysis (FEA). This is a general method to numerically solve a system of partial differential equations and widely used in all engineering disciplines. The listed software packages exploit the finite difference method (FDM) and the finite element method (FEM).

In these methods, the investigated model is divided into small elements of finite size. The splitting up of the model is usually referred to as “meshing”. The accuracy of the interpolation can be influenced by the mesh density, i.e. the edge length of the

elements. Furthermore, the approximation of curved surfaces is related to the chord angle and chord height control[2].

The meshing procedure goes along with the discretization of the governing differential equations. Together with the corresponding boundary conditions, the discretized partial differential equations can be solved in these small domains, yielding in the sum a numerical approximation of the solution for the continuous partial differential equations of the entire model. In this way, the software calculates the behavior of the plastic flow, the temperature development, the warpage of the plastic part, etc. The flexibility in handling complex geometries and irregular boundaries is a major asset of the FEM method [43].

What is referred to as "model" in the following is the discretized representation for FEM analysis of the entities that are to be investigated by means of the simulation. Preparing the model as well as the computation precision are therefore not dependent on material or process information.

3.3.2 Meshing strategies

Following up on the first aspect of the previous section, the meshing, i.e. the discretization of the investigated geometry, is the first step, when creating the simulation model. The mesh is of eminent importance for the accuracy of the simulation, since it influences the goodness of the numerical results and also the necessary computation time. In general, the numerical accuracy and the computation time increase with decreasing specific element edge length or decreasing mesh density. For one and the same geometry, the resulting mesh can look very different, depending on the settings of the numerous meshing parameters. Two approaches for the meshing can be defined:

1. Homogeneous mesh
   The homogeneous mesh shows approximately the same mesh size all over the modeled geometry, independently from the actual size of the geometry's entities. It is suited for systems which exhibit small differences in the dimensions of single entities and between the entities. The major drawback is the necessary application of fine meshes, if small geometries are contained in the model and the size varies considerably between the entities. This leads to a very large number of elements for the total system and excessive computation times. Coarse meshes provoke losses in the reproducibility of the shape of the investigated features and also numerical accuracy.

[2] "Chord" denotes a straight line segment connecting two points on any curve. The chord height describes the maximum distance allowed between the chord and the approximated curve. The chord angle describes the angle formed by the two lines through the end points of the chord and the center of curvature. The smaller the chord height or angle, the finer the mesh of curved surfaces.

2. Multi-scale mesh
   The multi-scale mesh combines a large span of mesh sizes. The mesh density is adjusted to the size of the meshed geometry and entities. This ensures the appropriate mesh size for all included entities and is a compromise between the necessary fine mesh for small entities and the adequate coarse mesh for large entities.

Micro injection molding exhibits in general large variations in the size of the involved parts. The actual plastic part has very small dimensions or micro features, whereas machine and mold parts are of conventional size. The application of a multi-scale mesh extending several orders of magnitude regarding the mesh size is therefore inevitable.

3.3.3 Mold and cooling analysis

Apart from the actual part, the process simulations of injection molding can also comprise the implementation and analysis of the actual mold block and the whole cooling system. The performance and properties of the cooling circuit itself, but also its influence on the filling and part quality can be examined. This can be done in a later design phase during product development, when information about the planned mold concept is available.

ASMI offers the option to run an additional cooling analysis. The computed results of the cooling analysis like temperature distribution in the mold block are taken into account for the subsequent filling, packing, and warpage analysis. Moreover, computational fluid dynamics (CFD) enable to investigate the cooling circuit itself and gain knowledge of the coolant, the flow, and the circuit layout.

However, there will be scenarios in which information about some or all entities except for the part is not available, e.g. in the early design phase of a new product when no mold is existent yet. In this case, the actual mold cannot be considered in the model. The software assumes instead a virtual, infinitely large mold block. Mold temperature and mold material must hence still be specified. Furthermore, the software assumes a perfectly vented mold as default in either case, if no dedicated venting analysis is performed.

3.4 State-of-the-art of micro injection molding process simulations

3.4.1 Issues of micro injection molding simulations

The aforementioned software packages have in common that they are officially made for conventional injection molding. However, micro injection molding is not just simply scaling down the conventional injection molding process. Relevant microscopic effects are not or only insufficiently implemented. This causes the drawback that up till now applying these simulation packages to micro injection molding still results in improper quantitative results. There are major differences to conventional injection molding which significantly influence the accuracy of the simulations of micro parts. [1, 2, 26, 36, 38, 44, 57–60]

1. There are dedicated micro injection molding machines for improved metering and more precise injection. Hence, these machines show different characteristics than conventional machines—the standard for process simulations. Micro machines show for instance a different geometry regarding the feeding and injection part of the machine with pistons instead of screws for the injection, or they are equipped with electric motors for better response, higher acceleration, and better position accuracy.
2. Due to the larger surface-to-volume ratio and the smaller thickness, the no longer negligible surface roughness and the resulting possible changes in the heat transfer coefficient, the cooling and heat loss happens much faster for micro parts. In addition, the morphological structure of the micro parts can change and the frozen layer at the part surface accounts for a larger share of the total volume.
3. Microscopic effects such as wall-slip, surface tension, viscous heating, or microscale viscosity might become relevant.
4. The commonly used 2.5-dimensional Hele-Shaw flow approximation might not be valid, and full 3D modeling is recommended.
5. The small cavities lead to high shear rates with all possible consequences like polymer degradation and shear heating or the need for the extrapolation of measured material data.

3.4.2 Simulation and validation of polymer micro injection molding

In order to investigate the differences of micro injection molding and possibly improve the simulations results, a multitude of studies on the process and simulation validations have been carried out in science and research in the recent years.

The reported simulation investigations and validations are often based on simple test geometries like plaques of constant thickness. This enables again the application of mid plane or dual domain meshes which reduces the complexity of the model and the necessary computation time. However, mid plane and dual domain were found to be insufficient for the accurate simulation of micro parts by several groups of researchers, and more advanced 3D models were recommended for superior performance. [6, 40, 46, 61–63]

Further comparative studies have shown the suitability of simulations to identify the most important process parameters linked to the part quality and to defects like air entrapment [46, 61, 64–66].

As summarized by Choi and Kim [63], in-house code is often applied for the simulation of micro injection molding at universities. The advantages such as implementation flexibility, overcoming software limitations, and achieving improved results come however for a price; the industrial interest and applicability as well as reproducibility of the results are significantly reduced.

Costa et al. [36] published best practice strategies with experiments on dedicated micro molding machines and a simple micro test part. The researchers pointed out several vital aspects, such as the importance of the right meshing parameters when creating the simulation model, the visualization of the flow front as a supportive validation method, or improved pressure prediction by the implementation of the nozzle of the injection molding machine.

Tosello et al. [18, 60] reported validation studies with time-controlled and pressure-controlled simulations and a model comprising the part and the feed system; giving the right trends, but still underestimating the real injection time and injection pressure. Furthermore, the molding and experimental short shots were monitored to gain input data for the simulations which yielded good prediction of the injection time, pressure, part mass, and flow length.

Cramer et al. [44] and Nguyen-Chung et al. [67, 68] emphasized the importance of proper boundary conditions of the simulation. The focus of the first study was the necessity for extensive material characterization and the modification of the deployed software for the incorporation of relevant microscopic effects, similar to the aforementioned in-house approaches. The latter studies dealt with the adaptation of the heat transfer coefficient (HTC) in micro injection molding. In a reverse engineering approach, the HTC was investigated for cavity thicknesses of 200 µm and

500 µm and for multiple injection speeds from 20 mm s^{-1} to 200 mm s^{-1}. The HTC increased with decreasing cavity thickness as typically assumed for micro cavities, but decreased with increasing injection speed, leading to lower values at typical speeds for micro injection molding. The determined HTC values were in the range from adiabatic up to 25 000 W m^{-2} K^{-1}.

As summarized by Heinle and Drummer [69], the HTC depends on the surface roughness, the contact pressure, the thermal conductivities of the bodies in contact, and the interstitial fluid, and the time-dependency of the heat transfer. In injection molding, the significance is also determined by the dimensionless Biot number *Bi* which depends on the HTC h, the part thickness t, and the thermal conductivity λ of the plastic according to [69, 70]

$$Bi = \frac{t}{2}\frac{h}{\lambda}. \tag{3.16}$$

The HTC cannot be disregarded, if the Biot number is low. According to Equation 3.16, this can become true, when the part thickness is small like in micro molding or when the thermal conductivity of the material is high like for polymers and feedstocks with thermally conductive fillers.

However, Nakao et al. [71] actually measured the heat flux in micro cavities of less than 10 µm thickness and determined the HTC as 850 W m^{-2} K^{-1} and 2700 W m^{-2} K^{-1} during the filling phase of polystyrene (PS) and polymethyl methacrylate (PMMA), respectively. These values are lower than the default values of about 5000 W m^{-2} K^{-1} often assumed in conventional injection molding and in simulation software and are hence in contrast to the frequent assumption of higher HTC in micro molding. Furthermore, Tosello et al. [60] presented successful simulations and flow validation of a 1 mm thick miniaturized part. The simulations were run with the default values of the HTC. In conclusion, the adaptation of the HTC was not necessary in this order of magnitude of cavity thickness which is comparable to the micro plastic parts in this thesis. As a consequence of all the aforementioned facets, the HTC value was not adapted in the present work and kept at the default values.

This Ph.D. thesis followed up on the latest research by further elaborating on and combining the necessary aspects of the simulation validation, such as investigations on the influence of the applied mesh or simulated venting, the implementation of the machine geometry and behavior, the collection and application of measured, comprehensive material data, and the application of sound models and simulations to complex, real-life prototypes of industrial relevance as compared with the reviewed literature where researchers addressed simplified test geometries.

3.4.3 Simulation and validation of micro powder injection molding

The simulations of the powder injection molding process address the whole process chain of mixing, molding, debinding, and sintering. The mixing is essential for the homogeneity of the feedstocks properties and thus the uniformity of the final part. The debinding is crucial for material defects. The sintering is an important step regarding the final shape and properties of the manufactured component [27, 43]. This brief discussion is however limited to the process simulations of the molding step. Regarding the molding step, the simulation and validation efforts are less advanced than in polymer micro injection molding, but the paid attention increases noticeably [16].

Examinations with conventional software tools exist, but predominantly various in-house software approaches were reported in the literature. Examples for these special approaches are for instance new material models based on the smoothed particle hydrodynamics (SPH) with added yield stress and powder segregation for the prediction of the powder distribution as summarized by Piotter [9] or the dissipative particle dynamics (DPD) with a discretized continuum fluid as discussed by Löhe and Haußelt [1]. The simulations thus happen rather on a scientific level with individual code having the aforementioned drawbacks than on an application-oriented level with industrially applied and accepted software. This circumstance can be attributed to the special characteristics of feedstocks and the limitations of available software regarding feedstocks and micro parts [1, 9, 16, 27, 43, 51, 72, 73].

Similar to micro injection molding, these simulation studies—whether conducted by means of commercial or in-house software—are however often of simple nature and based on test parts, because the topic is still young. Heldele et al. [73] for instance reported the successful application and validation of DPD simulations on a simple strip. Simple specimen for tensile tests were investigated experimentally and by simulations by Quinard et al. [72].

An example for a more complex geometry examined by commercially available software was illustrated by Piotter et al. [74] who showed the application of simulations to a micro gear wheel made by powder injection molding. The researchers found the numerical results insufficient in comparison to the experimental values, but pointed out that the simulation can be quite a helpful tool to optimize the part design and identify possible issues like powder-binder segregation due to high shear rates.

Furthermore, Martin et al. [75] recently published the manufacturing of miniature turbine stators by powder injection molding where simulations were bolstered up by prior material characterization and subsequently successfully applied for studying the feasibility and process window of the molding. Likewise, Lenz et al. [76] reported material characterization and the application of simulations for the successful part

design of an engine part. Nevertheless, both parts could be rather considered as miniaturized parts than true micro parts.

Also, the lack of material data for reliable simulations and of methods for acquiring such data is criticized [45], although there are plenty of studies available about either the rheological or thermal properties of feedstocks, as discussed later in chapter 4. Comprehensive studies are hardly available. Hence, it seems like the link between the numerous publications on the characterization of powder feedstocks on the one hand and the simulation trials on the other hand has not yet been truly established.

SIGMA Engineering, the manufacturer of the simulation software SigmaSoft®, published a validation study in 2012 and pointed out the necessity of adapting the viscosity model for feedstocks. Simulations and experimental short shots of a simple ladder part were compared [45, 55, 56].

The available number of studies employing common software tools is thus narrow. The present work connects the material characterization to the process simulations. The available knowledge on the simulation and validation of powder feedstocks is expanded to new materials and widespread simulation tools. The simulations are applied as supportive tool for the design of micro parts.

3.4.4 Recommendations for micro injection molding process simulations

In order to improve the numerical results of the micro injection molding process simulations, several aspects could be derived from existing work in literature as important [36, 44, 60, 67]:

1. The mesh size should be adapted to the dimensions of the investigated micro part and is hence much smaller than in conventional injection molding.
2. The usage of temperature and pressure dependent data of material properties is recommended.
3. Detailed material characterization with data at high shear rates and pressures is recommended.
4. Coupling and modeling of part and entire mold should be done.
5. The implementation of the machine characteristics like the speed profile, of the geometry of the machine nozzle, and of the used barrel volume is recommended.

The researchers pointed out necessary adaptations for the successful simulation of the micro injection molding process. However, merging all the mentioned aspects has not been done yet. This Ph.D. project followed up on this shortcoming and combined the mentioned aspect. The present work outlines in the following chapters

how to take the relevant aspects into consideration and apply it in the design and manufacture of micro parts.

3.4.5 Systematic concept and methodology for the concurrent development of molded micro parts

The combination of the aforementioned aspects being relevant for micro molding process simulations as well as the work and findings of this Ph.D. project have led to the analysis of all elements that should be taken into account for the development of new molded micro parts. It was found that a broad spectrum of factors can become relevant and play a very essential role in the entire part design, development, and manufacturing. Most aspects can be found in conventional injection molding, as well, but they are not of such great importance.

Hence, it is strongly believed that solely a holistic and concurrent approach can increase the value of molded micro products and enhance part quality. Consequently, such an approach—consisting of a systematic concept about the holistic consideration of the involved aspects in the part and mold development as well as of a systematic methodology for the concurrent development of molded micro products, in particular micro-patterned components—has been elaborated and is proposed to fully exploit the potential of micro injection molding and the resulting products in the near future.

The proposed concept can be seen as the framework of this Ph.D. project. The entire work and the presented chapters will deal with some of the considered aspects. The overview of the concept with all the treated facets is depicted in Figure 3.3. In compliance to the project objectives and the tackled research gaps, the concept will thus address aspects such as material characterization, modeling, testing, and selection, the treatment of the injection molding machine, the design of the part and the corresponding feed system, examinations on the part quality, simulation validations, mold conception and manufacture, as well as the analysis of the mold's cooling system and its effect on the part quality.

Concurrent engineering, sometimes also called simultaneous engineering, is not a new concept. After being applied already for many years, one of the first concrete definitions was presented by Pennell and Winner [77] and Pennell et al. [78] in 1989 where

> "Concurrent engineering is a systematic approach to the integrated, concurrent design of products and their related processes, including manufacture and support."

This definition is still valid and picked up today or concurrent engineering is interpreted in very akin ways in modern literature as for instance presented by Stjepandić et al. [79, 80]. Concurrent engineering is commonly characterized by promoting higher

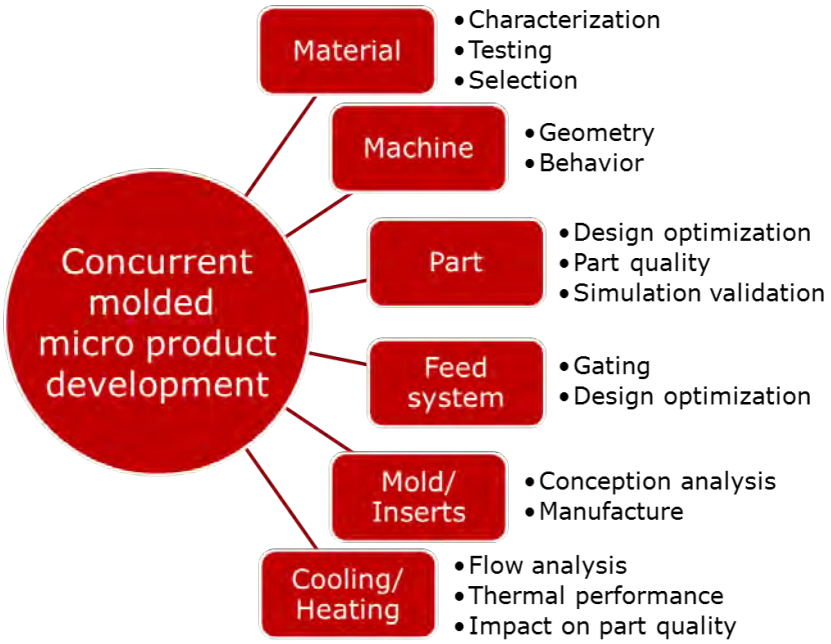

Figure 3.3: Proposed compilation for the systematic concept and its aspects for the concurrent development of molded micro parts.

productivity, lower costs, shorter product development time and time-to-market. Based on this definition, the methodology for the concurrent engineering and design of micro molded components is introduced in this work. The diagram in Figure 3.4 shows the course of action and interconnections of the single steps of the methodology. The core concept is linked to the previously mentioned comprehensive consideration of all relevant elements and leads to the concurrent engineering design of part and mold strongly supported by computer simulations. The concurrent engineering design thus deals with the issues of the feasibility, the moldability, the structural integrity, and the material choice of part and mold or in other words simultaneously with the design, manufacture, and process.

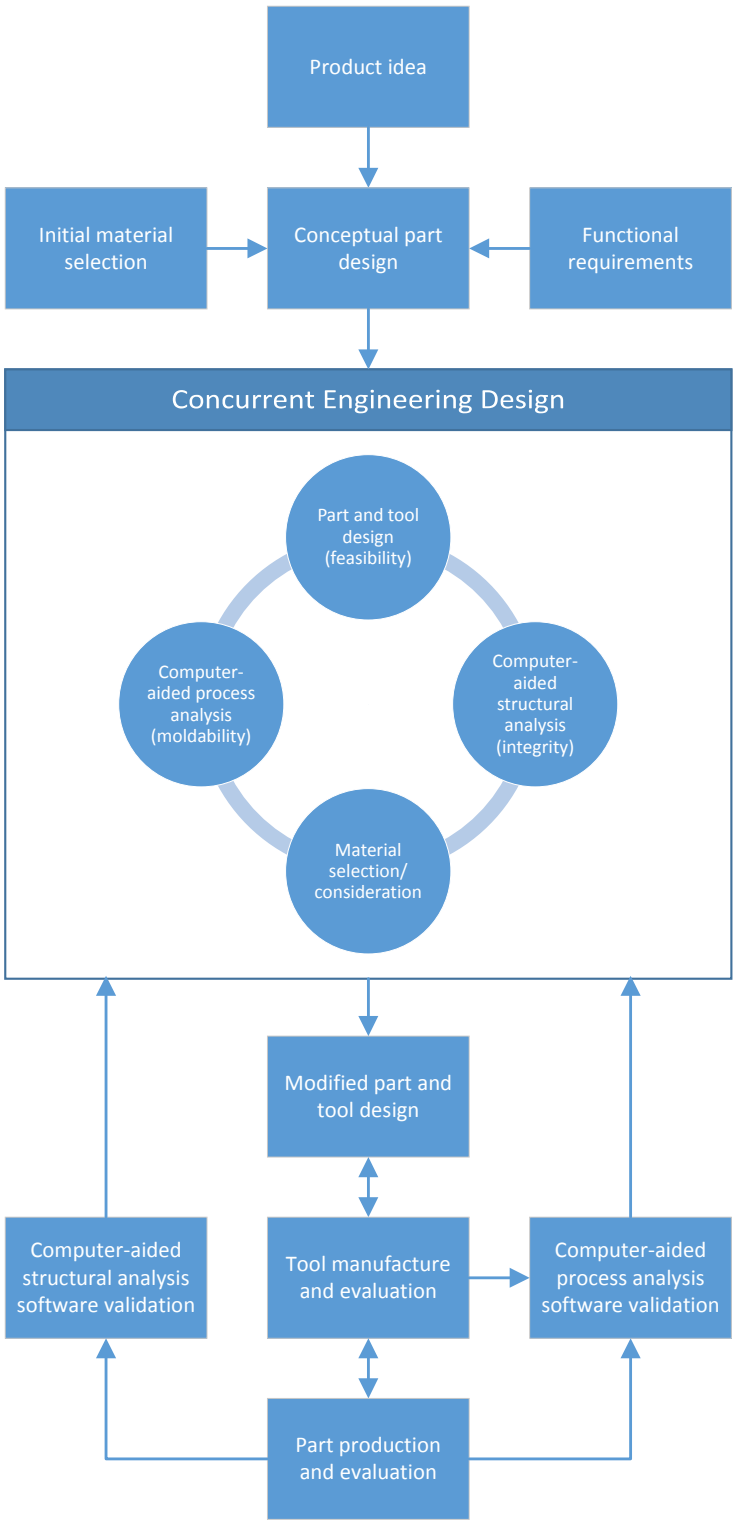

Figure 3.4: Proposed flow diagram for the systematic methodology for the concurrent development of molded micro parts.

3.4.6 Software and standard settings for this work

In this work, the software Autodesk Simulation Moldflow Insight® (ASMI) in the versions 2013 to 2015 was used for the presented simulations.

All investigated parts were analyzed using the 3D domain, so that any reported settings apply to 3D meshes and simulation models. The simulation settings are kept at the default value of the software, if not otherwise specified.

This includes for instance the value of the HTC which is kept at $5000\,\mathrm{W\,m^{-2}\,K^{-1}}$ and $2500\,\mathrm{W\,m^{-2}\,K^{-1}}$ in the filling and packing phase, respectively. An adjustment was assumed to not be necessary as discussed in subsection 3.4.2. The HTC depends on the surface roughness of the mold, but simulation software does in general not allow to model the surface roughness and its influence on the HTC at cavity-mold or cooling-mold interfaces.

The contributions of gravity and inertia were enabled for all simulations by default—despite the commonly accepted aspect that gravity is negligible for micro parts [24, 47, 48, 81, 82]. The significance of inertial forces is often assumed inferior to viscous forces or surface tension in conventional and micro injection molding. Yet, this issue is discussed controversially, especially in powder injection molding because of the heavy powder [1, 28, 48, 63, 81, 83].

The injection molding process analysis by means of FEA requires the meshing or discretization of the simulated entities. The preparation of a functional mesh with the appropriate mesh dimensions is essential, as also pointed out in section 3.3. The application of a multi-scale mesh was a central issue in this work. The mesh preparation included always the same procedure, comencing first with an assessment of the right mesh size depending on the dimensions of the part and the local features. As a rule of thumb, the aim was to get a mesh with about ten elements through the thickness of the meshed section. However, this rule of thumb could not always be followed for practical reasons. First, the software has a lower limit in the element edge length setting of the mesh. Since the meshing was applied to micro features, this limit could be easily reached. Second, choosing the element edge length larger, so that less than ten elements through the thickness are created, might be necessary to cap the number of elements and allow for computation in an economically reasonable time span. The final choice of the mesh and the element edge length was done by trial and error in an iterative process:

1. The local element edge length was assigned to the faces of the CAD models of the investigated entities.
2. The mesh was created and a visual inspection was conducted.
3. If the mesh refinement was not satisfactory, i.e. the number of elements through the thickness of the inspected section did not meet the requirements, the mesh

was discarded and the local element edge length was adapted accordingly, starting again at the beginning of the

Moreover, ASMI provided an automatic mesh inspection which would have come up with a warning, if the mesh refinement was lower than the value required and set by the user.

It should be pointed out that remeshing the existing mesh and hence creating elements with shorter edge length was in general not adequate. The reason is that the originally created mesh determines about how well the CAD surfaces are reproduced. Creating a coarse mesh and successively adapt the mesh refinement by multiple remeshing steps would have led to an appropriate mesh size, but the contour fidelity of the mesh compared to the CAD surfaces would have suffered.

Furthermore, the first step of the meshing is in general choosing the right mesh type [49]:

- Mid plane mesh: one-dimensional representation of the part, the thickness is represented by a thickness value applied to the mesh elements, suitable for fully thin-walled parts.
- Dual domain (surface) mesh: surface representation of the part as a hollow body with a surface shell, the thickness is equal to the distance between opposite surfaces of the mesh, suitable for thin-walled parts with minimum lateral dimensions being at least four to ten times larger than the thickness at any local region of the part.
- 3D mesh: volume mesh with solid tetrahedral elements, suitable for chunky parts with varying thickness and features with lateral dimensions smaller than four times their thickness.

All demonstrators investigated in this work can be classified as micro-patterned or micro precision parts. The application of a 3D mesh is crucial, as they all show large variations in thickness or features where the lateral dimensions and the thickness are of similar size.

The optimization of the mesh was also done by means of the mesh statistics. It was ensured for any of the presented meshes that the orientation of the mesh elements was correct and that there were no free or intersecting elements. Moreover, the aspect ratio (i.e. the ratio between the longest edge and the height perpendicular to that edge) was ensured to be below the recommended value of 50:1 [49]. The match mesh percentage is only relevant for Dual Domain meshes and was therefore neglected.

3.5 Summary and conclusion

In conclusion, simulations are a powerful engineering tool where the virtual investigation and manipulation of the system or process is practicably impossible or easier, less expensive, and less dangerous than performing the investigations or changes on the real system or process.

Process simulations are commonly applied in the area of conventional injection molding where they are beneficial part of the regular design process. Similar to other fields of engineering, they assist the product development regarding material selection, design, prototyping, and understanding of the process.

This chapter showed the basic mathematics that work in the background of the nowadays available simulation software. The viscosity is modeled by the Cross-WLF model which captures well the nature of plastics. Nevertheless, the Herschel-Bulkley extension is recommended to be added to the Cross-WLF model for the proper modeling of powder feedstocks. Alternative viscosity models exist and are subject of current research.

The Navier-Strokes equations are the basis of general fluid dynamics and are also applied for describing the flow of plastics and feedstocks. The thermodynamics of the injection molding process is usually treated by the 2-domain Tait model which describes the equation of state of the material in pvT diagrams.

Commercially available software tools were introduced. However, they are made for macroscopic parts and still show limitations in the capability to handle micro parts and powder injection molding. Consequently, process simulations are not as widely applied in micro and powder molding. Microscopic and powder-related effects or the characteristics of dedicated micro molding machines are still insufficiently implemented. The modeling strategies must be adapted to the special needs of micro parts to predict the nature of micro molding more correctly.

The state-of-the-art in the emerging field of application and validation of process simulations in the area of micro polymer and powder injection molding was discussed. The influence of microscopic effects and the necessity of their implementation is still being discussed and investigated in the scientific community. Available publications on this topic deal rather with simple structures and do not link the material model with the simulation model in powder injection molding. In polymer micro injection molding, attention is paid to many facets of the injection moldings system and its simulation, but a fully comprehensive concept has still not been presented. Many approaches also exploit in-house code which does not have the prospect of applicability and attention in the industry.

In conclusion, the present Ph.D. thesis contributed to expand the boundaries beyond the currently existing state-of-the-art in the field of high accuracy micro injection molding simulation boundaries. The material characterization and the process

simulations are combined for superior performance. Moreover, the simulations are run with commercially available and industrially accepted software and were applied to complex, industrially relevant prototypes.

4 Materials and material characterization

Abstract First, the state-of-the-art in material characterization and the material properties that are necessary for running a process simulation in injection molding are described. Furthermore, the materials used throughout the present PhD project are introduced. The materials comprise plastics and powder feedstocks. The final part of the chapter deals with the different aspects of the conducted, broad material characterization of the powder feedstocks.

All the experiments in connection to the characterization of the powder feedstocks were carried out during the external stay at the Karlsruhe Institute of Technology (KIT), Eggenstein-Leopoldshafen, Germany.

4.1 State-of-the-art

Understanding material properties is essential for the successful processing and simulation of the material in conventional and micro injection molding. Knowledge about the material helps to improve part quality and to reduce molding defects [84, 85]. Therefore, the determination of material properties of unfilled and filled polymers as well as feedstocks was always important in connection with injection molding technology.

Hence, much attention is paid in research to the whole spectrum of material properties of mainly powder feedstocks and filled plastics: rheological properties, heat conductivity and capacity, or pvT data. Still, the investigations focus even until today only on parts of all relevant material properties—mostly either on the rheological or thermal aspects.

Regarding the rheological properties, rotational rheometers are often applied for the determination of dynamic viscoelastic properties. Capillary rheometers are however the work horse for the collection of viscosity and pvT data [48]. Still, the connected data interpretation often exhibits deficiencies in the application of vital data correction methods (discussed in section 4.9) [85]. The thermal properties of feedstocks are measured by means of methods like the differential scanning calorimetry (DSC)

or laser flash analyses. Mechanical properties can be determined by established approaches like tensile or compression tests.

Filled polymers were for instance subject in research, as Boudenne et al. [86] and Weidenfeller et al. [87] presented work on the determination of the thermal properties of filled polypropylene in 2004. Thermal properties of a metallic feedstock were for instance published in 1999 by Kowalski and Duszczyk [88].

Many studies on the rheological characterization of feedstocks were reported recently within the last couple of years. The rheological characterization of stainless steel or zirconium oxide feedstock were presented by Ibrahim et al. [89] and Wang [24] and Wang [90]. Liu et al. [91] or Choi et al. [84] investigated the rheological behavior during mixing and the viscosity in dependency on the powder content of metal powder feedstock for injection molding in 2005 and 2014, respectively. Also in 2014, material characterization comprising rheological and pvT data with subsequent mathematical fitting was accomplished by Drummer and Messingschlager [26] and Jung et al. [92]. One year later, Hidalgo et al. [93] performed another experimental study on the viscosity of powder feedstock of stainless steel by means of a capillary rheometer. Also, Hausnerova [85] published a thorough review on the rheological, but only on the rheological properties of feedstocks—admitting that the rheological characterization is important, yet not always a simple undertaking.

Apart from the quite recent characterizations of a few feedstocks by a research group at the Oregon State University, Corvallis, OR, USA [52, 75, 76, 94] and single publications by Bilovol et al. [95] or Heldele et al. [73] from 2003 and 2006, respectively, really comprehensive material studies are virtually not existent. Taking up this shortcoming, the present work establishes an inclusive material characterization of four powder feedstocks for injection molding with the prospect of compiling the collected data to a material model for process simulations.

In contrast to feedstocks and filled polymers, unfilled polymers are well characterized and their properties are established for years in conventional injection molding. Consequently, extensive material information about thermoplastic materials are already available in the data base of ASMI.

Research on micro injection molding showed however that scaling effects do exist, and the plastic flow in micro channels is affected by viscous heating, surface tension, size-dependent viscosity, and the wall-slip phenomenon. Viscous heating can in general be ignored though for micro molding. Surface tension and size-dependent viscosity can be neglected for micro channels of few 100 µm—exactly the regime of the micro features of the miniaturized plastic parts in this work. [6, 58, 59, 63, 96].

Wall-slip plays an important role and causes a significant drop in viscosity in micro channels at high shear rates, i.e. larger than $10^4\,\mathrm{s}^{-1}$, as indicated by Chen et al. [96] in 2008. However, Choi and Kim [63] recommended the consideration of wall-slip in channels smaller than 10 µm based on the findings of simulation validations. Furthermore, Kelly et al. [97] measured viscosity over a large range of shear rates

with different instruments. As indicated by Martyn et al. [98] already in 2003, the viscosity was likewise found to increase at very high shear rates, i.e. beyond $10^6\,s^{-1}$, like they can occur in micro molding with dedicated micro machines at high injection speeds. Molding at such high speeds and shear rates nonetheless comes with the risk of material degradation.

Ito et al. [99] combined and integrated a rheometer and a high-pressure dilatometer into a super compact electric injection molding machine comparable to micro machines. The researchers proved that the measured rheological and pvT material properties were similar to data collected by classical methods.

Although still being micro parts, the molding in this work with conventional, screw-based injection molding machines instead of piston-based micro machines promoted processing conditions as in conventional molding, i.e. lower injection velocities and shear rates up to the order of magnitude of $10^4\,s^{-1}$. Hence, there is no experimental indication for disbelieving in the available viscosity and pvT data. Additional microscale material characterization of the used standard thermoplastics was therefore not necessary in this work. Moreover, the thermoplastic materials used throughout this work were among the most well characterized materials (with the so-called "gold status" [100]). The provided data of these materials does not originate from the standard tests of the material suppliers, but from calibrated experiments in special testing laboratories and has to be frequently updated to maintain the gold status.

The used plastic material types are mentioned in the corresponding sections of this thesis. The exact material grades are not mentioned in every section due to the confidentiality agreements with the Hi-MICRO partners. Any presented material properties are either taken from the ASMI material data base or from the official data sheets provided by the material suppliers.

4.2 Necessary material properties for simulations

Following up on the previous section, extensive material properties must be known for the proper simulation of the injection molding process. However, the required material properties depend on the type of simulation that is applied. The filling, packing, and cooling phase are governed by the flow of the plastic or feedstock. Therefore, the following properties are needed [42, 74]:

- viscosity,
- specific heat capacity,
- thermal conductivity,
- no-flow temperature, glass transition temperature, or melt temperature,
- pvT data.

Simulations of the shrinkage and warpage of the molded part are governed by the mechanics of the part. Hence, the following properties are additionally required [42]:

- elastic modulus,
- shear modulus,
- Poisson's ration,
- coefficient of thermal expansion.

In general, ASMI and comparable simulation software tools are primarily made for the plastic industry, i.e. their databases contain plenty of plastics, but no entries about powder feedstocks. This chapter is motivated by the fact that for feedstocks precise material data and guidelines for the acquisition of such data as well as the application of material models do not exist yet [26, 45]. The used feedstocks were characterized accordingly to the first property list above, since the application of the process simulations to powder injection molding was limited to the filling phase. The measured properties enabled to create a material data base entry for all characterized materials and to finally run the simulations in ASMI.

4.3 Powder feedstocks used and characterized in this work

Four different powder feedstocks, two commercial and two non-commercial, were used and characterized in this work. The two commercial feedstocks with trade name Catamold® were supplied by BASF, Ludwigshafen, Germany. Their key properties are shown in Table 4.1. The commercial feedstocks are based on polyoxymethylene (POM, also referred to as polyacetal) as binder, and the debinding happens catalytically by exposing it to a nitric acid atmosphere. As a result, the POM is decomposed in its monomers below its actual melt temperature. The efficient debinding and the good dimensional control are the main advantages of the materials. [22]

The two non-commercial powder feedstocks were compounded on-site at KIT. The feedstocks from KIT are referred to as "GoMikro". The key properties of the non-commercial feedstocks are shown in Table 4.2. The feedstocks are based on a mixture of polyethylene (PE) and wax as the binder system. The debinding happens usually thermally or in a solvent. The major advantage is the easy setup and low investment for debinding. The composition was known and the density and powder content were therefore not measured as outlined for the commercial feedstocks in the following sections.

Table 4.1: Key specifications of the characterized commercial powder feedstocks from BASF.

Trade name	Catamold® TZP-A	Catamold® 17-4PHA
Type	ceramic	metallic
Powder material	yttrium oxide-stabilized zirconium dioxide	stainless steel 17-4PH (1.4542, X5CrNiCuNb16-4)
Powder density / ($g\,cm^{-3}$)	6.06	7.6
Binder material	POM	POM
Debinding	catalytically	catalytically
Binder density[a]/ ($g\,cm^{-3}$)	1.40–1.42	1.40–1.42
Melt temperature / °C		
recommended	170–175	160–190
maximum	180	200
Mold temperature / °C		
recommended	138	128
maximum	145	140
References	[101]	[102]

[a] Since BASF did not disclose any binder information, the reference for the binder density was the data sheet of a typical co-polymeric POM produced by BASF (standard injection molding grade Ultraform® N2320 003) [103], the simulation software database [100], and other literature [104, 105].

Table 4.2: Key specifications of the characterized non-commercial powder feedstocks from KIT.

Name	GoMikro ZrO_2	GoMikro 17-4PH
Type	ceramic	metallic
Powder material	zirconium dioxide	stainless steel 17-4PH (1.4542, X5CrNiCuNb16-4))
Binder material	PE and wax	PE and wax
Powder volume fraction / vol%	50	63
Powder weight fraction / wt%	87	94
Debinding	thermally	thermally
Melt temperature / °C		
recommended	150–170	150–180
maximum	200	200

4.4 Molding of disc samples for measurements of density and thermal properties

The samples for the measurement of the density and the thermal properties of the feedstocks were circular discs with a thickness of 2 mm and a diameter of 10 mm. The disc was molded prior to the measurements on a Wittmann-Battenfeld Microsystem 50 micro injection molding machine.

The processing conditions for each feedstock are listed in Table 4.3. The processing parameters were individually adjusted to the used feedstocks for best filling and sample quality. Detailed information can be found in Appendix A.

Table 4.3: Processing conditions of the circular disc specimen for the material characterization of the feedstocks.

Parameter	Catamold®		GoMikro	
	TZP-A	17-4PHA	ZrO_2	17-4PH
Nozzle temperature / °C	175	180	165	165
Cylinder temperature / °C	170	170	165	160
Mold temperature / °C	23	23	23	23
Injection speed / mm s^{-1}	400	350	200	350
Injection stroke / mm	2.0	2.0	1.5	2.0
Packing	speed profile vs time			
	0 s: 0 mm s^{-1}, 1.2 s: 5 mm s^{-1}, 4.2 s: 5 mm s^{-1}			
Cooling time / s	10	10	13	13

4.5 Powder content determination

4.5.1 Measurement methods

Powder feedstocks consist of a polymer binder and a large fraction of metal or ceramic powder, as described before in chapter 2. The massive powder content in the feedstocks heavily affects the rheological, thermal, and mechanical properties of the feedstock and also the quality of the final part. Knowledge about the exact powder content is therefore essential. The determination of the powder content is often the first step when characterizing powder feedstocks.

The two commercial feedstocks came with information from the supplier about the approximately expected powder content. Still, the powder content was measured for both compounds in different ways because of the different powder material:

- Method 1:
  The granules were heated in a debinding furnace (Carbolite HT6/28, resolution: 0.5 °C) in air from approximately 23 °C (room temperature) up to 600 °C with a heating rate of 2 °C min^{-1} and again cooled down to room temperature. The total mass of the feedstock was measured before and after the heating with a lab scale (Kern EG 620-3NM, resolution: 1 mg). The binder burnt during the heating and caused the difference in mass. This method was not applicable to the metal feedstock, because the metal powder oxidized in the air and gained mass.
- Method 2:
  The ready-to-mold granules were heated in a combined debinding-sintering furnace (MUT ISO 15, resolution: 2 °C) in hydrogen/argon atmosphere from approximately 23 °C (room temperature) up to 600 °C with a heating rate of 10 °C min^{-1} and again cooled down to room temperature. The total mass of the feedstock was measured before and after the heating with a precision scale (Sartorius BP211D, resolution: 0.01 mg).
- Method 3 (in accordance to ASTM E 1269):
  The granules were heated in a differential scanning calorimetry (DSC) device (Netzsch STA 409 C/CD) in nitrogen atmosphere from 25 °C up to 1000 °C with a heating rate of 10 °C min^{-1} and again cooled down to 23 °C (room temperature). The mass was measured during the entire process by the DSC device. The DSC curves can be found in Appendix A.

All heating rates were typical values for the applied devices. Heating up to at least 600 °C ensured that the binder and all organic additives burnt completely, so that the left over mass could be related to the powder.

The powder content by weight ϕ_{wt} was calculated from the mass measurements, and the powder content by volume ϕ_{vol} was derived based on the densities of the binder and the powder according to

$$\phi_{\mathrm{vol}} = \frac{V_{\mathrm{p}}}{V_{\mathrm{tot}}} = \frac{\dfrac{m_{\mathrm{p}}}{\rho_{\mathrm{p}}}}{\dfrac{m_{\mathrm{p}}}{\rho_{\mathrm{p}}} + \dfrac{m_{\mathrm{b}}}{\rho_{\mathrm{b}}}} \tag{4.1}$$

where V_{p} and V_{tot} are the powder volume and total volume, respectively. m_{p} and ρ_{p} are the mass and density of the powder, m_{b} and ρ_{b} are the mass and density of the polymer binder. The mass and density of additives were neglected.

4.5.2 Results and discussion

The result of the measurements are summarized in Table 4.4. The powder content given by the supplier was derived from the recommended oversizing factor in the

material certificate supplied with each batch. The measured values are in good agreement with each other with up to about 1 % difference, whereas the measurements give all up to about 5 % higher powder contents than the values derived from the certificate and the density measurements. This discrepancy could be attributed to deviations between the assumed and true density for the binder and powder materials. For the density, the values from Table 4.1 were used.

Table 4.4: Determined powder content of the commercial powder feedstocks.

Reference	Catamold® TZP-A		Catamold® 17-4PHA	
	ϕ_{wt} / wt%	ϕ_{vol} / vol%	ϕ_{wt} / wt%	ϕ_{vol} / vol%
Certificate	79.3	46.9	87.3	55.8
Method 1	81.7	50.8	n.a.	n.a.
Method 2	n.a.	n.a.	88.9	59.5
Method 3	81.0	49.6	89.4	60.8
Density	77.8	44.7	87.6	56.5
Average	80.0	48.0	88.3	58.2

4.6 Density measurements

The density of the molded feedstocks was determined by means of the Archimedes' principle. For each compound, the mass of six discs was determined with a precision scale (Sartorius BP211D, resolution: 0.01 mg, equipped with the density measurement kit Sartorius YDK, resolution: 0.1 °C) in air and in water. The temperature of the water was monitored in order to gain information about the change in the density of the water ρ_{water}. The density of air $\rho_{\mathrm{air}} = 0.0012\,\mathrm{g\,cm^{-3}}$ was assumed to be constant. The density of the feedstock ρ was calculated according to

$$\rho = \frac{m_{\mathrm{air}}\,(\rho_{\mathrm{water}} - \rho_{\mathrm{air}})}{k\,(m_{\mathrm{air}} - m_{\mathrm{water}})} + \rho_{\mathrm{air}} \tag{4.2}$$

where m_{air} and m_{water} are the sample mass measured in air and in water, respectively, and the correction factor $k = 0.99983$ to account for the contribution of the immersed sample holder to the buoyant force. The determined density of the two compounds is listed in Table 4.5.

Independently from the aforementioned measurements, the density for all feedstocks was also determined in the context of the determination of the thermal conductivity (see section 4.8). The measurement was again based on the Archimedes' principle. Instead of water, ethanol was used as the liquid in which the sample was immersed. The procedure was similar with the difference of the density of ethanol $\rho_{\mathrm{ethanol}} =$

$0.0012\,\mathrm{g\,cm^{-3}}$ assumed to be constant. The results are based on measurements of three samples and are also listed in Table 4.5.

The discrepancy between the measurements in water and ethanol might be explained by the density of ethanol which was assumed as constant. The metal feedstock shows the greater density because of the heavier powder and larger powder content.

Table 4.5: Determined densities of the used powder feedstocks.

Compound	Density ρ / $(\mathrm{g\,cm^{-3}})$	
	water[a]	ethanol[b]
Catamold® TZP-A	3.482 ± 0.008	3.487 ± 0.009
Catamold® 17-4PHA	4.905 ± 0.031	4.954 ± 0.011
GoMikro ZrO_2	n.a.	3.494 ± 0.010
GoMikro 17-4PH	n.a.	4.798 ± 0.002

[a] Average of six measurements, confidence level: 95 %
[b] Average of three measurements, confidence level: 95 %

4.7 Measurements of the specific heat capacity

The specific heat capacity (at constant pressure) was measured by means of the high pressure differential scanning calorimeter Netzsch DSC 204 made by Netzsch-Gerätebau, Selb, Germany. The sample mass was in the range of 53 mg to 85 mg. For every material, three measurement cycles were run in argon atmosphere. The reported value for the specific heat capacity is hence the mean value of all three cycles. Every cycle consisted of a heating phase from 25 °C to 180 °C and a cooling phase back to 25 °C with a heating or respectively cooling rate of $10\,^{\circ}\mathrm{C\,min^{-1}}$ (complies with ASTM E 1269). In order to cover the entire processing window of Catamold® 17-4PHA, the temperature range of the analysis was expanded to 200 °C for this material. The heat capacity was determined during the heating phase at temperature steps of 10 °C. The results are shown in Table 4.6 and Figure 4.1.

As expected, the heat capacity is a function of temperature for all feedstocks. It must also be kept in mind that the heating rate influences the results of heat capacity measurements [88]. The specific heat capacity of the Catamold® compounds vary from $0.6\,\mathrm{J\,g^{-1}\,K^{-1}}$ to $2.2\,\mathrm{J\,g^{-1}\,K^{-1}}$, i.e. by a factor three. The heat capacity and the measurement uncertainty show show a significant increase in the temperature range of 160 °C to 180 °C. This correlates to the melting of the crystalline areas in the POM binder at its melting temperature of about 170 °C. The peak is however differently strongly pronounced because of the different types of powders and the varying powder loads.

The specific heat capacities of the GoMikro feedstocks vary in the range from $0.6\,\mathrm{J\,g^{-1}\,K^{-1}}$ to $1.2\,\mathrm{J\,g^{-1}\,K^{-1}}$, i.e. approximately by a factor two. The GoMikro compounds show two noticeable, but less pronounced increases in heat capacity and measurement uncertainty compared to Catamold®, namely at about 60 °C and at about 100 °C. Likewise, these peaks correlate to the melting temperatures of the wax and the PE in the binder system, respectively.

The dependency of the heat capacity on the temperature is much less pronounced compared to plastics. A reference curve for the specific heat capacity of pure POM from BASF is included in Figure 4.1, where the heat capacity shows a much more volatile behavior and varies from about $1.4\,\mathrm{J\,g^{-1}\,K^{-1}}$ to $10.1\,\mathrm{J\,g^{-1}\,K^{-1}}$, i.e. by a factor of roughly seven. In general, the heat capacity of the feedstocks is much lower compared to pure plastics.

The investigated compounds exhibit nevertheless typical values and qualitatively similar variations compared to other powder feedstocks. In literature, values of $0.7\,\mathrm{J\,g^{-1}\,K^{-1}}$ to $0.9\,\mathrm{J\,g^{-1}\,K^{-1}}$ for mullite-zirconia, $0.8\,\mathrm{J\,g^{-1}\,K^{-1}}$ to $1.2\,\mathrm{J\,g^{-1}\,K^{-1}}$ for silicon nitride, $0.9\,\mathrm{J\,g^{-1}\,K^{-1}}$ to $1.5\,\mathrm{J\,g^{-1}\,K^{-1}}$ for aluminum nitride, and $0.6\,\mathrm{J\,g^{-1}\,K^{-1}}$ to $4.5\,\mathrm{J\,g^{-1}\,K^{-1}}$ for 316L stainless steel feedstocks are reported [52, 75, 76, 88, 94].

Furthermore, the measured heat capacity of the two ceramic compounds is in general higher compared to the corresponding metallic compounds. This can be explained by the about 10 % higher heat capacity of the ceramic powder compared to the metallic powder [106–108]. The difference between the commercial and non-commercial compounds are caused by the different binder systems with their varying specific heat capacity and the varying powder load.

4.8 Measurements of the thermal conductivity

4.8.1 Measurement method

The thermal conductivity of the feedstocks was determined indirectly by the measurement of the thermal diffusivity in a laser flash analysis. The thermal diffusivity was measured by means of the laser flash apparatus Netzsch LFA 427. In the laser flash analysis, the top surface of the sample was heated up with a short laser flash and the introduced heat spread over the specimen. An infrared sensor monitored the time-dependent temperature distribution on the lower surface of the sample from which the thermal diffusivity could be inferred.

For each material, the laser flash analysis was conducted with one of the molded disc samples. The temperature range was the same as for the heat capacity measurements, 25 °C to 180 °C. For Catamold® 17-4PHA, the temperature range was also expanded and covered 25 °C to 200 °C. The temperature step was 10 °C. The reported value of

Table 4.6: Measured values for the specific heat capacity of the investigated feedstocks. The measurement was directly done by a DSC analysis. The values are the average of three heating and cooling cycles at a rate of $10\,°C\,min^{-1}$, confidence level: 95 %.

Temperature T / °C	specific heat capacity c_p / $(J\,g^{-1}\,K^{-1})$			
	Catamold®		GoMikro	
	TZP-A	17-4PHA	ZrO_2	17-4PH
25	0.70 ± 0.03	0.62 ± 0.09	0.72 ± 0.04	0.64 ± 0.03
30	0.70 ± 0.03	0.63 ± 0.08	0.74 ± 0.04	0.65 ± 0.03
40	0.72 ± 0.04	0.64 ± 0.07	0.82 ± 0.04	0.69 ± 0.02
50	0.73 ± 0.06	0.65 ± 0.07	0.99 ± 0.09	0.81 ± 0.02
60	0.75 ± 0.07	0.66 ± 0.06	1.17 ± 0.09	1.05 ± 0.12
70	0.77 ± 0.07	0.68 ± 0.06	1.05 ± 0.01	0.96 ± 0.01
80	0.78 ± 0.06	0.69 ± 0.06	0.93 ± 0.02	0.78 ± 0.01
90	0.79 ± 0.06	0.71 ± 0.05	0.95 ± 0.03	0.79 ± 0.01
100	0.81 ± 0.06	0.73 ± 0.05	1.08 ± 0.19	0.90 ± 0.16
110	0.83 ± 0.06	0.74 ± 0.04	0.91 ± 0.11	0.71 ± 0.01
120	0.86 ± 0.05	0.73 ± 0.05	0.81 ± 0.04	0.69 ± 0.03
130	0.90 ± 0.05	0.76 ± 0.04	0.82 ± 0.03	0.69 ± 0.03
140	0.95 ± 0.04	0.80 ± 0.04	0.83 ± 0.03	0.70 ± 0.03
150	1.05 ± 0.05	0.88 ± 0.05	0.83 ± 0.04	0.71 ± 0.03
160	1.52 ± 0.17	1.13 ± 0.07	0.84 ± 0.04	0.71 ± 0.03
170	2.20 ± 1.60	1.79 ± 1.30	0.84 ± 0.04	0.72 ± 0.04
180	0.89 ± 0.04	0.75 ± 0.03	0.85 ± 0.04	0.72 ± 0.04
190	n.a.	0.75 ± 0.03	n.a.	n.a.
200	n.a.	0.75 ± 0.04	n.a.	n.a.

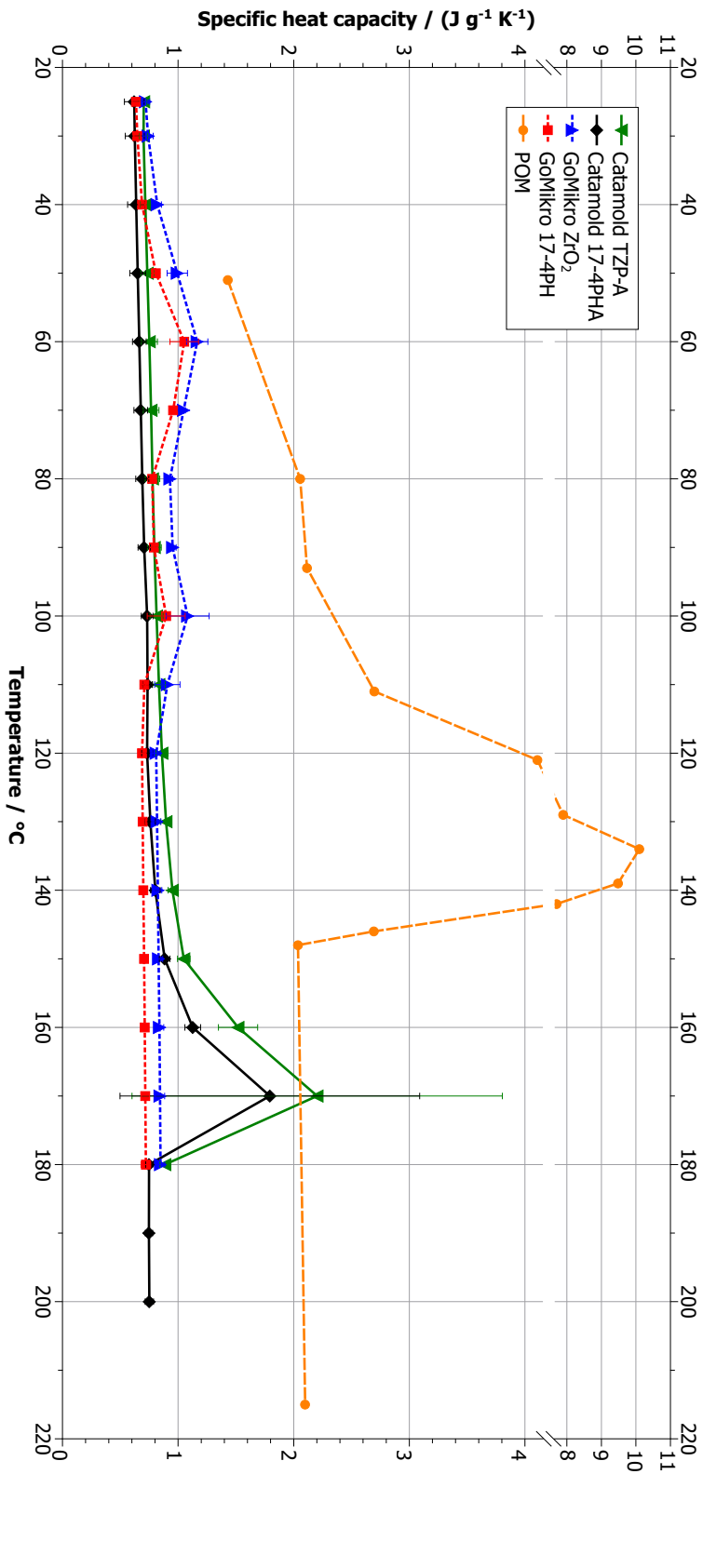

Figure 4.1: Measured values for the specific heat capacity of the investigated feedstocks and typical values for POM from BASF (from ASMI data base [100]). The measurement was directly done by a DSC analysis. The values are the average of three heating and cooling cycles at a rate of 10 °C min^{-1}, the error bars represent the standard measurement uncertainty, confidence level: 95 %.

the temperature conductivity is the average of five measurements at every temperature step.

The thermal conductivity λ was derived from the thermal diffusivity α by taking into account the density ρ and the specific heat capacity c_p as [1]

$$\lambda = \alpha \, \rho \, c_\mathrm{p}. \tag{4.3}$$

According to Equation 4.3 and the error propagation, the measurement uncertainty $u(\lambda)$ of the thermal conductivity is given by

$$\frac{u(\lambda)}{\lambda} = \sqrt{\left(\frac{u(\alpha)}{\alpha}\right)^2 + \left(\frac{u(\rho)}{\rho}\right)^2 + \left(\frac{u(c_\mathrm{p})}{c_\mathrm{p}}\right)^2}. \tag{4.4}$$

The values for the heat capacity were taken from section 4.7. For the density, the values determined and reported in section 4.6 were used. This is a simplification and introduces deviations, since the density was measured at room temperature and not for every temperature step in accordance to the heat capacity and thermal diffusivity.

4.8.2 Theoretical determination

Theoretically, the thermal conductivity λ of a powder feedstock can be computed by the direct rule of mixtures for powders and binders with comparable conductivities as [94, 109]

$$\lambda = (1 - \phi_\mathrm{vol}) \, \lambda_\mathrm{b} + \phi_\mathrm{vol} \, \lambda_\mathrm{p} \tag{4.5}$$

or accordingly to the inverse rule of mixtures for powders with significantly different conductivities from the binder as [28, 109]

$$\frac{1}{\lambda} = \frac{(1 - \phi_\mathrm{vol})}{\lambda_\mathrm{b}} + \frac{\phi_\mathrm{vol}}{\lambda_\mathrm{p}} \tag{4.6}$$

with the powder volume fraction ϕ_vol and the thermal conductivities λ_b and λ_p of the binder and powder, respectively.

4.8.3 Results and discussion

The measurement results are summarized in Table 4.7 and Figure 4.2. The theoretical and measured values for the thermal conductivities of the feedstocks, the powders, and the binder components are compared in Table 4.8. Due to the dependency of the thermal conductivity on the heat capacity, the Catamold® compounds also showed significant peaks from 160 °C to 180 °C. The large measurement uncertainty was

also caused by the heat capacity, the density and thermal diffusivity measurements showed much smaller errors.

Except for the characteristic peaks of both materials, the two ceramic feedstocks show very similar thermal conductivity of about $1\,\mathrm{W\,m^{-1}\,K^{-1}}$. Their theoretical conductivity was determined according to Equation 4.5 as about $1\,\mathrm{W\,m^{-1}\,K^{-1}}$ to $2\,\mathrm{W\,m^{-1}\,K^{-1}}$. Thus, the measured values are in good agreement with the theoretical value. The investigated compounds exhibit furthermore typical values and qualitatively similar variations compared to other ceramic feedstocks. Values of $0.7\,\mathrm{W\,m^{-1}\,K^{-1}}$ to $1.0\,\mathrm{W\,m^{-1}\,K^{-1}}$ for mullite-zirconia, $1.1\,\mathrm{J\,g^{-1}\,K^{-1}}$ to $1.4\,\mathrm{J\,g^{-1}\,K^{-1}}$ for silicon nitride, and $2.7\,\mathrm{J\,g^{-1}\,K^{-1}}$ to $4.3\,\mathrm{J\,g^{-1}\,K^{-1}}$ for aluminum nitride are reported in literature [52, 75, 76, 94].

The thermal conductivity of the ceramic feedstocks is moreover situated at the lower end of the typical range of pure zirconium oxide of about $1\,\mathrm{W\,m^{-1}\,K^{-1}}$ to $3\,\mathrm{W\,m^{-1}\,K^{-1}}$ [101, 107, 110], but noticeably higher than for the pure binder of typically about $0.3\,\mathrm{W\,m^{-1}\,K^{-1}}$ [28, 105]. The reference curve of pure POM from BASF in Figure 4.2 depicts this difference.

The two metallic feedstocks show thermal conductivities in the range of $1.5\,\mathrm{W\,m^{-1}\,K^{-1}}$ to $2.5\,\mathrm{W\,m^{-1}\,K^{-1}}$ apart from the peaks. The generally higher thermal conductivity of the metallic feedstocks can be attributed to the much higher thermal conductivity of the metal powder which is typically in the range of $14\,\mathrm{W\,m^{-1}\,K^{-1}}$ to $19\,\mathrm{W\,m^{-1}\,K^{-1}}$ for the pure steel [106, 108, 111, 112]. The theoretical value of about $1\,\mathrm{W\,m^{-1}\,K^{-1}}$ for the metallic feedstocks resulting from Equation 4.6 appears only suitable as estimation downwards. The measured values are noticeably higher and in agreement with the value of about $3\,\mathrm{W\,m^{-1}\,K^{-1}}$ reported by Heaney [28].

Also, the conductivities of the two metallic feedstocks differ from each other. GoMikro 17-4PH shows the lower thermal conductivity, although the powder content is much higher. Consequently, the binder dominates the conductivity and must presumably be less conductive than the Catamold® binder system. Additionally, the powder particle size and size distribution could be of relevance and cause the higher thermal conductivity of Catamold® 17-4PHA compared to GoMikro 17-4PH. Discrepancies are also introduced by the measurement uncertainties of density and heat capacity.

Table 4.7: Measured values for the thermal conductivity of the investigated feedstocks. The measurement was indirectly done by measuring the thermal diffusivity with a laser flash analysis. The values are the average of five measurements, confidence level: 95 %.

Temperature T / °C	thermal conductivity λ / ($\mathrm{W\,m^{-1}\,K^{-1}}$)			
	Catamold®		GoMikro	
	TZP-A	17-4PHA	ZrO_2	17-4PH
25	0.89 ± 0.05	2.79 ± 0.40	1.10 ± 0.12	1.95 ± 0.11
30	0.88 ± 0.07	2.59 ± 0.43	1.10 ± 0.08	1.95 ± 0.20
40	0.89 ± 0.11	2.61 ± 0.33	1.12 ± 0.10	1.91 ± 0.20
50	0.90 ± 0.08	2.56 ± 0.31	1.23 ± 0.13	1.86 ± 0.31
60	0.88 ± 0.11	2.53 ± 0.26	1.12 ± 0.13	1.93 ± 0.39
70	0.89 ± 0.08	2.52 ± 0.25	1.07 ± 0.12	1.81 ± 0.07
80	0.87 ± 0.07	2.50 ± 0.24	0.89 ± 0.05	1.35 ± 0.17
90	0.87 ± 0.07	2.58 ± 0.22	0.93 ± 0.09	1.60 ± 0.09
100	0.86 ± 0.06	2.53 ± 0.19	1.17 ± 0.23	1.70 ± 0.34
110	0.84 ± 0.06	2.48 ± 0.14	0.94 ± 0.12	1.40 ± 0.11
120	0.80 ± 0.06	2.25 ± 0.20	0.81 ± 0.04	1.52 ± 0.10
130	0.78 ± 0.07	2.14 ± 0.14	0.85 ± 0.05	1.54 ± 0.11
140	0.82 ± 0.04	1.84 ± 0.11	0.88 ± 0.04	1.59 ± 0.08
150	0.85 ± 0.05	2.01 ± 0.11	0.89 ± 0.04	1.65 ± 0.07
160	1.21 ± 0.14	2.48 ± 0.19	0.87 ± 0.04	1.62 ± 0.09
170	1.71 ± 1.25	3.88 ± 2.80	0.84 ± 0.04	1.62 ± 0.08
180	0.69 ± 0.03	1.58 ± 0.07	0.83 ± 0.04	1.59 ± 0.10
190	n.a.	1.59 ± 0.08	n.a.	n.a.
200	n.a.	1.56 ± 0.08	n.a.	n.a.

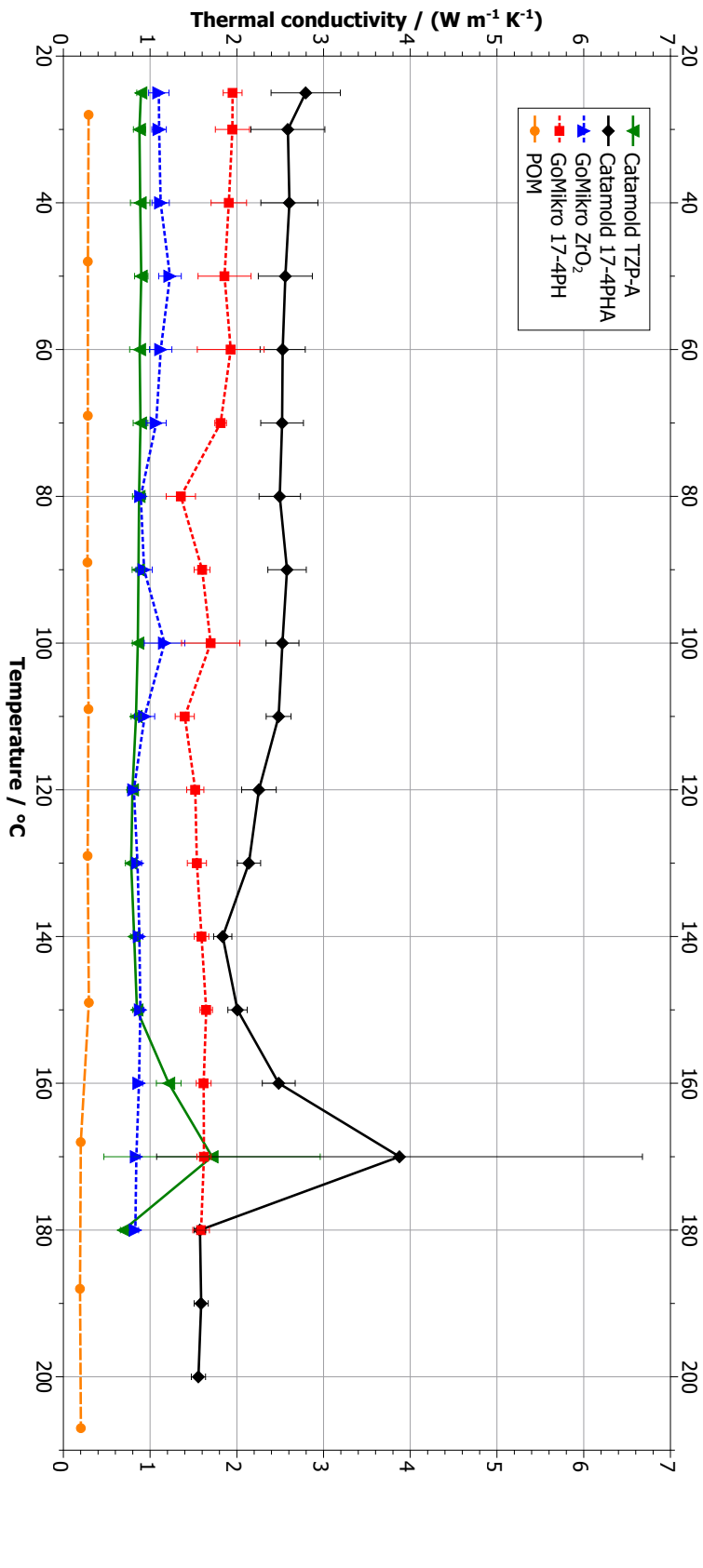

Figure 4.2: Measured values for the thermal conductivity of the investigated feedstocks and typical values of pure POM from BASF (from ASMI data base [100]). The measurement was indirectly done by measuring the thermal diffusivity with a laser flash analysis. The values are the average of five measurements. The error bars represent the standard measurement uncertainty, confidence level: 95 %.

Table 4.8: Measured and theoretical thermal conductivities of the powder feedstocks as well as of the pure powders and binders. Approximated and averaged values for temperatures of about 25 °C to 200 °C.

Material	thermal conductivity λ / ($W\,m^{-1}\,K^{-1}$)		reference
	theoretical	measured	
ZrO_2	1–3	n.a.	[101, 107, 110]
17-4PH	14–19	n.a.	[106, 108, 111, 112]
POM, PE, wax	0.3	n.a.	[28, 104, 105, 113]
Metal feedstocks	3	n.a.	[28]
Ceramic feedstocks	1–4	n.a.	[75, 94]
Catamold® TZP-A	1–2	0.9	Equation 4.5
Catamold® 17-4PHA	1	2.4	Equation 4.6
GoMikro ZrO_2	1–2	1.0	Equation 4.5
GoMikro 17-4PH	1	1.7	Equation 4.6

4.9 Theoretical background of rheological and thermodynamic measurements

4.9.1 Rheometers

In general, rotational or capillary rheometers are used for the measurement of the viscosity of plastics. In a rotational rheometer, the analyzed material is located between two contact surfaces of the rheometer. The contact surfaces are typically formed by plates, cones, or cylinders which are separated by the material gap. In such kind of rheometers, the shear force is directly applied to the heated material by rotating one or both contact surfaces. The viscosity is measured indirectly by recording the required torque for the rotation.

The pressure-driven capillary rheometers consist of a heated cylinder where the material is pushed by a piston from a material reservoir through a capillary. The viscosity is indirectly measured by monitoring the pressure drop over the capillary with a sensor in the cylinder and the flow rate of the material. The schematic structure is shown in Figure 4.3a.

The capillary rheometer involves however inhomogeneous flow—the drawback of capillary rheometers. Still, they are widely used because of their advantages like simple and inexpensive design and the applicability of high shear rates. Additionally, they provide the most accurate and most process-relevant data [47, 48].

viscosity.

ndard ISO 11443 [10] defines two possible methods: either measuring the volume
y rate Q or the test pressure p, while keeping the other parameter constant. It
ecommended to use capillaries with a length l of either 16 mm or 20 mm and a
meter of 1 mm. For highly filled materials, the diameter may be changed with T
tain specifications.

Measured parameters

This material characterization regarding the viscosity data was carried out by means of the high pressure capillary rheometer Göttfert Rheograph 25 (depicted in Figure 4.3b) made by Göttfert Werkstoff-Prüfmaschinen, Buchen, Germany.

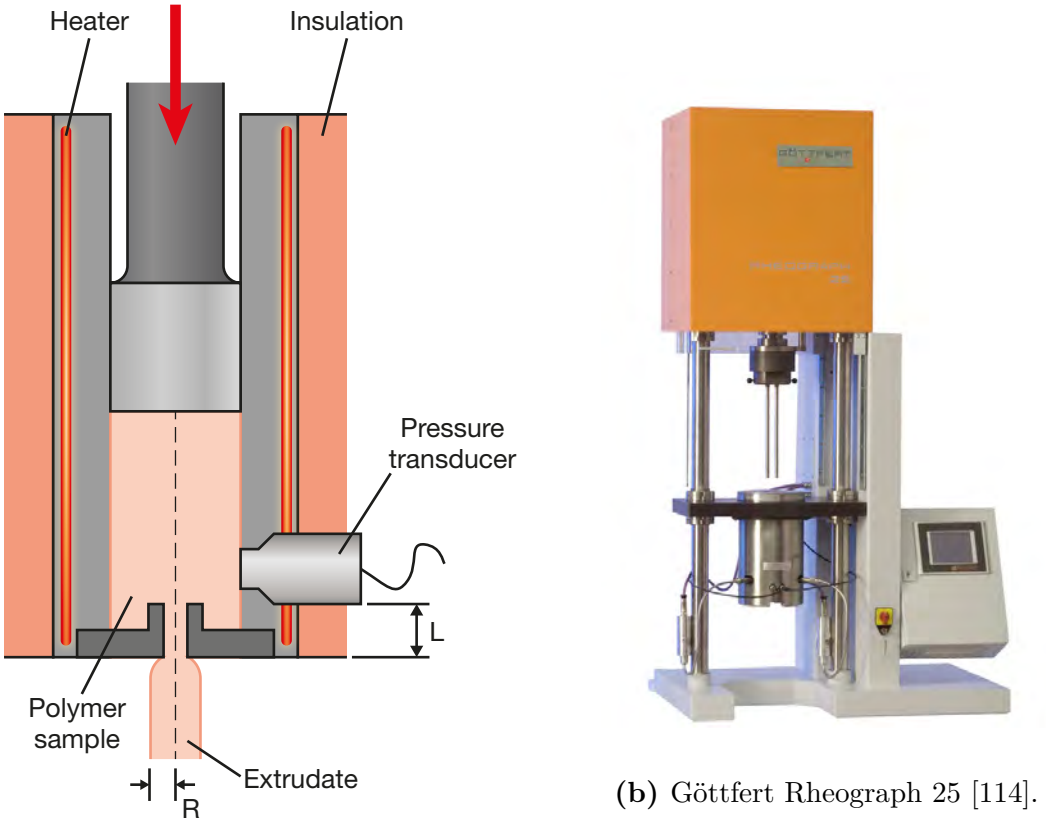

(a) Schematic view [48].

(b) Göttfert Rheograph 25 [114].

re 6.6 Schematic diagram of a capillary viscometer.

Figure 4.3: Schematic (left) and real device (right) of the high pressure capillary rheometer used for the material characterization of the powder feedstocks. The piston compresses the heated plastic material which flows through the orifice while the resulting pressure drop is monitored.

4.9.2 Fitting method

The collected data of the rheological and thermodynamic measurements were firstly processed with the software Göttfert WinRheo II version 1.7.13. The software automatically extracted all necessary data like the applied flow rate, pressure, volume, and temperature from the rheometer. The subsequent fitting of the collected material data was done by an add-on of ASMI, Autodesk Moldflow Plastics Labs Data Fitting release 2.0. The ASMI add-on used the input data to create a data base file for ASMI.

The coefficients of the fitted Cross-WLF and 2-domain Tait model for the viscosity and *pvT* data, respectively, could be extracted from there. The viscosity and *pvT* parameters were also fit with SigmaSoft® which was available at KIT. The values gained by SigmaSoft® are only for cross-check and were not used for any plots. The reason for this check was the fact that the exact algorithms of neither of the software packages were not known. Additionally, the goodness of the fit could not be evaluated in greater detail, since neither ASMI nor SigmaSoft® provided any sound quality indicators of the fit, e.g. residuals, R^2 values, or the χ^2 test. ASMI only provided an "error percentage" which was not further specified. Trials to fit the data fully with software like Wolfram Mathematica® or OriginLab Origin® did not succeed in reasonable time, possibly due to the large number of unknown parameters and the generalization of fitting algorithms.

4.9.3 Mathematical corrections

The mathematical derivation of the viscosity from the measured pressure and flow rate in a capillary rheometer requires the following assumptions [48]:

1. The flow is steady, isothermal, and laminar.
2. There is no flow in radial or angular direction in the capillary.
3. The plastic is incompressible.

However, these idealizing assumptions do not match to what is happening in reality. The viscosity data collected by means of a capillary rheometer should consequently be mathematically corrected. The following corrections can be relevant for processing the recorded viscosity data [47, 115–117]:

1. Bagley correction:
   The Bagley correction accounts for the entrance effects in the capillary rheometer. The measured pressure drop over the capillary is not only caused by the melt's flow resistance, but also by turbulent flow in the entrance region of the capillary. Besides, the melt must be accelerated from the low flow velocity in the reservoir to the high flow velocity in the capillary. Since plastics are viscoelastic materials, they temporarily absorb some of the applied pressure. This energy is again recovered after leaving the capillary and appears as an expansion of the material, the so-called die swell of the extrudate.
2. Weissenberg-Rabinowitsch correction:
   The Weissenberg-Rabinowitsch correction compensates for the non-Newtonian (shear thinning) behavior of the plastics and computes the "real" shear stress at the wall of the capillary out of the "apparent" shear stress.

3. Mooney correction:
   The Mooney correction is used to correct the velocity of the melt. Plastic melts do not always fulfill the assumption of no wall slip inside the capillary. In this case, the wall slip speed thus contributes apart from the melt velocity to the total flow rate.

4. Dissipation correction:
   The dissipation correction is used, if the assumption of isothermal flow inside the capillary is not true anymore. At high shear rates, the melt might heat up due to internal friction and the resulting dissipative heating.

4.10 Viscosity measurements

4.10.1 Measurement method

The viscosity data of the feedstocks was measured using the Göttfert Rheograph 25. The rheometer determined the wall shear rate and wall shear stress based on the measurement of the pressure drop over the capillary and a given flow rate. For every material, the measurement procedure was conducted for three differently long capillaries (diameters of 10 mm, 20 mm and 30 mm) and three different temperature levels (low, medium, high) in the recommended processing window of each individual material. This enabled to apply the necessary corrections to the collected raw viscosity data. The chosen temperature levels are listed in Table 4.9. The viscosity was measured at shear rates in the order of approximately $1\,s^{-1}$ to $10^4\,s^{-1}$. The measurement and data processing procedure was established as follows (in accordance to ASTM D 3835):

1. Heating up the rheometer to the softening temperature of investigated material and filling in of the material.
2. Adjustment of the rheometer to the desired temperature level for the measurement.
3. Viscosity measurement with automatic control of the plunger movement and pressure monitoring by the capillary rheometer.
4. Data processing with Göttfert WinRheo II. The software applied the Weissenberg-Rabinowitsch and Bagley correction to the recorded viscosity data to calculate the true viscosity data by consideration of the different capillary lengths and temperature levels.
5. Visualization and inspection of corrected viscosity data.
6. Data fitting to the Cross-WLF viscosity model and parameter extraction using ASMI and SigmaSoft®.

Table 4.9: Chosen temperature levels for the viscosity measurements and recommended processing window of the investigated feedstocks for reference.

Compound	Temperature level / °C			
	low	medium	high	processing
Catamold® TZP-A	170	175	180	170–180
Catamold® 17-4PHA	170	180	190	160–200
GoMikro ZrO_2	150	160	170	150–170
GoMikro 17-4PH	150	160	170	150–170

4.10.2 Results and discussion

The finally gained viscosity measurements are depicted in Figure 4.4. The results of the model fitting for the viscosity are shown in Table 4.10 and Figure 4.5 where they are compared to typical values of the pure POM binder of the Catamold® feedstocks. A comparison to the PE/wax binder was not possible due to the unknown amounts of PE and wax as well as the complex structure and hence the general unavailability of viscosity data of waxes.

The curves show that in contrast to plastics, the powder feedstocks do not exhibit a Newtonian plateau at low shear rates which is typical for feedstocks. The critical shear stress τ^*, i.e. the transition from Newtonian to power-law region, is situated at very low values (maximum of about 12 000 Pa) compared to POM (about 320 000 Pa) which illustrates this absence of the Newtonian plateau.

The GoMikro feedstocks show lower viscosity than the POM at medium viscosity values which proves their applicability for thin walled and micro plastic parts. Besides the characteristic viscosity increase at low shear rates, Catamold® TZP-A exhibits similar viscosity than the pure POM. Catamold® 17-4PHA reaches the viscosity of POM only in a narrow shear rate spectrum at about $5000\,\mathrm{s}^{-1}$ and is significantly more viscous than the pure binder.

According to the Cross-WLF model, the term $1-n$ describes the slope of the viscosity curves in the power-law region, i.e. the sensitivity of the shear thinning to the shear rate. Since the determined power-law index n of the feedstocks is higher than for POM, the feedstocks seem less sensitive to shear thinning. This is true for high shear rates ($\gtrapprox 5000\,\mathrm{s}^{-1}$) where the power-law region of POM is fully developed. At low shear rates though, the feedstocks show stronger shear thinning tendency, but also much higher absolute viscosity values.

The dent in the curve of GoMikro 17-4PH at low shear rates could indicate the Newtonian plateau, as it was previously shown in Figure 3.2, but could also be an outlier of the measurement. The remaining materials do not show a similar behavior,

so that the simple Cross-WLF model or even a power-law model could be sufficient for describing the viscosity.

Table 4.10: Data-fitted parameters for the Cross-WLF model describing the viscosity of the feedstocks and reference values of a pure POM from BASF (from ASMI data base [100]). The values given are partially rounded for easier perception.

Parameter		Catamold®		GoMikro		POM
Name	unit	TZP-A	17-4PHA	ZrO_2	17-4PH	
n	1	0.3683	0.4636	0.4378	0.4499	0.212
τ^*	Pa	1305	503	577	11 904	322 188
D_1	Pa s	$1.707 \cdot 10^{23}$	$8.125 \cdot 10^{16}$	$1.038 \cdot 10^{19}$	$7.317 \cdot 10^{13}$	$1.180 \cdot 10^{12}$
D_2	K	223.15	223.15	233.15	233.15	223.15
D_3	$K\,Pa^{-1}$	0	0	0	0	0
A_1	1	47.741	31.047	38.841	29.775	25.13
A_2	K	51.6	51.6	51.6	51.6	51.6

4.11 Measurements of *pvT* data

4.11.1 Measurement method

The *pvT* data of the feedstocks was measured using the Göttfert Rheograph 25. The rheometer offered an automatic program for the measurements, so that the investigated material only had to be filled into the rheometer. The measurements were carried out starting at the maximum individual allowed processing temperature for each feedstock and then sweeping the temperature down to 40 °C to cover the entire processing and cooling window of the materials. The chosen temperature steps were different for each feedstock in order to have good resolution of the acquired data in the process window and at the transition temperature.

At each temperature level, the rheometer applied a force accordingly to the investigated pressure level to the finite material sample. The contraction of the sample with temperature was measured from which the sample volume could be derived. Before acquiring data at any temperature, the material was allowed to rest and settle to prevent from any influence of possible material relaxation.

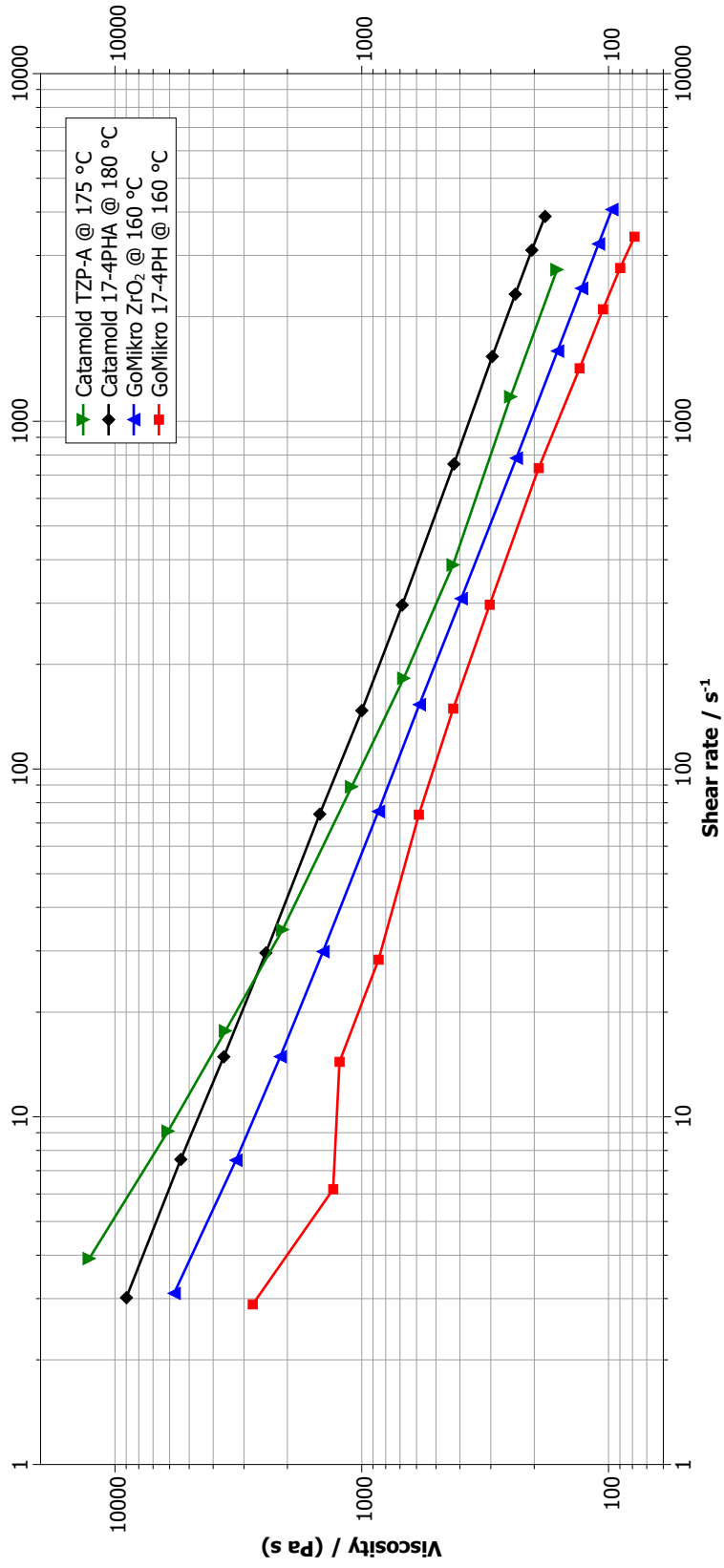

Figure 4.4: Example of measured raw viscosity data of the investigated feedstocks at their typical processing temperature and for a capillary ratio of $L/D = 10$.

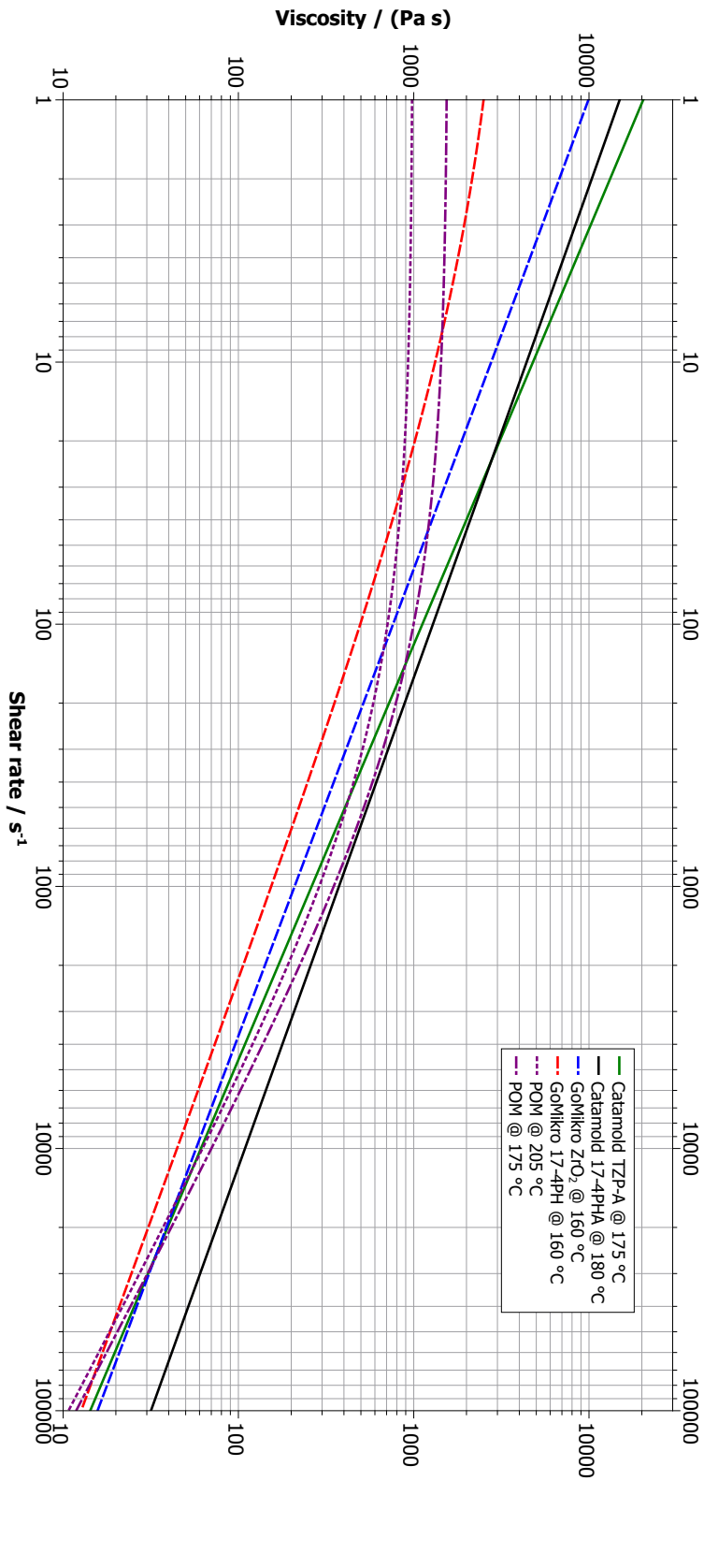

Figure 4.5: Fitted viscosity curves of the investigated feedstocks at their typical processing temperature and reference curves of POM according to the Cross-WLF model and the parameters from Table 4.10.

4.11.2 Results and discussion

The measured data and the fits for all four tested feedstocks are shown in Figure 4.6 to Figure 4.9. The main contributor to the increase in specific volume is the binder. The thermal expansion of the metal and ceramic powders only reaches $< 1\,\%$ for a temperature difference of 160 °C (at standard pressure). The increase in specific volume of the feedstocks nonetheless reaches values of more than 12 %.

The semi-crystalline polyacetal binder is clearly reflected in the *pvT* curves of the Catamold® feedstocks. Both data sets show typical curves of a semi-crystalline material, in this case with a very distinct increase in specific volume and a change of the average slope at around 160 °C to 180 °C. This corresponds to the melt temperature of 170 °C (at standard conditions) of the POM binder, as the melting of the crystalline regions in the material goes along with a significant increase in specific volume. The higher powder load of Catamold® 17-4PHA is also indicated in the *pvT* curves, as the specific volume shows smaller absolute values of $200\,\mathrm{mm^3\,g^{-1}}$ to $220\,\mathrm{mm^3\,g^{-1}}$ and a variation of about 10 % at the lowest pressure, whereas Catamold® TZP-A shows values of $285\,\mathrm{mm^3\,g^{-1}}$ to $315\,\mathrm{mm^3\,g^{-1}}$ and slightly higher variation of 11 %.

On the other hand, both GoMikro data sets show neither clear semi-crystalline nor amorphous behavior. The curves indicate a semi-crystalline behavior with a change in slope at about 110 °C to 120 °C which correlates to the melt temperature of the PE part in the binder. However, the transition from the solid to the molten region is indistinct and the semi-crystalline curve can only be sensed in the fit. Especially the data points of GoMikro ZrO_2 could also be fitted linearly.

Wax typically melts in the temperature range of approximately 40 °C to 90 °C [118]. Consequently, it is believed that the wax influences the shape of the curve below the melt temperature of PE and masks the semi-crystalline characteristics. Nonetheless, the exact influence is difficult to estimate, since wax is a very complex material. It would be necessary to collect *pvT* data with finer temperature resolution to investigate the effect of the wax and to perform a more reliable fitting.

The corresponding fitting parameters for the measured data for the 2-domain Tait model are listed in Table 4.11. The determined values of the parameters show good agreement between the fitting by ASMI and SigmaSoft® for the Catamold® feedstocks. Deviations are likely caused by the different fitting algorithms of the software.

In case of the GoMikro feedstocks, the agreement of the parameters between ASMI and SigmaSoft® is less positive, and some of the parameters are even negative. The fitting of GoMikro ZrO_2 was most challenging. These aspects might be related to the atypical shape of the *pvT* curves which is caused by the bimodal binder system. There is no clear distinction between the solid and liquid domain of the 2-domain Tait model. The transition phase where the wax is already molten and the PE still solid, is quite broad because of the indefinite melting temperature of wax. Consequently,

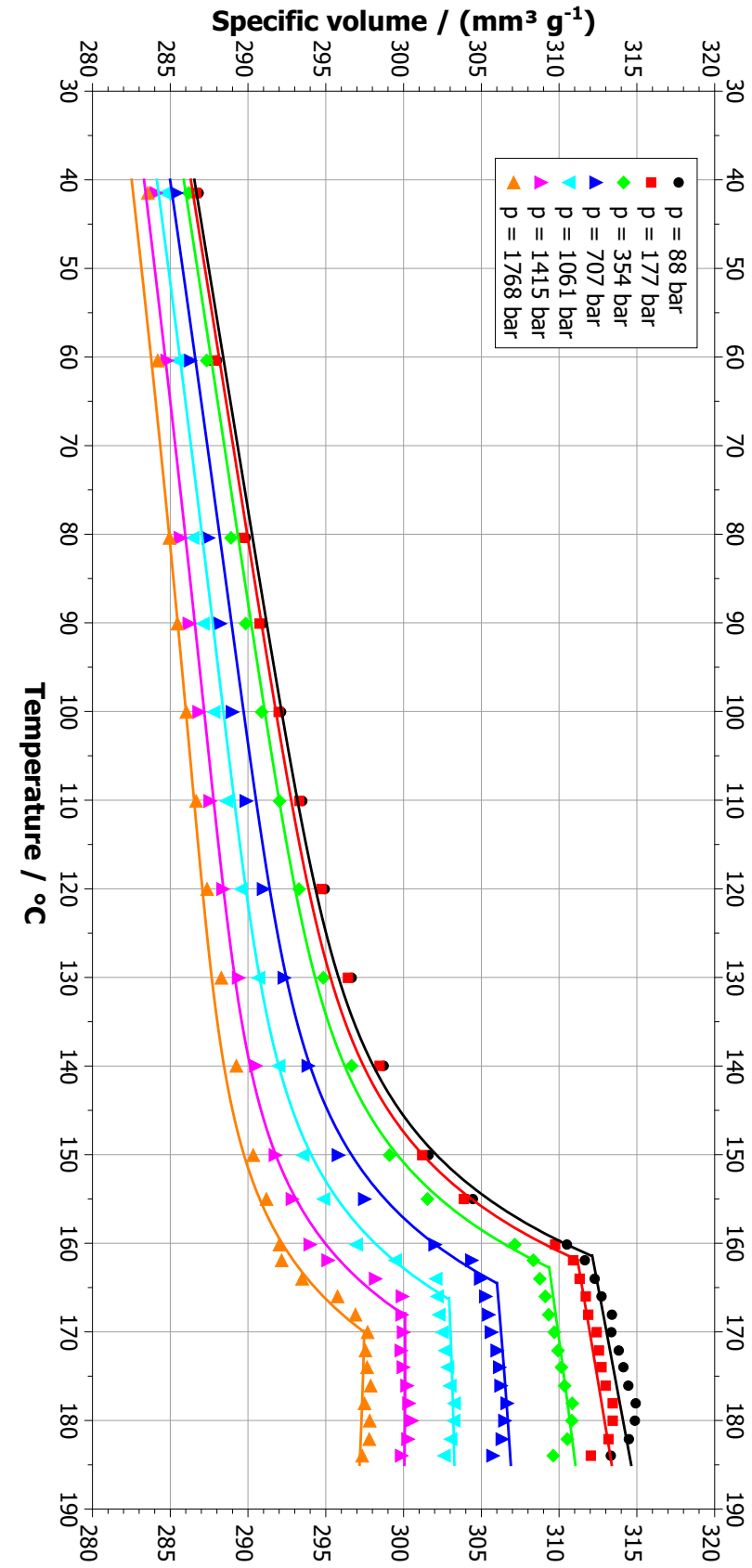

Figure 4.6: Measured pvT data and fitting curves for BASF Catamold® TZP-A.

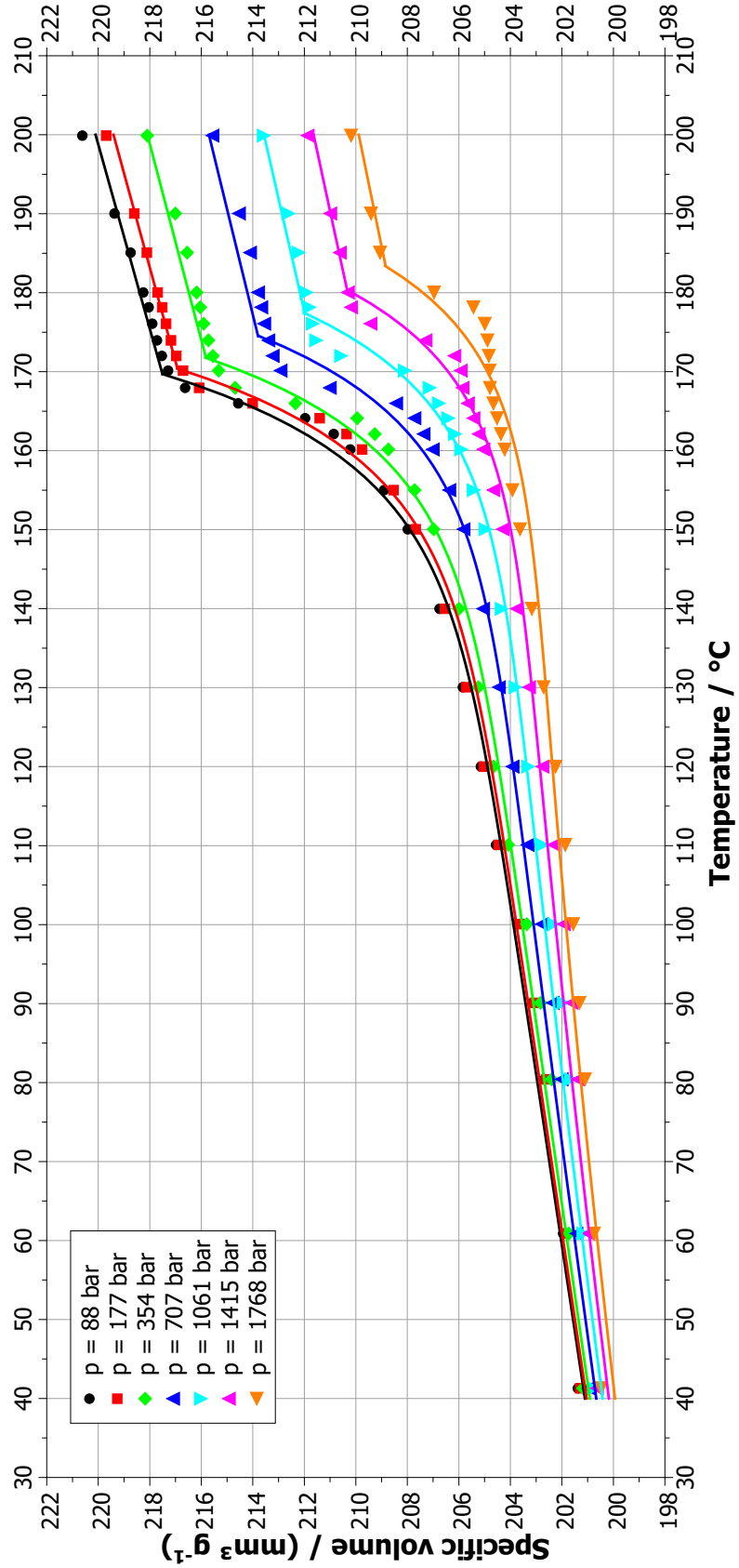

Figure 4.7: Measured pvT data and fitting curves for BASF Catamold® 17-4PHA.

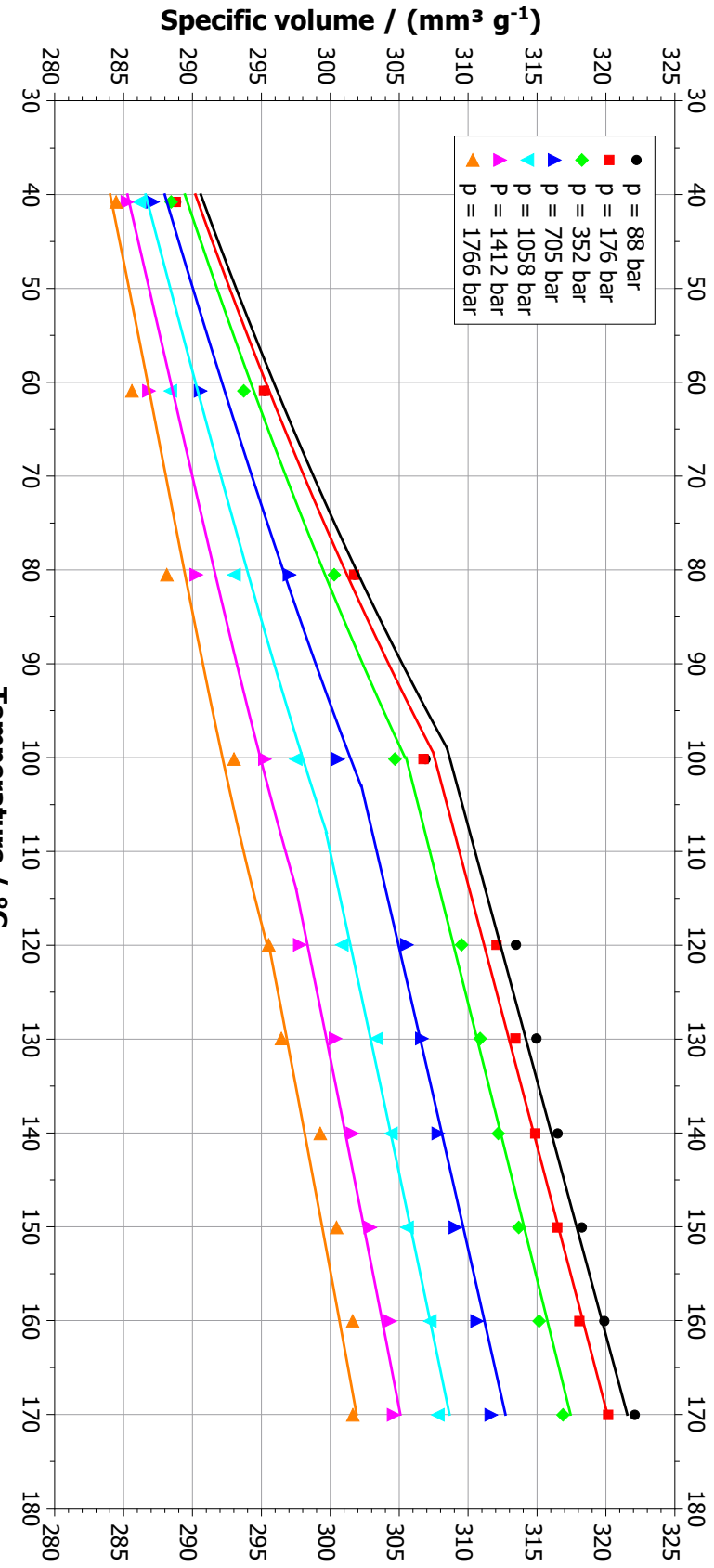

Figure 4.8: Measured pvT data and fitting curves for GoMikro ZrO_2.

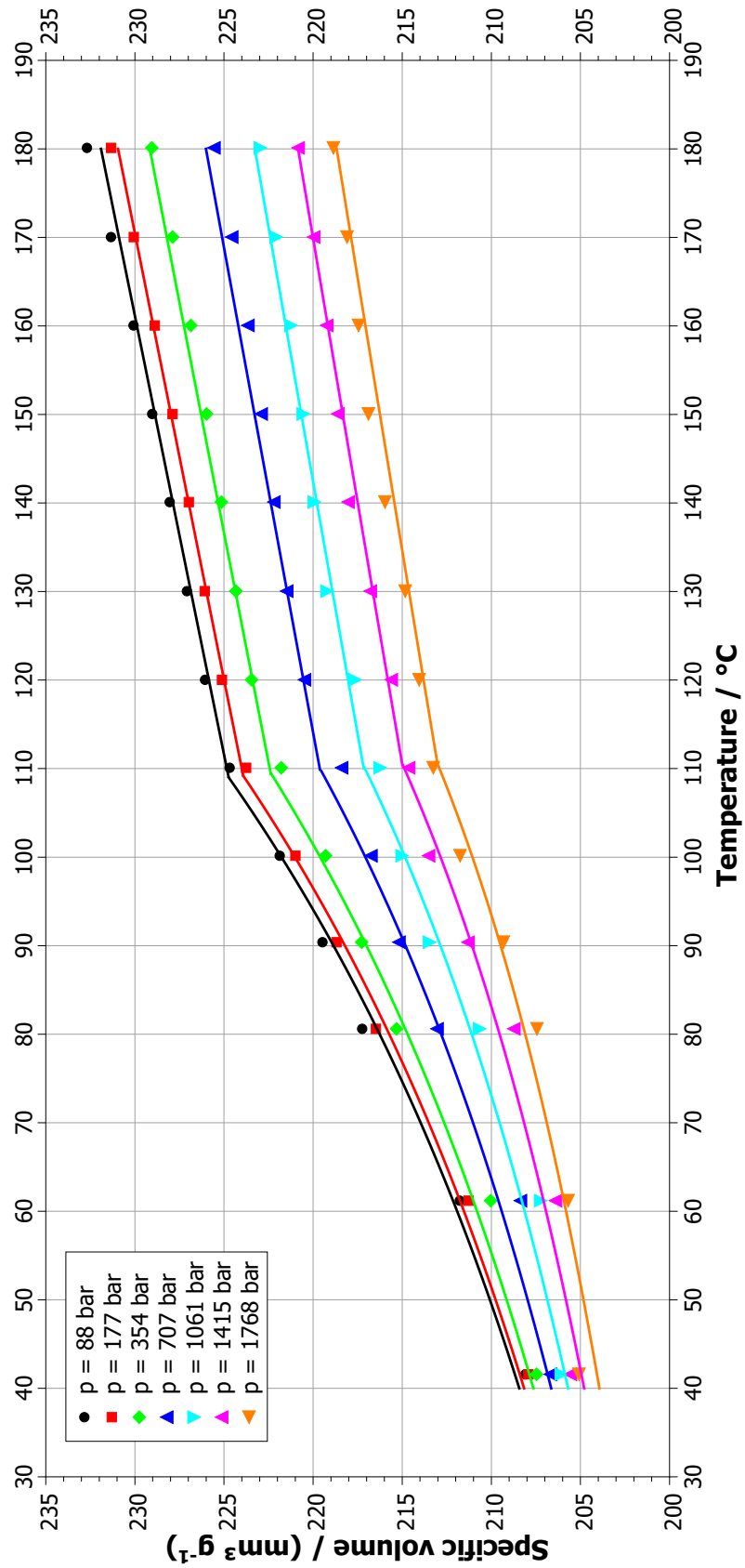

Figure 4.9: Measured pvT data and fitting curves for GoMikro 17-4PH.

Table 4.11: Data-fitted parameters for the modified 2-domain Tait model describing the pvT data of the investigated feedstocks, determined with ASMI and SigmaSoft®, and reference values of a pure POM from BASF (from ASMI data base [100]). The values are shown as generated by the fitting software.

Parameter		Catamold® TZP-A		Catamold® 17-4PHA		GoMikro ZrO_2		GoMikro 17-4PH		POM
name	unit	ASMI	SigmaSoft®	ASMI	SigmaSoft®	ASMI	SigmaSoft®	ASMI	SigmaSoft®	
b_{1s}	$10^{-4}\,m^3\,kg^{-1}$	2.982	2.935	2.072	2.075	2.953	3.026	2.043	0.657	7.427
b_{2s}	$10^{-8}\,m^3\,kg^{-1}\,K^{-1}$	9.438	9.738	4.677	5.050	16.79	23.217	4.758	-0.38184	27.39
b_{3s}	$10^{8}\,Pa$	4.0432	3.3399	7.4382	7.6931	1.85838	1.4419961	1.71485	0.3400786	3.21847
b_{4s}	$10^{-3}\,K^{-1}$	7.296	9.984	9.394	8.612	18.79	15.7	17.71	36.5	2.427
b_{1m}	$10^{-4}\,m^3\,kg^{-1}$	3.131	3.131	2.181	2.176	3.096	3.116	2.256	2.252	8.496
b_{2m}	$10^{-7}\,m^3\,kg^{-1}\,K^{-1}$	1.179	1.646	0.877	1.040	1.896	1.8880	1.027	1.1226	3.689
b_{3m}	$10^{8}\,Pa$	2.38286	2.19627	2.58211	2.57587	2.11054	2.05382	2.01520	2.04885	1.26898
b_{4m}	$10^{-3}\,K^{-1}$	9.976	7.532	2.500	2.418	3.59	3.8699	1.549	1.9632	2.514
b_5	K	434.15	435.37	442.15	440.31	372.04	382.00	382.15	382.28	443.15
b_6	$10^{-8}\,K\,Pa^{-1}$	4.9	3.3824	7.8	8.4587	7.2	14.0	1.0	-1.9651	3.75
b_7	$10^{-5}\,m^3\,kg^{-1}$	1.484	1.43	1.087	0.99987	1.437	0.93654	2.135	16.08	10.7
b_8	$10^{-2}\,K^{-1}$	8.505	7.530	9.036	11.930	1.598	1.33	1.481	46.622	5.729
b_9	$10^{-9}\,Pa^{-1}$	7.389	4.795	11.250	14.437	0.001616	-1.7548	0.00001165	0.080996	5.289

the fitting of the parameters was quite challenging. It is even doubtful, whether the 2-domain Tait model is suitable and can properly grasp the material behavior and if the collected data is sufficient. More information about the goodness of fit would have been helpful, and it is recommended to elaborate on this in future work.

4.11.3 Material compressibility

According to Equation 3.12, the term $B(T)$ corresponds to the pressure sensitivity. The pressure dependency of the specific volume of the feedstocks is of interest, as the injection molding happens at very high pressure levels. Since the molding happens at elevated temperatures, the discussion of the pressure sensitivity is limited to the molten material phase at $T > T_\mathrm{t}$. The normalized specific volume v_n versus the pressure and depending on the pressure sensitivity is given as

$$v_\mathrm{n}(p,T) = \frac{v(p,T)}{v_0(T)} = 1 - C \ln\left(1 + \frac{p}{B(T)}\right). \tag{4.7}$$

With the parameters from Table 4.11, the normalized specific volume can be plotted, as shown in Figure 4.10. It should be noted that the pressure sensitivity is a function of the temperature. Furthermore, the graph proves that feedstocks are in general much less compressible than the pure binder due to the rigid powder particles. At their typical processing temperatures and 2000 bar, POM can be compressed by about 9 %, whereas Catamold® 17-4PHA and Catamold® TZP-A are only about 5 % and 6 % compressible, respectively.

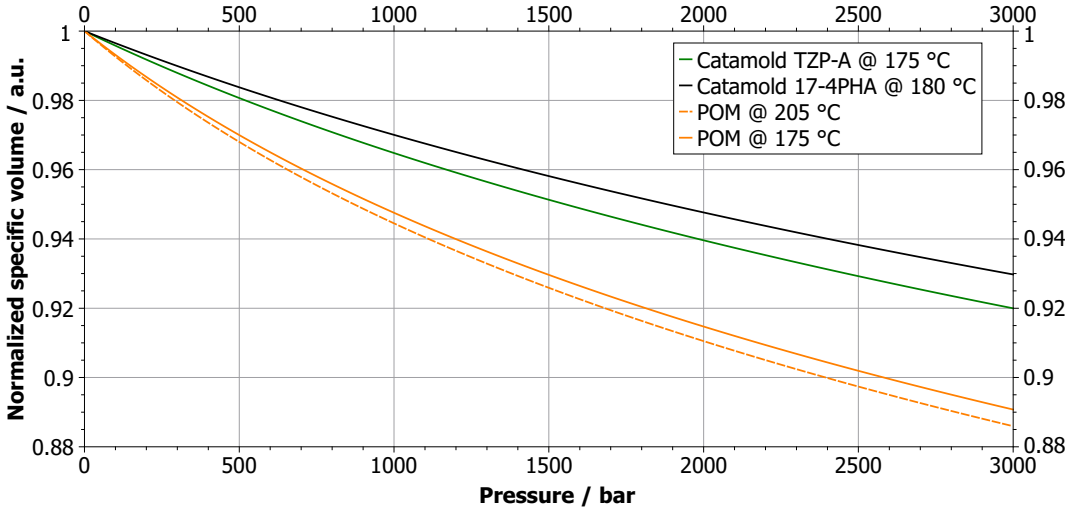

Figure 4.10: Normalized specific volume of the Catamold® feedstocks and the pure POM binder to illustrate the pressure dependency of the specific volume and compressibility of the materials.

4.12 Summary and conclusion

First, the powder load of the two Catamold® feedstocks were determined because of missing information, resulting in values of about 81 wt% (50 vol%) and 89 wt% (60 vol%) for the ceramic and metallic compound, respectively. The density was also measured, yielding values of approximately $3.5\,\mathrm{g\,cm^{-3}}$ and $4.9\,\mathrm{g\,cm^{-3}}$. These values illustrated that feedstocks are in general much heavier than pure plastics. Inertial forces certainly influence the filling behavior and can lead to wall-slipping or jetting.

Continuing with all four feedstocks, the specific heat capacity was measured by DSC with special attention to the temperature dependency. The results of all compounds were in the range of $0.6\,\mathrm{J\,g^{-1}\,K^{-1}}$ to $1.0\,\mathrm{J\,g^{-1}\,K^{-1}}$—typical values for powder feedstocks. Nevertheless, the compounds showed distinct peaks in the heat capacity curve reaching values up to about $2.2\,\mathrm{J\,g^{-1}\,K^{-1}}$. These peaks could be attributed to the melting temperatures of the binder components. The melting however did not happen at a distinct temperature and introduced hence significant measurement uncertainties around the melting temperature, especially for the Catamold® feedstocks with maximum uncertainties of $1.6\,\mathrm{J\,g^{-1}\,K^{-1}}$. It was proven that the heat capacity of the feedstocks is much lower than for plastics.

The thermal conductivity was measured indirectly by the determination of the thermal diffusivity in a laser flash analysis covering the full range from room to processing temperature. The dependency of the thermal conductivity on the heat capacity, the density, and the thermal diffusivity was taken into account by the calculation of the measurement uncertainty. The thermal conductivity also showed significant peaks and an increase in measurement uncertainty around the melting temperatures of the binder components which was caused by the contribution of the heat capacity. In addition, the theoretically expected values of the thermal conductivity were calculated.

The ceramic feedstocks showed with values of about $1\,\mathrm{W\,m^{-1}\,K^{-1}}$ good agreement both with the theory and typical values from literature. The metal feedstocks exhibited conductivities in the range of $1.5\,\mathrm{W\,m^{-1}\,K^{-1}}$ to $2.5\,\mathrm{W\,m^{-1}\,K^{-1}}$ which exceeded the theoretical values, but matched data from literature. The generally higher conductivity compared to the ceramic feedstocks could be attributed to the higher conductivity of the used metal powder and the higher powder load. Compared to the pure plastic binder, it was found that the feedstocks show a greater thermal conductivity.

The lower heat capacity and higher thermal conductivity can both be an issue during the filling phase. The heat carried by the feedstock is less than for plastics and in addition released more quickly which leads to an increased risk of premature solidification and short shots as well as larger pressure drops.

The rheological measurements were done by means of a capillary rheometer coming with the advantage of easy use and applicability to high shear rates as occurring in injection molding. The drawback was the necessity to apply the presented mathematical correction to the raw viscosity data. However, the viscosity was successfully measured and fitted by the Cross-WLF model for all four feedstocks. The curves showed the typical behavior of feedstocks with a missing Newtonian plateau. Literature discusses the necessity of extended viscosity models like Herschel-Bulkley to fully describe feedstocks.

Regarding the model, the viscosity measurements could be subject of future investigations. The resolution in shear rate should be significantly increased to identify a possible Newtonian plateau. If the Newtonian plateau was absent or covered a small negligible range, the viscosity might still be properly modeled by the Cross-WLF approach. This would facilitate the applicability of existent simulation tools to powder injection molding.

The collected pvT data of the Catamold® feedstocks reflected clearly their semi-crystalline polyacetal binder with a significant change in specific volume at the melting temperature. The data was successfully fitted by the 2-domain Tait model. In contrast, the curves of the non-commercial GoMikro feedstocks resembled neither clearly the typical shape of semi-crystalline nor amorphous materials. The curves were influenced by the different melting points of the two binder components, PE and wax. Furthermore, the distinction between the solid and liquid domain of the 2-domain Tait model is problematic, since the transition phase—where the wax is molten, the PE still solid—is quite broad. Hence, the fitting of the parameters is challenging, too. Nevertheless, the detailed analysis of the fitted parameters could reveal the much smaller material compressibility of feedstocks.

In conclusion, collecting and processing material data turned out as an extensive and time-consuming, but vital task for conducting injection molding simulations. Material data base files might not be available or outdated, especially in case of powder feedstocks. The necessary material properties for establishing a material data base file were outlined and covered by the performed detailed characterization of two commercial and two non-commercial feedstocks. The material characterization finally enabled to create material data files for the process simulations which are shown in chapter 8 and 9.

5 Validation of polymer micro injection molding simulations

Abstract This chapter deals with the validation of the process simulations of micro injection molding and the influence of the implementation of the mold and venting channels in the simulation model. The investigations are preformed on a micro channel test structure. The component is first introduced. Afterwards, the molding of the component as well as the simulation model and analysis are described. Finally, the results are compared, and the validation is discussed.

5.1 Study case

The first study case was a micro channel test structure with channels and walls of various widths and depths representing microfluidic structures, as depicted in Figure 5.1. The part had outer dimensions of about 13 mm × 13 mm × 3 mm (length × width × height). The channels and walls with dimensions in the micrometer range down to 200 µm made it a micro-patterned plastic part.

The part was given with the feed system consisting of a fan gate with a gate land thickness of 0.8 mm and the same width as the part. The runner had a diameter of 4 mm and a length of about 24 mm. The sprue featured a taper of 2°, a sprue puller, an inlet diameter of about 2.6 mm, and a total length of 40 mm. The injection volume of the part including the feed system was about 1.2 cm^3. More information about the dimensions of the part and feed system can be found in the drawings in Appendix B.

The component originated from test purposes [119]. The substantial challenge with the part was the molding of the fine ribs with a thickness in the micrometer range and at the same time a length of several millimeters, making the ribs to “elongated” micro features. Besides, the ribs and channels showed aspect ratios of up to four and the aspect ratio is often a crucial parameters for the filling of micro features.

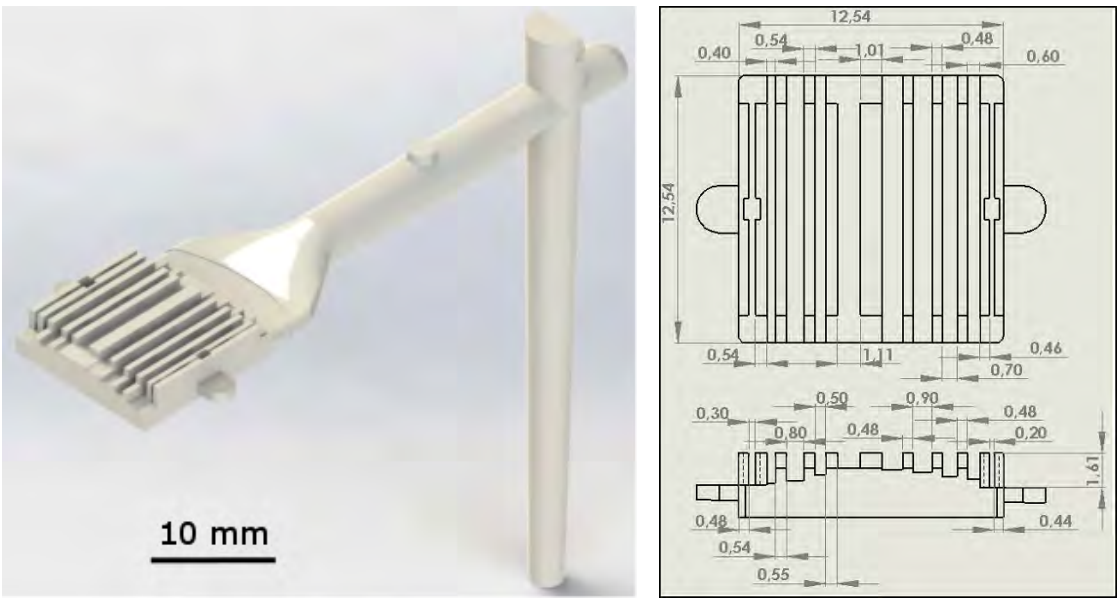

(a) CAD model of part and feed system. **(b)** Drawing.

Figure 5.1: Model and dimensions of the micro channel test structure [119].

5.2 Molding

The micro channel test structure was molded with the settings listed in Table 5.1. The experiments were carried out on the standard hydraulic injection molding machine Engel ES 80/25 HL-Victory with 18 mm screw diameter and 250 kN clamping force made by Engel Austria, Schwertberg, Austria, using the acrylonitrile butadiene styrene (ABS) Novodur P2H-AT provided by Styrolution, Frankfurt am Main, Germany. The mold temperature was set to 80 °C and measured as 82 °C. The four heating zones of the barrel of the machine were set from 205 °C to 220 °C in steps of 5 °C and increasing temperature towards the nozzle. The temperature of the plastic melt was measured as 220 °C.

The injection speed was set to $50\,\mathrm{mm\,s^{-1}}$. The real speed profile was monitored and extracted from the machine. Figure 5.2 illustrates the average speed profile of eight shots during serial production. The standard deviation over the entire curve was $<1.8\,\mathrm{mm\,s^{-1}}$. The calculation of the mean curve is described in more detail in Appendix B. The speed profile showed that the limited response time of the machine resulted in a delay of about 20 ms and inferior repeatability (higher standard deviation) at the start of injection. Besides, the machine had a limited acceleration, ramped up the speed, and did not reach the target value of $50\,\mathrm{mm\,s^{-1}}$ during injection.

Besides the speed, the pressure profile, the injection or fill time, i.e. the time until the switch-over point is reached, and the part mass were part of the investigation.

Table 5.1: Process settings for the molding and simulation of the micro channel test structure.

Parameter	setting
Material type	ABS
Material grade	Novodur P2H-AT
Melt temperature / °C	220
Mold temperature / °C	80
Dosage stroke / mm	11.5
Decompression / mm	4.0
Back pressure / bar	3
Switch-over point / mm	4.5
Injection speed / mm s^{-1}	50
Packing time / s	2.0
Packing pressure / bar	50
Cooling time / s	20
Machine	Engel ES 80/25 HL-Victory (18 mm)

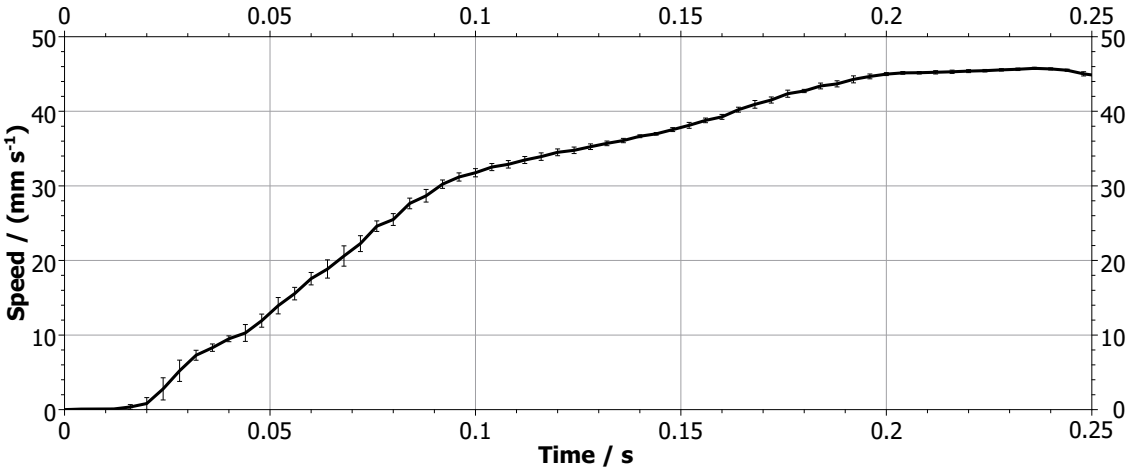

Figure 5.2: Monitored speed profile versus time of the used injection molding machine for the molding of the micro channel test structure. The error bars denote the standard deviation of the data points with a maximum value of about $\pm 1.8\,\mathrm{mm\,s^{-1}}$.

The reported pressure and time are the mean value of eight independent shots. The mass measurement was performed by means of the electronic scale Shimadzu AW 220 (resolution: 0.1 mg, repeatability: 0.2 mg), made by Shimadzu Corporation, Kyoto, Japan. The part mass reported for the experiments is the average of the mass of 45 individual parts including the feed system.

5.3 Simulation

5.3.1 Models

The micro channel test structure was simulated for validation purposes. Multiple simulation models of different complexity (described in the following) were analyzed to demonstrate the influence of the modeling of the injection molding machine and of the implementation of venting in the model. The models are described in the following, more information about the implementation of the venting can be found in the next section. The actual mold block was not implemented in any of the models. The overview about the models is shown in Table 5.2 The evaluation of the simulation was done in agreement with the experiments based on the predicted filling time, maximum injection pressure, and part mass. All evaluation criteria were directly given by the simulation software.

A: Part
The simulation model comprised the feed system, the fan gate, and the actual part. Other modules like the mold or machine were not modeled.

B: Part + machine
In addition to the part and feed system, the simulation model also included the geometry of the used injection molding machine. The nozzle and used part of the barrel of the machine were set up as hot runner in the simulation software.

C: Part + machine + venting (5 µm)
Based on the previous one, this model contained additionally venting structures with a thickness of 5 µm.

D: Part + machine + venting (2 µm)
Similar to the previous one, this model also featured venting structures but with a smaller thickness of 2 µm.

E: Part + machine + venting (front only)
This model also included venting structures, but the implemented venting channel was limited to the front (opposite of the fan gate) side of the part. The model was implemented for demonstration purposes of the venting analysis.

Table 5.2: Incorporated entities of the different simulation models of the micro channel test structure to assess the influence of the machine geometry and venting analysis on the predicted process outcome.

Model	A	B	C	D	E
Part	✓	✓	✓	✓	✓
Feed system	✓	✓	✓	✓	✓
Machine speed profile	✓	✓	✓	✓	✓
Machine geometry	✗	✓	✓	✓	✓
Venting	✗	✗	✓ (5 µm)	✓ (2 µm)	✓ (front only)

5.3.2 Venting

Venting structures are widely applied to efficiently remove the entrapped air from cavities, runners, and sprues. During injection, the air is displaced and highly compressed by the plastic melt. As the machine and plastic melt have to work against the counter pressure of the compressed air, more time and higher pressure for filling the cavity may be necessary. [14, 81]

If no venting structure exists in the mold, the air in the cavity escapes through the gaps between the two closed halves of the mold and between ejectors and mold, when the plastic is injected. The size of this gap and hence the occurring pressure caused by the compressed air depends on the clamping force and the surface roughness of the mold plates.

Full venting of the mold, equivalent to the application of vacuum to the mold prior to injection, is assumed as default setting in ASMI. This holds true, whether just the part with the surrounding virtual mold is modeled or an actual mold block is added to the simulation. To account for actual venting structures and the air present in the cavity, ASMI provides the option for running a venting analysis. However, certain limitations do exist regarding the implementation of the venting structures in ASMI:

- The venting channels can be connected to any area of the part, but it must be connected perpendicularly to the surface of the part.
- The venting channels can only be cuboid with rectangular cross-section. Neither tapered or round channels nor fillets are possible. Accordingly, the channels are implemented by assigning the length, width, and thickness.
- The venting channels cannot be applied to curved or rounded surfaces of the part.

The mold of the micro channel test structure did not exhibit special venting structures. The venting channels applied in the simulation modeled the escape of air through the

gaps between the mold plates. The contribution to the air purge by the ejector pins was not feasible and expected to be small in comparison. Thus, the implemented venting structures were in the parting plane of the mold and spreading from the straight faces of the part and runner to the boundary of the mold, as shown in Figure 5.3. The thicknesses of the implemented venting channels was chosen in accordance to typical values of the roughness of machined standard mold plates in the low micrometer range. The length of the venting channels was given by the position of the part in the mold and the mold dimensions. The width resulted from the accessible faces of the part and runner. To check the influence of the venting analysis in the simulation software, the models C, D, and E were equipped with venting structures of varying thickness. The dimensions of the venting channels are listed in Table 5.3.

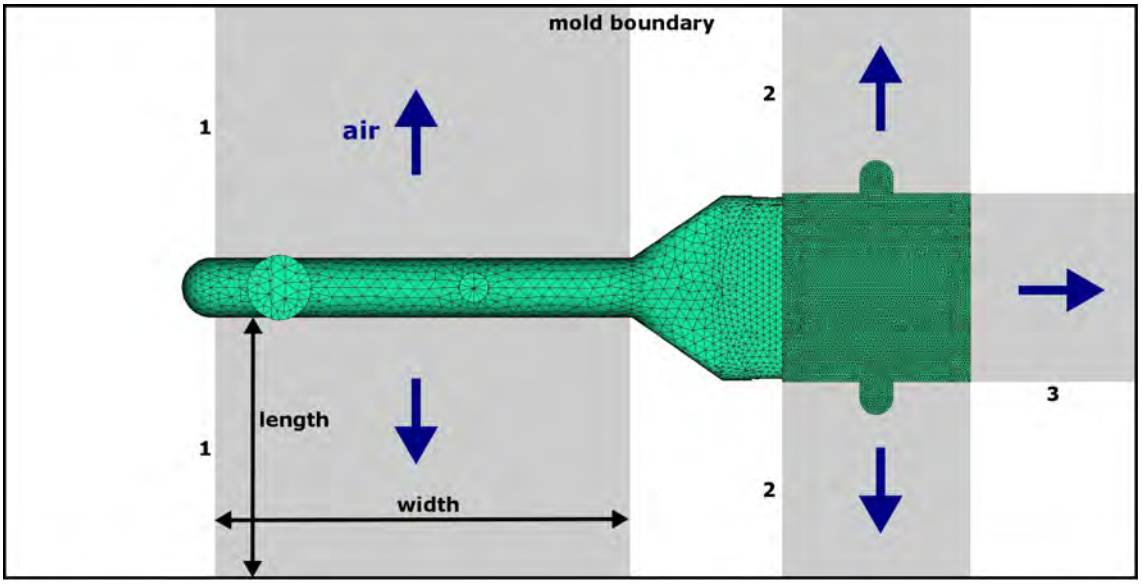

Figure 5.3: Schematic (not true to scale) of the implementation of the venting structure for the venting analysis in ASMI. The grey areas illustrate the implemented venting channels. Their dimensions were given by the part position and the mold size. The dimensions of the venting channels are listed in Table 5.3.

5.3.3 Meshing

The micro channel test structure was meshed with the settings listed in Table 5.4. The part and gate were assigned specific element edge lengths leading to local mesh enhancement. The meshed part is shown in Figure 5.4. The models B, C, D, E were created by adding the machine geometry consisting of the inner volume of the nozzle, the adapter between nozzle and barrel, and the barrel which was occupied

Table 5.3: Dimensions of the implemented venting channels of the models C, D, E of the micro channel test structure. The numbering of the venting channels corresponds to Figure 5.3. All dimensions in mm, corresponding to length × width × thickness.

Model	Channel 1	Channel 2	Channel 3
C	48.0 × 28.2 × 0.005	43.7 × 12.5 × 0.005	43.7 × 12.5 × 0.005
D	48.0 × 28.2 × 0.002	43.7 × 12.5 × 0.002	43.7 × 12.5 × 0.002
E	not implemented	not implemented	3.0 × 3.0 × 0.005

by the plastic. The machine geometry was divided into multiple beam elements[1] with the property of a hot runner in the simulation software. The beam elements were given the inner dimensions of the machine parts (shown in Appendix B). The hot runner was set to the same temperature as the plastic melt. The result of the implementation is depicted in Figure 5.5. Additionally, the venting channels were added for the models C, D, E as outlined in the previous section.

Table 5.4: Meshing settings of the micro channel test structure. Unspecified settings were kept at the default values.

Parameter	setting
Specific element edge length / µm	
part	150
fan gate	500
Beam element edge length / mm	
nozzle (tapered section)	1.0
nozzle (straight section)	3.0
adapter	2.0
barrel	4.0
Global edge length / mm	1.0
Merge tolerance / µm	20
Chord height / µm	30
Minimum number of elements through thickness	12
Maximum edge length in thickness direction / mm	1.0
Bias ratio	1.2
Total number of elements	1 300 000

[1] In contrast to the usual tetrahedral elements constituting the mesh, beam elements are two-noded elements with defined length and diameter which can be used for the representation of simple geometries like tapered or non-tapered channels or beams. [49]

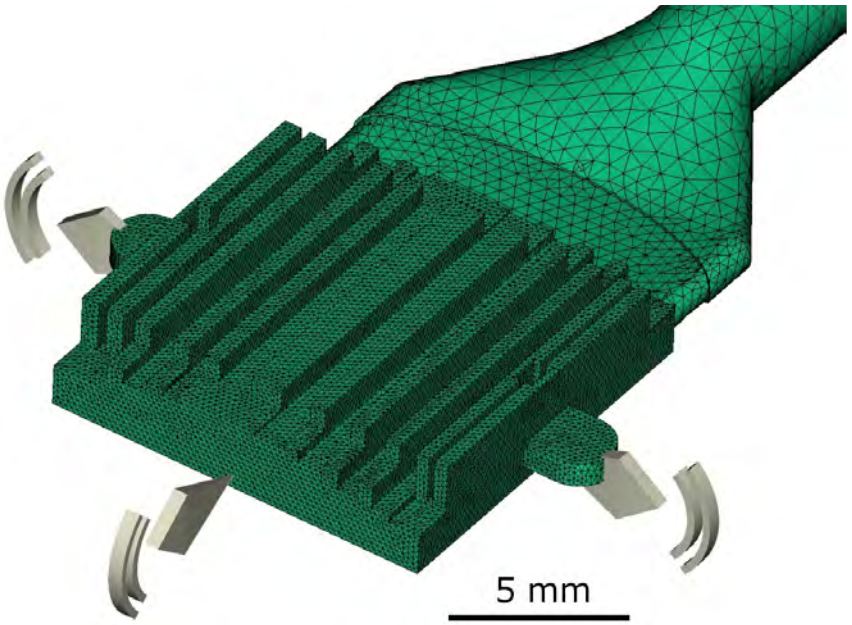

(a) Complete part with venting indicators.

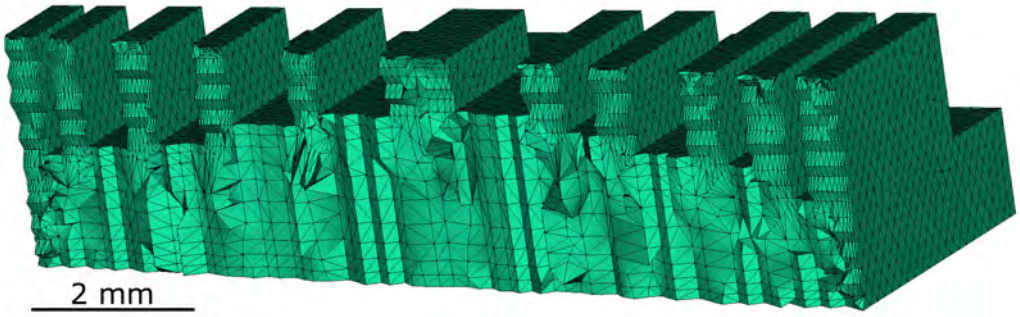

(b) Cut through the meshed part.

Figure 5.4: Meshed model of the micro channel test structure. The part and gate were meshed with smaller, individual specific element edge lengths.

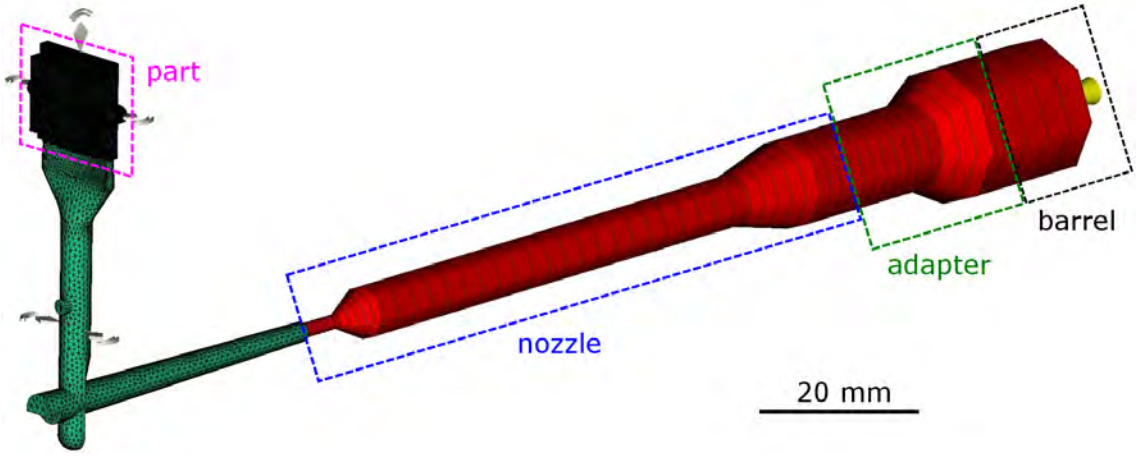

Figure 5.5: Meshed model of the part with feed system, additional machine geometry modeled as hot runner, and pointers indicating the venting channels. The geometry resembles the actual nozzle and barrel of the machine.

5.3.4 Simulation settings

The processing conditions as well as the material and machine choice of the simulations were in accordance to the experiments for most accurate results. The common settings are listed in Table 5.1 in the previous section, additional settings are listed in Table 5.5. ASMI 2013 was used for the simulations of the filling, packing, warpage, and venting of the micro channel test structure.

Especially in case of micro and fully electrical injection molding machines, the assumptions of the simulation software are often not sufficient to describe the machine characteristics properly. Major influences such as the delay due to the actual machine acceleration and the resulting true polymer flow rate are not taken into account. It is hence recommended to implement manually the speed profile of the injection molding machine based on experimental data to reproduce its characteristics as realistically and accurately as possible. [60]

Since the software can on the one hand reproduce basically any machine acceleration, and the Engel injection molding machine proved to exhibit limited response time on the other hand, the monitored speed profile was hence imported to the simulation software to model the real process more accurately.

The injection location diameter was set to the diameter of the nozzle of 2.0 mm for the default simulation. The diameter was adapted to the diameter of the modeled barrel of 18.0 mm in the other studies.

Table 5.5: Additional simulation settings of the micro channel test structure. Unspecified settings were kept at the default values.

Parameter	setting
ASMI version	2013
Analysis type	Fill+Pack+Vent
Virtual mold material	Uddeholm Orvar Supreme
Injection location diameter / mm	model A: 2.0, else: 18.0

5.4 Results and discussion

The experimental molding yielded an injection time of about 0.32 s and a maximum detected pressure of about 123 MPa. The determined standard deviation of the pressure was over the entire curve <3 MPa. The simulation studies proved that the implementation of the machine geometry and the venting analysis can improve the results, as illustrated in Figure 5.6 to 5.7. The more features were implemented, the closer the predictions were to the actual values. All simulations of the test part underestimated the injection time, the injection pressure, and the part mass though. This underestimation was most likely caused by the limitations of the software to handle micro parts and microscale effects. The part mass was still the most stable parameter, and already the default simulation setup reached 96 % of the actual value.

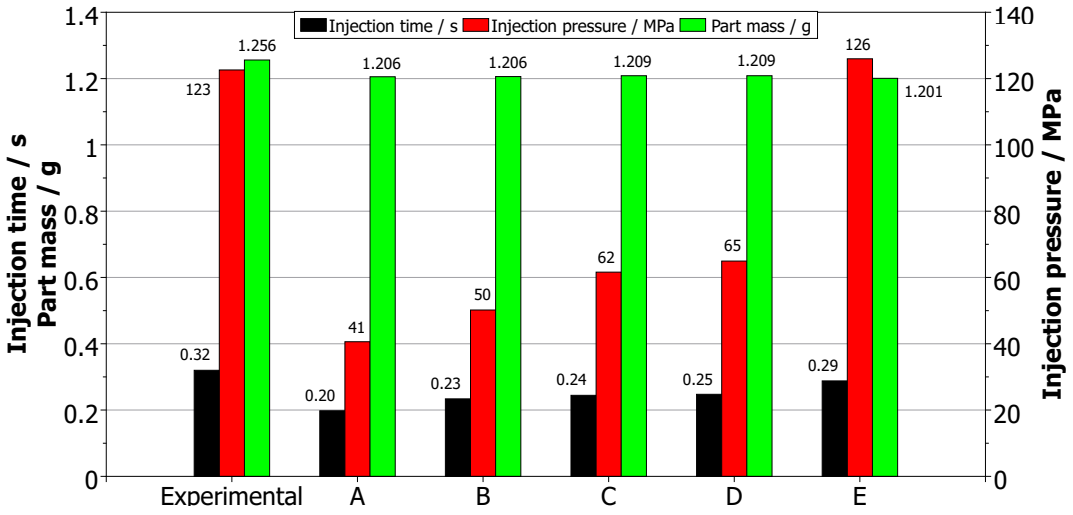

Figure 5.6: Injection time, injection pressure, and part weight of the experiments and different simulation models of the micro channel test structure. The studies A, B, C, D, E refer to the models described in subsection 5.3.1.

The implementation of the machine geometry improved the fill time and injection pressure by 15 % and 22 %, respectively. This improvement could first be attributed

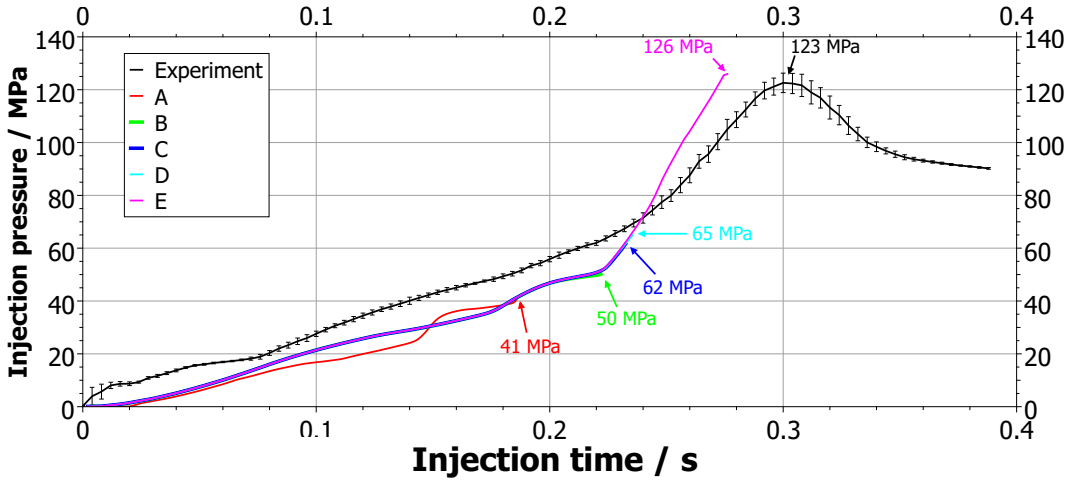

Figure 5.7: Injection pressure versus time for experiments and the simulated models of the micro channel test structure. The error bars indicate the standard deviation of the experimentally recorded pressure with a maximum value of about ±3 MPa.

to the additionally introduced plastic located between the screw and the nozzle and in the melt cushion during both injection and packing. This plastic cushion contributed largely to the material compressibility, when the pressure was applied.

Regarding the prediction of the injection pressure, it was moreover advantageous to model nozzle and barrel, since it accounted better for the additional pressure drop than the default internal assumptions of the software. Accurate injection pressure simulation is generally important, because it is the crucial process parameter and directly linked to the part quality. Yet, this procedure of modeling the machine geometry had to be seen critical and applied carefully. In ASMI, the barrel volume stayed constant, whereas in reality the barrel volume decreased during injection due to the movement of the screw.

Although no venting structures were existent in the real mold, implementing a venting analysis was found to enhance the results, as the default complete venting is a critical assumption. Depending on the thickness of the venting channel modeling the gap at the parting plane of the mold, the additional venting analysis was capable of improving the output again by up to 9 % and 30 % for the fill time and injection pressure, respectively. As expected, the time and pressure increased with decreasing channel thickness due to the more difficult air escape. The very small venting channel exposed the possible impact and importance of the venting analysis on the injection pressure.

Figure 5.8 depicts the comparison of the flow front of the investigated simulation models at different positions. The over-all pattern of the flow front did not vary

noticeably. Because of the deviation in filling time, the same flow front occurred at different times. In case of the model B, the flow front was slightly ahead of the models C, D, and E which is in agreement with the slightly shorter fill time. The polymer flow rate inside the cavity was higher for model A, especially at the beginning. This could be identified by the fact that the time step between the shown flow front positions is shorter. In case of model A, the shown flow fronts are separated by 7 ms and 15 ms, whereas in case of the other models the time step is 19 ms and 16 ms.

5.5 Summary and conclusion

The introduced micro channel test structure was molded to collect information about the process and to perform a simulation validation. The molding was done on a conventional injection molding machine. The injection speed of the machine was monitored, and the records revealed that the settings and the real speed profile differed much. This behavior must be considered in the process simulations, because the software can basically reproduce any acceleration and response time and the default assumptions might not reflect the really deployed machine.

The subsequent investigation of the study case comprised several simulation models of different comprehensiveness. The models varied in the extent of the implemented machine geometry and venting structures. The machine geometry or rather the plastic volume inside the machine was modeled as hot runner to account for the additional fill time due to compression and the occurring pressure drop. The mold did not feature any specific venting structures. Still, the application of a venting analysis with venting channels representing the air purge of the cavity through the parting plane of the mold was conducted. The machine characteristics were moreover accounted for in the models by the use of the measured speed profile.

All simulation models underestimated the actual values of injection time, injection pressure, and part mass. The shape of the flow front did not differ noticeably between the models. Nevertheless, the enhancements of the default model, i.e. the incorporation of the actual process boundary conditions, machine geometry, machine behavior, and venting, proved to boost the predicted results significantly. Furthermore, the trends of the fill time and pressure were predicted correctly. Keeping this limitation in mind, the process simulations can also be applied in the design of micro products. As a result, the scope of the implementation of the simulation model can have large impact on the simulation results. Regarding micro injection molding, the entire injection molding system should be modeled. Otherwise, the software can yield inaccurate results, caused by its purpose for macroscopic plastic parts.

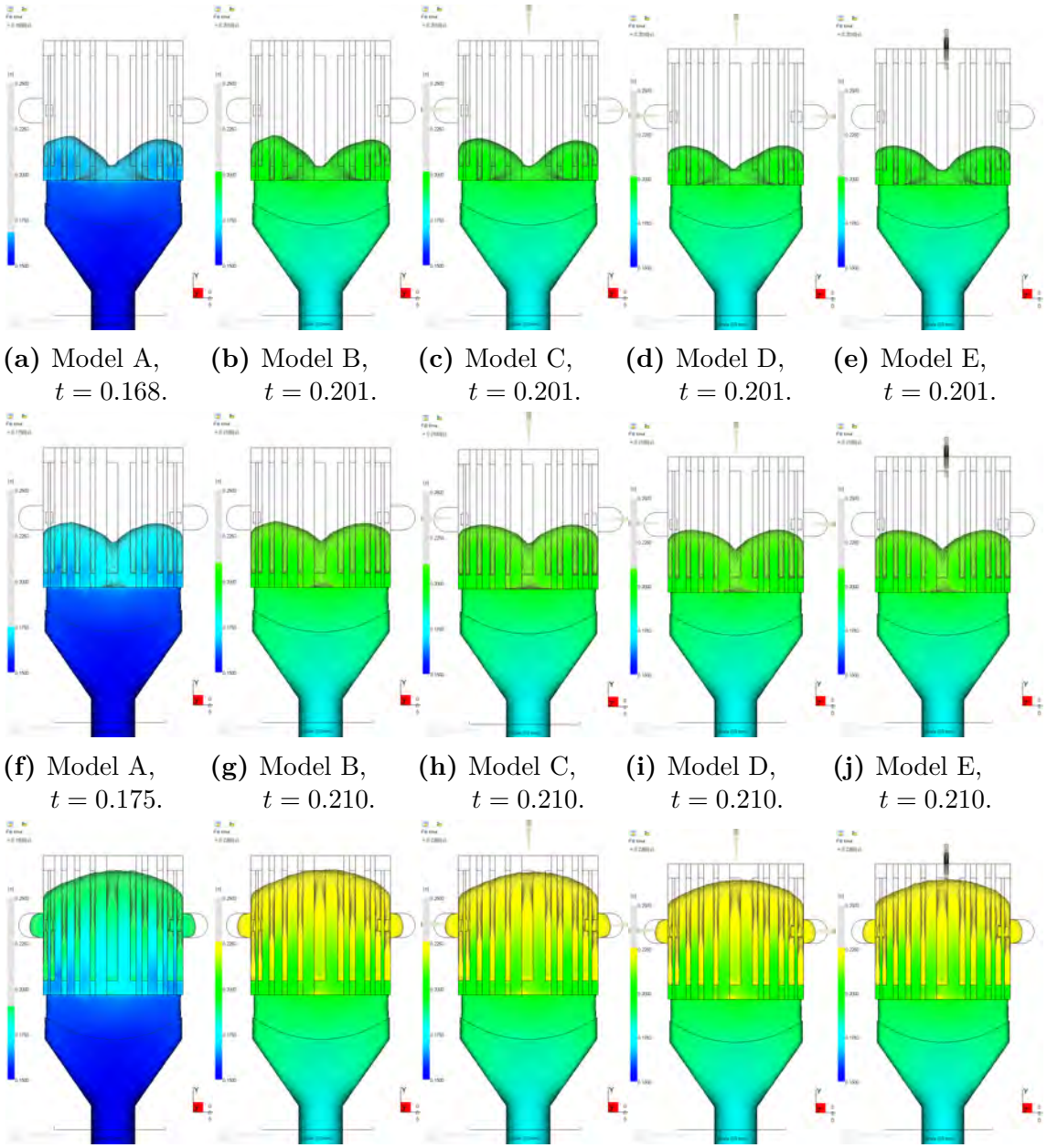

(a) Model A, $t = 0.168$. **(b)** Model B, $t = 0.201$. **(c)** Model C, $t = 0.201$. **(d)** Model D, $t = 0.201$. **(e)** Model E, $t = 0.201$.

(f) Model A, $t = 0.175$. **(g)** Model B, $t = 0.210$. **(h)** Model C, $t = 0.210$. **(i)** Model D, $t = 0.210$. **(j)** Model E, $t = 0.210$.

(k) Model A, $t = 0.190$. **(l)** Model B, $t = 0.226$. **(m)** Model C, $t = 0.226$. **(n)** Model D, $t = 0.226$. **(o)** Model E, $t = 0.226$.

Figure 5.8: Comparison of the flow fronts of the different simulation models of the micro channel test structure at two positions. The shape of the flow front did not differ significantly between the studies. Color scale: fill time from 0.15 s to 0.25 s (blue to red).

6 Simulation-aided part design

Abstract This chapter deals with the simulation-aided design of a micro product, when no mold is available and the design should be optimized. The work is therefore limited to the investigation and editing of the part, the mold was not designed. Firstly, the study case being subject to the design optimization is introduced. Afterwards, the analysis of the part design by simulations and design of experiments is outlined, and the design optimization based on the results of the analysis is discussed. The motive of this chapter is to promote the application of simulations in micro injection molding.

The first part of the chapter about the early design iteration was conducted together with a master student. The work was closely supervised by the author of this Ph.D. and took place at the Department for Mechanical Engineering at DTU.

6.1 Study case

6.1.1 Component

The simulation-aided part design was applied to a microfluidic dispenser for water-based solutions. Its purpose was to widen the flow from a narrow inlet at the top to a wide channel outlet at the bottom, while maintaining uniformity of flow velocity and pressure. The initial design of the dispenser is shown in Figure 6.1.

The dispenser had outer dimensions of 25 mm × 7 mm × 2 mm (length × width × height) and a total part volume of 190 mm^3. The device exhibited microfluidic channels on its front and back side which were symmetrical. The channels were down to 500 µm wide and less than 200 µm deep. The walls separating and limiting the fluidic channels reached thicknesses down to about 100 µm. The ribbing and coring out in non-fluidic areas was to retain strength, while enabling more uniform part thickness in accordance to general injection molding design guidelines.

The part was supposed to be assembled to other components which acted as lids on both sides. To avoid leakage, all the parts had to perfectly fit together. Thus, the most critical quality criterion of the part was the flatness of the faces with the fluidic channels. The allowed flatness tolerance was given as $f \leq 10\,\mu m$.

Figure 6.1: CAD model of the microfluidic dispenser which was used as study case for the simulation-assisted part design, captured in SolidWorks®. Shown is the front part, the back looked exactly the same because of the part symmetry.

One of the major challenges regarding the microfluidic dispenser was the large variation in thickness due to the ribs and coring out. The minimal thickness was only about one third of the total thickness. The manufacturing of this part was therefore expected to be challenging with flow distortion. The thickness variation and micro features made the part a truly 3D structured component requiring a full 3D modeling approach also in prospect of the injection molding simulations. Additionally, the required flatness value was quite demanding, as typical minimum flatness tolerances for injection molding are just in the range of 10 µm with slightly smaller values for amorphous plastics and higher values for crystalline and reinforced plastics [120, 121].

6.1.2 Material selection

For the preselection of possibly applied materials in the device, several requirements had to be taken into consideration:

- The component handled aqueous, but still chemically potentially reactive solutions of a pH range from 6 to 10. The device's material had to withstand the solution over longer time in operation—the exact life time was not specified—without deterioration to not compromise the functionality.
- Due to the water-based solutions, the part's water absorption had to be minimal to maintain dimensional stability of the part and the microfluidic channels. Otherwise, throughput and dispensed volume might be distorted.
- The material was not allowed to release any particles or chemicals to prevent from contamination of the distributed solution.

- The material had to show low thermal expansion to maintain dimensional stability and prevent from thermal stress during service, as it is applied in a large temperature range up to about 65 °C.

Based on these requirements, three thermoplastics with suitable chemical and thermal properties were identified [15, 122, 123]:

- Liquid crystal polymer (LCP)
  LCPs are generally inert and show good chemical resistance against acidic and alkaline solutions. They exhibit very low coefficient of thermal expansion and high thermal stability with heat deflection temperatures of higher than 185 °C. LCPs provide low melt viscosity and thus easy molding even of thin parts.
- Polyether ether ketone (PEEK) with 30 % glass fibers
  PEEKs are very resistant against chemicals. Furthermore, they show low water absorption, low coefficients of thermal expansion, and good thermal stability. The stiffness can be improved by the addition of reinforcing fillers like glass fibers.
- Polyetherimide (PEI)
  PEIs are chemically resistant in a broad range of pH values even under load. This family of plastics shows low thermal expansion and high dimensional stability up to 210 °C. PEIs provide excellent melt flow rate and thus easy molding.

6.1.3 Initial gate designs

Three different gate configurations at different part locations were proposed by the responsible industrial partner from the beginning of the design phase. The CAD models of the part with gate and the technical drawings of the gate layouts are shown in Figure 6.2 and 6.3, respectively.

A: Fan gate at the long face with a fan width of 25 mm and a fan thickness of 0.24 mm to 0.65 mm (Figure 6.2a and 6.3a). The total volume of part and feed system was about 450 mm^3.

B: Fan gate at the short face with a fan width of 6.6 mm and a fan thickness of 0.5 mm (Figure 6.2b and 6.3b). The total volume was about 390 mm^3.

C1: Pin gate at the long face with approximated semi-circular cross-section of 0.5 mm diameter and located close to the end of the part (Figure 6.2c and 6.3c). The total volume was about 370 mm^3.

Moreover, the author of this work proposed another design based on the existing configurations later during the design phase. The design was added in order to be able to conduct the gate investigations in a systematic design of experiments (DOE) approach.

C2: Pin gate centered on the short face with approximated semi-circular cross-section of 0.5 mm diameter (Figure 6.2d). The total volume weight yielded also about 370 mm^3, as the pin gate was the same as of design C1.

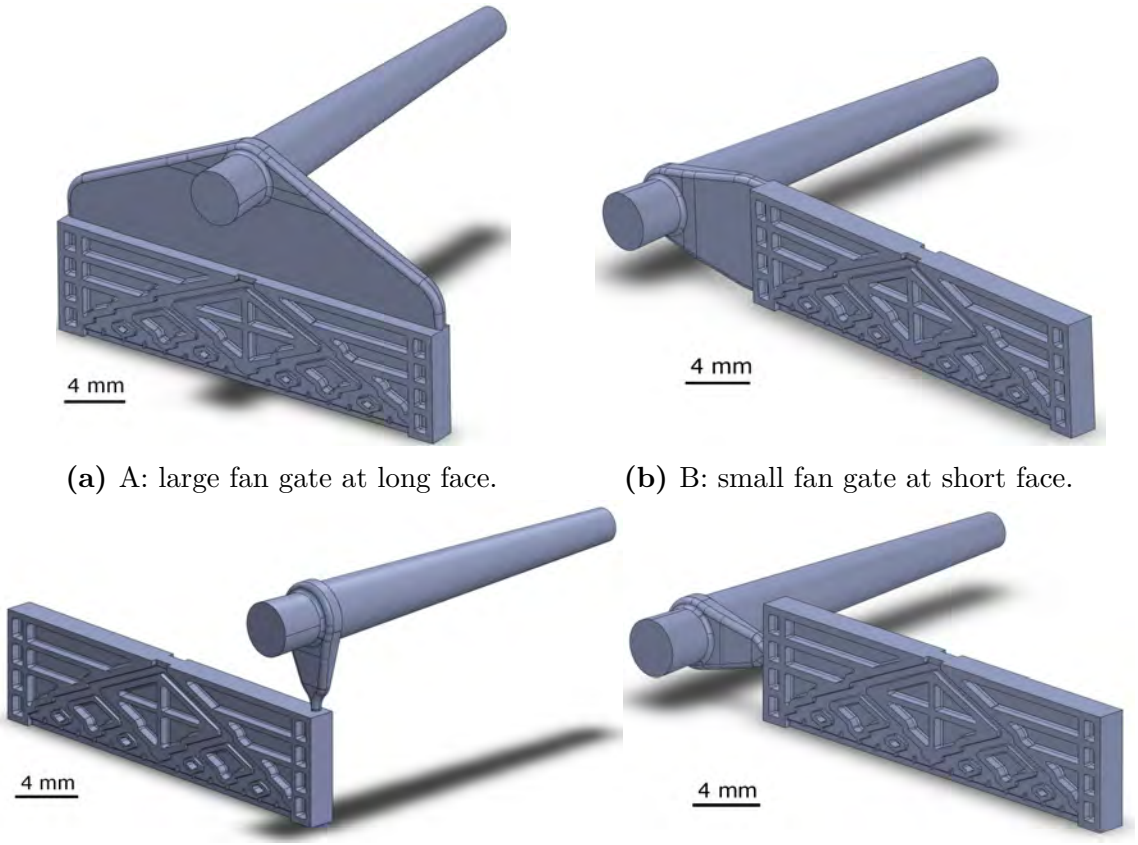

(a) A: large fan gate at long face.

(b) B: small fan gate at short face.

(c) C1: pin gate at long face.

(d) C2: pin gate at short face.

Figure 6.2: CAD models of the different gate configurations with the part for the microfluidic dispenser, captured in SolidWorks®.

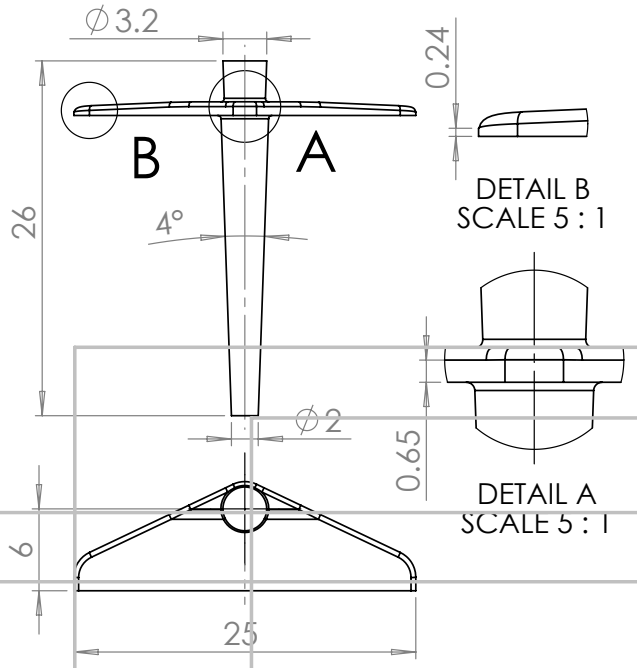

(a) A: large fan gate.

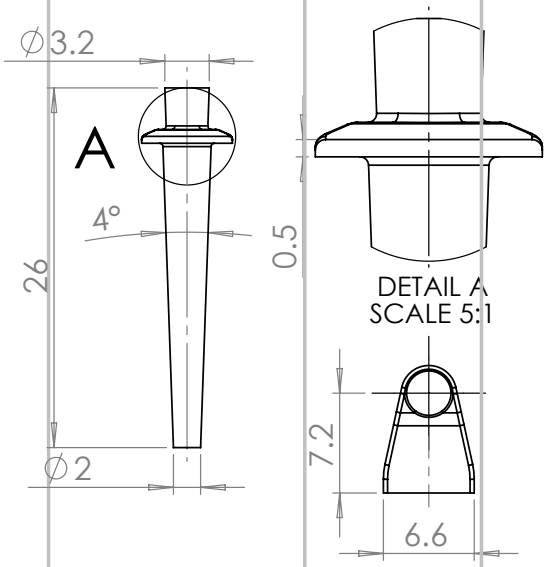

(b) B: small fan gate.

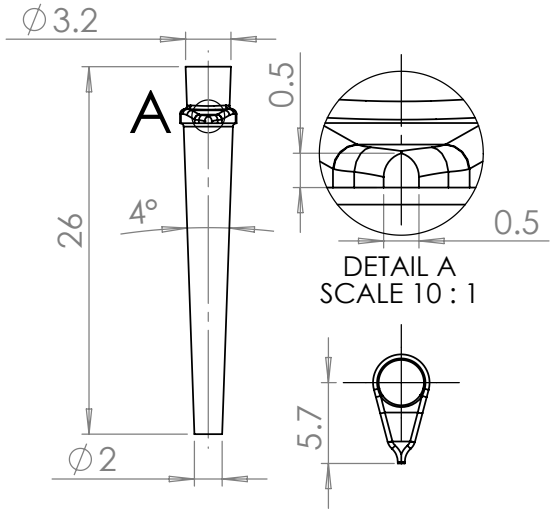

(c) C: pin gate.

Figure 6.3: Drawings of the different gate designs for the microfluidic dispenser, made in SolidWorks®. All dimensions in mm.

6.2 First design iteration

6.2.1 Introduction

The previously described CAD models were initial designs of the part according to common design guidelines for plastic parts. However, the ribbing and coring out created a complex geometry. In opposition to simple parts like boxes, the combination of the gate designs and the complexity of the shape made it impossible to assess the flow behavior and pressure distribution inside the cavity analytically and empirically. It was therefore necessary to investigate the flow behavior of the plastic by numerical simulations.

The goal of the investigations was to optimize the design for homogeneous flow—the prerequisite for homogeneous shrinkage and hence low warpage. This flow analysis was done by examining the flow front of the proposed gate designs over time on a qualitative basis. Since on the other hand the final decision about the material and gate design was still pending, these aspects were systematically examined by means of a DOE analysis.

6.2.2 Design of experiments

The objective of the DOE of the first design iteration on the microfluidic dispenser was to optimize the part design and find the best combination of the material, gate design, and gate position for maximized part and process quality in a suitable and economic process window. The DOE was set up and evaluated with the statistical software Minitab® 16.2.2, developed by Minitab, State College, PA, USA.

Output variables describe the result of the experiments. They must be clearly distinguishable, quantitatively measurable, and closely related to the aim of the investigation [124]. The following output variables were accordingly chosen and evaluated as measure of process window and part quality:

- maximum injection pressure p,
- fill time t,
- time to freeze at gate t_{fg},
- time to ejection t_{e},
- the average volumetric shrinkage s_{avg},
- maximum shear rate $\dot{\gamma}_{\mathrm{max}}$,
- flatness f_{f} on the front/top side of the part (front/top referred to the face pointing in the same direction as the sprue),

- flatness f_b on the back/bottom side of the part (back/bottom referred to the face pointing in the same direction as the sprue puller).

Besides the flatness, all output variables were directly given as simulation result by ASMI 2014. The maximum injection pressure, the fill time, and the maximum shear rate were measures for the processing window. The time to freeze at gate was evaluated by determining the time until the entire gate reached the glass transition or melt temperature. The gate was assumed completely solidified below this temperature, so that packing was no longer possible. The time to freeze at gate was relevant regarding the possibility to apply packing to the part.

The time to ejection was the time from when the cavity was filled completely to when the part reached the ejection temperature. At the ejection temperature, the material was assumed to have sufficient mechanical stability, so that the part could be ejected without the risk of being permanently damaged or deformed. The time to ejection was used to assess the minimum cycle time and thus the economic efficiency of the process with perspective to serial production. It was given smaller priority than the other factors though, because focus was on the feasibility study of the part and not on serial production. The flatness as the measure of the warpage of the part was manually evaluated by measuring the peak-to-valley value on the front and back surfaces of the warped part which was yielded by the simulation.

The volumetric shrinkage s in ASMI is defined as the percentage change in density from when the cavity is entirely filled to when the part has completely reached the ambient temperature of 25 °C. It is mathematically given as

$$s = 1 - \frac{\rho}{\rho_{25\,^\circ\mathrm{C}}} \tag{6.1}$$

with the density ρ at complete cavity fill and the density $\rho_{25\,^\circ\mathrm{C}}$ at 25 °C and atmospheric pressure. The determination of the density is based on the pvT data of the deployed material. The volumetric shrinkage as well as the part thickness should be uniform across the plastic part in order to minimize warpage [49, 81]. Low average volumetric shrinkage does hence not necessarily mean low warpage. It can be a first indicator though, as the extent of non-uniform shrinkage decreases with over-all shrinkage.

Input variables are parameters or interactions of parameters which directly influence the process output. The aforementioned plastics, the gate type, and the gate location were used as the so-called factors for the DOE—the input variables of which the influence on the output variables is investigated. They must be independently adjustable [124, 125]. The four previously presented gate designs A, B, C1, and C2 were investigated. The chosen factor levels are listed in Table 6.1. The DOE was conducted with a full factorial design giving in total 12 different simulation studies.

Experiments are of stochastic nature, i.e. measurements always go along with variance in the measured values, even for the exact same input. Simulations however are

deterministic, i.e. the same input will always yield the identical output, without any variance in the results. In other words, simulations provide perfect repeatability. Different from experiments, randomization and repetitions of the runs of a simulation-based DOE is therefore in general not necessary. [125]

Table 6.1: Factors and the chosen factor levels of the DOE for the first design iteration of the microfluidic dispenser.

#	factor	type	factor levels		
			–	0	+
1	material	discrete	LCP	PEI	PEEK
2	gate type	discrete	fan gate		pin gate
3	gate location	discrete	long face		short face

6.2.3 Simulation set up

The simulation model only comprised the part and feed system, because information about the mold was not available in this early design phase. The CAD models of the different designs were imported to ASMI and subsequently meshed. The exact mesh settings of the simulation models are listed in Table 6.2. The resulting multi-scale meshes and the mesh density are depicted in Figure 6.4 and 6.5. The mesh of the dispenser showed refined areas at the micro walls at the end of the fluidic channels. Due to the assigned mesh densities, the part had in general a small mesh edge length than the sprue. Roundings of the part and the sprue were also refined because of the chord angle control. The gate of the pin gate designs was in particular assigned its own mesh density because of the small size. The fan gates showed sufficient refinement by default. Design A exhibited the largest number of tetrahedral elements because of its much larger volume. Although design B had the higher volume than C1 and C2, the number of elements was compensated in case of C2 and even exceeded in case of C1 by the increase due to the assigned local mesh densities.

The conducted analysis in ASMI 2014 included filling, packing, and warpage of the part. The previously mentioned materials LCP, PEEK, and PEI were chosen. The default processing settings of the ASMI data base were used for all the materials due to the unavailability of actual values. The values did not change between the gate designs to rule out any influence of the processing. The molding of the part was supposed to be carried out at DTU on the available Arburg injection molding machine with 18 mm screw diameter and 600 kN clamping force. Besides this machine, common tool steel was selected as mold material. The injection location diameter was chosen in accordance to the nozzle size of the Arburg machine as 2.0 mm. The filling control was set to be governed by the screw speed which is the usual setting for experimental molding. The simulation settings are summarized in Table 6.3.

Table 6.2: Meshing settings of the microfluidic dispenser with pin gate for the simulation validation. Unspecified settings were kept at the default values.

Parameter	value
Specific element edge length / µm	
part	150
gate (C1 and C2 only)	150
micro walls	40
Global edge length / µm	800
Merge tolerance / µm	20
Chord height / µm	30
Minimum number of elements through thickness	10
Maximum edge length in thickness direction / µm	960
Bias ratio	1.2
Total number of elements	
design A	3 800 000
design B, C2	2 900 000
design C1	3 400 000

Table 6.3: Machine and process settings of the microfluidic dispenser with film gate. Unspecified settings were kept at the default values.

Parameter	setting		
ASMI version	2014		
Analysis type	Fill+Pack+Warp		
Material type	LCP	PEEK	PEI
Mold temperature / °C	80	190	160
Melt temperature / °C	335	375	380
Injection location diameter / mm	2.0		
Filling control	absolute ram speed vs ram position		
Target ram speed / ($\mathrm{mm\,s^{-1}}$)	10		
Cushion / mm	2.0		
Switch-over volume / %	99		
Packing pressure / MPa	60		
Packing time / s	30		
Cooling time / s	20		
Machine	Arburg Allrounder 370 A 600-70 (18 mm)		
Virtual mold material	1.1730 (C45W)		

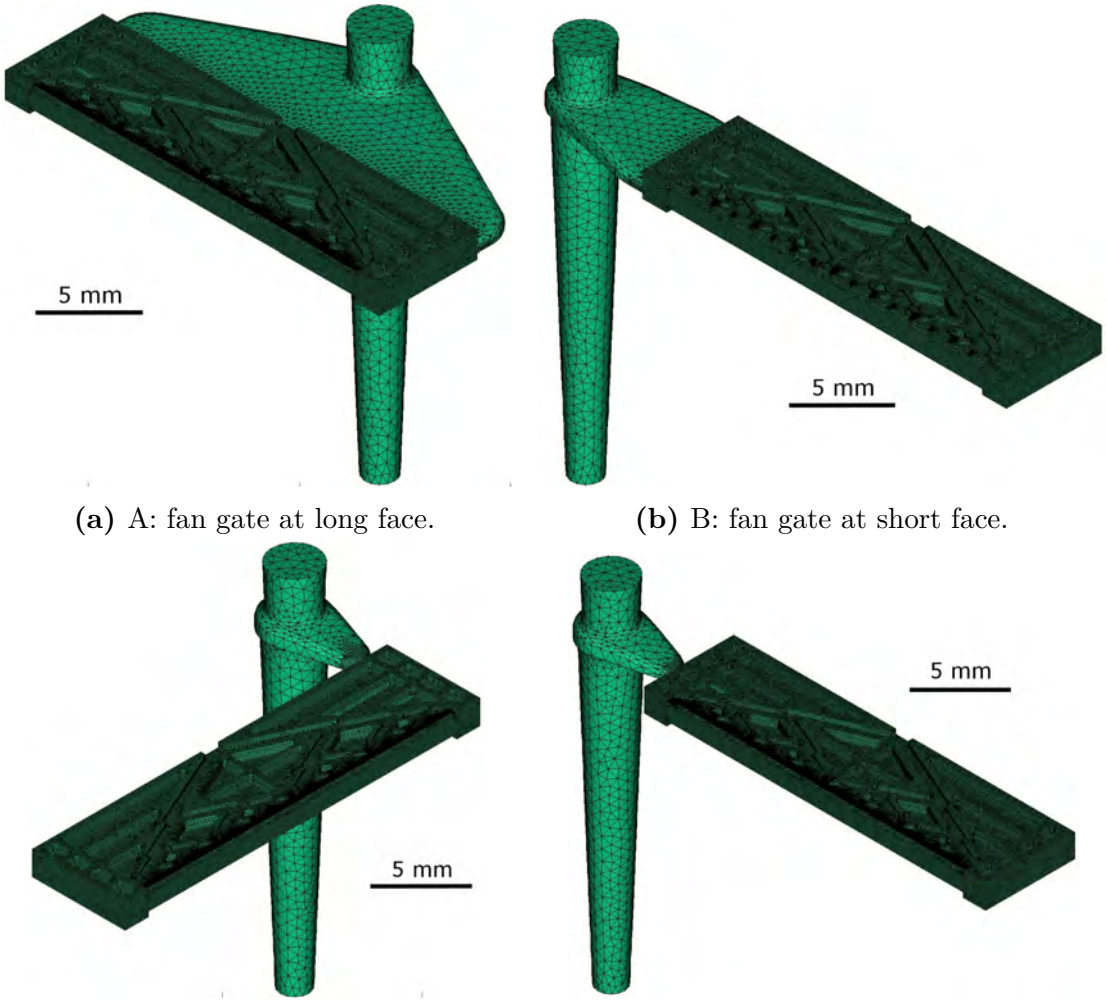

(a) A: fan gate at long face.

(b) B: fan gate at short face.

(c) C1: pin gate at long face.

(d) C2: pin gate at short face.

Figure 6.4: Meshed models of the proposed gate designs of the microfluidic dispenser in ASMI.

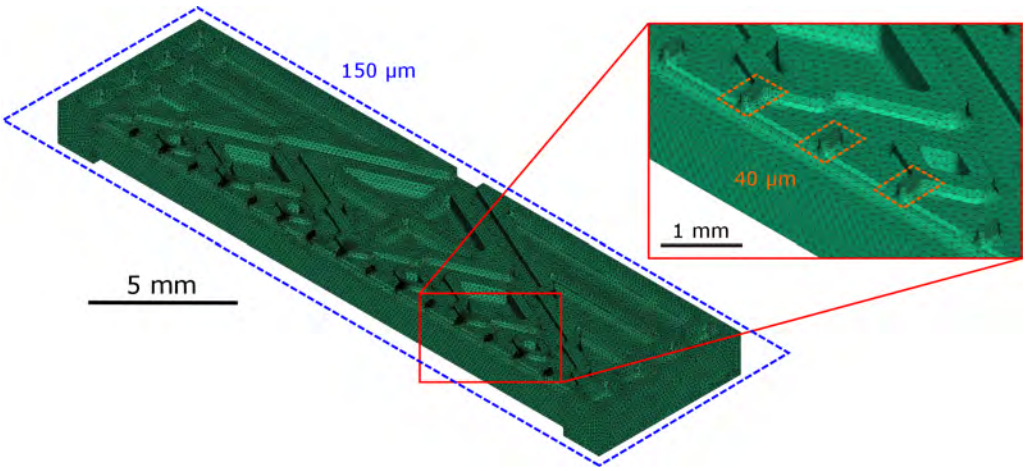

Figure 6.5: Meshed model of the actual part of the microfludic mixer with detailed view on some of the micro features and highlighted assigned specific element edge length.

6.2.4 Flow front comparison

The shape of the flow front during filling is illustrated in Figure 6.6 for gate design A and B and in Figure 6.7 for C1 and C2. For clarity, the pictures only depict the conditions for PEI, but the other materials showed similar trends.

Design A showed clearly the most inhomogeneous flow front, whereas B, C1, and C2 yielded more uniform flow fronts. The observed flow disruptions in the actual cavity—leading there again to an uneven flow front—were caused by the ribs and the significant thickness variation of the part (depicted in Figure 6.8a) as a consequence of the coring out and the microfluidic structures.

All ribs were introduced in accordance to common plastic design guidelines to minimize the part thickness and all disadvantages linked to chunky parts such as long time to freeze, noticeable sink marks, or packing difficulties, but to maintain structural stability at the same time. The ribs were thinner than the actual bulky body, and therefore they acted as flow restrictors, i.e. the flow front lagged behind in the rib, as illustrated in Figure 6.8b. The thickness variation of the part had a similar effect. The plastic flow was restricted in the thinner regions and moved more quickly in the thicker regions. The cored out depressions between the ribs showed only about one third of the total part thickness. In contrast, the microfluidic channel areas exhibited more than three quarter of the total thickness and thus acted as flow leader in direct comparison.

In case of design A, the flow length from the sprue to the actual cavity was additionally much shorter in the center of the gate than at the outer fringes, so that the flow reached the cavity much earlier there. When the flow reached the center of the cavity, the fringes of the gate were finally filled. The flow leading effect of the thicker regions

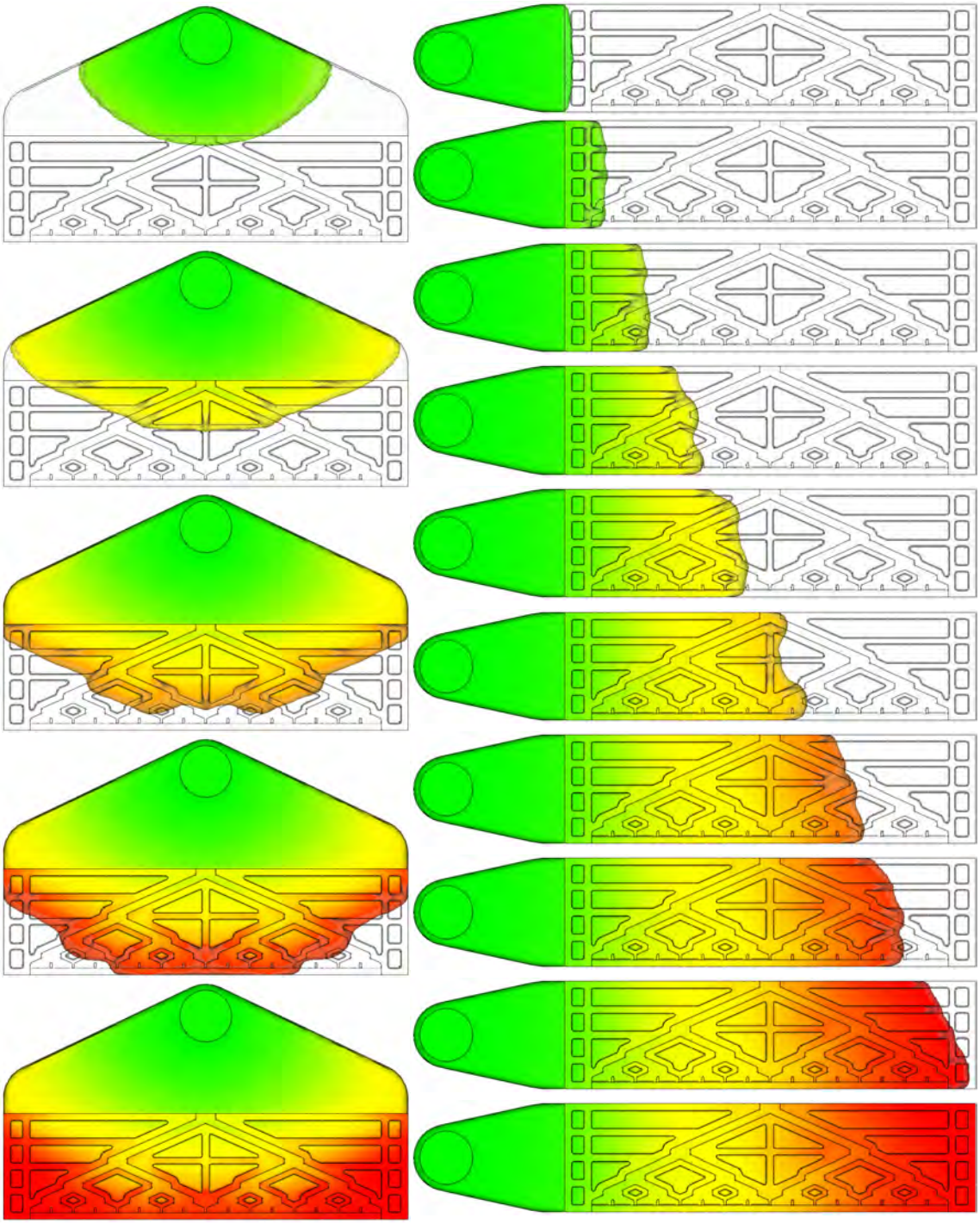

(a) Design A. **(b)** Design B.

Figure 6.6: Visualization of predicted flow front in the part cavity of the different gate designs of the microfluidic mixer. Color scale from red to blue: normalized filling time from 0 to 1.

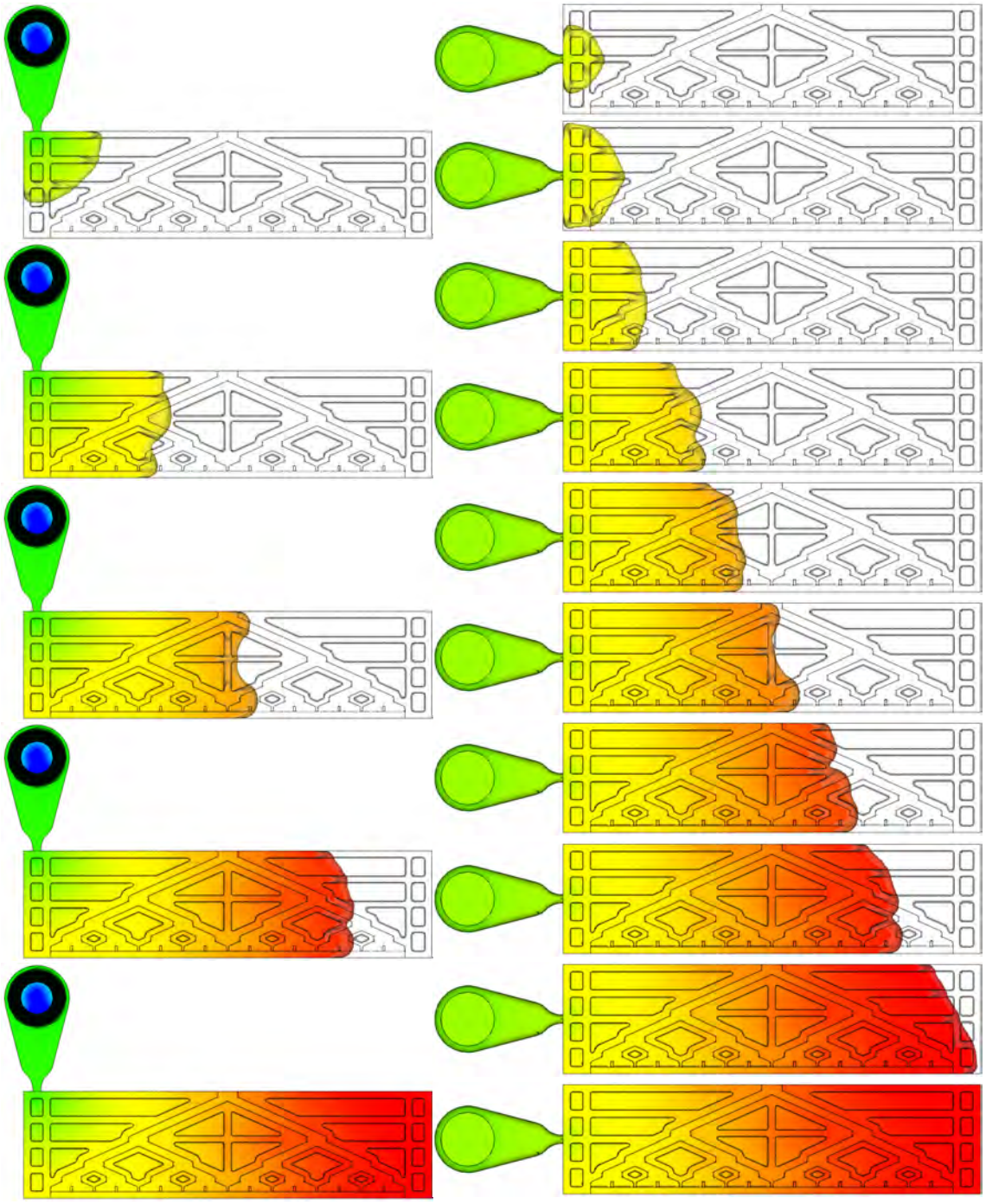

(a) Design C1. **(b)** Design C2.

Figure 6.7: Visualization of predicted flow front in the part cavity of the different gate designs of the microfluidic mixer. Color scale from red to blue: normalized filling time from 0 to 1.

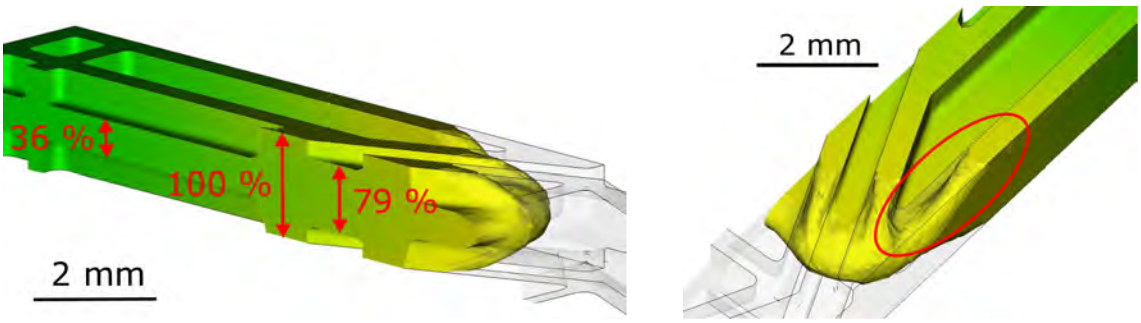

(a) Thickness variation. **(b)** Flow restriction in rib.

Figure 6.8: Influence of the ribbing and coring out of the microfluidic dispenser on the plastic flow. The ribs act as flow restrictor, because they are thinner than the bulk part which exhibited a large thickness variation. The color index represents the fill time.

of the fluidic channels magnified the effect of the non-uniform flow front. This also had the negative effect that the flow front suddenly accelerated considerably, when only the two lower corners of the part were left empty, since the machine maintained a constant flow rate.

Design B proved that a more appropriate fan gate could provide an even flow front entering the cavity which is maintained at the beginning of the fill. Since the microfluidic channels exhibited a tree-like structure, the dispenser's edge with the fluidic outlets was significantly thicker than the edge with the fluidic inlets. Therefore, the flow lagged behind from shortly after entering the cavity until the end of the filling. The flow showed again an acceleration just before filling the upper corner.

Design C2 showed a similar behavior to design B. The flow front initially developed into the shape of a circular arc. Again, the flow moved more rapidly at the edge with the microfluidic outlets, so that an inhomogeneous flow front appeared, the flow moved ahead at the lower edge, and accelerated again before filling the last corner.

The flow leading effect at the lower edge of the dispenser was anticipated by the design C1. Positioning the pin gate at the upper edge counteracted the flow restricting effect and helped to balance the flow front. Still, the considerable coring out in the center of the part slowed down the flow there, and the flow front at the upper edge could not keep up with the flow front at the lower edge over the entire cavity length. Consequently, the flow front was not entirely uniform either, but more balanced than for the other designs.

C1 was hence the number-one choice from a flow front perspective. In order to further improve the balance of the flow front, the design of the dispenser was modified. The center was on both sides of the part equipped with two ribs instead of one to increase the cross section and accelerate the flow front there, as shown in Figure 6.9.

(a) Original design. **(b)** Revised design.

Figure 6.9: Design optimization at the microfluidic dispenser. It was equipped with one more rib for more uniform flow on both sides.

The aforementioned flow acceleration—to some extent existent in all designs—was very sudden and significant. Consequently, the risk of burn marks provoked by the Diesel effect or of air entrapment emerged in these areas. This risk could be addressed during mold manufacture by the implementation of venting channels at the end of the cavity. Alternatively, the injection speed could be adjusted at the end of fill to prevent from the flow acceleration. Furthermore, the simulation identified that the flow restriction in the numerous ribs promoted also the risk of air entrapment in corners or ends of the ribs. This outcome was to be paid attention to during the positioning of the ejector pins, since they also contributed to the venting.

6.2.5 Filling analysis

The most relevant results of the DOE are presented in Table 6.4 and Figure 6.10. All main effect and interaction plots can be found in Appendix C. The simulations predicted the maximum injection pressure to be in the range from 18 MPa to 114 MPa. The pin gate required as expected the higher maximum injection pressure because of its narrow cross-section. On the other hand, design A required the lowest injection pressure due to its large cross-section with a maximum value of about 57 MPa (run 11). Among the materials, LCP decreased the injection pressure significantly, whereas the gate position had only small influence. Still, all values were clearly within the limits of the machine capability—the maximum clamping force likewise—and were therefore not evaluated in more detail. Considering the very low part volume and low injection speed, the fill time in the range from 0.20 s to 0.35 s was short, but for micro parts acceptable.

The permitted shear rate was nonetheless exceeded by most of the simulation studies. The gate type had the largest influence among the investigated input factors. The pin gate showed in general very high shear rates always violating the maximum limit and leading to serious risk of material degradation. In comparison, the fan gates showed both very low shear rates with the short fan gate yielding the twofold of the large one. Just the short fan gate in combination with LCP (run 9) exceeded the allowed limit. The gate position did not noticeably influence the occurring maximum shear rate, as the shear was dominated by the thickness of the gate. LCP showed

Table 6.4: Results of the simulation DOE for the analysis of the influence of the gate type and position and the material on the process and part quality of the microfluidic dispenser.

#	design	gate		material	p/MPa	t/s	t_{fg}/s	t_e/s	$\dot{\gamma}_{max}$/s^{-1}	s/%	f_f/µm	f_b/µm
		type	position									
1	C2	pin	short	PEEK	109	0.34	1.58	10.8	251 000	6.2	57	59
2	C2	pin	short	PEI	109	0.35	1.58	17.3	260 000	4.1	10	9
3	C2	pin	short	LCP	27	0.29	1.00	3.4	424 000	5.0	10	8
4	C1	pin	long	PEEK	114	0.28	1.53	11.5	242 000	4.4	58	58
5	C1	pin	long	PEI	114	0.27	0.95	21.0	255 000	6.2	6	5
6	C1	pin	long	LCP	27	0.21	0.83	4.4	342 000	5.0	38	38
7	B	fan	short	PEEK	73	0.25	1.46	11.2	19 000	4.7	6	10
8	B	fan	short	PEI	92	0.24	1.54	18.9	18 000	3.3	10	9
9	B	fan	short	LCP	23	0.20	1.61	3.3	109 000	4.8	19	8
10	A	fan	long	PEEK	46	0.26	1.61	14.1	10 000	4.6	47	55
11	A	fan	long	PEI	57	0.24	1.57	17.3	10 000	4.8	25	18
12	A	fan	long	LCP	18	0.24	1.65	9.2	9000	4.8	56	59
				PEEK	250				50 000		10	10
Limit				PEI	250				50 000		10	10
				LCP	250				60 000		10	10

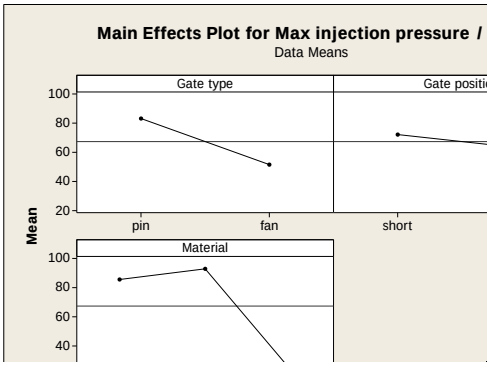

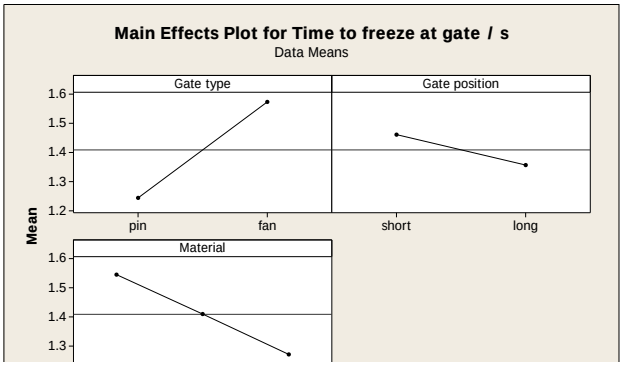

(c) Time to ejection.

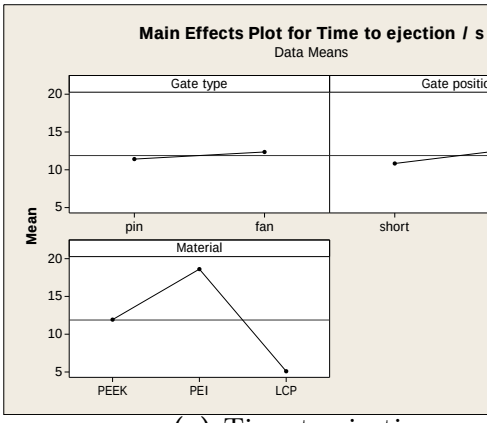

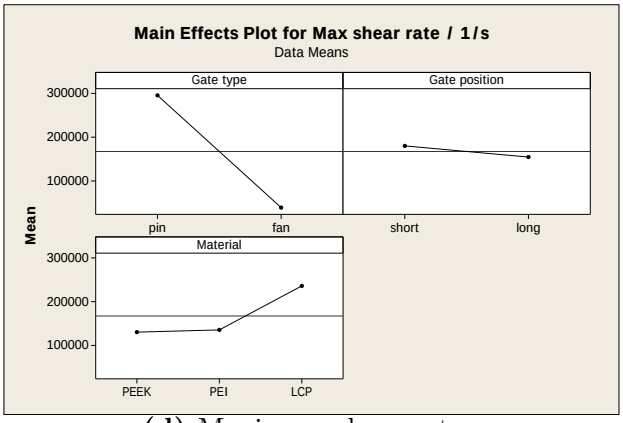

(d) Maximum shear rate.

Figure 6.10: Main effect plots of the responses of the DOE investigating the influence of the gate type and position as well as the material on the process and part quality of the microfluidic dispenser.

clearly the highest shear rates in average, whereas PEEK and PEI showed very similar values for all relevant DOE runs.

Due to the much larger cross-section and thickness, the fan gates showed as expected the longer time to freeze at gate. The gate position was of minor influence, as the gate shape dominated the time to freeze. Moreover, a linear trend could be found for the materials with PEEK solidifying the latest and LCP the earliest. Still, none of the gates or materials caused really an early gate freeze off, so that the packing could proceed for about 1 s.

The sprue dominated the time to ejection, because it was much thicker than the actual part. The gate type and position had no noticeable influence compared to the materials. PEI showed the highest, LCP the lowest time to ejection. The cause was most likely the temperature difference between the ejection and melt processing temperatures of the materials. With a temperature difference of 135 °C, PEI needed the most time to cool down. LCP and PEEK showed with values of 88 °C and 90 °C, respectively much lower differences and would therefore have enabled the more efficient production with shorter cycle times.

6.2.6 Warpage analysis

The numerical results for the warpage prediction of the simulations for all DOE runs are listed in the previous Table 6.4. The influence of the input parameters on the warpage and the linked flatness as the main criteria for the part quality is shown in Figure 6.11. The main effects and interactions of the input factors on the warpage of the front and back exhibited similar mean values and trends.

The deflection of the warped part in PEI is visualized in Figure 6.12. LCP and PEEK showed similar trends with varying numerical values. The color scales were adjusted to cover only the part, but not the sprue which was also included in the calculations. Additionally, the smallest deflection of the bottom face (not visible) was set as reference for the deflection of the part. Design A showed the larges warpage among all gate designs. Moreover, gating at the long side of the part provoked the warped part to bend approximately symmetrically and buckle up in the center. In contrast, gating at the short side of the part caused unsymmetrical warpage and the part bend up more with the edge of the microfluidic outlets, so that the corner there away from the gate experienced the largest deflection.

PEI gave with about 10 µm in average the significantly lowest flatness among all materials. The reason here might have been the amorphous structure and hence isotropic shrinkage of the material. The glass fiber reinforcement in PEEK and the high crystallinity in LCP might have led to an anisotropic material behavior. The flow-induced orientation of fibers and molecules in regions of linear flow is in general in parallel to the flow. In regions of radial flow, they orient in perpendicular to the flow direction [126]. The complex geometrical structure and resulting complex

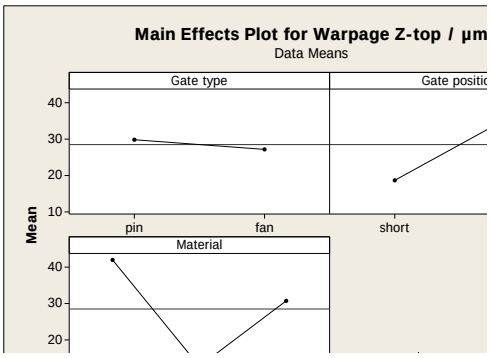

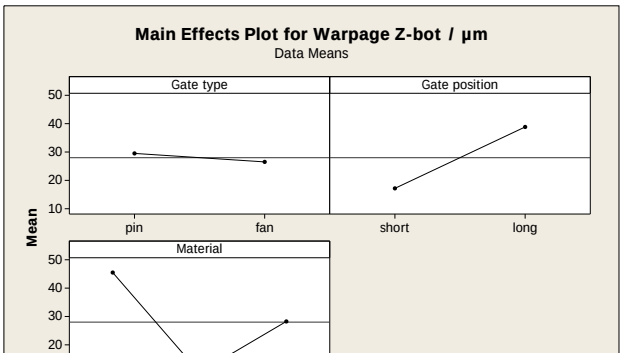

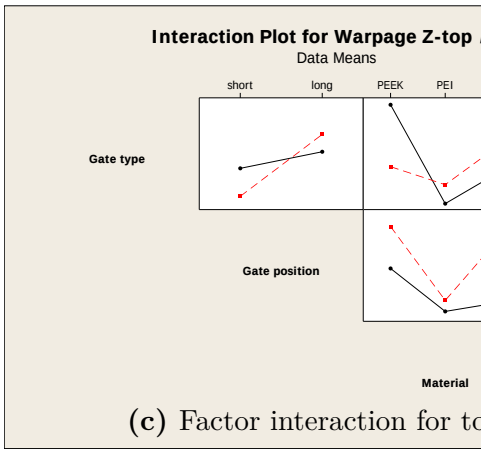

(c) Factor interaction for to

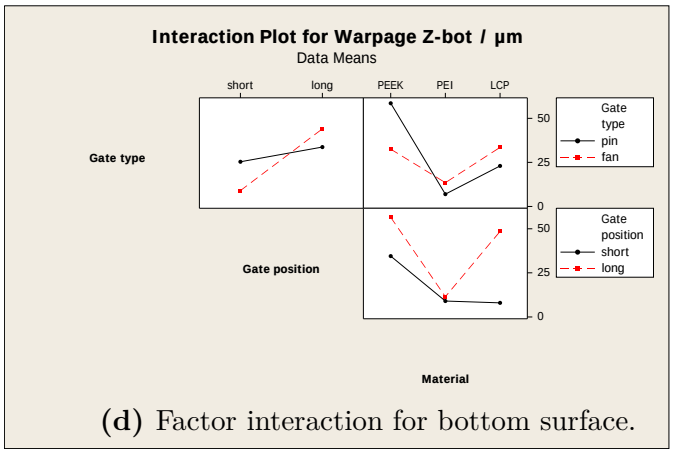

(d) Factor interaction for bottom surface.

Figure 6.11: Main effect and interaction plots for the examination of the influence of the gate type and position as well as the material on the warpage of the microfluidic dispenser.

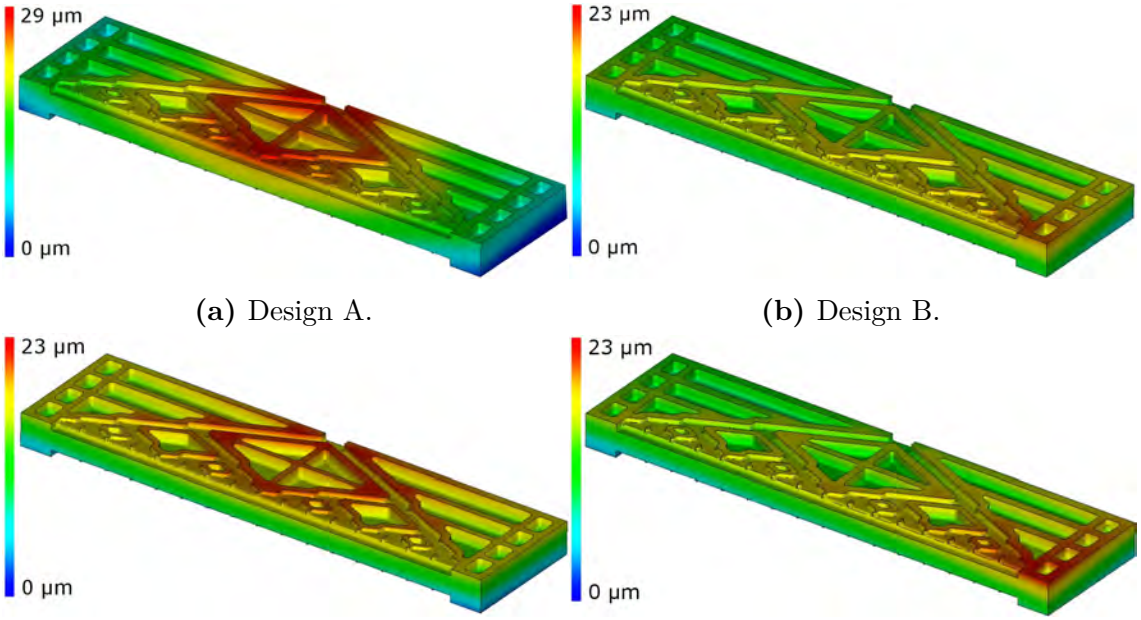

(a) Design A. **(b)** Design B.

(c) Design C1. **(d)** Design C2.

Figure 6.12: Exemplary visualization of the z-component (along the shortest side of the part) of the warpage of the microfluidic dispenser with different gate design. Please note the different deflection range for design A. Because of the inclusion of the sprue, the color scales were adjusted to match the deflection of the part only.

flow possibly resulted in domains of changing orientation and hence inhomogeneous shrinkage. Since the anisotropy for aligned fibers is more pronounced than for the polymer molecules, this effect and the deflections were strongest for PEEK.

Generally, the flatness benefited from having the gate at the short side of the part. According to the interaction plots, the effect was however more pronounced for the fan gate. The reason here was possibly the larger variation in flow length. The flow length of the pin gate did not change as significantly due to its uncentered position on the long side of the part. Furthermore, the variation caused by the gate position was small for PEI compared to PEEK and LCP. This might have been attributed to the homogeneity of the flow in the cavity. Having the gate at the short side led to a uniform flow basically in a single direction. As seen in the section about the filling behavior, the pin gate located at the long side caused at the beginning material flow in perpendicular direction to the longest side of the part. The flow-induced and hence different orientation of glass fibers or crystalline areas generated uneven shrinkage of the part. The fan gate at the large side caused a non-uniform flow front and again anisotropic shrinkage.

The gate type had in average only little influence on the resulting flatness with slightly lower values for the fan gate. The fan gate was expected to generate much lower flatness in direct comparison, since it provided a much larger cross-section for more effective packing and less shrinkage. The moderate difference could be explained by the mechanical connection between the part and the fan gate. Thus, the warpage of the part was constrained or magnified to some extent by the gate's warpage—for the large fan gate more distinct than for the small fan gate. In fact, the large fan gate gave higher warpage, the small fan gate lower warpage than the pin gate independently from its position.

In case of PEEK, the pin gate caused the strongest warpage. This might have been attributed to the difference in flow inside the cavity close to and far from the gate. Radial flow dominated close to the gate, whereas the flow was linear further from the gate in the major volume of the part. The aforementioned orientation effects caused different shrinkage close and far from the gate.

Only few factor combinations of the DOE were able to cope with the given flatness limit of 10 µm. Especially PEEK exceeded the requirement considerably with values of up to 59 µm. The processing of PEEK was moreover expected to be challenging and problematic because of the glass fibers, the required high temperatures, and the relatively high viscosity. PEEK was therefore discarded for the microfluidic dispenser.

LCP was discarded owing to the very high shear rates and the higher mean flatness values leaving PEI as the material of choice. The drawbacks of PEI showing the longest time to ejection and hence probably the less economic process was tolerated to meet the part requirements. However, the cycle time and efficiency of PEI could be improved in serial production by the adjustment of the processing conditions or

by the modification of the cooling concept. This would likely influence again the warpage of the part. Yet, the good warpage results of PEI showed that there was room to the allowed flatness tolerance which could be traded for improved cycle time.

PEI, pin gate, and long side (run 5)—that was the configuration providing minimum flatness of the dispenser on both sides and the final choice for the best gate design.

It must be critically noticed that the meaningfulness of the warpage assessment was somewhat limited. The reason here was the evaluation of the flatness of the part with attached gate. Removing the constrains of the gate on the part would have changed the flatness outcome. However, the investigations were not limited to the warpage only and gave good insight into the process and part quality.

6.3 Second design iteration

6.3.1 General simulation set up

As a first option, the excessive shear stress of design C1 could have been lowered by modifying the cross-section of the semi-circular pin gate. Derived from runners, a fully round or trapezoidal shape would have been more efficient, i.e. causing lower pressure drop and shear levels. The excessive shear stress was counteracted in this work alternatively by simply increasing the width of the gate.

Three different CAD models based on design C1 with gate sizes of 0.50 mm, 0.75 mm and 0.90 mm (yielding total volumes of 367.4 mm^3, 368.5 mm^3 and 369.3 mm^3) were investigated. The objective of this design iteration was the optimization of the previously approved pin gate and to tackle the problem of the excessive shear rate at the gate. The evaluation of the different gate designs was mainly done on the basis of the resulting maximum shear rate and the achieved part flatness. The part flatness still had to comply with the required maximum value of 10 µm. The major process parameters were also evaluated to remain in a feasible molding window.

The simulations were set up modeling the part with feed system. Information about the mold was not available, and the mold was hence not modeled. The exact mesh settings of the simulation models are listed in Table 6.5. The result of the meshing and the assigned mesh densities are depicted in Figure 6.13. The dispenser showed as in previous simulations refined areas at the micro walls at the end of the fluidic channels. Roundings of the part and the sprue were also refined because of the chord angle control. Due to the comparable volume, all models exhibited approximately the same number of elements.

The conducted analysis in ASMI included filling, packing, and warpage of the part. The sprue was included in the warpage computations as default. Due to

Table 6.5: Meshing settings of the microfluidic dispenser with pin gate for the simulation validation. Unspecified settings were kept at the default values.

Parameter	value
Specific element edge length / µm	
part	150
gate	150
micro walls	40
Global edge length / µm	800
Merge tolerance / µm	20
Chord angle / °	3
Minimum number of elements through thickness	10
Maximum edge length in thickness direction / µm	400
Bias ratio	1.2
Total number of elements	2 800 000

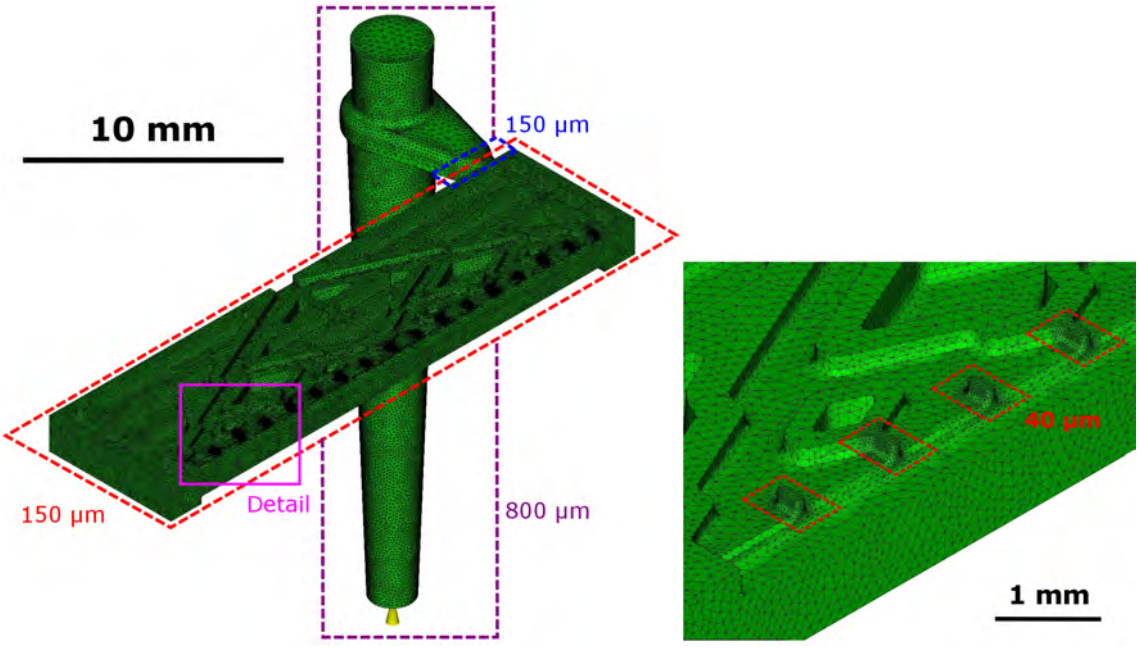

(a) Entire dispenser. **(b)** Detailed view on micro features.

Figure 6.13: Meshed microfluidic dispenser with feed system and indicated mesh densities in ASMI.

the unawareness of the possibility to exclude chunks of the part from the warpage calculation, the analysis was run with the default in ASMI 2014. The real part was however intended to be assembled without the sprue. The simulations were therefore later repeated in ASMI 2015 with the sprue included in the warpage calculation to investigate the influence of the software version and with the sprue being excluded from the warpage computations to resemble the real part. All these studies were based on the aforementioned same simulation models and meshes.

The material choice for the simulations was the PEI because of the superior performance in the previous investigations. The default processing settings of the ASMI data base were used due to the unavailability of actual values. The available Arburg machine and common tool steel were selected as injection molding machine and mold material, respectively. The simulation settings are summarized in Table 6.6.

Table 6.6: Machine and process settings of the microfluidic dispenser with film gate. Unspecified settings were kept at the default values.

Parameter	value
ASMI version	2014 and 2015
Analysis type	Fill+Pack+Warp
Material type	PEI
Mold temperature / °C	160
Melt temperature / °C	380
Filling control	absolute ram speed vs ram position
Target ram speed / ($\mathrm{mm\,s^{-1}}$)	10
Cushion / mm	2.0
Switch-over volume / %	99
Packing pressure / MPa	60
Packing time / s	30
Cooling time / s	20
Machine	Arburg Allrounder 370 A 600-70 (18 mm)
Virtual mold material	1.1730 (C45W)
Injection location diameter / mm	2.0

6.3.2 Design of experiments for filling and packing analysis

The influence of the gate size regarding filling and packing performance and the effect of the software version on the process outcome was analyzed by means of a DOE approach in Minitab® 16.2.2. The following output variables were chosen as measure of the filling and packing performance and the general feasibility of the processing:

- fill time t,

- maximum injection pressure p,
- total mass after fill m_{f},
- total mass after pack m_{p},
- difference of total mass after fill and pack Δm,
- part mass after pack m_{pp},
- volumetric shrinkage s,
- maximum shear rate $\dot{\gamma}_{\mathrm{max}}$.

All output variables except from the mass difference were directly provided by ASMI. The fill time, maximum injection pressure, the masses, the volumetric shrinkage and the maximum shear rate were measures of the process window. The part mass was only yielded in ASMI 2015 due to the distinction between sprue and part for the warpage computation. The volumetric shrinkage (definition in Equation 6.1) as first indicator for possible warpage was split into the maximum, minimum, and average value.

The proposed gate sizes of 0.50 mm, 0.75 mm and 0.90 mm and the two ASMI versions were taken as input. Including or excluding the sprue from the warpage calculations did not influence the filling and packing results of ASMI 2015. Therefore, only one result is reported for ASMI 2015. The chosen factor levels are listed in Table 6.7. The DOE was carried out as full factorial design without randomization or repetitions giving in total six different simulation studies.

Table 6.7: Factors and the chosen factor levels of the DOE analyzing the filling and packing of the microfluidic dispenser.

#	factor	type	factor levels			unit
			–	0	+	
1	gate size	continuous	0.50	0.75	0.90	mm
2	ASMI version	discrete	2014		2015	

6.3.3 Filling and packing analysis

Table 6.8 and Figure 6.14 summarize the major simulation results from the DOE with both ASMI versions. All main effect and interaction plots can be found in Appendix C. In general, the investigation revealed that the influence of the gate size is much larger than the influence of the applied software version. The software had generally only little impact on the predicted outcome of the filling phase (injection pressure and shear rate), whereas the results related to the packing phase (mass

increase by packing and average volumetric shrinkage) changed by about 10 %. This indicated that the algorithms for the packing and shrinkage were revised in the new release. The filling time was affected by the software version, too. Nonetheless, ASMI 2015 showed some irregularities in the plastic flow. The entering of the plastic in the cavity was delayed and the flow rate was close to zero at the beginning of the filling phase. Therefore, the actual fill time was estimated based on the delay. This effect limited the meaningfulness of the analysis of the fill time with regard to the software version. Still, the smallest gate thickness of 0.50 mm solely showed an increase in the fill time.

All gate sizes showed acceptable levels of fill time and did not exceed the injection pressure limit of the machine independently from the software version. The fill time was with about 0.3 s at a typical level for micro parts. The injection pressure decreased and the packing performance—illustrated by the mass increase, the part mass after packing, and the volumetric shrinkage—improved with increasing gate size. This behavior was in accordance to expectations, because the larger gate cross-section enabled the better packing pressure transmission. Over-packing or flash was not an issue. The total mass of the part was not a direct indicator for the packing performance though, because the volume and hence the total mass varied with the gate size.

In addition, the total mass increase and the volumetric shrinkage had to be critically evaluated, as the sprue was also considered for these values. Due to the separation between feed system and actual part, separate values for the mass were reported in ASMI 2015. The numerical trend of better packing for larger gate size was also true for the actual part mass only, with the largest gate getting closest to the maximum part weight. Thin-walled parts normally shrink less than bulky parts, i.e. the actual dispenser was expected to shrink less than the sprue. Hence, the minimum volumetric shrinkage was assumed more of an indicator of the shrinkage behavior of the part, whereas the maximum volumetric shrinkage was assumed to be rather related to the sprue. For both measures, the larger gate size was beneficial, with little effect on the minimum volumetric shrinkage though.

The evaluation of the shear rate at the gate in ASMI 2014 is additionally depicted in Figure 6.15. Only the gate with 0.90 mm diameter did not exceed the critical shear rate of the used PEI. The bulk shear rate was noticeably lower than the maximum, but there was still a risk of material degradation and surface flaws because of the locally high shear rate. The pictures show the results of ASMI 2014, but the statements also held true for ASMI 2015, as the divergence of the yielded shear rates was negligible.

Table 6.8: General simulation results for the second design iteration of the microfluidic dispenser with different gate size in ASMI.

#	gate/mm	ASMI	t^{a}/s	p/MPa	m_f/g	m_p/g	Δm/g	m_{pp}/g	s_{max}/%	s_{min}/%	s_{avg}/%	$\dot{\gamma}_{max}$/s^{-1}
1	0.50	2014	0.289	109.9	0.4394	0.453	0.014	n.a.	10.3	0.761	4.1	255 000
2	0.50	2015	0.308	109.5	0.4392	0.455	0.015	0.2298	10.2	0.660	3.8	255 000
3	0.75	2014	0.335	97.9	0.4406	0.457	0.016	n.a.	9.5	0.761	3.7	128 000
4	0.75	2015	0.304	97.4	0.4404	0.459	0.018	0.2395	9.4	0.658	3.3	129 000
5	0.90	2014	0.339	93.5	0.4411	0.460	0.019	n.a.	8.9	0.759	3.3	47 000
6	0.90	2015	0.303	93.0	0.4409	0.461	0.020	0.2404	8.8	0.658	3.1	47 000
mean ASMI 2014			0.321	100.4	0.4404	0.457	0.016	n.a.	9.6	0.760	3.7	143 000
mean ASMI 2015			0.305	99.9	0.4402	0.458	0.018	0.2366	9.5	0.659	3.4	144 000
ΔASMI^{c}/%			−4.9	−0.5	0.05	0.3	10.3	n.a.	−1.2	−13.3	−8.7	0.3
Limit				250				0.2483				50 000

[a] Due to the erroneously delayed start of the plastic flow at the beginning of the filling phase in the simulation, ASMI 2015 yielded unusual fill times in the range of 1.6 s to 1.7 s. For comparison to ASMI 2014, the delay and true fill time were hence manually estimated.

[b] The part mass after pack is not available for ASMI 2014, since no distinction between the sprue and actual part was made.

[c] ΔASMI denotes the difference of the means between ASMI 2014 and ASMI 2015. The calculation is based on the exact values, not on the rounded values shown in the table.

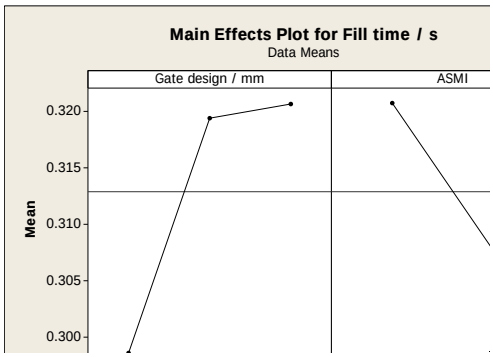

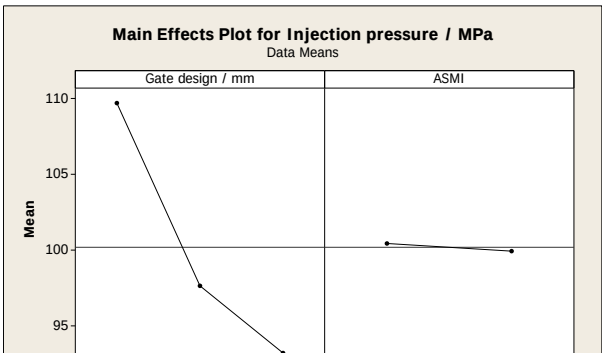

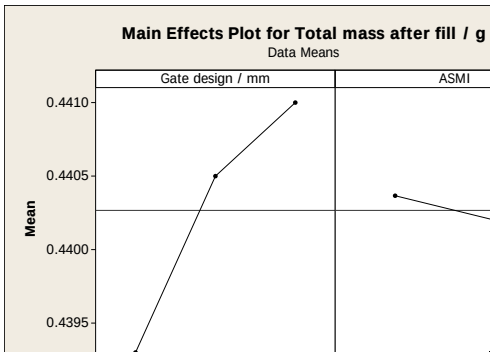

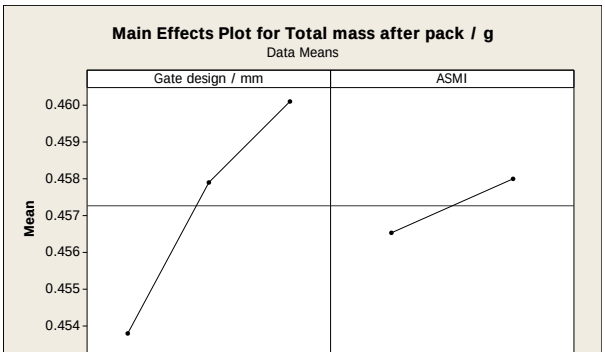

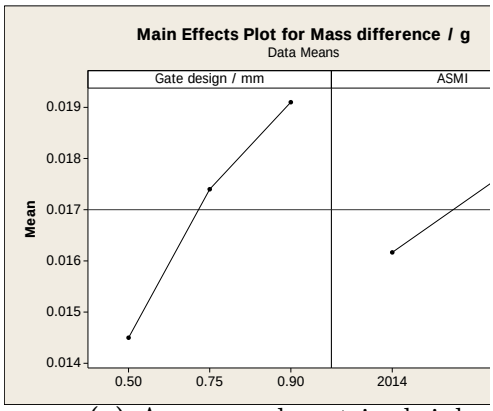

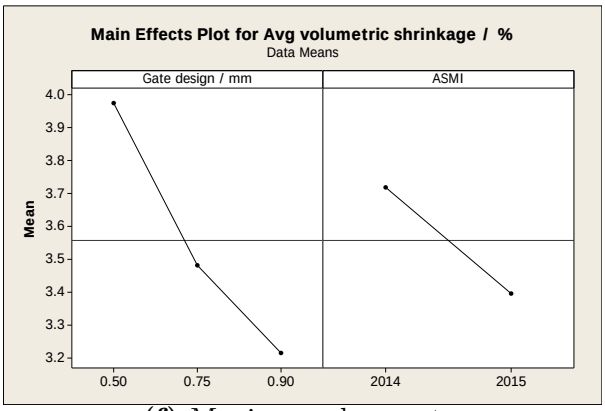

(e) Average volumetric shrinkag

(f) Maximum shear rate.

Figure 6.14: Main effect plots of the DOE analyzing the effect of the input factors "gate thickness" and "ASMI version" on the simulated process outcome of the microfluidic dispenser with pin gate.

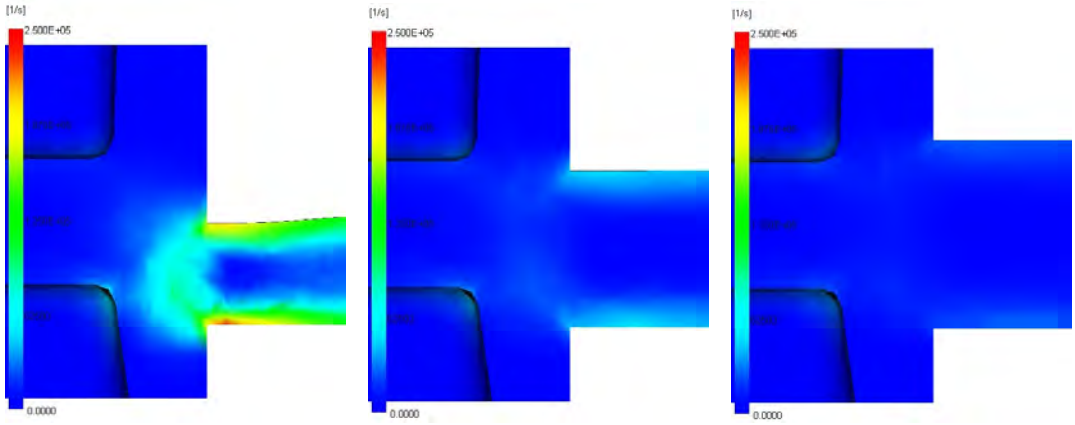

(a) 0.50 mm. **(b)** 0.75 mm. **(c)** 0.90 mm.

Figure 6.15: Maximum shear rate during filling at the investigated pin gates of different size in ASMI 2014. The presented results are also representative for ASMI 2015, since the shear rate results of both software releases were very close. Color scales from blue to red: shear rate from $0\,\mathrm{s}^{-1}$ to $250\,000\,\mathrm{s}^{-1}$.

6.3.4 Design of experiments for warpage analysis

The influence of the gate size, the ASMI version, and the evaluation method on the part flatness was analyzed by extending the previously described DOE approach—again implemented and evaluated by Minitab® 16.2.2. The reason was the possibility to distinguish the sprue from the part for the warpage analysis in ASMI 2015. The following output variables were chosen as measure of the flatness of the part:

- flatness f_f on the front side of the part (front referred to the side pointing in the same direction as the sprue),
- flatness f_b on the back side of the part (back referred to the side pointing in the same direction as the sprue puller).

ASMI calculated the warped shape based on the residual internal stresses of the plastic part. The assessment of the flatness by the manual evaluation of the peak-to-valley distance of the warped surfaces was laborious and introduced an error in the measurements. Therefore, the assessment was done by two more advanced methods in accordance to the flatness definition and evaluation described in ISO 1101, ISO 12781, and geometric dimensioning and tolerancing (GD&T) [127–129]. The flatness of a surface is defined as the minimum distance between two planes being parallel to the reference plane of the investigated surface and enclosing the entire actual surface, as depicted in Figure 6.16. The reason for the application of the two methods was to improve the measurement strategy, to comply with international standards, and to investigate the pertinence and applicability of the evaluation tools. The following two software tools were used:

Figure 78

Definition of the tolerance zone

The tolerance zone is limited by two parallel planes a distance t apart.

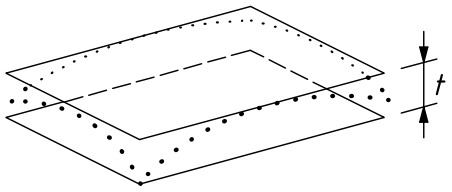

Figure 79

Figure 6.16: Definition of flatness according to ISO 1101 and as applied for the flatness measurements in the second design iteration of the microfluidic mixer [127]: the flatness of a surface is the distance between the two planes enclosing this surface.

1. ASMI

   The flatness evaluation was done directly in ASMI. The simulation software offered the possibility to evaluate the flatness of the warped part by an integrated script. For running the script, all nodes constituting the relevant surface had to be selected. Based on the selected nodes, the script calculated an averaged reference plane of the warped surface and yielded the flatness in compliance to the ISO standards.

   The main advantage was the accurate evaluation, since the entire surface was taken into account. However, the method had the drawback of the time-consuming selection of all relevant nodes. An exemplary node selection is shown in Figure 6.17.

2. GOM

   The flatness evaluation was done in the software GOM Inspect V8 Hotfix 10 (GOM) developed by GOM Gesellschaft für optische Messtechnik, Braunschweig, Germany. This software is made for 3D inspection and dimensional metrology. The warped plastic parts were exported from ASMI as stereolithography CAD file[1] (STL) and imported into GOM. The flatness of front and back was evaluated by the integrated flatness evaluation tool. This tool worked similar to ASMI. It fitted an averaged reference plane to the actual surface and yielded the flatness in compliance to GD&T.

   The advantage of this method was the quick and simple workflow. The major disadvantage was the less accurate measurement compared to ASMI, because not all data points could be selected on the relevant surface. All nodes within a given distance from the original CAD surface were selected and evaluated, leaving out some areas of the surface. An exemplary selection and evaluation are shown in Figure 6.17.

[1] Stereolithography CAD files, denoted as file format STL, are triangulated 3D surface representations of the described body or geometry. [130]

39

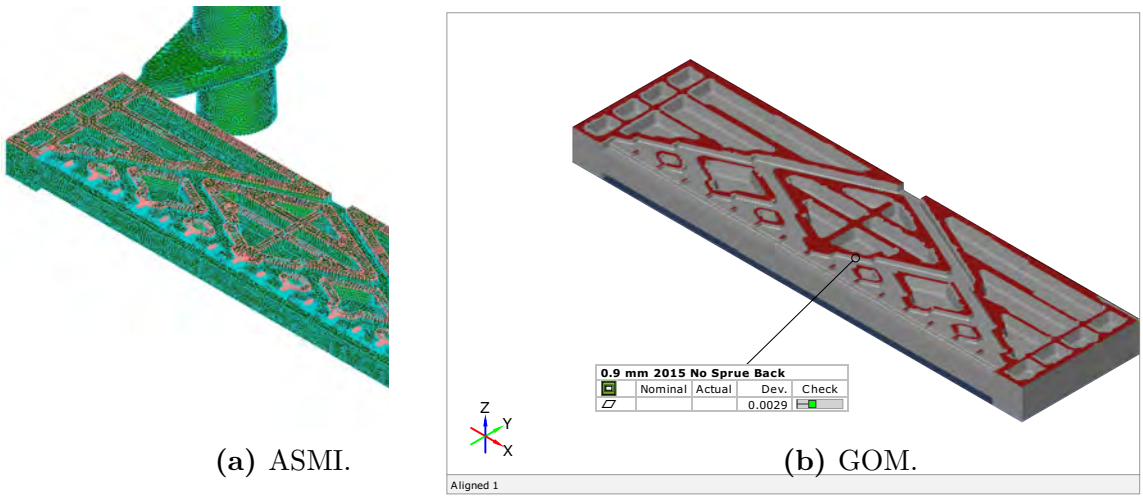

(a) ASMI. **(b)** GOM.

Figure 6.17: Exemplary surface selection and flatness evaluation of warped microfluidic dispenser in the deployed evaluation software. The flatness was in both cases evaluated according to GD&T, ISO 1101, and ISO 12781 as the distance between the two parallel planes enclosing the investigated surface. Displayed values in mm.

The proposed gate sizes of 0.50 mm, 0.75 mm and 0.90 mm, the flatness evaluation methods, and the two ASMI versions were taken as input variables. The simulation studies including and excluding the sprue in the warpage computation in ASMI 2015 were distinguished and are denoted as “2015” and “2015 No Sprue” in the following. The chosen factor levels are summarized in Table 6.9. The DOE was carried out with a full factorial design without randomization and repetitions giving in total 18 different simulation studies.

Table 6.9: Factors and the chosen factor levels of the DOE analyzing the flatness of the microfluidic dispenser.

#	factor	type	factor levels			unit
			−	0	+	
1	gate size	continuous	0.50	0.75	0.90	mm
2	ASMI model	discrete	2014	2015	2015 No Sprue	
3	evaluation software	discrete	ASMI		GOM	

6.3.5 Warpage analysis

In general, the warpage of the part could be caused by the variation in part thickness, the resulting distortion of the plastic flow, and the flow entering the cavity from the side which all led to differential and anisotropic shrinkage. The results of the

warpage analysis are shown in Table 6.10 and Figure 6.18. The flatness of the front and back side of the part differed noticeably from each other with the greater values at the front, so that the residual stresses were not homogeneous, although the part was symmetrical. Major differences in the plastic flow inside the cavity causing the variation in warpage could not be identified, since the part was symmetrical, and the flow was governed by the part geometry, not by the gate size.

Table 6.10: Simulation results of the DOE for analyzing the flatness of the microfluidic dispenser with different gate sizes.

#	gate / mm	ASMI	evaluation	f_f / µm	f_b / µm
1	0.50	2014	GOM	5.1	3.5
2	0.50	2014	ASMI	5.4	3.7
3	0.50	2015	GOM	4.6	3.3
4	0.50	2015	ASMI	5.1	3.6
5	0.50	2015 No Sprue	GOM	2.5	2.3
6	0.50	2015 No Sprue	ASMI	2.6	2.5
7	0.75	2014	GOM	5.2	3.3
8	0.75	2014	ASMI	5.8	3.6
9	0.75	2015	GOM	6.2	3.7
10	0.75	2015	ASMI	6.5	4.0
11	0.75	2015 No Sprue	GOM	3.7	2.9
12	0.75	2015 No Sprue	ASMI	4.2	3.2
13	0.90	2014	GOM	6.2	3.6
14	0.90	2014	ASMI	6.5	4.2
15	0.90	2015	GOM	5.0	3.2
16	0.90	2015	ASMI	5.2	3.7
17	0.90	2015 No Sprue	GOM	3.1	2.9
18	0.90	2015 No Sprue	ASMI	3.1	3.4
mean GOM				4.6	3.2
mean ASMI				4.9	3.5

Increasing the gate size could help to reach acceptable shear rates, but increased the flatness. Yet, all gate sizes still yielded flatness levels clearly below the limit of 10 µm with differences between the mean values of up to about 15 % and 11 % for the front and back, respectively. The smallest gate of 0.50 mm gave the smallest flatness value, as shown in Figure 6.18a and 6.18b. This was in contrary to the over-all analysis of the packing performance where the smallest gate gave the highest values of volumetric shrinkage and lowest values of the predicted mass.

This behavior can be explained by the fact that the smallest gate reduced the influence of the applied packing. The resulting deflection was consequently the most homogeneous because of the minimized gradient of packing pressure and shrinkage

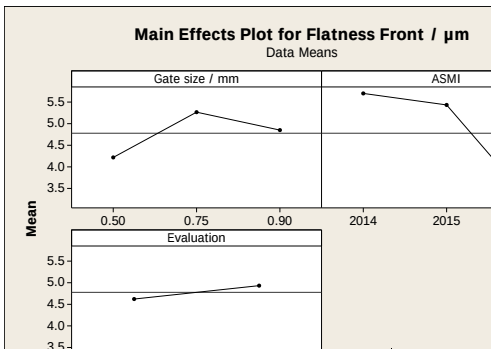

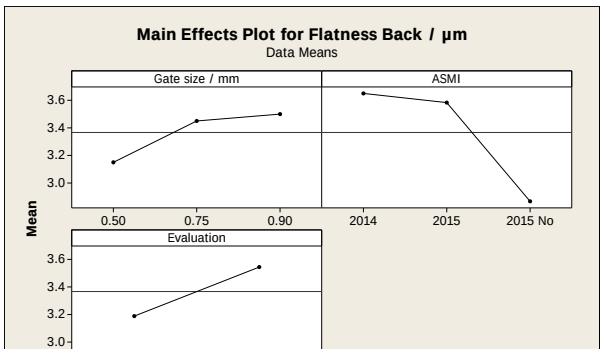

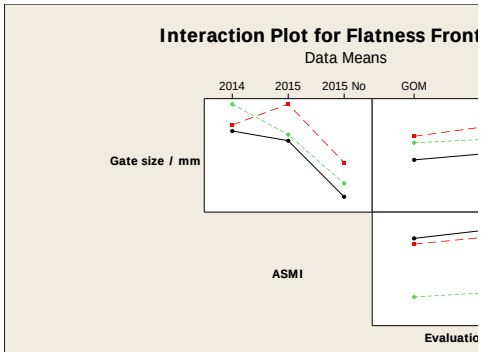

(c) Interactions for flatne

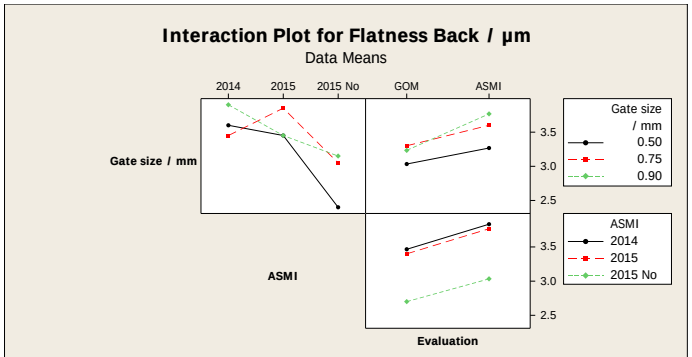

(d) Interactions for flatness at back.

Figure 6.18: Main effect and interaction plots of the DOE analyzing the effect of the input factors “gate size”, “ASMI configuration”, and “evaluation software” on the simulated flatness of the microfluidic dispenser with pin gate.

from the gate to the end of the part. The deflection is exemplary shown for the simulations in ASMI 2015 (No Sprue) in Figure 6.19. The gradient in the deflection along the part was most pronounced for the largest gate. The extent of the deflection increased at the top and bottom edge with the distance from the gate. In contrast, the deflection was the most uniform along the top and surface edge for the smallest gate.

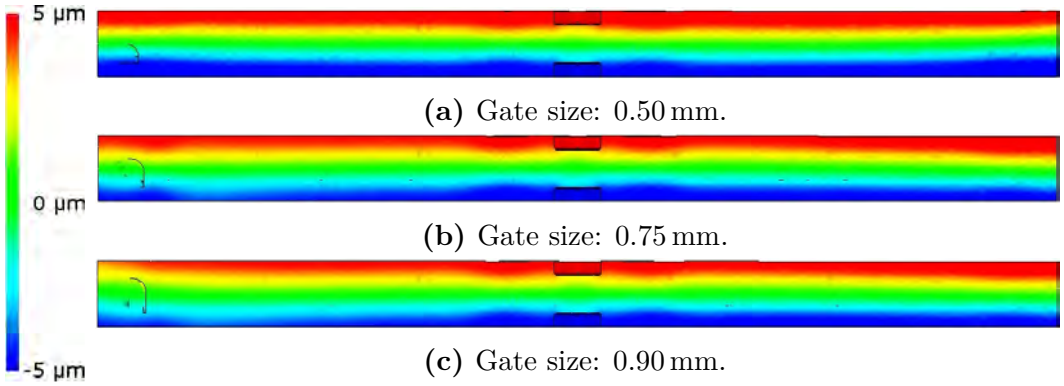

(a) Gate size: 0.50 mm.

(b) Gate size: 0.75 mm.

(c) Gate size: 0.90 mm.

Figure 6.19: Comparison of z-component (along the shortest dimension of the part) of the part warpage of the microfluidic dispenser for different gate thicknesses. The view is in the direction of the gate on the face with the fluidic inlet, the gate is indicated on the left. Color scale: deflection from −5 µm to 5 µm.

The evaluation by GOM yielded always lower values than by ASMI, in average by about 0.3 µm. The systematic underestimation of the flatness by GOM might have been connected to the selected and evaluated area on the front and back side. It was not possible to select the entire surfaces in GOM. Hence, there was the risk of not including some points on the surface which might have pushed the enclosing planes further apart and thus increased the flatness value.

Nonetheless, the trends were predicted similarly to ASMI with the larger flatness values at the front compared to the back and the in average decreasing flatness value with changing software configuration. The only deviation was the predicted flatness at the back, as seen in Figure 6.18d. GOM evaluated the gate size of 0.75 mm giving the largest flatness, whereas ASMI evaluated the gate size of 0.90 mm giving the largest value. The difference in flatness of the back was also significantly greater for the 0.90 mm large gate which was most likely related to GOM's inability to capture the entire surface area.

Both evaluation tools turned out as suited and effective for the flatness evaluation with the previously described pros and cons. It must nevertheless be kept in mind that GOM underestimated the flatness due to the inferior surface selection. The evaluation could be carried out more quickly though. Besides, GOM would have been more appropriate, if additional actions like dimensional measurements had to be performed. For flatness measurements only, it was recommended to use ASMI.

ASMI 2014 gave slightly larger flatness values than ASMI 2015 for gates sizes of 0.50 mm and 0.90 mm, whereas the trend was vice versa for 0.75 mm, as depicted in Figure 6.18c. The former was in agreement with the simulated packing outcome. The lower predicted mass and higher predicted shrinkage of ASMI 2014 could have caused higher residual stress and thus larger warpage.

Excluding the sprue from the warpage calculations decreased the predicted flatness of the dispenser as expected. The sprue was mechanically not connected anymore and could not magnify the part deflection by its own warpage. With variations of more than 40 % and 20 % for the flatness of the front and back, respectively, the effect was however quite tremendous, when considering that the sprue was connected to the part only by a small area compared to the total dimension of the dispenser. The configuration with excluded sprue resembled the reality best, and greater importance should therefore be paid to its outcome.

6.3.6 Mold

The actual mold layout and manufacture was not part of this work, but it was carried out by an industrial partner in the Hi-MICRO project. The mold was in fact fabricated with the knowledge and insight from the presented simulations and design optimization including recommendations about the venting. The cavity of the microfluidic dispenser with 0.90 mm gate size was implemented. The fabricated mold is depicted in Figure 6.20. It was used for the part production and the short shots in connection to the simulation validation described in the next section.

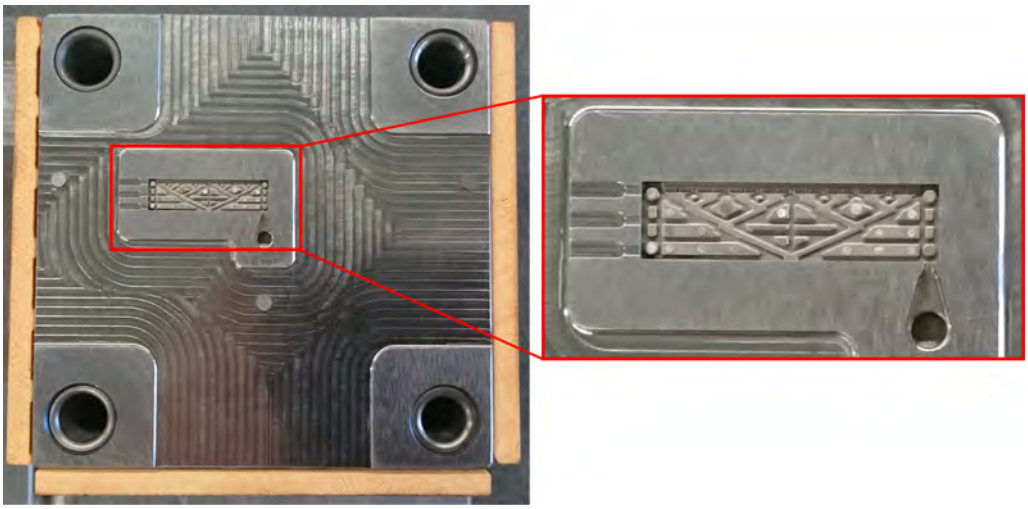

Figure 6.20: Finalized mold with the machined cavity of the microfluidic dispenser with 0.90 mm large semi-circular pin gate. The design was based on the knowledge gained in the simulation-aided optimization.

6.4 Simulation validation

6.4.1 Molding and sample preparation

For the simulation validation, short shots of the microfluidic dispenser were molded by the respective industrial partner of the Hi-Micro Project. The part included the actual microfluidic dispenser, the finally approved pin gate with 0.9 mm diameter and the sprue. The used material was a generic polypropylene (PP). The study was still conducted to qualitatively investigate how the simulation performed with regard to the general prediction accuracy of the flow front pattern. The investigation was split into the comparison of the flow front on the global level, i.e. looking at the flow front of the part as a whole, and on the local level, i.e. looking at some of the details of the part.

For the investigation on global part level, the samples were mapped with a DeltaPix Infinity X-32 digital camera from DeltaPix, Smørum, Denmark, mounted on a Zeiss Stemi 2000 stereo microscope made by Carl Zeiss, Oberkochen, Germany. For the investigation on local feature level with a scanning electron microscope (SEM), the samples had to be conductive. Consequently, the samples were coated at room temperature with approximately 40 nm of gold by means of a Polaron Thermo CG Scientific SC7620 sputter coater made by Quorum Technologies, Laughton, UK. They were investigated with a JEOL JSM-5900 SEM made by Nihon Denshi K.K. JEOL, Akishima, Japan. The very thin layer of gold was not expected to influence the geometry of the molded part or its features.

6.4.2 Simulation set up

The meshed simulation model of the last design iteration was used for the simulation validation. The model included the part, the feed system, and the sprue. In agreement with the experiments, the final gate design with the pin gate at the long side of the dispenser and a diameter of 0.90 mm was analyzed. The creation of the model, the used mesh settings, and the meshed part can be found in the previous section 6.3.

The simulations were run in ASMI 2015. For the comparison to the short shots, only a fill analysis was necessary. The material choice for the simulations was in accordance to the short shots a generic PP. The available Arburg machine at DTU was selected because of the availability of the machine model.The simulation settings are summarized in Table 6.11.

Table 6.11: Simulation process settings of the microfluidic dispenser for the simulation validation. Unspecified settings were kept at the default values.

Parameter	value
ASMI version	2015
Analysis type	Fill
Material type	PP
Material grade	generic
Mold temperature / °C	50
Melt temperature / °C	220
Filling control	injection time
Target injection time / s	0.4
Switch-over volume / %	99
Machine selection	Arburg Allrounder 370 A 600-70 (18 mm)
Virtual mold material	1.1730 (C45W)
Injection location diameter / mm	2.0

6.4.3 Results and discussion

The comparison between the actual flow front of the short shots and the predicted flow front of the simulation was done on a qualitative basis. The flow front patterns on the global part and on local feature level are illustrated in Figure 6.21 and Figure 6.22, respectively.

The overlay of the simulated and real flow front showed good agreement on the global level. The previously identified flow leading and restriction effect was described. On closer examination, the simulated flow front nonetheless constantly moved slightly ahead in the lower half of the cavity, whereas it lagged slightly behind in the upper half.

The simulated flow pattern on the local feature level was also in satisfactory agreement with the actual shape of the short shots. Nevertheless, the simulation predicted the filling of the micro features too early. The real parts showed only indications of the filling of the micro features which most likely happened later at the end of the filling phase or in the packing phase. The simulation on the other hand showed complete filling already at an early stage of the filling phase.

Moreover, it should be noted that for the single short shots the time step for the best fit on part level often differed from the time step for the best fit on feature level. The differences were in the range of up to about 3 % of the individual filling time. This small divergence might be explained by the limited capability of describing the flow in the micro features.

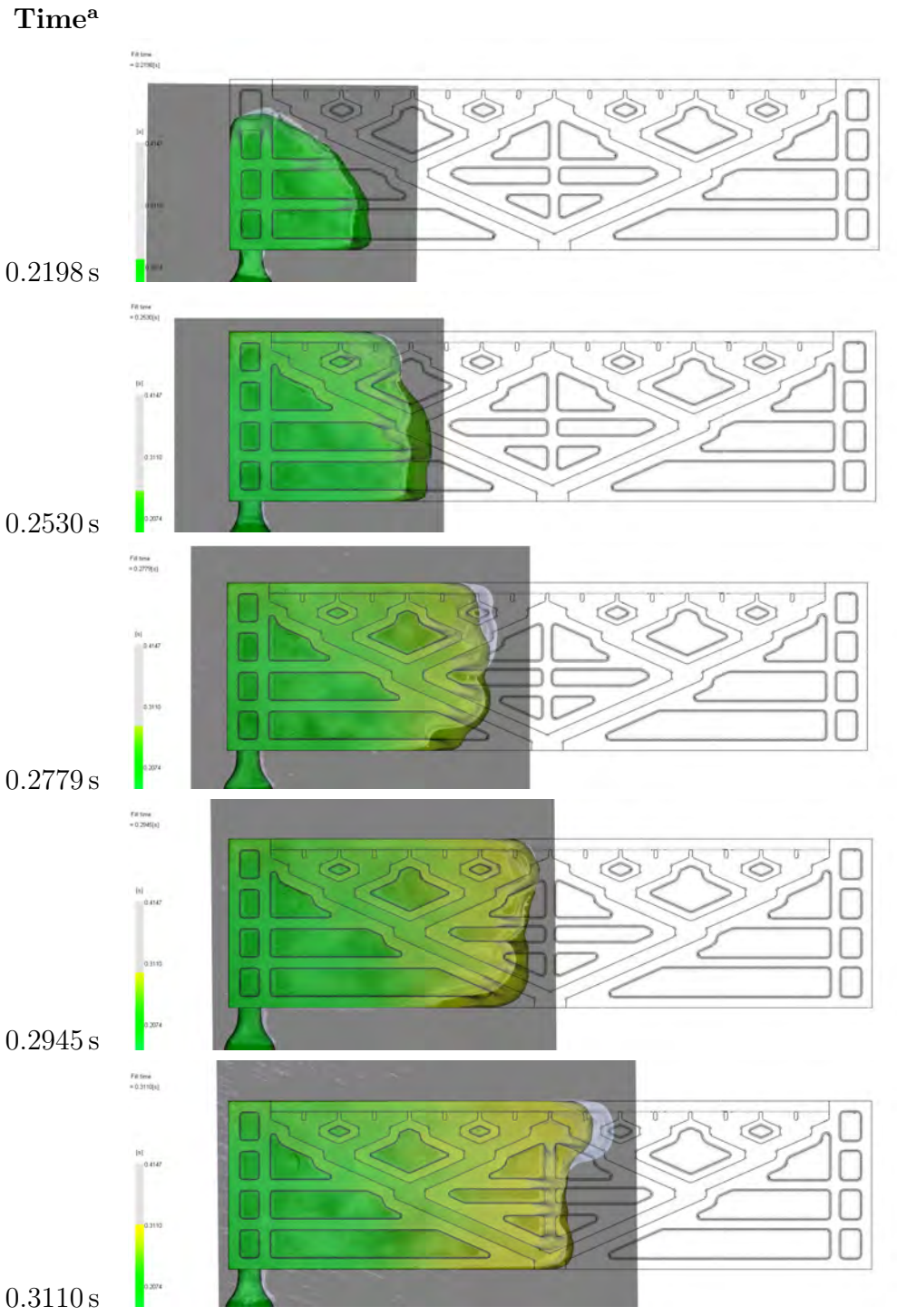

Figure 6.21: Comparison of molded short shots and the simulated flow front pattern on global part level of the microfluidic dispenser.
[a] Filling time in simulation of the best fit to the actual short shot.

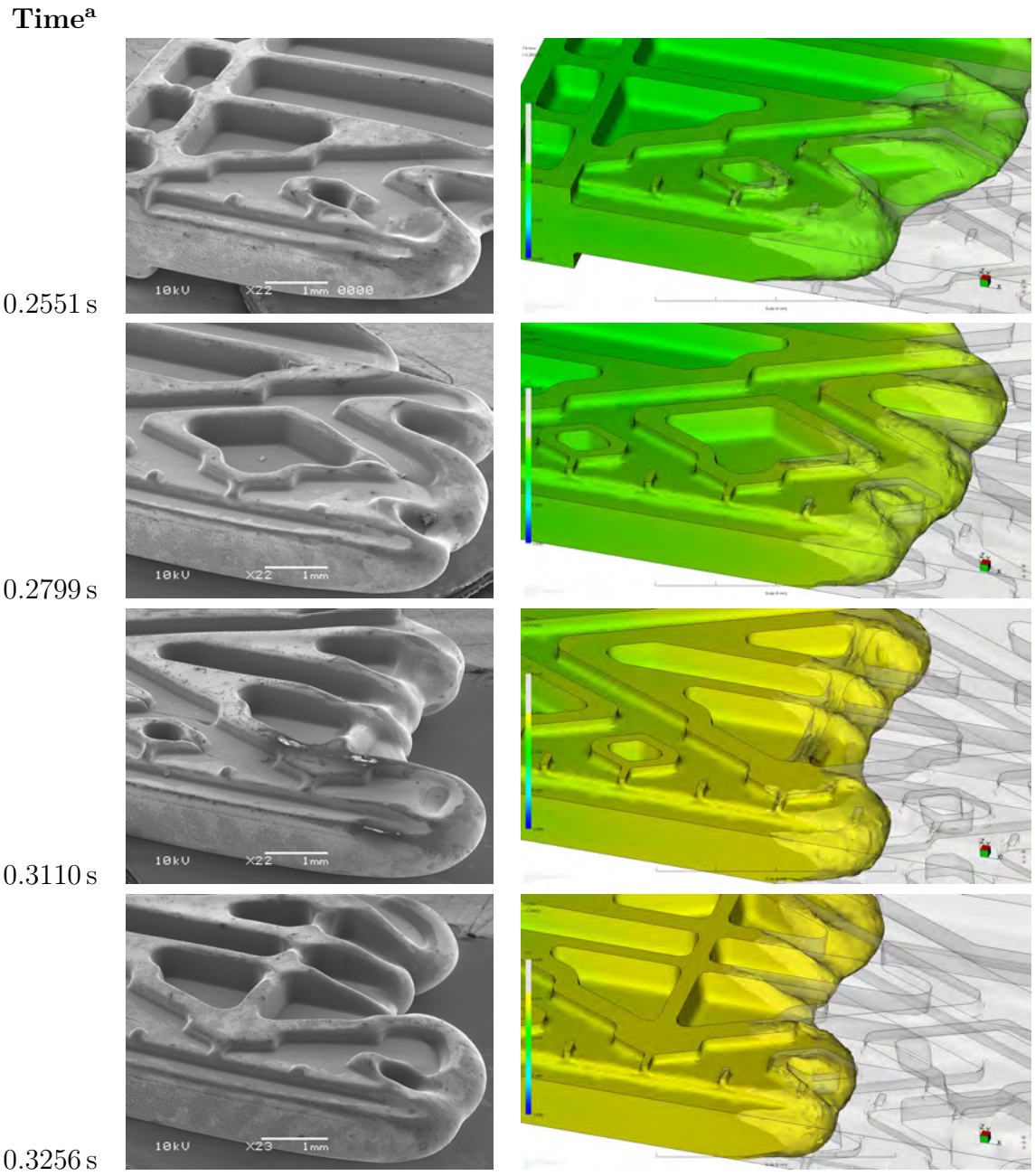

Figure 6.22: Comparison of molded short shots and the simulated flow front pattern on local feature level of the microfluidic dispenser.
[a] Filling time in simulation of the best fit to the actual short shot.

In general, the small divergences between simulations and experiments could also be explained by the limited repeatability of the short shots. The simulations were deterministic and always yielded the exact same result. Yet, the short shots were of stochastic nature, so that even for the same settings and shot dosage, variations in the flow front shape could be observed.

At last, it can be concluded that the simulation was able to catch and predict the pattern of the real flow front, both on global part and local feature level with some small inadequacy for the micro walls. It was believed that the key for the good match was the application of a sufficiently fine mesh. Nevertheless, the numerical results could probably still be improved by implementing a more comprehensive simulation model.

6.5 Summary and conclusion

The study case for the concurrent part design was a microfluidic dispenser. First, the dispenser was introduced with its functional specifications, mainly the required flatness limit, and LCP, glass fiber reinforced PEEK, and PEI were selected as compatible materials. The part design started with four given gate designs—two fan gates and two pin gates. The gates and materials were evaluated by means of a systematic DOE approach based on process simulations. The focus of the investigation was on the resulting flow front in and filling of the cavity, the feasibility of the process window, the packing performance, and the resulting flatness of the gate configurations.

The DOE showed that the large fan gate was not able to provide a uniform flow front, and the flatness of the part exceeded significantly the required value. The pin gates gave in average better flatness values than the fan gates, but had issues with excessive shear. The small fan gate performed better than the large fan gate with regard to flatness and showed acceptable shear rates. However, issues with the degating were expected for the fan gates. Based on the over-all picture, the pin gate at the long side of the part was approved as the best layout, still with the issue of an excessive shear rate and risk for material degradation.

Additionally, the simulations could identify possible issues linked to the plastic flow, such as air entrapment and unfavorable flow acceleration with risk of burn marks. This outcome was to be considered in the tool design. Furthermore, the filling studies showed inhomogeneous flow inside the cavity because of the complex part geometry and varying thickness. The warpage and flatness of the part was anticipated to suffer from this. Therefore, it was decided to modify the part design and change the ribbing to enhance the uniformity of the flow front and the part's structural stiffness.

Regarding the selected plastics, the simulations predicted that PEEK showed inferior part quality and much higher warpage and flatness values. LCP yielded the highest

shear rates. It was therefore decided to use PEI as the first material of choice for the microfluidic dispenser.

The second design iteration was used to optimize the size of the previously approved pin gate and to address the shear rate issue which was previously proven as crucial. Gates of varying size were proposed and investigated in a DOE approach. In a first step, the filling performance of the gates was examined. The increase in gate diameter enabled to push the maximum shear rate to an acceptable level. The remaining process conditions were less critical and were all at suitable levels.

In a second step, the flatness of the microfluidic distributor as the most important specification was successfully investigated. Besides the gate sizing, the comprehensive examination assessed also the influence of the simulation and evaluation software. Although the smallest gate of 0.50 mm minimized the effect of the gate and yielded the lowest flatness, all gate designs could cope with the required flatness level.

Mostly due to the shear rate evaluation, the design of the prototype was finalized including the semi-circular pin gate with a diameter of 0.90 mm. The cavity was in fact realized in the steel mold with the optimized gate design and additional venting structures. In conclusion, the knowledge originating from the simulations and design process was applied in practice.

Ultimately, the simulation validation was carried out by comparing actual plastic parts and the simulations. Parts and short shots were molded with the manufactured mold. The simulation settings were accordingly adjusted and the studies repeated. The comparison of the short shots and the predicted flow behavior revealed a good agreement of the flow front on a global part level. The simulation showed also good agreement on the local feature level, but it was proven that the filling of the micro features is challenging for the software and deviations between the real and predicted behavior can occur, if the features are very small.

In conclusion, it has been demonstrated that simulations are a precious and supportive tool for the design and manufacture of the presented micro plastic part. The simulation-aided investigations could enhance and accelerate the design phase of the micro plastic part.

7 Complete part and mold design and manufacture

Abstract This chapter treats the concurrent and comprehensive part and mold design of a microfluidic mixer—the second industrial study case made from plastics—from the first design draft until the finally molded part. First, the study case and the material selection and testing are described. By means of simulations, the part design is optimized, a possible gate design is systematically established, and the mold is subsequently built up. The manufactured mold and mold components are introduced, demonstrating the application of the previously gained simulation insight to industrial manufacture. The chapter finishes with the simulation validation by comparing molded parts to simulation results.

In micro injection molding, the application of simulation-aided design has low dissemination. The motivation of this chapter is to prove the applicability of structural and process simulations and to apply a holistic approach in the product development of a micro molded part.

7.1 Study case

The study case for the concurrent and simulation-aided part and mold design was a microfluidic mixer with two chambers for aqueous solutions. The entire device (in the following referred to as DEV) is illustrated in Figure 7.1. It consisted of three sub-units: the bottom part (BOT), a middle segment (SUB), and the top part (TOP).

The TOP provided fluidic connections on the back side where silicon tubes could be inserted to supply the whole device. On the front side, a circular microfluidic chamber with flow guiding micro pillars was incorporated. Two of the fluidic connectors supplied this chamber, the other two were fed through to the BOT next to the chamber. The two vias and the chamber were equipped with an integrated rubber sealing. The whole assembly was enabled by four pins which featured a press-fit connection from TOP to BOT.

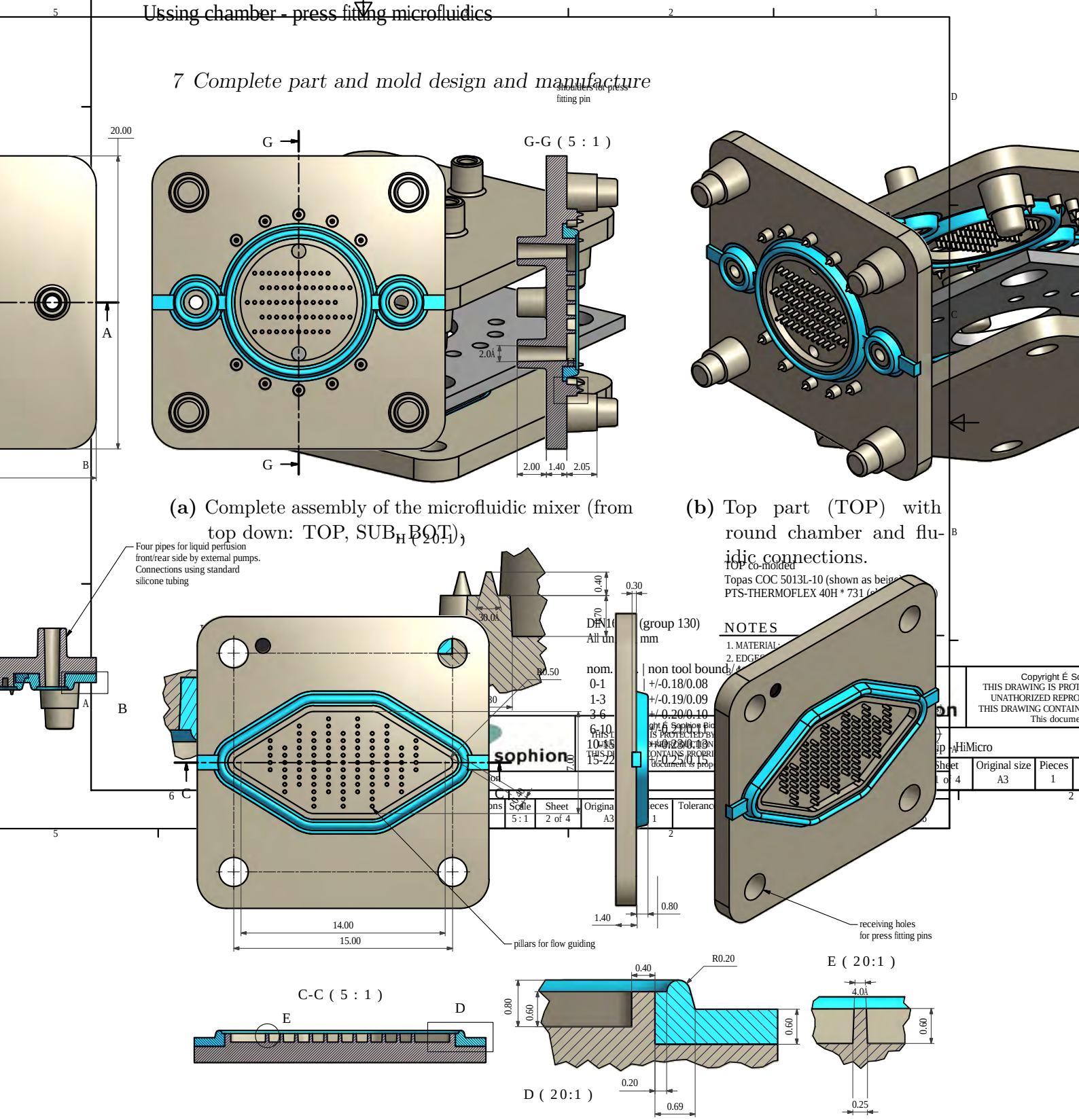

(a) Complete assembly of the microfluidic mixer (from top down: TOP, SUB, BOT).

(b) Top part (TOP) with round chamber and fluidic connections.

(c) Bottom part (BOT) with oval fluidic chamber.

Figure 7.1: Schematic CAD models of the initial design of the microfluidic mixer with two chambers. The BOT was relevant for this investigation. The blue structure is the TPE used for sealing, the brownish part is the thermoplastic base.

The middle segment (SUB) was inserted between TOP and BOT and was used as separator. It was provided ready-to-use by the respective industrial partner in the Hi-Micro project and was therefore not part of this work.

The BOT provided a second, oval-like fluidic chamber with another set of flow guiding pillars. The chamber was supplied from the two vias of the TOP. The chamber was also equipped with a sealing structure to prevent from leakage. Four holes at the corners of the BOT were used as the receiving parts for the pins of the press-fit connection.

The performed investigation and design optimization were limited to the thermoplastic of BOT because of time constraints. The findings about design optimization, gating, and manufacture were transferred to the thermoplastic base of the TOP part because of its similar shape. Hence, in the following "microfluidic mixer" refers to the thermoplastic part of BOT.

The BOT itself had outer dimensions of about 20 mm × 20 mm × 2 mm (length × width × height). It can be classified in fact as a micro-patterned part because of the microfluidic features. The channel depths were in the range of 300 µm to 600 µm, the width less than 1 mm, and the wall thickness about 400 µm. The pillars in the center of the part were used as flow guides and were the most prominent micro features. They were 600 µm high, slightly tapered with a draft angle of 2°, and 200 µm to 250 µm in diameter. They had thus an aspect ratio of three. The part volume was approximately 540 mm^3 which gave a part weight of about 0.54 g for a typical polymer density of approximately 1.0 $g\,cm^{-3}$.

The part was of great interest in this simulation-based investigation because of the 97 micro pillars. The large number and their regular pattern enabled to use them as flow markers during the filling analysis. This aspect eased to perform a qualitative comparison of the simulations with short shots. The presence of the vast number of micro pillars came along with exceptional demands on the filling and demolding because of the large total surface area. Moreover, the modeling of the micro pillars was expected to require a thorough approach and the meshing to be challenging.

7.2 Material selection

For the material selection of the hard thermoplastic and the soft sealing part, the following main requirements regarding the functionality of the device had to be considered:

- the materials had to be compatible with aqueous solutions of slightly alkaline or acidic nature,
- the materials were not allowed to release any contaminants or additives into the used solutions,

- the materials had to fulfill all these requirement at room temperature for the storage time of up to six months and at elevated temperatures of 40 °C for the service time of up to two weeks,
- the whole part should be fabricated by two-component (2k) injection molding,
- the thermoplastic part of the device had to be transparent for optical inspection during operation,
- the soft sealing material had to provide enough compression set to ensure the proper sealing over the entire life time of about six months.

The bulk material of the TOP and BOT was supposed to provide the mechanical stability. Therefore, it had to be a rigid thermoplastic material suitable for injection molding. Based on these requirements, three thermoplastics with suitable chemical and thermal properties were identified due to their properties. [15, 122, 123]

- Cyclic olefin copolymer (COC)
  COCs combine excellent transparency, moisture insensitivity, and resistance towards alkaline and acidic solutions. They provide high dimensional stability and good biological and food compatibility because of their very high chemical purity and low emissions. Drawbacks are the quite challenging processing and the high price.
- Polystyrene (PS)
  PS is a low cost material with good transparency. Food compatible grades are available and it has good dimensional stability and low water absorption. PS is well-known and uncritical to process. The largest disadvantage is its brittleness.
- Polypropylene (PP)
  PP is actually not transparent per se because of its semi-crystalline structure. Nevertheless, tailor-made grades with transparency are available. Its versatile properties comprise good chemical resistance and easy processing. It is however difficult to bond and the expected shrinkage is higher than in case of COC and PS.

COC was actually the preferable material of the industrial partner in the Hi-MICRO Project because of its excellent transparency and chemical compatibility. It was therefore used as the standard material in the following simulations, as the material tests run in parallel.

The sealing structure was intended to work as a gasket and prevent from leakage. Rubber-like properties and the ability to injection mold the material narrowed the material selection to a thermoplastic elastomer (TPE). TPEs can be processed like thermoplastics, but they show similar properties to rubber because of their block copolymer structure. Blocks of thermoplastics and blocks of elastomers are combined in the material and constitute the thermoplastic or rubbery properties,

respectively. Tailor-made grades for the adhesion to different materials exist. Hence, three matching TPE for good adhesion to the proposed thermoplastics were selected. All selected TPEs belonged to the family of styrene TPE, usually called TPS or TPE-S, in which the thermoplastic blocks are made of polystyrene.

7.3 Material testing

7.3.1 Purpose

All selected thermoplastics and TPE were tested regarding the bonding strength. The bonding strength should be high, because the sealing was not allowed to fall off after the overmolding or to be torn off during the handling or assembly of the whole device. However, the criterion for a high bonding strength was not quantified. Instead, all possible combinations of the three thermoplastics and TPEs were investigated and compared among each other to find the best performing material combination.

7.3.2 Sample preparation

The shape and dimensions of the molded specimen were in accordance to type 1B in ISO 527-2 [131]. The processing was conducted similarly to ISO 294-1 [132]. Nevertheless, only one instead of two dog bones were molded in one shot due to the layout of the available mold at DTU. Furthermore, the recommended processing conditions stated in ISO 294-1 could not be entirely fulfilled. The processing parameters differed and the stated requirements regarding the injection molding machine and lab equipment could not be fully guaranteed.

With regard to the course of action, full “dog bone” specimens were molded with every shot for all materials. The runner and gate were removed by cutting. The resulting burr was ground by using grinding paper with grain size P120. The dog bone could then be used as specimen for the tensile test of the pure thermoplastics and TPEs. This step was done as control of the gained results by comparing the values to the theoretical values given by the material supplier. Furthermore, the test provided a reference to classify the values of the bonding strength.

In order to prepare the thermoplastic sample for the overmolding with TPE and the subsequent bonding test, the dog bones were manually cut by means of a band saw. The cut was done in perpendicular at half of the length of the specimen. Burr was again removed by slight grinding with P120 grinding paper. The halves were then inserted in the empty mold occupying half of the dog bone cavity. After inserting, the hard component was overmolded by a second shot with the TPE, as shown in Figure 7.2.

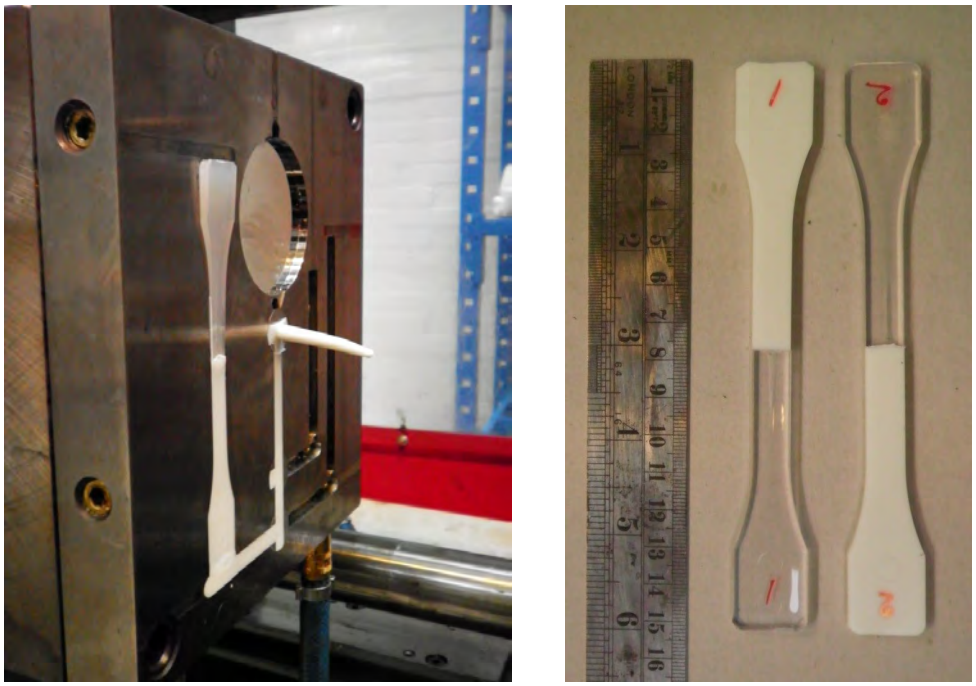

(a) Inserted thermoplastic half with TPE overmolding in dog bone mold.

(b) 2k dog bones ready for testing.

Figure 7.2: 2k injection molding of material samples for bonding strength tests in relation to the material selection of the microfluidic mixer. The used mold is multi-purpose, so that other cavities are integrated, but not active.

The molding was done on a Ferromatik Milacron K60 injection molding machine with 35 mm screw diameter, made by Ferromatik Milacron, Malterdingen, Germany. The machine was equipped with an external oil heater of type Wittmann Tempro Plus 190, made by Wittmann, Vienna, Austria. The chosen process parameters for all the materials can be found in Appendix D. Elevated temperatures were chosen to increase the chance for bonding and the bonding strength.

7.3.3 Tensile testing

The bond strength of the molded sample was evaluated as the tensile strength, given that the material bond breaks before the pure materials. The tensile tests were conducted by measuring the force and then calculating the material stress by means of the initial cross-section of the specimen. Five specimens were tested for each material and material combination. The tensile tests for the specimens of pure PP and all TPE could not be completed, because the elongation of the material exceeded the working distance of the tensile testing machine, so that no break in the material could be achieved. An exemplary tensile test with a clamped sample and the excessive elongation of PP is shown in Figure 7.3.

The tests were run in accordance to ISO 527-2/1B/50 on an Instron 1115 tensile testing machine made by Illinois Tool Works, Glenview, IL, USA. The chosen speed for elongation was $50\,\mathrm{mm\,min^{-1}}$. The force signal was recorded by means of LabVIEW®, made by National Instruments, Austin, TX, USA, with a sampling frequency of 1613 Hz.

7.3.4 Data processing

The measurement of the tensile testing machine showed huge noise on the measured signal, especially recognizable at low bond strength, i.e. for most of the 2k specimen. Figure 7.4 depicts an exemplary recorded data set. The raw data was first analyzed by a fast Fourier transformation (FFT) in order to identify the type of noise and find any frequency of the superimposed noise. An example of the FFT analysis is show in Figure 7.5.

Since the tensile test was a very slow motion, the actual data was represented by the peak at about 0 Hz. The frequency plot showed additionally much small peaks at multiples of 50 Hz which represent noise originating from the supplying global electricity grid. Besides these peaks, the general spectral density did not show any trend, but remained constant which indicated white noise. To filter out the noise, a low pass filter with a cut-off frequency of 10 Hz and a symmetrical and rectangular moving average filter with a window size of 60 data points were applied.

(a) PP specimen in machine during test.

(b) Initial and stretched PP specimen.

Figure 7.3: PP specimens being clamped in the tensile testing machine and showing necking during test and comparison between the initial and stretched PP sample. Break could not be reached, because the material elongation exceeded the machine working distance.

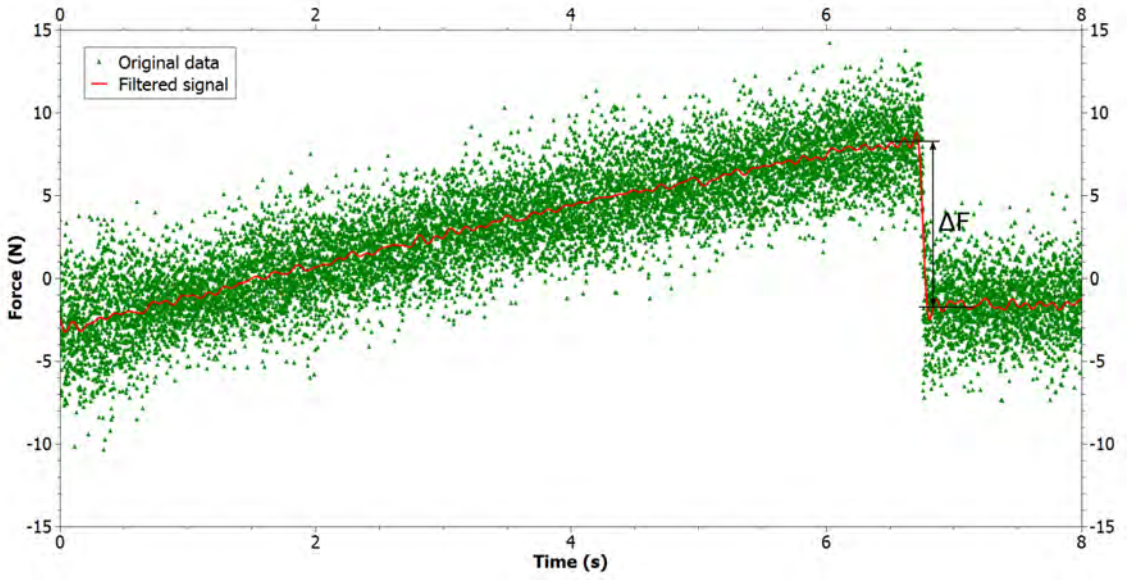

Figure 7.4: Exemplary originally monitored and filtered data of the 2k tensile test. The highlighted difference after sample break was considered for calculating the tensile strength.

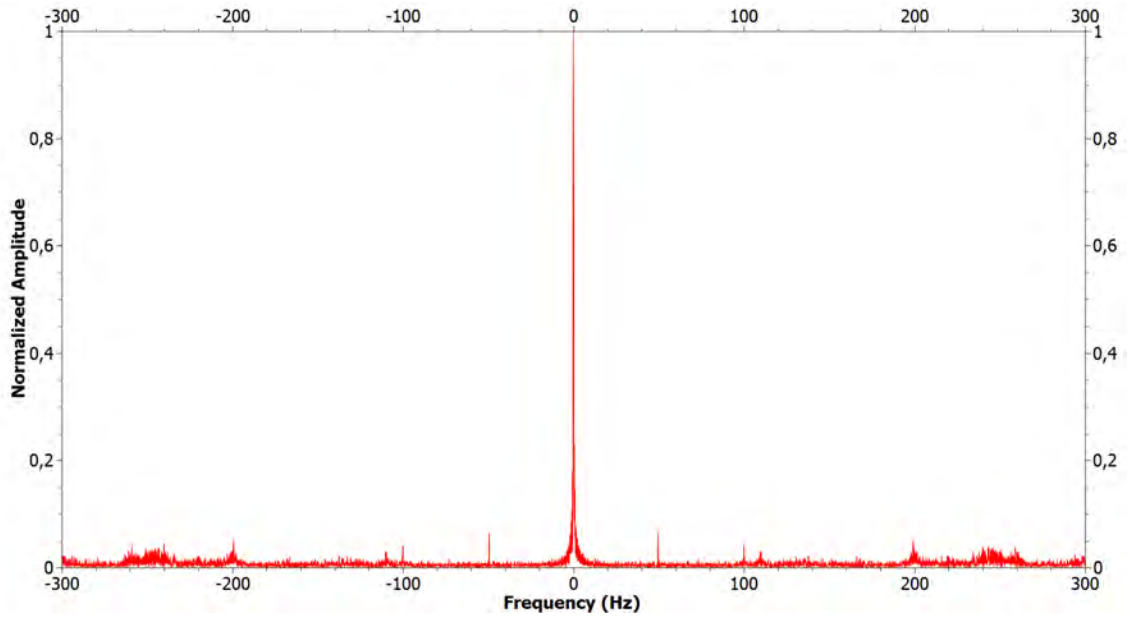

Figure 7.5: Exemplary frequency spectrum of the FFT analysis of the measured tensile test data for a 2k specimen.

The tensile strength was of main interested for the bonding strength. However, the peak in tensile stress could still not be clearly identified in the filtered signals. In addition, an offset in the signal could be sometimes recognized after the sample broke. Hence, the tensile strength was estimated in the graph as the difference between the high and low signal before and after breakage, respectively, as indicated in Figure 7.4.

7.3.5 Results and discussion

The results for the tensile strength of the pure thermoplastics and the bonding strength of all 2k combinations are summarized in Figure 7.6. The detailed results can be found in Appendix D. The measured values of (44.9 ± 0.4) MPa and (39.8 ± 2.0) MPa for the tensile strength of COC and PS, respectively, were close to the theoretical values from the data sheet. The tensile strength of PP and the TPE could not be measured, since the elongation exceeded the machine's working distance.

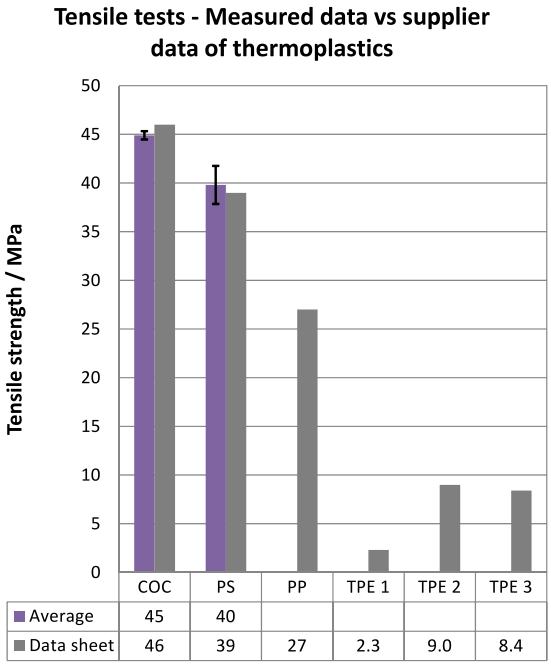

(a) Pure thermoplastics and TPEs.

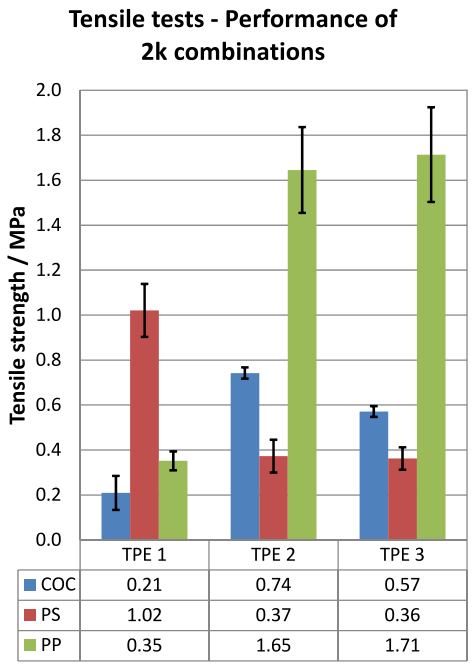

(b) 2k combinations.

Figure 7.6: Results of the tensile tests of the 1k and 2k specimens. The shown values are the average of five measurements. The error bars mark the standard measurement uncertainty, confidence level: 95 %.

In general, bonding could be achieved for all 2k material combinations. However, some bonds were very weak and broke already while handling the sample, i.e. they

had very little tensile strength. As rule of thumb, a tensile strength of about 2 MPa is considered as very good bond which is not achieved by any of the investigated material combinations. Nevertheless, high tensile loads on the interface were not expected in the service scenario of the demonstrator.

The best bonds were achieved with PP in combination with TPE 2 and TPE 3 with values for the tensile strength of about (1.7 ± 0.2) MPa. However, the PP appeared milky after molding and showed thus much lower transparency compared to COC and PS. The transparency could perhaps be improved by reducing the material thickness. The microfluidic mixer was not a thin foil though, but still had a material thickness of about 1.4 mm. It was assumed that the transparency would likely still be insufficient for visual inspection, and it was consequently decided to discard PP and all 2k combinations with PP.

The combination of PS and TPE 1 showed the third largest bonding strength with a value of approximately (1.0 ± 0.1) MPa. It was therefore the preferable material combination for the production of the prototypes of the microfluidic mixer.

7.4 Design of press-fit connections

Press-fits are simple, but effective features for the connection and assembly of two parts [133]. The major dimensions and resulting stresses of an assembled press-fit are illustrated in Figure 7.7. The interference of the shaft and the hub, i.e. the difference between the outer shaft diameter d_o and the slightly smaller inner hub diameter D_i, introduces a pre-stress in the material and determines the strength of the press-fit. Regarding the layout, the minimum interference is given by the minimum required axial bearing capacity of the press-fit. The maximum interference is given by the mechanical strength of the deployed material.

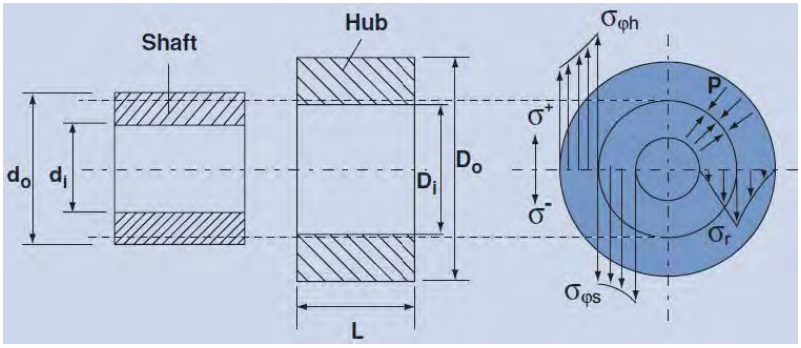

Figure 7.7: Schematic of the shaft and hub of a press-fit with the major dimensions and the resulting stresses in the material and pressure between the shaft and the hub [133].

The axial bearing capacity F of the press-fit is mathematically given as [133, 134]

$$F = \pi\,\mu\,d_\mathrm{o}\,L\,p = \pi\,\mu\,d_\mathrm{o}\,L\,\frac{(d_\mathrm{o} - D_\mathrm{i})\,E}{d_\mathrm{o}\,(A + B)} \tag{7.1}$$

with the coefficient of friction μ and the elastic modulus E of the used material, the length of interference L and the pressure p between shaft and hub, and the geometrical factors A and B again given as

$$A = \frac{1 + \left(\frac{d_\mathrm{i}}{d_\mathrm{o}}\right)^2}{1 - \left(\frac{d_\mathrm{i}}{d_\mathrm{o}}\right)^2} \quad \text{and} \quad B = \frac{1 + \left(\frac{d_\mathrm{o}}{D_\mathrm{o}}\right)^2}{1 - \left(\frac{d_\mathrm{o}}{D_\mathrm{o}}\right)^2} \tag{7.2}$$

with the inner shaft diameter d_i and the outer hub diameter D_o.

When in service, a pressure of up to 1 bar was supposed to be applied to the assembled device to drive the liquid through the system. This pressure introduced a force on BOT and TOP which the press-fits had to withstand, otherwise BOT and TOP would have leaked or split. The force on the liquid chamber of BOT was greater than on the liquid chamber of TOP due to the larger surface area. Taking the projected area in direction of the press-fits into account, the applied maximum pressure of 1 bar correlated to a maximum force and thus the required aggregate bearing capacity of all four press-fits of about 6.7 N.

The outer hub diameter correlated to the radius of the fillet of the BOT and was hence set to $D_\mathrm{o} = 6\,\mathrm{mm}$. The outer and inner shaft diameters were set to $d_\mathrm{o} = 2\,\mathrm{mm}$ and $d_\mathrm{i} = 0\,\mathrm{mm}$. The length of interference was equal to the thickness of BOT in the non-functional area and hence $L = 1.4\,\mathrm{mm}$. The tensile modulus of the previously investigated COC and PS showed similar values of $T_\mathrm{COC} = 3.20\,\mathrm{GPa}$ and $T_\mathrm{PS} = 3.25\,\mathrm{GPa}$, so that this part of the dimensioning of the press-fits was universal. The coefficient of friction for both materials was estimated as $\mu = 0.25$. The force resulting from the liquid pressure inside the system was distributed to four press-fits and a safety factor of two was introduced. As a result, the maximum inner hub diameter was yielded by means of Equation 7.1 as $D_{\mathrm{i\ max}} = 1.991\,\mathrm{mm}$.

The maximum allowed interference I_max of the press-fit is given as [134]

$$I_\mathrm{max} = \frac{\sigma_\mathrm{y}\,d_\mathrm{o}\,(W + 1)}{E\,W} \tag{7.3}$$

with the yield strength σ_y of the used material and the geometrical factor W which is again given as

$$W = \frac{D_\mathrm{o}^2 + d_\mathrm{o}^2}{D_\mathrm{o}^2 - d_\mathrm{o}^2}. \tag{7.4}$$

The yield strengths of COC and PS were assumed to be equal to the tensile strengths, as this is a common assumption for brittle materials. By means of Equation 7.4, the

yield strengths of $\sigma_{y\ COC} = 46\,\text{MPa}$ and $\sigma_{y\ PS} = 39\,\text{MPa}$ for COC and PS resulted in minimum inner hub diameters of $D_{i\ min\ COC} = 1.974\,\text{mm}$ and $D_{i\ min\ PS} = 1.978\,\text{mm}$, respectively. In accordance to the upper and lower limits, the inner hub diameter was finally chosen as $D_i = 1.98\,\text{mm}$. Detailed information about the calculations regarding the press-fit layout can be found in Appendix D.

The mechanical stability of the press-fit connection was additionally checked by mechanical FEM simulations of the stress inside the material in SolidWorks®. The check was based on the comparison of the von-Mises stress and the yield strength of the material. The mesh density of SolidWorks® was set to "fine", and the default mesh parameters were used. The resulting mesh is shown in Figure 7.8a. The pressure p resulting from the press-fit (correlating to Figure 7.7) was applied to the inner face of the holes of BOT—about 13 MPa and 15 MPa for COC and PS, respectively. Moreover, the gravity was applied to BOT in the direction of the thickness. The exemplary simulation result for the von-Mises stress distribution in the part is depicted in Figure 7.8b. The simulation gave a maximum stress of about 29 MPa for COC and 31 MPa for PS which was both below the yield strength.

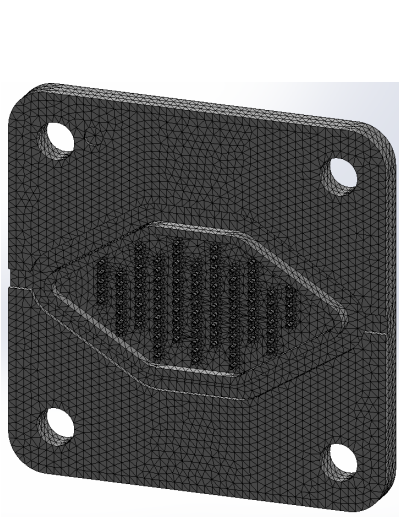

(a) Meshed BOT.

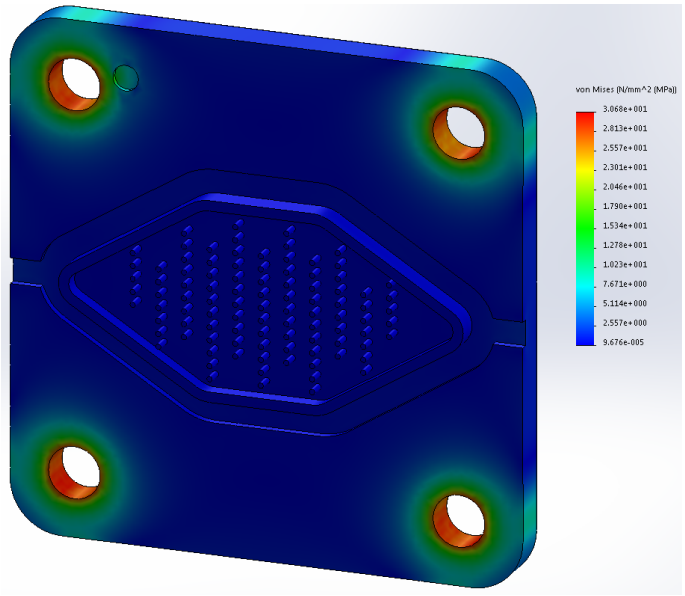

(b) Stress distribution.

Figure 7.8: Mechanical FEM simulation of the von-Mises stress distribution in BOT for PS. The stress distribution for COC matched PS, the numerical values varied. The simulation showed that the von-Mises stresses for both materials were clearly below the yield strengths.

7.5 Mold design and gate optimization—pin gates

7.5.1 Gate properties

The pin gate is a commonly applied and simple type of gate. It was therefore the starting point of the mold design of the microfluidic mixer. The major advantage is the easy degating after molding. However, the small cross-section of the gate can cause excessive shear rates and quick gate freezing preventing from sufficient packing.

The pin gate is also advantageous, because it can be modeled with circular cross-section in the simulation software without additional precautions. The injection location in ASMI has to be assigned to a single node of the mesh. The size of the injection location can be specified by the diameter of the projected area around the node. The plastic flow enters the cavity from there, similarly to a small pin gate. ASMI provides the possibility to analyze the most suitable injection location. The evaluation criterion is the injection pressure which is minimized.

The applicability of pin gates was investigated by simulations in ASMI 2014 in two stages. First, the focus was on finding the most suitable gating location. Subsequently, different pin gate configurations were evaluated. Both stages are described in the following. They are however based on the same simulation model and mesh presented in the next section.

7.5.2 Simulation set up

The general simulation set up included the part only without feed system or any mold or machine components, since no information on them was available so early in the design phase. The CAD file of the BOT was directly imported to ASMI.

The analysis of the gating location and the subsequent investigation on various pin gate configurations were carried out with the same simulation model. The exact mesh settings of the BOT are listed in Table 7.1. The result of the meshing is shown in Figure 7.9. Specific mesh densities were not assigned. The mesh showed refined areas at round surfaces because of the use of the chord height control. The small value led to a good interpolation of rounded edges in the model.

Since the mold design was performed in parallel to the material tests, the outcome of the tests was not known yet. The material choice for the simulations was therefore the COC as the number-one choice of the industrial partner among the selected thermoplastics. The default processing settings of the ASMI data base for the chosen COC were used due to the unavailability of actual values. The machine properties were set to the Arburg Allrounder 370 A 600-70 with 18 mm screw diameter and 600 kN clamping force being available at DTU. This machine was meant to be used

for the part production. All relevant technical specifications were implemented in the machine model in ASMI. The material and machine settings were used for any design investigations on the pin gates.

Table 7.1: Meshing settings of the microfluidic mixer with film gate. Unspecified settings were kept at the default values. The total number of elements varies slightly due to the different thickness of the investigated film gates.

Parameter	setting
Global edge length / µm	600
Merge tolerance / µm	10
Chord height / µm	30
Minimum number of elements through thickness	10
Maximum edge length in thickness direction / µm	600
Bias ratio	1.2
Total number of elements	2 100 000

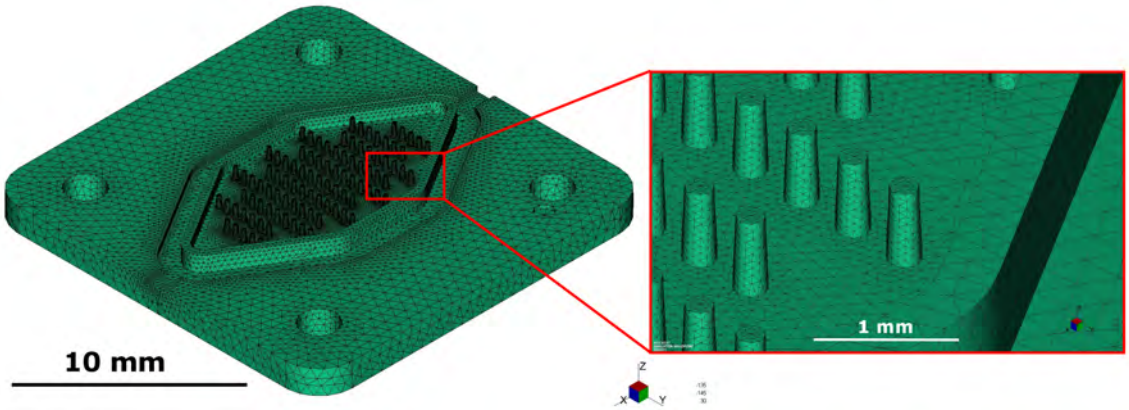

Figure 7.9: Overview and details of the meshed microfluidic mixer. The global edge length was 0.6 mm. The mesh refinement at the gate and micro features is due to the use of the chord height control.

7.5.3 Settings for gating location analysis

A gate location suitability analysis was conducted in ASMI 2014. The analysis was done in order to find the most suitable location for a single pin gate with regard to minimized injection pressure. The aforementioned COC and Arburg injection molding machine as well as standard processing parameters were selected for the simulation. The simulation settings are summarized in Table 7.2.

Table 7.2: Machine and process settings for the simulations of the microfluidic mixer with pin gate. Unspecified settings were kept at the default values.

Parameter	setting
ASMI version	2014
Analysis type	gate location
Method	minimization of injection pressure
Material type	COC
Mold temperature / °C	110
Melt temperature / °C	280
Machine	Arburg Allrounder 370 A 600-70 (18 mm)
Number of gates	1

7.5.4 Results and discussion of gating location analysis

The results of the gating suitability analysis is illustrated in Figure 7.10. Regarding flow considerations to minimize pressure, the most suitable gating location was in the center of the top or bottom surface of the part. The top surface could however not be used because being a functional surface with integrated micro structures. The micro pillars did not leave space to integrate a pin gate and the gate vestige would have influenced the flow in the fluidic chamber.

Gating at any location on the bottom or top surface with a pin gate would have made necessary the use of a three-platen mold instead of a two-platen mold. This option was ruled out for economic reasons and to maintain the mold simple. The possibility to use a sprue gate was not considered, as the mold was intended to be used with two cavities, so that up to two parts could be molded at a time. Hence, runners were necessary to supply both cavities, and the part's side walls were left as the only option for placing pin gates.

The footprint of 20 mm × 20 mm of the BOT suggested that the part could be gated from four equal sides. The symmetry of the part however implied gating possibilities on two sides: the "front", resulting in flow of the plastic parallel to the fluidic chamber, and the "side", resulting in plastic flow perpendicular to the fluidic chamber. Because of the high width-to-thickness ratio (20 mm to 1.4 mm), gate configurations with one, two, and three pin gates per face appeared suitable and were investigated, leading to six gating scenarios in total.

The sizing guidelines of pin gates in tool engineering recommend 40 % to 100 % of the wall thickness where the gate is attached [81, 133, 135]. Still, small sizes can cause high shear rates, larger pin gates are more difficult to remove and leave gate vestige. Intending to keep good balance between the shear rate and the necessary degating, a gate thickness of 1.0 mm equal to approximately 70 % of the wall thickness was selected.

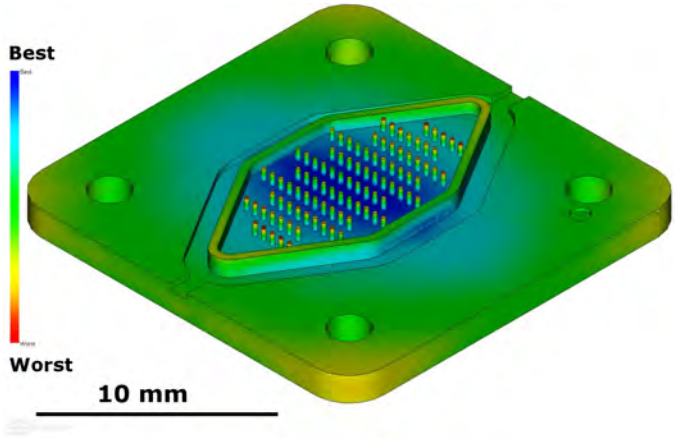

Figure 7.10: Results of the gating suitability analysis. Color scale from "best" to "worst".

7.5.5 Settings for pin gate analysis

The pin gates were directly modeled by placing the injection location and adjusting the injection location diameter in ASMI. Only the number of injection locations and their placement at the front or side varied between the studies, so that the total number of tetrahedral elements did not differ. The simulation was based on the same model and mesh as the gate injection location analysis. Meshing settings and results are hence shown in the previous Table 7.1 and Figure 7.9, respectively.

The simulations of the various pin gate configurations were performed to evaluate the filling characteristics of the plastic, e.g. over-all flow pattern, weld lines, shear stress, etc. The focus was on the whole part and the meshing was not optimized, so that the filling performance of the micro pillars was only of secondary importance. A complete filling, packing, and warp analysis of the part with filling control by ram speed was conducted in ASMI 2014.

The aforementioned COC and Arburg injection molding machine as well as standard processing parameters were selected for the simulation. A machine speed profile was not implemented because of the lack of according data. The screw speed was set to a constant value of $20\,\mathrm{mm\,s^{-1}}$. The software however accounts for the machine response time.

The tool steel "Orvar Supreme" from Uddeholm, Hagfors, Sweden, was chosen as material of the virtual mold. Orvar supreme is an alloyed, thermally stable, and shock-resistant steel of type 1.2344 (AISI H13). Due to its special production, it shows superior quality than conventional 1.2344 steels and meets the requirements for premium H13 steel. Ovar surpreme is well suitable for parts subjected to thermal and mechanical stress [136]. It was hence planned to fabricate the prototype mold inserts from this type of steel. The injection location size was chosen as 1.0 mm equal to the intended gate size. All settings are summarized in Table 7.3.

Table 7.3: Machine and process settings for the simulations of the microfluidic mixer with pin gate. Unspecified settings were kept at the default values.

Parameter	setting
ASMI version	2014
Analysis type	Fill+Pack+Warp
Material type	COC
Mold temperature / °C	110
Melt temperature / °C	280
Filling control	absolute ram speed vs ram position
Target ram speed / ($mm\,s^{-1}$)	20
Cushion / mm	2.0
Switch-over volume / %	99
Packing pressure / MPa	60
Packing time / s	10
Cooling time / s	20
Machine selection	Arburg Allrounder 370 A 600-70 (18 mm)
Virtual mold material	Orvar Supreme (1.2344, AISI H13)
Injection location diameter / mm	1.0

7.5.6 Results and discussion of pin gate analysis

The major simulation results of the pin gate analysis are listed in Table 7.4. All gates gave approximately the same filling time of about 0.11 s. The value matches the expected value considering the part volume and the material flow rate given by the injection speed. The value only accounted for the part, any feed system was not included and was expected to increase the injection time significantly. The fact that the acceleration and geometry of the machine were not modeled probably mattered also for the short injection time.

The filling study of the BOT revealed also the risk of possible air entrapment at the rib forming the border of the fluidic chamber. The rib was thinner than the bulk structure and acted therefore as flow restrictor. The effect of the rib with the possible air entrapment is exemplary shown for two pin gate layouts in Figure 7.11.

The necessary injection pressure was expected to reach values in the range of 2.6 MPa to 4.2 MPa. The addition of a feed system would increase the injection pressure significantly, but the machine would still most likely be able to provide the necessary pressure and clamping force.

One gate at the front or side and two gates placed at the side caused high shear rates exceeding the recommended limit for COC. It was therefore debatable, if one or two pin gates of 1 mm size would lead to possible material deterioration.

Table 7.4: Simulation results for the predicted values of the injection time and pressure and the shear rate of the pin gate analysis.

Gate location	side			front			limit
Number of gates	1	2	3	1	2	3	
Filling time / s	0.1068	0.1069	0.1067	0.1067	0.1068	0.1069	–
Injection pressure / MPa	3.4	2.8	2.6	4.2	3.3	2.9	250
Max. shear rate / s^{-1}	59 000	61 000	41 000	84 000	37 000	36 000	40 000

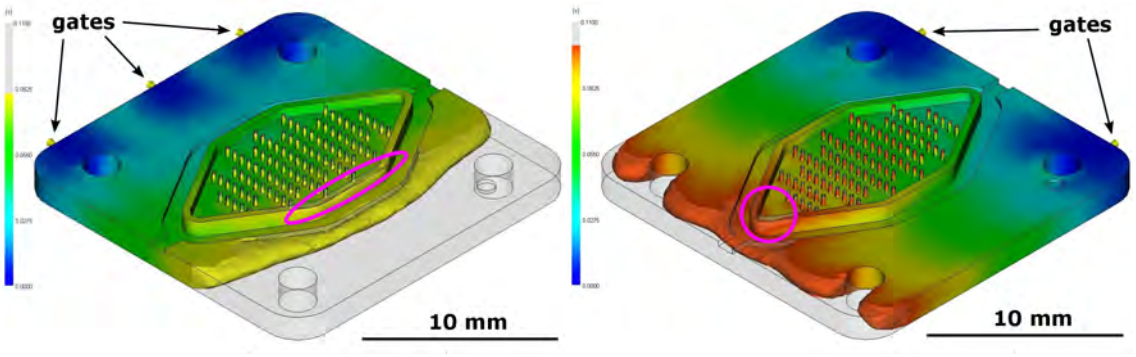

(a) Three gates at side. **(b)** Two gates at front.

Figure 7.11: Filling analysis of two pin e microfluidic mixer with indicated possible air entrapment because of the rib acting as flow restrictor. Color scale: fill time from 0 s to 0.11 s.

The weld line analysis is depicted for all gate configurations in Figure 7.12. The indicated weld lines represent flow fronts meeting at an angle of up to 135° (default value of ASMI). Larger values were assumed to not cause any mechanically weak spots or surface notches which are usually associated to weld lines. [15, 137, 138]

In general, all gate configurations led to two weld lines and hence mechanically weaker spots at the holes of the press-fit on the opposite side to the gates. The weld lines reached the outer edge of the part. This introduced higher risk of material breakage and hence failure of the press-fit, since mechanical stress was applied to the material surrounding the holes of the BOT after the insertion of the press-fit pins of the TOP part.

Applying one pin gate resulted in noticeable weld lines from all four holes of the press-fits to the outer edge which was even more critical than having only two weld lines in this area. The weld lines of the two holes closer to the gate are less pronounced for two and three gates and disappear within the bulk material, so that a noticeable mechanical influence was not expected.

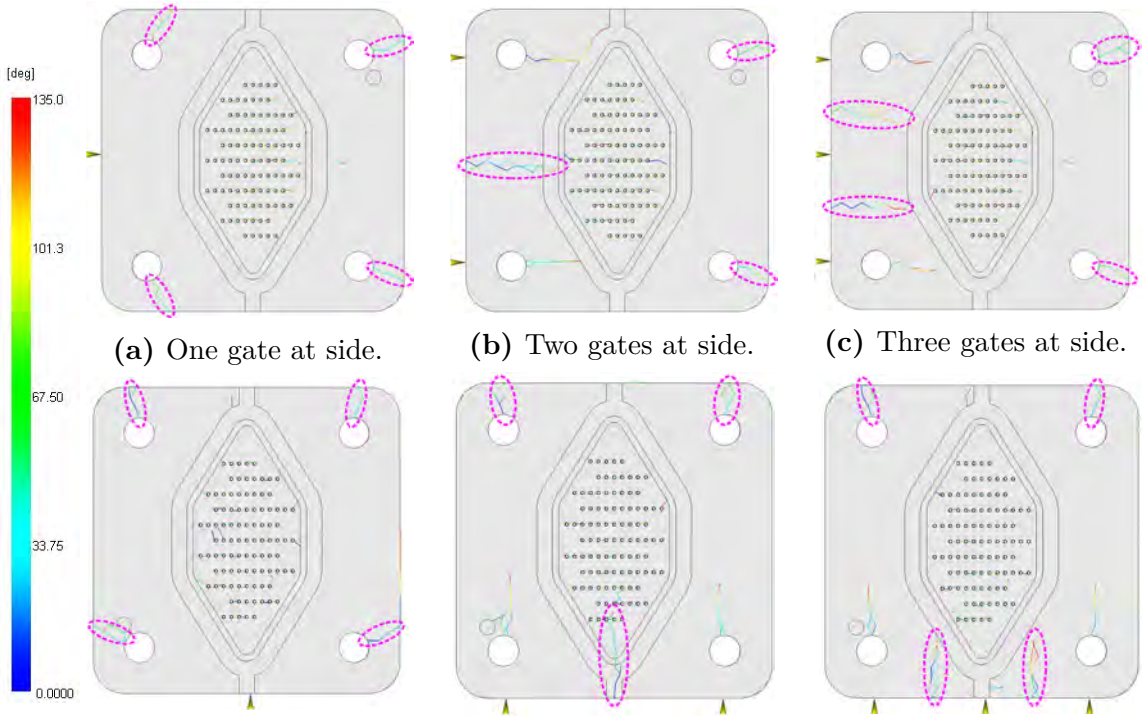

(a) One gate at side. **(b)** Two gates at side. **(c)** Three gates at side.

(d) One gate at front. **(e)** Two gates at front. **(f)** Three gates at front.

Figure 7.12: Weld line analysis in ASMI for the investigated pin gate configurations. The lines show the formation of weld lines where flow fronts meet at an angle of up to 135° (the default value of ASMI). Larger values were assumed to not cause any mechanically weak spots or surface notches. Critical weld lines are particularly highlighted. Color scales: weld line angle from 0° to 135°.

Two pin gates led independently from the location of the gates to one long weld line approximately at the center in between the two gates[1]. The weld line extended from the edge of the part towards the center. In case of the the gates located at the front, they reached with a length of about one third of the part the functional structures on the top surface. In case of the gates located at the side, the length was shorter, but the weld lines still came dangerously close. The resulting surface notches could compromise the proper function of the fluidic channels, since the channels required an even surface for undisturbed flow.

Three pin gates caused two weld lines between the gates. However, their length was smaller than for two pin gates. The risk of an influence on the functional structures was hence less.

The average volumetric shrinkage of the part for all gate layouts is shown in Figure 7.13. The volumetric shrinkage of the part was predicted to decrease and thus the packing performance to be better with an increasing number of pin gates. This was due to the larger cross-section of the gates in aggregate by which the packing pressure could be applied to the cavity.

The extent of the volumetric shrinkage was also influenced by the chosen location of the gates. Gating at the side gave higher values for the volumetric shrinkage than gating at the front. The reason here might have been the influence of the pocket where the BOT was supposed to be overmolded with TPE. This pocket also represented an area of lower part thickness. In case of gating at the side, the pocket extended over the entire width of the part. This narrow section reduced the transmission of the pressure and the material flow during the packing phase. In contrast, the pocket was in parallel to the flow direction when gating at the front, and the packing pressure could be consequently transmitted more easily. Although the predicted shrinkage is symmetrical, lower shrinkage was beneficial, because the holes of the press-fit remained where they were intended to be.

Considering all results, the application of three pin gates at the front side of the part appeared as the best solution. The general trend was that the gate performance increased with increasing number of pin gates, so even more pin gates would have been the logical consequence. The implementation of more pin gates was however practicably linked to large investments in the tooling phase of the mold manufacture. It was therefore decided to investigate the possible implementation of a film gate or a fan gate which basically resemble in their behavior a massive number of pin gates along the side.

[1] Weld lines occurring due to feeding the cavity with multiple gates are sometimes differentiated from weld lines occurring due to obstacles in the flow path and are referred to as “meld lines” [138].

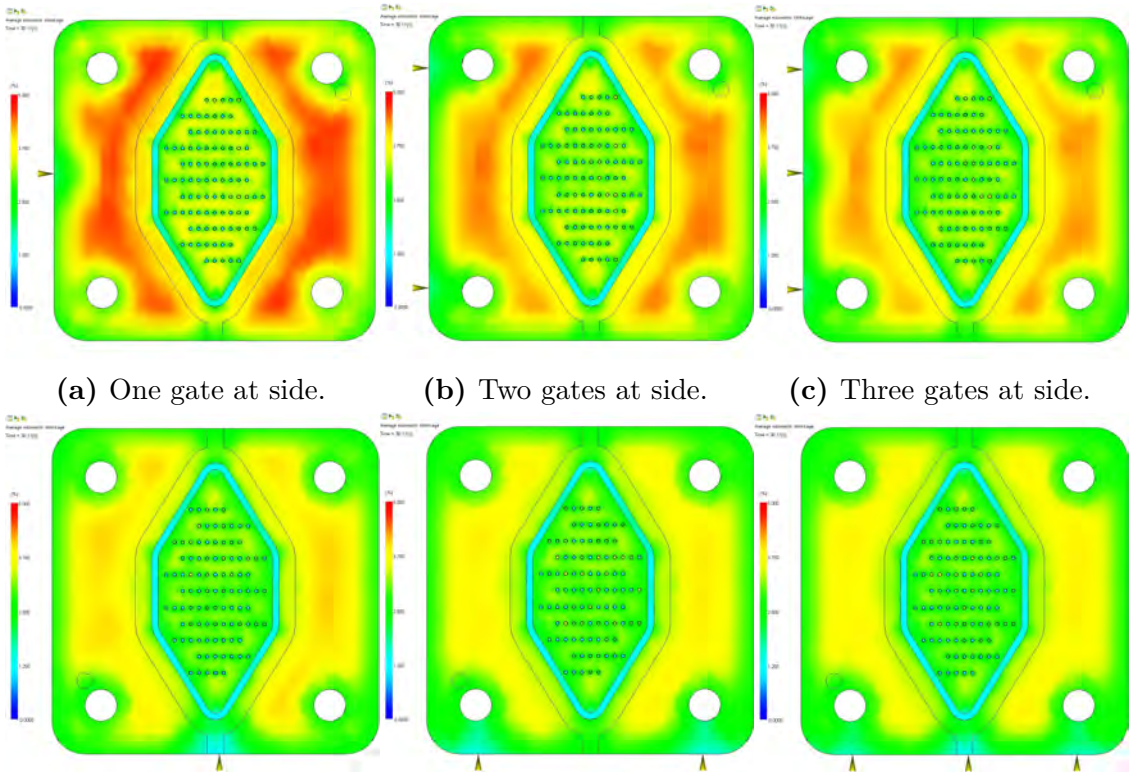

(a) One gate at side. **(b)** Two gates at side. **(c)** Three gates at side.

(d) One gate at front. **(e)** Two gates at front. **(f)** Three gates at front.

Figure 7.13: Analysis of volumetric shrinkage in ASMI for the investigated pin gate configurations. The configuration with three gates at the front was preferred, as it gave the lowest shrinkage. Color scale: average volumetric shrinkage from 0 % to 5 %.

7.6 Mold design and gate optimization—film gates

7.6.1 Gate design considerations

The application of film gates, also called flash gates, or fan gates can prevent from weld lines caused by several pin gates. Advantages are the reduced risk for jetting, low residual stress in the gate area, and reduced shear rates. The main benefit of these types of gates is the flow entering the cavity with a broad uniform flow front, making these types of gates well suited for wide and flat parts where dimensional stability is important. The major drawback is the large cross-section which can cause difficult degating and gate vestige at the part.

Since the BOT is a flat, plate-like component, a feed system consisting of a film gate, runner, and sprue was designed in addition to the actual BOT, as shown in Figure 7.14. The fan gate was not investigated because of time constraints. The gate location resulted from the considerations regarding the pin gates. The gate thickness resulted from available best practice recommendations about film gate design in tooling engineering. The gate thickness should be in the range of 20 % to 70 % of the wall thickness where the gate is attached [15, 81, 133, 135, 137]. In connection to the part thickness of 1.4 mm, this corresponds to 0.28 mm to 0.96 mm. Because of easier degating, it was decided to use three gate sizes at the lower end of the recommended range: 0.28 mm, 0.42 mm and 0.56 mm (equal to 20 %, 30 % and 40 % of the wall thickness). The gate was moreover 1 mm long (recommended <1.5 mm) and 16 mm wide (derived from the total part width neglecting the fillets).

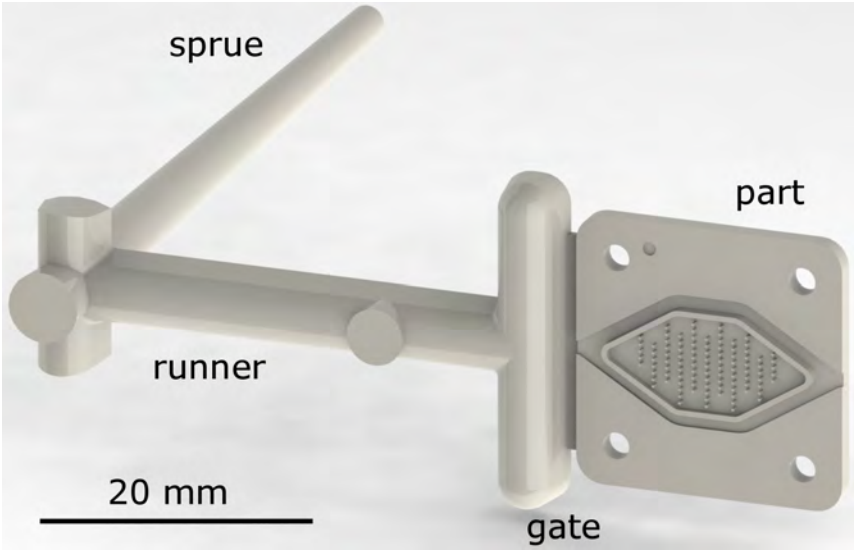

Figure 7.14: Bottom part (BOT) of the microfluidic mixer with the proposed film gate, runner, and sprue. The gate thickness was varied, the feed system showed an ejection spot and a sprue puller.

7.6.2 Feed system design

The film gate of the part was connected to the runner and sprue which supplied the plastic from the machine. It was decided to use a cold runner and sprue as feed system for economic reasons. Detailed information about the runner and sprue can be found in the technical drawings in Appendix D.

The sprue is formed by the sprue bushing. It must not be frozen before any other section of the feed system to ensure the transmission of the packing pressure. Safe and reliable demolding from the stationary mold plate must be ensured. This can be achieved by the following considerations and design recommendations [81, 139]:

- The bushing inlet diameter should be at least about 0.8 mm larger than the nozzle diameter of the injection molding machine to prevent from undercuts and not smaller than 2.5 mm.
- The bushing should be tapered by 1° to 4° depending on the expected shrinkage of the used plastic.
- The minimum outlet diameter of the sprue bushing is recommended to be at least 1.5 mm larger than the part wall thickness.

It was planned to use the Arburg Allrounder 370 A 600-70 (18 mm) injection molding machine with 2.0 mm nozzle diameter for the molding of the part. For the BOT with 1.4 mm wall thickness, this required an inlet and outlet diameter of 2.8 mm and 2.9 mm, respectively. However, not all arbitrary sizes of sprue bushings are available as standard parts which were planned to be used for building the mold. It was therefore decided to use the available standard sprue bushing Hasco Z511/12x46/2,5/15,5 with a taper of 1° per side and an inlet and outlet diameter of 2.5 mm and 4.6 mm, respectively. The sprue was moreover equipped with a sprue puller to ensure that the part stayed with the movable plate for demolding.

If falsely designed, the runner can cause a large pressure drop. It is recommended to use a runner with fully round, parabolic, or trapezoidal cross-section. The draft angle should be 5° to 10°, and the diameter of the runner should be at least 150 % of the part wall thickness where the gate is attached or in more conservative cases of the thickest section of the part. [81]

As a result, a parabolic runner with a draft angle of 10° was designed. Since parts of the runner were manufactured in the cavity plates, it was decided to double the recommended size of the runners to 4.2 mm. In that way, it could be ensured that the mold is also suitable for the future molding of thicker parts. For this part, the drawbacks of larger material consumption per shot and more scrap because of the runner and sprue were of minor importance. The runner was moreover equipped with an ejection spot.

The total volume of the part increased because of the gate and feed system from about 0.54 cm^3 to 2.3 cm^3 (equal to an increase in mass from approximately 0.54 g to 2.3 g for COC). The part volume did not differ very much with the gate thickness.

7.6.3 Simulation set up

The simulation was set up modeling and meshing the feed system, the film gate, and the actual part. The modeled entities were represented as one common CAD body in the imported CAD files. Since the mold was not existent yet in this design stage either, the mold and cooling circuit was not considered for the simulation.

The simulations of the different gate layouts was conducted in order to evaluate filling characteristics of the plastic, e.g. over-all flow pattern, filling of the micro pillars, shear stress, temperature, etc. Furthermore, the simulations should reveal information about the packing performance of the gates and warpage of the part. The warpage was crucial inasmuch as the deflection of the part could possibly cause the press-fits of the BOT and TOP to not fit together anymore and hence to jeopardize the assembly. It was therefore the objective to minimize the warpage and shrinkage of the part. Because the gate thickness was situated at the lower end of the recommended range, it was also of interest whether the gates produce a short short due to insufficient cross-section. The general process window was also analyzed regarding its feasibility with the molding equipment available at the facilities of DTU MEK.

The exact mesh settings for the three models of the microfluidic mixer are listed in Table 7.5. The result of the meshing is depicted in Figure 7.15. The total number of elements slightly differed because of the variation in gate thickness. The mixer showed refined areas at the gate area and at the micro features according to the mesh densities which were assigned to the various surfaces of the entities.

A complete filling, packing, and warp analysis of the part was conducted in ASMI 2015. The material choice for the simulations was the same COC as the preferred material of the industrial partner like in case of the pin gates. The default processing settings of the ASMI data base for the chosen COC were used due to the unavailability of actual values. Furthermore, the machine properties were set to the aforementioned Arburg Allrounder 370 A 600-70. All the technical specifications were implemented in an according machine model.

The previously selected Orvar Supreme as insert material was discarded from the simulations because of questionable availability. In the simulation settings, it was therefore switched to the tool steel 1.1730 as an alternative. This steel was supposed to be used at least for the majority of the mold plates. 1.1730 is an unalloyed tool steel commonly deployed for mold plates and risers and provides good machinability.

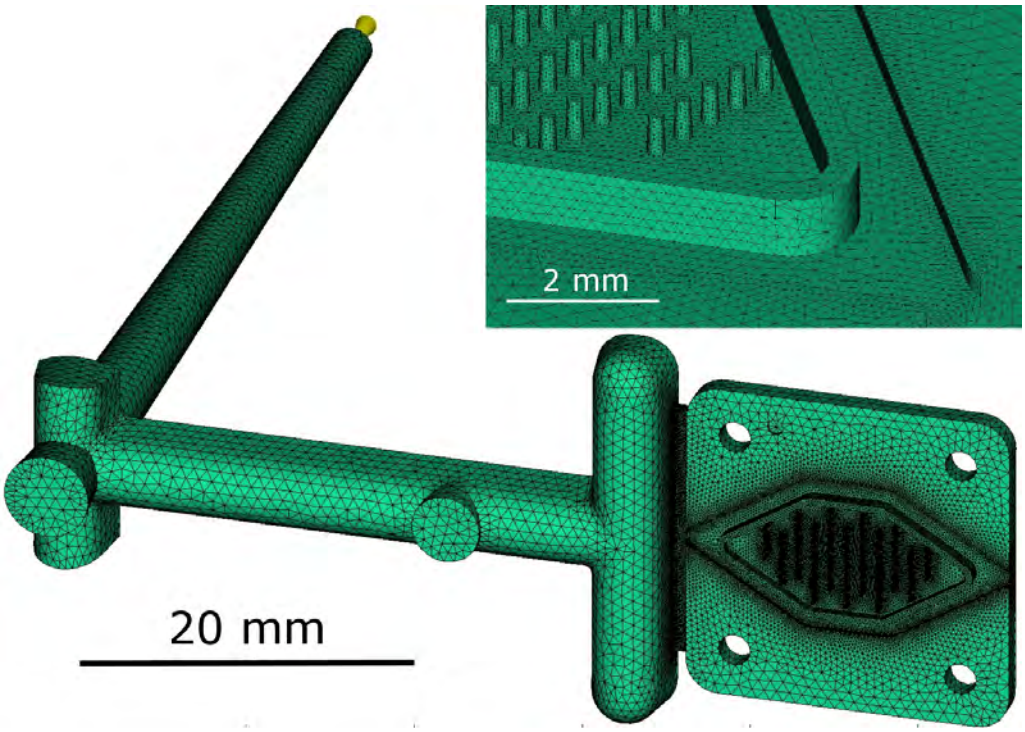

(a) Complete part and feed system and detailed view (top right).

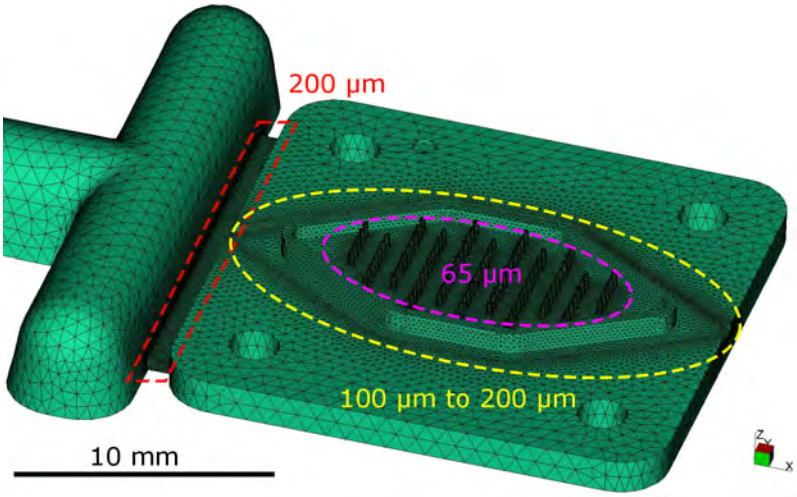

(b) Closeup on part with indicated mesh densities.

Figure 7.15: Overview and closeup of the meshed microfluidic mixer, captured in ASMI 2015. The global edge length was 0.8 mm. The mesh refinement at the gate and micro features is due to the assignment of the highlighted local mesh densities.

Table 7.5: Meshing settings of the microfluidic mixer with film gate. Unspecified settings were kept at the default values. The total number of elements varied slightly due to the different thickness of the investigated film gates.

Parameter	setting
Mesh density / µm	
micro pillars	65
wall of fluidic chamber	200
rim of groove around the wall	100
top of gate	200
sides of gate	65
Global edge length / µm	800
Merge tolerance / µm	20
Chord height / µm	30
Minimum number of elements through thickness	10
Maximum edge length in thickness direction / µm	960
Bias ratio	1.2
Total number of elements	4 100 000

The injection location size was chosen as 2.4 mm slightly smaller than the actual face of the sprue to prevent from flow distortions due to misalignment. The settings are summarized in Table 7.6.

7.6.4 Results and discussion

First, it could be proven with the simulations that the film gate was in general well suited for the microfluidic mixer. All three gate layouts enabled the polymer flow to enter the cavity uniformly across the entire gate width, as depicted in Figure 7.16.

Additionally, the simulation identified hesitation of the polymer flow at the micro pillars, as illustrated Figure 7.17. It is characterized by the easier flow into the bulky substrate, i.e. in the actual main flow direction, than into the micro pillars. The hesitation effect is a common phenomenon for cavities of very different thicknesses [81], like for micro structures on substrates. This led to the flow actually reaching the end of the cavity before the micro pillars are completely filled which had to be considered for setting up the packing phase when producing the part.

The simulation results of the film gate investigation are summarized in Table 7.7. Because the filling was governed by the constant injection speed and the part volume was approximately the same, the predicted filling time of about 0.46 s showed only little deviations between the gate layouts. Short shots could not be detected for

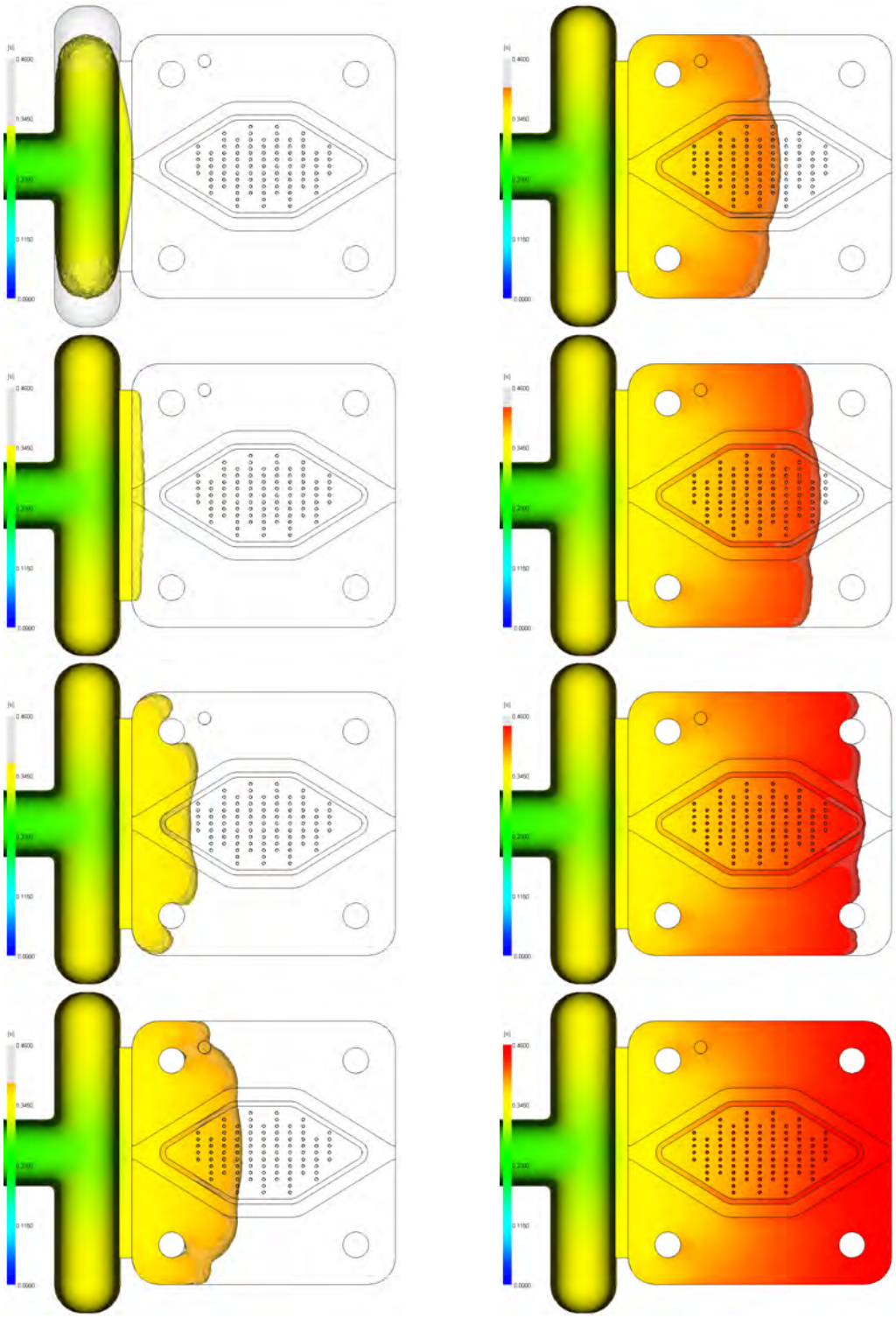

Figure 7.16: Flow front visualization of the microfluidic mixer with film gate in ASMI 2015. Color scale from blue to red: filling time from 0 s to 0.46 s.

Table 7.6: Machine and process settings for the simulations of the microfluidic mixer with film gate. Unspecified settings were kept at the default values.

Parameter	setting
ASMI version	2015
Analysis type	Fill+Pack+Warp
Material type	COC
Mold temperature / °C	110
Melt temperature / °C	280
Filling control	absolute ram speed vs ram position
Target ram speed / ($mm\,s^{-1}$)	20
Cushion / mm	2.0
Switch-over volume / %	99
Packing pressure / MPa	60
Packing time / s	30
Cooling time / s	20
Machine	Arburg Allrounder 370 A 600-70 (18 mm)
Virtual mold material	1.1730 (C45W)
Injection location diameter / mm	2.4

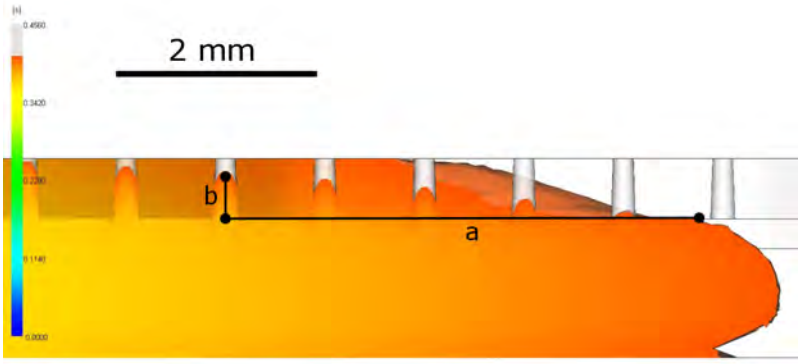

Figure 7.17: Cross-sectional view of the flow inside the cavity of the microfluidic mixer with distinct hesitation effect at the micro pillars: the filling in bulk direction is faster than in the direction of the micro pillars, i.e. the flow length a in bulk direction is larger than the flow length b in direction of the micro pillars. Color scale from blue to red: filling time from 0 s to 0.46 s.

any of the gates. The molding could be handled by the proposed Arburg injection molding machine regarding injection pressure and clamping force.

Table 7.7: General simulation results for the second design iteration of the microfluidic dispenser in ASMI 2015.

Gate thickness / mm	0.28	0.42	0.56	limit
Filling time / s	0.4549	0.4550	0.4560	–
Injection pressure / MPa	30	33	38	250
Clamping force / tons	1.1	1.4	2.0	60
Total mass after fill / g	2.10	2.11	2.14	2.32
Total mass after pack / g	2.24	2.24	2.25	2.32
Maximum volumetric shrinkage / %	6.8	7.6	7.0	–
Minimum volumetric shrinkage / %	0.33	0.34	0.37	–
Average volumetric shrinkage / %	2.6	2.5	2.4	–
Maximum shear rate / s^{-1}	120 000	87 000	26 000	40 000

The thinnest gate showed the smallest injection pressure with about 30 MPa, whereas the thickest gate reached an about 27 % higher level of 38 MPa. This was in contrast to expectation considering their cross-section and the resulting pressure loss. The injection speed and hence the flow rate were kept constant for all gate sizes. This conflicting behavior could therefore be explained by the thinnest film gate causing the highest acceleration and thus shear rate. The material showed consequently a significant drop in viscosity due to shear thinning. Hence, it is believed that the pressure decrease owing to the shear thinning was suspected to exceeded the pressure increase due to the smaller gate size.

Nonetheless, the shear rate was at an acceptable level for the thickest gate only, as shown in Figure 7.18, whereas for the small and medium gates the risk of polymer degradation emerged.

The average volumetric shrinkage for all three gates is depicted Figure 7.19. The thickest gate proved to achieve the lowest average volumetric shrinkage, the highest part mass (mass increase due to larger gate thickness was negligible), and thus the best packing performance. In addition, the shrinkage was quite symmetrical for any of the gates. Uniform and low shrinkage was important, as the BOT was assembled to TOP and SUB by means of the four press-fit holes. Any displacement or misalignment would have jeopardized the assembly.

In total, the film gate with 0.56 mm thickness showed the best performance and was therefore selected to be incorporated in the final design of the mold.

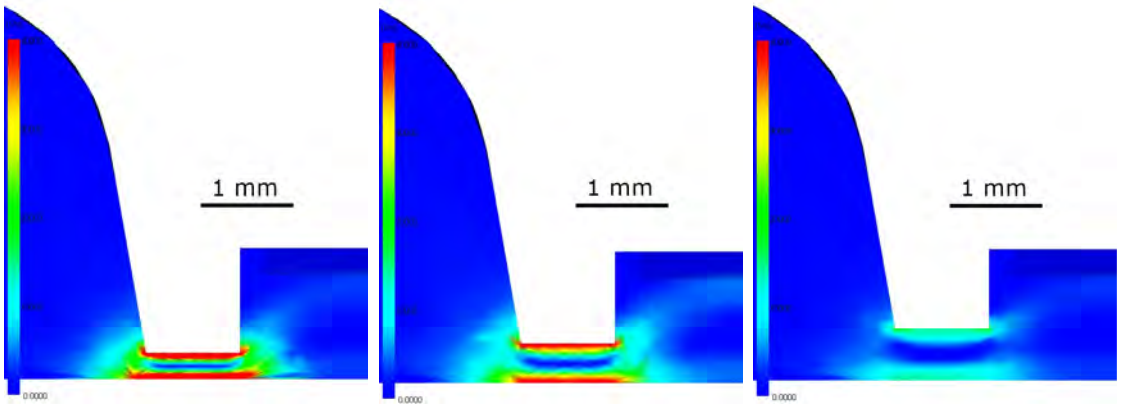

(a) Thickness: 0.28 mm. **(b)** Thickness: 0.42 mm. **(c)** Thickness: 0.56 mm.

Figure 7.18: Predicted shear rate at the film gates of different thickness. Only the largest gate showed acceptable shear rates. Color scales from blue to red: shear rate from $0\,s^{-1}$ to $40\,000\,s^{-1}$ (allowed limit for COC).

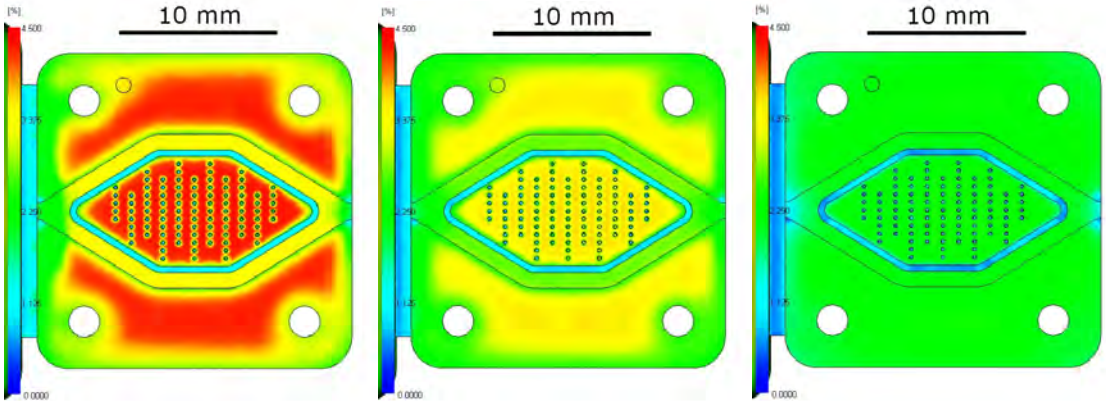

(a) Thickness: 0.28 mm. **(b)** Thickness: 0.42 mm. **(c)** Thickness: 0.56 mm.

Figure 7.19: Predicted average volumetric shrinkage of BOT for different film gate thicknesses. The packing performance increases with thickness. Color scales from blue to red: shrinkage from 0 % to 4.5 %.

7.7 Mold design and manufacture

7.7.1 Mold block

The mold layout of the microfluidic mixer was done in accordance to best practice recommendations in tooling engineering. Furthermore, standard units for mold making from Hasco Hasenclever, Lüdenscheid, Germany, were used in order to comply with common industrial practice and to minimize expenses.

The presumably used Arburg Allrounder 370 A 600-70 injection molding machine with 18 mm screw diameter and 600 kN clamping force required a minimum mold height of 200 mm and allowed a maximum mold width and depth of 370 mm × 370 mm. It was decided to implement a prototype mold which is characterized by low investment, simple structure, and interchangeable inserts [123].

The mold was created as simple two-plate version for economical reasons and versatility. The rectangular mold block had dimensions of 156 mm × 196 mm × 209 mm (width × depth × height, without locating ring and heat insulation) with the clamping plates being actually 206 mm wide. All mold plates consisted of 1.1730 tool steel. A cross-sectional view with some of the used mold plates and components is sketched in Figure 7.20. Detailed information on the whole mold as well as the part list can be found in Appendix D.

The mold was intended to provide a flexible platform with four inserts. The inserts could be replaced to mold first the BOT and later the TOP, to enable the overmolding by the TPE with separate inserts, but also the molding of other prototypes in the future. Due to the incorporation of four large inserts (more information in the next section), the cavity plates were considerably weakened in their mechanical stiffness. Therefore, it was decided to use a back-up plate in the movable half of the mold to counteract the loss in stiffness.

The cavity plates were equipped with two drilled, straight cooling channels for the basic heating of the mold plates. Owing to the presumed molding of COC and PEI and their very high mold temperatures, the mold had to be equipped with heat insulation plates on the outside.

7.7.2 Inserts

The first step of the design of the inserts was to decide about the parting line. It was decided to use a flat parting line and to position it at the flat back surface of BOT. Since the part had to stay with the movable half of the mold when opening, did not show any undercuts, and could be equipped with draft angles on the top surface, the cavity could be entirely incorporated in the insert of the movable platen.

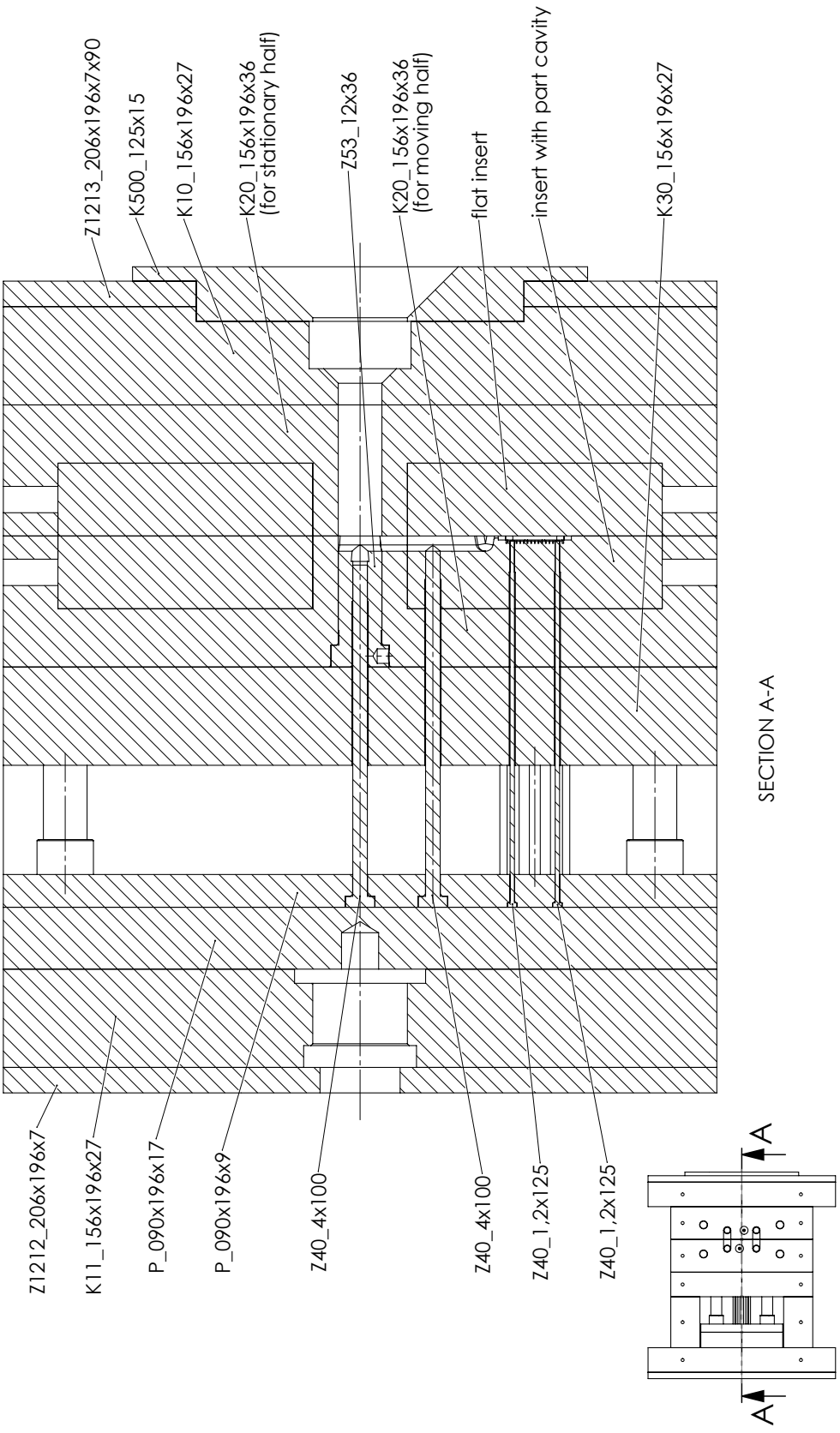

Figure 7.20: Cross-sectional view of the created prototype mold for the BOT of the microfluidic mixer. The two-plate mold consisted of Hasco standard parts and featured four interchangeable inserts for flexibility of the molded plastic parts enabling the 2k production of the BOT and TOP as well as other parts in the future.

As an advantage, the machining could be limited to one insert only saving time and resources.

The initial mold concept shown in Figure 7.21 included screwless inserts. The inserts were supposed to have the same thickness as the cavity plate. Massive undercuts enabled to clamp them from the back by means of the back-up plate. This fixation with tight fit between the cavity plate and the insert would provide good mechanical support for the inserts. However, the inserts could only be exchanged by dismounting and disassembling the mold. Moreover, it was planned to equip the cavity plates with electrical cartridge heaters.

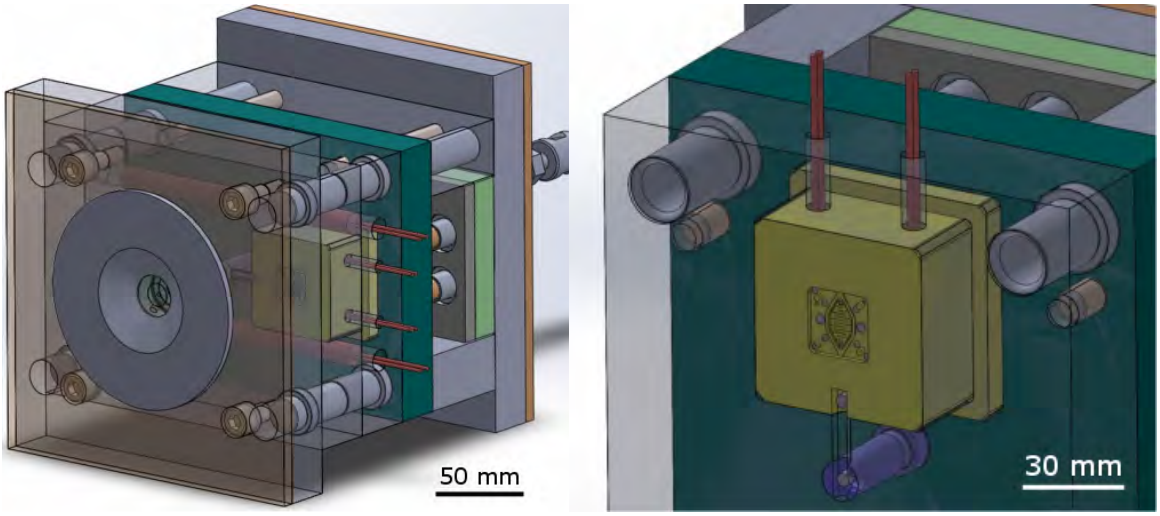

(a) Entire mold assembly. **(b)** Insert of movable half.

Figure 7.21: CAD models of the initial mold concept with plugged insert (highlighted in yellow) clamped from the back by the back-up plate. The heating was supposed to be fully electrical. The film gate is not shown at the insert.

The final mold concept is shown in Figure 7.22. In order to ease and quicken the exchange of the insert, it was decided to clamp the inserts from the front by screw joints. The inserts were therefore provided symmetrically four holes to homogeneously transmit any load and to avoid tilted fixation of the inserts. Furthermore, the heating concept of the cavity plates was changed to liquid heating due to the available equipment and the limited electrical connections of the Arburg machine.

The final inserts had outer dimensions of 70 mm × 70 mm × 20 mm (length × width × thickness). Moreover, the inserts were equipped with two exchangeable electrical heaters to enable quick and independent heating of the inserts which could be necessary to mold the micro parts. In that way, an independent heating zone concept was implemented with six zones in total (counting all inserts and the movable and stationary cavity plates). The integrated thermocouple was meant for the feedback control of the temperature of each insert.

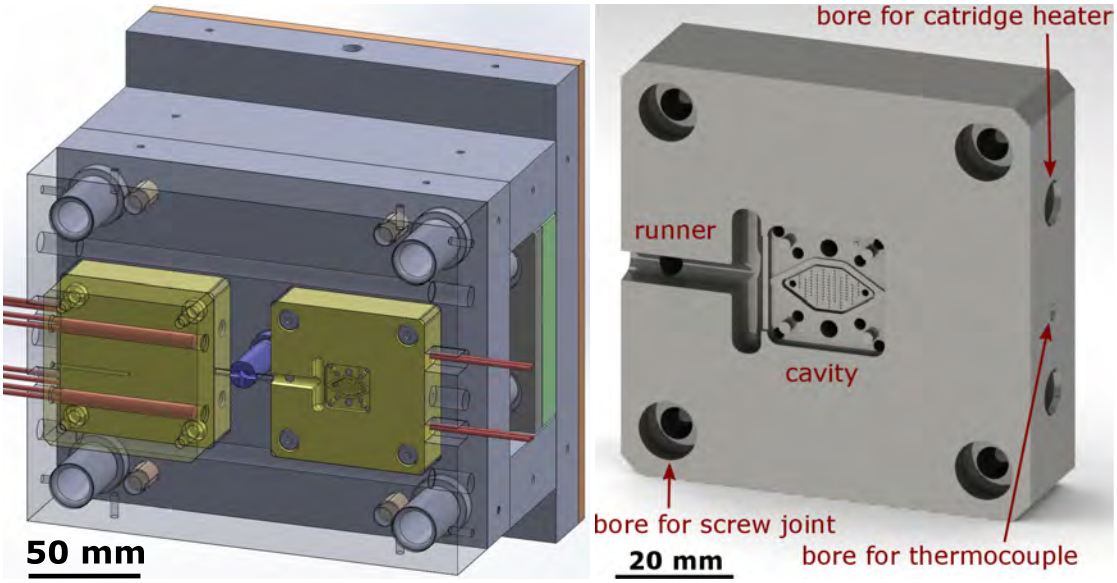

(a) Assembly of movable mold half. **(b)** Final insert.

Figure 7.22: CAD models of the final, realized mold concept with inserts fixed by four screw joints and liquid heating of the cavity plates and electrical heating of the inserts.

The part cavity was manufactured as negative image of the designed plastic part including the film gate. Part of the runner and the gate was also implemented in the insert. The runner and gate were machined with the initial dimensions. The cavity was scaled up by 0.5 % in all directions to compensate for the expected shrinkage of the part, no matter if COC or PS was finally selected. The value was in agreement with the mold shrinkage of 0.4 % to 0.7 % and 0.3 % to 0.6 % for the chosen COC and PS, respectively, given by the material suppliers. The values could be confirmed by the simulation shrinkage analysis. The simulation yielded a value of 2.4 % for the average volumetric shrinkage of COC which relates to approximately 0.8 % average linear shrinkage.

After the design was finalized, the inserts were manufactured in the tool shop at DTU. The production happened in several steps: the inserts were first cut to the proper outer dimensions, the general features like through holes and fillets were then added, the larger structures of the cavity were subsequently fabricated by milling, and the fine machining was ultimately done by EDM sinking with several electrodes. The electrodes for the EDM sinking process were milled from pure copper also in the tool shop at DTU. The EDM electrode for fabricating the holes for the micro pillars and the finished mold insert are shown in Figure 7.23.

(a) EDM electrode.

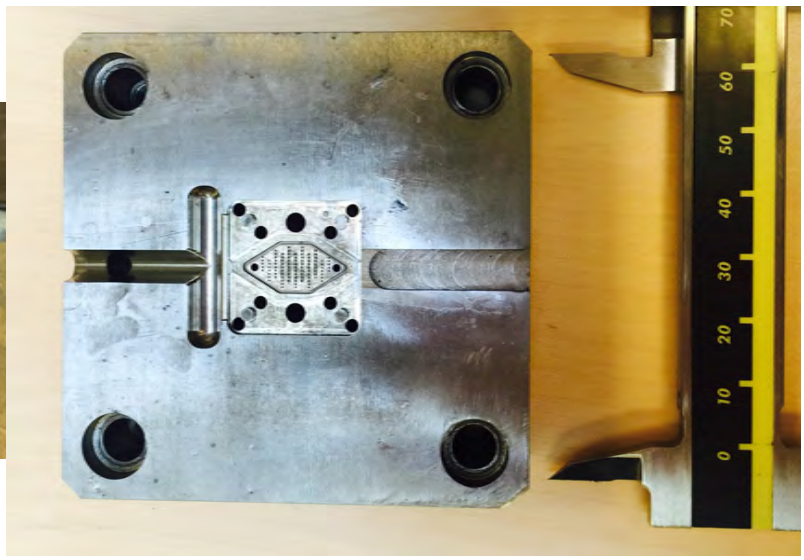

(b) Finished mold insert.

Figure 7.23: EDM electrode in copper for fabricating the holes of the micro pillars and finished mold insert of the microfluidic mixer. The cavity design was machined by milling and EDM accordingly to the finalized design based on the findings in the simulations. The insert was provided with an additional venting channel. Scale in mm.

7.8 Validation of simulations

7.8.1 Molding and sample preparation

For the simulation validation, short shots of the microfluidic mixer were produced. The material choice for the short shots was the polypropylene (PP) Sabic PP 579S made by Sabic, Riyadh, Saudi Arabia. The molding was conducted on an Arburg Allrounder 370 A 600-70 with a melt temperature of 230 °C, a mold temperature of 60 °C, and an injection speed of 40 mm s^{-1}. Packing was not applied, since this would have caused additional material to flow into the cavity and hence distorted the flow pattern. The process settings are summarized in Table 7.8. Similar to the microfluidic dispenser, the actual and simulated flow front patterns were compared on a qualitative basis on the global part level, i.e. over all pattern evaluation and the local feature level, i.e. pattern evaluation of the microfluidic pillars.

For the investigation on global part level, the samples were photographed with a Sony Alpha 5000 digital camera made by Sony Corporation, Tokyo, Japan. For the investigation on local feature level, the samples were coated with approximately 40 nm of gold by means of a Polaron Thermo CG Scientific SC7620 sputter coater at room temperature to make the surface conductive. Afterwards, they were investigated with

a JEOL JSM-5900 SEM. The very thin layer of gold was not expected to influence the geometry of the molded part or its features.

Table 7.8: Process settings for the molding of the short shots of the microfluidic mixer in PP.

Parameter	setting
Material type	PP
Material grade	Sabic PP 579S
Melt temperature / °C	230
Mold temperature / °C	60
Dosage length range / mm	$11.0 - 13.4$
Dosage stroke increment / mm	0.6
Switch-over point / mm	4.0
Stroke length range[a]/ mm	$7.0 - 9.4$
Injection speed / $\mathrm{mm\,s^{-1}}$	40
Machine	Arburg Allrounder 370 A 600-70 (18 mm)

[a] The stroke length was not an actual setting, but resulted from the set dosage length and switch-over position.

7.8.2 Simulation set up

The meshed simulation model of the film gate analysis was used for the simulation validation. The model included the part, the feed system, and the sprue. In correspondence to the real mold, the film gate with 0.56 mm thickness was analyzed. The creation of the model, the used mesh settings, and the meshed part can be found in the previous section 7.6.

A filling analysis of the part was conducted in ASMI 2015. The material choice for the simulations was in accordance to the short shots Sabic PP 579S. The experimental material processing conditions, the deployed Arburg injection molding machine, and the mold material of the real mold were used for the simulations. The injection speed was adjusted to the experimental value of $40\,\mathrm{mm\,s^{-1}}$. The settings of the simulation validations are summarized in Table 7.9.

7.8.3 Results and discussion

The comparison of the flow front patterns on the global part and on local feature level are illustrated in Figure 7.24 and Figure 7.25, respectively.

The overlay of the simulated and real flow front showed good agreement between the flow fronts with minimal deviations. The simulation could forecast the actual

Table 7.9: Machine and process settings of the simulations of the microfluidic mixer with film gate. Unspecified settings were kept at the default values.

Parameter	setting
ASMI version	2015
Analysis type	Fill
Material type	PP
Material grade	Sabic PP 579S
Mold temperature / °C	60
Melt temperature / °C	230
Filling control	ram speed vs ram position
Target ram speed / $\mathrm{mm\,s^{-1}}$	40
Cushion / mm	4.0
Machine	Arburg Allrounder 370 A 600-70 (18 mm)
Mold material	1.1730 (C45W)
Injection location diameter / mm	2.4

flow front behavior more accurately than in case of the dispenser (section 6.4). The reason was possibly that the mixer exhibited a lower thickness variation, so that the flow was less distorted.

In the comparison on the feature level, the effect of a depression at the base of the pillars was noted in the plastic samples. Possibly, they were caused by air in the cavity which created a counterpressure and leaves an imprint or by surface tension effects holding the flow back. This effect was seen for all pillars. Although the simulation assumes perfect venting, the plastic flow also showed narrow depressions at the base shortly before entering the pillars.

Despite the fact that the match for the flow front on part level was better, the filling of the micro features was predicted less accurately than in case of the microfluidic dispenser. The pillars filled too early in the simulation, likely for the same reason as for the dispenser: the simulation assumed an evacuated mold, whereas in reality the air might cause a counterpressure in the pillars which holds back the plastic flow. Additionally, the time steps in the simulation giving the best fit on part level or respectively on the feature level showed differences of up to about 1 % of the individual filling time.

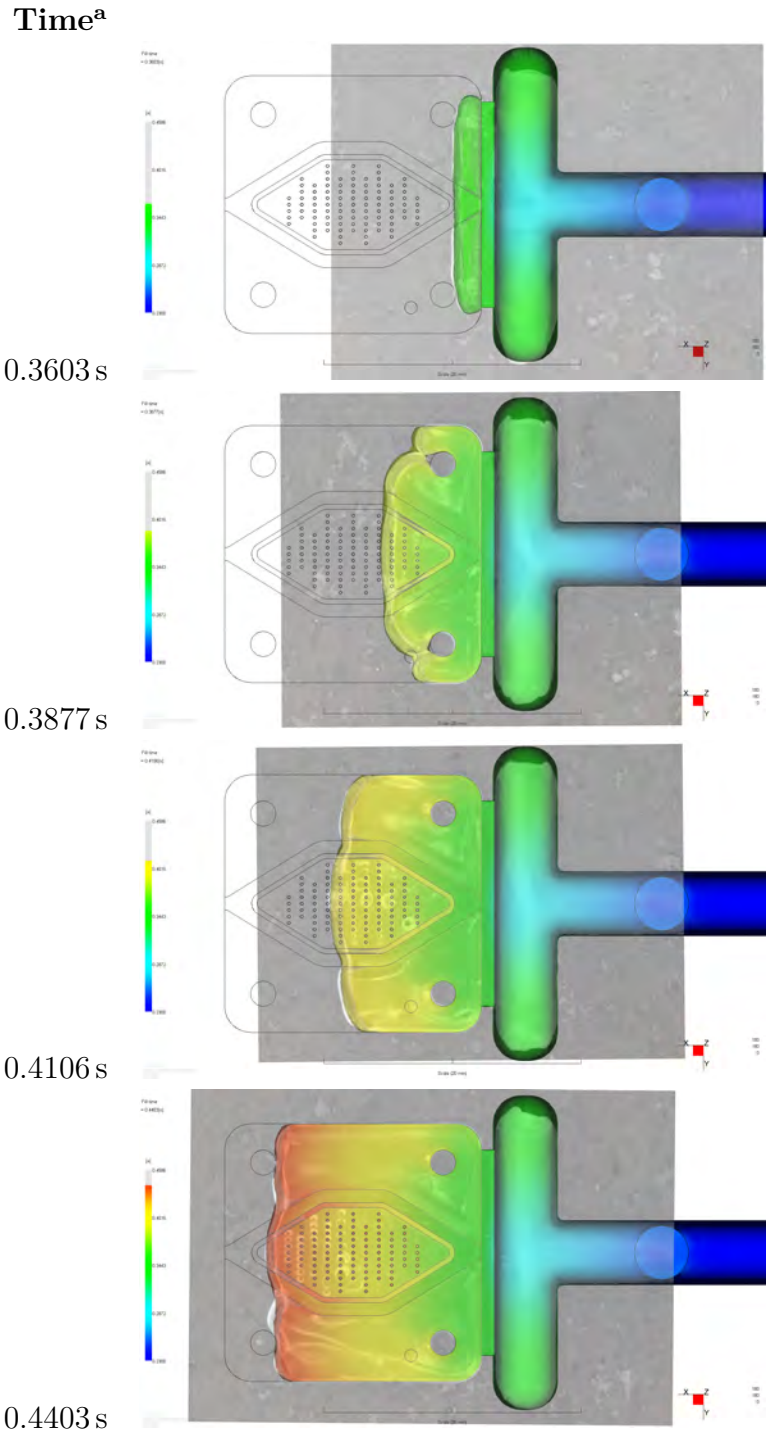

Figure 7.24: Comparison of molded short shots and the simulated flow front pattern on global part level of the microfluidic mixer.
[a] Filling time in simulation of the best fit to the actual short shot.

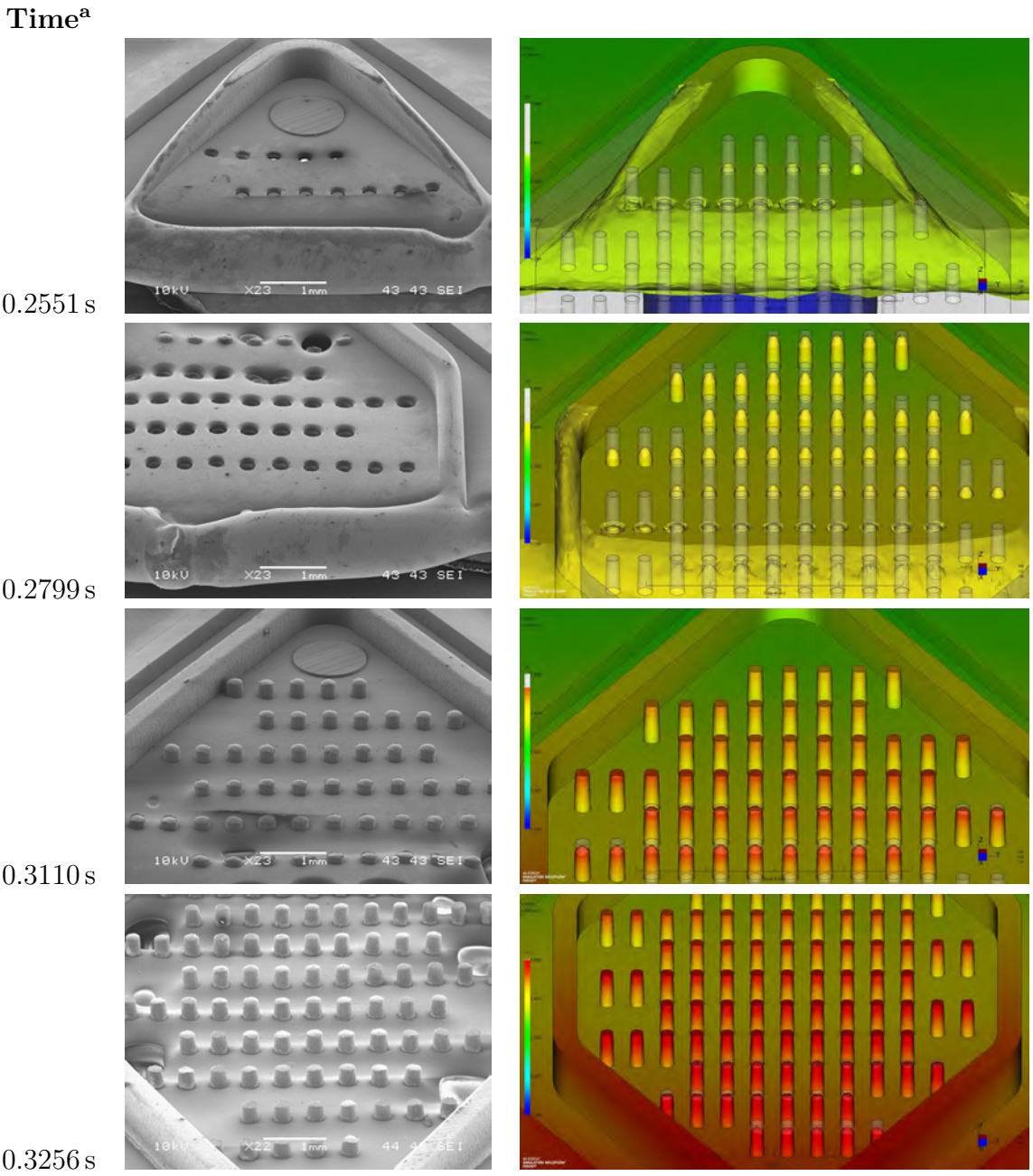

Figure 7.25: Comparison of molded short shots and the simulated flow front pattern on local feature level of the microfluidic dispenser.
[a] Filling time in simulation of the best fit to the actual short shot.

7.9 Summary and conclusion

The study case for the complete micro design and manufacture was a microfluidic mixer. The entire product development from the first design draft through the material selection and testing, different design iterations on the gate design, the mold layout and fabrication to the production of the plastic part was performed.

Its components and the most important micro features of the sub-device of interest were outlined. Based on the requirements on the material in connection to the part, the material selection declared COC, PS, and PP as possible candidates for the thermoplastic base and TPE for the sealing structures.

Since the sealing structures were supposed to be made by 2k overmolding of the thermoplastic by the TPE, the material compatibility regarding bonding strength was evaluated. The molding of the 2k specimens and the subsequent tensile tests showed that the configurations PP/TPE and PS/TPE showed the best bonding performance. However, PP was discarded because of the insufficient transparency which was essential for the part inspection during operation, leaving PS/TPE as the preferable material combination for the production.

The starting point of the gate and mold design was the investigation of possible gate locations. It was found that the part had to be gated from the side due to geometrical constrains given by the incorporated micro features on microfluidic mixer and mold layout reasons. Subsequently, several pin gate configurations were evaluated. Based on simulation results, the application of three pin gates at the front side of the part, i.e. leading to parallel flow of the plastic to the fluidic chamber, was expected to have the lowest impact on the material and the best packing performance.

The subsequently designed film gate of the microfluidic mixer was investigated to find a suitable gate thickness. The simulation results showed that the thickest gate of 0.56 mm provided superior properties with respect to the filling and packing. The smaller gates led to unacceptably high shear rates and inferior packing performance. The simulation proved the general suitability of the film gate and the hesitation of the polymer flow at the micro pillars as the most challenging features of the part.

After the most suitable gate was found, the actual mold design and manufacture commenced with the selection of the components for the mold block and the layout of the feed system and the insert concept. With multiple inserts, the proposed mold provided a flexible and versatile base for conducting the 2k molding of the BOT and TOP or other plastic parts in the future. The mold and inserts could be at last successfully manufactured with the appropriate dimensioning from the previous simulation steps.

The simulation validation was carried out by comparing the simulated and real flow front on the global part and local feature level. The comparisons showed good agreement on the global level, i.e. the simulation was successfully able to

predict the over-all flow front of the part. The comparisons on feature level revealed some deviations and thus the limitations of the simulation software. The micro pillars on the surface filled to early in the simulations. The hesitation effect was indicated as outlined in the investigations before, but the extent of the effect was underestimated. However, the real flow experienced depressions at the location of the micro pillars before entering the micro cavities which were successfully captured by the simulations.

In conclusion, the part could be successfully designed and produced, effectively supported by the application of process simulations. The simulations turned out as precious tool in case of this micro plastic component and contributed significantly to the design optimization of the part and gate. With the successful manufacture of the mold being largely based on the findings of the simulation analyses, the simulations proved to be applicable and helpful tool in the mold design and manufacture, as well.

8 Validation of powder injection molding simulations

Abstract This chapter is intended to report all experiments and simulations in connection to the validation of powder injection molding simulations. The chapter first introduces the used part and machinery. Later on, the carried out experiments and simulations are outlined. Finally, the results of both are generally discussed and compared with regard to the validation and performance of the simulations. The incentive of this chapter is to evaluate the applicability of process simulations in conventional and micro powder injection molding.

All experiments in connection to the validation of the powder injection molding simulations were carried out during the external stay at the Karlsruhe Institute of Technology (KIT), Eggenstein-Leopoldshafen, Germany. The used injection molding machine was an Arburg Allrounder 420 C 600-100 with a screw and nozzle diameter of 15 mm and 2.0 mm, respectively, and made by Arburg, Loßburg, Germany. The simulations were conducted with ASMI 2015.

8.1 Study case

8.1.1 Part

The geometry being used for the validation of the powder injection molding simulations was a double spiral test geometry. The double spiral is depicted in Figure 8.1. It consisted of the actual spirals and a feed system with a sprue and a sprue gate, i.e. without a runner. The flow entered the cavity directly from the sprue. It was moreover equipped with a sprue puller. The two incorporated spirals were symmetrical and based on an arithmetic spiral. The cross-section of the spiral tube had a nominal thickness of 1.0 mm and a nominal width of 2.6 mm. The maximum flow length was about 100 mm at the center of the flow path.

The flow spiral could be classified as micro precision part, because of the tight tolerances in the micrometer range. However, it still is a test geometry without direct industrial or practical application. The part was nevertheless picked because of the advanced mold with a sensor array (described in the next section) allowing for a live process monitoring and characterization. The scientific value was the extensive data

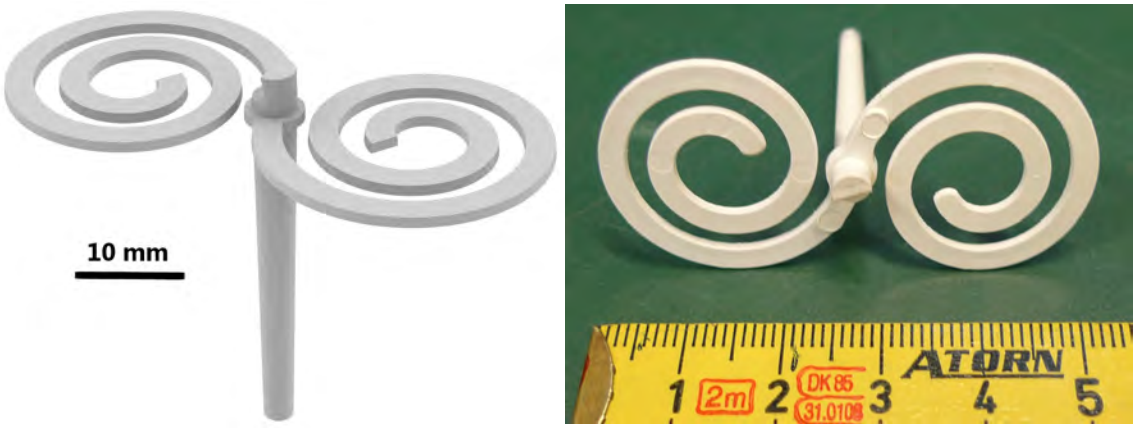

(a) CAD model. **(b)** Real spiral molded in POM.

Figure 8.1: CAD model and real part of the test spiral being used for the powder injection molding simulations and experiments.

acquisition which laid the foundation for the performance assessment of the powder feedstocks regarding micro parts and for the process simulations of the injection molding process.

8.1.2 Mold

The used two-plate steel mold was made of 1.2767 tool steel and already existent for flow length testing purposes. The mold provided three pressure and three temperature sensors along the flow path of the two separate spiral cavities. The pressure sensors were integrated in one spiral, the temperature sensors in the other. Their exact position and the layout of the cavity can be seen in Figure 8.2. Figure 8.3 shows the stationary half of the steel mold with the integrated sensors. More pictures of the machine and the mold can be found in Appendix E.

The sensor array allowed to investigate the pressure and temperature evolution in the cavity live during the filling phase of the injection molding process. The pressure sensors are of type 6003B and the temperature sensors were of type 4008B (type N thermocouple) made by Priamus System Technologies, Schaffhausen, Switzerland. The sensors were exposed to the melt on a diameter of 2.5 mm and 1.0 mm, respectively. The sampling frequency of the sensors was 200 Hz. The signals of the pressure sensors are denoted in the following sections as p1, p2, and p3; the temperature sensors were not used in this investigation. In addition to the sensors, the injection molding machine also monitored the applied injection pressure of the hydraulic drive which is denoted as pM in the following.

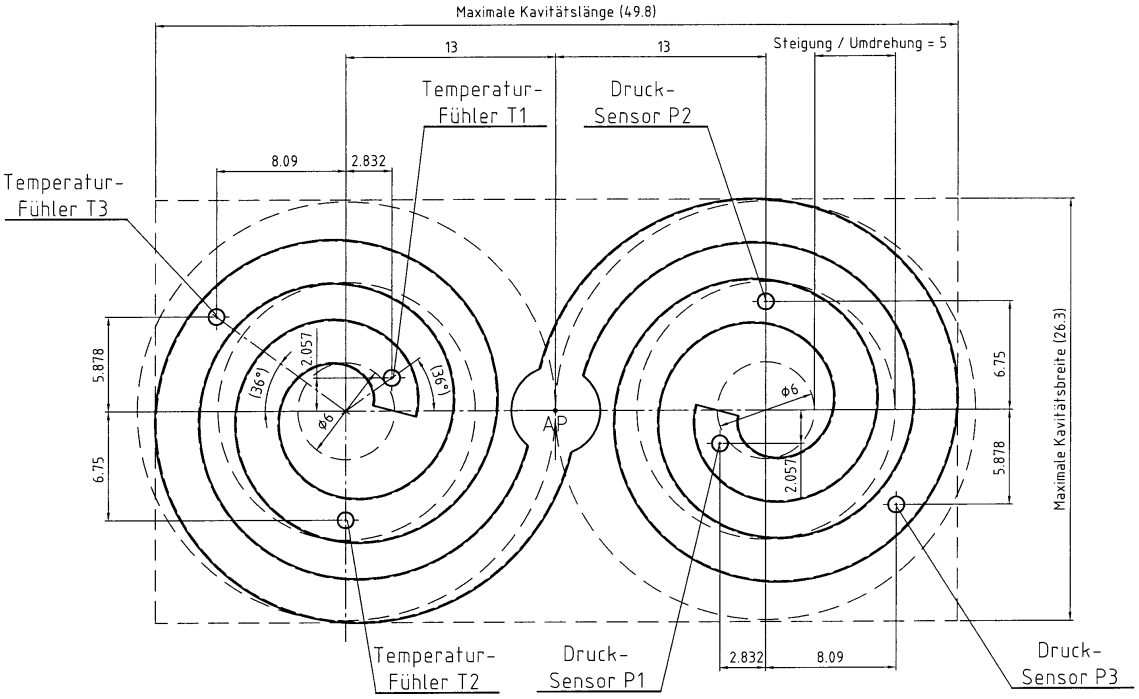

Figure 8.2: Drawing of the cavity layout of the double spiral. The mold enables to investigate the pressure and temperature evolution in the cavity with three integrated pressure sensors (pressure signals denoted as p1, p2, and p3) in one spiral and three integrated temperature sensors (not used) in the other spiral. All values in mm.

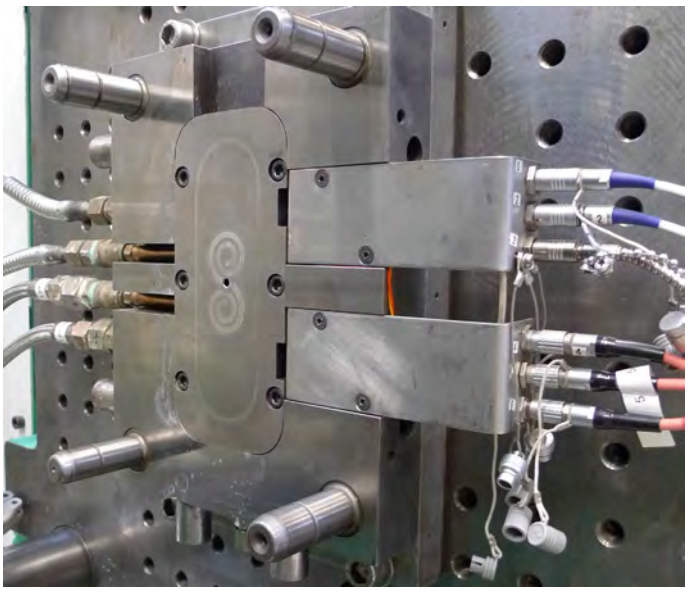

Figure 8.3: Stationary half of the double spiral test mold with pressure and temperature sensors (not visible) and their connections (cables on the right) used for the powder injection molding experiments.

8.2 Experiments

8.2.1 Full shot study

Full shots of the double spiral were molded with all four feedstocks introduced in chapter 4: Catamold® TZP-A, Catamold® 17-4PHA, GoMikro ZrO_2, and GoMikro 17-4PH. The goal was to investigate the pressure and temperature development in the cavity as well as to evaluate the flow length and thus the applicability of the feedstocks to micro structures. The flow length was evaluated by an angular measurement of the spirals from which the spiral length could be calculated. The process settings were chosen accordingly to the molded material and are listed in Table 8.1.

Table 8.1: Process settings for the molding of the full shots of the double spiral geometry with all four characterized feedstocks.

Parameter		Catamold®		GoMikro	
Name	unit	17-4PHA	TZP-A	17-4PH	ZrO_2
Melt temperature	°C	170–200	172–180	170–195	178–200
Mold temperature	°C				
stationary half		130	145	51	51
movable half		135	145	51	51
Dosage	mm	20.0	20.0	20.0	20.0
Decompression	mm	2.0	2.0	2.0	2.0
Back pressure	bar	80	80	80	80
Switch-over point	mm	12.7	9.7	10.0	7.0
Stroke length[a]	mm	7.3	10.3	10.0	13.0
Injection speed	$mm\,s^{-1}$	35	35	40	40
Packing pressure	bar	1200	800	650	850
Packing time	s	2.68	2.68	2.68	2.68
Cooling time	s	35	35	35	35

[a] The stroke length was no actual setting, but resulted from the set dosage and switch-over position.

The melt and mold temperatures of the Catamold® feedstocks were chosen as high as allowed (compare to section 4.3) to achieve the best filling and largest flow length. The mold halves of Catamold® 17-4PHA showed different values to prevent from the part sticking to the stationary half, when the mold opened. The GoMikro feedstocks were also molded at elevated temperatures slightly above the recommended processing window to achieve the best filling.

8.2.2 Short shot study with design of experiments

For the GoMikro ZrO_2 feedstock, the experimental investigation could be expanded to a more detailed DOE in Minitab® 16.2.2. GoMikro ZrO_2 was chosen over the Catamold® feedstocks, because it showed the longer flow length at the full shots and over GoMikro ZrO_2 because of material availability.

The investigation included the variation of the switch-over point, cushion size, the injection stroke, and the injection speed and was hence a short shot study. The aim of the DOE was to deepen the understanding of the powder injection molding process and to investigate the influence of the aforementioned factors on the pressure evolution in the cavity, the injection pressure, and the flow length in the mold. Moreover, the influence of the stroke length and cushion size was supposed to be additional validation for the simulations regarding the necessity of implementing the used volume covered by the polymer in the nozzle and the barrel of the machine.

An overview of the chosen input factors and their factor levels is given in Table 8.2. The minimum value of the stroke length was derived from the minimum stroke length necessary for the material flow to reach the actual spiral tube, the minimum value of the injection speed from the range of typical injection speeds for the feedstock, and the minimum value of the cushion from the smallest value without risking to damage the machine. The maximum values of all factors were derived from the full shots. The switch-over point was however not an actual setting or factor, since it depended on the stroke length and cushion size.

Apart from the factors, the remaining process conditions were tallied with the settings of the full shot studies. The settings for GoMikro ZrO_2 can thus be found in the previous Table 8.1.

Table 8.2: Input factors and their factor levels for the DOE with the GoMikro ZrO_2 feedstock.

	Factor	unit	levels		
			low	high	increment
1.	Stroke length s	mm	2	13	1
2.	Injection speed v	$mm\,s^{-1}$	30	40	10
3.	Cushion c	mm	2	7	5

8.3 Simulation set up

The simulation model of the double spiral was prepared without taking the mold or the cooling into consideration. The part was modeled together with the feed system. The objective of the simulations was the investigation of the predicted fill time and fill pressure. The simulation outcome was supposed to be compared to the experimental data, in particular the pressure curves of the machine and the sensors in the mold.

The meshed double spiral is shown in Figure 8.4. The mesh settings are summarized in Table 8.3. The mesh density of the side walls of the spirals was adjusted to 150 µm to reach about ten elements through the thickness. The value was chosen larger than one tenth of the thickness of the spiral tube of 1.0 mm, but the meshing yielded smaller side length for the elements than the set value.

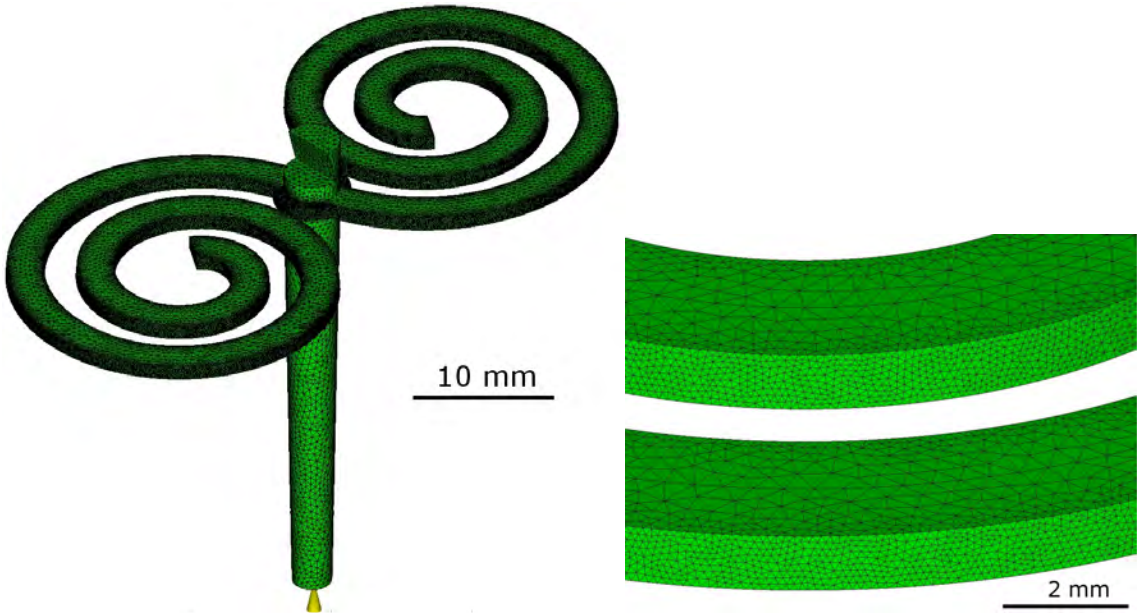

(a) Entire double spiral. **(b)** Detailed view on spiral.

Figure 8.4: Meshed double spiral with sprue and defined injection location, captured in ASMI.

The simulation settings for the filling and packing analysis in ASMI 2015 tallied with the experimental settings of the full shots. Additional settings are summarized in Table 8.4. The processing settings like melt and mold temperature of the feedstocks were adjusted to the experiments. The material choice of the feedstocks, the virtual mold, and the machine were in accordance to the experiments. However, the simulation was not run with the GoMikro ZrO_2 feedstock due to the issues of the data fitting and the resulting unavailability of a reliable material model. The injection

Table 8.3: Meshing settings of the double spiral together with the feed system. Unspecified settings were kept at the default values.

Parameter	value
Specific element edge length / µm	
side walls of spiral tube	150
Global edge length / µm	500
Merge tolerance / µm	20
Chord angle / °	20
Minimum number of elements through thickness	10
Maximum edge length in thickness direction / µm	600
Total number of elements	930 000

location size was chosen as 2.0 mm in accordance to the size of the nozzle of the injection molding machine.

In addition, the injection speed of the screw which was monitored by the machine was introduced to ASMI in several ways to evaluate their influence:

1. Ram speed versus ram position with constant speed profile
   The speed was assumed to be constant and at the same nominal speed, i.e. $35\,\mathrm{mm\,s^{-1}}$ for the Catamold® feedstocks and $40\,\mathrm{mm\,s^{-1}}$ for the GoMikro feedstocks, over the entire stroke length of 20 mm as in the real experiments.
2. Ram speed versus time with true speed profile
   The speed profile was set up with multiple data points approximating the true monitored speed profile.

The implemented speed profiles are shown exemplary for Catamold® TZP-A in Figure 8.5. The true speed profile clearly accounts for the finite acceleration and the response time of about 60 ms of the injection molding machine. The controller first ramped up the screw speed and then tried to adjust it to the nominal value before the speed dropped again at the end of injection.

For the comparison to the experiments, the pressure at the injection location and the pressure at four nodes at the same location as the sensors in the real mold were determined.

Table 8.4: Additional simulation settings of the simulations of the test spiral. The process settings were in accordance to the experiments (see Table 8.1). Unspecified settings were kept at the default values.

Parameter	setting
ASMI version	2015
Analysis type	Fill+Pack
Filling control	ram speed profile
Machine	Arburg Allrounder 420 C 600-100 (15 mm)
Virtual mold material	1.2767
Injection location diameter / mm	2.0

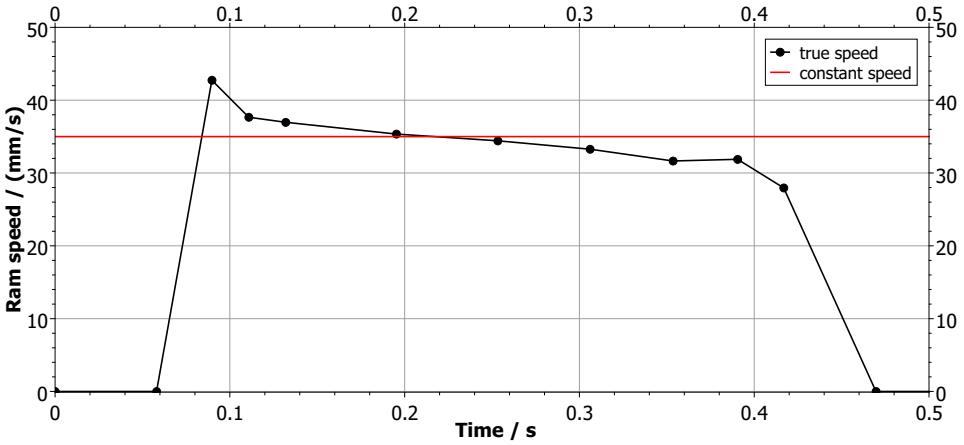

Figure 8.5: Comparison of the true and constant speed profile used for the simulation of the double spiral in ASMI. The curves are exemplary shown for Catamold® TZP-A.

8.4 Results and discussion

8.4.1 Experimental results of full shot study

The injection time and pressure of the full shots are listed in Table 8.5. First, it can be noticed that the necessary injection pressures to mold the parts were very high for all four feedstocks—exceeding for three materials in fact the nominal maximum injection pressure of the machine of 250 MPa. Except for Catamold® TZP-A, the measurement uncertainty was less than 1 %. The higher uncertainty of Catamold® TZP-A could be attributed to the smaller number of measured full shots. The high pressure levels indicated the high viscosity of the feedstocks. Only GoMikro 17-4PH allowed to mold at lower pressures of about 164 MPa. At this pressure level, the machine still worked within the specifications and was able to handle the material more easily. Hence, the metallic GoMikro also showed with about 0.36 s a shorter injection time than the other three feedstocks with at least 0.42 s.

Table 8.5: Experimental results for the full shots of the molded test spirals.

Feedstock	fill time t / s	fill pressure p / MPa	flow length L / mm or %
Catamold® TZP-A	0.45	262.5 ± 3.6[a]	95
Catamold® 17-4PHA	0.45	271.1 ± 0.9[b]	84
GoMikro ZrO_2	0.45	263.3 ± 1.2[b]	100
GoMikro 17-4PH	0.36	163.6 ± 1.1[b]	100

[a] Average of four measurements, confidence level: 90 %
[b] Average of 16 measurements, confidence level: 90 %

The resulting samples of the full shots of the double test spiral are shown in Figure 8.6. The two GoMikro feedstocks are actually compounded especially for easy flow and the molding of thin-walled and micro parts. This property was indicated, since they yielded complete filling of the cavity, whereas the two Catamold® feedstocks led to short shots. The early solidification and difficult molding of the Catamold® 17-4PHA spiral is reflected in the highest injection pressure and shortest flow length of approximately 84 mm among all feedstocks. This result also matched the findings of chapter 4 where Catamold® 17-4PHA showed the highest viscosity at shear rates higher than $10\,s^{-1}$. The task of micro injection molding with these compounds can therefore be evaluated as challenging and very dependent on the aspect ratio and flow length of the molded part.

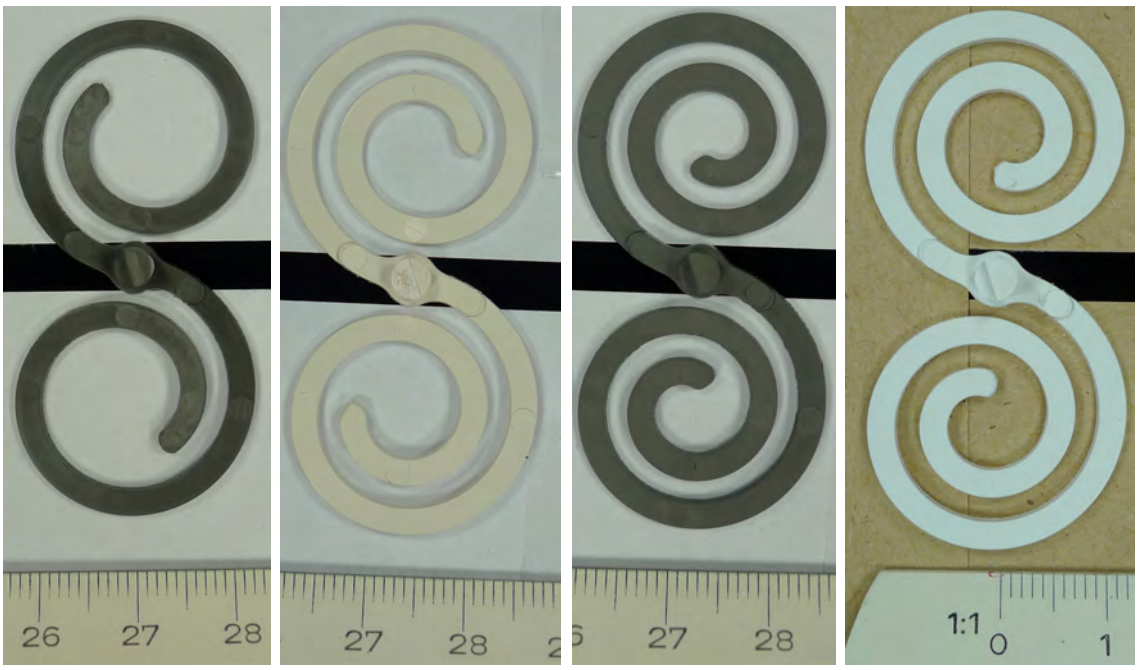

(a) Catamold® 17-4PHA. **(b)** Catamold® TZP-A. **(c)** GoMikro 17-4PH. **(d)** GoMikro ZrO_2.

Figure 8.6: Comparison of the molded spirals for all four used feedstocks. Shown scale in cm.

8.4.2 Comparison of full shot study and simulations

The successful application of the established material model could be first reported. All simulations showed complete filling of the spiral. The numerical values of the simulation results and the experiments are listed in Table 8.6. Additionally, Figure 8.7 shows the injection pressure of the simulations with the two implemented speed profiles and of the experimental molding exemplary for Catamold® 17-4PHA. When comparing first the simulations, the introduction of the full speed profile increased the simulation results of the pressure by only few percent for the Catamold® feedstocks, but by about 53 % in case of GoMikro 17-4PH. The injection time was increased by 28 %, 11 % and 53 % for Catamold® TZP-A, Catamold® 17-4PHA, and GoMikro 17-4PH, respectively. This time difference was partially related to the response time of the machine which went along with a short delay at the beginning and which is better matched by the simulation with full speed profile. Also, the filling of the sprue which could be identified by the first section up to the steep pressure rise was longer.

Still, a significant discrepancy between the simulation results and the experimental values for the injection time and pressure could be observed. Since the full speed

Table 8.6: Predicted process results of the simulations with constant and true speed profile of the test spirals and experimental results from above for comparison (given in the row denoted by "experiment").

Feedstock	speed profile	fill time t / s	fill pressure p / MPa	flow length L / mm or %
Catamold® TZP-A	constant	0.18	149	100
	true	0.23	150	100
	experiment	0.45	263	95
Catamold® 17-4PHA	constant	0.18	222	100
	true	0.20	230	100
	experiment	0.45	271	84
GoMikro 17-4PH	constant	0.15	97	100
	true	0.23	175	100
	experiment	0.36	164	100

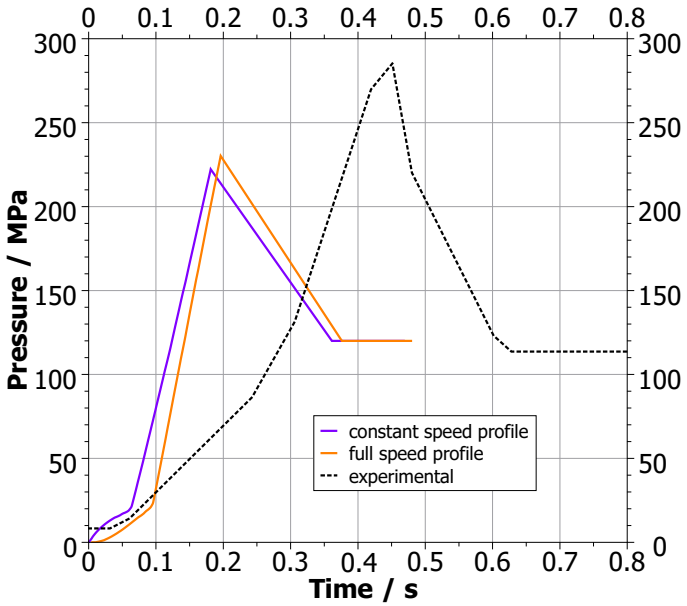

Figure 8.7: Comparison of the predicted injection pressure over time for the two implemented simulation with the implemented constant and true speed and the experimental results for Catamold® 17-4PHA.

profile yielded the better results, the following analysis of the pressure in the cavity was done with the full speed profile as the simulation reference.

Figure 8.8 shows the pressure signal of the machine and the sensors of the mold as well as the pressure level at the corresponding positions of the simulation based on the true speed profile. The simulations of the Catamold® feedstocks underestimated the pressure and fill time levels and gave a discrepancy not only between the pressure at injection location (machine signal pM) as discussed above, but also between the signal of the sensors (sensor signals p1, p2, p3). In fact, the experimental signals "p2 exp" and "p1 exp" remained at zero, since the flow length was too short to reach the sensors. The pressure level "p3 exp" reached about 50 MPa as maximum value. The standard deviation of the measured signals were up to 13 MPa and 3 MPa for Catamold® 17-4PHA and Catamold® TZP-A, respectively. The maximum standard deviation was however observed during the rise of the signal when reaching approximately 20 MPa. The standard deviation decreased and reached values at the peak of the signal of about 1 MPa for both materials. The simulation on the other hand gave values of about 200 MPa for all three sensor positions. The signals decayed subsequently to the respective packing pressure level afterwards, so that the feedstock was still assumed liquid at that point in time by the software. Due to the incomplete filling and premature solidification in the real molding, the packing pressure could not be applied hydrostatically to the whole cavity. Additionally, there was the time shift of the curves because of the much quicker filling in the simulation.

This time shift also applied to the GoMikro 17-4PH feedstock. Nonetheless, the pressure predicted by the simulation was much closer to the actual values. Owing to the complete filling of the spiral, all mold sensors yielded pressure signals for this feedstock. The injection pressure (signal pM) of the molding and the simulations was in fact at the same peak level, and also the shape of the curve was very similar. The slope to the peak was however steeper for the simulation. Moreover, the simulation again predicted similar maximum values of about 140 MPa for the pressure at the sensor locations (signals p1, p2, p3). The pressure dropped from the peak down to zero without a trend of approaching the packing pressure. This behavior indicated the quick solidification of the material, so that the packing pressure applied by the machine was not transferred to the cavity. In the experiments, the pressure level was much lower, up to approximately 70 MPa, 50 MPa and 20 MPa for the sensor signals p3, p2, and p1, respectively. The observed standard deviation increased and decreased with the pressure curves, so that the determined maximum of about 11 MPa was observed at the peak. The pressure decayed more slowly than in the simulations; however again without a noticeable constant pressure level induced by the ongoing packing phase.

The material data base was excellent and up-to-date because of the conducted characterization. Furthermore, the spiral was no micro part, so that deviations due to software limitations regarding insufficiently implemented microscale effects could be safely ruled out. The unsatisfactory results of the Catamold® feedstocks might

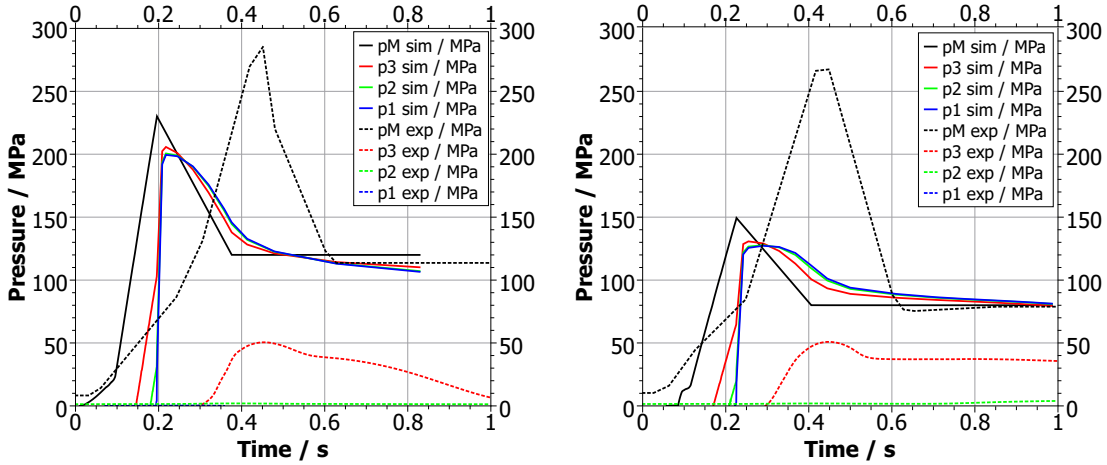

(a) Catamold® 17-4PHA. **(b)** Catamold® TZP-A.

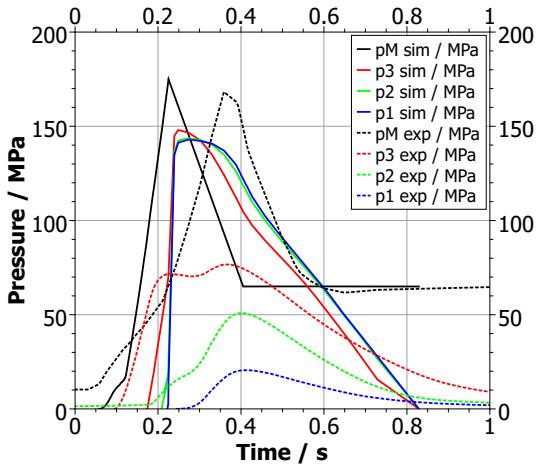

(c) GoMikro 17-4PH.

Figure 8.8: Injection pressure over time of the experiments and simulations with three different feedstocks. The plot contains the pressure signals from the pressure sensors (p1, p2, p3) and the machine (pM).

therefore be attributed to the inadequate viscosity model, as the introduction of the Herschel-Bulkley extension to the Cross-WLF model is recommended by many researchers. On the other hand, this would give rise to the question of where the matching results of the GoMikro 17-4PH feedstock came from.

A modification of the viscosity model was not feasible in this work because of time constrains. Nevertheless, Autodesk allows to modify the solver of ASMI and introduce for instance a new viscosity model—advanced programming skills assumed [49]. The influence of the viscosity model could therefore be investigated in future work by incorporating the Herschel-Bulkley extension in the software. The applicability of current commercial simulation tools employing the regular Cross-WLF model could be evaluated as limited.

8.4.3 Short shot study

In prospect of the analysis of the short shots, the pressure drop of laminar shear flow of polymer shall be introduced. The pressure drop p of the polymer flow in a thin slit like the spiral tube is given as [140]

$$p = \frac{m\,L}{B}\left(\frac{\dot{Q}\,(\frac{1}{n}+2)}{2\,W\,B^2}\right)^n \tag{8.1}$$

with the viscosity parameter m, the power-law index n, the flow rate $\dot{Q}$, and the length L, the width W, and the thickness B of the slit.

The graphical evaluation of the DOE is illustrated in Figure 8.9. The main effect plot shows that the injection pressure did not depend linearly on the stroke length. According to Equation 8.1, the pressure on the other hand depends linearly on the flow length. The stroke length was related to the flow length of the feedstocks, as the larger injected volume resulted in more material present in the cavity. This conflict indicated presumably the compressibility of the feedstock which consumed some of the energy applied by the screw.

The non-linearity might also be caused by the varying injection speed and thus material flow rate of the injection molding machine due to acceleration and inertial effects of the heavy feedstock. In addition, the feedstock showed much higher thermal conductivity than regular plastics, so that the frozen layer is not as insulating. Possibly, the thickness of the frozen material layer on the mold surface grew with the stroke length and injection time and led effectively to a narrower cross-section of the flow channel.

With higher injection speed, i.e. with higher flow rate of the material, the injection pressure rose in agreement to Equation 8.1. A decision about the nature of the relation (linear, non-linear, exponential, etc.) could not be taken with just two data points. However, the difference was smaller than mathematically expected. The

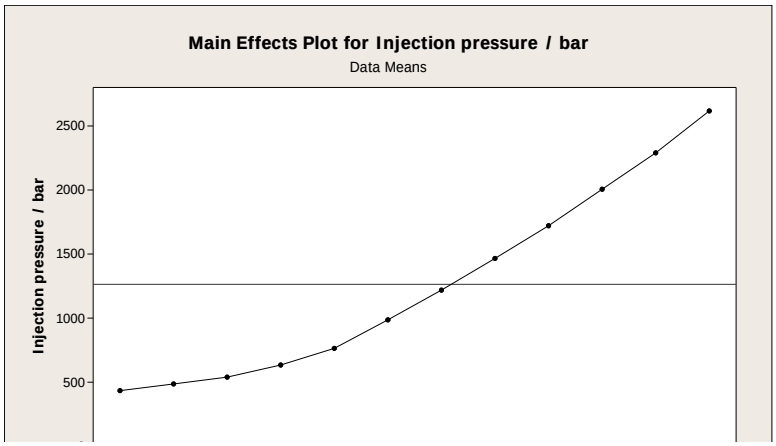

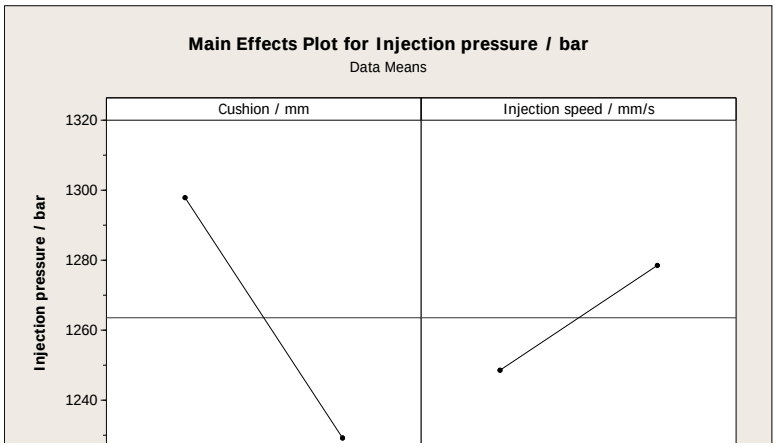

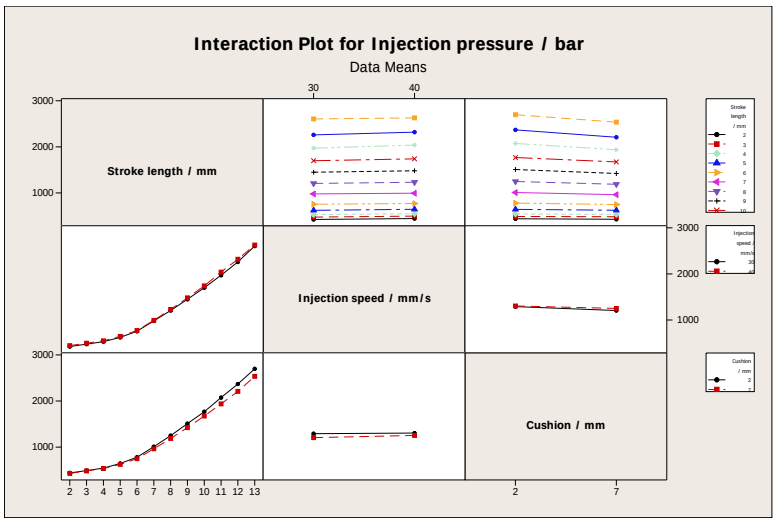

(c) Interaction plot of all factors.

Figure 8.9: Graphs of the results of the short shot DOE with GoMikro ZrO_2.

real increase in pressure was about 3 %. Taking into account a power-law index of $n = 0.44$ correlating approximately with the values of the material characterization, the expected increased would have been approximately 12 %. This difference might be attributed to the acceleration of the machine. As a consequence, the set nominal injection speed was not maintained during the entire filling phase, as depicted previously in Figure 8.5, so that the flow rate varied accordingly.

The increase in size of the cushion resulted in about 5 % lower injection pressure, although there should have been an additional pressure drop for the longer used barrel length. A theory for explanation might be related to the fact that the thermal melt homogeneity can be improved by a reduction of the melt cushion [15]. Most of the dosage volume was used with the small cushion, so that only little backflow from the used volume to the volume remaining as cushion could happen while the screw was moving. In case of the long cushion, preferably warmer and thus less viscous material was pushed into the cavity. In case of the long cushion the melt homogeneity was worse and caused lower average viscosity of the actually injected material. Moreover, the effect was more distinct for longer stroke length, so that the described effect might have had more time to develop more pronounced.

Every run of the DOE was repeated three times. The reported data is therefore every time the average of the three corresponding short shots. In general, the higher the injection pressure was, the higher also the standard deviation. For instance the maximum process standard deviation of the injection pressure was determined as approximately 3 MPa or 1 % at pressure levels of 270 MPa for a stroke length of 13 mm. On the other hand, the standard deviation for a stroke length of 2 mm was computed as being smaller than about 1 MPa or 2 % at pressure levels of 45 MPa.

The samples of the short shots are shown in Figure 8.10 and 8.11. The flow length was a function of the process parameters. In accordance to expectation, the higher the injection speed was, the longer the flow length was owing to the higher shear rate and thus lower viscosity. In general, the short cushion of 2 mm gave the greater flow length for all stroke lengths with the effect more noticeable for the higher injection speed of $40\,\mathrm{mm\,s^{-1}}$. This observation could also explain the aforementioned larger injection pressure for the shorter cushion. Given one stroke length setting and thus theoretically a certain injected volume, the flow length and hence the pressure drop over this length was higher for the 2 mm cushion.

Moreover, the stroke length and thus the theoretically injected volume would have been the same for each step, if the material was incompressible. As already pointed out in section 4.11, feedstocks are generally much less compressible than pure plastics due to the rigid powder, but can still be considered and were proven compressible. Figure 8.12 recalls the compressibility chart derived from the material characterization. The example shows that the binder can be compressed by about 9 %, whereas the feedstocks are only about 5 % and 6 % compressible at 2000 bar. Similar behavior applied also to the GoMikro feedstocks. As a consequence, the melt cushion absorbed some energy of the applied pressure like a spring. The energy was released again

(a) Melt cushion of $c = 2\,\mathrm{mm}$.

(b) Melt cushion of $c = 7\,\mathrm{mm}$.

Figure 8.10: Overview of the different short shot studies with varying stroke length at an injection speed of $v = 30\,\mathrm{mm\,s^{-1}}$. Scale in cm.

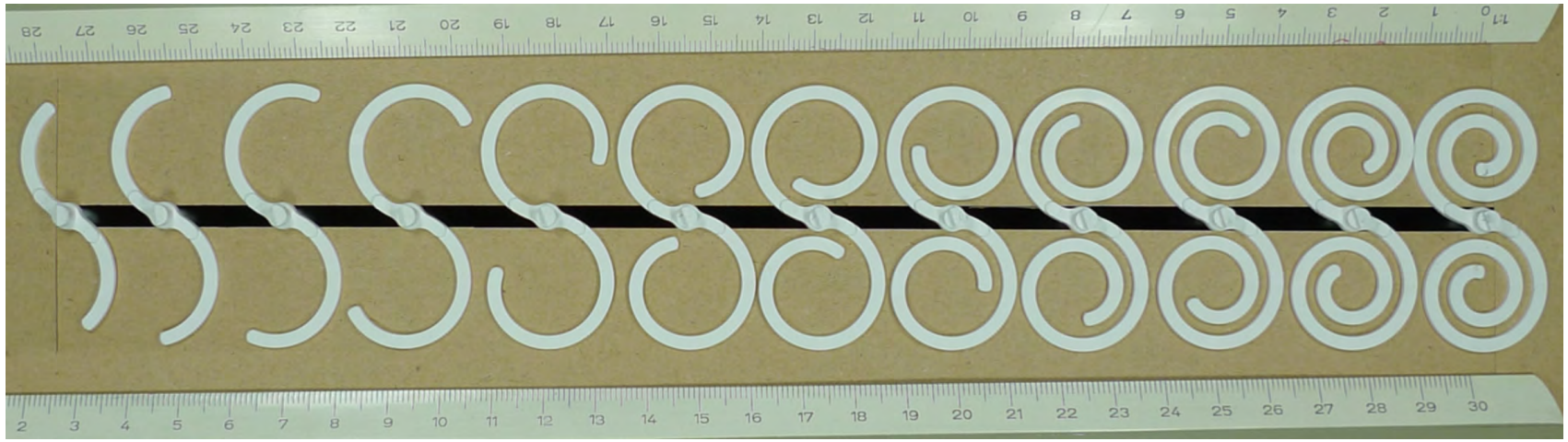

(a) Melt cushion of $c = 2\,\mathrm{mm}$.

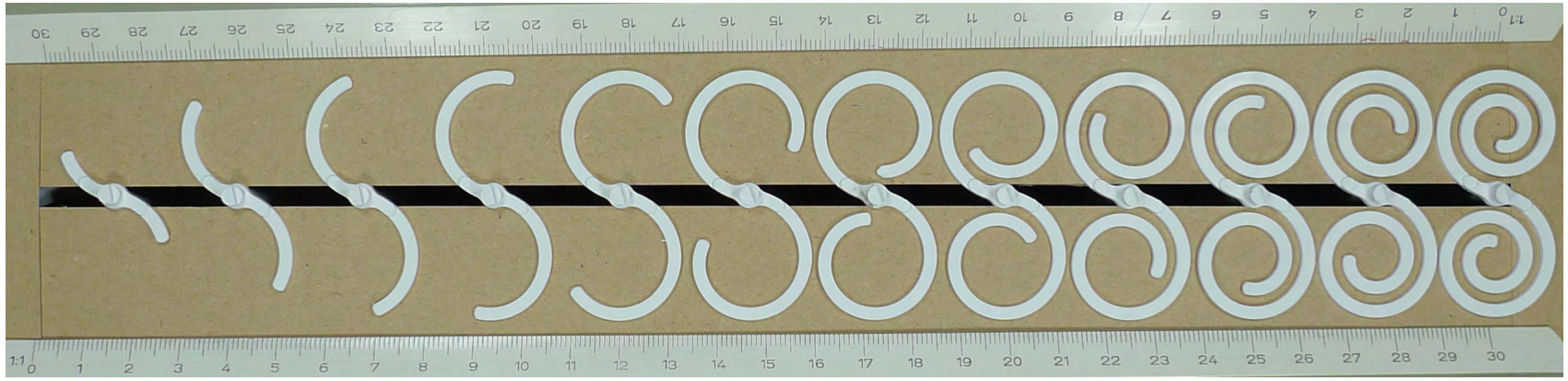

(b) Melt cushion of $c = 7\,\mathrm{mm}$.

Figure 8.11: Overview of the different short shot studies with varying stroke length at an injection speed of $v = 40\,\mathrm{mm\,s^{-1}}$. Scale in cm.

later when the material started freezing already, and could hence not contribute to the material flow. The large cushion could be compressed and absorb energy more extensively than the short cushion which led to the variation in the flow length.

The melt cushion could thus be proven to have a noticeable influence on the injection pressure and flow length of the material. The short cushion gave the more direct response, i.e. the longer flow length and higher pressure. This aspect should be considered in simulation models for micro injection molding in the future, as the default software assumptions might not reflect this characteristic of the process properly.

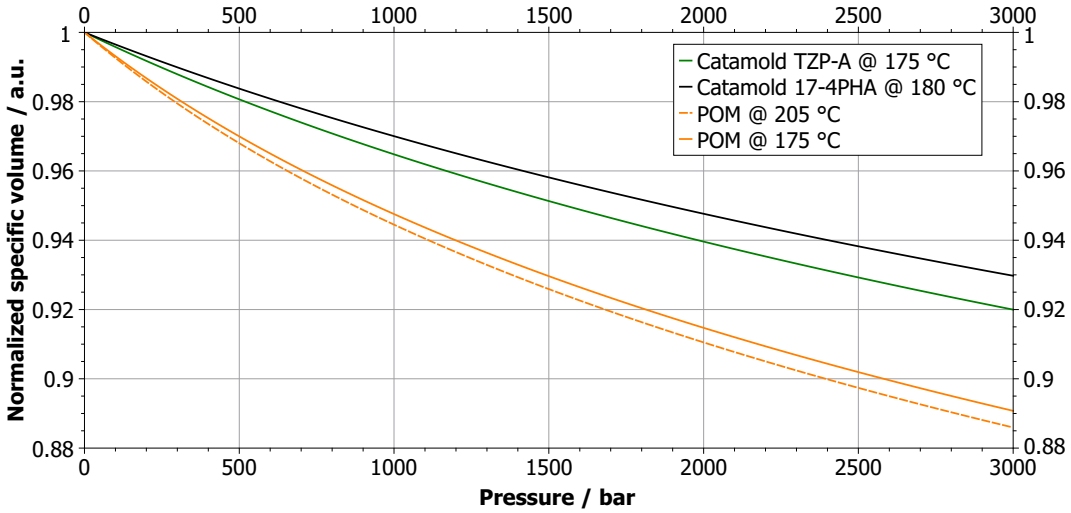

Figure 8.12: Normalized specific volume versus pressure of the Catamold® feedstocks and the pure POM binder to illustrate the pressure dependency of the specific volume and the compressibility of the materials.

8.5 Summary and conclusion

The investigations on powder injection molding commenced with the presentation of the study part: a double spiral test geometry in the millimeter range. The mold of the double spiral was equipped with pressure and temperature sensors enabling the monitoring of the pressure and temperature inside the cavity live during injection.

First, a full shot study was performed to investigate the molding and as basis for comparison to the later conducted simulations. The experiments yielded full shots of the non-commercial feedstocks from KIT and short shots of the commercial feedstocks from BASF. All tested feedstocks caused very high injection pressures near or beyond the machine's nominal maximum pressure. The KIT feedstocks could be evaluated as presumably suitable for micro parts. Micro molding with the Catamold® feedstocks

on the other hand was expected to be challenging because of the high viscosity and short flow length.

The simulations of the double spiral comprised the part and were compared to the experiments. The introduction of the speed profile monitored during the molding was proven to yield the better results in comparison to a simple constant speed profile. Furthermore, the investigation of the injection pressure measured by the machine and by the sensors revealed that the simulations underestimated both the pressure levels and fill times for the Catamold® feedstocks. This was also related to the false prediction of a full shot. However, the results turned out to be more promising for GoMikro 17-4PH, as the fill pressure was predicted correctly. Still, the predicted fill time was too short and the pressure levels inside the cavity too low. The main reason for the reported discrepancies was most likely the inadequate viscosity model. The simulation of powder injection molding had therefore to be evaluated as critical and not entirely reliable with the current tools. However, adapted viscosity models and access to the core of the software provide the potential for enhancements.

Additionally, series of short shots were carried out with the ceramic GoMikro ZrO_2 at different process conditions in a DOE. The short shots could prove the influence of the melt cushion size on the injection pressure and material flow length. Consequently, future work should also address this aspect in process simulations and elaborate on it in greater detail. The parts and data of the short shots are available, and a quantitative flow length determination as well as simulations of the short shots to elaborate on the effect of inertia and the flow length prediction could be part of future research.

9 Ceramic micro component design and manufacture

Abstract This chapter deals with a micro-mechanical part. The study case and the different mold concepts of the early and late design phase are introduced. Afterwards, the influence of a multi-scale mesh in comparison to a homogeneous mesh in the process simulations are shown.

The process simulations on this study case do not only comprise the part design, but also the analysis of the mold and the implemented cooling system. The layout of the cooling system is optimized and the consequences on the part quality are outlined with a study on similar models containing different cooling systems.

The chapter is stimulated by the possibility to expand the simulation-aided design concept to micro powder injection molding. Furthermore, the applicability and limitations of the previously established feedstock material models to a real component was intended to be checked. The chapter was also motivated by the idea to enhance the awareness and application of process simulations in the area of micro powder injection molding.

9.1 Study case

9.1.1 Actual component

The third industrial study case was a ceramic lever with pure mechanical functionality for a micro-mechanical system. The lever featured a through hole for bearing and sharp edges for the interaction with gear wheels. Moreover, the limited space in the micro-mechanical system gave it a unique shape and outer dimensions of approximately 12.0 mm × 3.0 mm × 0.8 mm (length × width × height). The part was in fact only 0.36 mm thick, but exhibited a thicker "tail" of 0.76 mm thickness. The part and its major dimensions are shown in Figure 9.1. The over-all dimensions of the part were in the millimeter range. Still, the part could be considered as a micro part and the process as micro injection molding, because the knocker exhibited dimensional tolerances and radii down to the low micrometer range.

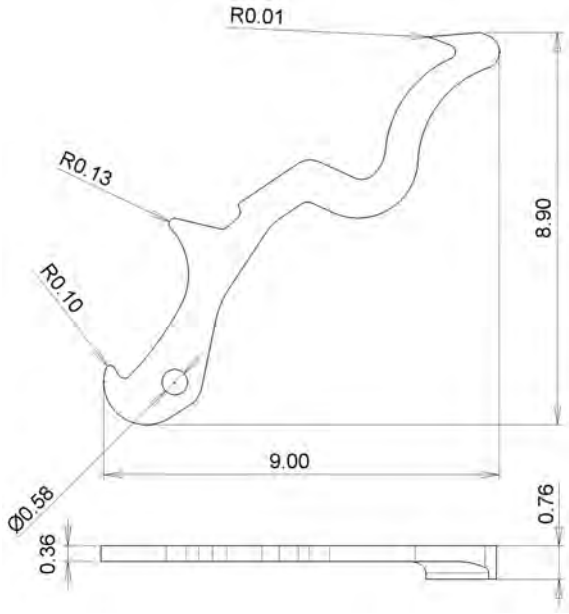

(a) Drawing with major dimensions.

(b) CAD model.

Figure 9.1: Drawing and CAD model of the ceramic lever for a micro-mechanical system [141]. All dimensions in mm.

The part was intended to be made by ceramic powder injection molding. The scope was on the design for the molding step only, so that the presented part is in fact the green part. The subsequent debinding and sintering to yield the final part was not part of this Ph.D. project.

The part and the whole micro-mechanical system was expected to have a life time of several years. Failure or replacement of the lever was not an option. Hence, high reliability promoted by superior wear resistance and exceptional stiffness against the mechanical loads and possible abrasion coming from the interaction with the surrounding mechanical parts was essential. The complete part was therefore implemented in ceramic. Zirconium dioxide (ZrO_2) was the material of choice because of its excellent elastic modulus, the high abrasion resistance, and the applicability in micro powder injection molding. It is moreover compatible to steel parts due to its comparable thermal expansion and elastic modulus. [107, 110]

Instead of a classical feed system of runner and sprue, the prototype was initially equipped with a reversed sprue gate in a single-cavity layout. The material for the ceramic molding was the previously presented BASF Catamold® TZP-A feedstock featuring ZrO_2 powder and POM binder. This feedstock was not available in the default material data base of ASMI. Consequently, the simulations with feedstock were enabled by the material characterization and resulting material model described in chapter 4.

This component was picked as study case because of the required high accuracy in the low micrometer range, the micro roundings with tight radii, and the use of ceramic feedstock and powder injection molding. This enabled to apply the previously established material models of the ceramic feedstock not only to a simple test structure, but a complex industrial prototype. Furthermore, the extraordinary shape with lots of curved edges required careful modeling and the fine tuning of the mesh for good contour fidelity in the simulation model. With regard to the mold manufacturing by additive manufacturing within the Hi-MICRO project and the resulting freedom in the design of the mold's cooling system greatly induced the need for an analysis of the cooling circuit regarding flow and impact on part quality which could hardly be done by other means than flow and process simulations.

9.1.2 Mold conception of early design stage

The intended mold concept in the early design phase of the ceramic lever was given by the industrial partner in the Hi-MICRO project and is shown in Figure 9.2. The mold size was not decided, so that the mold plates were not considered. Two inserts with outer dimensions of 46 mm × 46 mm × 17 mm were intended to be mounted to the cavity plates of the stationary and movable half by two through holes and clamped by undercuts. Both inserts were provided with complex 3D cooling channels leaving space for the presumed ejectors and the sprue. The sprue was connected to the part by a pin gate and was moreover inversely tapered, so that a three-plate would have been necessary for the demolding of the sprue and the part. The complexity of the cooling channels did not allow to produce them conventionally. Instead, the inserts were supposed to be manufactured from steel by selective laser sintering (SLS). This additive manufacturing process empowered the implementation of the internal free-form surfaces of the channels during the layer-by-layer fabrication of the inserts.

9.1.3 Mold conception of late design stage

The mold concept of the ceramic lever was changed during the design process by the industrial partner in the Hi-MICRO project for several reasons.

1. The previously shown cooling channels of the inserts exhibited too much unsupported and free-standing surfaces which would have collapsed or been deformed during the SLS process.
2. The gating design was changed to simplify the planed mold and to gate the part at the thickest area for better packing.

The later mold conception is shown in Figure 9.3. Both cavity plates of the two-plate mold showed straight cooling channels. The channels were aligned in U-shape

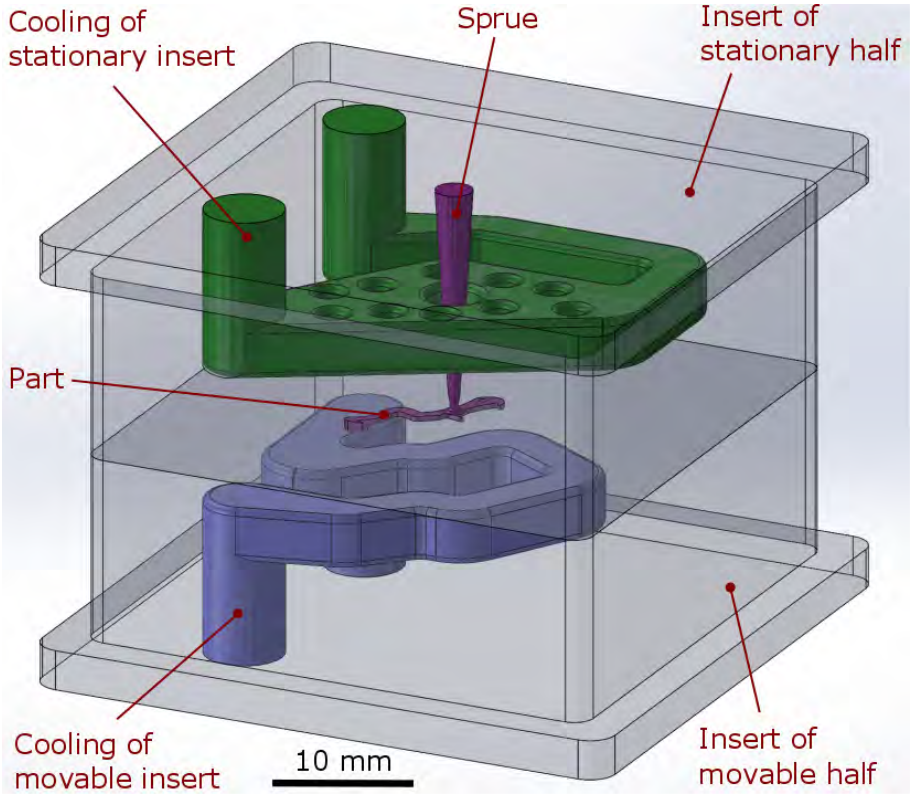

Figure 9.2: Mold conception for the ceramic lever with two inserts, integrated cooling channels, and actual part in the early design stage.

through the plates and were to be manufactured conventionally by drilling. The tail of the part was extended and the part was gated there by means of an approximately semi-circular pin gate, as shown in Figure 9.3a. Furthermore, the movable cavity plate was provided with a pocket for an insert exhibiting the part cavity, the gate, a runner-like extension of the sprue to the gate, and the sprue puller. Four screw joints in the corners of the insert were allocated for the symmetrical fixation of the insert in the cavity plate. The insert with outer dimensions of 32 mm × 32 mm × 8 mm was equipped with a fine conformal cooling channel following in two branches the contour of the part. The conformal cooling channels were again too complicated in shape for the conventional manufacture. As a consequence, the channels were planned to be integrated during the SLS fabrication of the whole insert.

The design of the late conception was finally realized. The insert with the integrated conformal cooling channels was manufacture by SLS. The mold plates were standard parts and modified by milling. The cooling channels in the mold plates were produced by drilling. The movable half of the mold with mounted insert is depicted in Figure 9.4. The mold manufacture was not part of this work and is therefore not discussed in more detail.

9.2 Comparison of homogeneous and multi-scale mesh

9.2.1 Simulation set up

The ceramic lever was the smallest prototype with regard to its absolute outer dimensions and volume which was studied in this work. The following investigation was meant to investigate the influence of the application of a multi-scale mesh in comparison to a homogeneous mesh for the same geometry with a micro component as study case.

The simulation models comprised the layout of the early design stage (shown in subsection 9.1.2): the ceramic lever and two inserts which incorporated the revised complex 3D cooling channels. The mold block was neglected, because no information was available. The whole system was meshed with the homogeneous and the multi-scale approach (introduced in subsection 3.3.2) yielding two simulation models: the homogeneous mesh (HM) with one single edge length and the multi-scale mesh (MM) in which all CAD faces were assigned the mesh density matching the rule of thumb of ten elements across the thickness was fulfilled. The mesh settings of both models are listed in Table 9.1. A closer look on the resulting mesh and the mesh densities is depicted in Figure 9.5.

(a) Part with revised feed system.

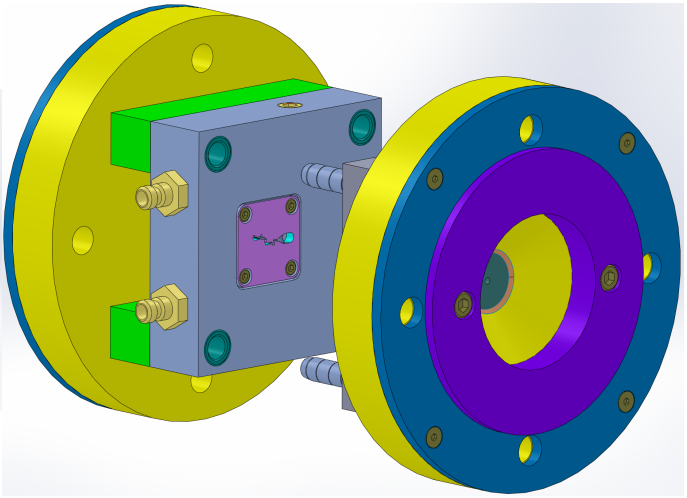

(b) Full mold assembly.

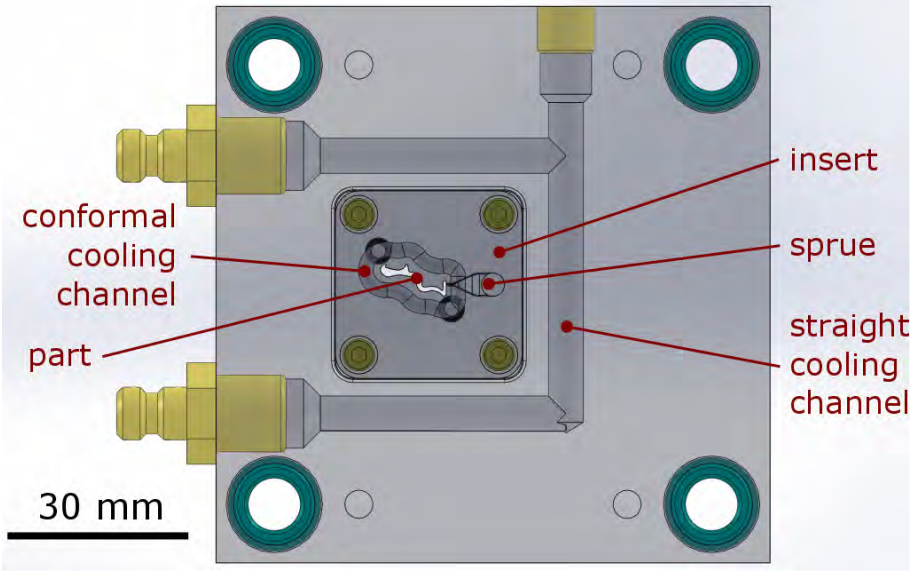

(c) Movable cavity plate with insert and cooling.

Figure 9.3: Mold conception for the ceramic lever in the later design stage. The gating of the part was changed, and the part cavity was incorporated in a single insert in the movable half of the mold.

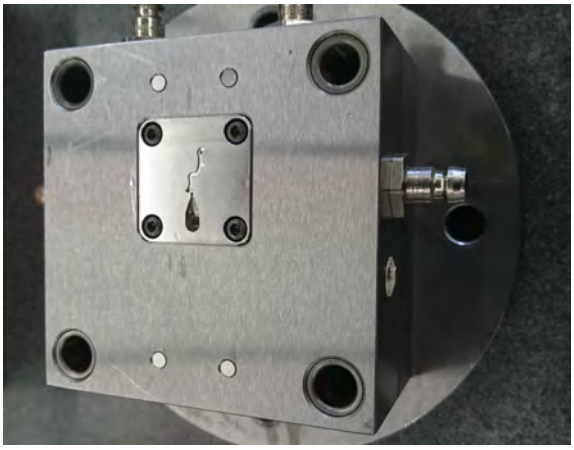

Figure 9.4: Realized mold (movable half) with mounted insert made by SLS.

Table 9.1: Meshing settings of the homogeneous mesh (HM) and multi-scale mesh (MM) of the micro-mechanical lever with insert and cooling. Unspecified settings were kept at the default values. The numbers of elements are rounded.

Parameter	setting	
	HM	MM
Mesh density / µm		
part, side walls	500	40
part, front+back	500	100
gate	500	100
cooling channels	500	500
CFD mesh for cooling	no	yes
Global edge length / µm	500	500
Merge tolerance / µm	10	10
Chord angle / °	10	10
Min. number of elements through thickness	10	10
Max. edge length in thickness direction / mm	0.5	0.5
Bias ratio	1.2	1.2
Total number of elements	5 600 000	4 700 000
part (including feed system)	70 000	830 000
insert	5 000 000	2 400 000
cooling circuit	610 000	1 500 000
Part mesh volume / mm^3	48.8	50.0

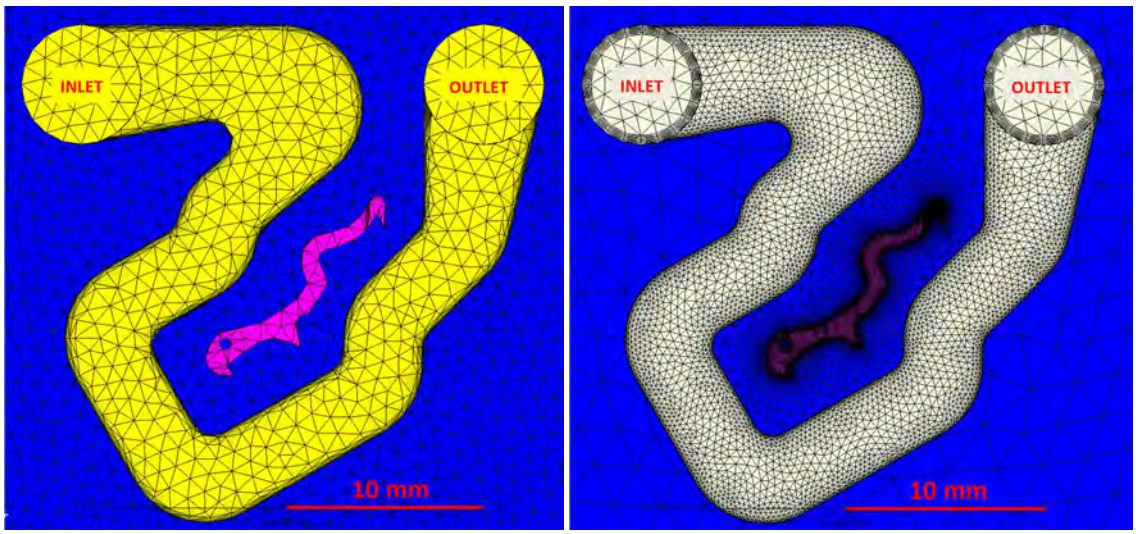

(a) Homogeneous mesh. **(b)** Multi-scale mesh.

Figure 9.5: Comparison between homogeneous and multi-scale mesh applied to the micro-mechanical lever. The homogeneous mesh was created with 500 µm mesh size, the multi-scale mesh comprised mesh sizes in the range from 40 µm to 500 µm. The part (magenta), one of the cooling channels (yellow or beige), and partially the insert (blue) are shown.

It should be noted that the total number of tetrahedrons—which is related to the computation time—was in fact larger for the HM model. Nevertheless, the distribution of the tetrahedrons among part, cooling channels, and insert varied and correlated to their volume in case of the HM. Especially, the part consisted of much less tetrahedral elements, whereas the insert clearly consumed most of the elements in accordance to its much larger size. The reproducibility of the original CAD geometry suffered from the coarse mesh, so that some edges and surfaces were only roughly interpolated, and the meshed part volume was smaller for the HM model.

The effect of the MM was reflected in the much better distribution of the elements between the part, the insert, and the cooling channels. Defining local mesh densities at the CAD faces clearly gave a dynamic multi-scale mesh with high resolution at the part and at the interface between the part or the cooling channels and the insert. The mesh size of the insert increased towards the outer areas of the insert. In addition, the special CFD mesh of the cooling channels exhibited mesh enhancement at the channel surface for more accurate flow calculations. The mesh enhancement is visible at the inlet and outlet as very dense circular slices along the circumference.

Table 9.2 summarizes the simulation settings. The conducted analysis included cooling, filling, packing, and warpage. The material choice for the simulations was the POM Ultraform N2320C BK120 Q600 from BASF. This material was chosen in

perspective to the ceramic feedstock from BASF with POM binder. Moreover, the chosen POM provided comprehensive material data in the ASMI data base. The default processing settings of the ASMI data base were used.

The coolant governed the temperature of the insert which was at the start of the injection hence also at 75 °C. The pressure applied to the coolant inlets was chosen as 1 bar, the outlets were set to 0 bar, giving a total pressure drop of 1 bar at each channel. Standard external temperature controllers for injection molding machines running with water can typically provide about 4 bar to 6 bar of pump capacity [142, 143]. A large share of the maximum pump capacity was assumed to be consumed already by the pressure drop over the supply pipes. The mold's cooling channels were most likely shorter in direct comparison. The available Arburg machine was deployed for the simulation. The injection location diameter was chosen accordingly to the nozzle of 2.0 mm in diameter. The decision on the mold material was still pending, so that common tool steel of type 1.1730 was employed in the simulations.

Table 9.2: Machine and process settings of the simulations for the comparison of the homogeneous and multi-scale mesh of the ceramic lever. Unspecified settings were kept at the default values.

Parameter	setting
ASMI version	2015
Analysis type	Cool(FEM)+Fill+Pack+Warp
Material type	POM
Material grade	BASF Ultraform N2320C BK120 Q600
Melt temperature / °C	205
Coolant temperature / °C	75
Coolant type	water
Cooling pressure drop / bar	1
Filling control	absolute ram speed vs ram position
Target ram speed / ($mm\,s^{-1}$)	50
Cushion / mm	2.0
Switch-over volume / %	98
Packing pressure	80 % of filling pressure
Packing time / s	20
Machine	Arburg Allrounder 370 A 600-70 (18 mm)
Mold material	1.1730 (C45W)
Injection location diameter / mm	2.0

9.2.2 Results and discussion

The major simulation results for the HM and MM models are listed in Table 9.3. The results related to flow—the polymer flow inside the cavity or the coolant flow

inside the channels—differed much for the two mesh types, although the relevant simulation settings like the injection speed or applied coolant pressure were the exact same. This was most likely due to the higher resolution and hence smaller step size in computation of the multi-scale mesh and demonstrated its necessity and impact. Both models predicted complete fill, but the HM model yielded less than half of the injection time of the MM. As a result, the injection pressure in case of the MM was lower by about 26 %, the maximum occurring shear rate also about 25 %.

Table 9.3: Major simulation results of the homogeneous and multi-scale mesh of the ceramic lever.

Model	HM	MM	Δ/%
Filling	complete	complete	
Fill time / s	0.05	0.12	118
Max. injection pressure / MPa	49	36	−26
Total mass after fill / g	0.0595	0.0600	1
Total mass after pack / g	0.0637	0.0642	1
Mass increase by pack / g	0.0042	0.0042	0
Max. shear rate / s^{-1}	27 000	20 000	−25
Avg. volumetric shrinkage / %	3.4	3.8	10
Max. coolant velocity / ($m\,s^{-1}$)	1.07	1.29	21

The flow analysis of the cooling channels is illustrated in Figure 9.6. The CFD analysis of the cooling channel of the HM mesh could be carried out with the given mesh, but the resolution and the results suffered from the missing mesh enhancement and refinement at the surface of the cooling structure. Consequently, the HM model was not able to compute the flow near the surface of the cooling channels and thus capture the flow acceleration in turns. Therefore, the maximum observed flow velocity in the cooling channel of the MM model was greater by about 21 %. Such a flow acceleration however would have had a considerable effect on the cooling performance of the coolant, as the heat transfer depends on the flow rate at the channel's surface.

In fact, the dissimilar mesh influenced the cooling and hence the warpage of the part, as illustrated in Figure 9.7. The HM model showed the larger deflection of the warped part which was especially visible at the tail of the part.

The results which were related to the volume like average volumetric shrinkage and part mass were not affected as much by the different mesh types. The reason was probably the limited variation in meshed volume. However, the comparison of the mass was problematic, since the packing pressure as 80 % of the maximum injection pressure was thus higher for the HM model.

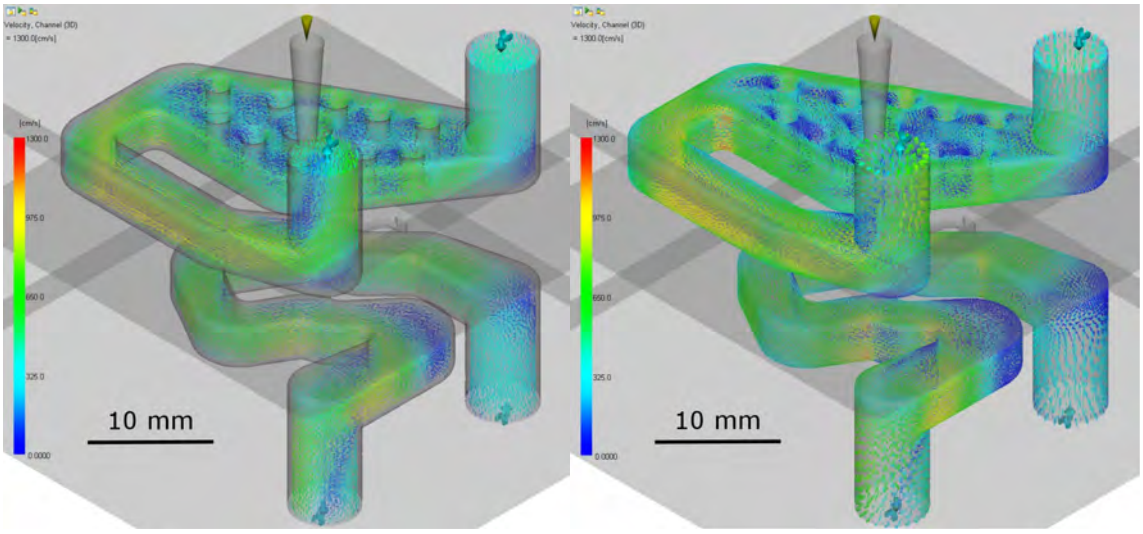

(a) Homogeneous mesh. **(b)** Multi-scale mesh.

Figure 9.6: Comparison between the coolant flow and velocity inside the cooling channels of the planned insert for the homogeneous and multi-scale mesh of the ceramic lever. Color scale from blue to red: velocity from $0\,\mathrm{m\,s^{-1}}$ to $1.3\,\mathrm{m\,s^{-1}}$.

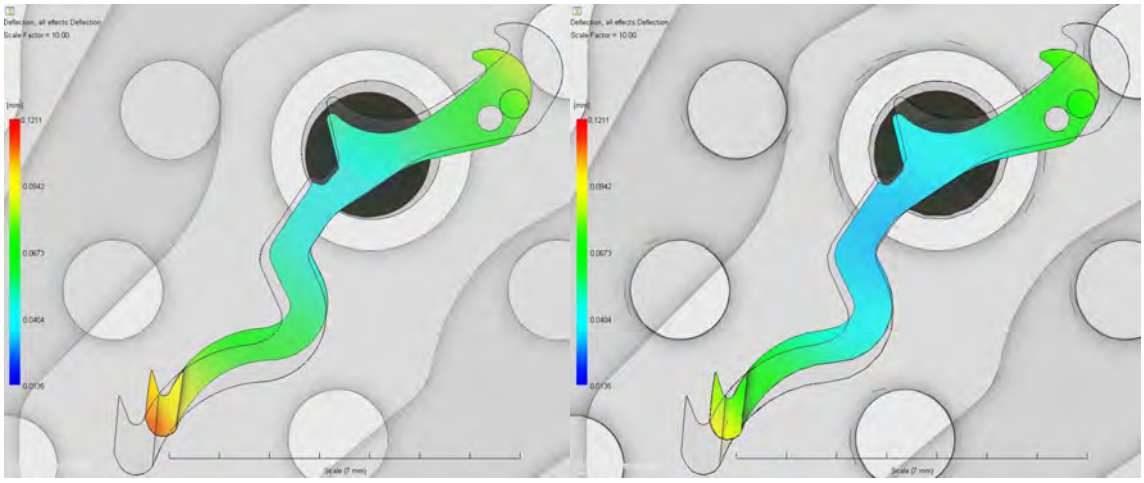

(a) Homogeneous mesh. **(b)** Multi-scale mesh.

Figure 9.7: Comparison between the total warpage (sum of x, y, and z-component of deflection) of the ceramic lever for the homogeneous and multi-scale mesh. The original shape of the part is indicated and the deflection is scaled by a factor ten. Color scale from blue to red: deflection from $14\,\mu\mathrm{m}$ to $121\,\mu\mathrm{m}$.

9.3 Influence of mold and cooling implementation

9.3.1 Investigated simulation models

The following investigation was conducted to assess the impact of the mold and cooling system implementation on the predicted simulation results regarding the process and part quality. The three different models were based on the revised mold conception of the late design stage with the lever, one insert, and the mold block, as shown in subsection 9.1.3. They varied in the extent of the considered injection molding entities (mold, inserts, and cooling system). The comprehensiveness of the models is summarized in Table 9.4.

PO: Part only
Only the part and the feed system were considered in the model. The surrounding mold was not implemented, so that the software assumed it as the default infinite block of the set mold temperature and the given material. Insert and cooling channels were not included.

SC: Simple cooling
In addition to part and feed system, the mold was modeled as dedicated finite steel block of the given mold material with actual dimensions. The mold consisted of the simplified representation of the movable and stationary half. Both halves incorporated the simple network of large, straight, conventional cooling channels. The movable half additionally contained the insert with the actual part cavity.

CC: Conformal cooling
This configuration was similar to the SC model, but the mold insert also featured conformal cooling structures besides the straight channels.

Table 9.4: Incorporated entities of the different simulation models of the ceramic lever to assess the influence of mold and cooling circuit on the simulation outcome.

Model	part only (PO)	simple cooling (SC)	conformal cooling (CC)
Part	✓	✓	✓
Feed system	✓	✓	✓
Mold block	✗(default virtual)	✓(actual)	✓(actual)
Mold cooling	✗(fixed temperature)	✓(conventional)	✓(conventional)
Insert	✗	✓	✓
Insert cooling	✗	✗	✓(conformal)

9.3.2 Meshing

The simulation model of PO did not include any mold entities. The SC and CC models however included also the mold, inserts, and cooling channels. Since the size varied a lot between the mold and the actual part, the application of a multi-scale mesh was of great importance, and numerous local mesh densities were assigned. The exact mesh settings for all models and their entities are listed in Table 9.5. The meshed lever and the assigned mesh densities are depicted in Figure 9.8. Details of the mesh of the mold and the cooling can be found in Figure 9.9 and 9.10. The assigned mesh densities caused mesh refinement in the relevant areas of the model. Roundings were also slightly refined because of the chord angle control. The cooling channels featured mesh enhancement at the channel surface due to the deployed CFD mesh.

Table 9.5: Meshing settings of the microfluidic dispenser with pin gate for the simulation validation. Unspecified settings were kept at the default values. The numbers of elements are rounded.

Parameter	setting		
	PO	SC	CC
Mesh density / µm			
part	50	50	50
gate	50	50	50
sprue, gate connection	100	100	100
sprue, tapered extension	200	200	200
sprue, general	800	800	800
insert, side walls	n.a.	800	800
insert, bottom surface	n.a.	1600	1600
cooling channels	n.a.	500	500
CFD mesh for cooling	n.a.	yes	yes
Global edge length / mm	0.8	3.0	3.0
Merge tolerance / µm	20	20	20
Chord angle / °	20	20	20
Min. number of elements through thickness	10	10	10
Max. edge length in thickness direction / mm	0.8	3.0	3.0
Total number of elements	810 000	4 900 000	5 000 000
part (including feed system)	810 000	1 800 000	2 000 000
mold (including insert)	n.a.	1 500 000	1 300 000
cooling circuit	n.a.	1 700 000	1 800 000

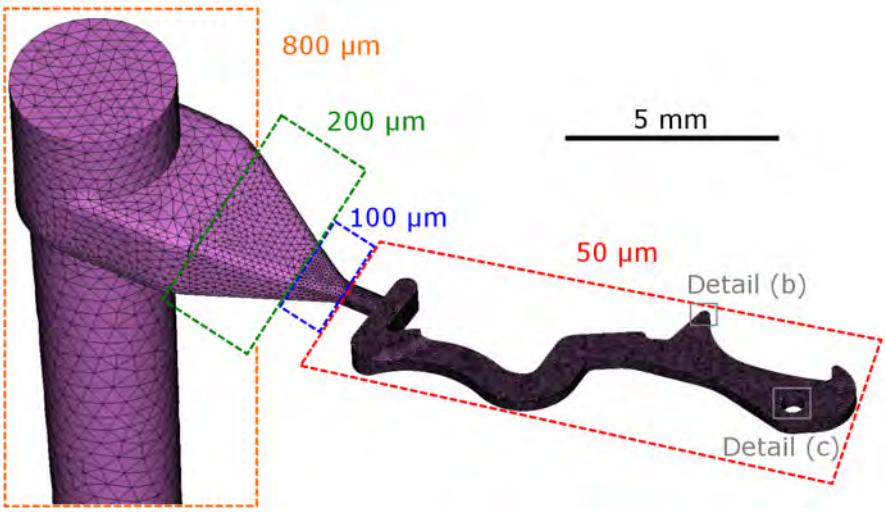

(a) Entire lever with assigned mesh densities.

(b) Radius.

(c) Hole.

Figure 9.8: Meshed micro-mechanical ceramic lever with feed system (sprue is not shown completely), detailed views on micro features, and indicated mesh densities in ASMI.

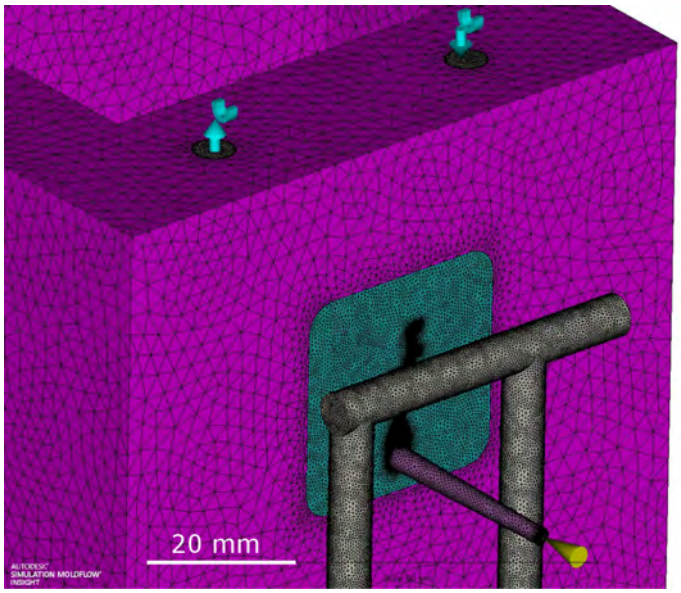

Figure 9.9: Meshed mold block with insert, part, and cooling channels of the SC model of the ceramic lever. The mold plate of the stationary half is not shown, the cooling inlet and outlet are indicated.

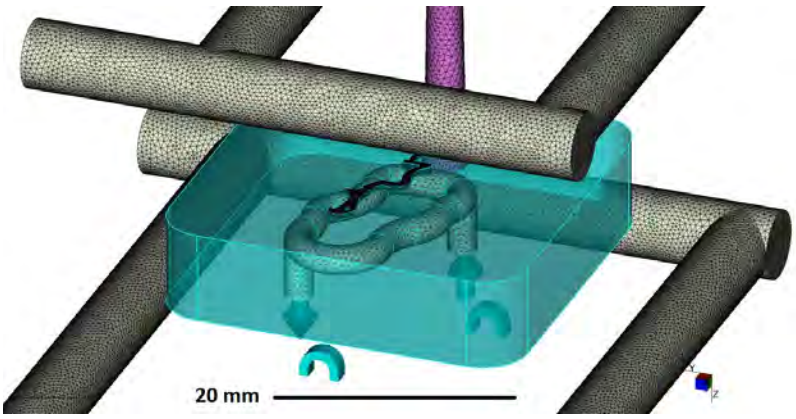

Figure 9.10: Meshed cooling channels and part and indicated insert of the CC model of the ceramic lever. The mold plates are not shown.

The total number of elements varied quite significantly. Although the settings did not change, the SC and CC models yielded more elements for the part because of the interfaces of the part to the insert and the mold. The meshing algorithms tried to adapt and match the meshes of the part and the insert where in contact for precise calculation of temperature distribution and heat transfer. This constraint might have caused the difference in elements. Variations between the SC and CC model could be explained by the fact that the CC model included additional conformal cooling channels. Due to their close location to the part, they probably still affected the meshing of the part and did not only change the number of elements of the mold and cooling circuit.

9.3.3 Simulation settings

The simulation settings are summarized in Table 9.6. The conducted simulation included filling, packing, and warpage for the PO model and an additional cooling analysis for the SC and CC models. In case of the PO model, the mold temperature was hence set, whereas in case of the SC and CC models the coolant governed the temperature of the mold. The pressure applied to the cooling circuit was 1 bar like in the previous analyses.

Likewise, the material choice for the simulations was again the POM Ultraform N2320C BK120 Q600 from BASF. The default processing settings of the ASMI data base were used due to the unavailability of actual values. The available Arburg machine and common tool steel were selected as injection molding machine and mold material, respectively. The injection location diameter was adjusted to the nozzle diameter of the machine of 2.0 mm.

Table 9.6: Machine and process settings of the simulations models of the ceramic lever. Unspecified settings were kept at the default values.

Parameter	setting
ASMI version	2015
Analysis type[a]	Cool(FEM)+Fill+Pack+Warp
Material type	POM
Material grade	BASF Ultraform N2320C BK120 Q600
Melt temperature / °C	205
Mold/coolant[a] temperature / °C	75
Coolant type[a]	water
Cooling pressure drop[a] / bar	1
Filling control	absolute ram speed vs ram position
Target ram speed / ($mm\,s^{-1}$)	40
Cushion / mm	2.0
Switch-over volume / %	99
Packing pressure	80 % of filling pressure
Packing time / s	20
Cooling time / s	20
Machine	Arburg Allrounder 370 A 600-70 (18 mm)
Virtual mold material	1.1730 (C45W)
Injection location diameter / mm	2.0

[a] The cool analysis and all information about the coolant were only relevant for the SC and CC model.

9.3.4 Results and discussion

Table 9.7 summarizes the major results of the three presented and investigated simulation models. The maximum injection pressure was about 47 MPa and almost equal for all models, whereas the SC model showed a greater injection time than the other two models. Due to some erroneous artifact in the flow at the end of fill, the simulation time was manually estimated to be 0.35 s (about 17 % higher compared to the other models).

Table 9.7: Major simulation results of the three different models of the ceramic lever.

Model	PO	SC	CC	limit
Filling	complete	complete	complete	
Fill time / s	0.295	0.35[a]	0.299	
Max. injection pressure / MPa	46.6	46.8	46.7	250
Total mass after fill / g	0.336	0.338	0.335	
Total mass after pack / g	0.349	0.350	0.348	
Mass increase by pack / g	0.013	0.012	0.013	
Max. shear rate / s^{-1}	61 000	56 000	62 000	40 000
Avg. volumetric shrinkage / %	6.2	6.5	6.8	
Flatness front / µm	3.6	2.7	3.3	
Flatness back / µm	2.9	2.7	3.2	

[a] The fill time of the SC model was estimated manually because of the occurrence of a flow artifact at the end of fill.

The simulation predicted a complete fill for every model. However, the position of the flow front became different, when the flow reached the last third of the cavity. The pattern of the polymer flow front is depicted in Figure 9.11. After passing at the through hole of the part, the flow in the SC model lagged behind compared to the PO and CC model. This correlated to the longer injection time of the SC model.

The shear rate predictions of the simulation differed considerably between the models, as the SC model gave an about 8 % lower shear rate. The PO and CC models did not vary significantly in direct comparison. The lower shear rate of the SC model was generated by slower flow which proved the longer injection time. All models exceeded the tolerated shear rate for the used POM. However, this issues was not followed up in further detail, as the actual part was supposed to be produced in ceramic, and this study was done for comparison between the simulation models.

The warpage is illustrated in Figure 9.12. The illustrated and numerical results of the warpage and flatness also differed noticeably. Compared to the PO model, the SC model yielded about 25 % less warpage. The flatness of the CC model was predicted to be lower at the front, but higher at the back of the part. The deviations in warpage

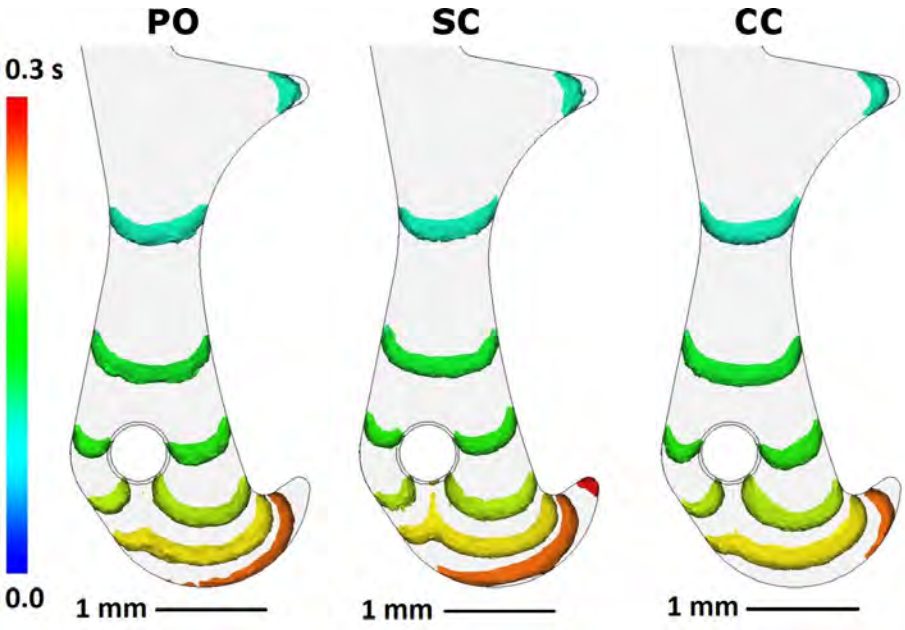

Figure 9.11: Comparison of filling of the cavity for the three different simulation models of the ceramic lever. Color scale from blue to red: filling time from 0 s to 0.3 s.

were induced by the contrasting cooling which changed the filling characteristics, but especially the temperature distribution and heat transfer of the system. The dissimilar results of the evaluated warpage and flatness proved that the process simulations can also be applied for the optimization of the cooling system of the mold with regard to the part quality. Various cooling layouts can easily be investigated and compared without the need for expensive machining of prototypes and molding trials.

All variations could be attributed to the different extent of the simulation models, since the same simulation settings were given. It can hence be concluded that attention must be paid to how the simulation models are built up in micro injection molding. Some of the predicted parameters might change with the comprehensiveness of the simulation model.

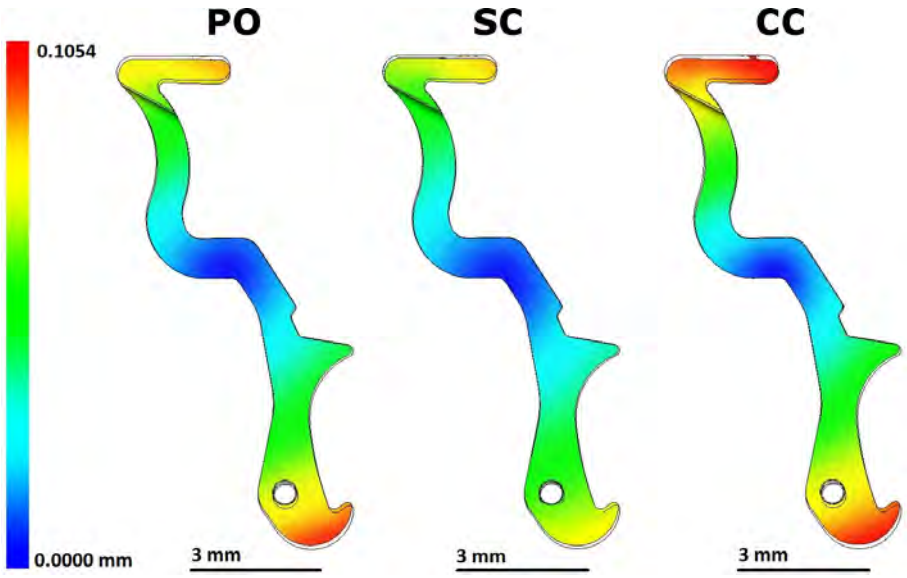

Figure 9.12: Comparison of the total deflection (sum of x, y, and z-component) for the three different simulation models of the ceramic lever. Color scale from blue to red: deflection from 0 mm to 0.1054 mm

.

9.4 Simulation validation of powder injection molding

9.4.1 Molding

The mold for the ceramic lever was realized with straight cooling channels in the mold plates and conformal cooling channels in the single insert, as shown in the revised mold conception.

Table 9.8 summarizes the processing conditions of the ceramic lever. The material choice was a ceramic feedstock very similar to Catamold® TZP-A. The two feedstocks alter inasmuch as the deployed powder feedstocks contained besides the polycrystalline yttria-stabilized zirconium dioxide also about 6 % other, unspecified materials. This leads to slightly lower density and inferior mechanical properties of the final product. Moreover, the melt-flow index tested by ISO 1133 is typically about the twofold of Catamold® TZP-A, so that deviations in viscosity and flow behavior can be expected. The processing conditions recommended by the material supplier BASF retain however the same.

The molding was conducted by the responsible industrial Hi-MICRO project partner on an Arburg Allrounder 270 S 250-60 with 15 mm screw diameter, 2.0 mm nozzle diameter, and a maximum clamping force of 250 kN. The filling was performed flow rate controlled at 8 $cm^3 s^{-1}$. Afterwards, a packing pressure profile was applied with the pressure decreasing in 1 s from 120 MPa to 90 MPa and dropping further in 1 s

from 90 MPa to 7.5 MPa. The detailed process settings of the machine can be found in Appendix F.

The profile of the injection pressure and the injection time were monitored by the machine. The resulting values were used for the comparison and validation of the powder injection molding simulations with the created material model of Catamold® TZP-A.

Table 9.8: Machine and process settings of the powder injection molding experiments of the ceramic lever.

Parameter	setting
Material type	ceramic feedstock (ZrO_2)
Barrel temperature / °C	164–172
Mold temperature / °C	140
Flow rate / ($cm^3\,s^{-1}$)	8
Switch-over pressure / MPa	152
Cushion / ($cm^3\,s^{-1}$)	1.1
Packing	pressure profile vs time
	0 s: 120 MPa, 1 s: 90 MPa, 2 s: 7.5 MPa
Total packing time / s	2
Machine	Arburg Allrounder 270 S 250-60 (15 mm)

9.4.2 Simulation models and meshing

The experimental molding was compared to two simulation models of varying comprehensiveness. The models were based on the late mold concept and included the full spectrum of part, feed system, mold, cooling channels, and insert. The mold block was a simplified version of the real mold disregarding the details such as screws, bolts, ejectors, etc. The second model differed by the incorporation of the machine geometry. The geometry was modeled by implementing the inner volume of the nozzle and the barrel which was filled by the plastic as hot runner. The hot runner was represented by beam elements and realized after the tetrahedral mesh of the remaining components was created. The temperature of the hot runner was set to the melt temperature. Besides the hot runner, the employed mesh and mesh settings of both models were consequently identical.

The mesh settings are listed in Table 9.9. The chosen values were similar to the mesh settings of the previous investigation; slightly adapted to optimize the computation time of the simulation. The meshed part and mold entities were hence comparable to what was shown and described previously in section 9.3. The meshed mold assembly with the machine geometry implemented as hot runner is illustrated in Figure 9.13.

Table 9.9: Meshing settings of the micro-mechanical lever. Unspecified settings were kept at the default values. The numbers of elements are rounded.

Parameter	value
Specific element edge length / µm	
part, side walls	50
part, front	100
part, back	200
gate	50
sprue, gate connection	100
sprue, tapered extension	200
sprue, general	400
insert, side walls	800
insert, front+back	1600
mold plates, back	6000
cooling channels	500
Beam element edge length / mm	1.0
CFD mesh for cooling	yes
Global edge length / mm	3.0
Merge tolerance / µm	20
Chord angle / °	20
Min. number of elements through thickness	10
Max. edge length in thickness direction / mm	3.0
Total number of elements	3 900 000
part (including feed system)	1 200 000
mold (including insert)	900 000
cooling circuit	1 800 000

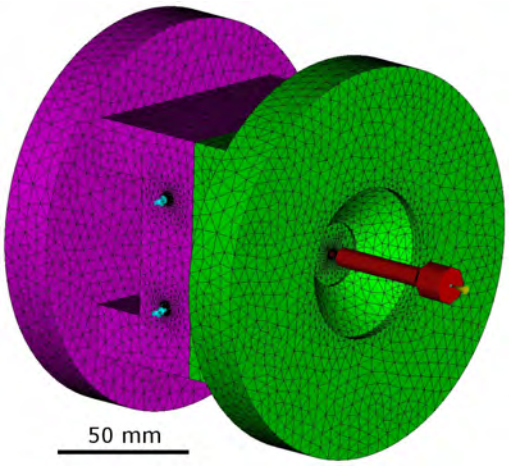

(a) Meshed mold assembly.

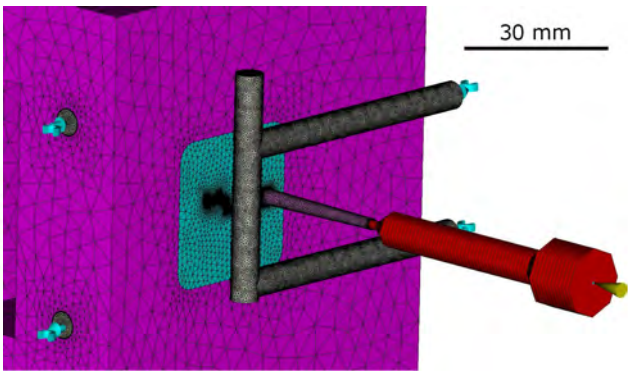

(b) Detailed view on the insert, part, machine geometry, and cooling channel of the stationary half, with hidden plates of stationary mold half.

Figure 9.13: Meshed part and mold assembly with indicated machine geometry modeled as hot runner beam elements. The mesh is based on a simplified version of the mold block.

9.4.3 Simulation settings

The simulation settings are summarized in Table 9.10. The material choice for the simulations was the Catamold® TZP-A feedstock. The processing conditions, the flow rate, the pakcing pressure profile, and the injection molding machine were chosen in accordance to the experiments. The set flow rate of $8\,\mathrm{cm^3\,s^{-1}}$ tallied with an injection speed of $45.3\,\mathrm{mm\,s^{-1}}$ based on the screw diameter. Still, flow rate controlled filling was applied. The injection location diameter was set to the nozzle diameter of the machine. The material choice for the mold was common tool steel.

9.4.4 Results and discussion

The results of the simulations and experiments are shown in Figure 9.14. Both simulations, the first one including the mold and the second one including the mold and machine geometry, underestimated the values of the experimental filling time and total injection pressure. The implementation of the machine geometry provoked a more accurate prediction of the fill time and less accurate prediction of the pressure at the same time. The trend of an increase in fill time, when the machine geometry was implemented as shown in chapter 5, could hence be confirmed—unlike the trend of an additional pressure drop and thus an increase in the total injection pressure.

The pressure drop and fill time of the sprue was given by the first section of the pressure curve to the sharp bend (at about (0.06 s/15 MPa) and (0.04 s/25 MPa) in case of the experiments and both simulations, respectively). When comparing the fill

Table 9.10: Machine and process settings of the powder injection molding simulation of the ceramic lever. Unspecified settings were kept at the default values.

Parameter	setting
ASMI version	2015
Analysis type	Cool(FEM)+Fill+Pack+Warp
Material type	ceramic feedstock (ZrO_2)
Material grade	BASF Catamold® TZP-A
Melt temperature / °C	172
Coolant temperature / °C	140
Coolant type	water
Cooling pressure drop / bar	1
Filling control	flow rate
Target flow rate / ($cm^3\,s^{-1}$)	8
Switch-over volume / %	99
Packing	pressure profile vs time 0 s: 120 MPa, 1 s: 90 MPa, 2 s: 7.5 MPa
Total packing time / s	2
Machine	Arburg Allrounder 270 S 250-60 (15 mm)
Mold material	1.1730 (C45W)
Injection location diameter / mm	2.0

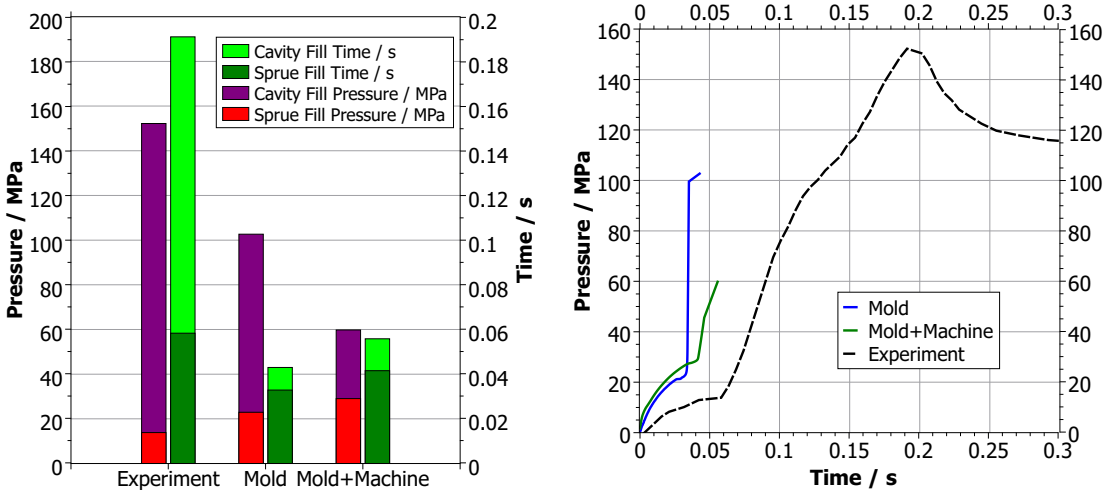

(a) Fill time and fill pressure.

(b) Pressure versus time.

Figure 9.14: Comparison of the experiments and the two investigated models of the simulations of the lever made of ceramic feedstock.

time and fill pressure for the sprue, the values of the experiments and the simulations did not differ as much as for the cavity. The underestimation of the process outcome could therefore be attributed mainly to the insufficient prediction of the fill time and pressure drop of the cavity. Especially the experimental fill time of the cavity was much larger than in the simulations.

The second simulation model yielded a higher pressure drop of the sprue, a smaller pressure drop of the cavity, a higher injection time of the sprue, and a higher injection time for the cavity than the first simulation model. Besides the cavity pressure, all parameters benefited from the implementation of the machine geometry.

Since the experimentally used feedstock had the double melt-flow index than the feedstock applied in the simulations, one would have expected a higher viscosity and thus necessary injection pressure in the simulations. Nevertheless, the reason for the deviation of the predicted values from the real values is most likely the employed viscosity model of the simulation software. The simulations could be successfully accomplished with the material model established by means of chapter 4 and the employed Cross-WLF viscosity model. The model was proven to not be satisfactory for the process simulation of micro powder injection molding in ASMI. Consequently, further improvement of the software or the separate introduction of the more advanced Cross-WLF model with Herschel-Bulkley extension is recommended to really benefit in powder injection molding from the potential of process simulations. Notwithstanding the difference in the exact used material grade, deficiencies in relation to the material data could be ruled out because of the extensive and up-to-date material characterization.

9.5 Summary and conclusion

When looking at the micro-mechanical ceramic lever and the linked micro powder injection molding, the simulation-aided design approach was applied to two new aspects in comparison to the previous chapters. Furthermore, the evolution of the mold conception from the early design with two inserts and sprue gating to the late design with a single insert and pin gating at the tail of the component was shown. Both concepts comprised mold inserts with complex internal cooling channels intended to be made by additive manufacturing.

The early design of the mold was used to investigate the influence of the multi-scale meshing approach on the model and the simulation results. In comparison to the homogeneous mesh, the element distribution of the multi-scale mesh was proven to be beneficial for the part where the mesh exhibited finer resolution. Furthermore, the simulation was still as economic, since the number of elements did not change significantly. The simulations confirmed that the mesh noticeably influenced the

process outcome related to the plastic flow during filling, the analysis of the cooling circuit, and the part warpage.

The late design of the mold was deployed in an assessment of the influence of the mold and cooling system implementation. The assessment revealed that the three models of altering comprehensiveness yielded close results for the filling and packing of the part. Yet, varying results regarding the warpage of the part were observed and could be attributed to the different cooling circuits.

Both investigations on the micro-mechanical lever had the character of a feasibility study, since the material choice of POM varied from the actually allocated ceramic feedstock. However, the full simulation of the mold and cooling circuits demonstrated that the process simulations were also beneficial for the layout and optimization of the cooling system. With regard to the emerging mold manufacture by additive manufacture and the prospect of integrating complex 3D cooling structures, the simulation and visualization of the flow, of the cooling performance, and of the impact on the part quality will become absolutely essential and reach a whole new level.

Furthermore, the conditions of the molding and the simulations for the validation with the actually allocated ceramic feedstock were discussed and enabled by the previously established material model. The molding was done by means of the finally realized mold based on the late mold conception and the knowledge previously gained from the simulations. The process simulations were successfully applied to the ceramic lever. Nonetheless, the comparison showed that the numerical results were still not satisfactory for the competitive application in the industrial design process of micro molded metallic or ceramic components. This deficiency could be mainly attributed to the particular characteristics of feedstocks, like heavy powder load or greater viscosity, in conflict with the inadequate viscosity models of the simulation software, as the material was well characterized.

10 Executive summary

Abstract This chapter summarizes the findings from the previous chapters about simulation accuracy and validation. The gained knowledge is combined into a systematic strategy for improved simulations of micro plastic parts. The most important considerations and and implementation steps are outlined.

10.1 Improved simulation strategy – entities to model

New opportunities for improved accuracy have opened up due to current and quick developments of the simulation technology. With every new release of their software packages, the software manufacturers provide new tools and improved features. Keeping up with this evolution has the objective of achieving more accurate and more reliable simulation results for micro injection molding. Consequently, new and comprehensive strategies for simulation models in micro injection molding are necessary for full benefit. The aspects of such a strategy were investigated and established in this work. The implementation methodology and model of the process simulations were demonstrated to be essential for improving the results for micro plastic parts.

In conclusion, an implementation strategy of the simulation model of a typical micro plastic part is suggested—inspired by the recommended aspects for improvement in section 3.4 and largely stimulated by the content and findings of this Ph.D. project. This strategy is based on the analysis of the whole injection molding system including the actual part, the feed system, the inserts, the mold block, the cooling or heating system, the deployed material, and the injection molding machine as described in the following and as indicated in Figure 10.1.

Nonetheless, less sophisticated simulations with the part only can be run to support major design decisions. Regarding newly developed components, the mold is not designed and available yet or the mold and molding machine are possibly still to be decided on at an early design stage. The accuracy can however be compromised.

This strategy focuses on the procedure for micro injection molding of micro plastic parts—in particular micro-patterned components. With little adaptation, it can however also be applied to process variants like multi-component molding or insert molding. The guidelines are valid for the used simulation software ASMI, but the principle can also be applied to other software tools.

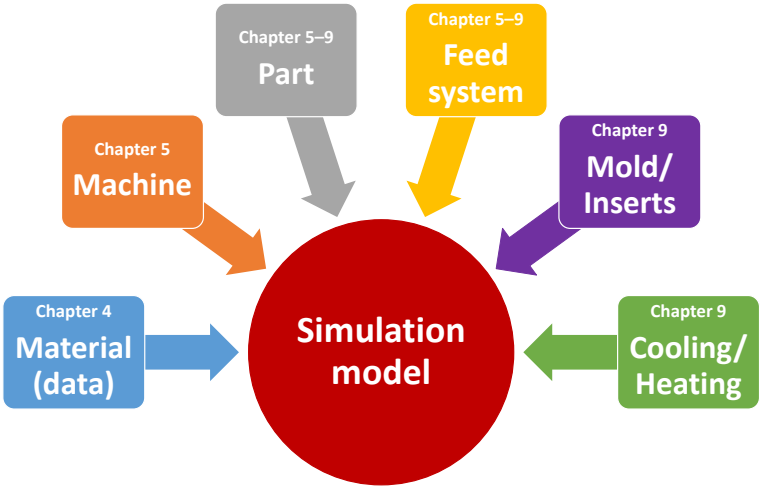

Figure 10.1: Recommended aspects to consider for a comprehensive simulation model of micro plastic parts.

1 **Material data (chapter 4)**
Although elaborate and time-consuming, correct and comprehensive material data is essential, because it is the foundation for the proper simulation of the plastic or feedstock flow. The principle "garbage in, garbage out" [144] applies, i.e. accurate simulations can only be achieved with accurate material data. The vital material data comprises information about the viscosity, the pvT behavior, the thermal properties, and the degree of filling.

2 **Injection molding machine (chapter 5)**
The implementation of the characteristics of the injection molding machine is important. The injection happens very quickly and especially conventional, hydraulic machines influence the the filling because of limited response, acceleration, and positioning accuracy. The technical specifications of the machine are supposed to be implemented in a machine model. Furthermore, the geometry of the machine should be implemented additionally for instance as hot runner. By doing so,the material compressibility and pressure drop over the nozzle and barrel are taken into account.

3 **Part (chapter 5 to 9)**
The simulation is obsolete without the part. The CAD model of the actual plastic part is therefore crucial.

4 **Feed system (chapter 5 to 9)**
The CAD model of the part should also include the complete feed system. With regard to micro parts, the feed system contributes to a large extent of the total volume and flow length. Including the feed system is thus inevitable for micro parts in order to predict the injection phase correctly. However, attention

must be paid to the warpage prediction, since the feed system mechanically constrains the part, if included in the warpage computation.

5 **Mold block and inserts (chapter 9)**
The implementation of the mold block and inserts are recommended, since they significantly influence the thermal characteristics of the whole system and hence the filling, packing, and warpage of the part. The CAD model should be a rudimentary version of the mold not considering geometrical details such as holes, fillets, screws, bolts, ejector pins, etc. Otherwise, the model becomes very complex and the time for setup and computation dramatically increases, making it impossible for user and computer hardware to handle the model in the worst case. The mold is supposed to be simplified to one CAD body for the stationary and movable platen each. Nonetheless, cavities for possible cooling channels or inserts must still be included as indicated in Figure 10.2. All aforementioned recommendations also apply to mold inserts. Unnecessary geometrical details besides the actual cavity of the plastic part should be removed from the CAD model.

6 **Cooling circuit (chapter 9)**
When the mold or inserts are implemented, cooling or heating structures must be added for providing information about the mold temperature. The CAD model must include a solid representation of the cooling channels being deployed in the mold block and inserts. The shape of the cooling channel must seamlessly fit to the respective cavities in the mold block. In the real mold, connectors between cooling channels closing the circuit are possibly located outside of the mold block or inserts. Their fluidic volume should be modeled as part of the CAD geometry of the cooling channels for proper analysis of the coolant flow.

10.2 Improved simulation strategy – implementation procedure

The improved simulation procedure for micro injection molding is summarized in the flow chart in Figure 10.3. It is based on taking into consideration the previously mentioned modules and the fact that ASMI includes a mesh algorithm. External meshers can however be used, too. The externally meshed part can be imported and subsequently analyzed in ASMI. The following details and recommendations of the approach were elaborated during this Ph.D. project.

1 **Create CAD models**
First, the CAD models of the entire assembly with part, feed system, insert, mold, and thermal management or solely of the part, if no information about the other modules is available, are created. This step is common practice for

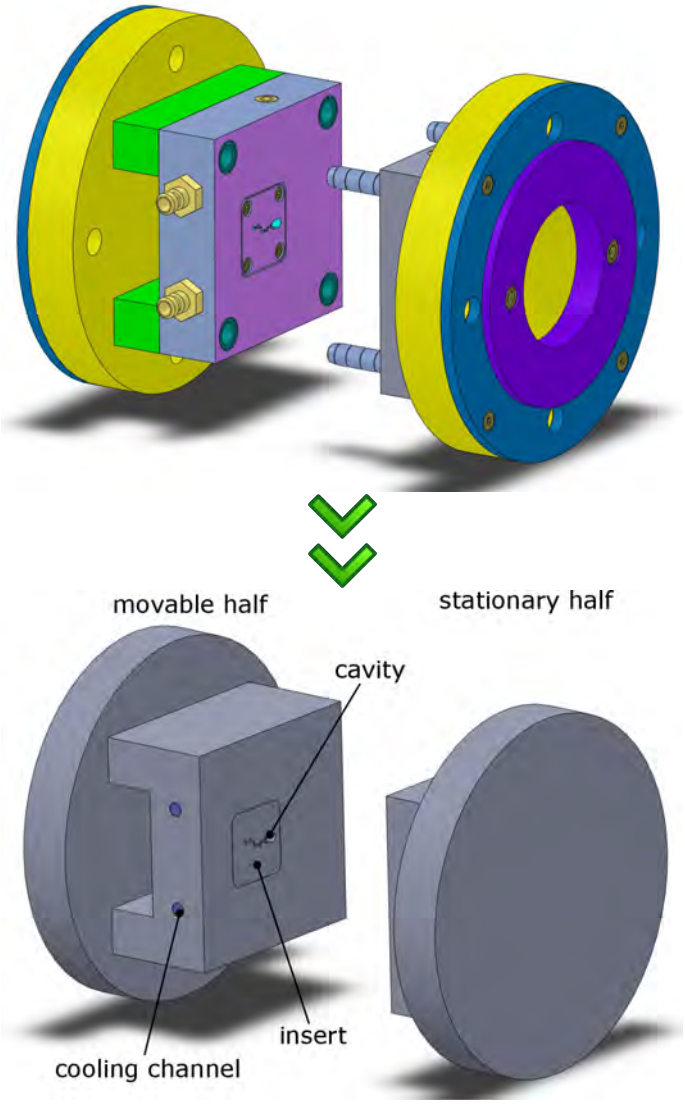

Figure 10.2: Simplification of the full CAD model of a mold including all components such as screws and bolts (top) to a reduced version suitable for process simulations in ASMI (bottom), captured in SolidWorks®.

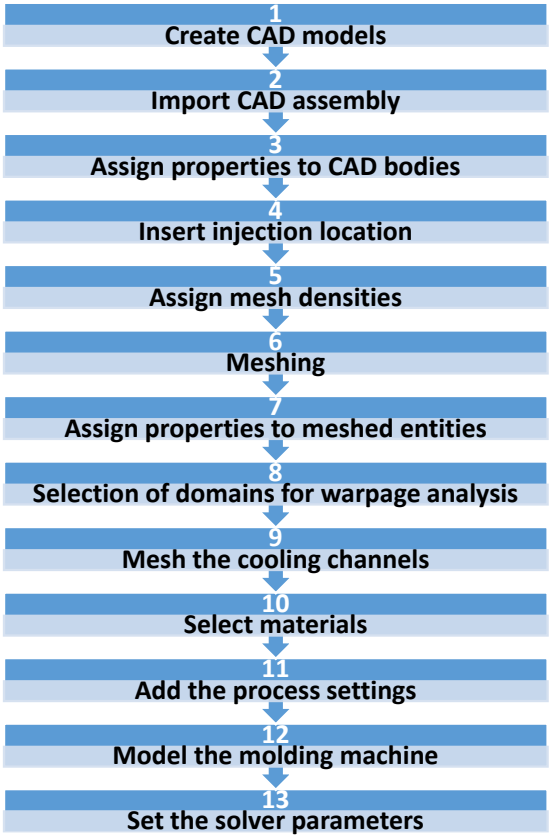

Figure 10.3: Implementation procedure for process simulations of micro plastic parts with ASMI.

the design of a new product. It can be done for instance in CAD programs like SolidWorks® or Autodesk Inventor®.

2 Import CAD assembly
The CAD files of the complete assembly or the part only are imported to ASMI. The import of the assembly as a whole is recommended to maintain correct alignment of all entities. An assembly of imported CAD bodies in ASMI is exemplary shown in Figure 10.4.

3 Assign properties to CAD bodies
The corresponding property type for meshing is assigned to the imported CAD bodies:

Part and feed system	→	"Part (3D)"
Inserts	→	"Part (3D)"
Mold halves	→	"Part (3D)"
Cooling channels	→	"Channel (3D)"

The cooling channels will be specially meshed with a CFD mesh refinement at the surface of the channels to model better the fluid flow and to capture better the heat transfer at the contact area between coolant and mold. All other elements should be meshed together to maintain mesh alignment.

4 Insert injection location
The placement prior to the meshing will lead to a mesh refinement around the injection location for smoother entering of the plastic flow.

5 Assign mesh densities
The investigated micro plastic parts can be of very different shape and complexity. Besides, the micro features can be several orders of magnitude smaller than the insert or mold. Specific elements edge lengths (mesh densities) are therefore assigned to all entities on their CAD faces. The assignment proceeds from the largest to smallest size to overwrite sequentially the edge length. As a rule of thumb, ≥ 10 elements across the thickness of the part or the shortest length of the surface are recommended, i.e. one tenth of the dominant dimension as mesh element edge length. Still, the assignment of sufficient mesh size is accompanied by visual inspection with trial and error.

6 Meshing
All entities expect for the cooling channels are meshed. It is recommended to create a 2D mesh and fix possible errors first, because the repair in the 2D domain is easier than in the 3D domain.

7 Assign properties to meshed entities
The corresponding property type is assigned to the meshed entities:

Part	→	"Part (3D)"
Feed system	→	"Cold Runner (3D)"
Inserts	→	"Mold Insert (3D)"
Mold halves	→	"Mold Block (3D)"

8 Selection of domains for warpage analysis (if conducted)
The feed system is usually removed from the actual plastic part. The warped shape of the part is therefore to be evaluated without the feed system. The relevant elements that constitute the feed system must be excluded from the warpage calculations.

9 Mesh the cooling channels
The channel inlets and outlets as well as the boundary conditions, e.g. coolant and flow control, are added before meshing. The meshing parameters have to be chosen accordingly to the channel size and shape. If the channels vary very much in size, different mesh densities can again be used. An example of meshed cooling channels inside mold inserts is depicted in Figure 10.5.

10 Select materials
The used materials for the part, the inserts, and the mold are selected. The material data can originate from the data base or independent material characterizations like in chapter 4. The data base comprises mainly unfilled and filled plastics and metals for the part and mold, respectively. Attention has to be paid to the comprehensiveness and time of acquisition of the material data.

11 Add the process settings
The general process settings, e.g. the melt and mold temperature, are defined. In order to achieve more precise results, the same type of filling and packing control as in reality is recommended to be applied, e.g. ram speed vs ram position for filling and pressure vs time for packing. The actual speed and packing profile of the allocated injection molding machine should be implemented in the software. The speed profiles can be directly derived from the injection molding cycle of existing and comparable plastic parts or estimated based on experience.

12 Model the molding machine
The specifications of the deployed injection molding machine are set. Various standard models of mainly hydraulic machines can be used or customized hydraulic or micro machines can be compiled to account for their special specifications. Additionally, the nozzle and used part of the barrel are modeled as hot runner.

13 Set the solver parameters
Since the aim is to simulate micro and small high precision plastic parts, it is necessary to adapt the solver settings of the software. Additional physical effects and software options, e.g. inertia, gravity, thermal expansion of the mold, mold core shift, are recommended to be included. Due to the very small shot size and often high injection speeds, the filling time of micro plastic parts is usually shorter than for macroscopic parts. The actual solver parameters such as time step, iterations, convergence criteria, should be adjusted accordingly.

Macroscopic plastic parts can be simulated with a model set up in the same way. However, for macro parts often a less sophisticated model without the mold block already yields accurate results. Yet, the trend in conventional injection molding goes towards modeling the whole system. Due to the very different size of the micro plastic parts and the mold, the mesh edge length often extends over several orders of magnitude from tens of micrometers up to millimeters leading to the previously seen multi-scale mesh. This multi-scale mesh is essential for micro parts.

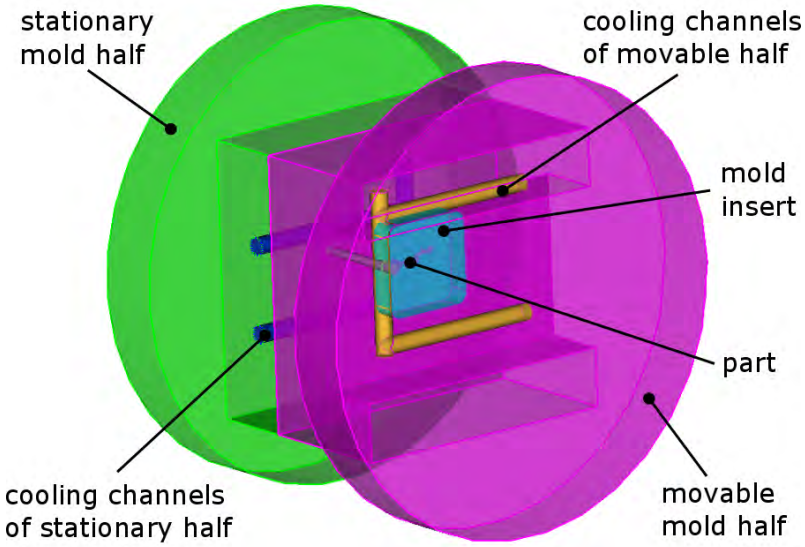

Figure 10.4: Imported assembly for the simulation including the mold platens, the insert, the cooling channels, and the actual part, captured in ASMI 2015.

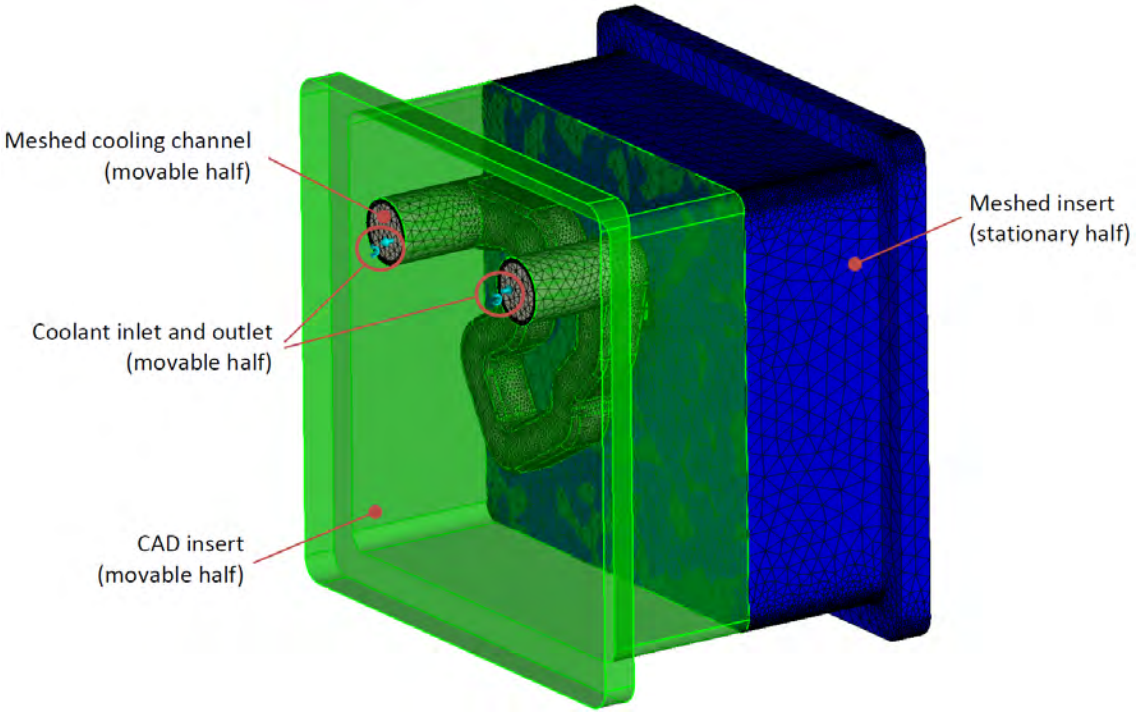

Figure 10.5: Meshed insert of stationary half (blue) and meshed cooling channel (greyish) with cooling inlet and outlet and overlay of original CAD model (green), captured in ASMI 2015.

11 Conclusion and outlook

11.1 Conclusion

Micro injection molding is widely approved as one key technology for the economic large-scale production of precise micro plastic components. This thesis was devoted to the development, design, and manufacture of complex micro parts made by micro and powder injection molding. The main focus was on the simulation-aided design for manufacture and assembly in a holistic approach and the establishment of a corresponding systematic methodology applicable to micro parts.

The development of this methodology was hence based on comprehensive material characterization and tests, the application and validation of process simulations in micro molding, mechanical simulations, concurrent engineering, design for manufacture and assembly, dimensional and geometrical tolerancing and metrology, as well as analysis and experimental characterization of the micro and powder injection molding process. The actual methodology and all its aspects reflect the initially mentioned objectives.

Methodology for process simulations of micro injection molding
The actual methodology for micro molding was developed by combining the individual parts of the simulation model for micro plastic parts to a fully comprehensive concept and taking the recommendations of previous research in this field into account. The parts being investigated throughout this thesis comprised for instance the influence of venting, the influence of the meshing, the material data, the machine characteristics, the part, the feed system, the mold and inserts, and finally the cooling and heating system of the mold. It was shown that the scope of the implementation of the simulation model can have a large impact on the simulation results, so that the relevance of these elements was proven, and the applicability and performance of process simulation software in micro molding was thus developed further. It should be mentioned that the presented methodology cannot overcome the natural limitations of simulations. Consequently, the application of the methodology is always linked to the need for sufficient computation power and for more preparation time than in conventional injection molding.

Material research
The foundation was laid by the conducted material research on the applied materials to enable concurrent simulation-aided design methods in the area of powder injection molding. Collecting and processing material data turned out as an extensive and time-consuming, but vital task for conducting injection molding simulations. The extensive material characterization on the powder feedstocks combined the thermal and rheological properties to establish a comprehensive and reliable material model. The drawn link between the material and simulation model enabled the application of process simulations to powder injection molding in the first place. Although not an innovative activity, conducting comprehensive material characterization will also remain necessary in the future for reliable simulations, since reliable data is the crucial basis, and currently available data might not be complete or already outdated.

Application of process simulations in powder injection molding
The investigations on powder injection molding and the application and validation of process simulations appeared somewhat ambiguously. The material models resulting from the material characterization could be successfully applied. In a study with a test geometry, the powder injection molding process was monitored in detail and turned out to be much more challenging than plastic injection molding—for the employed machinery as well as with regard to the simulations—due to the special properties of feedstocks. The comparison to the simulations demonstrated some insufficiency of the predicted process outcome. The simulations underestimated the fill time and pressure for the commercial feedstocks, but could match the pressure for the non-commercial feedstock. This evaluation could be confirmed by the molding and simulation of an industrially relevant ceramic micro part. The fill time and pressure were again predicted too low. Furthermore, the investigations proved the significant difference of powder feedstocks compared to plastic which needs again an additional adaptation and enhancement of design practice and tools.

The main reason for the reported deficiencies was most likely the conflict between the special characteristics of feedstocks and the inadequate viscosity model in the simulation software, as the material data was solid. Consequently, simulation of powder injection molding could be evaluated as promising, although the numerical results were still not satisfactory for the sound and competitive application of the current simulation tools in the industrial design process of micro molded metallic or ceramic components.

Characterization of the molding process by experiments and simulations
The design optimization, the development of the simulation and design methodology, the simulation validations, as well as the study on the applicability of the simulations in powder injection molding was accompanied by the analysis of the molding process. The major design decisions of the investigated micro parts were based on the predicted molding process and the analysis of various process parameters. The polymer injection

molding process was monitored as basis for the simulation validation. Besides, the machine behavior was recorded, too, in order to complete the presented simulation and modeling strategy. The integration of the machine was proven to enhance the simulation outcome. The powder injection molding process was investigated in greater detail with a mold equipped with a sensor array and provided data for the comparison between experiments and simulations. The conducted short shot study could disclose the effect of the melt cushion on the flow length.

Optimization of micro product design by concurrent engineering
The optimization of the design of the micro molded component and the corresponding mold, the core of the thesis, was performed for several industrially relevant micro products. The concurrent approach was applied to assist the material selection and testing, the part design optimization, the fulfillment of the demanded part quality, the analysis of possible feed systems, and the mold layout; basically the entire product development from the first draft to the production of the plastic part.

Suitable materials regarding the prerequisites of the parts and applications could be easily exchanged in the process simulations, and their effect on the process conditions could be studied by the design of experiments method. Design of experiments was also employed in the iterative design optimization of the examined plastic parts and their feed system. The design of experiments was again enabled by the process simulations which relatively effortlessly allowed to virtually evaluate and visualize the injection molding process of the investigated part design and material configurations. The resulting flow front, the process window, the packing, and the yielded part quality could be investigated. The gained knowledge was used again as feedback on the part and mold design. Moreover, possible issues in the filling and defects affecting the part quality could be identified promptly in the design phase avoiding costly revisions of part and mold. However, the carried out simulations did not only comprise the injection molding process, but also mechanical simulations on the loaded part in operation. The aforementioned dimensioning and tolerancing was part of the design optimization, too, for instance illustrated by the investigations on the gate thickness or the part flatness.

In conclusion, the conducted concurrent simulation-aided investigations could enhance the design phase of the presented micro plastic part. It has been demonstrated that simulations greatly supported and accelerated the design and manufacture of the micro parts which could ultimately successfully be molded. Additionally, the application- and industry-oriented nature of this work was supported by the deployment of industrially relevant software instead of particular in-house code. The present Ph.D. thesis contributed to the expansion and further development of the process simulations and their application in the process chain of high precision micro molded products.

Validation of process simulations in micro injection molding
The validation played also an important role. The validation was realized by quantitative and qualitative means. The molding of the components on conventional injection molding machines was monitored to collect information about the process and to yield plastic parts for examination. The collected process data showed the deviations of the actual machine behavior to the default software assumptions. The implementation of the machine in the software improved the simulations results. The validation of the simulations and comparison to experimental values showed that the default model underestimated the actual process outcome, but the advanced model could improve the results significantly. The flow pattern validation was carried out by comparing actual plastic parts and the simulations on a global part and local feature level. The simulation displayed good agreement on the global and local feature level, but it was proven that the filling of the micro features was challenging for the software. The hesitation effect typically occurring at micro cavities was also indicated. Hence, the simulations tools can also be used for predicting the general flow front of micro parts.

11.2 Outlook

Despite the presented advancements, process simulations linked to micro molded part remain challenging because of the particular characteristics of the micro injection molding process. As described at the beginning of this thesis, simulations are only valid in a certain context. The thesis provided sound evidence for the applicability and validity of the process simulations for the investigated micro plastic parts. However, the investigated micro parts could be classified on meticulous examination as micro-patterned parts molded by means of conventional injection molding machines. This scenario concerns the majority of industrial companies and products. Future work could therefore address the application and validation of the developed simulation strategy based on single micro parts and the employment of special micro molding machines. The even shorter shot volume and the different mechanics of the micro machines might make it necessary to adapt the simulation methodology. Furthermore, the simulation methodology aims at plastic parts made from one material. In prospect of the trend towards multi-material parts, the established holistic methodology for the design for manufacture and assembly and hence also the process simulations could be extended to the multi-component injection molding process. However, some challenges like how to implement and model the dynamic change of the mold and boundary conditions between the shots arise.

The emerging technology of additive manufacturing has arrived in the tooling and fabrication of molds for injection molding. Tools can for instance be made by selective laser sintering. This technology facilitates the incorporation of cooling channels of conformal layout or basically any other complex 3D shape in molds and insert in

order to enhance the product and process quality. However, the process of mold making will still be expensive. Therefore, process simulations including the full mold and cooling system will become even more important than they are already nowadays to optimize the cooling design and avoid design errors. The simulation and visualization of the flow, of the cooling performance, and of the impact on the part quality will become absolutely crucial—especially for micro parts which are even more delicate to the thermal management than the macroscopic parts. Still, validations have to be performed as well to be able to exploit the full potential of process simulations in the product development phase.

The development of software tools progresses fast. Practically every year, the software manufacturers release new versions with extended functionality. Due to the presented new simulation concept and these new software functionality, new questions nonetheless arise in micro injection molding, such as about the required degree of detail of the models of the mold or about the adequateness of simpler representations—both being related to the conflict between economic and accurate simulations. Another example is the known and outlined, but yet not thoroughly investigated effect of the melt cushion on molding and simulations in micro injection molding. The necessity for investigating new parameters has also arisen, and their influence on the simulation needs to be addressed in the future, e.g. the roughness of cooling channels or mold surfaces and its impact on the heat transfer coefficient. The analysis of the powder injection molding process demonstrated the influence of the cushion and its interaction with the injection speed on the flow length. This issue and the exact links between the process parameters could hence also be focus of future experimental research.

Future work linked to the powder injection molding activities should address the adaptation of the viscosity model and the necessary simulation validations to establish and exploit the potential of process simulations in the macro and micro powder molding area. Moreover, this would close a gap and empower the simulation of the complete process chain of a product made by powder injection molding, as simulations of the compounding, debinding, and sintering are also available. Because of the sparse number of powder feedstocks being generally available in software data bases, the characterization of feedstocks and compiling the available scattered data to comprehensive material models should have high priority to empower the process simulations in the first place. Furthermore, the performed short shot study provides a solid data base for a future comparison to simulated short shots. This is of interest, since the effect of the software's assumptions regarding the material compressibility and the connected size of the melt cushion and injected volume could be studied. In addition, the correct short shot prediction will be relevant especially in powder injection molding because of the heavy powder load and the resulting high inertia.

Bibliography

[1] D. Löhe and J. Haußelt. *Microengineering of Metals and Ceramics. Part I: Design, Tooling and Injection Molding*. Ed. by H. Baltes, O. Brand, G. K. Fedder, C. Hierold, J. G. Korvink, and O. Tabata. Vol. 3. Advanced Micro and Nanosystems. Weinheim, Germany: Wiley-VCH Verlag, 2005. ISBN: 9783527616725. DOI: 10.1002/9783527616725. URL: http://doi.wiley.com/10.1002/9783527616725%20http://d-nb.info/1055827579.

[2] C. Yang, X.-H. Yin, and G.-M. Cheng. "Microinjection molding of microsystem components: new aspects in improving performance". In: *Journal of Micromechanics and Microengineering* 23.9 (2013), p. 093001. ISSN: 0960-1317. DOI: 10.1088/0960-1317/23/9/093001. URL: http://iopscience.iop.org/0960-1317/23/9/093001/.

[3] C. A. Griffiths, S. S. Dimov, S. Scholz, H. Hirshy, and G. Tosello. "Process Factors Influence on Cavity Pressure Behavior in Microinjection Moulding". In: *Journal of Manufacturing Science and Engineering* 133.3 (2011), p. 031007. ISSN: 10871357. DOI: 10.1115/1.4003953. URL: http://manufacturingscience.asmedigitalcollection.asme.org/article.aspx?articleid=1439716.

[4] G. Tosello. "Precision Moulding of Polymer Micro Components". PhD Thesis. Technical University of Denmark, 2008. ISBN: 9780874216561.

[5] J. Giboz, T. Copponnex, and P. Mélé. "Microinjection molding of thermoplastic polymers: a review". In: *Journal of Micromechanics and Microengineering* 17.6 (June 2007), R96–R109. ISSN: 0960-1317. DOI: 10.1088/0960-1317/17/6/R02. URL: http://stacks.iop.org/0960-1317/17/i=6/a=R02?key=crossref.1433df5680278d815a739a8d69ab45b2.

[6] D. Yao and B. Kim. "Simulation of the filling process in micro channels for polymeric materials". In: *Journal of Micromechanics and Microengineering* 12.5 (2002), pp. 604–610. ISSN: 09601317. DOI: 10.1088/0960-1317/12/5/314. URL: http://stacks.iop.org/JMM/12/604.

[7] Micro Systems (UK) Ltd. *http://microsystems.uk.com/*. Warrington, UK. URL: http://microsystems.uk.com/ (visited on 10/29/2015).

[8] Grand View Research. *Polymer Microinjection Molding Market Analysis And Segment Forecasts To 2020*. San Francisco, CA, USA: Grand View Research, 2014. ISBN: 978-1-68038-062-0. URL: http://www.grandviewresearch.com/industry-analysis/polymer-microinjection-molding-industry.

[9] V. Piotter. "A review of the current status of MicroPIM". In: *Powder Injection Molding International* 5.3 (2011), pp. 27–42.

[10] M. Thornagel. "Simulating flow can help avoid mould mistakes". In: *Metal Powder Report* 65.3 (2010), pp. 26–29. ISSN: 00260657. DOI: 10.1016/S0026-0657(10)70072-2. URL: http://www.sciencedirect.com/science/article/pii/S0026065710700722.

[11] Hi-MICRO (High Precision Production Technologies). *http://www.hi-micro.eu*. URL: http://www.hi-micro.eu (visited on 09/04/2015).

[12] Hi-MICRO (High Precision Production Technologies). *High precision production technologies for high quality 3D micro-parts (Hi-MICRO) - Annex I - Description of Work*. 2012.

[13] G. Burkhardt, U. Hüsgen, M. Kalwa, G. Pötsch, and C. Schwenzer. "Plastics, Processing, 1. Processing of Thermoplastics". In: *Ullmann's Encyclopedia of Industrial Chemistry*. Vol. 28. Weinheim, Germany: Wiley-VCH Verlag, 2012, pp. 155–193. DOI: 10.1002/14356007.a20_663.pub2. URL: http://onlinelibrary.wiley.com/doi/10.1002/14356007.a20%7B%5C_%7D543/full%20http://doi.wiley.com/10.1002/14356007.a20%7B%5C_%7D663.pub2.

[14] D. O. Kazmer. *Injection Mold Design Engineering*. Munich: Carl Hanser Verlag, 2007. ISBN: 978-3-446-41266-8. URL: http://d-nb.info/984010149.

[15] V. Goodship. *Practical Guide to Injection Moulding*. Shawbury, UK: Rapra Technology Limited, 2004. ISBN: 1859574440.

[16] U. M. Attia and J. R. Alcock. "A review of micro-powder injection moulding as a microfabrication technique". In: *Journal of Micromechanics and Microengineering* 21.4 (Apr. 2011), p. 043001. ISSN: 0960-1317. DOI: 10.1088/0960-1317/21/4/043001. URL: http://stacks.iop.org/0960-1317/21/i=4/a=043001?key=crossref.b617dfa75908032fd8b4d79b9b9b78b7.

[17] T. V. Zhiltsova, M. S. A. Oliveira, and J. A. Ferreira. "Integral approach for production of thermoplastics microparts by injection moulding". In: *Journal of Materials Science* 48.1 (2013), pp. 81–94. ISSN: 0022-2461. DOI: 10.1007/s10853-012-6669-7. URL: http://link.springer.com/10.1007/s10853-012-6669-7.

[18] G. Tosello, A. Schoth, and H. N. Hansen. "Implementation strategies for the optimization of micro injection moulding simulations". In: *Proceedings of the 4th International Conference on Multi-Material Micro Manufacture (4M 2008)*. Ed. by S. S. Dimov and W. Menz. Cardiff, UK: Whittles Publishing, Sept. 2008.

[20] M. Philipp-Pichler. "MicroPower". In: *ATV-SEMAPP Micro-Nano Moulding: Technologies and Applications*. Odense, Denmark: ATV-SEMAPP, 2015.

[21] Klöckner DESMA Schuhmaschinen. *formicaPlast®*. Achim, Germany. URL: http://www.desma-tec.de/de/machines/micro%7B%5C_%7Dinjection/pdf/FormicaPlast%7B%5C_%7D1K%7B%5C_%7DE.pdf.

[22] M. Blömacher. *Catamold® – Ceramic and Metal Injection Molding*. 2013.

[23] D. W. Richerson. *Modern Ceramic Engineering: Properties, Processing, and Use in Design*. 3rd ed. CRC Press Taylor & Francis Group, 2005. ISBN: 9781574446937.

[24] J. Wang. *Some critical issues for injection molding*. Rijeka, Croatia: InTech, 2012. ISBN: 9789535102977. DOI: 10.5772/2294.

[25] R. Urval, S. Lee, S. V. Atre, S. J. Park, and R. M. German. "Optimisation of process conditions in powder injection moulding of microsystem components using a robust design method: part I. primary design parameters". In: *Powder Metallurgy* 51.2 (June 2008), pp. 133–142. ISSN: 0032-5899. DOI: 10.1179/174329008X284796. URL: http://www.maneyonline.com/doi/abs/10.1179/174329008X284796.

[26] D. Drummer and S. Messingschlager. "Ceramic injection molding material analysis, modeling and injection molding simulation". In: *Proceedings of the 29th International Conference of the Polymer Processing Society (PPS-29)*. Vol. 1593. AIP Publishing, 2014, pp. 582–586. ISBN: 9780735412279. DOI: 10.1063/1.4873848. URL: http://scitation.aip.org/content/aip/proceeding/aipcp/10.1063/1.4873848.

[27] H. S. Yunn, N. Muhamad, and A. B. Sulong. "Micro Powder Injection Molding (µPIM): Review". In: *Applied Mechanics and Materials* 52-54 (2011), pp. 91–96. ISSN: 16609336. DOI: 10.4028/www.scientific.net/AMM.52-54.91.

[28] D. F. Heaney. *Handbook of Metal Injection Molding*. 1st ed. Cambridge, UK: Woodhead Publishing, 2012. ISBN: 9780857090669. DOI: 10.1533/9780857096234.4.446. URL: http://www.sciencedirect.com/science/article/pii/B9780857090669500182.

[29] T. Hanemann, K. Honnef, T. Müller, and O. Weber. "New methacrylate-based feedstock systems for micro powder injection moulding". In: *Microsystem Technologies* 17.3 (Feb. 2011), pp. 451–457. ISSN: 0946-7076. DOI: 10.1007/s00542-011-1243-9. URL: http://link.springer.com/10.1007/s00542-011-1243-9.

[30] U. M. Attia, S. Marson, and J. R. Alcock. "Micro-injection moulding of polymer microfluidic devices". In: *Microfluidics and Nanofluidics* 7 (2009), pp. 1–28. ISSN: 1613-4982. DOI: 10.1007/s10404-009-0421-x. URL: http://link.springer.com/10.1007/s10404-009-0421-x.

[31] V. Piotter. *Nano- and Micro Injection Moulding of polymer, metal, and ceramic components for various applications*. 2013.

[32] H. N. Hansen, R. J. Hocken, and G. Tosello. "Replication of micro and nano surface geometries". In: *CIRP Annals - Manufacturing Technology* 60.2 (2011), pp. 695–714. ISSN: 00078506. DOI: 10.1016/j.cirp.2011.05.008. URL: http://dx.doi.org/10.1016/j.cirp.2011.05.008.

[33] T. Müller, V. Piotter, K. Plewa, M. Guttmann, H.-J. Ritzhaupt-Kleissl, and J. Haußelt. "Ceramic micro parts produced by micro injection molding: Latest developments". In: *Microsystem Technologies* 16.8-9 (2010), pp. 1419–1423. ISSN: 09467076. DOI: 10.1007/s00542-009-0992-1.

[34] P. Humphreys. "Computer Simulations". In: *PSA: Proceedings of the Biennial Meeting of the Philosophy of Science Association* 2 (1990), pp. 497–506. ISSN: 02708647. URL: http://www.jstor.org/stable/193093.

[35] S. Hartmann. "The World as a Process: Simulations in the Natural and Social Sciences". In: *Modelling and Simulation in the Social Sciences from the Philosophy of Science Point of View*. Ed. by R. Hegselmann, U. Mueller, and K. G. Troitzsch. Dordrecht: Springer Netherlands, 1996, pp. 77–100. ISBN: 978-90-481-4722-9. DOI: 10.1007/978-94-015-8686-3_5. URL: http://philsci-archive.pitt.edu/id/eprint/2412%20http://link.springer.com/10.1007/978-94-015-8686-3%7B%5C_%7D5.

[36] F. S. Costa, G. Tosello, and B. R. Whiteside. "Best practice strategies for validation of micro moulding process simulation". In: *Proceedings of the Polymer Process Engineering 2009 Conference*. University of Bradford, 2009, pp. 331–364. ISBN: 9781851432622.

[37] U. Vietri, A. Sorrentino, V. Speranza, and R. Pantani. "Improving the predictions of injection molding simulation software". In: *Polymer Engineering & Science* 51.12 (2011), pp. 2542–2551. ISSN: 00323888. DOI: 10.1002/pen.22035. URL: http://doi.wiley.com/10.1002/pen.22035.

[38] S. A. Khalilian, S. S. Park, and T. I. Freiheit. "The Application of Commercial Injection Molding Software to Micro-Component Design and Process Development". In: *Proceedings of the 8th Internation Conference on Micro Manufacturing (ICOMM 2013)*. 2013, pp. 50–56.

[39] G. Tosello, A. Gava, H. N. Hansen, H. Reinecke, G. Lucchetta, and A. Schoth. "Experimental validation of micro molding simulations using different process setting conditions". In: *Proceedings of the 67th Annual Technical Conference of the Society of Plastics Engineers 2009 (ANTEC 2009)*. Chigago, IL, USA: Society of Plastics Engineers (SPE), 2009, pp. 1787–1793. ISBN: 9781615673278.

[40] T. Nguyen-Chung, C. Loser, G. Jüttner, T. Pham, M. Obadal, and M. Gehde. "Simulation of the micro-injection moulding process: effect of the thermo-rheological status on the morphology". In: *Proceedings of the Institution of Mechanical Engineers, Part E: Journal of Process Mechanical Engineering*

225.4 (2011), pp. 224–238. ISSN: 0954-4089. DOI: 10.1177/0954408911415940. URL: http://pie.sagepub.com/lookup/doi/10.1177/0954408911415940.

[41] L. Chen, C. Kietzmann, D. Astbury, and L. Shao. *Advanced cooling simulation technologies for the injection molding process*. San Rafael, CA, USA, 2014.

[42] P. Kennedy and R. Zheng. *Flow Analysis of Injection Molds*. 2nd ed. Munich: Carl Hanser Verlag, 2013. ISBN: 9781569905128.

[43] S. J. Park, S. Ahn, T. G. Kang, S.-T. Chung, Y.-S. Kwon, S. H. Chung, S.-G. Kim, S. Kim, S. V. Atre, S. Lee, and R. M. German. "A review of computer simulations in powder injection molding". In: *International Journal of Powder Metallurgy* 46.3 (2010), pp. 37–46.

[44] A. Cramer, W. Michaeli, W. Friesenbichler, and I. Duretek. "Simulation des Spritzgießprozesses von Mikrobauteilen". In: *Zeitschrift Kunststofftechnik (Journal of Plastics Technology)* 3.1 (2007), pp. 1–26.

[45] M. Thornagel. "Injection moulding simulation: New developments offer rewards for the PIM industry". In: *Powder Injection Molding International* 6.1 (2012), pp. 65–68.

[46] C. A. Griffiths, S. S. Dimov, E. B. Brousseau, and M. S. Packianather. "The finite element analysis of melt flow behaviour in micro-injection moulding". In: *Proceedings of the Institution of Mechanical Engineers, Part B: Journal of Engineering Manufacture* 222.9 (2008), pp. 1107–1118. ISSN: 0954-4054. DOI: 10.1243/09544054JEM965. URL: http://pib.sagepub.com/lookup/doi/10.1243/09544054JEM965.

[47] J. M. Dealy and J. Wang. *Melt Rheology and its Applications in the Plastics Industry*. 2nd ed. Dordrecht, The Netherlands: Springer Science+Business Media, 2013. ISBN: 978-94-007-6394-4. DOI: 10.1007/978-94-007-6395-1. URL: http://link.springer.com/10.1007/978-94-007-6395-1.

[48] T. A. Osswald and N. Rudolph. *Polymer Rheology*. Munich: Carl Hanser Verlag, 2014. ISBN: 978-1-56990-517-3. DOI: 10.3139/9781569905234. URL: http://www.hanser-elibrary.com/doi/book/10.3139/9781569905234.

[49] Autodesk. *Autodesk Knowledge Network - Autodesk Moldflow Flex*. San Rafael, CA, USA, 2015. URL: https://knowledge.autodesk.com/support/moldflow-flex.

[50] S. Mueller, E. W. Llewellin, and H. M. Mader. "The rheology of suspensions of solid particles". In: *Proceedings of the Royal Society A: Mathematical, Physical and Engineering Sciences* 466.2116 (Apr. 2010), pp. 1201–1228. ISSN: 1364-5021. DOI: 10.1098/rspa.2009.0445. URL: http://rspa.royalsocietypublishing.org/cgi/doi/10.1098/rspa.2009.0445.

[51] G. Larsen, Z. Qiang Cheng, T. Barrière, B. S. Liu, and J. C. Gelin. "Simulation of micro injection moulding with emphasis on the formulation of feedstock viscosity: Use of non-equilibrium molecular dynamics for the determination of viscosity of multi-body fluid". In: *AIP Conference Proceedings* 1353 (2011), pp. 714–719. ISSN: 0094243X. DOI: 10.1063/1.3589599.

[52] K. H. Kate, V. P. Onbattuvelli, R. K. Enneti, S. W. Lee, S. J. Park, and S. V. Atre. "Measurements of Powder–Polymer Mixture Properties and Their Use in Powder Injection Molding Simulations for Aluminum Nitride". In: *JOM (The Journal of The Minerals, Metals & Materials Society)* 64.9 (Sept. 2012), pp. 1048–1058. ISSN: 1047-4838. DOI: 10.1007/s11837-012-0404-3. URL: http://link.springer.com/10.1007/s11837-012-0404-3.

[53] V. P. Onbattuvelli. "The Effects of Nanoparticle Addition on the Processing, Structure and Properties of SiC and AlN". PhD thesis. Oregon State University, 2010.

[54] H. Bruus. *Theoretical Microfluidics*. Oxford, UK: Oxford University Press, 2008. ISBN: 9780199235087.

[55] L. Florez. *MIM Spritzgießsimulation: Hoch entwickelte Rheologie-Modelle bieten erheblich verbesserte Präzision*. 2012. URL: http://plasticker.de/news/showartikel.php?id=121%7B%5C&%7Dbegriff=%7B%5C&%7Dbackto=/news/fachartikel.php (visited on 06/17/2015).

[56] SIGMA Engineering. "3D moulding simulation - The 'whole process' approach". In: *Metal Powder Report* 68.3 (2013), pp. 30–32. ISSN: 0026-0657. DOI: 10.1016/S0026-0657(13)70094-8. URL: http://www.sciencedirect.com/science/article/pii/S0026065713700948.

[57] D. Drummer, G. W. Ehrenstein, C. Hopmann, K. Vetter, S. Meister, T. Fischer, V. Piotter, and J. Prokop. "Innovative Prozesstechnologien für die Herstellung thermoplastischer Mikrobauteile - Analyse und vergleichende Bewertung". In: *Zeitschrift Kunststofftechnik (Journal of Plastics Technology)* 8.5 (2012), pp. 440–467.

[58] D. Yao and B. Kim. "Scaling Issues in Miniaturization of Injection Molded Parts". In: *Journal of Manufacturing Science and Engineering* 126 (Nov. 2004), pp. 733–739. ISSN: 10871357. DOI: 10.1115/1.1813479.

[59] R.-D. Chien, W.-R. Jong, and S.-C. Chen. "Study on rheological behavior of polymer melt flowing through micro-channels considering the wall-slip effect". In: *Journal of Micromechanics and Microengineering* 15 (2005), pp. 1389–1396. ISSN: 0960-1317. DOI: 10.1088/0960-1317/15/8/003. URL: http://stacks.iop.org/0960-1317/15/i=8/a=003?key=crossref.ee15bd4c7f093dc3d83dd3d54f96d1b3.

[60] G. Tosello, F. S. Costa, and H. N. Hansen. "Micro Injection Moulding High Accuracy Three-Dimensional Simulations and Process Control". In: *Proceedings of Polymer Process Engineering 11: Enhanced Polymer Processing*. Bradford, UK, 2011.

[61] L. Yu, C. G. Koh, L. J. Lee, K. W. Koelling, and M. J. Madou. "Experimental investigation and numerical simulation of injection molding with micro-features". In: *Polymer Engineering & Science* 42.5 (2002), pp. 871–888. ISSN: 1548-2634. DOI: 10.1002/pen.10998. URL: http://dx.doi.org/10.1002/pen.10998.

[62] W. B. Young. "Simulation of the filling process in molding components with micro channels". In: *Microsystem Technologies* 11.6 (2005), pp. 410–415. ISSN: 09467076. DOI: 10.1007/s00542-004-0474-4.

[63] S. J. Choi and S. K. Kim. "Multi-scale filling simulation of micro-injection molding process". In: *Journal of Mechanical Science and Technology* 25.1 (2011), pp. 117–124. ISSN: 1976-3824. DOI: 10.1007/s12206-010-1025-9. URL: www.springerlink.com/content/1738-494x.

[64] K. Tada, D. Fukuzawa, A. Watanabe, and H. Ito. "Numerical simulation for flow behaviour on micro- and nanomoulding". In: *Plastics, Rubber and Composites* 39.7 (2010), pp. 321–326. DOI: 10.1179/174328910X12777566997252.

[65] K. Tada, D. Fukuzawa, A. Watanabe, and H. Ito. "Computer Simulation for Flow Behavior on Micro- and Nano-Molding". In: *Proceedings of the 67th Annual Technical Conference of the Society of Plastics Engineers 2009 (ANTEC 2009)*. Chigago: Society of Plastics Engineers (SPE), 2009, pp. 1794–1798. ISBN: 9781615673278.

[66] C. A. Griffiths, S. S. Dimov, E. B. Brousseau, and M. S. Packianather. "Micro injection moulding: simulation of melt flow behaviour". In: *Proceedings of the 4th International Conference on Multi-Material Micro Manufacture (4M 2008)*. Ed. by S. S. Dimov and W. Menz. Cardiff, UK: Whittles Publishing, Sept. 2008, pp. 267–270. ISBN: 978-1-904445-76-0.

[67] T. Nguyen-Chung, G. Jüttner, T. Pham, G. Mennig, and M. Gehde. "Die Bedeutung präziser Randbedingungen für die Simulation des Mikrospritzgießens". In: *Zeitschrift Kunststofftechnik (Journal of Plastics Technology)* 4.6 (2008), pp. 1–25.

[68] T. Nguyen-Chung, G. Jüttner, C. Löser, T. Pham, and M. Gehde. "Determination of the heat transfer coefficient from short-shots studies and precise simulation of microinjection molding". In: *Polymer Engineering & Science* 50.1 (2010), pp. 165–173. ISSN: 00323888. DOI: 10.1002/pen.21536. URL: http://doi.wiley.com/10.1002/pen.21536.

[69] M. Heinle and D. Drummer. "Heat Transfer Coefficient in Injection Molding of Polymers". In: *International Polymer Processing* 30.4 (2015), pp. 434–441.

[70] K.-H. Grote and J. Feldhusen. *Dubbel – Taschenbuch für den Maschinenbau*. 23rd ed. Berlin: Springer-Verlag, 2011. ISBN: 9783642173059. URL: http://d-nb.info/1015041825%20http://www.springerlink.com/content/978-3-642-17306-6.

[71] M. Nakao, K. Tsuchiya, T. Sadamitsu, Y. Ichikohara, T. Ohba, and T. Ooi. "Heat transfer in injection molding for reproduction of sub-micron-sized features". In: *The International Journal of Advanced Manufacturing Technology* 38.3-4 (2008), pp. 426–432. ISSN: 0268-3768. DOI: 10.1007/s00170-007-1343-y. URL: http://link.springer.com/10.1007/s00170-007-1343-y.

[72] C. Quinard, T. Barrière, J. C. Gelin, J. P. Song, Z. Q. Cheng, and B. S. Liu. "Development of Metal/Polymer Mixtures Dedicated to Macro and Micro powder Injection Moulding : Experiments and Simulations". In: *Materials Processing and Design: Modeling, Simulation and Applications* (2007), pp. 787–792.

[73] R. Heldele, M. Schulz, D. Kauzlaric, J. G. Korvink, and J. Haußelt. "Micro powder injection molding: process characterization and modeling". In: *Microsystem Technologies* 12.10-11 (2006), pp. 941–946. ISSN: 09467076. DOI: 10.1007/s00542-006-0117-z. URL: http://www.springerlink.com/index/10.1007/s00542-006-0117-z.

[74] V. Piotter, W. Bauer, R. Knitter, M. Müller, T. Müller, and K. Plewa. "Powder injection moulding of metallic and ceramic micro parts". In: *Microsystem Technologies* 17.2 (2011), pp. 251–263. ISSN: 0946-7076. DOI: 10.1007/s00542-011-1274-2. URL: http://link.springer.com/10.1007/s00542-011-1274-2.

[75] R. Martin, M. Vick, M. Kelly, J. P. de Souza, R. K. Enneti, and S. V. Atre. "Powder injection molding of a mullite–zirconia composite". In: *Journal of Materials Research and Technology* 2.3 (2013), pp. 263–268. ISSN: 22387854. DOI: 10.1016/j.jmrt.2013.03.014. URL: http://linkinghub.elsevier.com/retrieve/pii/S2238785413000549.

[76] J. Lenz, R. K. Enneti, V. P. Onbattuvelli, K. H. Kate, R. Martin, and S. V. Atre. "Powder Injection Molding of Ceramic Engine Components for Transportation". In: *JOM (The Journal of The Minerals, Metals & Materials Society)* 64.3 (Mar. 2012), pp. 388–392. ISSN: 1047-4838. DOI: 10.1007/s11837-012-0264-x. URL: http://link.springer.com/10.1007/s11837-012-0264-x.

[77] J. P. Pennell and R. I. Winner. "Concurrent engineering: practices and prospects". In: *IEEE Global Telecommunications Conference and Exhibition. 'Communications Technology for the 1990s and Beyond' (GLOBECOM), 1989.* Vol. 1. Dallas, TX: IEEE, 1989, pp. 0647–0655. DOI: 10.1109/GLOCOM.1989.64049. URL: http://ieeexplore.ieee.org/lpdocs/epic03/wrapper.htm?arnumber=64049.

[78] J. Pennell, R. Winner, H. Bertrand, and M. Slusarczuk. "Concurrent engineering: an overview for Autotestcon". In: *Proceedings of the IEEE Automatic Testing Conference AUTOTESTCON '89: 'The Systems Readiness Technology Conference'. 'Automatic Testing in the Next Decade and the 21st Century'.* Philadelphia, PA, USA: IEEE, 1989, pp. 88–99. DOI: 10.1109/AUTEST.1989.81104. URL: http://www.scopus.com/inward/record.url?eid=2-s2.0-0024921638%7B%5C&%7DpartnerID=tZOtx3y1%20http://ieeexplore.ieee.org/lpdocs/epic03/wrapper.htm?arnumber=81104.

[79] J. Stjepandić, G. Rock, and C. Bil. *Concurrent Engineering Approaches for Sustainable Product Development in a Multi-Disciplinary Environment.* Ed. by J. Stjepandić, G. Rock, and C. Bil. London: Springer, 2013, p. 255. ISBN: 978-1-4471-4425-0. DOI: 10.1007/978-1-4471-4426-7. URL: http://link.springer.com/10.1007/978-1-4471-4426-7.

[80] J. Stjepandić, N. Wognum, and W. J. C. Verhagen. *Concurrent Engineering in the 21st Century - Foundations, Developments and Challenges.* Ed. by J. Stjepandić, N. Wognum, and W. J.C. Verhagen. Cham, Switzerland: Springer International Publishing, 2015, p. 836. ISBN: 978-3-319-13775-9. DOI: 10.1007/978-3-319-13776-6. URL: http://link.springer.com/10.1007/978-3-319-13776-6.

[81] J. P. Beaumont. *Runner and Gating Design Handbook - Tools for Successful Injection Molding.* 1st ed. Munich: Carl Hanser Verlag, 2004. ISBN: 1569903476.

[82] M. Gad-el-Hak. *MEMS - Introduction and Fundamentals.* The MEMS Handbook - Second Edition. Boca Raton, FL, USA: CRC Press Taylor & Francis Group, 2006. ISBN: 978-0-8493-9137-8.

[84] J. P. Choi, H. G. Lyu, W. S. Lee, and J. S. Lee. "Investigation of the rheological behavior of 316L stainless steel micro-nano powder feedstock for micro powder injection molding". In: *Powder Technology* 261 (2014), pp. 201–209. ISSN: 1873328X. DOI: 10.1016/j.powtec.2014.04.047. URL: http://dx.doi.org/10.1016/j.powtec.2014.04.047.

[85] B. Hausnerova. "Rheological characterization of powder injection molding compounds". In: *Polimery/Polymers* 55.1 (2010), pp. 3–11. ISSN: 00322725.

[86] A. Boudenne, L. Ibos, M. Fois, E. Gehin, and J. C. Majeste. "Thermophysical properties of polypropylene/aluminum composites". In: *Journal of Polymer Science Part B-Polymer Physics* 42.4 (2004), pp. 722–732. ISSN: 0887-6266. DOI: 10.1002/polb.10713.

[87] B. Weidenfeller, M. Höfer, and F. R. Schilling. "Thermal conductivity, thermal diffusivity, and specific heat capacity of particle filled polypropylene". In: *Composites Part A: Applied Science and Manufacturing* 35.4 (2004), pp. 423–429. ISSN: 1359835X. DOI: 10.1016/j.compositesa.2003.11.005.

[88] L. Kowalski and J. Duszczyk. “Specific heat of metal powder-polymer feedstock for powder injection molding”. In: *Journal of Materials Science Letters* 18 (1999), pp. 1417–1420.

[89] M. H. I. Ibrahim, N. Muhamad, and A. B. Sulong. “Rheological Investigation of Water Atomised Stainless Steel”. In: *International Journal of Mechanical and Materials Engineering (IJMME)* 4.1 (2009), pp. 1–8.

[90] M. W. Wang. “Microceramic injection molding of a multilayer micropatterned micropart”. In: *International Journal of Advanced Manufacturing Technology* 51.1-4 (2010), pp. 145–153. ISSN: 02683768. DOI: 10.1007/s00170-010-2597-3.

[91] L. Liu, N. H. Loh, B. Tay, S. B. Tor, Y. Murakoshi, and R. Maeda. “Mixing and characterisation of 316L stainless steel feedstock for micro powder injection molding”. In: *Materials Characterization* 54.3 (2005), pp. 230–238. ISSN: 10445803. DOI: 10.1016/j.matchar.2004.11.014. URL: http://linkinghub.elsevier.com/retrieve/pii/S1044580304002815.

[92] I. D. Jung, S. H. Kim, S. J. Park, S. J. Kim, T. G. Kang, and J. M. Park. “Rheological modeling of strontium ferrite feedstock for magnetic powder injection molding”. In: *Powder Technology* 262 (Aug. 2014), pp. 198–202. ISSN: 00325910. DOI: 10.1016/j.powtec.2014.04.073. URL: http://linkinghub.elsevier.com/retrieve/pii/S0032591014004033.

[93] J. Hidalgo, A. Jiménez-Morales, T. Barrière, J. C. Gelin, and J. Torralba. “Capillary rheology studies of INVAR 36 feedstocks for powder injection moulding”. In: *Powder Technology* 273 (2015), pp. 1–7. ISSN: 00325910. DOI: 10.1016/j.powtec.2014.12.027. URL: http://linkinghub.elsevier.com/retrieve/pii/S0032591014010092.

[94] K. H. Kate, R. K. Enneti, V. P. Onbattuvelli, and S. V. Atre. “Feedstock properties and injection molding simulations of bimodal mixtures of nanoscale and microscale aluminum nitride”. In: *Ceramics International* 39.6 (2013), pp. 6887–6897. ISSN: 02728842. DOI: 10.1016/j.ceramint.2013.02.023. URL: http://linkinghub.elsevier.com/retrieve/pii/S0272884213001843.

[95] V. V. Bilovol, L. Kowalski, J. Duszczyk, and L. Katgerman. “Characterisation of 316L powder injection moulding feedstock for purpose of numerical simulation of PIM process”. In: *Powder Metallurgy* 46.3 (2003), pp. 236–240. ISSN: 00325899. DOI: 10.1179/003258903225005367.

[96] C. S. Chen, S. C. Chen, W. L. Liaw, and R. D. Chien. “Rheological behavior of POM polymer melt flowing through micro-channels”. In: *European Polymer Journal* 44.6 (2008), pp. 1891–1898. ISSN: 00143057. DOI: 10.1016/j.eurpolymj.2008.03.007.

[97] A. L. Kelly, T. Gough, B. R. Whiteside, and P. D. Coates. "High Shear Strain Rate Rheometry of Polymer Melts". In: *Journal of Applied Polymer Science* 114 (2009), pp. 864–873.

[98] M. T. Martyn, B. R. Whiteside, P. D. Coates, P. S. Allan, G. Greenway, and P. Hornsby. "Micromoulding: consideration of processing effects on medical materials". In: *Proceedings of the 61st Annual Technical Conference of the Society of Plastics Engineers 2003 (ANTEC 2003)*. Nashville, TN, USA: Society of Plastics Engineers (SPE), 2003, pp. 2582–2586.

[99] H. Ito, T. Saito, T. Yasuhara, T. Kikutani, Y. Yamagiwa, and K. Muroi. "Evaluation of Material Properties and Processability Using The Intelligent Micro-scale Polymer Processing System". In: *Proceedings of the 63rd Annual Technical Conference of the Society of Plastics Engineers 2005 (ANTEC 2005)*. Boston, MA, USA: Society of Plastics Engineers (SPE), 2005, pp. 693–697. ISBN: 9781604234527.

[100] Autodesk. *Autodesk Simulation Moldflow Insight®*. San Francisco, CA, USA, 2015.

[101] BASF SE. *Catamold® TZP-A – Data sheet, Processing Instructions, Product Specification*. Ludwigshafen, Germany, 2008.

[102] BASF SE. *Catamold® 17-4PH – Data sheet, Processing Instructions, Product Specification*. Ludwigshafen, Germany, 2006.

[103] BASF SE. *Ultraform® N 2320 003 BK120 Q600 Polyoxymethylene – Product Information*. Ludwigshafen, Germany, 2014. URL: http://iwww.plasticsportal.com/products/dspdf.php?type=iso%7B%5C&%7Dparam=Ultraform+N+2320+003+BK120+Q600.

[104] M. Haubs, K. Kurz, and G. Sextro. "Polyoxymethylenes". In: *Ullmann's Encyclopedia of Industrial Chemistry*. Weinheim, Germany: Wiley-VCH Verlag, 2012. DOI: 10.1002/14356007.a21_591.pub2. URL: http://doi.wiley.com/10.1002/14356007.a21%7B%5C_%7D591.pub2.

[105] Merrem Materials. *Material Data Sheet POM-C natural*. Dinxperlo, The Netherlands. URL: http://www.merrem-kunststoffen.nl/UserFiles/File/Shop/pom-c%7B%5C_%7Dnatural.pdf.

[106] AMETEK Specialty Metal Products. *17-4 PH: The Workhorse of Precipitation-Hardening Stainless Steels*. Eighty Four, PA, USA. URL: http://www.ameteksmp.com/PDF/tech-sheets/08461%7B%5C_%7DAME%7B%5C_%7D17-4PH.pdf.

[107] Maxon Motor. *Innovative CIM / MIM Komponenten*. Sexau, Germany, 2010.

[108] Deutsche Edelstahlwerke. *Acidur 4542 – Werkstoffdatenblatt X5CrNiCuNb16-4 1.4542*. Witten, Germany, 2015. URL: http://bit.ly/23B5iCL.

[109] H. Lobo and C. Cohen. "Measurement of thermal conductivity of polymer melts by the line-source method". In: *Polymer Engineering and Science* 30.2 (1990), pp. 65–70. ISSN: 0032-3888. DOI: 10.1002/pen.760300202. URL: http://doi.wiley.com/10.1002/pen.760300202.

[110] E. Roos and K. Maile. *Werkstoffkunde für Ingenieure – Grundlagen, Anwendung, Prüfung*. 3rd ed. Berlin: Springer-Verlag, 2008. ISBN: 978-3-540-68398-8. DOI: 10.1007/978-3-540-68403-9. URL: http://link.springer.com/10.1007/978-3-540-68403-9.

[111] Gruppo Lucefin. *Technische Datenblätter Material X5CrNiCuNb16-4*. Esine, Italy, 2012.

[112] L. Lü, J. Y. H. Fuh, and Y.-S. Wong. *Laser-Induced Materials and Processes for Rapid Prototyping*. 1st ed. New York: Springer Science+Business Media, 2013. ISBN: 978-1461355694.

[113] R. R. Kraybill. "Estimation of thermal conductivity of polyethylene resins". In: *Polymer Engineering and Science* 21.3 (Feb. 1981), pp. 124–128. ISSN: 0032-3888. DOI: 10.1002/pen.760210303. URL: http://doi.wiley.com/10.1002/pen.760210303.

[114] Göttfert Werkstoff-Prüfmaschinen GmbH. *Product description Rheograph 25*. Buchen, Germany, 2007.

[115] G. Schramm. *A Practical Approach to Rheology and Rheometry*. 2nd ed. Karlsruhe, Germany: Gebrueder HAAKE, 1994. URL: http://www.polymer.cn/bbs/File/UserFiles/UpLoad/200904010309415s.pdf.

[116] E.-O. Reher. "Zur Rheologie von Polymerschmelzen". In: *Sitzungsberichte der Leibniz-Sozietät* 43 (July 2000), pp. 5–23.

[117] A. Göttfert, E.-O. Reher, and I. M. Balagula. "Kapillarrheometer für die Kunststoffverarbeitung. Simulation rheologischer Prozesse". In: *KGK Kautschuk Gummi Kunststoffe* 53.9 (2000), pp. 512–517. ISSN: 09483276.

[118] U. Wolfmeier, H. Schmidt, F.-L. Heinrichs, G. Michalczyk, W. Payer, W. Dietsche, K. Boehlke, G. Hohner, and J. Wildgruber. "Waxes". In: *Ullmann's Encyclopedia of Industrial Chemistry*. Vol. 39. Weinheim, Germany: Wiley-VCH Verlag, 2012, pp. 111–172. DOI: 10.1002/14356007.a28_103. URL: http://doi.wiley.com/10.1002/14356007.a28%7B%5C_%7D103.

[119] A. Islam. "Two component micro injection moulding for moulded interconnect devices". PhD Thesis. Technical University of Denmark, 2008.

[120] The Society of the Plastic Industry (SPI). *Standards & Practices of Plastics Molders - Guidelines for Molders and Their Customers*. Washington, D.C., USA, 1998.

[121] DesignInfoSystem. *Plastic Injection Molding Part Tolerance*. URL: http://www.designinfosystem.com (visited on 04/01/2016).

[122] T. A. Osswald, E. Baur, S. Brinkmann, K. Oberbach, and E. Schmachtenberg. *International Plastics Handbook*. 4th ed. Munich: Carl Hanser Verlag, 2006. ISBN: 9783446229051.

[123] A. E. Campo. *The Complete Part Design Handbook - For Injection Molding of Thermoplastics*. Munich: Carl Hanser Verlag, 2006. ISBN: 9781569903759.

[124] W. Kleppmann. *Versuchsplanung – Produkte und Prozesse optimieren*. 7th ed. Munich: Carl Hanser Verlag, 2011. ISBN: 9783446427747.

[125] K. Siebertz, D. van Bebber, and T. Hochkirchen. *Statistische Versuchsplanung – Design of Experiments (DoE)*. VDI-Buch. Berlin: Springer-Verlag, 2010. ISBN: 9783642054938. DOI: 10.1007/978-3-642-05493-8. URL: http://www.springerlink.com/index/10.1007/978-3-642-05493-8.

[126] E. Wintermantel and S.-W. Ha. *Medizintechnik*. 5th ed. Berlin: Springer-Verlag, 2009. ISBN: 9783540939351. DOI: 10.1007/978-3-540-93936-8. URL: http://link.springer.com/10.1007/978-3-540-93936-8.

[127] Comité Européen de Normalisation (CEN). *EN ISO 1101 – Geometrical product specifications (GPS) – Geometrical tolerancing – Tolerances of form, orientation, location and run-out (ISO 1101:2012, including Cor 1:2013)*. 2013.

[128] Comité Européen de Normalisation (CEN). *CEN ISO/TS 12781-1 – Geometrical product specifications (GPS) – Flatness – Part 1: Vocabulary and parameters of flatness (ISO/TS 12781-1:2003)*. 2007.

[129] GD&T Basics. *GD&T Basics*. URL: http://www.gdandtbasics.com/ (visited on 04/15/2015).

[130] M. Burns. *Automated Fabrication*. Prentice Hall, 1993. ISBN: 978-0131194625. URL: http://www.fabbers.com/tech/STL%7B%5C_%7DFormat.

[131] Comité Européen de Normalisation (CEN). *EN ISO 527-2 – Plastics – Determination of tensile properties – Test conditions for moulding and extrusion plastics (ISO 527-2:2012)*. 2012.

[132] Comité Européen de Normalisation (CEN). *EN ISO 294-1 – Plastics – Injection moulding of test specimens of thermoplastic materials – Part 1: General principles, and moulding of multipurpose and bar test specimens (ISO 294-1:1996)*. 1998.

[133] DSM Engineering Plastics. *Design Guide - Performance And Value With Engineering Plastics*. Evansville, IN, USA, 2005.

[134] Du Pont de Nemours International. *DuPont Technische Kunststoffe – Allgemeine Konstruktionsprinzipien – Modul I*. Genf, Switzerland, 1997.

[135] Bayer MaterialScience. *Part and Mold Design - A Design Guide*. Pittsburg, PA, USA, 2000.

[136] BÖHLER-UDDEHOLM Deutschland. *Uddeholm Orvar® Supreme*. Düsseldorf, Germany, 2008. URL: http://www.uddeholm.de/german/files/downloads/orvar%7B%5C_%7Dsupreme-ger%7B%5C_%7Dp%7B%5C_%7D0808%7B%5C_%7De3.pdf.

[137] G. Menges, W. Michaeli, and P. Mohren. *How to Make Injection Molds*. 3rd ed. Munich: Carl Hanser Verlag, 2001. ISBN: 978-3-446-21256-5. DOI: 10.3139/9783446401808. URL: http://www.hanser-elibrary.com/doi/book/10.3139/9783446401808.

[138] P. Jones. *The Mould Design Guide*. Shawbury, UK: Smithers Rapra Technology, 2008. ISBN: 9781847350886.

[139] F. Johannaber. *Kunststoff-Maschinenführer*. 4th ed. Munich: Carl Hanser Verlag, 2003. ISBN: 9783446220423.

[140] H. K. Rasmussen. *41736 Polymer Processes*. Tech. rep. Kongens Lyngby, Denmark: Technical University of Denmark, 2013, p. 106.

[141] Hi-MICRO (High Precision Production Technologies). *Technical Specifications of Part Demonstrators*. 2013.

[142] Wittmann Kunststoffgeräte Ges.m.b.H. *TEMPRO Temperiergeräte*. Vienna, Austria. URL: http://schroer-technik.de/PDF/temper/tempro%7B%5C_%7D02%7B%5C_%7D11%7B%5C_%7D07ges.pdf.

[143] gwk Gesellschaft Wärme Kältetechnik mbH. *Baureihe teco Temperiergeräteprogramm*. Meinerzhagen, Germany, 2015. URL: https://www.gwk.com/de/teco-cs.html?file=files/redakteur/downloads/prospekte/teco%7B%5C_%7Dtemperiergeraete/teco/teco%7B%5C_%7DDE.pdf.

[144] W. Lidwell, K. Holden, and J. Butler. *Universal Principles of Design*. 2nd ed. Beverly, MA, USA: Rockport Publishers, 2010. ISBN: 978-1592535873. URL: https://books.google.dk/books?id=l0QPECGQySYC%7B%5C&%7Dprintsec=frontcover%7B%5C#%7Dv=onepage%7B%5C&%7Dq%7B%5C&%7Df=false.

List of Publications

Peer-reviewed journal papers

- D. M. Marhöfer, G. Tosello, A. Islam, and H. N. Hansen. "Gate Design in Injection Molding of Microfluidic Components using Process Simulations". In: *Journal of Micro- and Nano-Manufacturing* 4.June (2016), p. 025001. DOI: 10.1115/1.4032302
- A. Islam, N. Giannekas, D. M. Marhöfer, G. Tosello, and H. N. Hansen. "Experimental investigation of comparative process capabilities of metal and ceramic injection moulding for precision applications". In: *Journal of Micro and Nano-Manufacturing* 4.September (2016), p. 031003. DOI: 10.1115/1.4033820
- D. M. Marhöfer, G. Tosello, A. Islam, H. N. Hansen, T. Müller, and V. Piotter. "Comprehensive characterization of metal and ceramic feedstocks for powder injection molding simulations". In: *(manuscript, to be decided)* (2016)

Conference proceedings as first author

- D. M. Marhöfer, T. Müller, G. Tosello, A. Islam, H. N. Hansen, and V. Piotter. "Validation of precision powder injection molding process simulations using a spiral test geometry". In: *Proceedings of the PPS2015 Regional Conference Europe & Africa*. Graz, Austria: Polymer Processing Society (PPS), 2015
- D. M. Marhöfer, G. Tosello, A. Islam, and H. N. Hansen. "Comparative analysis of different process simulation settings of a micro injection molded part featuring conformal cooling". In: *Proceedings of the 15th International Conference of the European Society for Precision Engineering and Nanotechnology (euspen)*. Leuven, Belgium, 2015, pp. 65–66. ISBN: 978-0-9566790-7-9
- D. M. Marhöfer, G. Tosello, A. Islam, and H. N. Hansen. "Gate design in injection molding of microfluidic components using process simulations". In: *Proceedings of the euspen Micro/Nano Manufacturing Workshop 2015*. Teddington, UK: European Society for Precision Engineering and Nanomanufacturing (euspen), 2015

- D. M. Marhöfer, G. Tosello, A. Islam, and H. N. Hansen. "Gate Design in Injection Molding of Microfluidic Components using Process Simulations". In: *Proceedings of the 11th International Conference on Multi-Material Micro Manufacturing (4M/ICOMM 2015)*. Milan, Italy: Research Publishing Services, 2015, pp. 546–549. ISBN: 978-981-09-4609-8. DOI: 10.3850/978-981-09-4609-8_136
- D. M. Marhöfer, G. Tosello, A. Islam, and H. N. Hansen. "Improving the accuracy of micro injection moulding process simulations". In: *Proceedings of the euspen Micro/Nano Manufacturing Workshop 2013*. Karlsruhe, Germany: European Society for Precision Engineering and Nanomanufacturing (euspen), 2013
- D. M. Marhöfer, G. Tosello, H. N. Hansen, and A. Islam. "Advancements on the Simulation of the Micro Injection Moulding Process". In: *Proceedings of the 10th International Conference on Multi-Material Micro Manufacture (4M)*. San Sebastian, Spain: Research Publishing Services, 2013, pp. 77–81. ISBN: 978-981-07-7248-2. DOI: 10.3850/978-981-07-7247-5-426

Conference proceedings as co-author

- A. Islam, N. Giannekas, D. M. Marhöfer, G. Tosello, and H. N. Hansen. "A Comparative Study of Metal and Ceramic Injection Moulding for Precision Applications". In: *Proceedings of the 11th International Conference on Multi-Material Micro Manufacturing (4M/ICOMM 2015)*. Milan, Italy: Research Publishing Services, 2015, pp. 567–570. ISBN: 9789810946098. DOI: 10.3850/978-981-09-4609-8_134
- A. Islam, N. Giannekas, D. M. Marhöfer, G. Tosello, and H. N. Hansen. "The shrinkage behavior and surface topographical investigation for micro metal injection molding". In: *Proceedings of the 30th International Conference of the Polymer Processing Society (PPS)*. Cleveland, OH, USA: AIP Publishing, 2015, p. 110007. ISBN: 978-0-7354-1309-2. DOI: 10.1063/1.4918482. URL: http://scitation.aip.org/content/aip/proceeding/aipcp/10.1063/1.4918482
- A. Islam, N. Giannekas, D. M. Marhöfer, G. Tosello, and H. N. Hansen. "Experimental investigation on shrinkage and surface replication of injection moulded ceramic parts". In: *Proceedings of the 4th International Conference on Nanomanufacturing (nanoMan 2014)*. Bremen, Germany, 2014

Miscellaneous publications and proceedings

- D. M. Marhöfer. "Implementation and application of material models in injection molding simulations using powder feedstocks". In: *Connect! European Moldflow User Meeting 2015*. Frankfurt, Germany: MF Software, 2015
- D. M. Marhöfer. "Gate design in injection molding of microfluidic components using process simulations". In: *ATV-SEMAPP Micro-Nano Moulding: Technologies and Applications 2015*. Odense, Denmark, 2015
- D. M. Marhöfer. "Advancements on the simulation of the micro injection moulding process". In: *ATV-SEMAPP Micro-Nano Moulding: Technologies and Applications 2013*. Kongens Lyngby, Denmark: ATV-SEMAPP, 2013

A Supplementary information to chapter 4

A.1 Processing data of the disc samples

The following section contains the detailed information of the molding of the disc samples used for the material characterization.

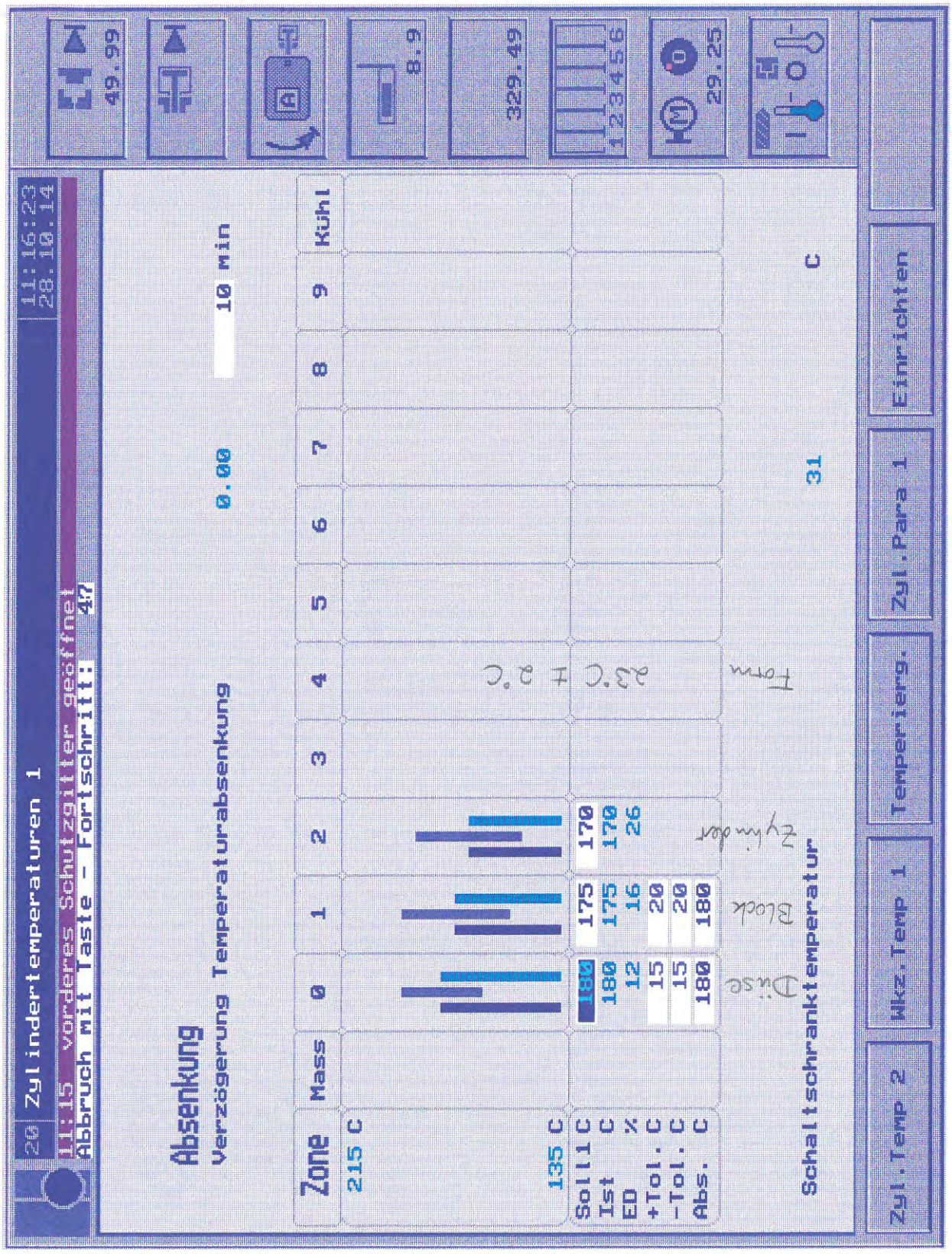

Catamold 17-4 PH A

Catamold TZP-A

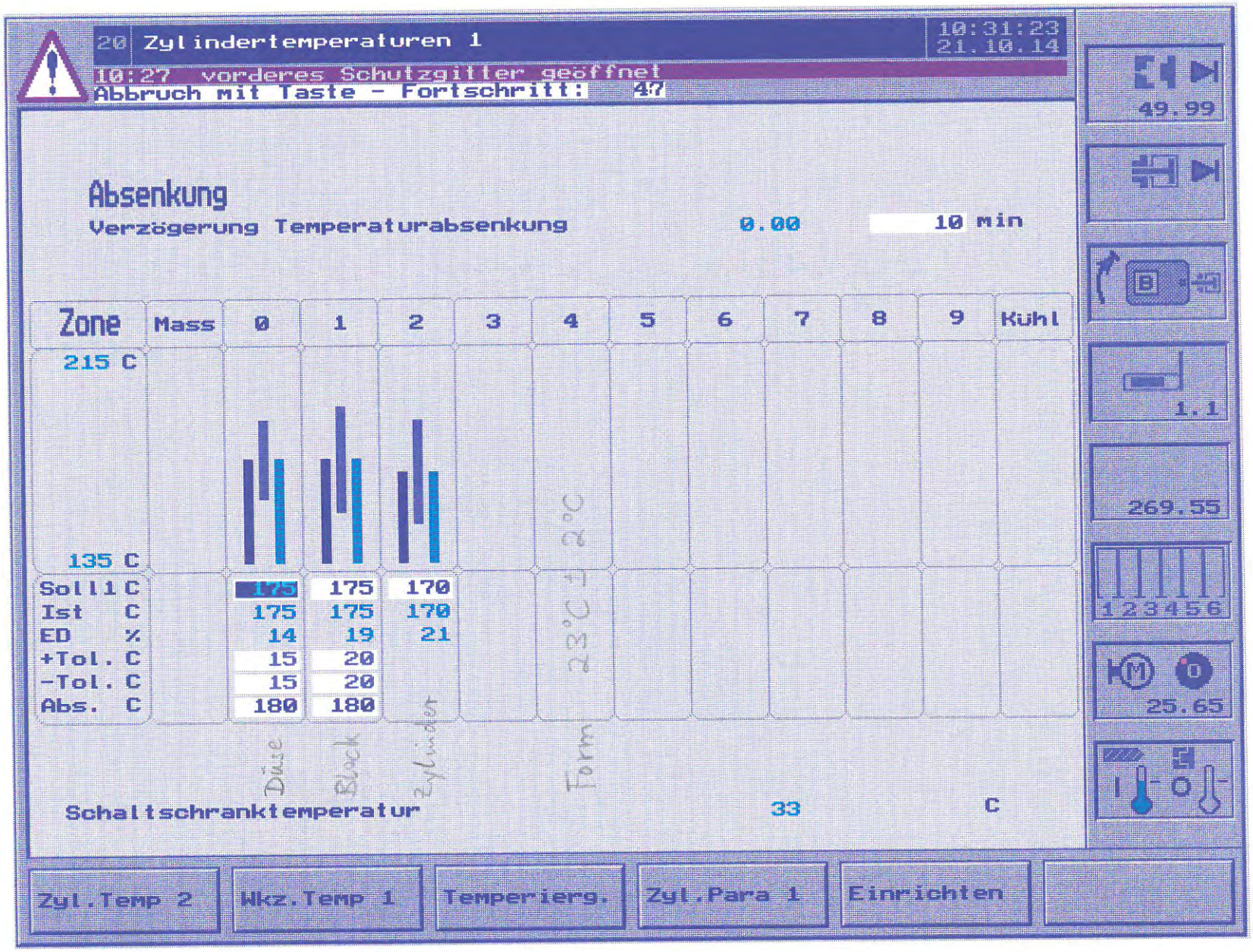

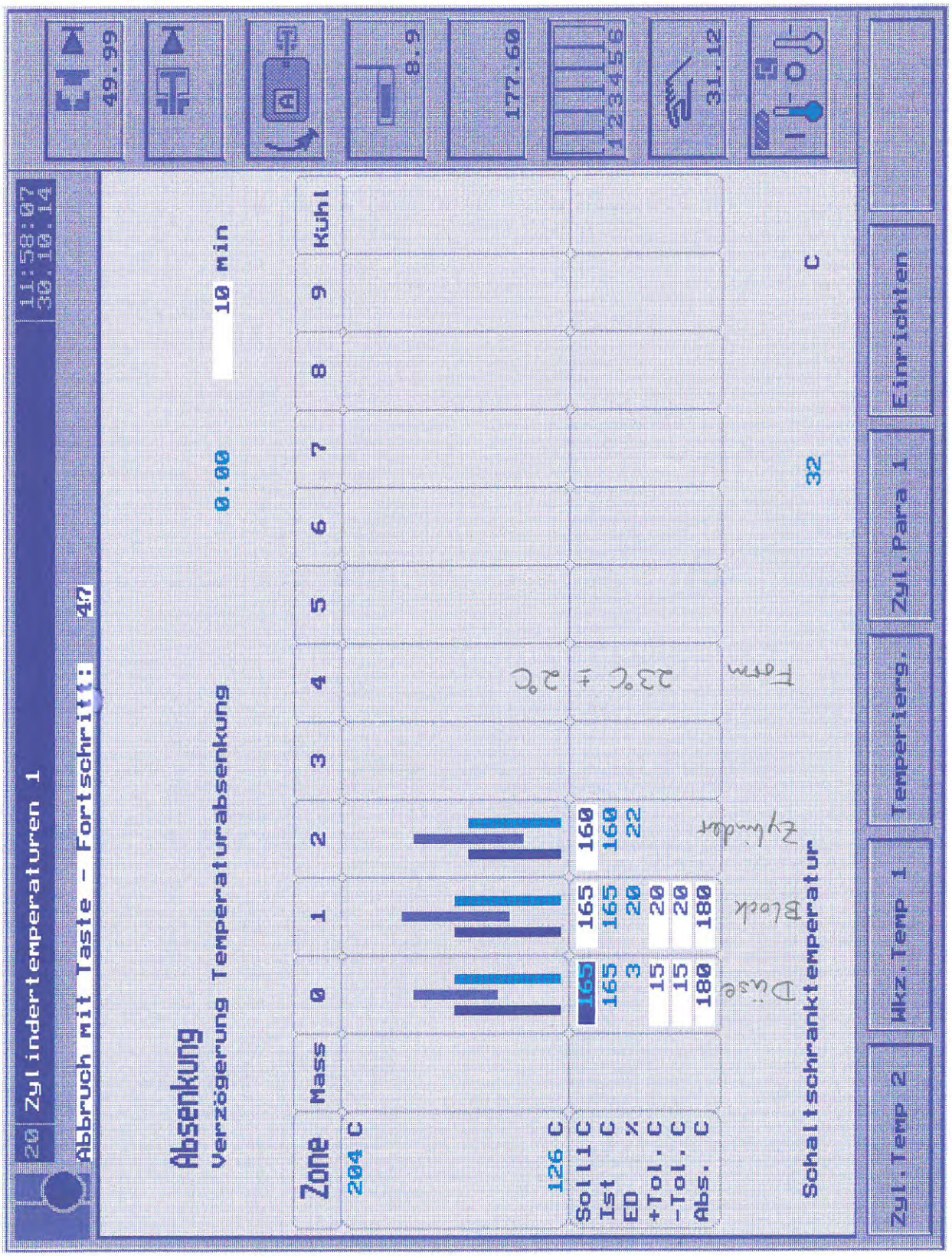
20 Zylindertemperaturen 1
11:58:07
30.10.14
Abbruch mit Taste - Fortschritt: 47
49.99
8.9
177.60
123456
31.12
Absenkung
Verzögerung Temperaturabsenkung
0.00
10 min
Zone
Mass
0 1 2 3 4 5 6 7 8 9 Kühl
204 C
126 C
Soll C 165 165 160
Ist C 165 165 160
ED % 3 20 22
+Tol. C 15 20
-Tol. C 15 20
Abs. C 180 180
Düse
Block
Zylinder
Form
23°C ± 2°C
Schaltschranktemperatur
32 C
Zyl.Temp 2
Wkz.Temp 1
Temperierg.
Zyl.Para 1
Einrichten

KIT 17-424

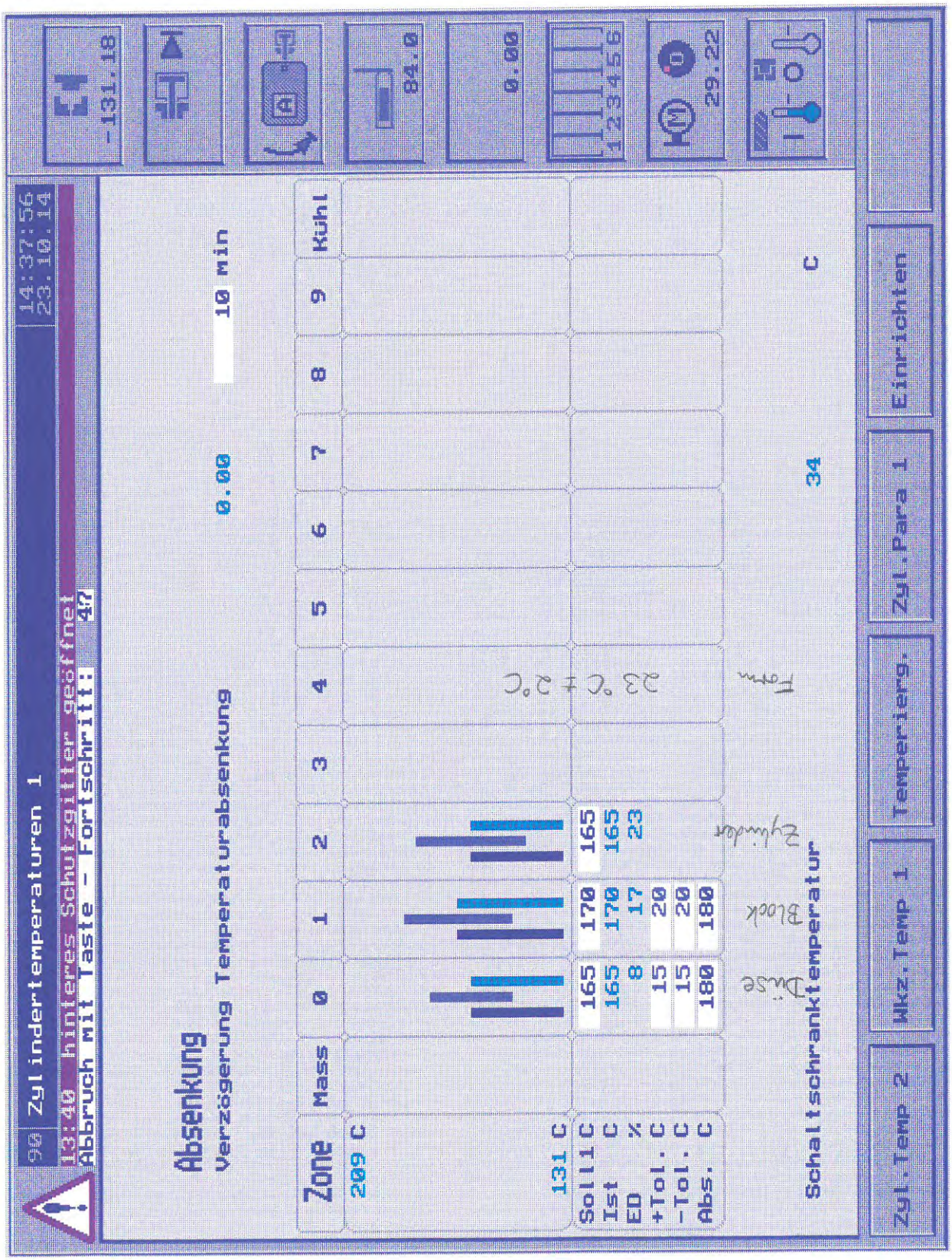
99 Zylindertemperaturen 1
14:37:56
23.10.14
13:40 hinteres Schutzgitter geöffnet
Abbruch mit Taste - Fortschritt: 47
-131.18
84.0
0.00
29.22
Absenkung
Verzögerung Temperaturabsenkung
0.00
10 min
Zone
Mass
0
1
2
3
4
5
6
7
8
9
Kühl
209 C
131 C
Soll C
Ist C
ED %
+Tol. C
-Tol. C
Abs. C
165 170 165
165 170 165
8 17 23
15 20
15 20
180 180
Düse
Block
Zylinder
Form
Schaltschrankkemperatur
34 C
Zyl.Temp 2
Mkz.Temp 1
Temperierg.
Zyl.Para 1
Einrichten

KIT ZrO_2

A.2 DSC curves for powder content determination of feedstocks

This section contains the measured DSC curves for Catamold® 17-4PHA and Catamold® TZP-A.

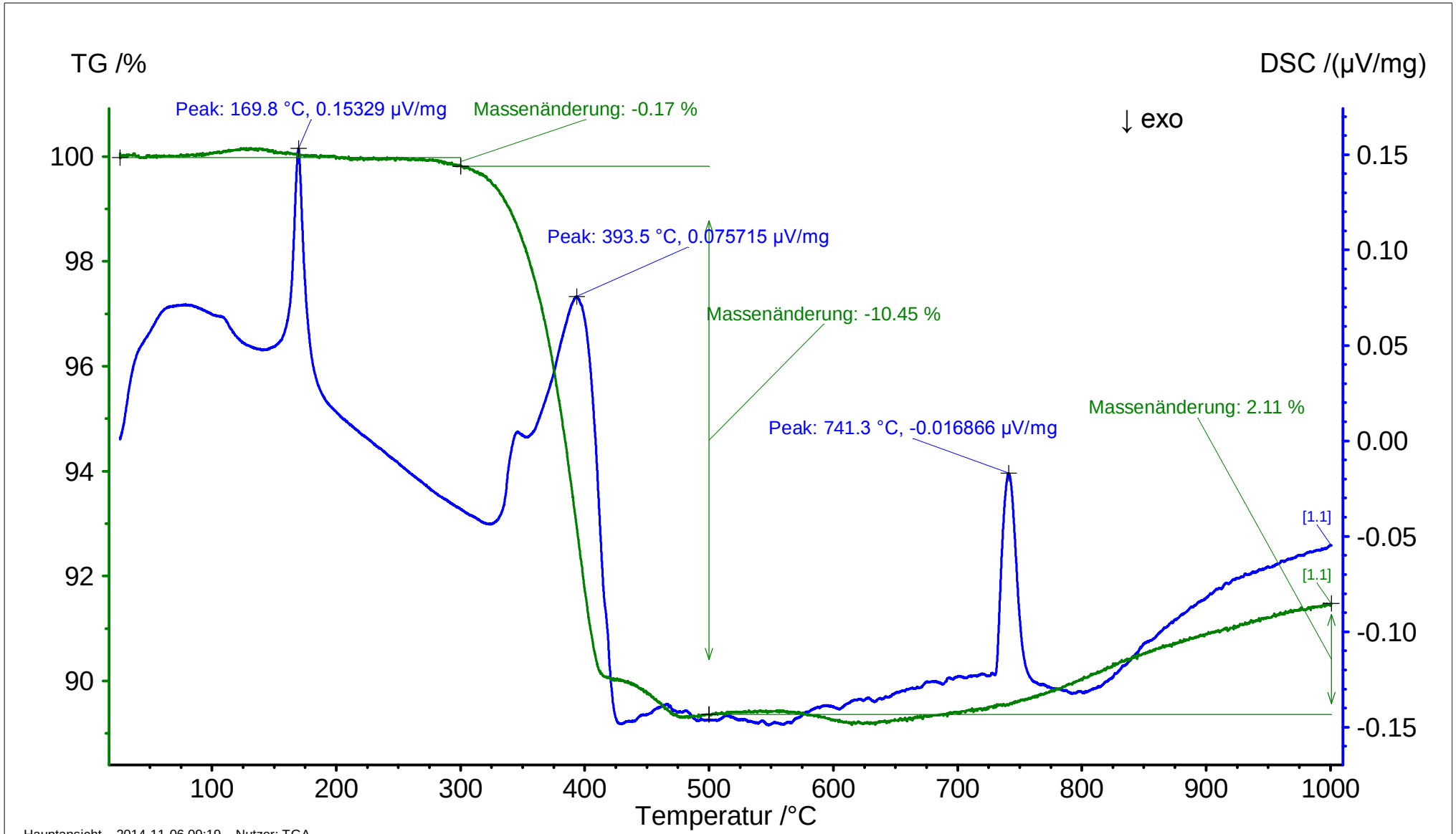

Hauptansicht 2014-11-06 09:19 Nutzer: TGA

Gerät :	NETZSCH STA 409 C/CD			**Datei :**	D:\TGA-Daten\TG-DSC\Messungen\Catamold_17-4PHA.ngb-dss		
Projekt :	Hanemann-Marhöfer	**Probe :**	Catamold_17-4PHA, 65.9 mg	**Probentr./TC :**	DSC(/TG) HIGH RG 3 / S	**TG Korr/Messber :**	020/500 mg
Proben-ID :	Catamold_17-4PHA	**Material :**	Feedstock	**Modus /Messtyp :**	DSC-TG / Probe + Korrektur	**DSC Korr/Messber :**	020/500 µV
Datum/Zeit :	05.11.2014 16:27:32	**Korrektur-Datei :**	Korr1000_10_N2.ngb-bss	**Segmente :**	1/3		
Labor :	WPT	**Tempkal./Empf. Datei :**	TCALZERO.TCX / SENSZERO.EXX	**Tiegel :**	DSC/TG pan Al2O3		
Operator :	UG	**Bereich :**	25°C/10.0(K/min)/1000°C	**Atmosphäre :**	<kein Gas>/--- / AIR(80/20)/--- / <kein Gas>/---		

Erzeugt mit NETZSCH Proteus Software

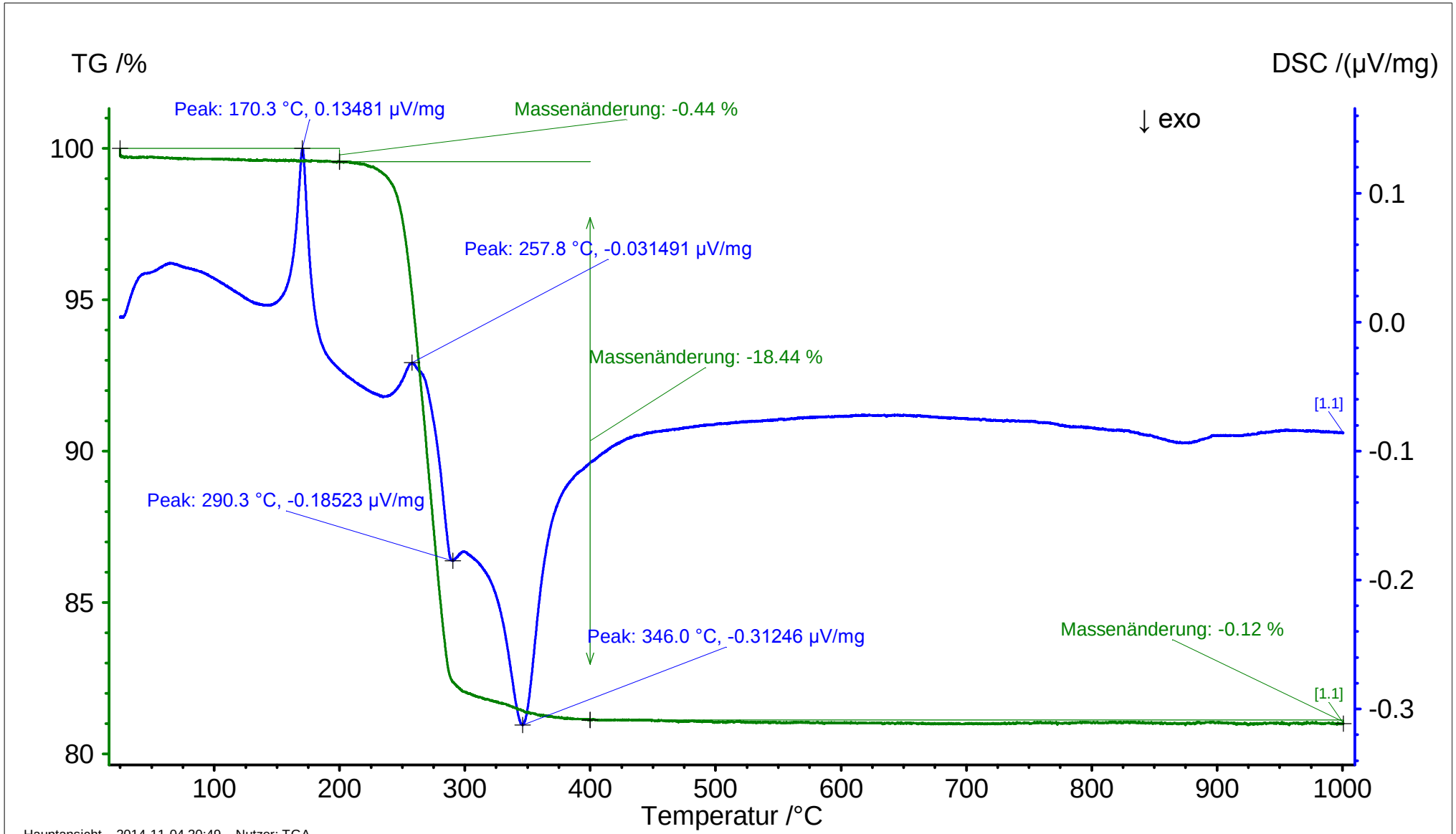

Hauptansicht 2014-11-04 20:49 Nutzer: TGA

Gerät :	NETZSCH STA 409 C/CD			**Datei :**	D:\TGA-Daten\TG-DSC\Messungen\Captamold_ZrO2_2.ngb-dss		
Projekt :	Hanemann-Marhöfer	**Probe :**	Captamold_ZrO2_2, 47.3 mg	**Probentr./TC :**	DSC(/TG) HIGH RG 3 / S	**TG Korr/Messber :**	020/500 mg
Proben-ID :	Captamold_ZrO2_2	**Material :**	Feedstock	**Modus /Messtyp :**	DSC-TG / Probe + Korrektur	**DSC Korr/Messber :**	020/500 µV
Datum/Zeit :	04.11.2014 15:14:04	**Korrektur-Datei :**	Korr1000_10.ngb-bss	**Segmente :**	1/3		
Labor :	WPT	**Tempkal./Empf. Datei :**	TCALZERO.TCX / SENSZERO.EXX	**Tiegel :**	DSC/TG pan Al2O3		
Operator :	UG	**Bereich :**	25°C/10.0(K/min)/1000°C	**Atmosphäre :**	<kein Gas>/--- / AIR(80/20)/--- / <kein Gas>/---		

Erzeugt mit NETZSCH Proteus Software

A.3 Viscosity and *pvT* fitting for Catamold® TZP-A

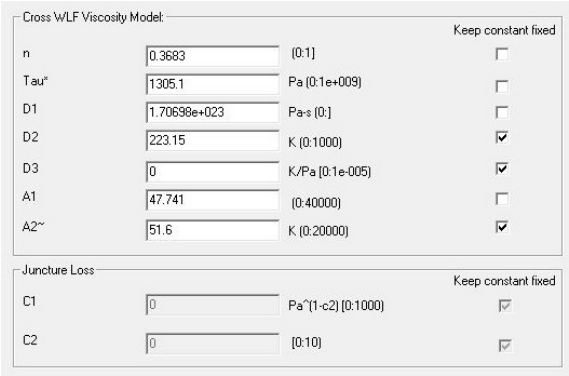

Figure A.2: Coefficients of the ASMI data fit for the viscosity of Catamold® TZP-A.

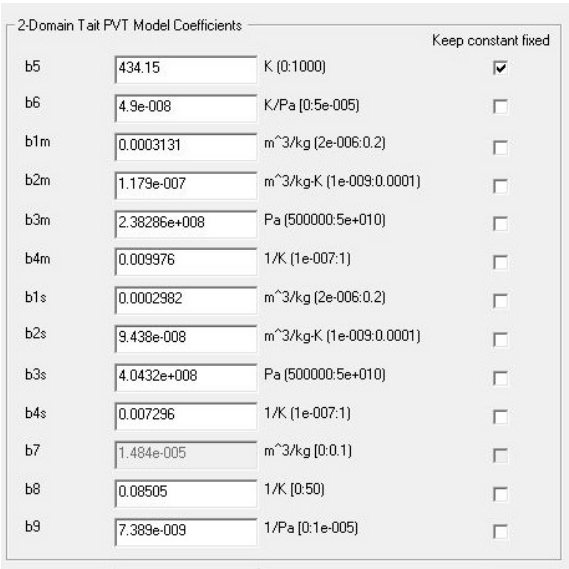

Figure A.4: Coefficients of the ASMI data fit for the *pvT* data of Catamold® TZP-A.

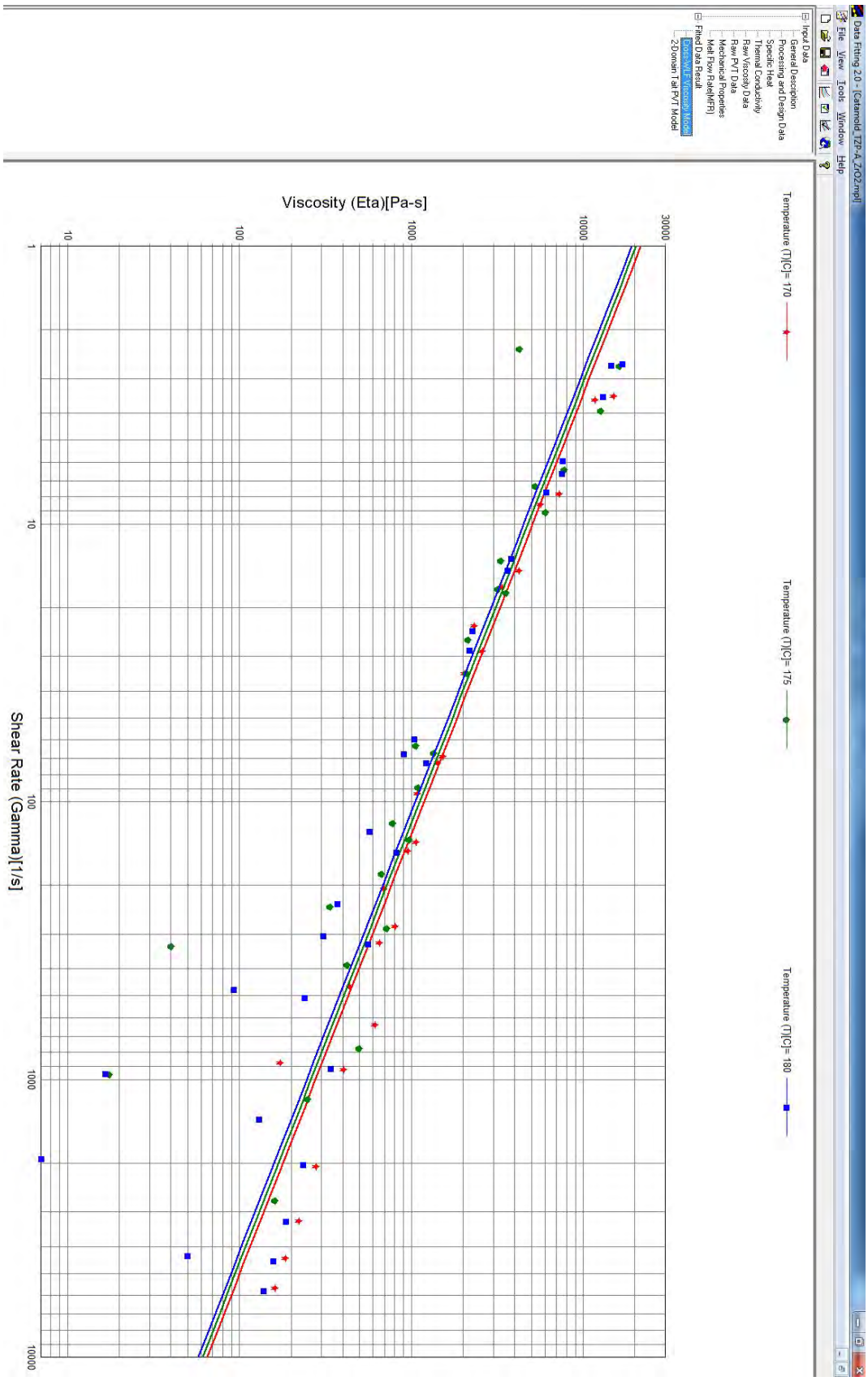

Figure A.1: ASMI data fit for the viscosity of Catamold® TZP-A.

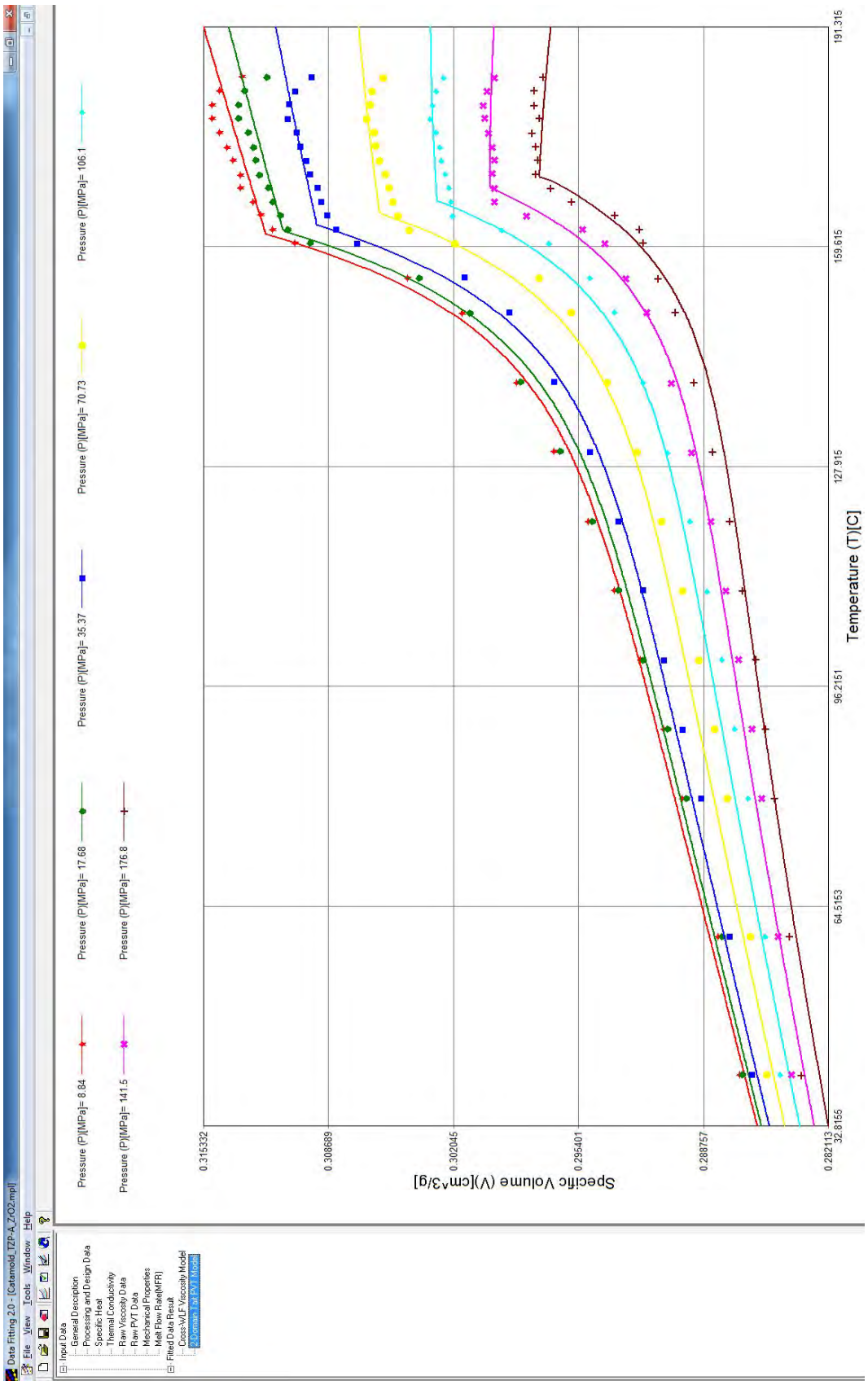

Figure A.3: ASMI data fit for the pvT data of Catamold® TZP-A.

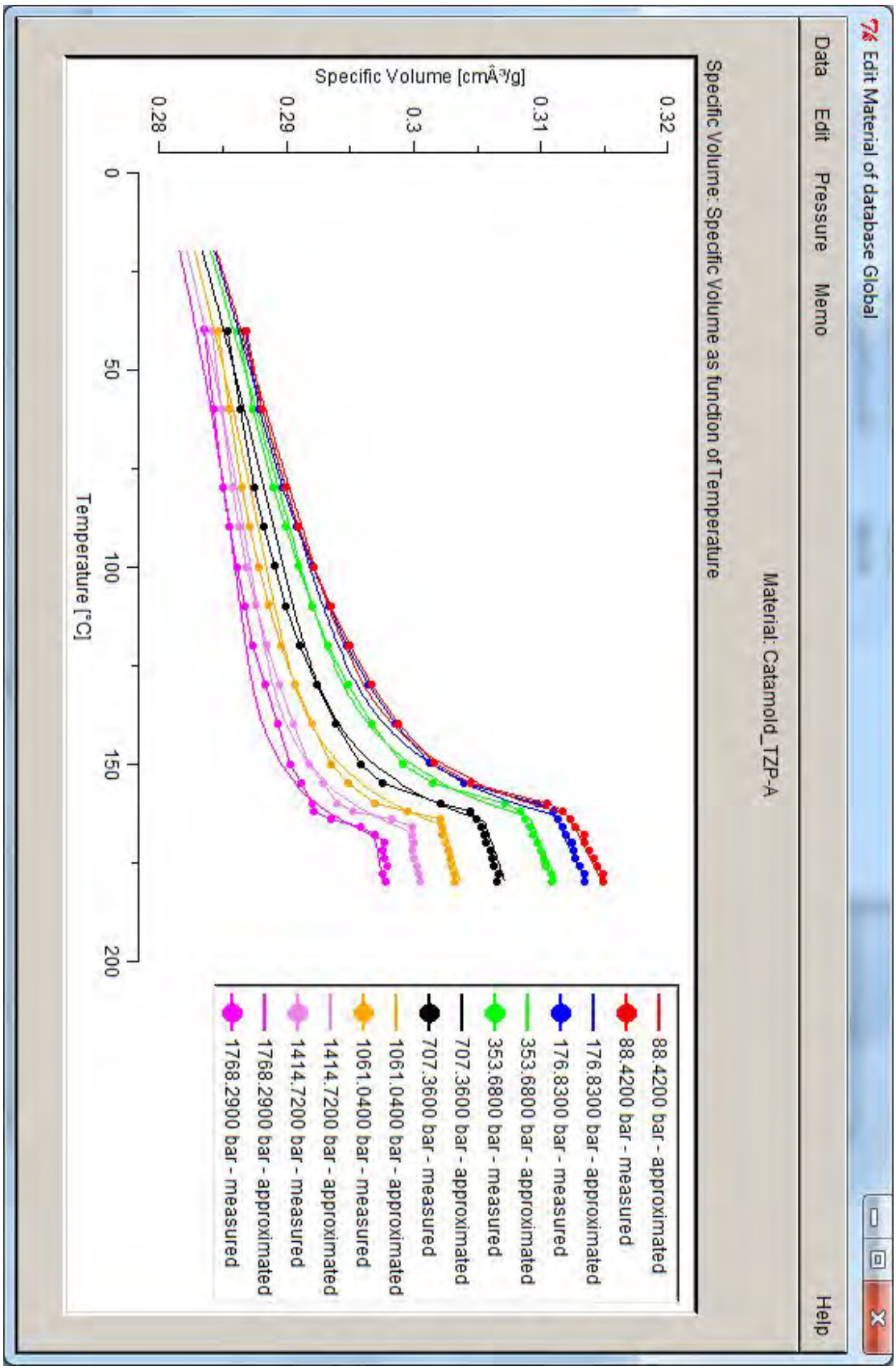

Figure A.5: SigmaSoft®data fit for the *pvT* data of Catamold® TZP-A.

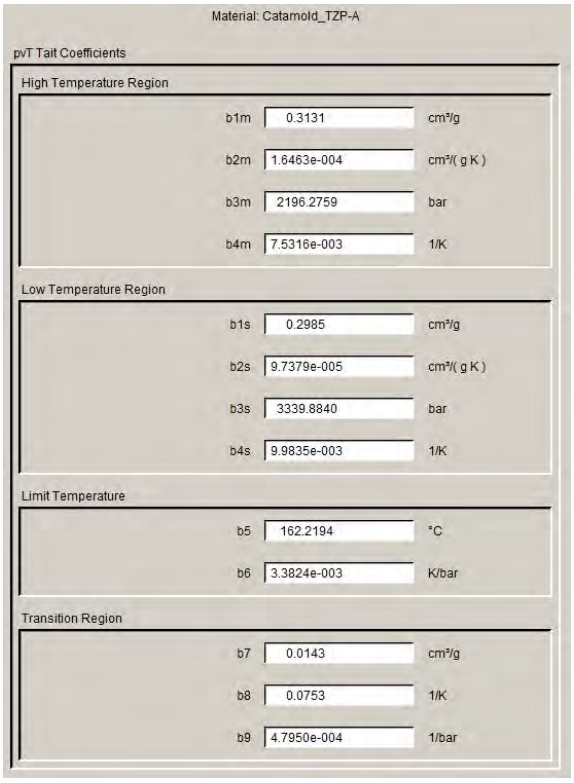

Figure A.6: Coefficients of the SigmaSoft®data fit for the *pvT* data of Catamold® TZP-A.

A.4 Viscosity and *pvT* fitting for Catamold® 17-4PHA

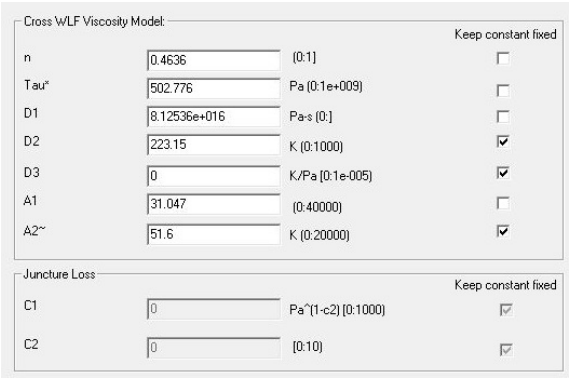

Figure A.8: Coefficients of the ASMI data fit for the viscosity of Catamold® 17-4PHA.

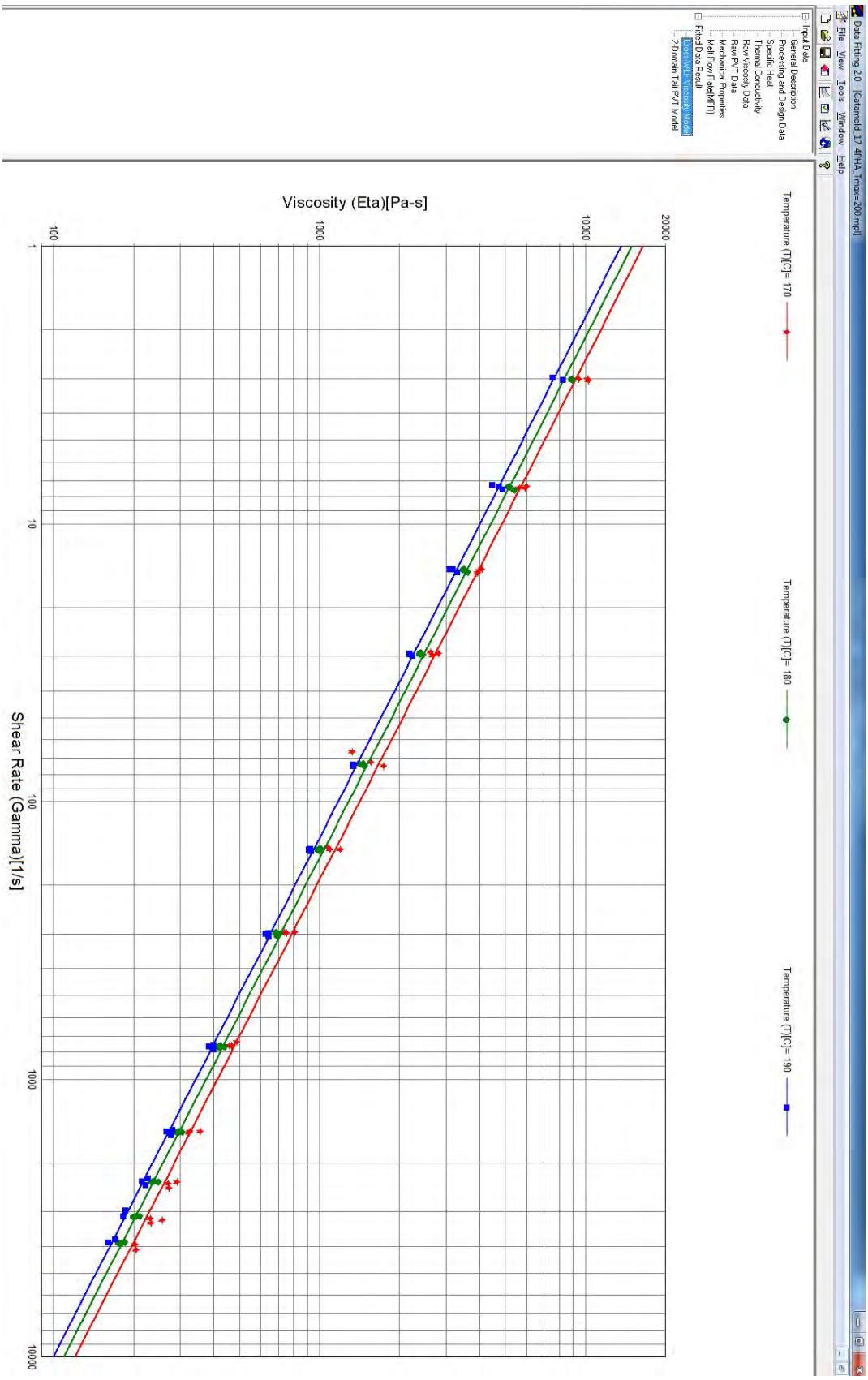

Figure A.7: ASMI data fit for the viscosity of Catamold® 17-4PHA.

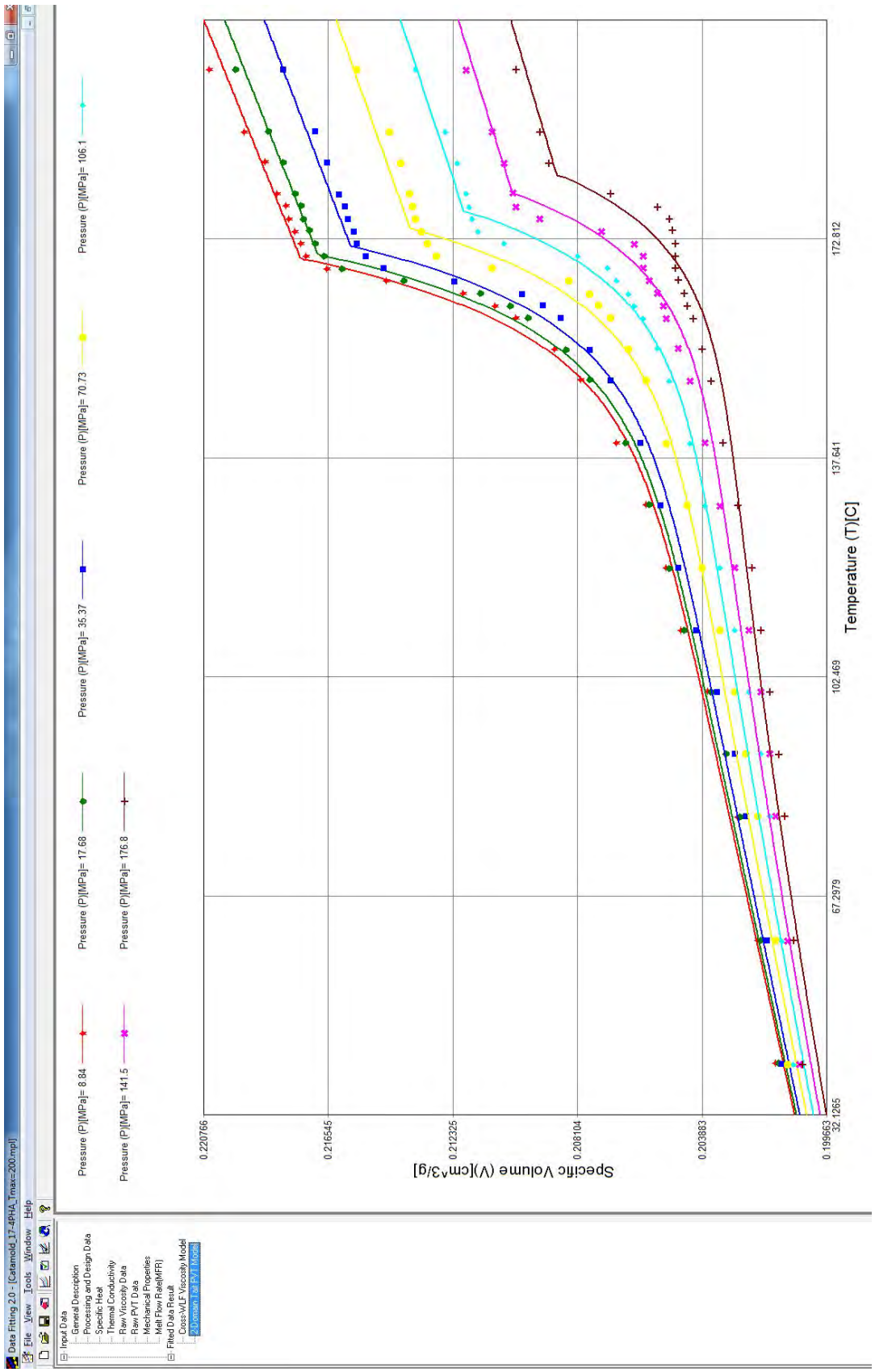

Figure A.9: ASMI data fit for the pvT data of Catamold® 17-4PHA.

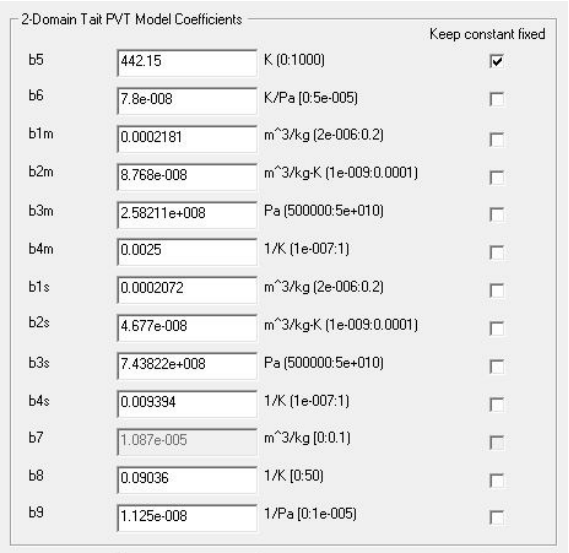

Figure A.10: Coefficients of the ASMI data fit for the pvT data of Catamold® 17-4PHA.

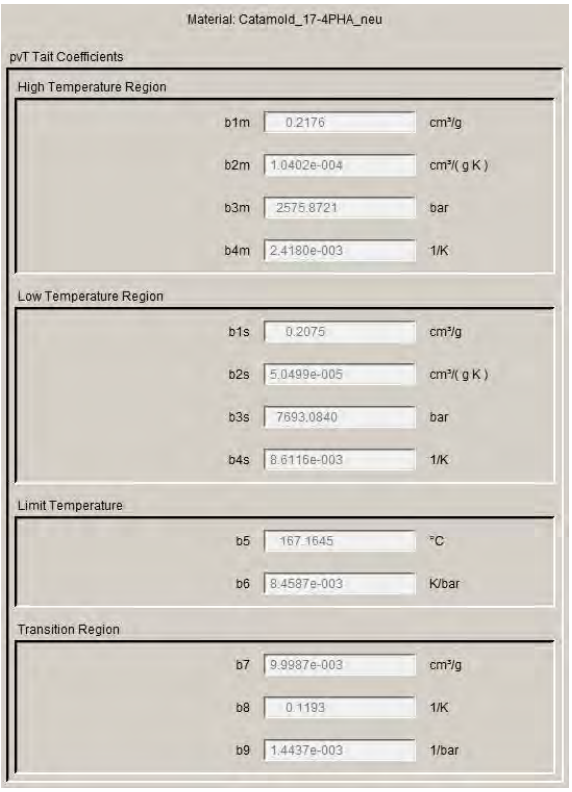

Figure A.12: Coefficients of the SigmaSoft®data fit for the pvT data of Catamold® 17-4PHA.

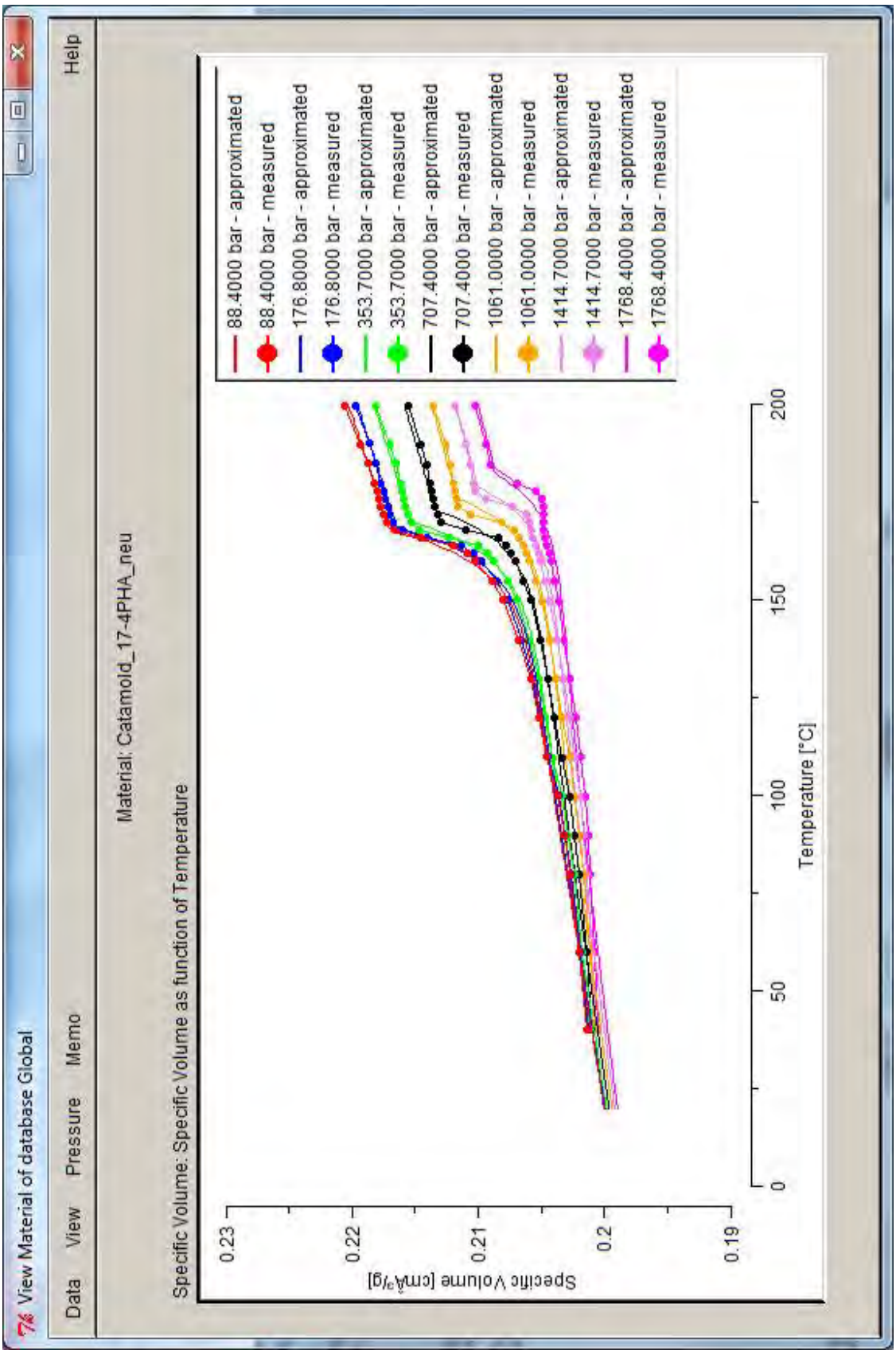

Figure A.11: SigmaSoft®data fit for the *pvT* data of Catamold® 17-4PHA.

A.5 Viscosity and *pvT* fitting for GoMikro ZrO_2

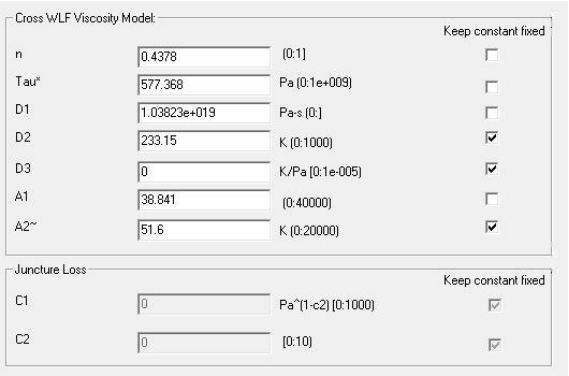

Figure A.14: Coefficients of the ASMI data fit for the viscosity of GoMikro ZrO_2.

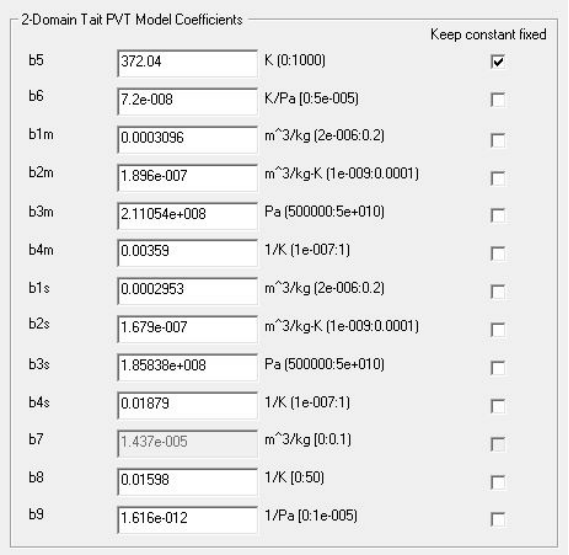

Figure A.16: Coefficients of the ASMI data fit for the pvT data of GoMikro ZrO_2.

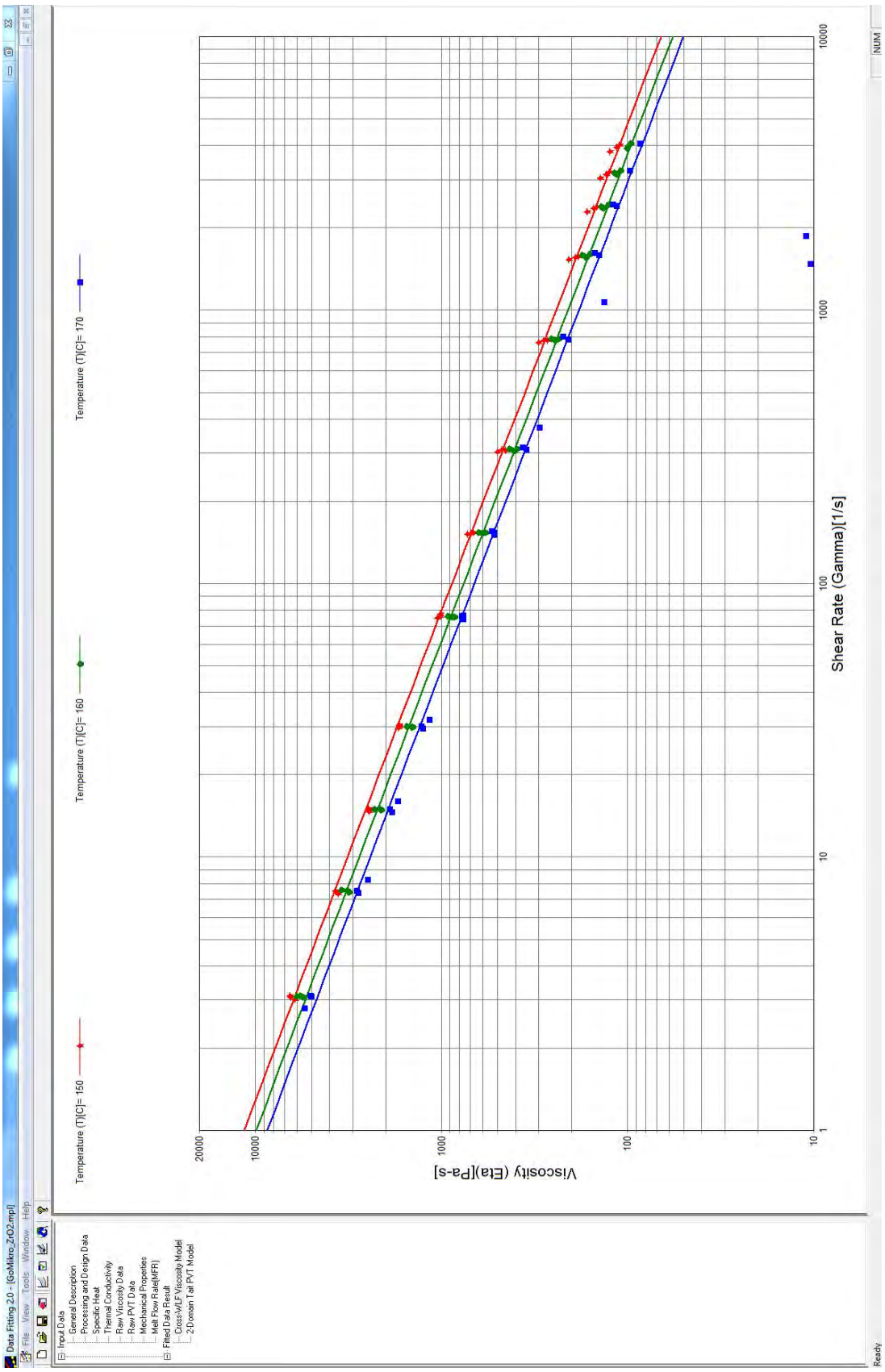

Figure A.13: ASMI data fit for the viscosity of GoMikro ZrO_2.

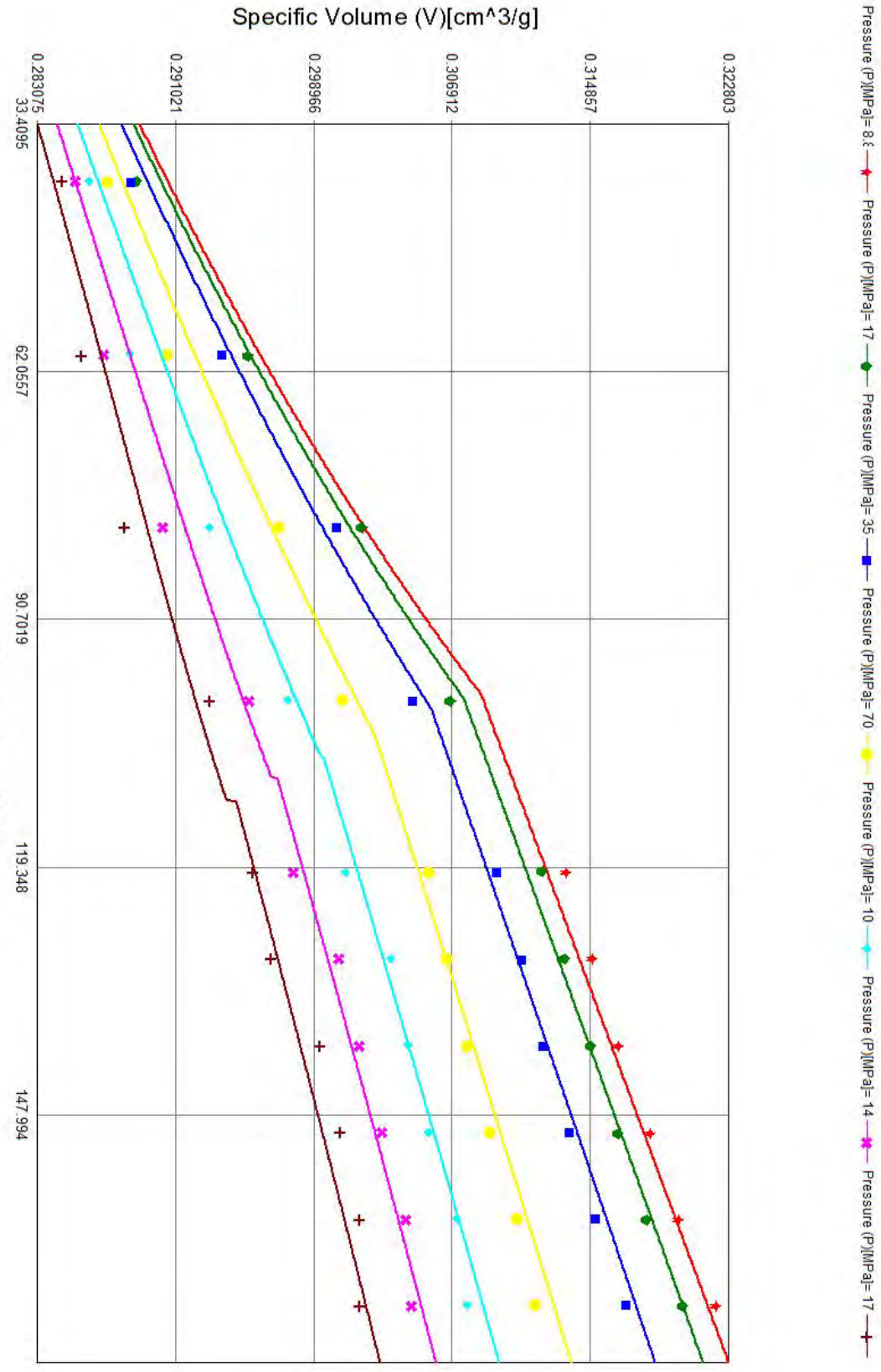

Figure A.15: ASMI data fit for the pvT data of GoMikro ZrO_2.

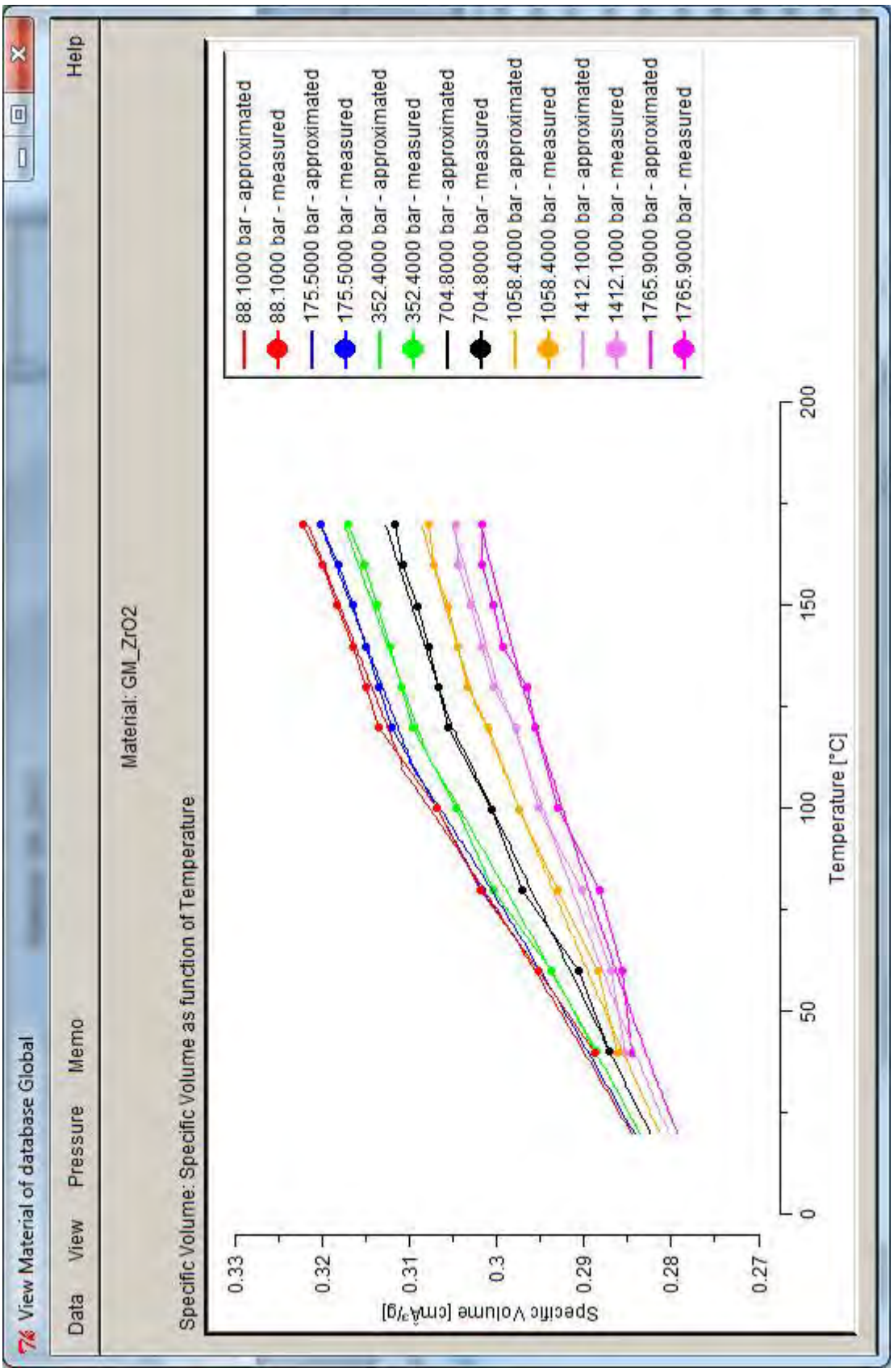

Figure A.17: SigmaSoft®data fit for the pvT data of GoMikro ZrO_2.

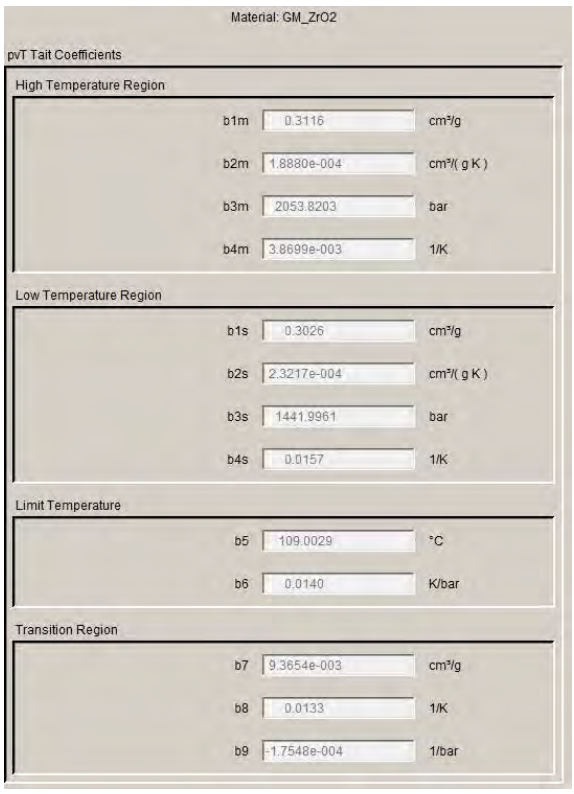

Figure A.18: Coefficients of the SigmaSoft®data fit for the *pvT* data of GoMikro ZrO_2.

A.6 Viscosity and *pvT* fitting for GoMikro 17-4PH

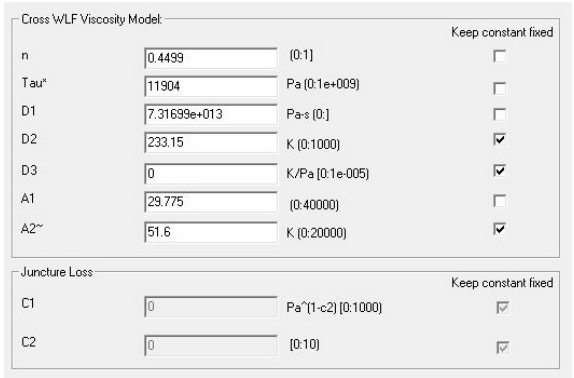

Figure A.20: Coefficients of the ASMI data fit for the viscosity of GoMikro 17-4PH.

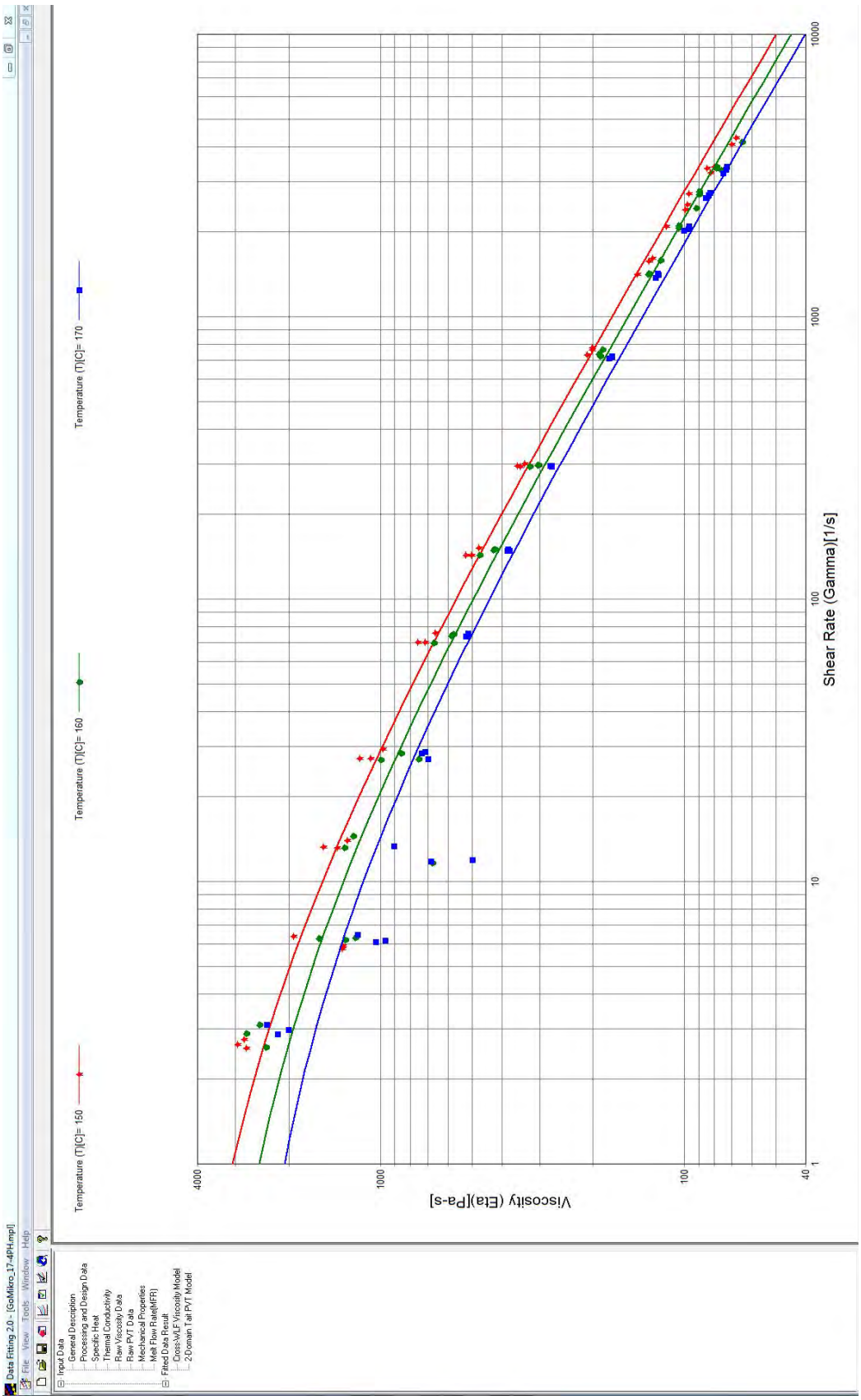

Figure A.19: ASMI data fit for the viscosity of GoMikro 17-4PH.

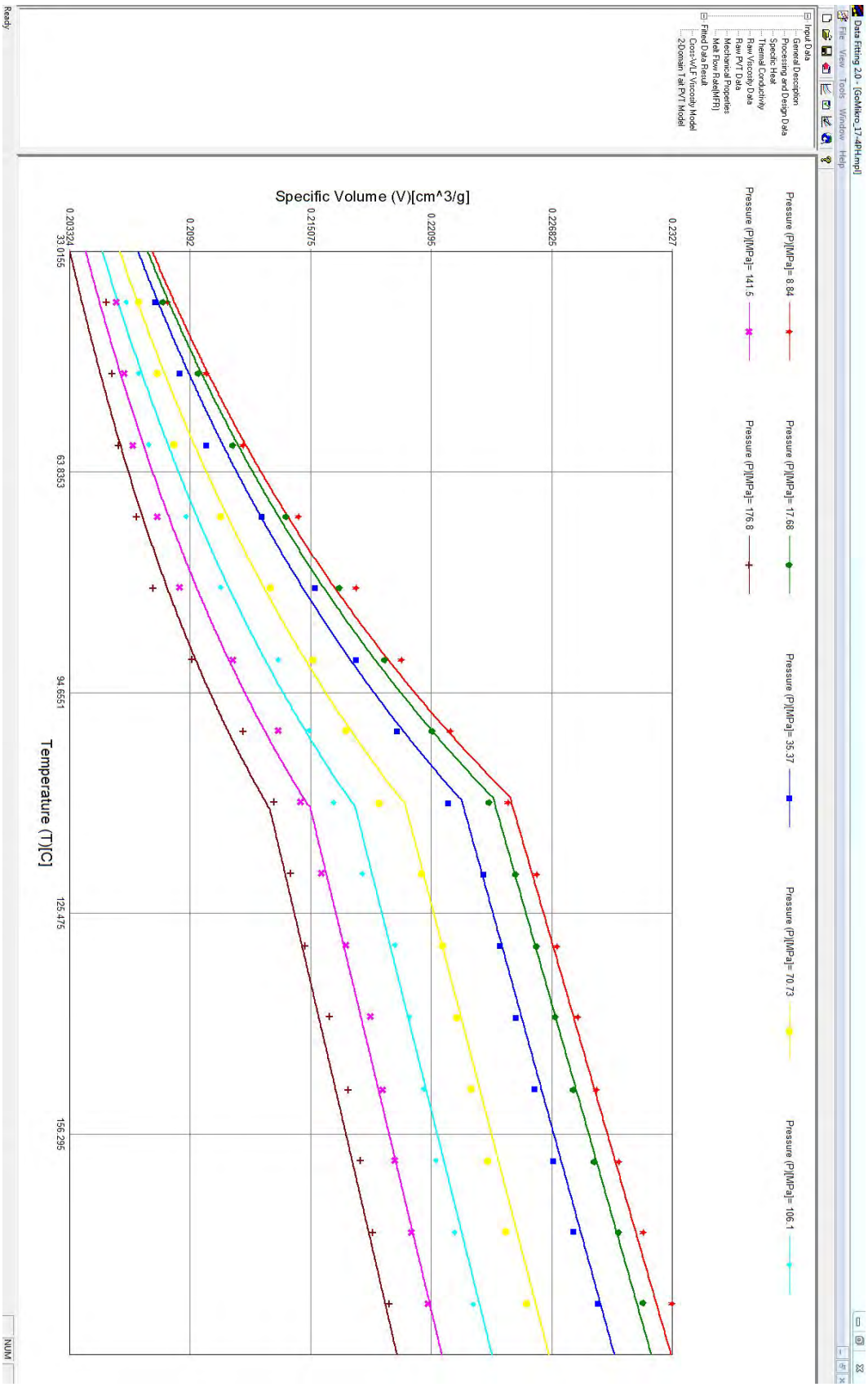

Figure A.21: ASMI data fit for the *pvT* data of GoMikro 17-4PH.

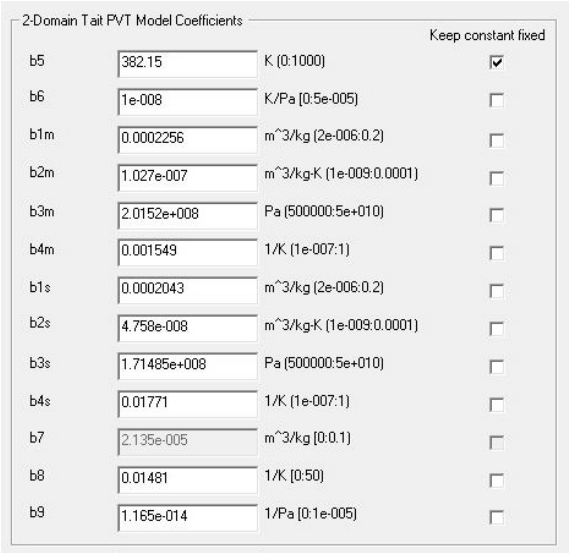

Figure A.22: Coefficients of the ASMI data fit for the *pvT* data of GoMikro 17-4PH.

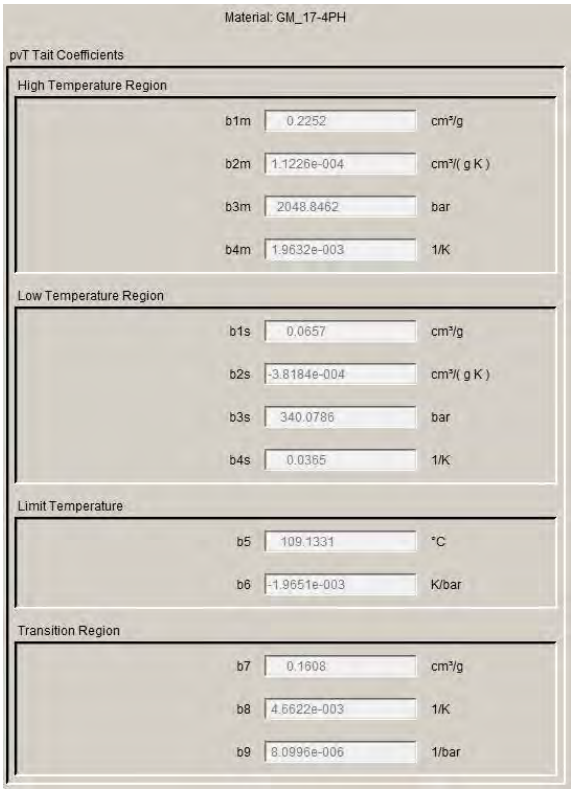

Figure A.24: Coefficients of the SigmaSoft®data fit for the *pvT* data of GoMikro 17-4PH.

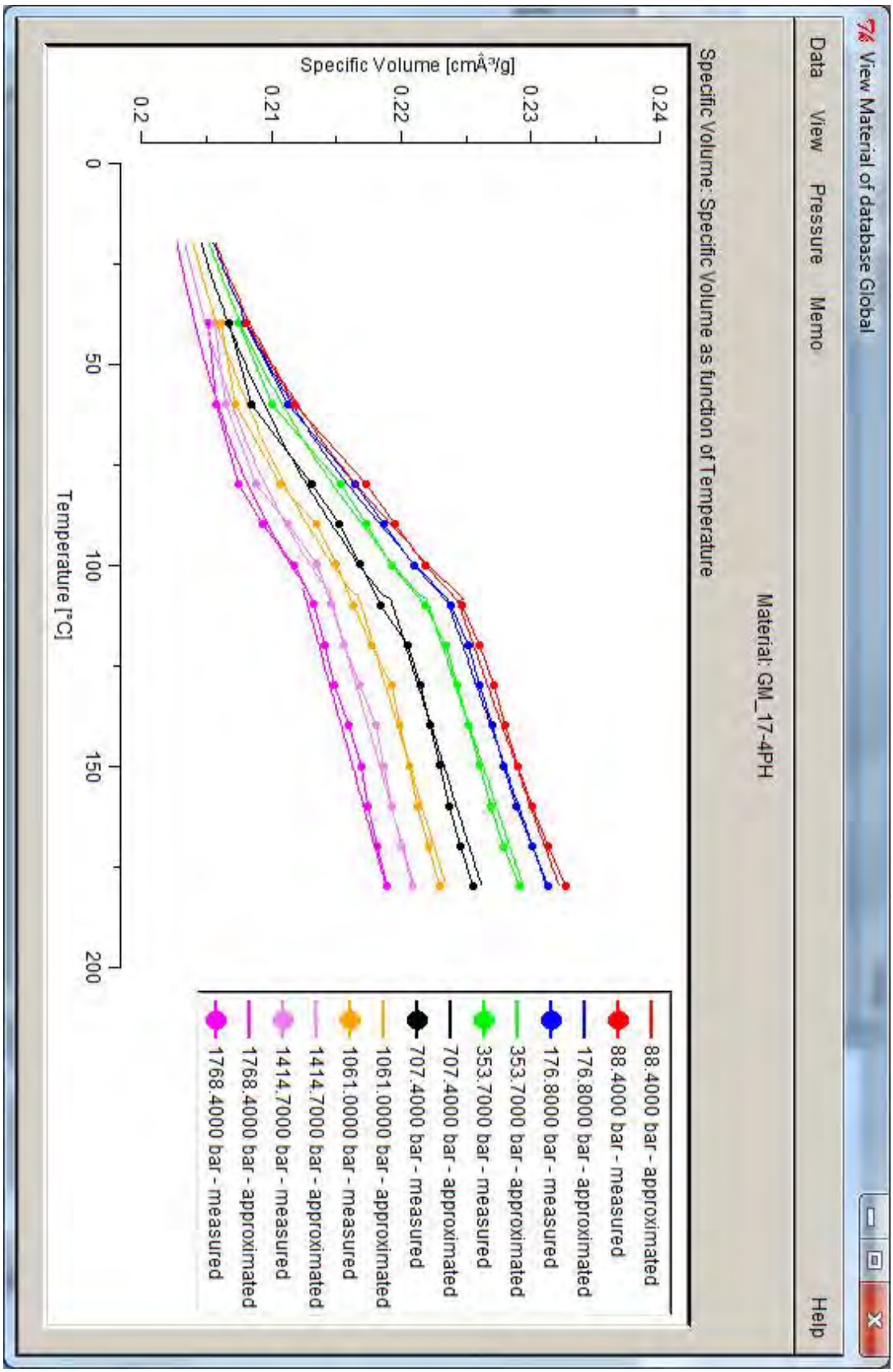

Figure A.23: SigmaSoft®data fit for the pvT data of GoMikro 17-4PH.

B Supplementary information to chapter 5

B.1 Technical drawing of the micro channel test structure

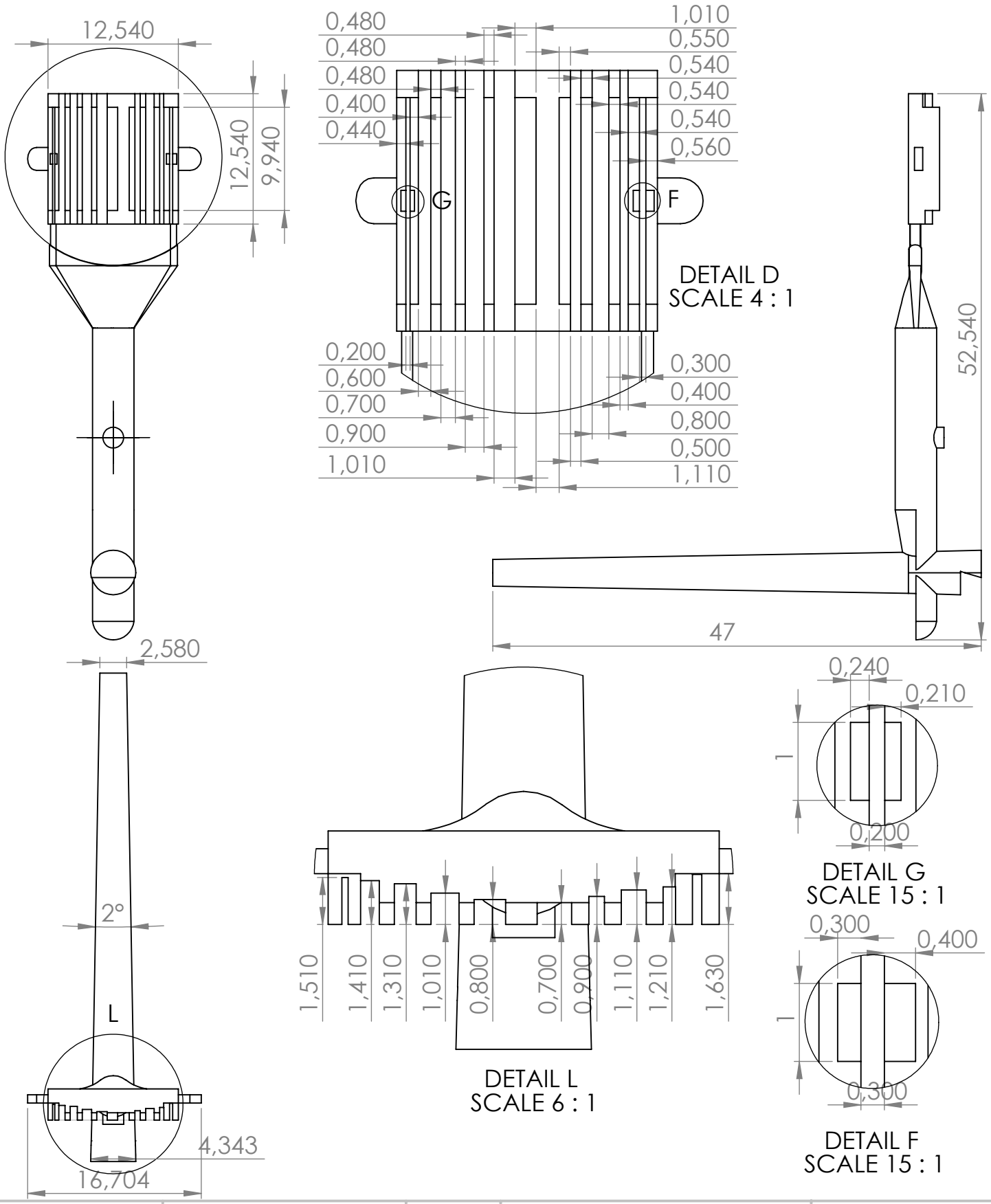

UNLESS OTHERWISE SPECIFIED: DIMENSIONS ARE IN MILLIMETERS SURFACE FINISH: TOLERANCES: LINEAR: ANGULAR:	FINISH:		DEBUR AND BREAK SHARP EDGES	DO NOT SCALE DRAWING	REVISION	
	NAME	SIGNATURE	DATE	TITLE:		
DRAWN						
CHK'D						
APPV'D						
MFG						
Q.A				MATERIAL:	DWG NO.	A4
				WEIGHT:	SCALE:1:1	SHEET 1 OF 1

Solid_works_part_drawing

B.2 Averaging of speed profile of injection molding machine

Importing and plotting the data points which were extracted from the pictures by means of Graph Digitizer.

The data is exported by Graph Digitizer in txt format with tabulator spacing. Due to the manual placement of data points in Graph Digitizer, the sampling frequency is not regular and not similar from file to file. Text files for ram speed vs time, ram position vs time, and injection pressure vs time exist. Multiple files can be imported and plotted again in *Mathematica*. The import procedure checks the existance of the imported file and automatically stops the import after the last file. For control reasons, the name of all imported files will be listed and for visualization, the imported data sets are plotted at the end of this section.

In[1]:=
```
filename = newfilename = "Speed_profile_1_Position_vs_time.txt";
filepath = StringJoin[NotebookDirectory[], filename];
(* automatic definition of name and path of first file *)

For[i = 2; Tposition = {}, FileExistsQ[filepath] == True,
 i++, T_i := Import[filepath, "Table"]; AppendTo[Tposition, T_i];
 Print[newfilename]; newfilename = StringReplace[filename, "1" → ToString[i]];
 filepath = StringJoin[NotebookDirectory[], newfilename]]
(* loop for importing the data files,
prints also the name of all imported files for control *)

filename = newfilename = "Speed_profile_1_Pressure_vs_time.txt";
filepath = StringJoin[NotebookDirectory[], filename];
(* automatic definition of name and path of first file *)

For[i = 2; Tpressure = {}, FileExistsQ[filepath] == True,
 i++, T_i := Import[filepath, "Table"]; AppendTo[Tpressure, T_i];
 Print[newfilename]; newfilename = StringReplace[filename, "1" → ToString[i]];
 filepath = StringJoin[NotebookDirectory[], newfilename]]
(* loop for importing the data files,
prints also the name of all imported files for control *)

filename = newfilename = "Speed_profile_1_Speed_vs_time.txt";
filepath = StringJoin[NotebookDirectory[], filename];
(* automatic definition of name and path of first file *)

For[i = 2; Tspeed = {}, FileExistsQ[filepath] == True, i++,
 T_i := Import[filepath, "Table"]; AppendTo[Tspeed, T_i]; Print[newfilename];
 newfilename = StringReplace[filename, "1" → ToString[i]];
 filepath = StringJoin[NotebookDirectory[], newfilename]]
(* loop for importing the data files,
prints also the name of all imported files for control *)

ListPlot[Tposition, PlotRange → {0, 100}]
ListPlot[Tpressure, PlotRange → {0, 100}]
ListPlot[Tspeed, PlotRange → {0, 100}]
(* list plot of all imported data files for control of data *)
```

```
Speed_profile_1_Position_vs_time.txt
Speed_profile_2_Position_vs_time.txt
Speed_profile_3_Position_vs_time.txt
Speed_profile_4_Position_vs_time.txt
Speed_profile_5_Position_vs_time.txt
Speed_profile_6_Position_vs_time.txt
Speed_profile_7_Position_vs_time.txt
Speed_profile_8_Position_vs_time.txt
Speed_profile_1_Pressure_vs_time.txt
Speed_profile_2_Pressure_vs_time.txt
Speed_profile_3_Pressure_vs_time.txt
Speed_profile_4_Pressure_vs_time.txt
Speed_profile_5_Pressure_vs_time.txt
Speed_profile_6_Pressure_vs_time.txt
Speed_profile_7_Pressure_vs_time.txt
Speed_profile_8_Pressure_vs_time.txt
Speed_profile_1_Speed_vs_time.txt
Speed_profile_2_Speed_vs_time.txt
Speed_profile_3_Speed_vs_time.txt
Speed_profile_4_Speed_vs_time.txt
Speed_profile_5_Speed_vs_time.txt
Speed_profile_6_Speed_vs_time.txt
Speed_profile_7_Speed_vs_time.txt
Speed_profile_8_Speed_vs_time.txt
```

Out[10]=

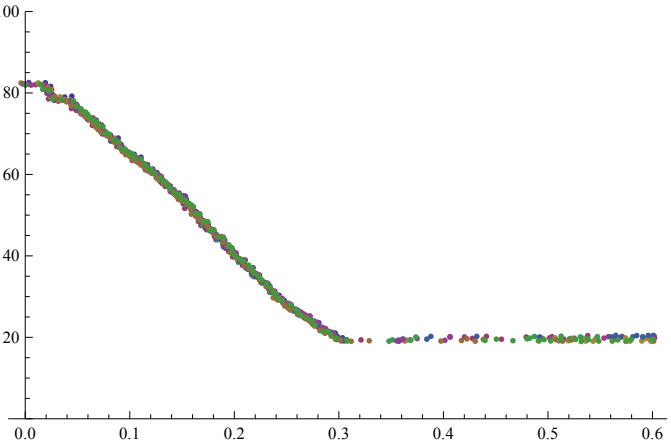

Out[11]=

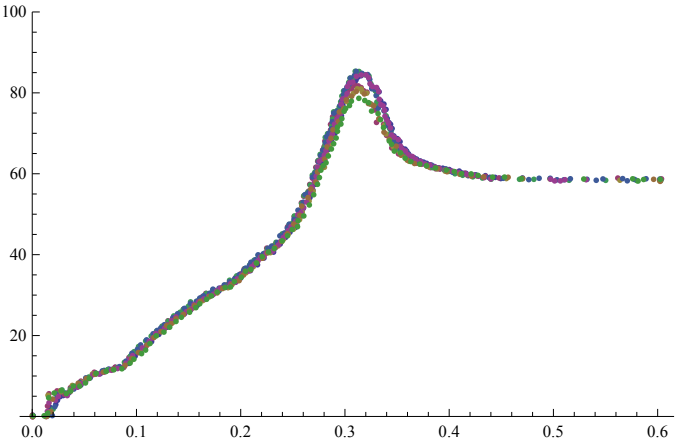

Out[12]=

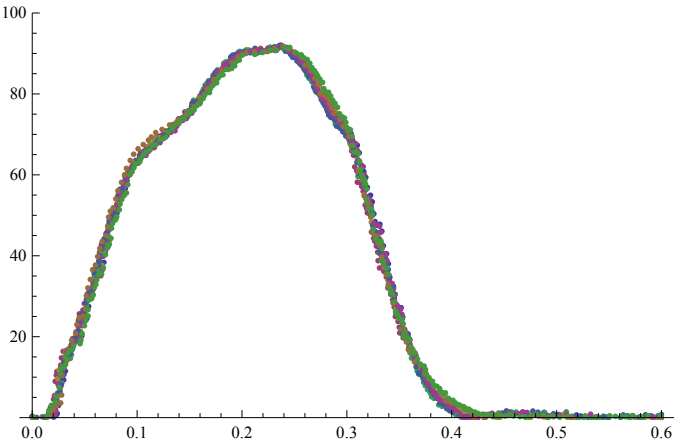

Creating manually a function that piecewisely interpolates the imported data points.

For every input value (x) an output (y) is given by the various interpolation curves. The inerpolation is necessary because of the different time scale of the sampled data points. This again enables averaging all the recorded curves at certain time steps to statistically determine the real machine behavior out of several curves. Second, it can be used for creating new data points, so that the different curves the injection molding machine provides can be connected and profiles like ram speed versus ram position can be computed. The yielded data can be then imported to Autodesk Moldflow for modeling the injection molding machine properly.

In[13]:=
$$f[x\_, T\_] := \frac{y2[x, T] - y1[x, T]}{x2[x, T] - x1[x, T]} (x - x1[x, T]) + y1[x, T]$$

```
(* Linear interpolation function between data points of table T *)
x1[x_, T_] := Max[Select[T[[All, 1]], # <= x &]]
(* Maximum of all values being smaller or equal than x in table T *)
x2[x_, T_] := Min[Select[T[[All, 1]], # > x &]]
(* Minimum of all values being greater than x in table T *)
p1[x_, T_] := Position[T, Max[Select[T[[All, 1]], # <= x &]]]
(* Position of previously determined maximum in list T*)
p2[x_, T_] := Position[T, Min[Select[T[[All, 1]], # > x &]]]
(* Position of perviously determined minimum in list T*)
y1[x_, T_] := T[[p1[x, T][[1, 1]], 2]]
(* y value corresponding to previously determined maximum in list T *)
y2[x_, T_] := T[[p2[x, T][[1, 1]], 2]]
(* y value corresponding to previously determined minimum in list T *)
```

Calculation of new data profiles.

This section uses the previously set up interpolation function for calculating new profiles with fixed time steps and than derive the average and standard deviation at every time step. Furthermore, the data is scaled to the right values by transfering it from % scale and by multiplying by the actual maximum value for position, pressure, and speed.

```
position = 20;(* in mm *)
pressure = 100;(* in bar *)
speed = 50;(* in mm/s *)
(* set maximum values for plotted parameters *)

tStep = 0.004;
(* time step for calculation of new profiles *)
tEnd = 0.4;
(* end time for calculation of new profiles,
correlates to the real injection time of abou 0.32 s *)

For[n = tStep; TpositionNew = {}, n ≤ tEnd, n = n + tStep, For[m = 1; T = {},
   m ≤ 8, m++, AppendTo[T, f[n, Tposition[[m]]]]]; AppendTo[TpositionNew,
   {n, Mean[T] * position / 100, StandardDeviation[T] * position / 100}]];

For[n = tStep; TpressureNew = {}, n ≤ tEnd, n = n + tStep, For[m = 1; T = {},
   m ≤ 8, m++, AppendTo[T, f[n, Tpressure[[m]]]]]; AppendTo[TpressureNew,
   {n, Mean[T] * pressure / 100, StandardDeviation[T] * pressure / 100}]];

For[n = tStep; TspeedNew = {}, n ≤ tEnd, n = n + tStep,
  For[m = 1; T = {}, m ≤ 8, m++, AppendTo[T, f[n, Tspeed[[m]]]]];
  AppendTo[TspeedNew, {n, Mean[T] * speed / 100, StandardDeviation[T] * speed / 100}]];

ListPlot[TpositionNew[[All, {1, 2}]], PlotRange → {0, position}]
ListPlot[TpressureNew[[All, {1, 2}]], PlotRange → {0, pressure}]
ListPlot[TspeedNew[[All, {1, 2}]], PlotRange → {0, speed}]
(* list plot of all averaged data files for control of data *)
```

Out[27]=

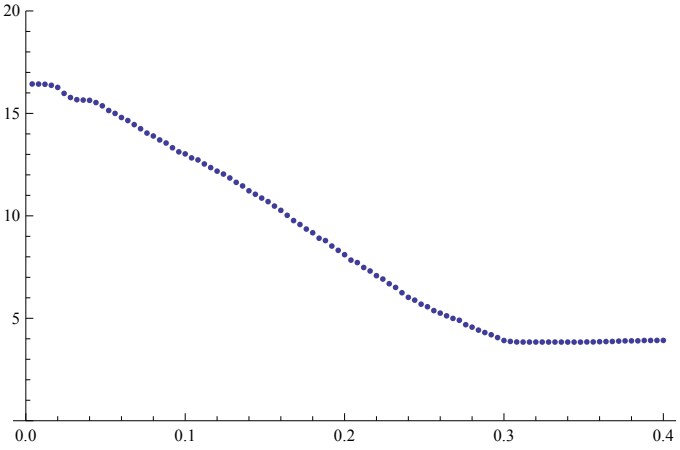

Out[28]=

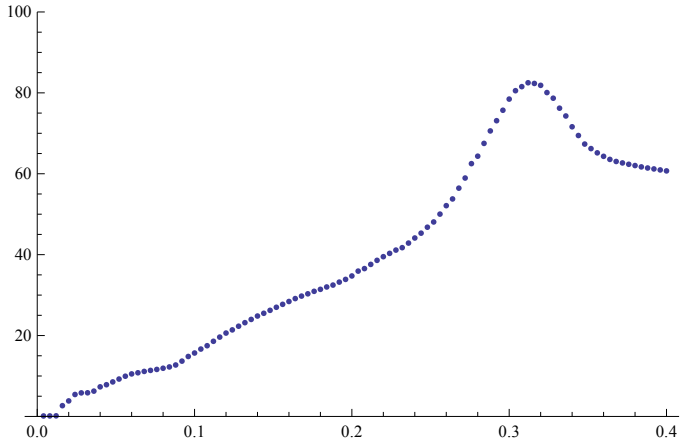

Out[29]=

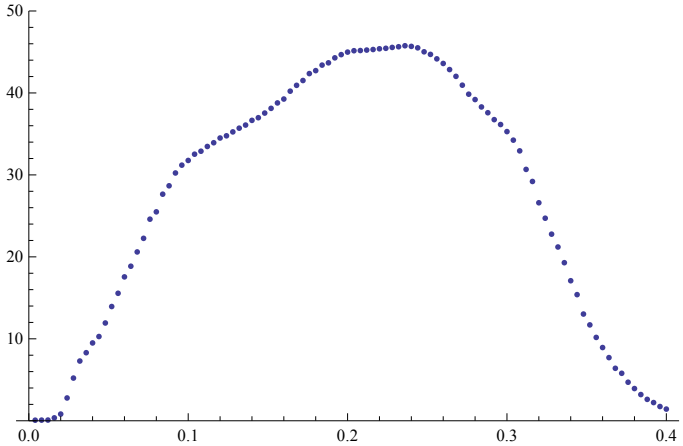

Exporting the interpolated and averaged data points.

Exports the processed data in three text files, one for position/pressure/speed, all containing the time step (column 1, unit: s), average (column 2, unit: mm, bar, mm/s), standard deviation (column 3, unit: mm, bar, mm/s). A headline is added with the name and the unit of the columns.

In[30]:=
```
TpositionExport = Insert[TpositionNew,
   {"Time in s", "Position average in mm", "Standard deviation in mm"}, 1];
TpressureExport = Insert[TpressureNew,
   {"Time in s", "Pressure average in bar", "Standard deviation in bar"}, 1];
TspeedExport = Insert[TspeedNew, {"Time in s", "Speed in mm/s",
    "Standard deviation in mm/s"}, 1];

Export[StringJoin[NotebookDirectory[],
  "Profile_Average_and_StandardDeviation_Position_vs_Time.txt"],
 TpositionExport, "Table"]
Export[StringJoin[NotebookDirectory[],
  "Profile_Average_and_StandardDeviation_Pressure_vs_Time.txt"],
 TpressureExport, "Table"]
Export[StringJoin[NotebookDirectory[],
  "Profile_Average_and_StandardDeviation_Speed_vs_Time.txt"],
 TspeedExport, "Table"]
```

Out[33]= U:\Production\Engel ES 80-25 HL-Victory\Machine Settings 2013-04-24 (Special Course Frederik)\Session 03 (finished)\Profile_Average_and_StandardDeviation_Position_vs_Time.txt

Out[34]= U:\Production\Engel ES 80-25 HL-Victory\Machine Settings 2013-04-24 (Special Course Frederik)\Session 03 (finished)\Profile_Average_and_StandardDeviation_Pressure_vs_Time.txt

Out[35]= U:\Production\Engel ES 80-25 HL-Victory\Machine Settings 2013-04-24 (Special Course Frederik)\Session 03 (finished)\Profile_Average_and_StandardDeviation_Speed_vs_Time.txt

B.3 Machine geometry

Engel ES 80/25 HL - Victory

not true to scale

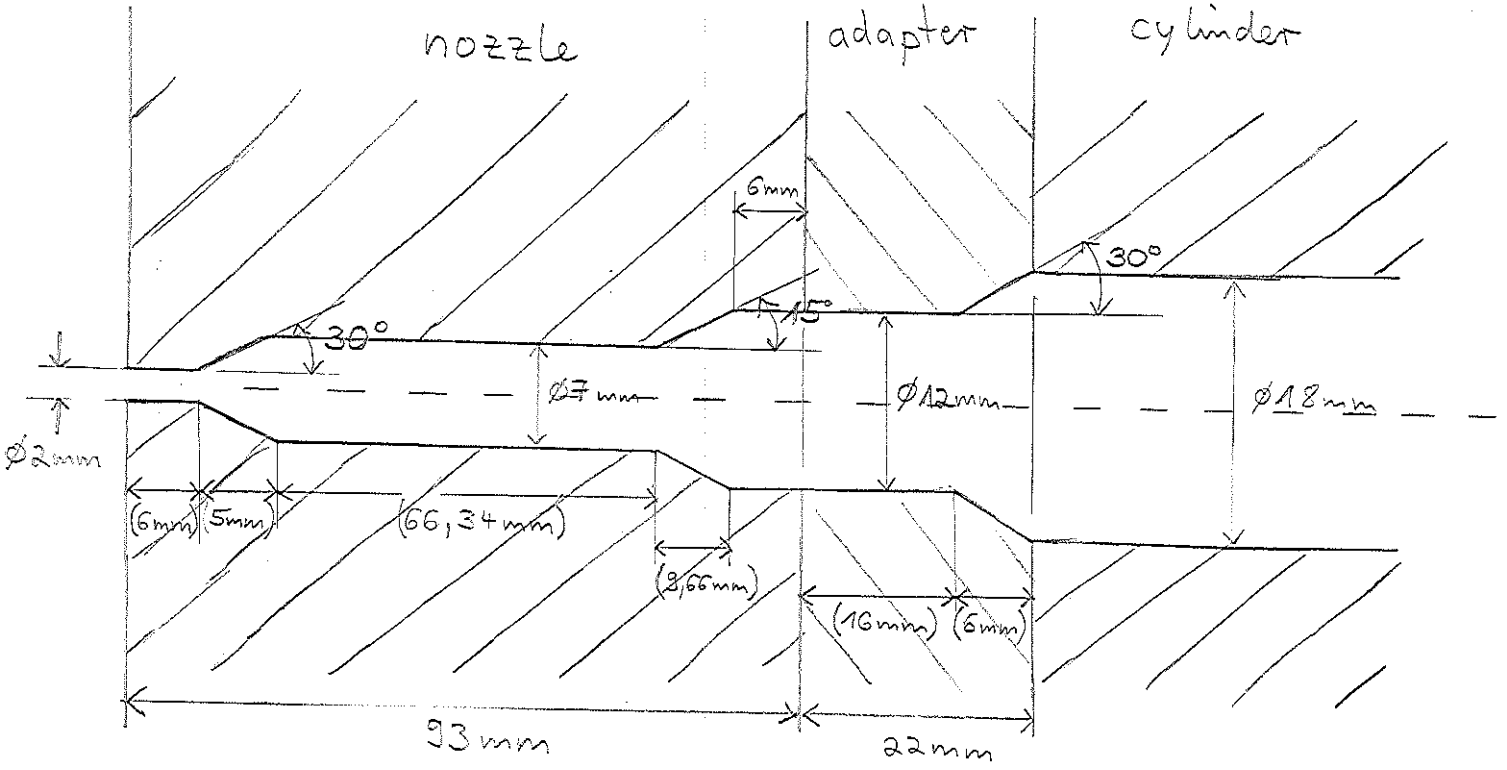

C Supplementary information to chapter 6

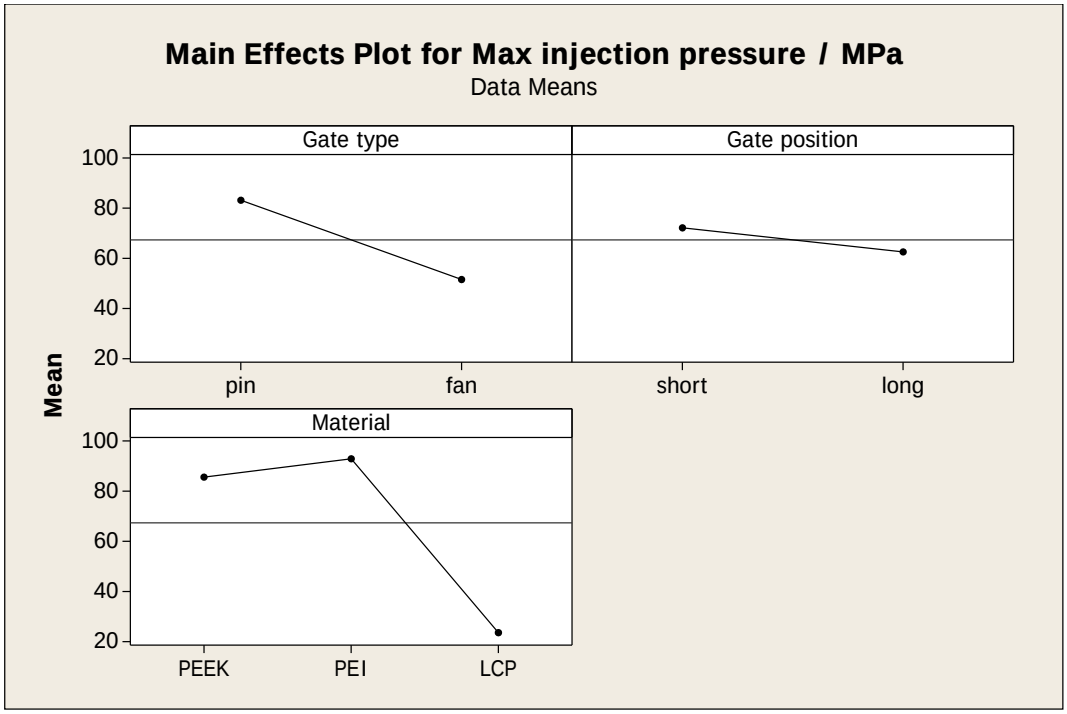

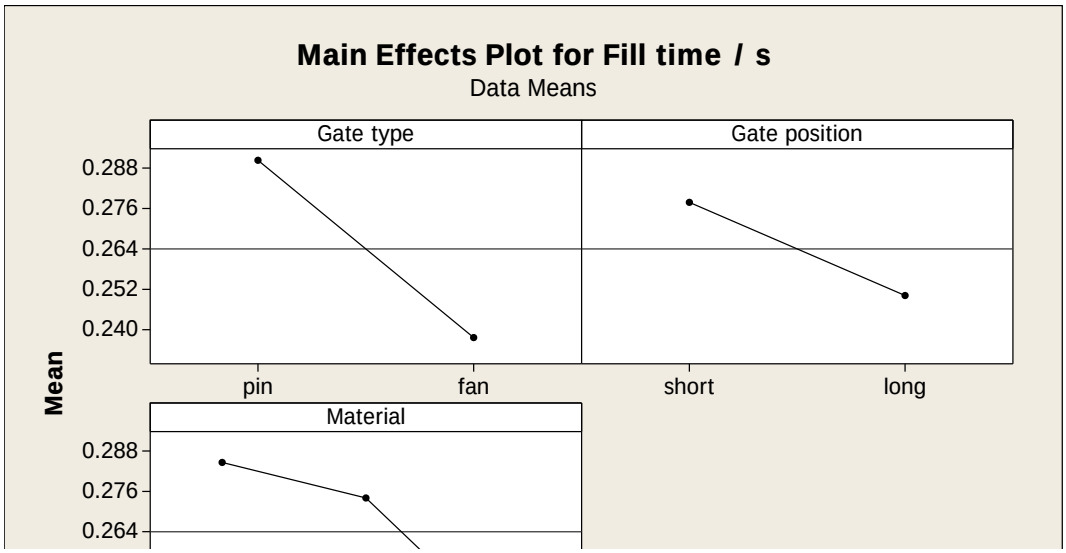
Main Effects Plot for Fill time / s
Data Means
Gate type
Gate position
Material
Mean
0.288
0.276
0.264
0.252
0.240
pin
fan
short
long

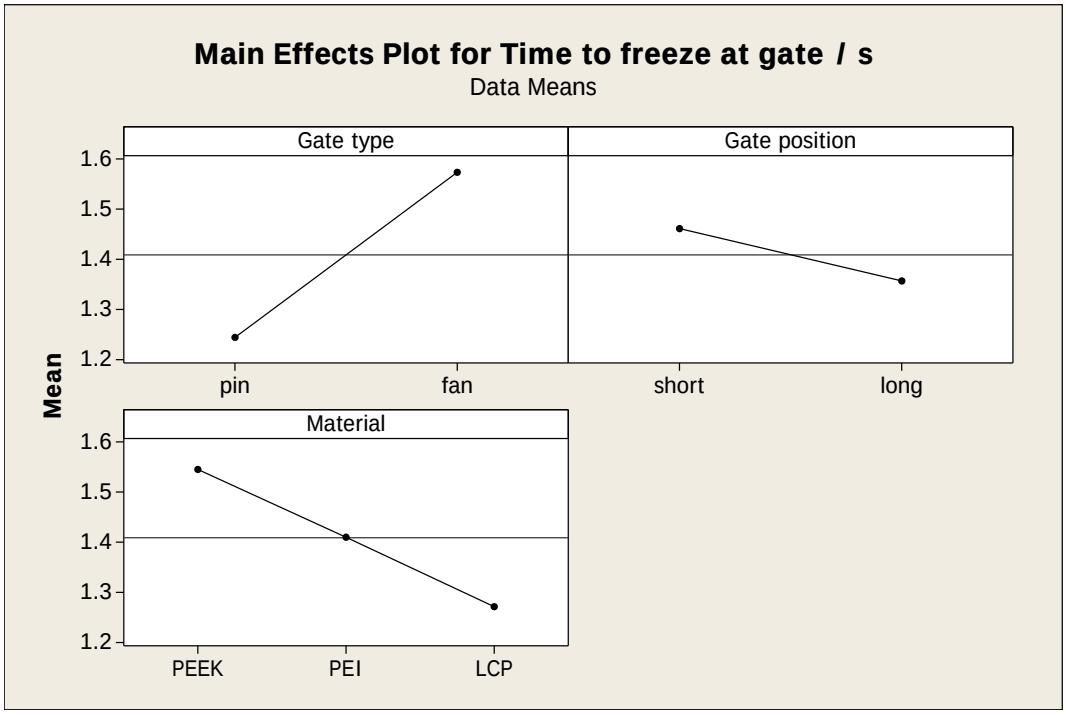
Main Effects Plot for Time to freeze at gate / s
Data Means
Gate type
Gate position
Material
Mean
1.6
1.5
1.4
1.3
1.2
pin
fan
short
long
PEEK
PEI
LCP

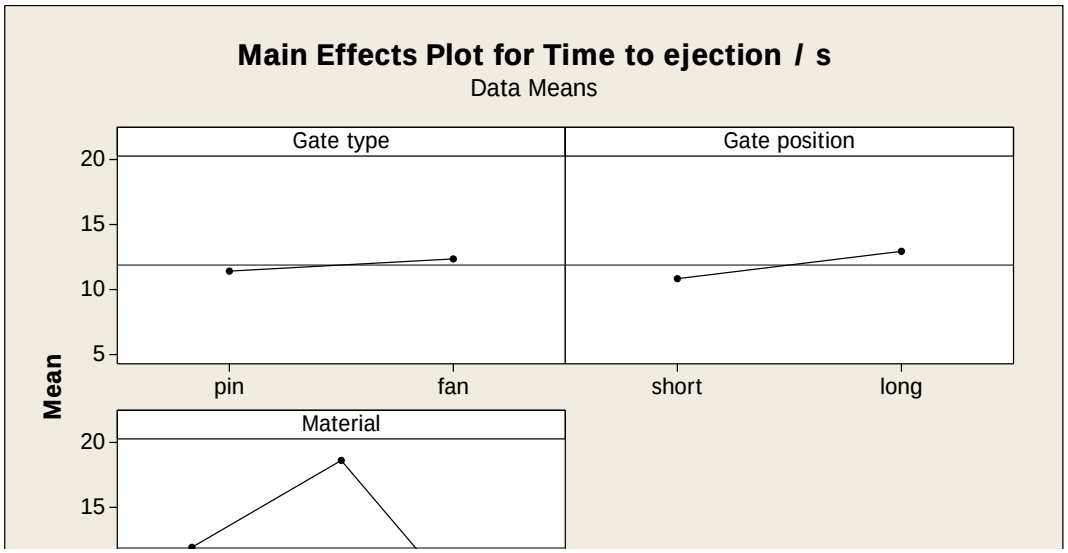
Main Effects Plot for Time to ejection / s
Data Means
Gate type
Gate position
Material
Mean
20
15
10
5
pin
fan
short
long

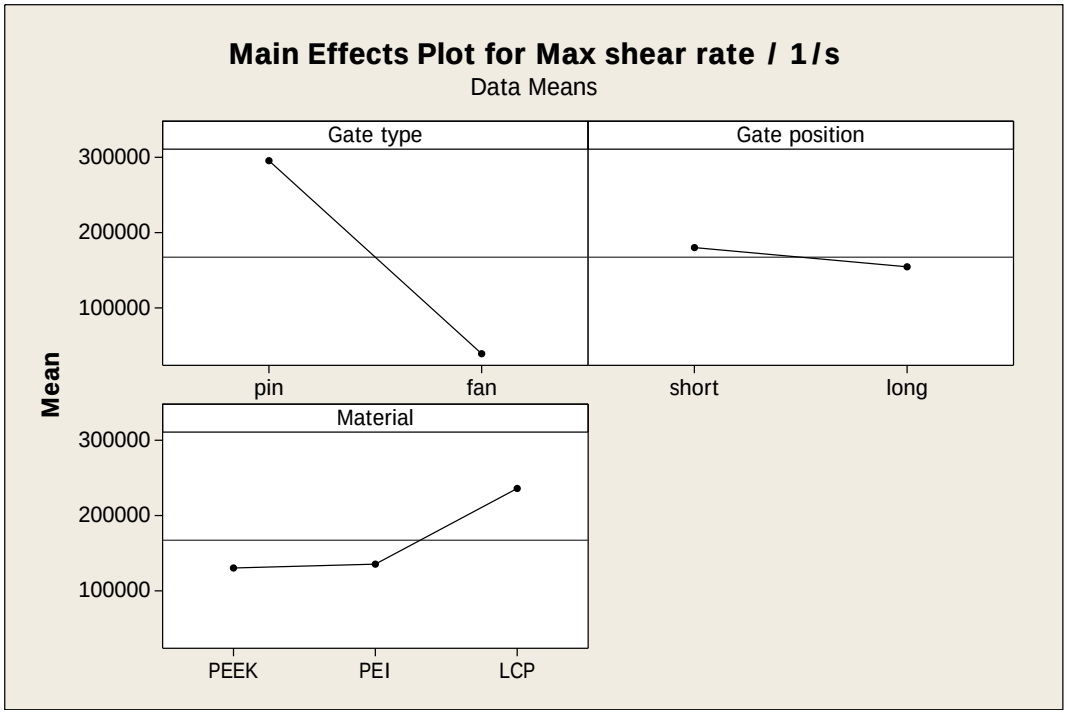
Main Effects Plot for Max shear rate / 1/s
Data Means
Gate type
Gate position
Material
Mean
300000
200000
100000
pin
fan
short
long
PEEK
PEI
LCP

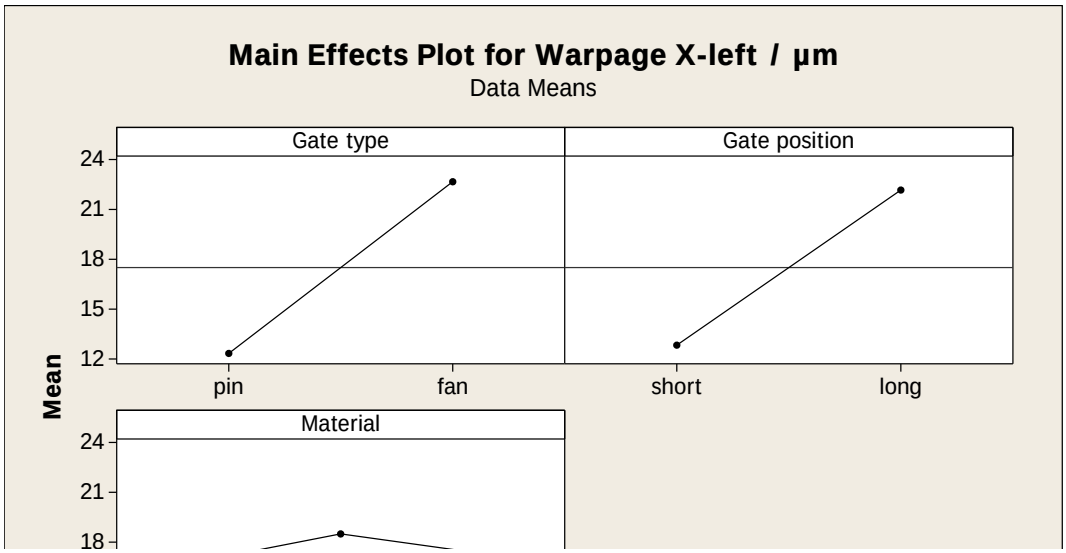
Main Effects Plot for Warpage X-left / µm
Data Means
Gate type
Gate position
Material
Mean
24
21
18
15
12
pin
fan
short
long
PEEK
PEI
LCP

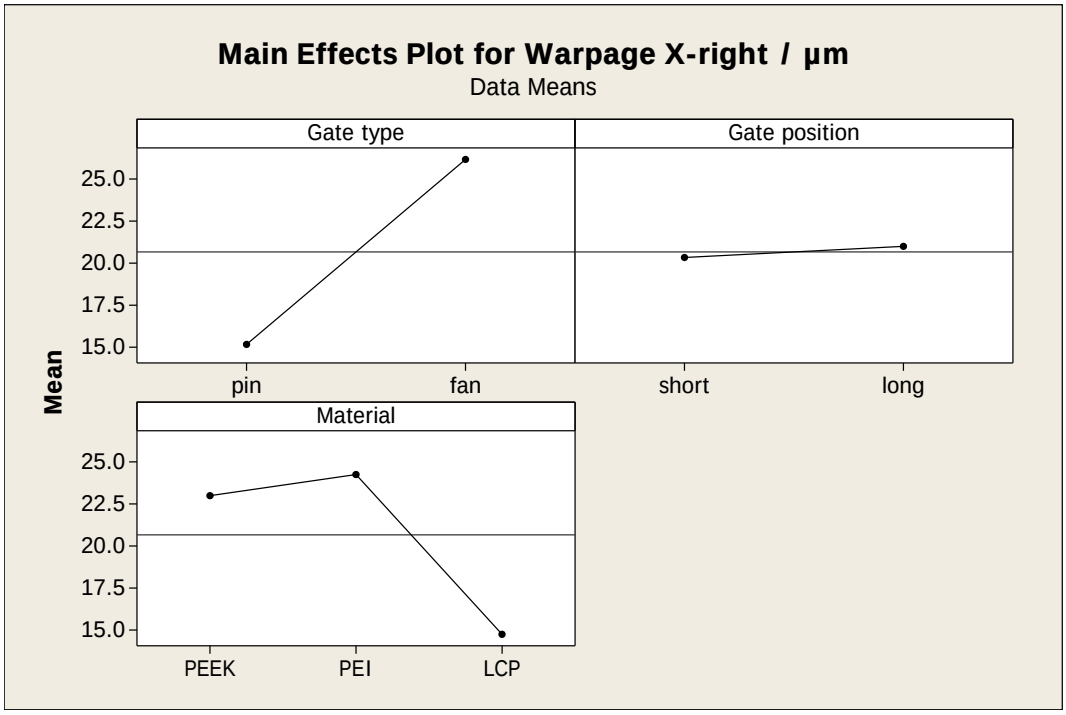
Main Effects Plot for Warpage X-right / µm
Data Means
Gate type
Gate position
Material
Mean
25.0
22.5
20.0
17.5
15.0
pin
fan
short
long
PEEK
PEI
LCP

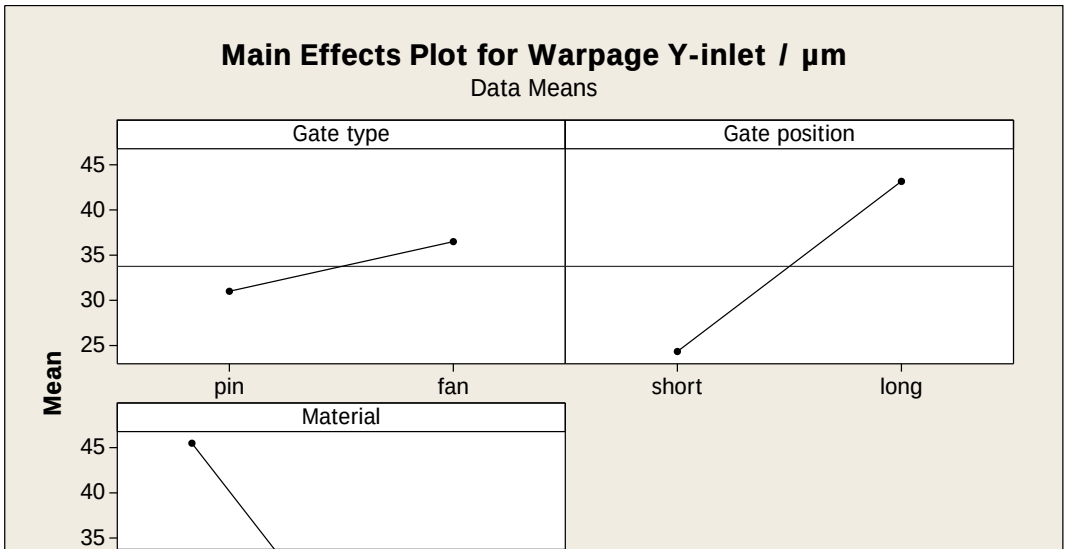
Main Effects Plot for Warpage Y-inlet / µm
Data Means
Gate type
Gate position
Material
Mean
45
40
35
30
25
pin
fan
short
long

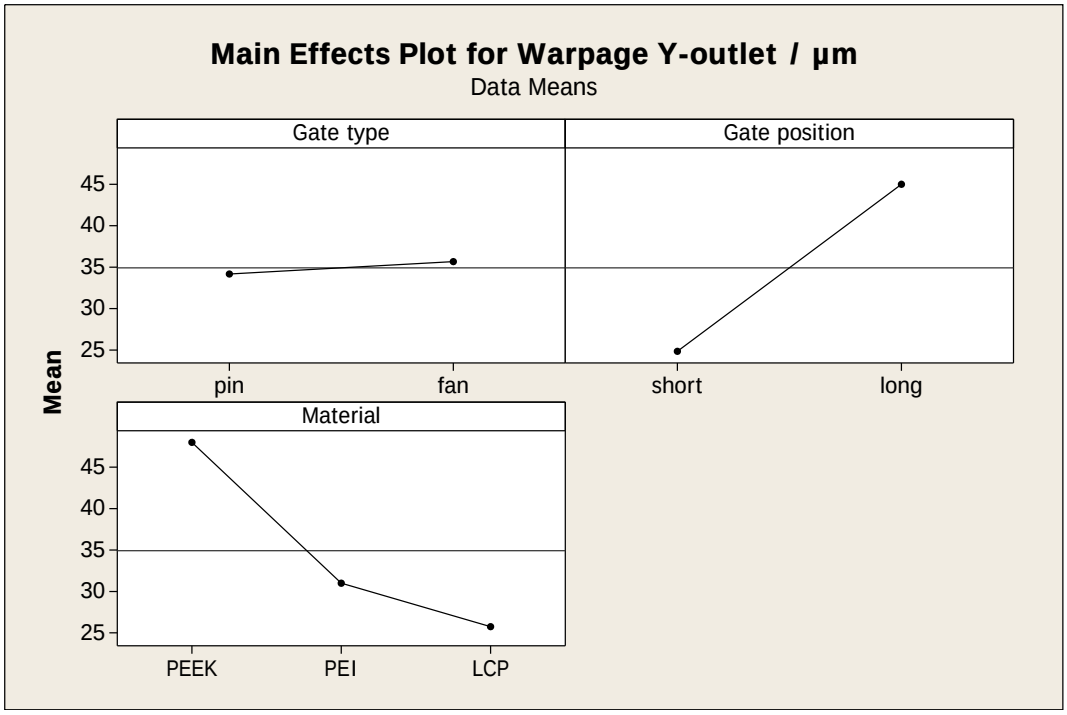
Main Effects Plot for Warpage Y-outlet / µm
Data Means
Gate type
Gate position
Material
Mean
45
40
35
30
25
pin
fan
short
long
PEEK
PEI
LCP

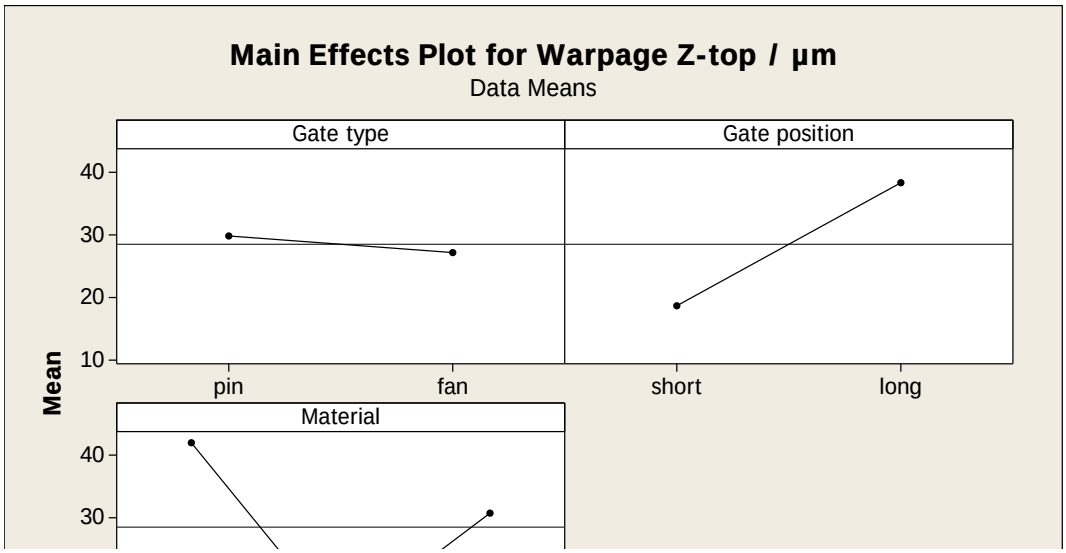
Main Effects Plot for Warpage Z-top / µm
Data Means
Gate type
Gate position
Material
Mean
40
30
20
10
pin
fan
short
long

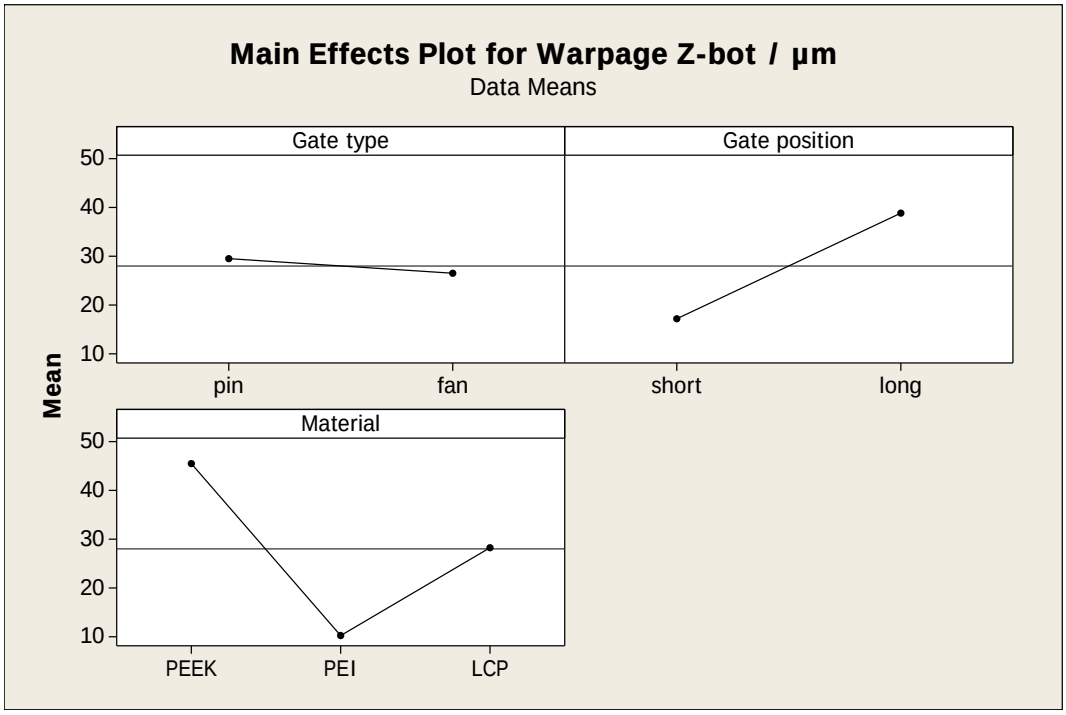
Main Effects Plot for Warpage Z-bot / µm
Data Means
Gate type
Gate position
Material
Mean
50
40
30
20
10
pin
fan
short
long
PEEK
PEI
LCP

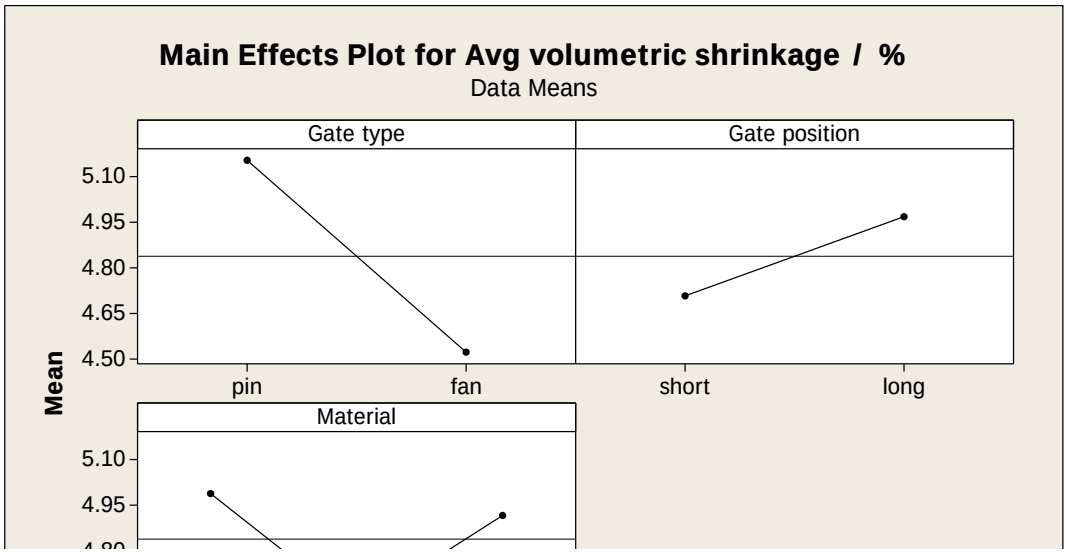
Main Effects Plot for Avg volumetric shrinkage / %
Data Means
Gate type
Gate position
Material
Mean
5.10
4.95
4.80
4.65
4.50
pin
fan
short
long

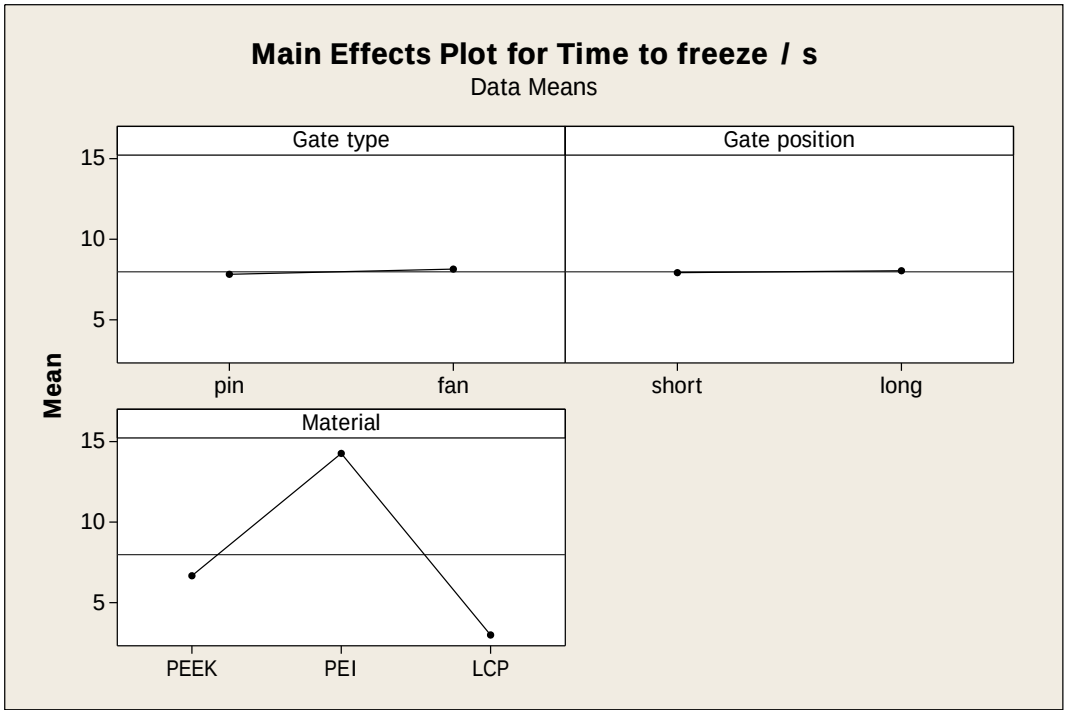
Main Effects Plot for Time to freeze / s
Data Means
Gate type
Gate position
Material
Mean
15
10
5
pin
fan
short
long
PEEK
PEI
LCP

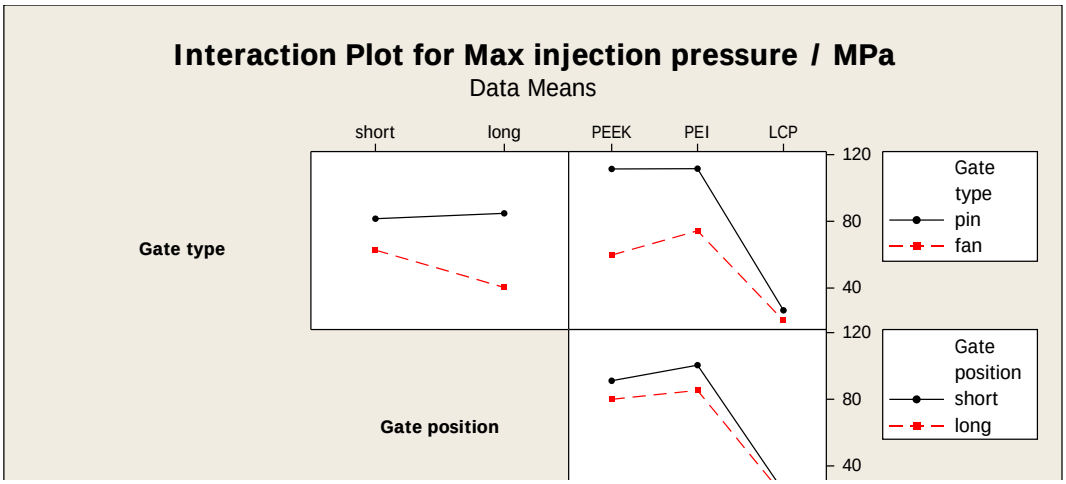
Interaction Plot for Max injection pressure / MPa
Data Means
short
long
PEEK
PEI
LCP
Gate type
Gate position
120
80
40
Gate type
pin
fan
Gate position
short
long

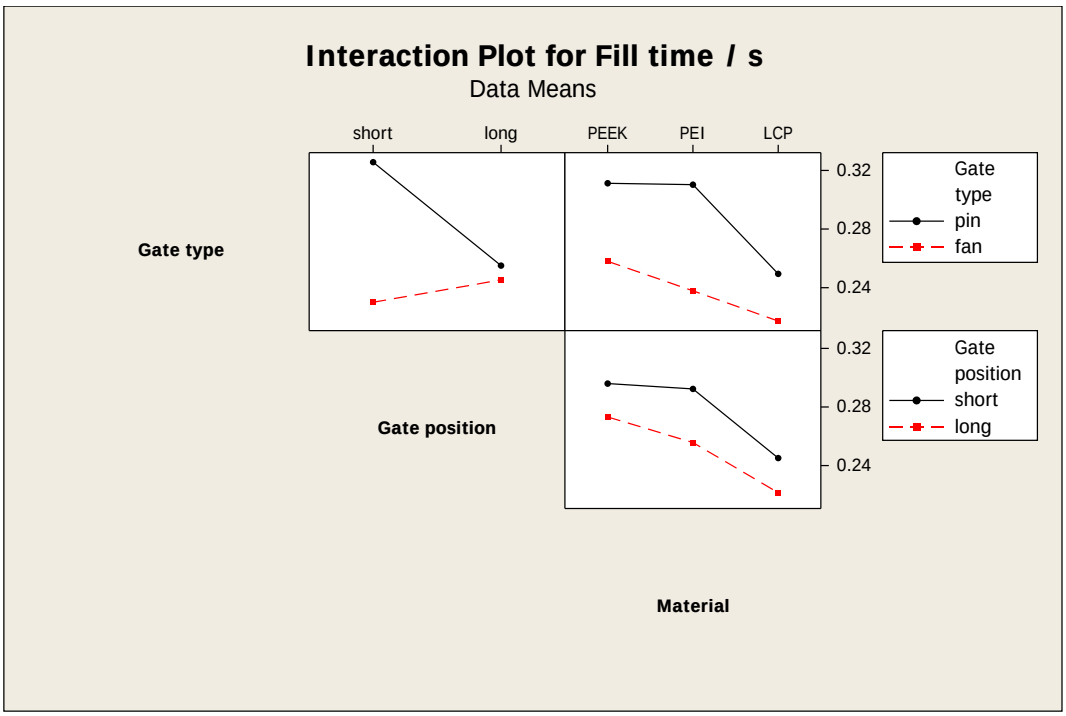
Interaction Plot for Fill time / s
Data Means
short
long
PEEK
PEI
LCP
Gate type
Gate position
0.32
0.28
0.24
Gate type
pin
fan
Gate position
short
long
Material

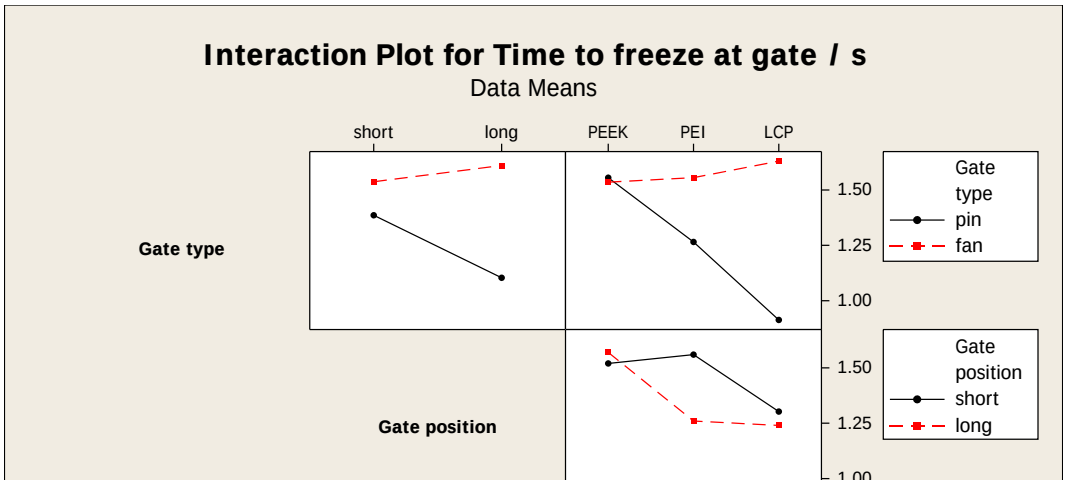
Interaction Plot for Time to freeze at gate / s
Data Means
short
long
PEEK
PEI
LCP
Gate type
Gate position
1.50
1.25
1.00
Gate type
pin
fan
Gate position
short
long

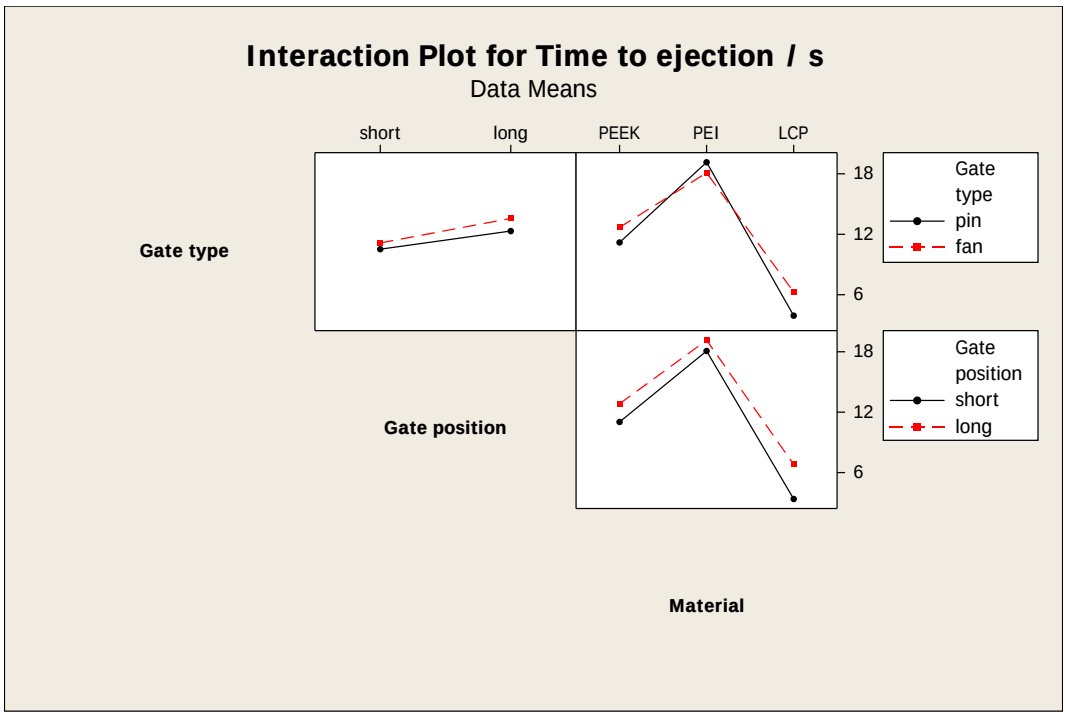
Interaction Plot for Time to ejection / s
Data Means
short
long
PEEK
PEI
LCP
Gate type
Gate position
18
12
6
Gate type
pin
fan
Gate position
short
long
Material

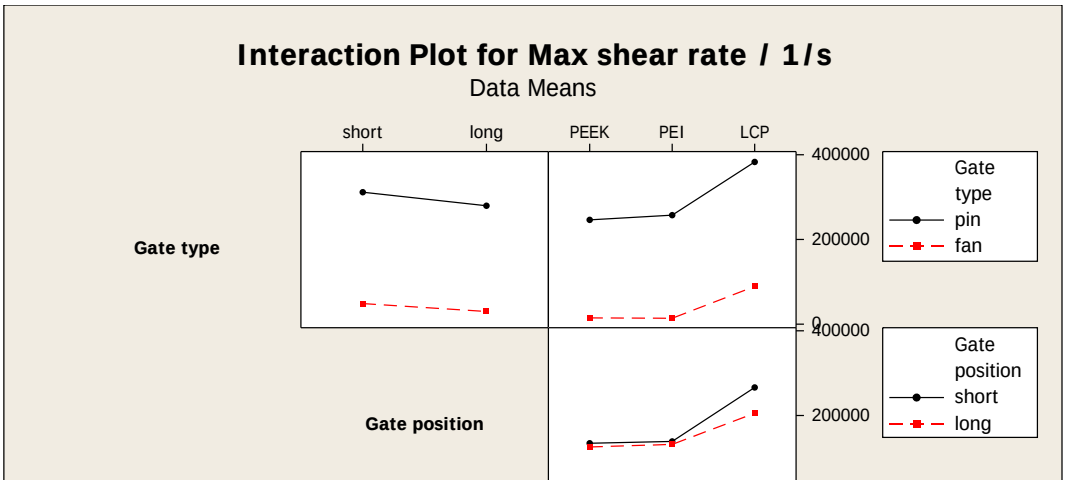
Interaction Plot for Max shear rate / 1/s
Data Means
short
long
PEEK
PEI
LCP
Gate type
Gate position
400000
200000
0
400000
200000
Gate type
pin
fan
Gate position
short
long

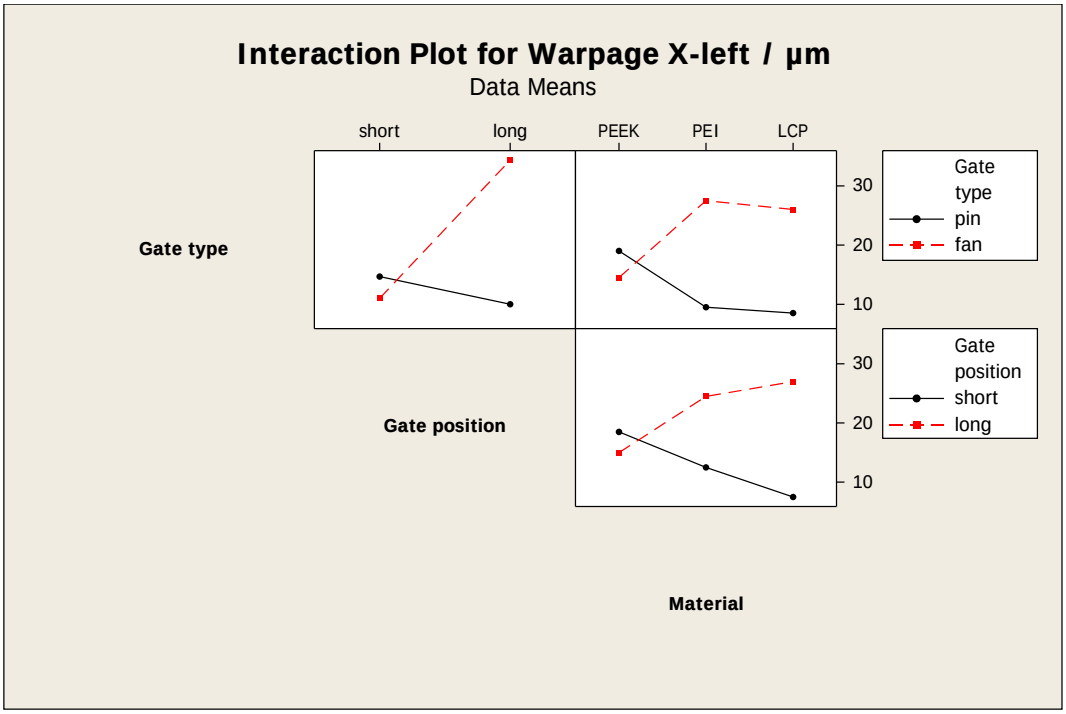
Interaction Plot for Warpage X-left / µm
Data Means
short
long
PEEK
PEI
LCP
Gate type
Gate position
30
20
10
30
20
10
Gate type
pin
fan
Gate position
short
long
Material

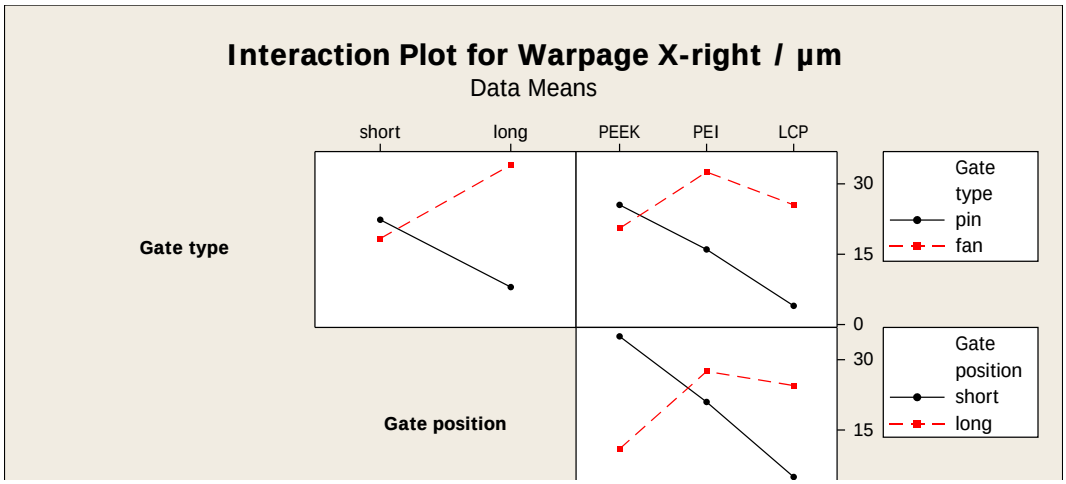
Interaction Plot for Warpage X-right / µm
Data Means
short
long
PEEK
PEI
LCP
Gate type
Gate position
30
15
0
30
15
Gate type
pin
fan
Gate position
short
long

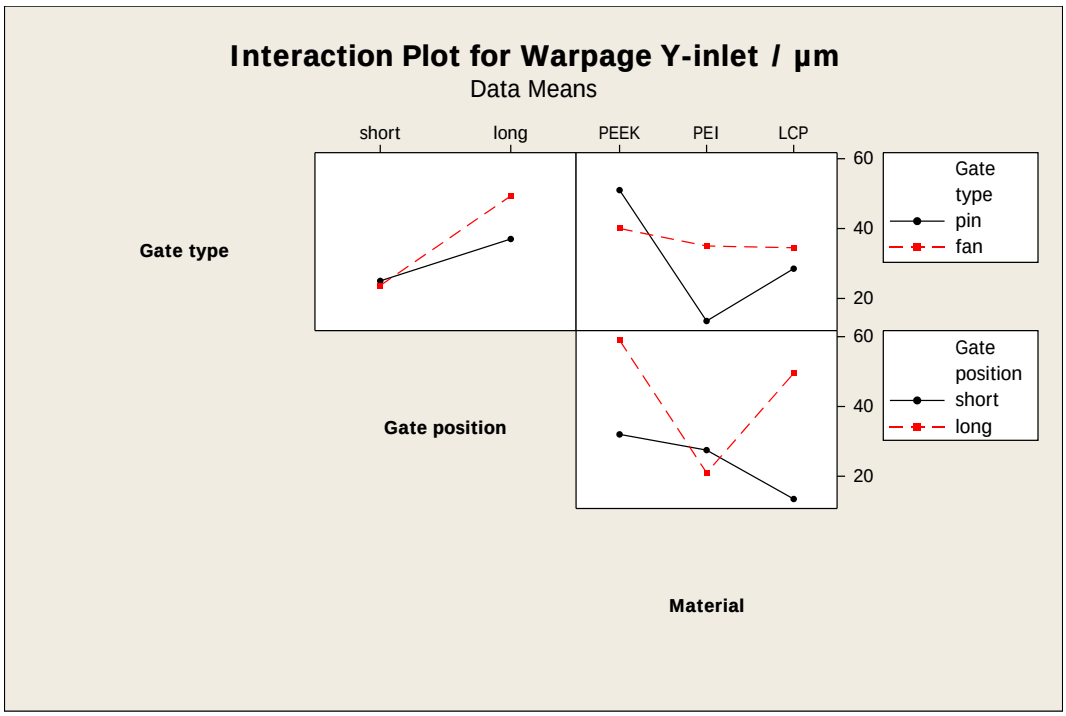
Interaction Plot for Warpage Y-inlet / µm
Data Means
short
long
PEEK
PEI
LCP
Gate type
Gate position
60
40
20
60
40
20
Gate type
pin
fan
Gate position
short
long
Material

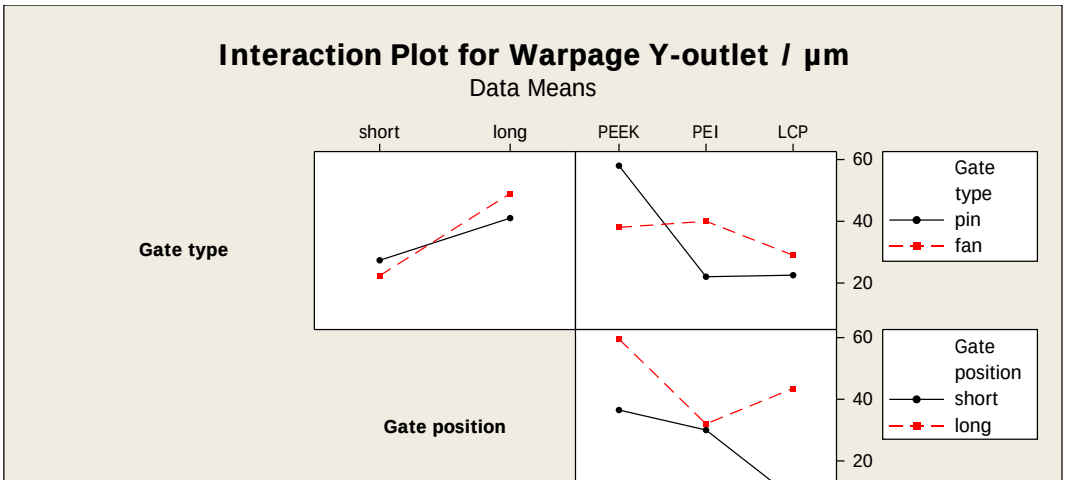
Interaction Plot for Warpage Y-outlet / µm
Data Means
short
long
PEEK
PEI
LCP
Gate type
Gate position
60
40
20
Gate type
pin
fan
Gate position
short
long

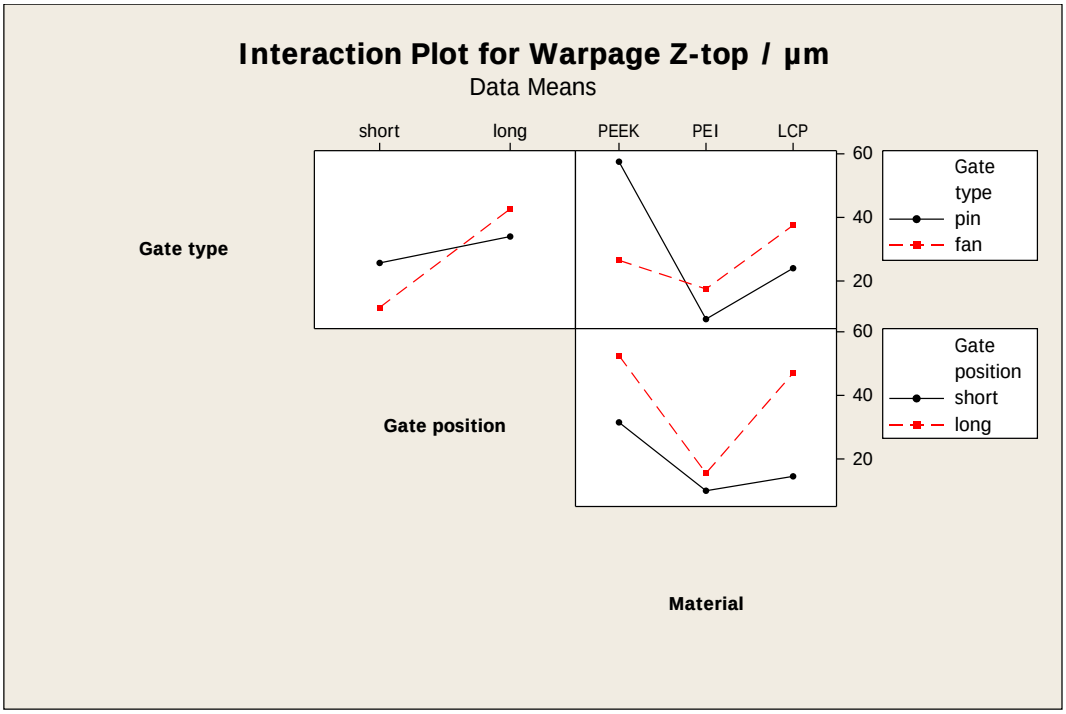
Interaction Plot for Warpage Z-top / µm
Data Means
short
long
PEEK
PEI
LCP
Gate type
Gate position
60
40
20
Gate type
pin
fan
Gate position
short
long
Material

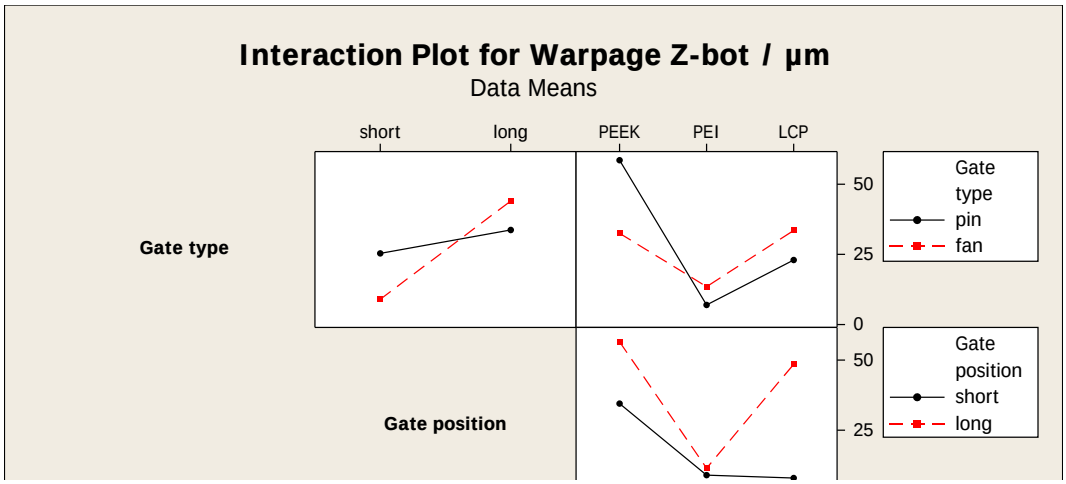
Interaction Plot for Warpage Z-bot / µm
Data Means
short
long
PEEK
PEI
LCP
Gate type
Gate position
50
25
0
50
25
Gate type
pin
fan
Gate position
short
long

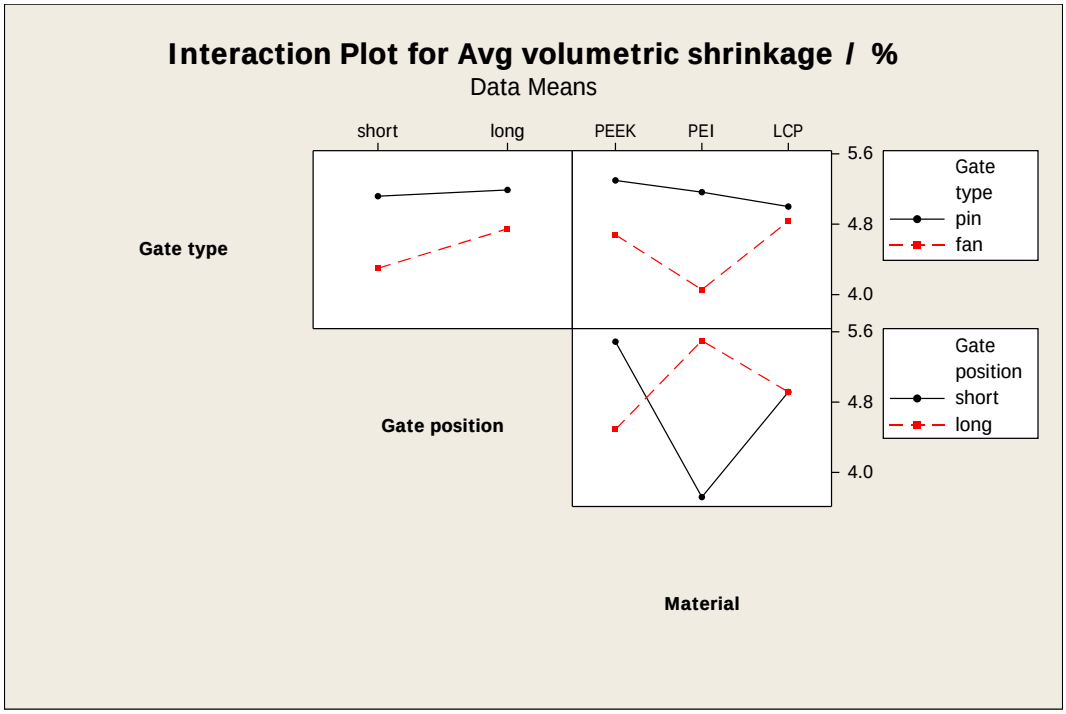
Interaction Plot for Avg volumetric shrinkage / %
Data Means
short
long
PEEK
PEI
LCP
Gate type
Gate position
5.6
4.8
4.0
5.6
4.8
4.0
Gate type
pin
fan
Gate position
short
long
Material

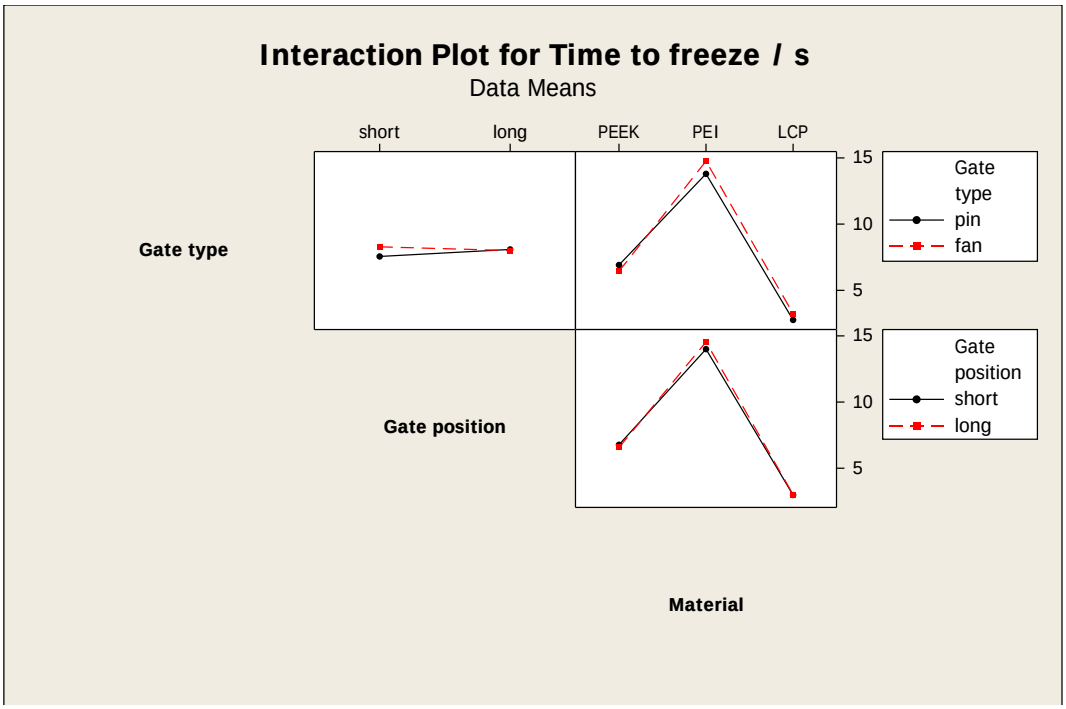
Interaction Plot for Time to freeze / s
Data Means
short
long
PEEK
PEI
LCP
Gate type
Gate position
15
10
5
Gate type
pin
fan
Gate position
short
long
Material

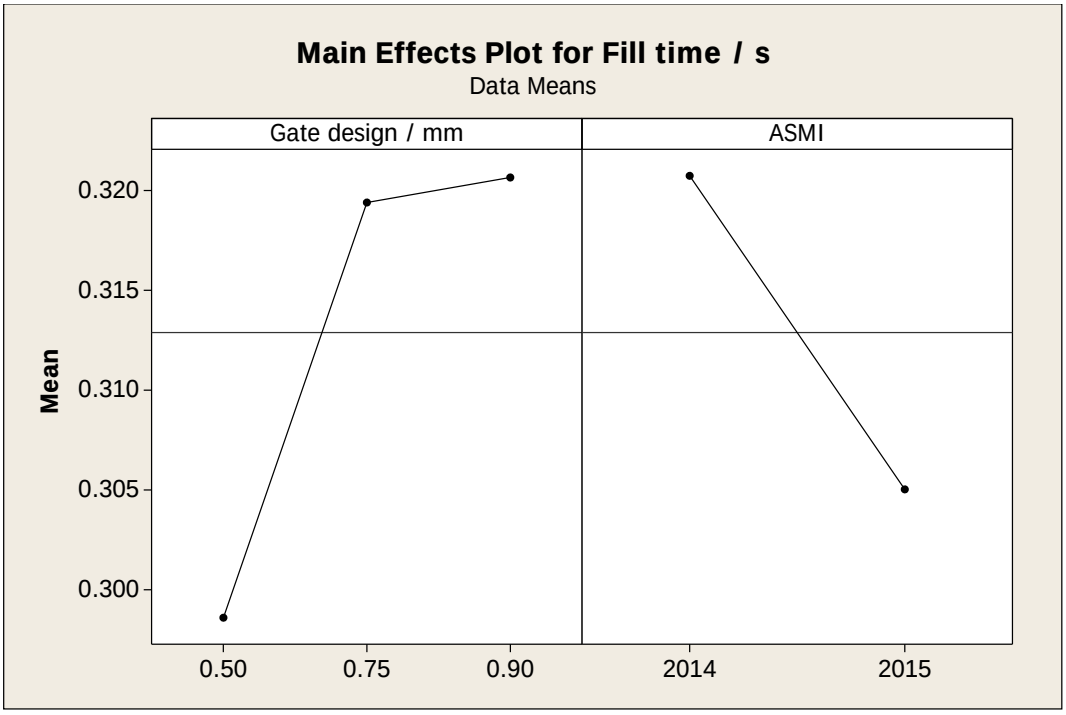
Main Effects Plot for Fill time / s
Data Means
Gate design / mm
ASMI
Mean
0.320
0.315
0.310
0.305
0.300
0.50
0.75
0.90
2014
2015

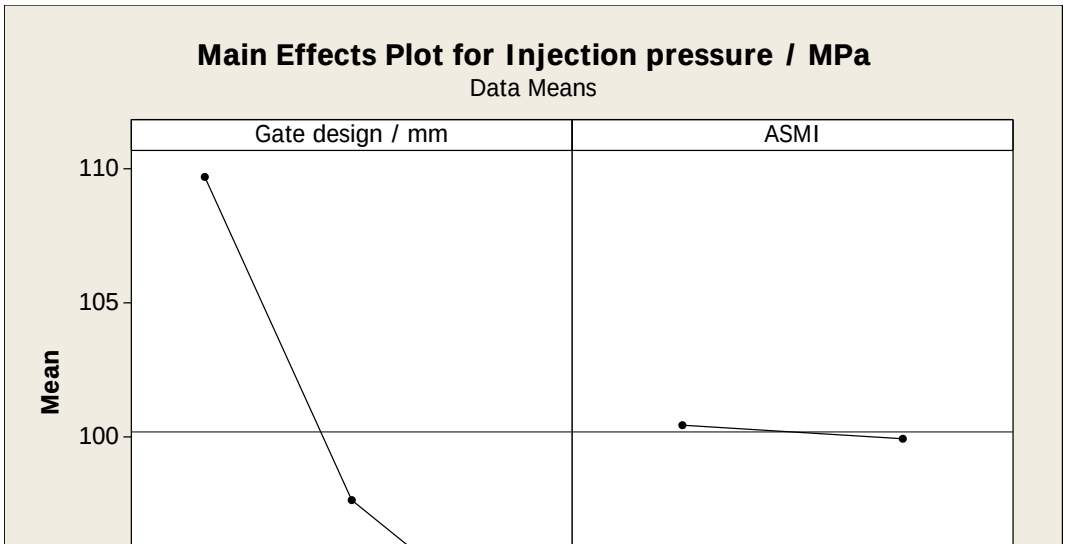
Main Effects Plot for Injection pressure / MPa
Data Means
Gate design / mm
ASMI
Mean
110
105
100

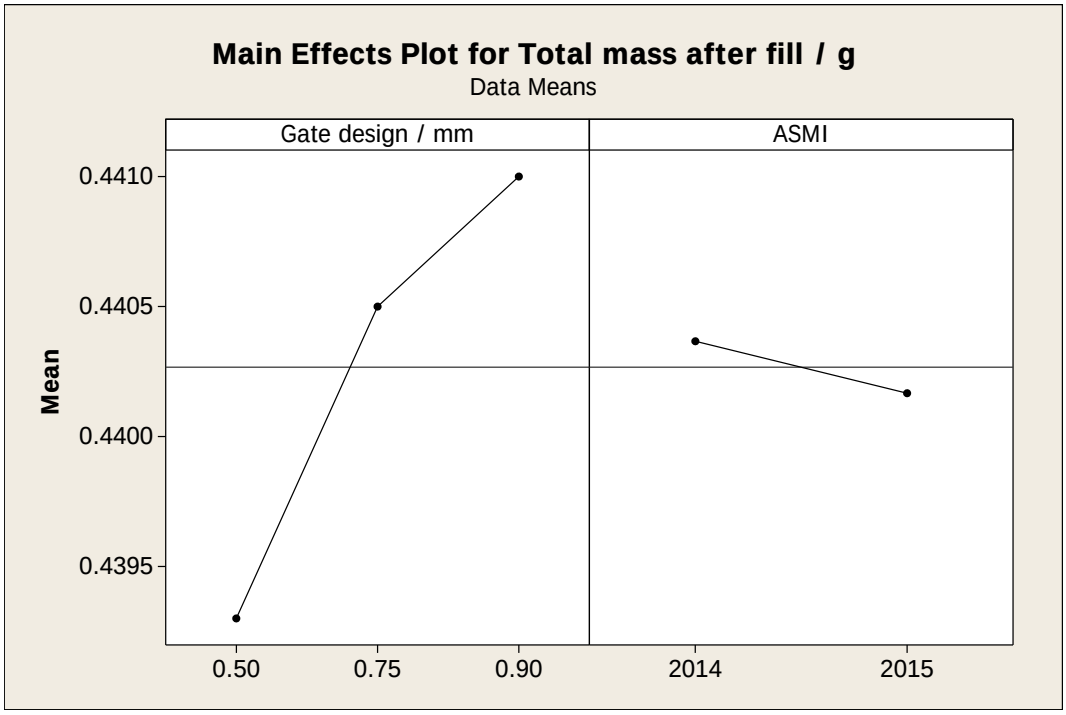
Main Effects Plot for Total mass after fill / g
Data Means
Gate design / mm
ASMI
Mean
0.4410
0.4405
0.4400
0.4395
0.50
0.75
0.90
2014
2015

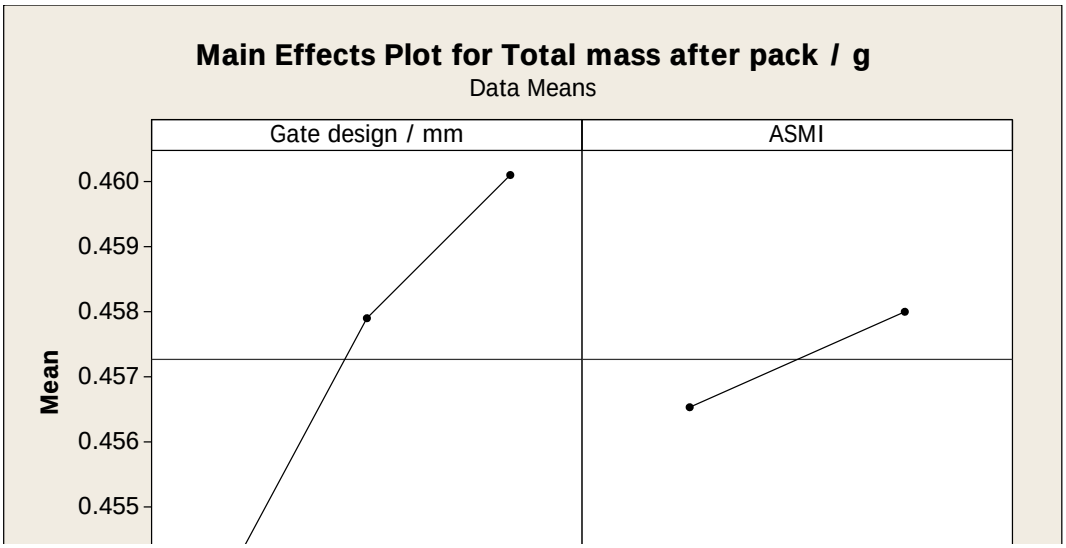
Main Effects Plot for Total mass after pack / g
Data Means
Gate design / mm
ASMI
Mean
0.460
0.459
0.458
0.457
0.456
0.455

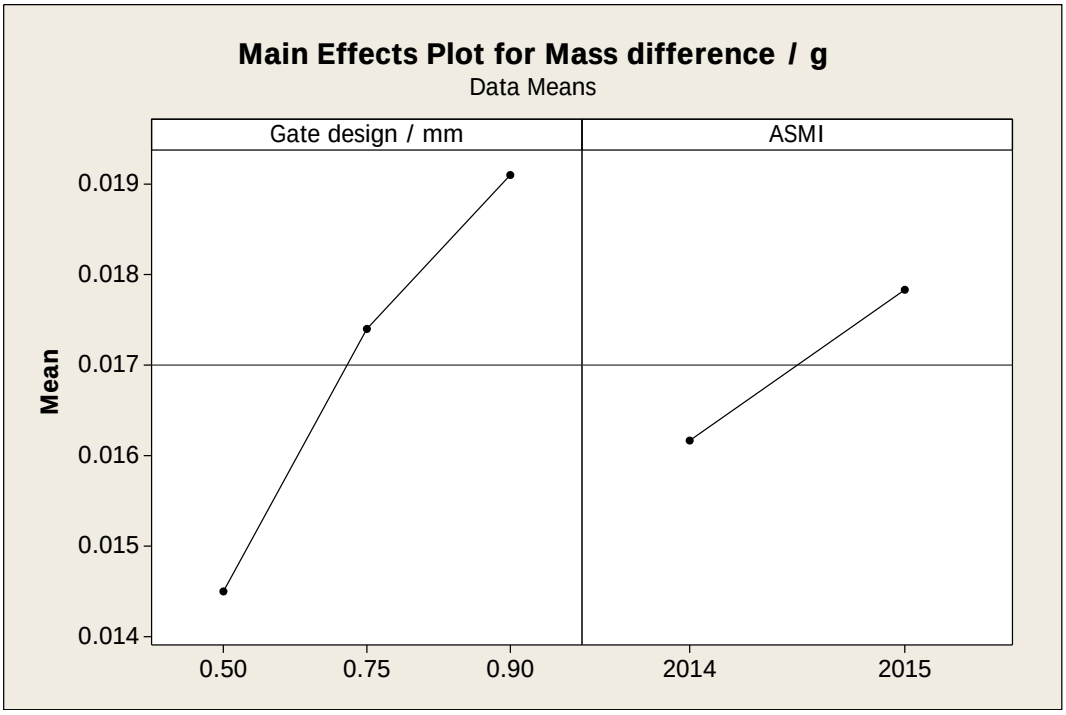
Main Effects Plot for Mass difference / g
Data Means
Gate design / mm
ASMI
Mean
0.019
0.018
0.017
0.016
0.015
0.014
0.50
0.75
0.90
2014
2015

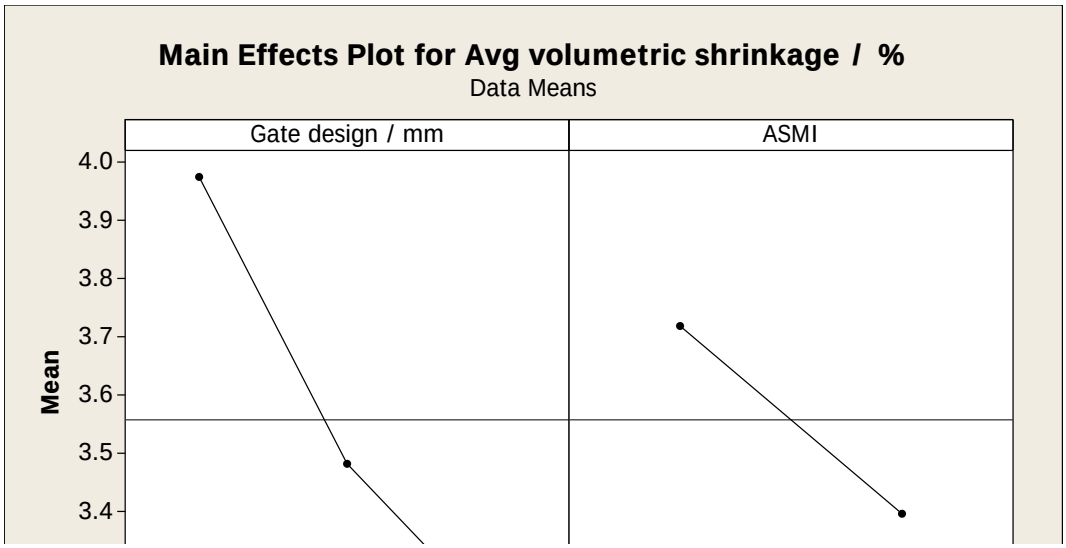
Main Effects Plot for Avg volumetric shrinkage / %
Data Means
Gate design / mm
ASMI
Mean
4.0
3.9
3.8
3.7
3.6
3.5
3.4

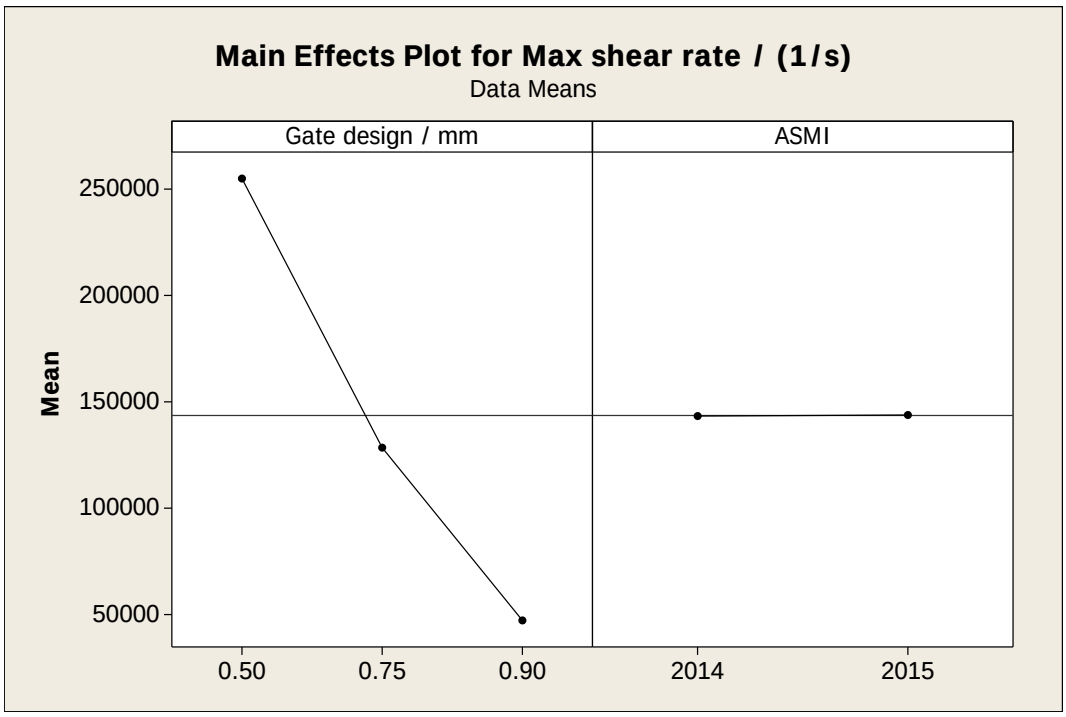
Main Effects Plot for Max shear rate / (1/s)
Data Means
Gate design / mm
ASMI
Mean
250000
200000
150000
100000
50000
0.50
0.75
0.90
2014
2015

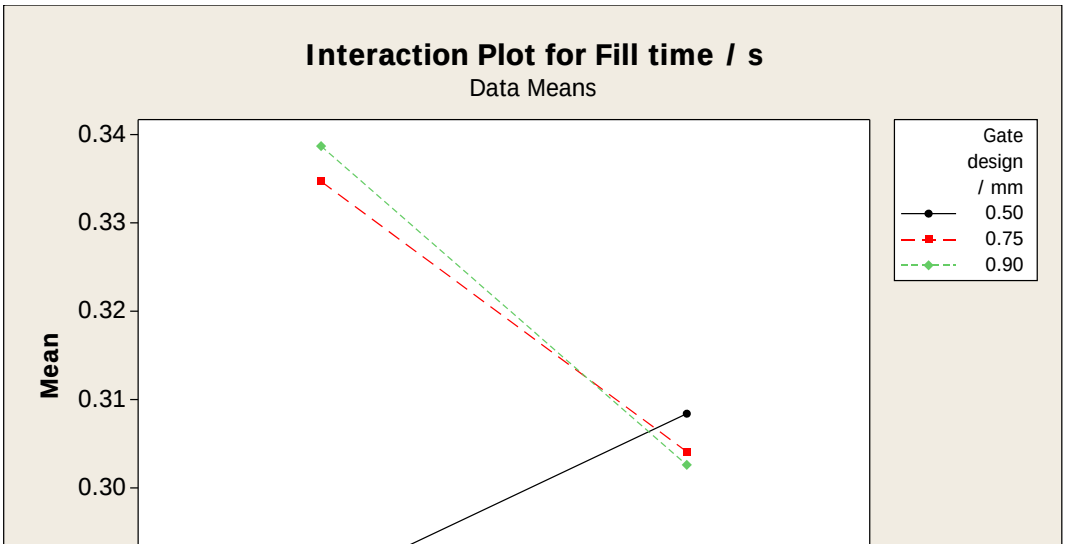
Interaction Plot for Fill time / s
Data Means
0.34
0.33
0.32
0.31
0.30
Mean
Gate design / mm
0.50
0.75
0.90

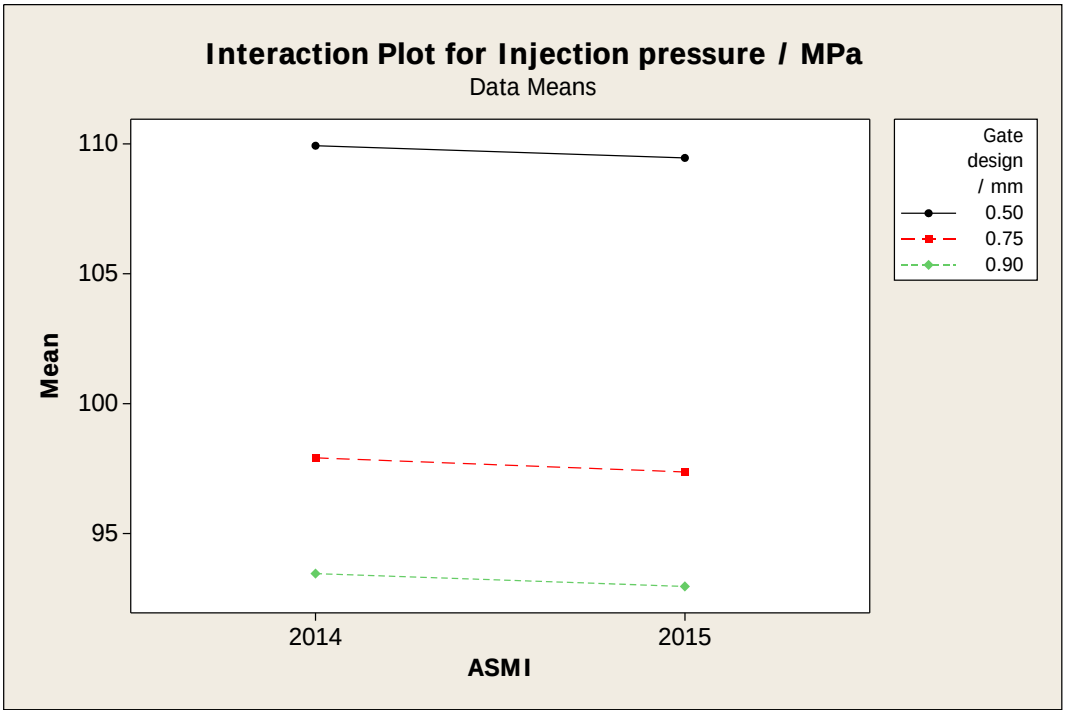
Interaction Plot for Injection pressure / MPa
Data Means
110
105
100
95
Mean
2014
2015
ASMI
Gate design / mm
0.50
0.75
0.90

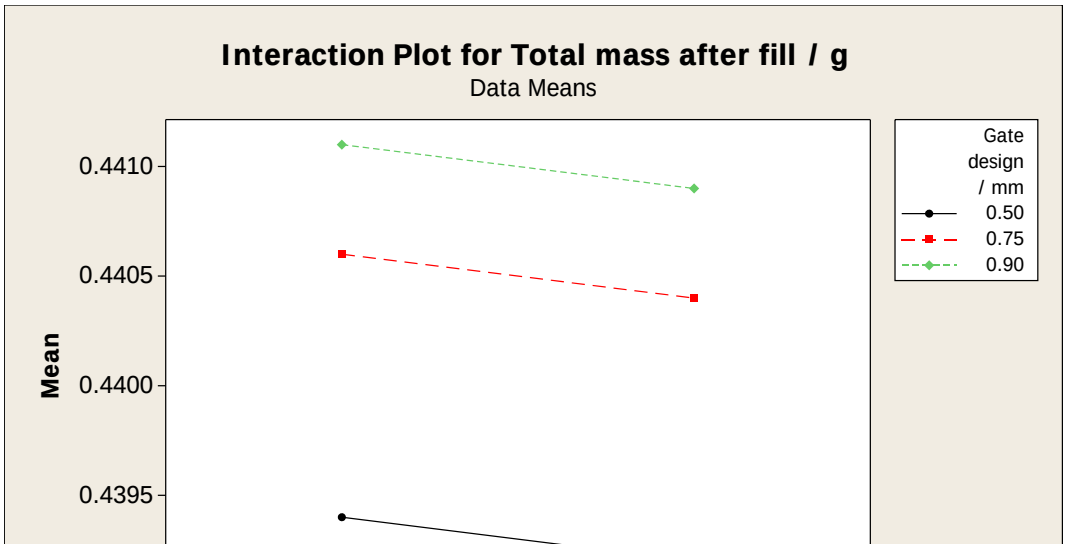
Interaction Plot for Total mass after fill / g
Data Means
Mean
0.4410
0.4405
0.4400
0.4395
Gate design / mm
0.50
0.75
0.90

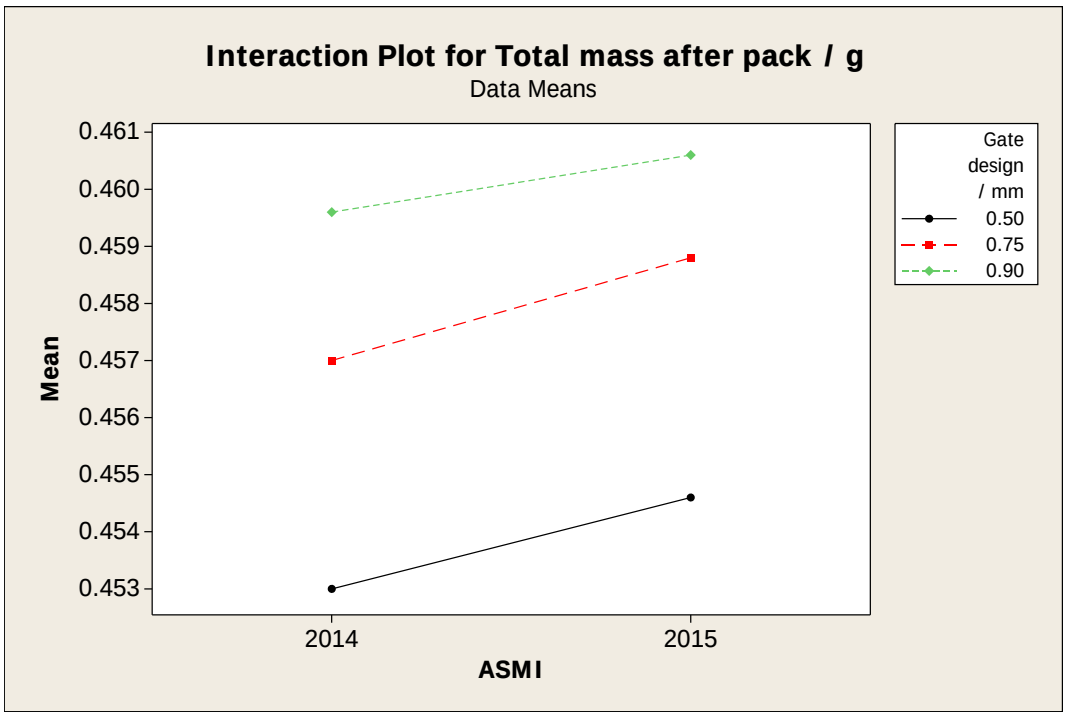
Interaction Plot for Total mass after pack / g
Data Means
Mean
0.461
0.460
0.459
0.458
0.457
0.456
0.455
0.454
0.453
2014
2015
ASMI
Gate design / mm
0.50
0.75
0.90

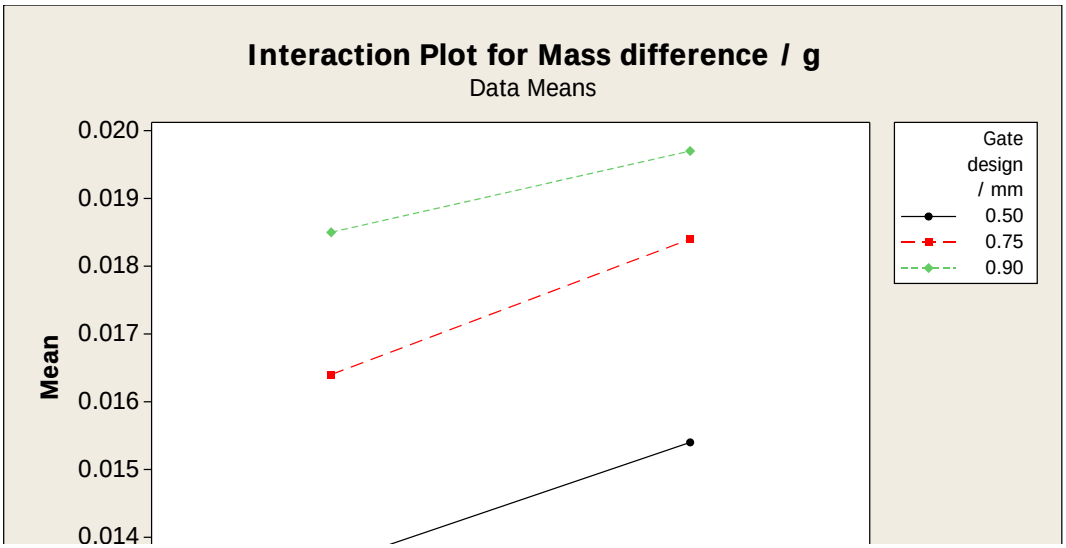
Interaction Plot for Mass difference / g
Data Means
Mean
0.020
0.019
0.018
0.017
0.016
0.015
0.014
Gate design / mm
0.50
0.75
0.90

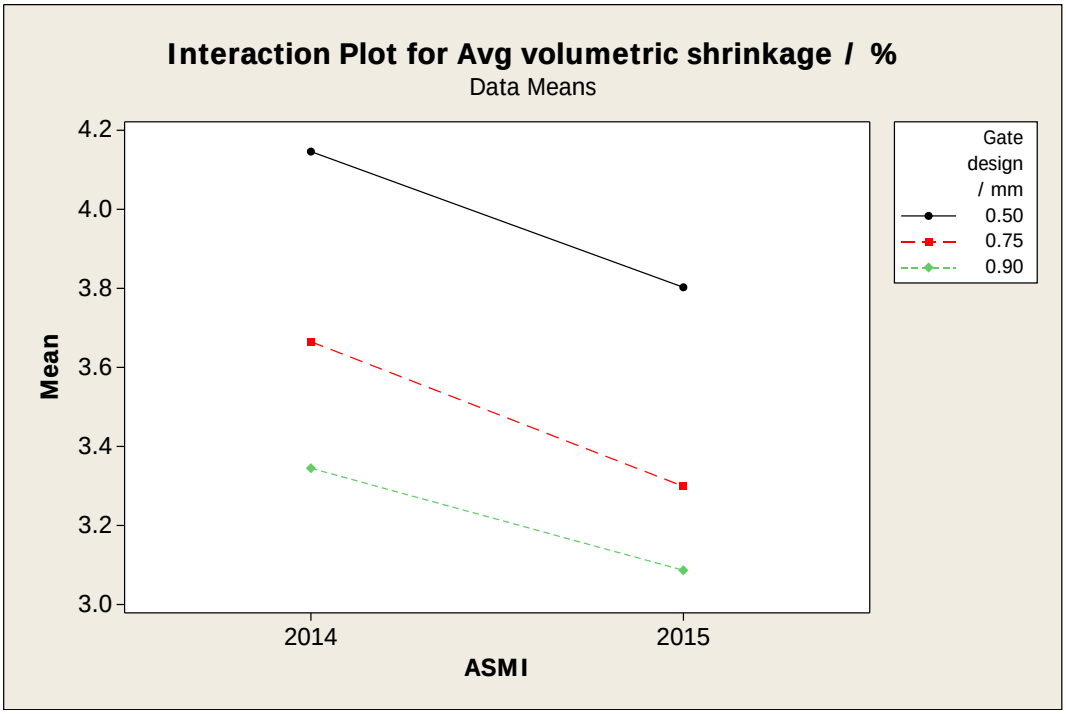
Interaction Plot for Avg volumetric shrinkage / %
Data Means
Mean
4.2
4.0
3.8
3.6
3.4
3.2
3.0
2014
2015
ASMI
Gate design / mm
0.50
0.75
0.90

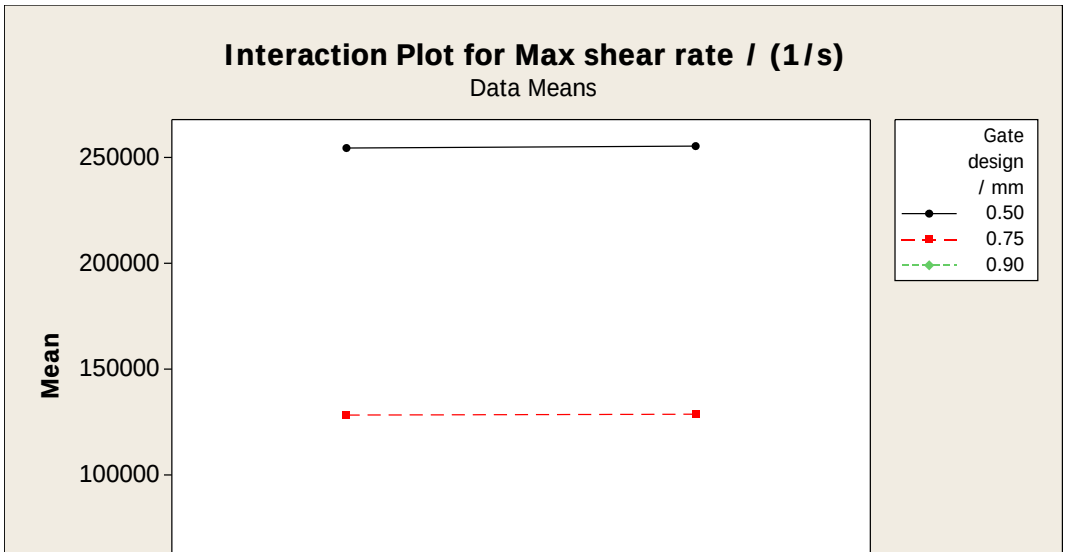
Interaction Plot for Max shear rate / (1/s)
Data Means
Mean
250000
200000
150000
100000
Gate design / mm
0.50
0.75
0.90

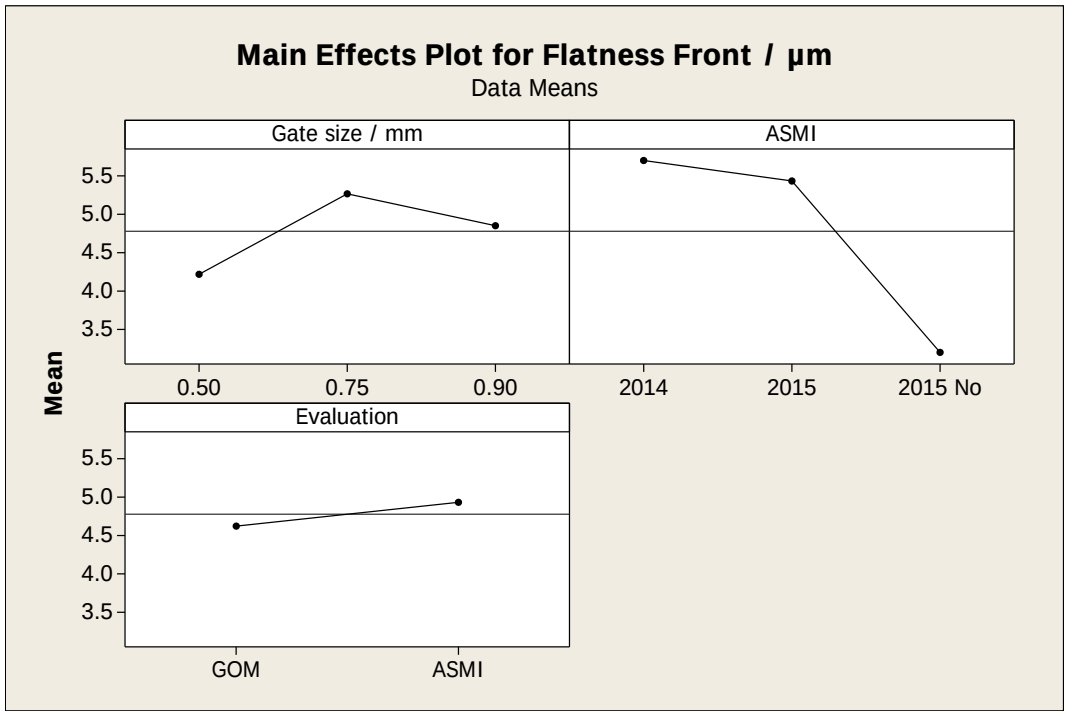
Main Effects Plot for Flatness Front / µm
Data Means
Gate size / mm
ASMI
Evaluation
Mean
5.5
5.0
4.5
4.0
3.5
0.50
0.75
0.90
2014
2015
2015 No
GOM
ASMI

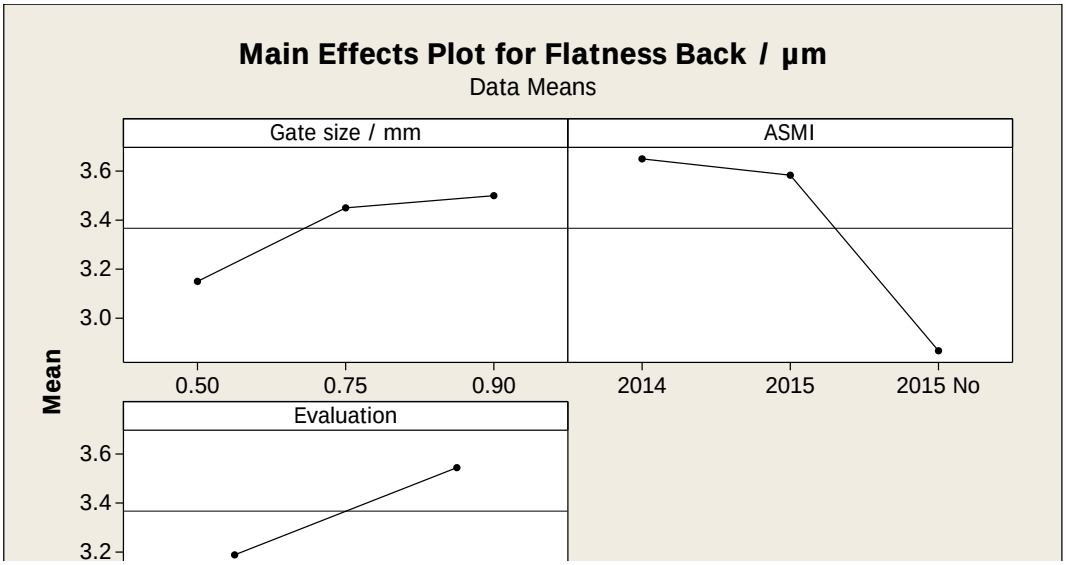
Main Effects Plot for Flatness Back / µm
Data Means
Gate size / mm
ASMI
Evaluation
Mean
3.6
3.4
3.2
3.0
0.50
0.75
0.90
2014
2015
2015 No

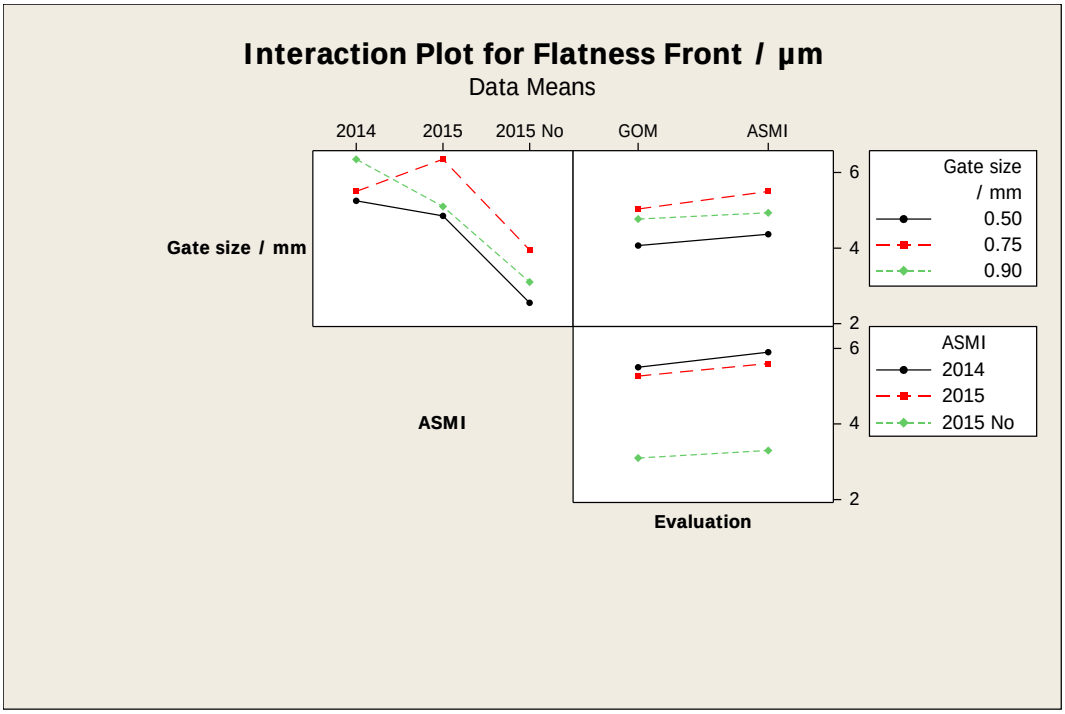
Interaction Plot for Flatness Front / µm
Data Means
2014
2015
2015 No
GOM
ASMI
Gate size / mm
ASMI
Evaluation
6
4
2
Gate size / mm
0.50
0.75
0.90
ASMI
2014
2015
2015 No

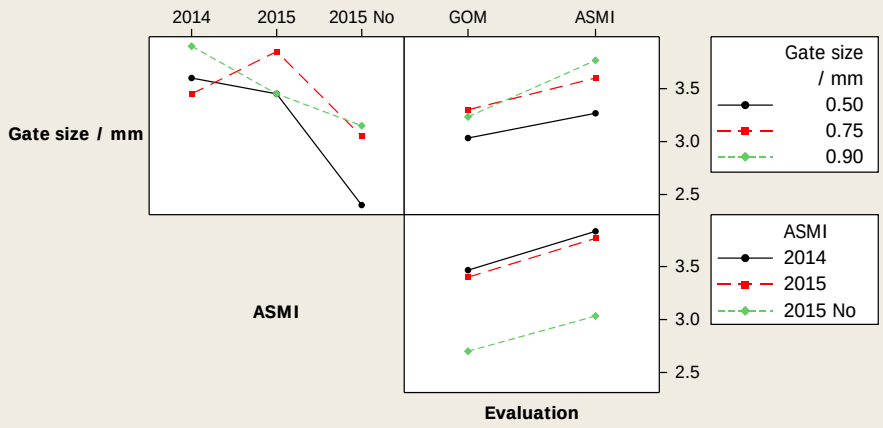

C.3 Pictures of instruments of the simulation validation

The following pages contain pictures of the equipment used for some of the experiments.

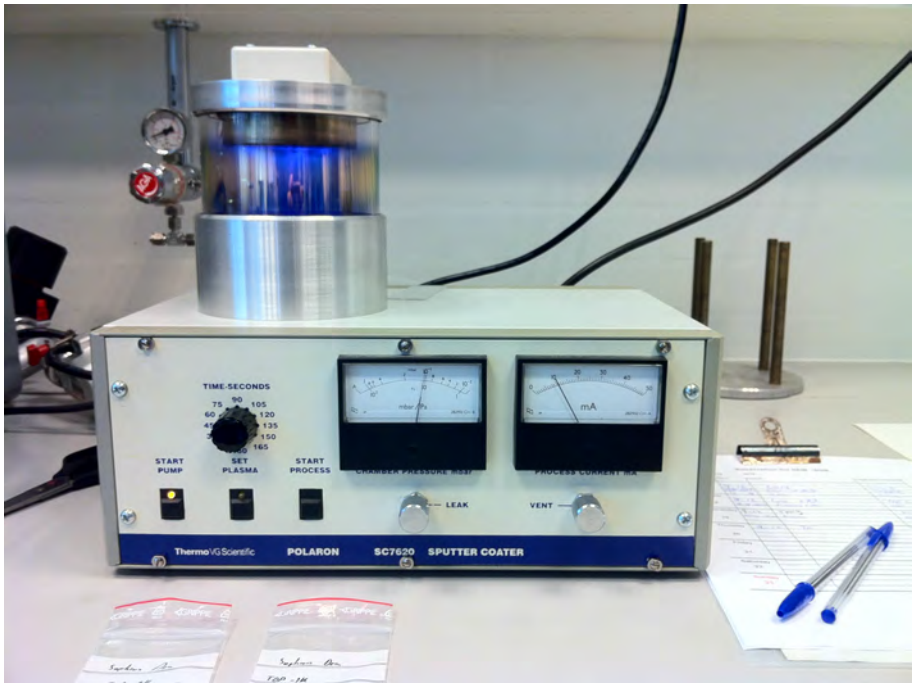

Figure C.1: Polaron Thermo VG Scientific SC7620 sputter coater.

Figure C.2: JEOL JSM-5900 scanning electron microscope.

D Supplementary information to chapter 7

D.1 Supplementary data to the tensile tests

The following pages contain the detailed molding parameters and tensile test results. Please not that the exact material grades could not be published due to confidentiality understandings and to protect the business knowledge of the industrial partners in the Hi-MICRO project.

2K injection molding of dog bone tensile test specimen for Sophion ussing chamber

Equipment:

Machine: Ferromatik Milacron K60 (screw Ø=35mm)
Mold heating: Wittmann Tempro plus 190 (external oil heater)
Thermometer: Digitalthermometer Viking 3000 (precision: ±(0,2 % + 0,1 °C), resolution: 0.1 °C)
Caliper: resolution: 0.1 mm

Material	melt temperature in °C					mould temperature in °C		injection speed in mm/s	injection pressure in bar	cooling time in s	injection length in mm	
	T1	T2	T3	T4	T5	set	measured*				1K	2K
COC	260	250	240	230	170	120	90	80	25-30	15	20	-
PS	220	215	210	205	190	30	50	80	20-25	15	20	-
PP	230	220	210	200	190	70	60	80	10-15	15	20	-
TPE 1	240	230	220	210	200	30	30	80	10-15	12	21	16
TPE 2	240	230	220	210	200	30	30	80	10-15	15	21	16
TPE 3	230	220	210	200	190	20	20	60	10-15	60	28	21

* one measurement at mold surface in between two arbitrary shots
** one measurement with caliper

Material	Switchover point in mm		packing speed in mm/s	packing pressure in bar	packing time in s	Size of dogbone in mm**		Drying	
	1K	2K				Length	thickness	Time in h	Temperature in °C
COC	n.a.	n.a.	30	n.a.	n.a.	149	4.0	4	130
PS	n.a.	n.a.	30	n.a.	n.a.	149	4.0	-	-
PP	n.a.	n.a.	30	n.a.	n.a.	147	3.9	-	-
TPE 1	18	13	30	40	20	147	3.8	-	-
TPE 2	18	13	30	40	20	148	3.9	-	-
TPE 3	17	14	30	40	40	147	4.1	-	-

Material	COC	PS	PP*	TPE 1	TPE 2	TPE 3
Data sheet**	46	39	27	2.30	9.00	8.40

*Note: Manufacturer provides only data about tensile strength at yield, but not at break

**Note: The provided tensile strength at break of the materials might be tested based on different norms and methods. Therefore, the comparison among materials and between data sheet and experiments has limited meaningfulness.

1st shot =	COC	PS	PP	COC	PS	PP
Specimen	Tensile force at break in N			Tensile stress at break in MPa		
1	1803	1501	n.a.	45.1	37.5	n.a.
2	1775	1637	n.a.	44.4	40.9	n.a.
3	1790	n.a.	n.a.	44.8	n.a.	n.a.
4	1810	1632	n.a.	45.3	40.8	n.a.
5	1802	1599	n.a.	45.1	40.0	n.a.
Average	1796	1592	#DIV/0!	44.9	39.8	n.a.
Std Dev	14	63	#DIV/0!	0.3	1.6	#DIV/0!
Uncertainty	17	78	#DIV/0!	0.4	2.0	#DIV/0!

Note: PP and all TPE could not be measured, because the machine traverse reached its end position before the sample broke

1st shot =	COC					
2nd shot =	TPE 1	TPE 2	TPE 3	TPE 1	TPE 2	TPE 3
Specimen	Tensile force at break in N			Tensile stress at break in MPa		
1	8.7	29.9	23.6	0.22	0.75	0.59
2	10.2	29.0	23.3	0.26	0.73	0.58
3	10.3	30.3	22.3	0.26	0.76	0.56
4	4.3	28.6	23.4	0.11	0.71	0.59
5	0.0	30.8	21.6	n.a.	0.77	0.54
Average	7	30	23	0.21	0.74	0.57
Std Dev	4	1	1	0.06	0.02	0.02
Uncertainty	6	1	1	0.08	0.03	0.02

Note: No bonding was achieved for the highlighted samples. The two components fell apart immediately after molding. The bond strength and tensile force is therefore set to F=0 N. The sample is not taken into consideration for the tensile strength average and standard deviation.

1st shot =	PS					
2nd shot =	TPE 1	TPE 2	TPE 3	TPE 1	TPE 2	TPE 3
Specimen	Tensile force at break in N			Tensile stress at break in MPa		
1	40.8	12.6	13.1	1.02	0.32	0.33
2	42.6	14.2	13.7	1.07	0.36	0.34
3	44.4	19.0	12.9	1.11	0.48	0.32
4	42.8	12.9	16.9	1.07	0.32	0.42
5	33.6	15.9	15.9	0.84	0.40	0.40
Average	41	15	15	1.02	0.37	0.36
Std Dev	4	2	2	0.09	0.06	0.04
Uncertainty	5	3	2	0.12	0.07	0.05

1st shot =	PP					
2nd shot =	TPE 1	TPE 2	TPE 3	TPE 1	TPE 2	TPE 3
Specimen	Tensile force at break in N			Tensile stress at break in MPa		
1	12.3	63.3	67.4	0.31	1.58	1.69
2	13.4	69.3	56.7	0.34	1.73	1.42
3	0.0	72.9	69.0	n.a.	1.82	1.73
4	15.9	55.2	77.1	0.40	1.38	1.93
5	14.7	68.5	72.5	0.37	1.71	1.81
Average	11.3	65.8	68.6	0.35	1.65	1.71
Std Dev	6.4	6.2	6.8	0.03	0.15	0.17
Uncertainty	8.0	7.6	8.4	0.04	0.19	0.21

Note: No bonding was achieved for the highlighted samples. The two components fell apart immediately after molding. The bond strength and tensile force is therefore set to F=0 N. The sample is not taken into consideration for the tensile strength average and standard deviation.

D.2 Supplementary calculations to the dimensioning of the press-fits

The following pages contain the detailed calculation of the dimensions of the press-firts of the microfluidic mixer. The calculations were conducted by means of Wolfram Mathematica® 9.

Calculation of geometrical design factors for press-fits

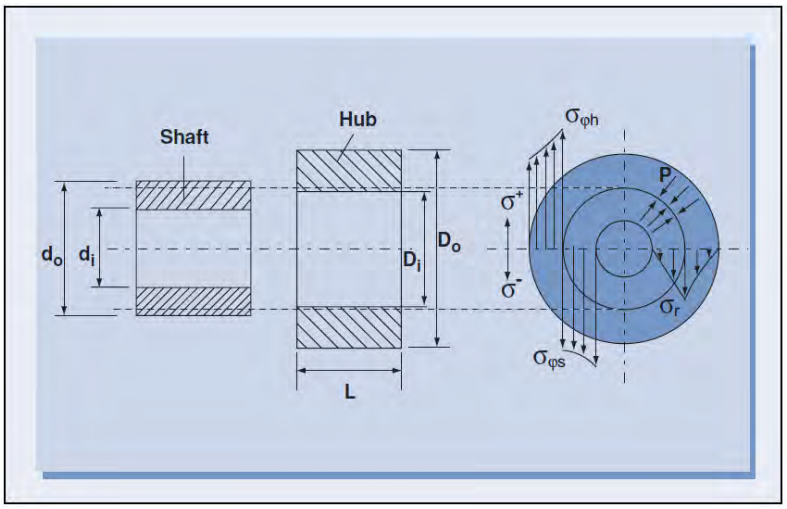

Designations of variables for design of press – fit connection.
(Source: DSM – Secondary Operations Guide – Assembly and Finishing of Engineering Plastics)

Assembly force

The assembly force/axial bearing capacity of the press-fit results from the frictional forces between hub and shaft. It is mathematically given as:
(Source: DSM - Secondary Operations Guide - Assembly and Finishing of Engineering Plastics)

$$F = \mu F_N = \mu S p = \mu \pi d_o L p$$

The pressure between shaft and hub is given as:

$$p = \frac{i T}{d_o (A+B)}$$

The interference *i* between hub and shaft ist given as:

$$i = d_o - D_i$$

A and B are geometrical factor of shaft and hub:

$$A = \frac{1+(d_i/d_o)^2}{1-(d_i/d_o)^2}$$
$$B = \frac{1+(d_o/D_o)^2}{1-(d_o/D_o)^2}$$

Dimensioning of press-fits (calculation of inner hub diameter)

All relevant equations for dimensioning of press-fits and solving for D_{in}:

In[1]:=
```
p = (Ds - dh) T / (Ds (A + B));(* pressure between shaft and hub for same plastic in Pa *)

Eq = F == μ S p;(* assembly force/axial bearing capacity in N *)

Solve[Eq, dh]
```

Out[3]= $\left\{\left\{\text{dh} \to -\frac{\text{Ds}\ (\text{A F} + \text{B F} - \text{S T}\ \mu)}{\text{S T}\ \mu}\right\}\right\}$

System pressure acting on press-fit (lower interference limit)

When the device is in service, a pressure of ±1 bar is applied to drive the liquid. Alternatively, ±450 mbar could be used. This pressure introduces a force on the device which the press-fits have to withstand, otherwise the device will open or leak. The force on the BOT liquid chamber will be greater than on the TOP liquid chamber due to the bigger surface area the pressure can act on.

In[4]:=
```
pmax = {1.0 × 10^5, 0.45 × 10^5};(* maximum system pressure in Pa *)

A = 67 × 10^-6;(* surface area of BOT liquid chamber in m² *)

Fmax = A pmax(* force acting on the press-fits in N *)
```

Out[6]= {6.7, 3.015}

Insertion of actual numerical values

Inserting numerical values and calculate D_{in} and p depending both on the hydrostatic pressure inside the device. Safety factors for the force and the tensile/relaxation modulus of the material in service are considered. Mean assumptions are taken for the coefficient of friction.

In[7]:=
```
dh[T_] := -(Ds (A F + B F - S T μ))/(S T μ);(* inner hub diameter in m *)
Int[T_] := Ds - dh[T];(* interference between hub and shaft in m *)
```

```
Ds = 2 × 10^-3;(* outer shaft diameter in m *)
A = 1;(* geometrical factor in units of 1 *)
F = (2 Fmax)/4;(* force on single press-fit including safety factor in N *)
B = (1 + (Ds / Dh)^2)/(1 - (Ds / Dh)^2);(* geometrical factor in units of 1 *)
Dh = 6 × 10^-3;(* outer hub diameter in m *)
S = 4 × 0.642 × 10^-6;
(* contact area between shaft and hub of single press-fit in m² *)
μ = 0.25;(* coefficient of friction for plastic vs plastic in units of 1*)

TCOC = 3.20 × 10^9;(* tensile/relaxation modulus of COC in Pa *)
TPP = 1.05 × 10^9;(* tensile/relaxation modulus of PP in Pa *)
TPS = 3.25 × 10^9;(* tensile/relaxation modulus of PS in Pa *)

{dh[0.8 TCOC], Int[0.8 TCOC]} * 10^3
{dh[0.8 TPP], Int[0.8 TPP]} * 10^3
{dh[0.8 TPS], Int[0.8 TPS]} * 10^3
```

Out[19]= {{1.99083, 1.99587}, {0.00917239, 0.00412757}}

Out[20]= {{1.97205, 1.98742}, {0.0279539, 0.0125793}}

Out[21]= {{1.99097, 1.99594}, {0.00903127, 0.00406407}}

⇒ maximum inner hub diameter // minimum interference for 1 bar fluid pressure:

COC:	**1.991 mm**	**9 µm**	**(10 µm)**
PP:	**1.972 mm**	**28 µm**	**(30 µm)**
PS:	**1.991 mm**	**9 µm**	**(10 µm)**

Maximum interference (upper interference limit)

The interference between shaft and hub is limited due to the limited mechanical strength of the material. The maximum allowed interference I_{max} for shaft and hub made out of the same material is given as:
(Source: DuPont - Technische Kunststoffe - Allgemeine Kunstruktionsprinzipien)

$$I_{max} = \frac{\sigma D_s (W+1)}{T W}$$

In[22]:=
```
σCOC = 46 × 10^6;(* tensile stress of COC in Pa *)
σPP = 27 × 10^6;(* tensile stress of PP in Pa *)
σPS = 39 × 10^6;(* tensile stress of PS in Pa *)

W = (Dh^2 + Ds^2)/(Dh^2 - Ds^2);(* geometrical factor in units of 1 *)

Imax[σ_, T_] := σ Ds (W + 1)/(T W);(* maximum allowed interference in m *)
Isafe[Dh_, Ds_] := Imax[Dh, Ds] / 1.5;
(* maximum allowed interference with safety factor in m *)

Isafe[σCOC, TCOC] * 10^3
Isafe[σPP, TPP] * 10^3
Isafe[σPS, TPS] * 10^3
```

Out[28]= 0.0345

Out[29]= 0.0617143

Out[30]= 0.0288

⇒ minimum inner hub diameter // maximum interference before breakage:

COC:	**1.966 mm**	**34 µm**	**(30 µm)**
PP:	**1.939 mm**	**61 µm**	**(60 µm)**
PS:	**1.972 mm**	**28 µm**	**(30 µm)**

Final proposal for dimensions

	hole	**shaft**
COC:	**(2.000 ± 0.005) mm**	**(1.980 ± 0.005) mm**
PP:	**(2.000 ± 0.010) mm**	**(1.960 ± 0.010) mm**
PS:	**(2.000 ± 0.005) mm**	**(1.980 ± 0.005) mm**

D.3 Technical drawings of mold and mold components

The following pages contain technical drawings of the mold and mold entities. Please note that some of the technical drawings could not be published due to confidentiality understandings and to protect the business knowledge of the industrial partners in the Hi-MICRO project.

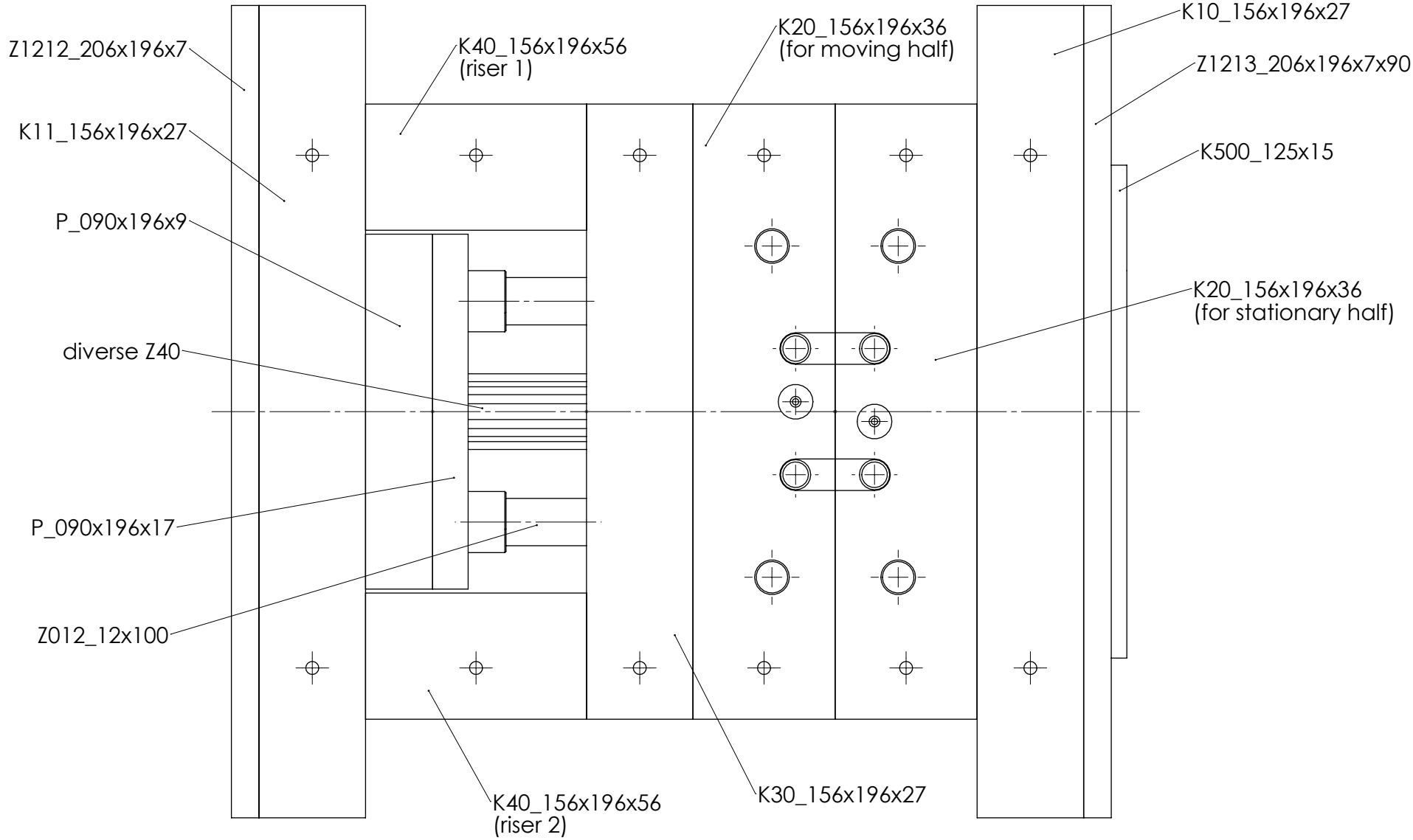

UNLESS OTHERWISE SPECIFIED: DIMENSIONS ARE IN MILLIMETERS SURFACE FINISH: TOLERANCES: LINEAR: ANGULAR:		FINISH:		DEBUR AND BREAK SHARP EDGES	DO NOT SCALE DRAWING	REVISION
	NAME	SIGNATURE	DATE		TITLE: Assembly drawing of the machined parts. Please note that some of the shown components are standard parts from HASCO. They will be used without any modifications or machining. Some of the standard HASCO parts are not shown for better overview.	
DRAWN	MAXMAR		23-05-2014			
CHK'D						
APPV'D						
MFG						
Q.A				MATERIAL:	DWG NO.	A3
				WEIGHT:	SCALE:1:1	SHEET 1 OF 3

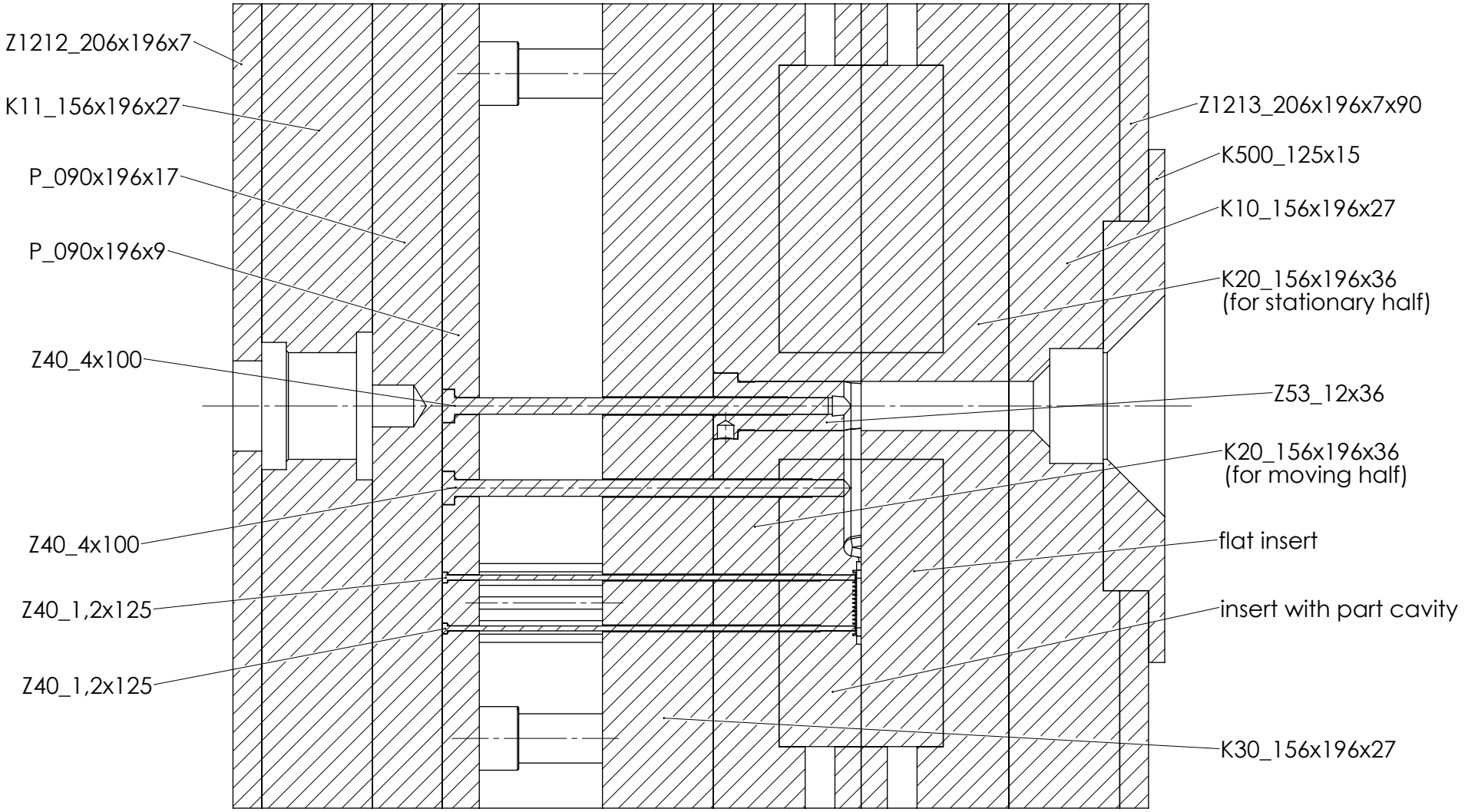

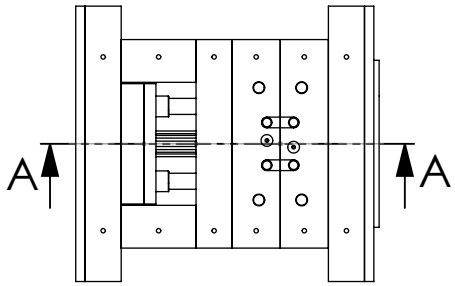

SECTION A-A
SCALE 1:1

UNLESS OTHERWISE SPECIFIED: DIMENSIONS ARE IN MILLIMETERS SURFACE FINISH: TOLERANCES: LINEAR: ANGULAR:	FINISH:				DEBUR AND BREAK SHARP EDGES	DO NOT SCALE DRAWING / REVISION
	NAME	SIGNATURE	DATE			TITLE: Assembly drawing of the machined parts. Please note that some of the shown components are standard parts from HASCO. They will be used without any modifications or machining. Some of the standard HASCO parts are not shown for better overview.
DRAWN	MAXMAR		23-05-2014			
CHK'D						
APPV'D						
MFG						
Q.A				MATERIAL:		DWG NO. / A3
				WEIGHT:		SCALE:1:4 / SHEET 2 OF 3

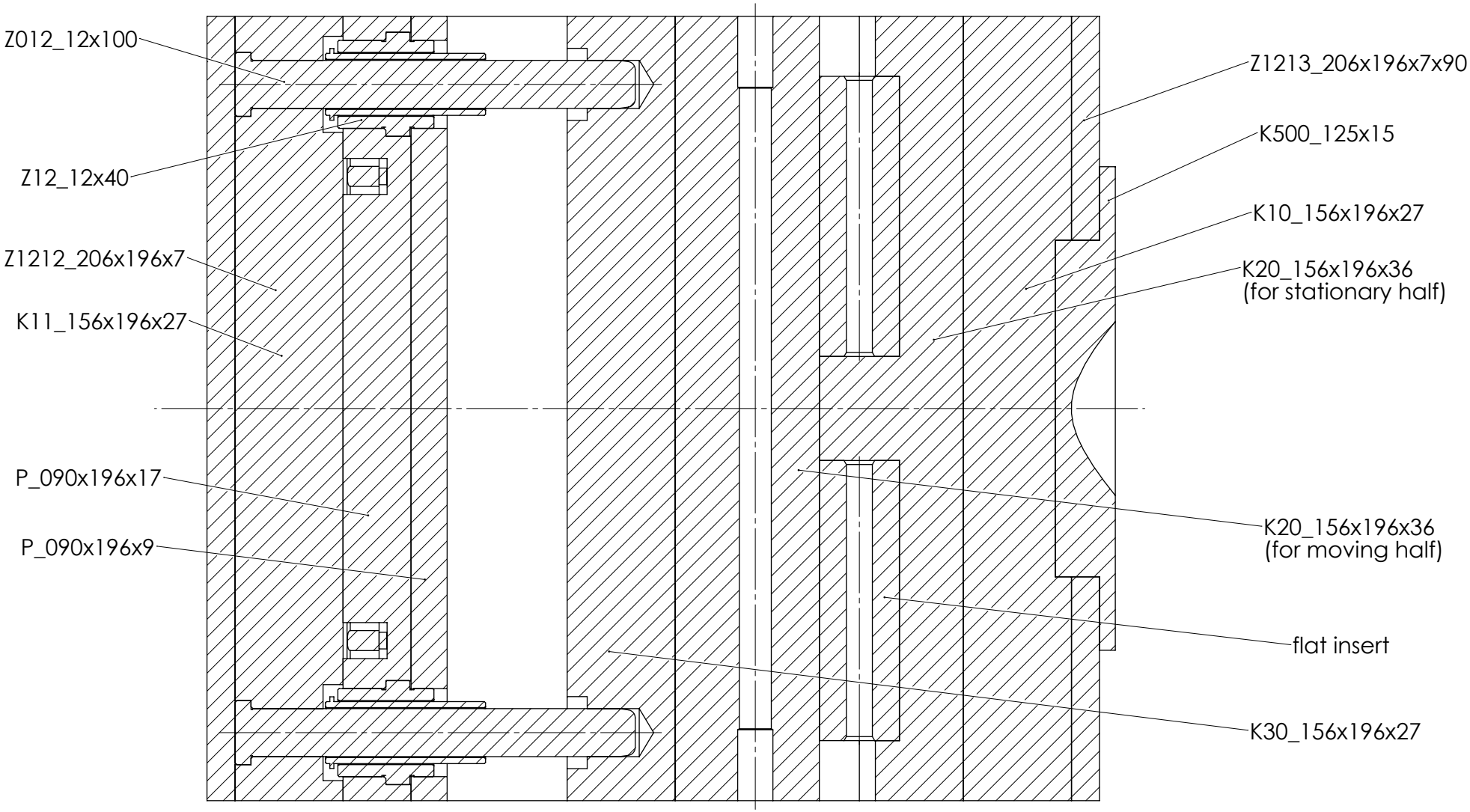

SECTION C-C
SCALE 1 : 1

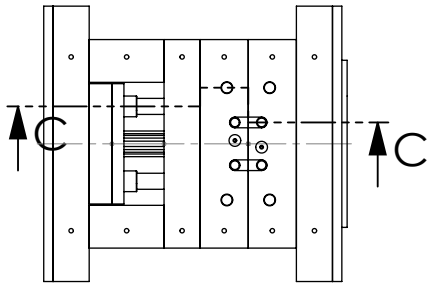

UNLESS OTHERWISE SPECIFIED: DIMENSIONS ARE IN MILLIMETERS SURFACE FINISH: TOLERANCES: LINEAR: ANGULAR:	FINISH:		DEBUR AND BREAK SHARP EDGES	DO NOT SCALE DRAWING	REVISION	
	NAME	SIGNATURE	DATE	TITLE: Assembly drawing of the machined parts. Please note that some of the shown components are standard parts from HASCO. They will be used without any modifications or machining. Some of the standard HASCO parts are not shown for better overview.		
DRAWN	MAXMAR		23-05-2014			
CHK'D						
APPV'D						
MFG						
Q.A				MATERIAL:	DWG NO.	A3
				WEIGHT:	SCALE:1:4	SHEET 3 OF 3

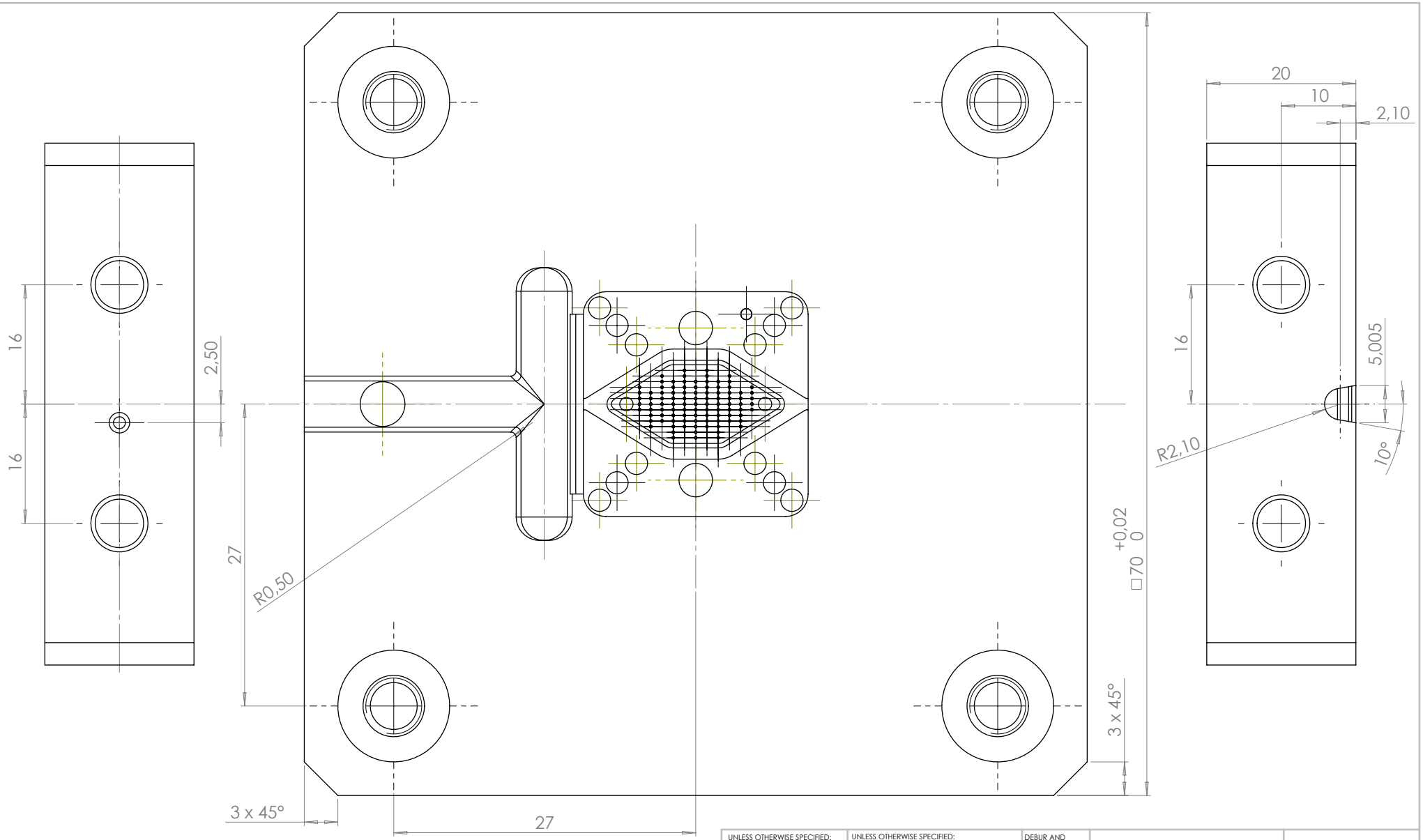

MAIN VIEW
SCALE 3:1

UNLESS OTHERWISE SPECIFIED: DIMENSIONS ARE IN MILLIMETERS SURFACE FINISH: ▽ Rz 10	UNLESS OTHERWISE SPECIFIED: TOLERANCES: LINEAR: DIN ISO 2768-1 fine ANGULAR: DIN ISO 2768-1 fine HOLES: DIN EN ISO 286-1 H7			DEBUR AND BREAK SHARP EDGES (NOT FOR EDGES DEFINING THE RUNNER OR CAVITY)	DO NOT SCALE DRAWING	REVISION V01
	NAME	SIGNATURE	DATE			
DRAWN	MAXMAR		19-05-2014			
CHK'D						
APPV'D						
MFG						
Q.A				MATERIAL: IMPAX	DWG NO. Insert	A3
				WEIGHT:	SCALE:2:1	SHEET 1 OF 8

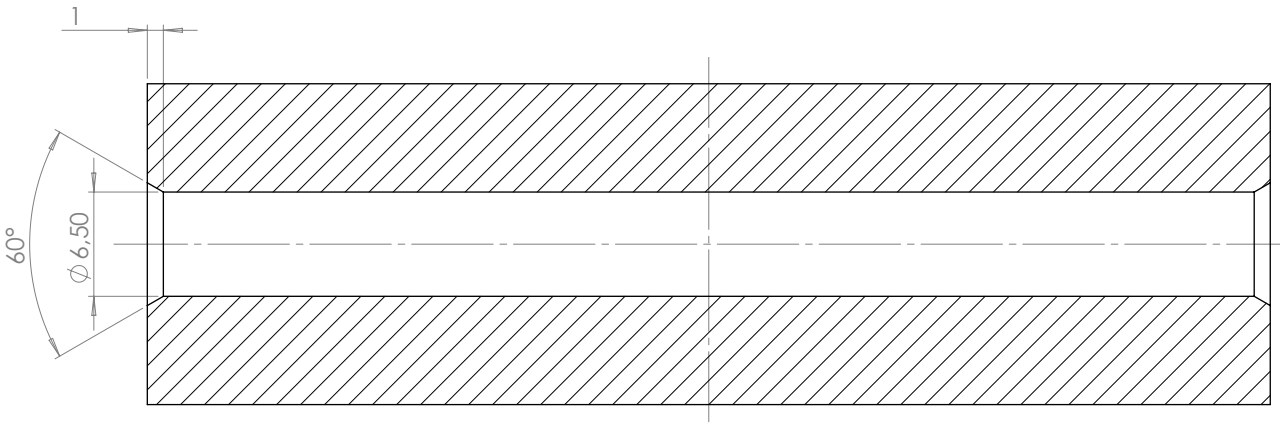

SECTION A-A
SCALE 3 : 1

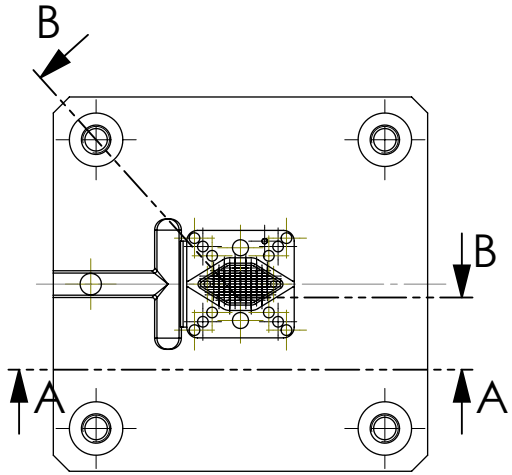

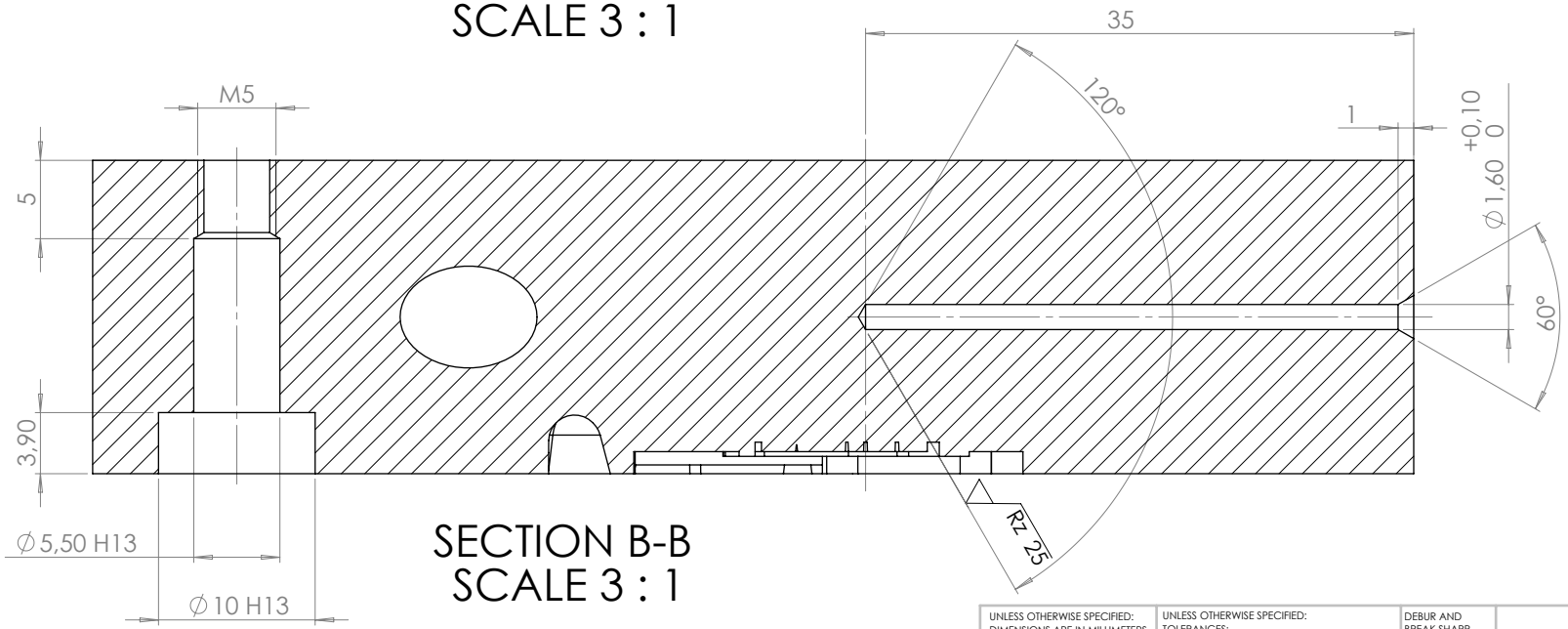

SECTION B-B
SCALE 3 : 1

UNLESS OTHERWISE SPECIFIED: DIMENSIONS ARE IN MILLIMETERS SURFACE FINISH: Rz 10	UNLESS OTHERWISE SPECIFIED: TOLERANCES: LINEAR: DIN ISO 2768-1 fine ANGULAR: DIN ISO 2768-1 fine HOLES: DIN EN ISO 286-1 H7		DEBUR AND BREAK SHARP EDGES (NOT FOR EDGES DEFINING THE RUNNER OR CAVITY)		DO NOT SCALE DRAWING	REVISION V01
	NAME	SIGNATURE	DATE			
DRAWN	MAXMAR		19-05-2014			
CHK'D						
APPV'D						
MFG						
Q.A				MATERIAL: IMPAX	DWG NO. Insert	A3
				WEIGHT:	SCALE:1:1	SHEET 2 OF 8

SECTION C-C
SCALE 5 : 1

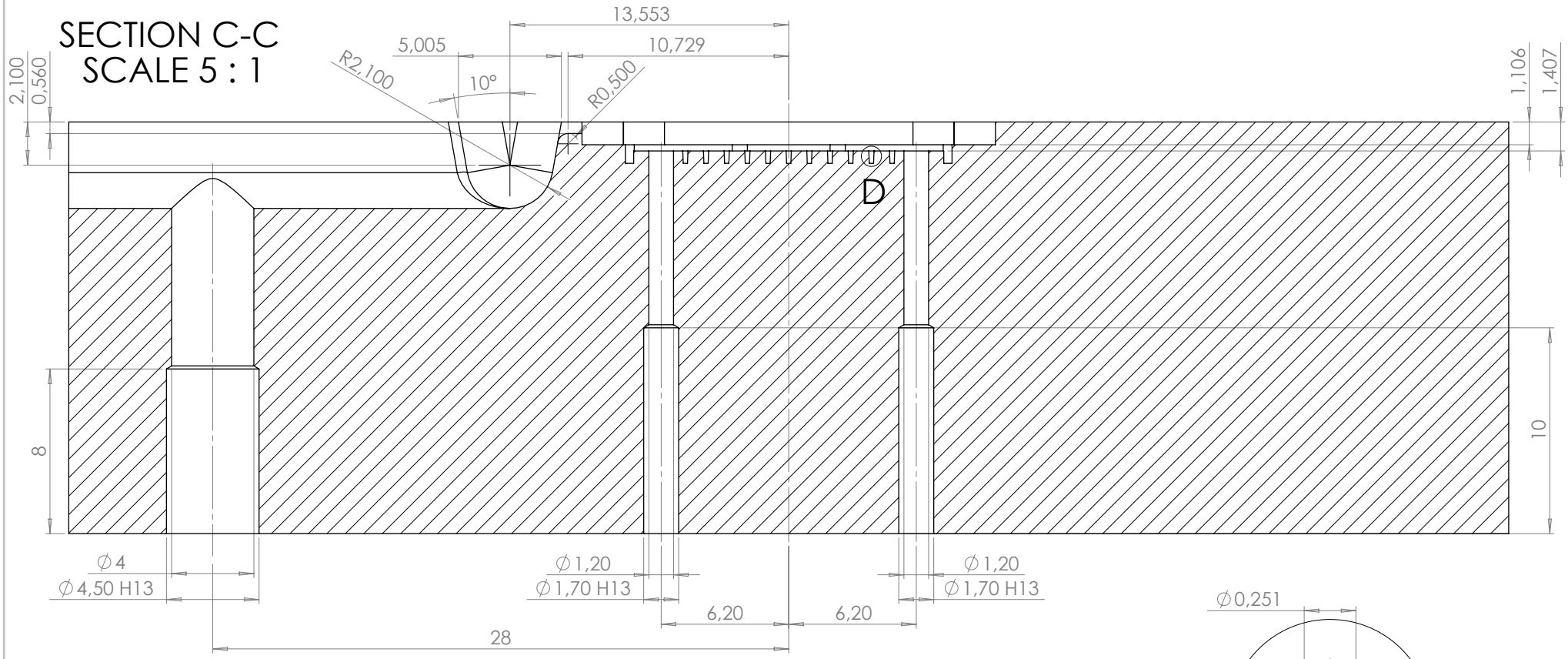

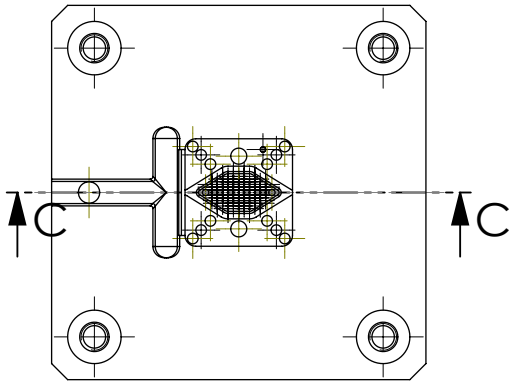

DETAIL D
SCALE 50 : 1

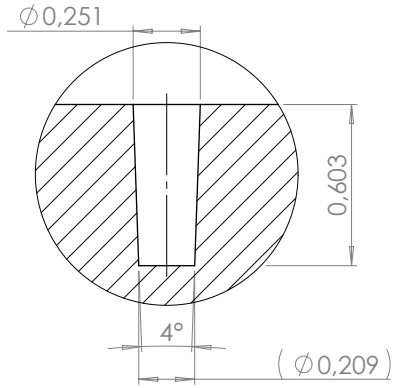

UNLESS OTHERWISE SPECIFIED: DIMENSIONS ARE IN MILLIMETERS SURFACE FINISH: Ra 10	UNLESS OTHERWISE SPECIFIED: TOLERANCES: LINEAR: DIN ISO 2768-1 fine ANGULAR: DIN ISO 2768-1 fine HOLES: DIN EN ISO 286-1 H7	DEBUR AND BREAK SHARP EDGES (NOT FOR EDGES DEFINING THE RUNNER OR CAVITY)	DO NOT SCALE DRAWING	REVISION V01		
	NAME	SIGNATURE	DATE			
DRAWN	MAXMAR		19-05-2014			
CHK'D						
APPV'D						
MFG						
Q.A				MATERIAL: IMPAX	DWG NO. Insert	A3
				WEIGHT:	SCALE:1:1	SHEET 3 OF 8

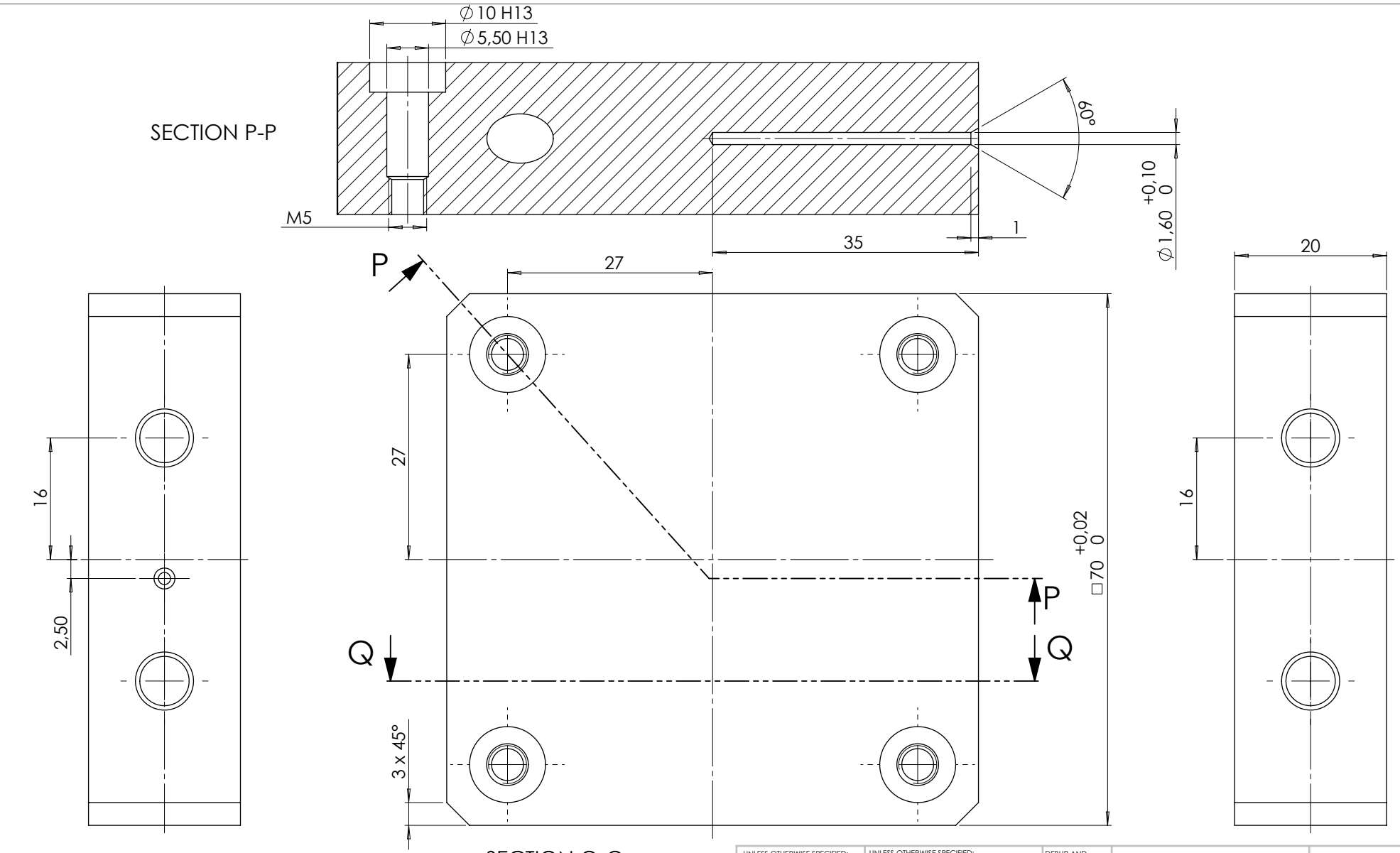

UNLESS OTHERWISE SPECIFIED: DIMENSIONS ARE IN MILLIMETERS SURFACE FINISH: Rz 10	UNLESS OTHERWISE SPECIFIED: TOLERANCES: LINEAR: DIN ISO 2768-1 fine ANGULAR: DIN ISO 2768-1 fine HOLES: DIN EN ISO 286-1 H7	DEBUR AND BREAK SHARP EDGES	DO NOT SCALE DRAWING	REVISION V01		
	NAME	SIGNATURE	DATE			
DRAWN	MAXMAR		23-05-2014			
CHK'D						
APPV'D						
MFG						
Q.A				MATERIAL: IMPAX	DWG NO. Insert	A3
				WEIGHT:	SCALE:2:1	SHEET 8 OF 8

D.4 Part list of the mold block

The following pages contain the mold part list with standard components from Hasco. Please note that the inserts are not included, as they were machined from available steel in stock.

ITEM NO.	PART NUMBER	QTY.
1	K10_156x196x27	1
2	K11_156x196x27	1
3	K20_156x196x36	2
4	K30_156x196x27	1
5	K40_156x196x56	1
6	K40_C2_156x196x56	1
7	K500_125x15	1
8	P_090x196x17	1
9	P_090x196x9	1
10	Z00_36_14x55	1
11	Z00_36_15x55	3
12	Z012_12x100	4
13	Z02_20x140	1
14	Z10_36_14	1
15	Z10_36_15	3
16	Z110_6,5x60_125	8
17	Z12_12x40-1	4
18	Z12_12x40-2	4
19	Z1212_206x196x7	1
20	Z1213_206x196x7x90	1
21	Z1215_116x246x6	2
22	Z1215_36x196x6	10
23	Z1215_56x196x6	4
24	Z1215_66x218x6	2
25	Z1295_5_1,5x100	4
26	Z1297_1,5x1-8	4
27	Z20_20x80	4
28	Z31_10x110	4
29	Z31_10x30	4
30	Z31_8x16	4
31	Z32_5x22	16
32	Z330_4x10	56
33	Z35_12x20	1
34	Z40_1,2x125	2
35	Z40_2x125	8
36	Z40_3x125	2
37	Z40_4x100	2
38	Z511_12x46_2,5_15,5	1
39	Z53_12x36	1
40	Z691_10x2,5	8
41	Z691_8x2	4

E Supplementary information to chapter 8

E.1 Experimental molding of KIT double spiral

The following pages contain pictures of the equipment used for some of the experiments at KIT.

Figure E.1: Arburg Allrounder 420 C 600-100 injection molding machine.

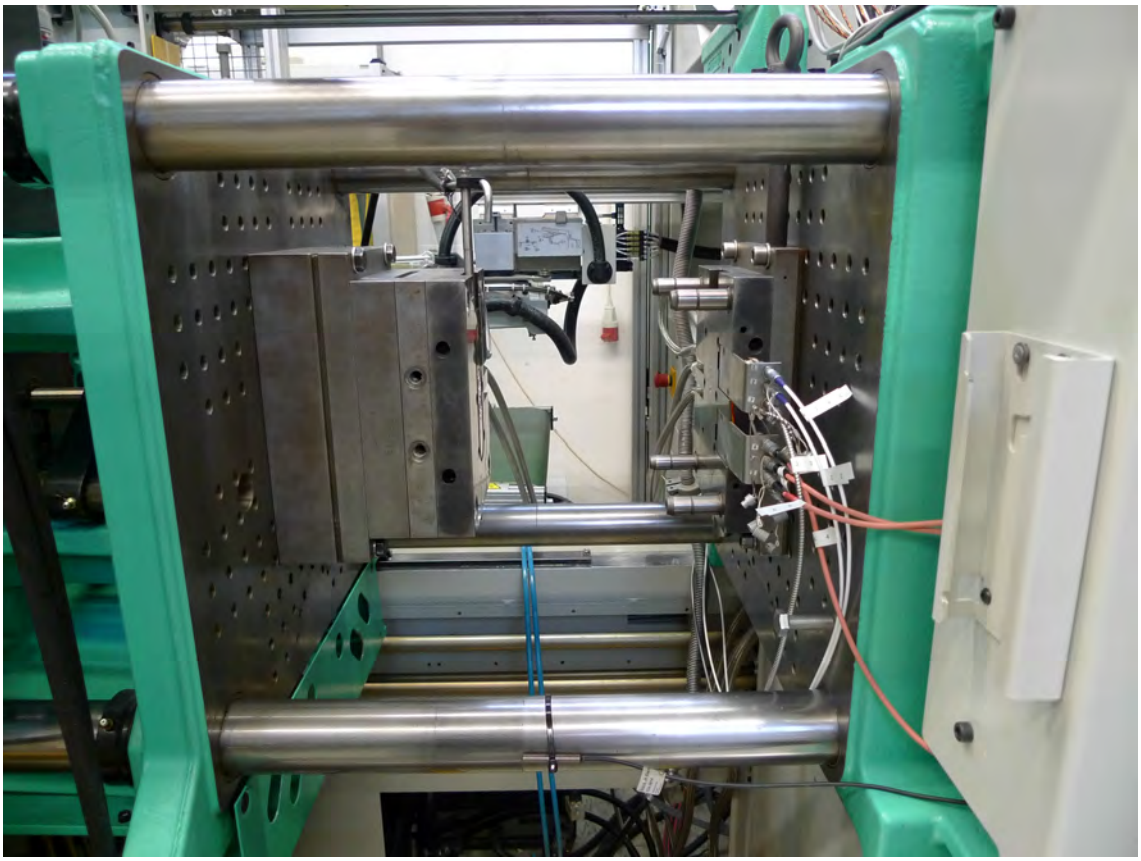

Figure E.2: Mold installed on the injection molding machine.

Figure E.3: Stationary half of the double test spiral geometry with sprue and pressure sensors.

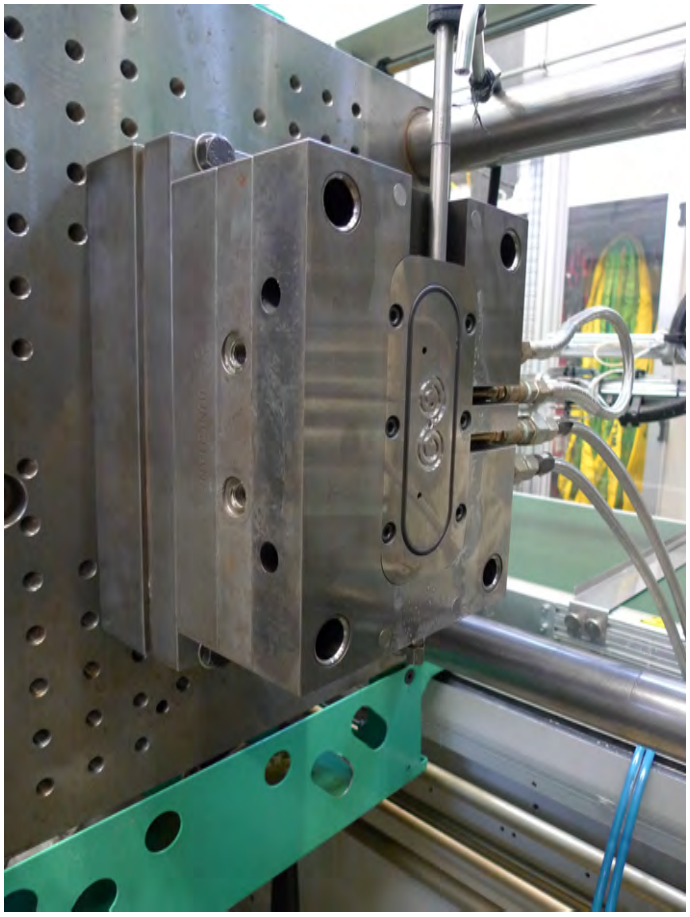

Figure E.4: Movable half of the double test spiral geometry with cavity.

E.2 Simulations of KIT double spiral

The following pages contain supplementary information about the simulations run on the double spiral from KIT. The screenshots about the sensor positions and sensor signals were taken in ASMI 2015.

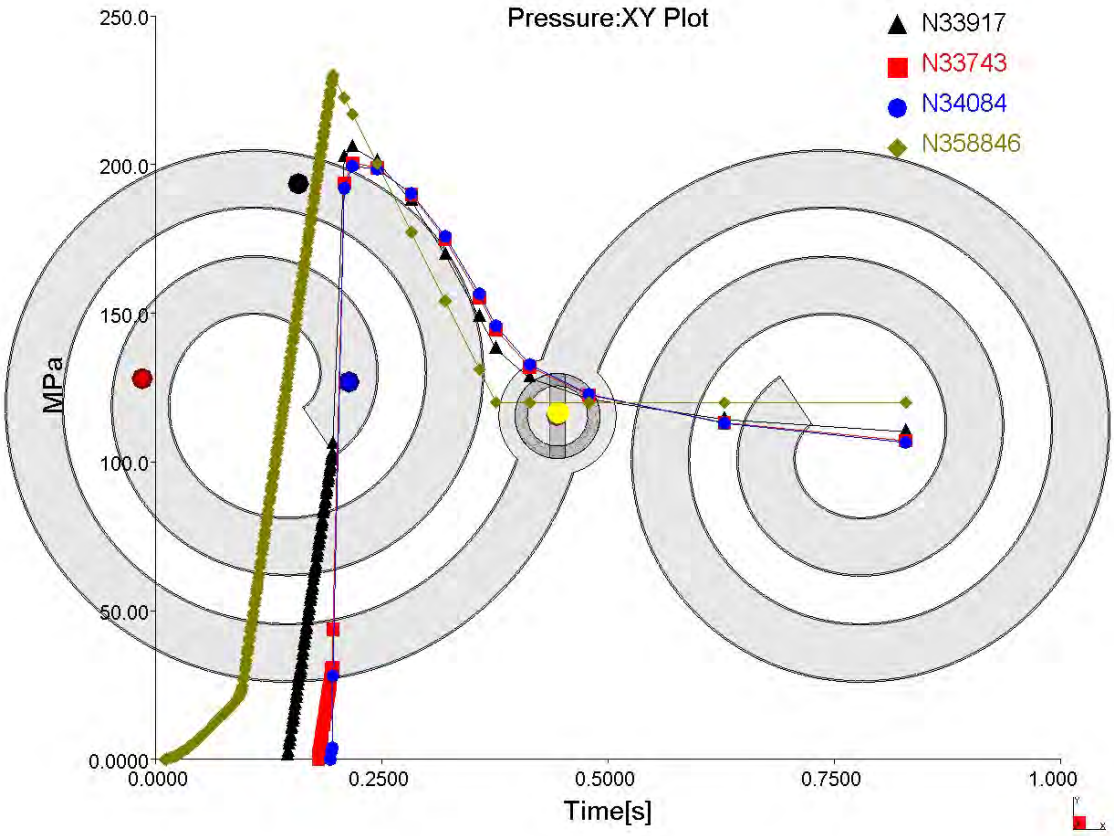

Figure E.5: Positions of the pressure measurements on the spiral with pressure curves for Catamold® 17-4PHA.

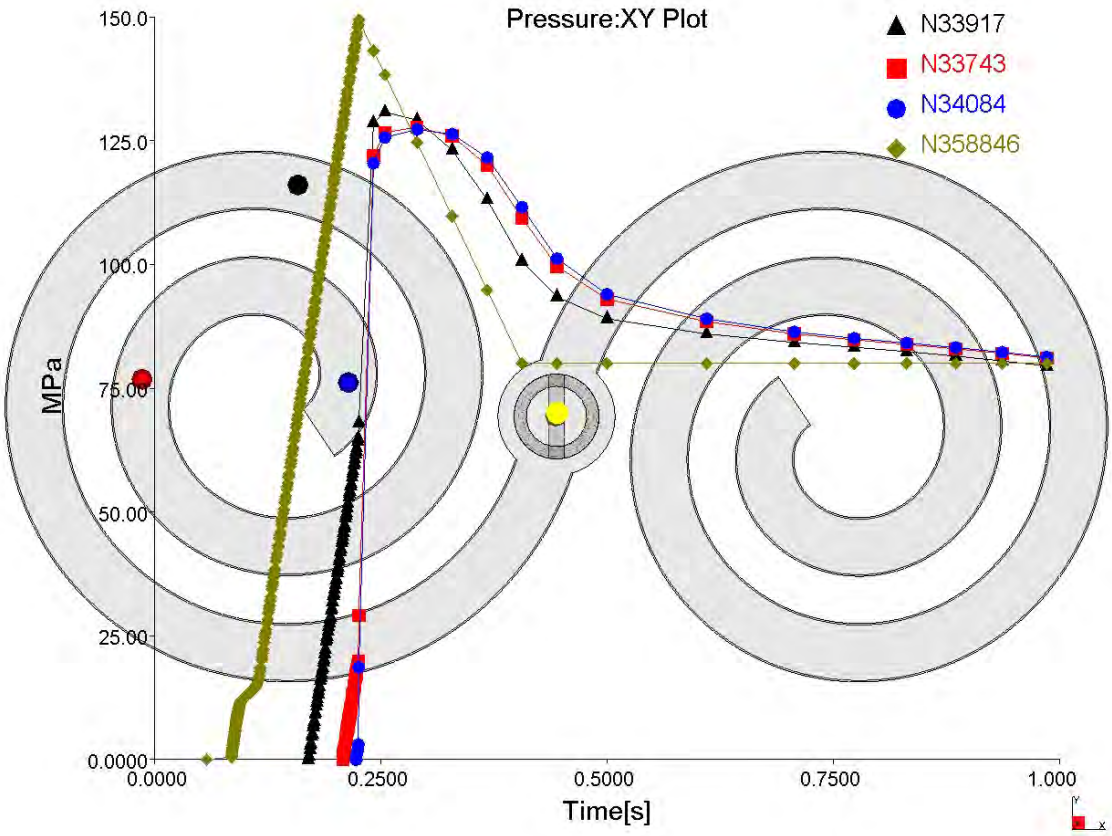

Figure E.6: Positions of the pressure measurements on the spiral with pressure curves for Catamold® TZP-A.

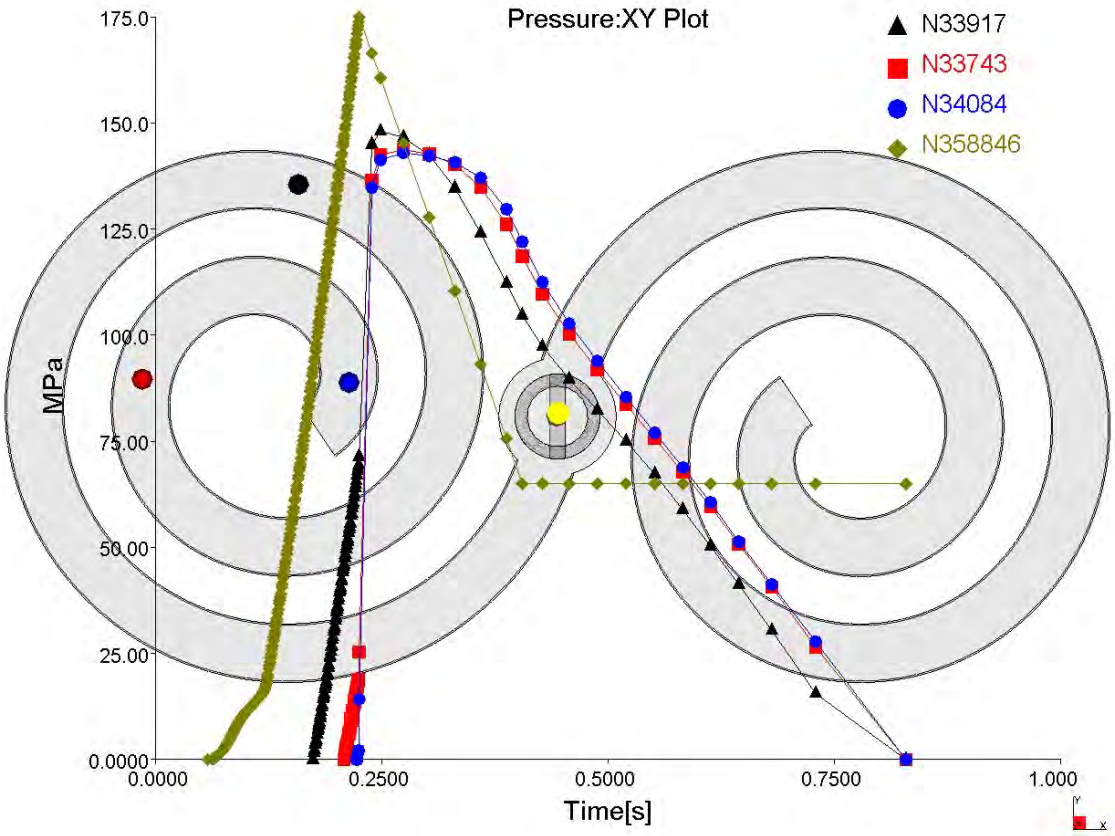

Figure E.7: Positions of the pressure measurements on the spiral with pressure curves for GoMikro 17-4PH.

F Supplementary information to chapter 9

F.1 Molding settings of molding machine for ceramic lever

The following pages contain the detailed processing parameters for the molding of the ceramic lever.

ARBURG - COPYLOG 8.0

Parameter list

Date: 29-05-2015

Time: 10:10:06 / ADMIN

Programme: Marhoefer last change: 28-05-2015 13:12

	Description	Parameter	Value	Unit
1	data set (internal)	f902E	HIMICRO-HOOK	
2	mould	f9100	HIMICRO-HOOK	
3	cavity count	f9103	1	
4	mould selection	.....	.....	.....
5	enable force reached (yes=1 no=0)	f131	0	
6	activate extended clamping program (on=1 off=0)	f132	1	
7	mould closing	.....	.....	.....
8	stage count	f101	2	
9	end of stage 1	s103	14	mm
10	closing speed stage 1	v103	150	mm/s
11	closing force stage 1	F103	3	kN
12	end of stage 2	s104	1	mm
13	closing speed stage 2	v104	30	mm/s
14	closing force stage 2	F104	2	kN
15	clamping	.....	.....	.....
16	stage count after mould closed	f133	1	
17	force after mould closed stage 1	F134	175	kN
18	stage count with holding pressure	f135	1	
19	force with holding pressure stage 1	F136	175	kN
20	stage count with cooling	f137	1	
21	force with cooling stage 1	F138	100	kN
22	mould opening	.....	.....	.....
23	stage count	f501	3	
24	end of stage 1	s502	5	mm
25	opening speed stage 1	v502	20	mm/s
26	opening force stage 1	F502	5	kN
27	end of stage 2	s503	170	mm
28	opening speed stage 2	v503	200	mm/s
29	opening force stage 2	F503	10	kN
30	end of stage 3	s504	175	mm
31	opening speed stage 3	v504	80	mm/s
32	opening force stage 3	F504	10	kN
33	ejector advancement	.....	.....	.....
34	delay time	t601	0,5	s
35	stage count	f601	1	
36	advancement speed stage 1	v603	30	mm/s
37	advancement force stage 1	F603	1	kN
38	end of stage 1	s603	4	mm
39	ejector retraction	.....	.....	.....
40	delay time	t611	0	s
41	stage count	f611	1	
42	retraction speed stage 1	v613	20	mm/s
43	retraction force stage 1	F613	2	kN
44	end of stage 1	s613	0	mm
45	mould temperature	.....	.....	.....
46	mould heating circuits	f9153	0	
47	lower enable tolerance	T8004	10	°C
48	upper switch-off tolerance	T8006	10	°C
49	hot runner channel sink temperature	T825	30	°C
50	mould temperature control devices	f9158	0	
51	dryer	.....	.....	.....
52	dryer 1 temperature	T961	0	°C
53	dryer 1 sink temperature	T962	0	°C
54	dryer 1 drying time	t881	0	h:min
55	injection unit 1	.....	Active	.....
56	material	f903E	TZP-F	
57	screw diameter	d9104	15	mm
58	cylinder temperature	.....	.....	.....
59	feed yoke cooling nominal value	T821	40	°C
60	feed yoke cooling tolerance	T821T	10	°C
61	cylinder heating zones	f9155	4	
62	cylinder heating zone 1 nominal value	T801	164	°C
63	cylinder heating zone 1 tolerance	T801T	10	°C
64	cylinder heating zone 2 nominal value	T802	168	°C
65	cylinder heating zone 2 tolerance	T802T	10	°C
66	cylinder heating zone 3 nominal value	T803	170	°C
67	cylinder heating zone 3 tolerance	T803T	10	°C
68	cylinder heating zone 4 nominal value	T804	172	°C
69	cylinder heating zone 4 tolerance	T804T	10	°C
70	lower enable tolerance	T8002	10	°C
71	upper switch-off tolerance	T8003	10	°C
72	sink temperature feed zone	T890	125	°C
73	sink temperature cylinder	T891	30	°C
74	injection	.....	.....	.....

Programme: Marhoefer **last change: 28-05-2015 13:12**

	Description	Parameter	Value	Unit
75	stage count	f301	1	
76	stage 1 injection flow	Q305	8	ccm/s
77	stage 1 injection pressure	p305	2300	bar
78	end of stage 1	V305	1,1	ccm
79	pressure ramp at switch-over point (on=1 off=0)	f313	1	
80	switch-over volume quality assurance nominal value	V4064	2,1	ccm
81	switch-over volume quality assurance tolerance	V4066	1	ccm
82	holding pressure	.....	.....	.....
83	number of pressure profile plotting points	f311	3	
84	holding pressure flow	Q311	8	ccm/s
85	ramp time	t311	0,05	s
86	plotting point 1	p311	1200	bar
87	time (1->2)	t312	1	s
88	plotting point 2	p312	900	bar
89	time (2->3)	t313	1	s
90	plotting point 3	p313	75	bar
91	sum t311 to t320	t300	2,05	s
92	dosage	.....	.....	.....
93	stage count	f401	1	
94	stage 1 circumferential speed	v403	6	m/min
95	stage 1 back pressure	p403	10	bar
96	end of stage 1	V403	2	ccm
97	remaining cooling time	t400	30	s
98	delay decompression after dosage	t405	0	s
99	decompression flow	Q412	5	ccm/s
100	decompression volume	V412	0,4	ccm
101	melt cushion quality assurance nominal value	V4061	1,6	ccm
102	melt cushion quality assurance tolerance	V4063	1	ccm
103	quality monitoring parameter	.....	.....	.....
104	cycle time nominal value	t4011	68	s
105	cycle time tolerance	t4013	5	s
106	dosage time nominal value	t4014	8	s
107	dosage time tolerance	t4016	5	s
108	injection time nominal value	t4017	0,31	s
109	injection time tolerance	t4019	0,03	s

Acknowledgments

I would like to thank everybody that supported me during my work as Ph.D. student and the writing of this Ph.D. thesis and helped me to successfully complete it.

First, I would like to thank especially Prof. Hans Nørgaard Hansen for offering me the opportunity to accomplish this Ph.D. project as well as all related research at the Section of Manufacturing Engineering at the Department of Mechanical Engineering at the Technical University of Denmark.

Special thanks go to Assoc. Prof. Guido Tosello for his exceptional supervision and guidance, numerous hints, and precious pieces of advice. With enormous experience and his open-door policy, he could answer many rising questions and help on any issues. The various discussions were very useful and informative. It was a great pleasure for me to work with him.

Aminul Islam is also greatly acknowledged as my co-supervisor. He contributed excellently with his great experience, helpful advice, discussions, and plenty of feedback on my work.

Thanks go also to the technician Michael Guldager and the head of the tool shop Jan Frank Pedersen. Michael brought in useful advice on practical issues with the injection molding equipment in the plastic laboratory, and he often prepared the machines, materials, and molds for this project. Jan helped me with useful advice, tips, and discussions on the mold design and manufacture done in this project.

Furthermore, I would like to thank all people in my office for several pieces of advice and discussions of problems. They also helped to sometimes get my mind off and created a pleasant atmosphere. I want to thank the entire staff of the Section of Manufacturing Engineering for the good time there.

I must also mention and thank Tobias Müller, Volker Piotter, Klaus Plewa, Prof. Thomas Hanemann, and all the other very pleasant people from the Karlsruhe Institute of Technology where I had the pleasure of staying three months for a fruitful external research stay. The received hospitality and support there was outstanding. Everybody was happy to help me to complete my work and contributed hence to a tremendous part of this thesis.

Finally, exceptional thanks go to my family for their enduring and intense support during all my studies. With their strong reassurance, they helped me to accomplish this Ph.D. thesis.